FRACTURE MECHANICS

Proceedings of the Thirteenth National Symposium on Fracture Mechanics

Richard Roberts, *editor*

ASTM STP 743

AMERICAN SOCIETY FOR TESTING AND MATERIALS

FRACTURE MECHANICS

Proceedings of the
Thirteenth National Symposium
on Fracture Mechanics

A symposium sponsored by
ASTM Committee E-24 on
Fracture Testing of Metals
AMERICAN SOCIETY FOR
TESTING AND MATERIALS
Philadelphia, Pa., 16–18 June 1980

ASTM SPECIAL TECHNICAL PUBLICATION 743
Richard Roberts
Lehigh University
editor

ASTM Publication Code Number (PCN)
04-743000-30

AMERICAN SOCIETY FOR TESTING AND MATERIALS
1916 Race Street, Philadelphia, Pa. 19103

Library of Congress Catalog Card Number: 81-65836

NOTE

The Society is not responsible, as a body,
for the statements and opinions
advanced in this publication.

Printed in Baltimore, Md.
November 1981

Foreword

This publication, *Fracture Mechanics,* contains papers presented at the Thirteenth National Symposium on Fracture Mechanics which was held 16–18 June 1980 at Philadelphia, Pennsylvania. The American Society for Testing and Materials' Committee E-24 on Fracture Testing of Metals sponsored the symposium. Richard Roberts, Lehigh University, presided as symposium chairman and editor of this publication.

Related ASTM Publications

Tables for Estimating Median Fatigue Limits, STP 731 (1981), $15.00, 04-731000-30

Fatigue of Fibrous Composite Materials, STP 723 (1981), $30.00, 04-723000-23

Crack Arrest Methodology and Applications, STP 711 (1980), $44.74, 04-711000-30

Commercial Opportunities for Advanced Composites, STP 704 (1980), $13.50, 04-704000-33

Fracture Mechanics (Twelfth Conference), STP 700 (1980), $53.25, 04-700000-03

Nondestructive Evaluation and Flaw Criticality for Composite Materials, STP 696 (1979), $34.50, 04-696000-33

Composite Materials: Testing and Design (Fifth Conference), STP 674 (1979), $52.50, 04-674000-33

Advanced Composite Materials—Environmental Effects, STP 658 (1978), $26.00, 04-658000-33

Fatigue of Filamentary Composite Materials, STP 636 (1977), $26.50, 04-636000-33

Composite Materials: Testing and Design (Fourth Conference), STP 617 (1977), $51.75, 04-617000-33

Thermal Fatigue of Materials and Components, STP 612 (1976), $27.00, 04-612000-30

A Note of Appreciation to Reviewers

This publication is made possible by the authors and, also, the unheralded efforts of the reviewers. This body of technical experts whose dedication, sacrifice of time and effort, and collective wisdom in reviewing the papers must be acknowledged. The quality level of ASTM publications is a direct function of their respected opinions. On behalf of ASTM we acknowledge with appreciation their contribution.

ASTM Committee on Publications

Editorial Staff

Contents

Introduction

Fracture mechanics has become one of the preeminent disciplines utilized in the evaluation of structural integrity during the past 20 years. This growth has been spearheaded in part by the efforts of ASTM Committee E24 on Fracture Testing of Metals. One aspect of this involvement by Committee E24 has been the development of a significant body of technical literature related to fracture mechanics. This literature generally represents the proceedings of specialist conferences dealing with fracture mechanics as well as the National Symposium on Fracture Mechanics. For the most part, these proceedings take the form of an ASTM *Special Technical Publication (STP).* The papers in this *STP* were presented at the 13th National Fracture Mechanics Symposium held June 16 through 18, 1980 at ASTM headquarters in Philadelphia, Pa.

The paper selection process for the national symposium has varied over the years. The procedure adopted for the 13th National Symposium on Fracture Mechanics was to have a general solicitation for technical papers in all areas related to fracture mechanics and structural integrity. Thus there was not a specific theme for the 13th National Symposium. It is interesting to note from the foreign contributors to the 13th National Symposium on Fracture Mechanics as well as the previous symposiums on fracture mechanics that the National Symposium on Fracture Mechanics truly represents an international event.

The papers contributed to the 13th Symposium fell into four broad categories. The first category was fatigue of engineering materials with principal applications to metals. Two conference sessions were devoted to this. The second indentifiable category at the conference was the calculation of stress-intensity factors. This represented a single session in the conference. The third subject area was elastic-plastic fracture mechanics as represented by the calculation of J_{Ic} and the tearing modulus T. Lastly, the fourth category represented a general potpourri of subjects dealing with fracture mechanics and structural integrities, with such topics as composites, R-curves, fracture mechanics applications, Charpy V-notch correlations, creep crack growth rate, and metallurgical effects finding coverage in these sessions. It is clear when reviewing previous proceedings that the distribution of subjects represented in the 13th Symposium is very similar to those presented at the previous symposiums.

This volume should provide a valuable source of information to all those interested in fracture mechanics. The assistance of the organizing committee, particularly Professor Jerry Swedlow; the authors and reviewers; J. J. Palmer, J. B. Wheeler, and Kathy Greene of ASTM and their staff along with all those who participated in the conference are gratefully acknowledged. Particular thanks go to Professor R. W. Hertzberg, Dr. R. Bucci, Professor C. W. Smith, Dr. W. R. Andrews, Mr. J. C. Lewis, Professor G. H. Sines, Dr. G. Clarke, and Dr. W. G. Clark for their assistance with the various technical sessions. A particular thanks is extended to Dr. John Barsom of the United States Steel Corp., Dr. R. Bucci of the Aluminum Corporation of America, and Mr. Ed Wessel of Westinghouse for their continued support to the National Symposium on Fracture Mechanics through their individual effort as well as the efforts and support of their industrial organizations. Without their support and encouragement, the 13th National Symposium could not have been as productive and valuable. It is also noted with great pleasure the award of the Geo. Irwin Medal to Dr. Steve Novak of the Applied Research Laboratory of the United States Steel Corp. Lastly, the support of the Materials Research Center at Lehigh University for my time is gratefully acknowledged along with the help of our girl Friday, Jone Svirzofsky.

Richard Roberts

Materials Research Center, Lehigh University, Bethlehem, Pa. 18015; symposium chairman and editor.

J. B. Chang,[1] *R. M. Engle,*[2] *and J. Stolpestad*[1]

Fatigue Crack Growth Behavior and Life Predictions for 2219-T851 Aluminum Subjected to Variable-Amplitude Loadings

REFERENCE: Chang, J. B., Engle, R. M., and Stolpestad, J., **"Fatigue Crack Growth Behavior and Life Predictions for 2219-T851 Aluminum Subjected to Variable-Amplitude Loadings,"** *Fracture Mechanics: Thirteenth Conference, ASTM STP 743,* Richard Roberts, Ed., American Society for Testing and Materials, 1981, pp. 3-27.

ABSTRACT: Fatigue crack growth behavior of 2219-T851 aluminum is characterized for variable-amplitude loading conditions which include the single and periodic tensile or compressive overload, single tensile overload followed by a single compressive load, multiple tensile and compressive overloads, high-low or low-high block loading, and compression-compression loads followed by tension-tension loads. A load interaction model which accounts for the overload retardation and compressive load acceleration effects on fatigue crack growth lives is introduced. Fatigue crack growth analyses are performed on all test cases using a computer program which employs this load interaction model. Analytical predictions are correlated with the test data. Results show that this model adequately predicted fatigue crack growth behavior and fatigue crack lives for most of the test loading conditions to within ±30 percent.

KEY WORDS: fatigue crack growth, variable-amplitude loading, fatigue life prediction, 2219-T851 aluminum alloy

Nomenclature

- a Crack size
- c Half crack length
- C Crack growth rate constant
- K Stress-intensity factor
- m Walker's stress ratio layering collapsing factor
- n Crack growth rate exponent
- N Cycles

[1]Program manager and technical staff, respectively, Rockwell International Corp., North American Aircraft Division, Los Angeles, Calif. 90009.
[2]Aerospace engineer, U.S. Air Force Flight Dynamics Laboratory, WPAFB, Ohio 45433.

R	Stress ratio
q	Chang's acceleration exponent
a_{ol}	Crack size at the overload
c_i	Initial half crack length
c_f	Final half crack length
c_{cr}	Critical half crack length
K_{eff}	Effective stress-intensity factor
K_{max}, K_{min}	Stress-intensity factor value at maximum and minimum cyclic stresses
$K_{max_{ol}}$	Stress-intensity factor value at maximum overload
$R_{cut}{}^{+}$	Positive stress ratio cutoff value
$R_{cut}{}^{-}$	Negative stress ratio cutoff value
R_{ol}	Overload ratio
$r_{y_{ol}}$	Plasticity zone size at overload
ΔK_{eff}	Effective stress-intensity factor range
ΔK_{th}	Threshold stress-intensity factor range
S_{so}	Shutoff overload ratio
da/dN	Fatigue crack growth rate
σ_{max}	Maximum cyclic stress
σ_y	Material tensile yield strength
α	Crack growth rate ratio
β	Plane stress plane strain coefficient
Φ	Generalized Willenborg model proportional constant
ϵ	Predicted life to tested life ratio

The implementation of fracture control plans on structures, such as airframes and bridges, subjected to random cyclic spectrum loadings requires the capability of accurate predictions of the growth behavior of cracks or cracklike flaws contained in primary structural components under such loadings. In reality, all spectrum loadings contain variable-amplitude load cycles. Various load interaction effects on the crack growth behavior under variable-amplitude loadings have been observed by many investigators. The significant effects observed can be summarized as follows:

1. Tensile overloads cause retardation of the crack growth in general. Some data indicate that if the overload ratio is sufficiently high, the crack might completely stop growing [*1-3*].[3]

2. Compressive loads in compression-tension load cycles cause the acceleration of crack growth [*4,5*].

3. Compressive loads in tension-compression load cycles tend to reduce the retardation effects of the tensile load cycles immediately following the compressive load [*6-8*].

[3]The italic numbers in brackets refer to the list of references appended to this paper.

4. A certain number of small tensile load cycles (underloads) in a low-high sequence of loading tend to accelerate the crack growth rate of the load cycle immediately following the low-high transition [9,10].

The need to develop a methodology capable of accounting for the load interaction effects on crack growth under variable-amplitude loading is obvious. Neglecting crack growth retardation effects caused by the tensile overloads can lead to unnecessary weight and cost penalties. On the other hand, an unsafe design often results if acceleration effects introduced through the compressive loads or underloads are not accounted for in design analysis and testing.

Various crack growth models have been proposed by numerous investigators in the past decades. A few of them in the literature have demonstrated the ability to provide consistently good predictions for certain types of variable-amplitude loadings, including the Wheeler [11], Willenborg [12], Elber [13], and Vroman [14] models and their modified versions. Yet, none of them is capable of accounting for all of the important load interaction effects. Recently, a research and development project [15] has been conducted at Rockwell to systematically investigate all significant stress parameters which control the crack growth rates and load interaction effects, such as tension overload retardation, compressive load acceleration, tension-tension underload acceleration, load sequences, and high-low and low-high block loading. The significant results of this investigation are reported in this paper.

Experimental Program

The test program consisted of a series of baseline crack growth rate tests and three groups of cyclic load tests varying in complexity from simple constant-amplitude tests to block loading tests, as listed in Table 1. All test specimens used in this experimental program were of the ASTM Test for Constant-Load-Amplitude Fatigue Crack Growth Rates Above 10^{-8} m/Cycle (E 647-78T) center-cracked-tension (CCT) design [16], fabricated from 5.35-mm-thick (0.25 in.) 2219-T851 aluminum plates. All plates were from the same lot of material. The specimen was 15.24 cm (6 in.) wide and 45.72 cm (18 in.) long.

TABLE 1—*Methodology development test program.*

Test Group	Type of Load	Tests
Baseline	constant amplitude (σ_{max} = 137.9 MPa (20 ksi)	8
I	constant amplitude (various load level)	10 (M-1 to M-10)
II	single or periodic overload/underload	20 (M-11 to M-30)
III	multiple overload/underload	30 (M-31 to M-60)

The center notches were installed by employing the electrical discharge machining (EDM) process, with the maximum width of the notch less than 0.254 mm (0.01 in.).

The entire test program was conducted by employing MTS Fatigue Testing Systems. Applied loads were controlled through a closed-loop servo system and load programmer test system, with load cells and servo valves optimized for the controllability and cyclic load rates. The spectrum sequences were stored in a digital PDP 8E computer. The EDM crack starter slot in each specimen was precracked to produce an initial crack length $2c$ of approximately 7.62 mm (0.3 in.). Precracking was performed under constant-amplitude cycling at a stress ratio of zero and with maximum cyclic stresses of 55.16 or 68.95 MPa (8 or 10 ksi). All tests were run at a cyclic rate of 6 Hz in ambient laboratory air at room temperature. Cyclic crack growth measurements were obtained by employing visual optical reading from precision scales attached to each side of the specimen adjacent to the EDM slot. The resolution of the crack length measurement was approximately 0.127 mm (0.005 in.).

Experimental Results and Discussions

Crack growth measurements from baseline crack growth rate tests, constant-amplitude tests (Group I), and variable-amplitude tests (Groups II and III) were taken and recorded throughout each test. The results are presented in the following paragraphs.

Baseline Crack Growth Tests and Data Reduction

The baseline tests consisted of eight CCT specimens; all were loaded at constant amplitude with a maximum stress level of 137.9 MPa (20 ksi). The cyclic stress ratios tested were $R = 0.01, 0.2, 0.3, 0.7, -0.1$, and -0.3. This group of test data was used to obtain the baseline crack growth rate constants. A computer program, PLOTRATE, developed by Chang et al [*16*], was used to process these data.

PLOTRATE is an interactive computer routine which calculates the fatigue crack growth rate, da/dN, through the seven-point incremental polynomial method from the crack length versus elapsed cycles data (a versus N) of each test, as recommended by the ASTM E 647-78T, and determines the crack growth rate constants C and n for various crack growth rate equations in the following general form, through a least-square-fitting routine

$$da/dN = C[f(K, R)]^n \tag{1}$$

where K is the stress-intensity factor and R is the cyclic stress ratio.

For a given set of (a versus N) data, PLOTRATE calculates the dependent variable da/dN and the independent variable $f(K, R)$ of the preceding fatigue crack growth rate equation and plots those calculated data points on log-log coordinates, with da/dN on the ordinate and $f(K, R)$ on the abscissa. PLOTRATE provides the user with options for selecting various commonly used fatigue crack growth equations, including the Paris [17] and Walker [18] equations. If the Paris equation, that is, $da/dN = C(\Delta K)^n$ is selected, the independent variable used in the plot will be $f(K, R) = (1 - R)K_{max}$ or ΔK. In the Walker equation, that is, $da/dN = C[(1 - R)^m K_{max}]^n$, the independent variable is then $f(K, R) = (1 - R)^m K_{max}$ or $(1 - R)^{m-1}\Delta K$, where m is Walker's stress ratio layer collapsing factor.

Baseline crack growth test data with positive stress ratios ($R = 0.01, 0.20, 0.30, 0.70$) were processed through the use of the PLOTRATE program. A da/dN versus ΔK plot provided by PLOTRATE is shown in Fig. 1. The straight line was the least-square-fitted line drawn by PLOTRATE.

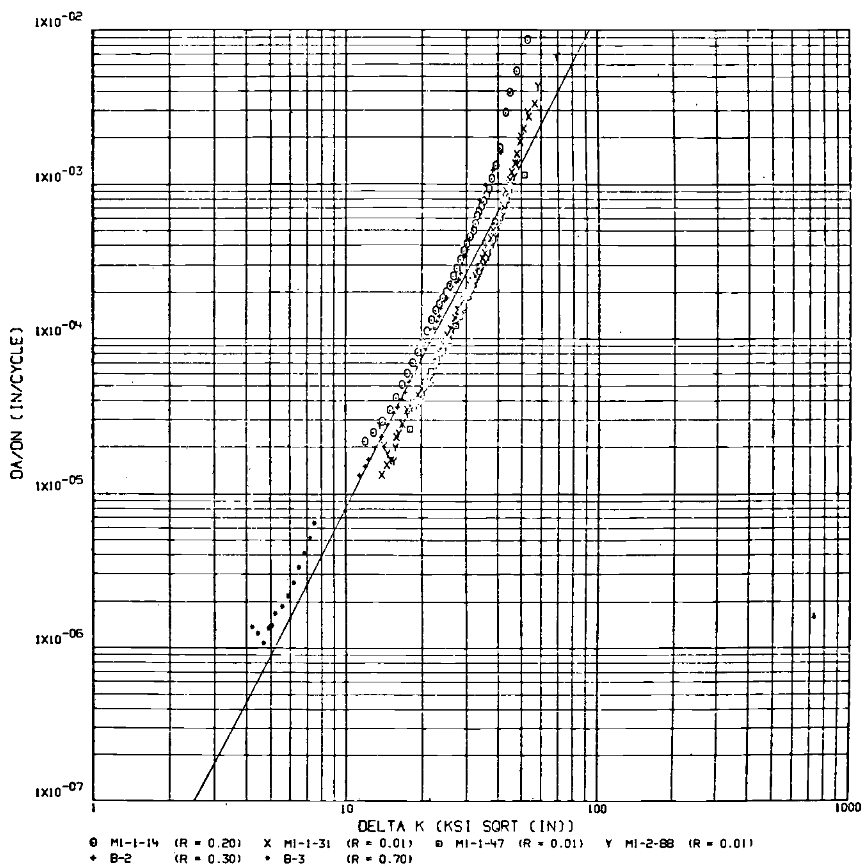

FIG. 1—*Baseline 2219-T851 aluminum crack growth rate data.*

Constant-Amplitude Tests

Tests conducted in this group were confined to constant-amplitude loading at different maximum stress levels and stress ratios, as shown in Table 2. Two maximum stress levels were tested: $\sigma_{max} = 55.16$ MPa (8 ksi) and 275.8 MPa (40 ksi). The stress ratios tested were $R = 0, 0.3, 0.7, -0.1, -0.3$, and -1. As expected, the higher the maximum stress level is, the faster the crack grows. The effect of stress ratios on crack growth is shown in Figs. 2 and 3. At 275.8-MPa (40 ksi) and 55.16-MPa (8 ksi) maximum stress levels, a significant reduction of crack growth rates was shown, respectively, in the test cases with negative stress ratios $R = -0.1, -0.3$, and -1.

Single or Periodic Overload/Underload Tests

As shown in Table 3, this test group consisted of 20 specimens subjected to relatively simple test load sequences which were basically constant-amplitude

TABLE 2—*Constant-amplitude test descriptions and crack growth data correlations.*

Test	Test condition: Applied base load: Loading profile	Applied base load: Max (ksi)	Applied base load: Min (ksi)	Over-/Under load: Max (ksi)	Over-/Under load: Min (ksi)	N_I (cycle)	N_{II} (cycle)	(C_i-C_f) Test life N_{test} (cycle)	EFFGRO with Forman/Chang model: N_{pred} (cycle)	ϵ	Cracks IV with Willenborg model: N_{pred} (cycle)	ϵ
M-1	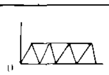	8	0	-	-	-	-	0.140-C_{CR} 555,810	584,500	1.09	587,250	1.09
M-2	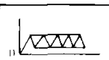	8	2.4	-	-	-	-	0.153-0.270 260,000	352,000	1.35	353,200	1.36
M-3	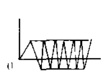	8	-8	-	-	-	-	0.193-0.970 129,240	120,000	0.93	>200,000	>2
M-4		8	-2.4	-	-	-	-	0.153-0.695 144,000	222,500	1.54	300,300	2.08
M-5	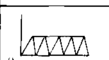	40	0	-	-	-	-	0.151-0.588 846	825	0.98	940	1.11
M-6	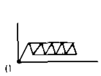	40	12	-	-	-	-	0.155-0.510 1,693	1,640	0.97	1,750	1.03
M-7		40	28	-	-	-	-	0.155-C_{CR} 14,870	12,050	0.81	12,250	0.82
M-8	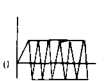	40	-4	-	-	-	-	0.155-C_{CR} 469	784	1.67	1,100	2.35
M-9		8	-0.8	-	-	-	-	0.153-0.735 175,000	270,700	1.55	305,400	1.74
M-10		40	-12	-	-	-	-	0.160-C_{CR} 251	624	2.48	950	3.78

Note: $\epsilon = \dfrac{N_{pred}}{N_{test}}$

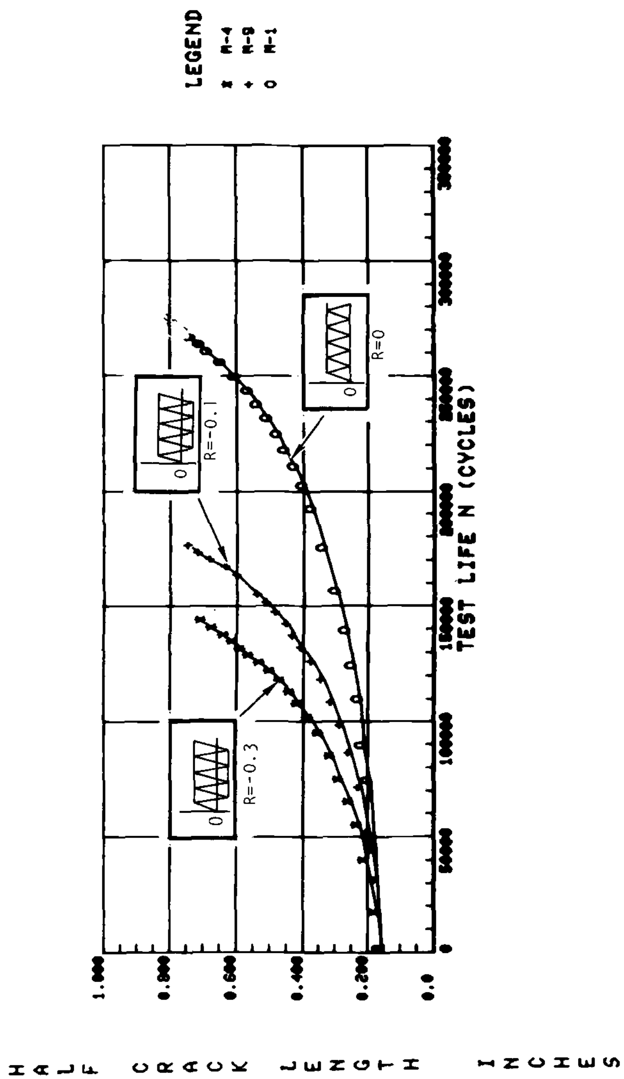

FIG. 2—Negative-stress-ratio effects on crack growth life, σ_{max} = 55.16 MPa (8 ksi).

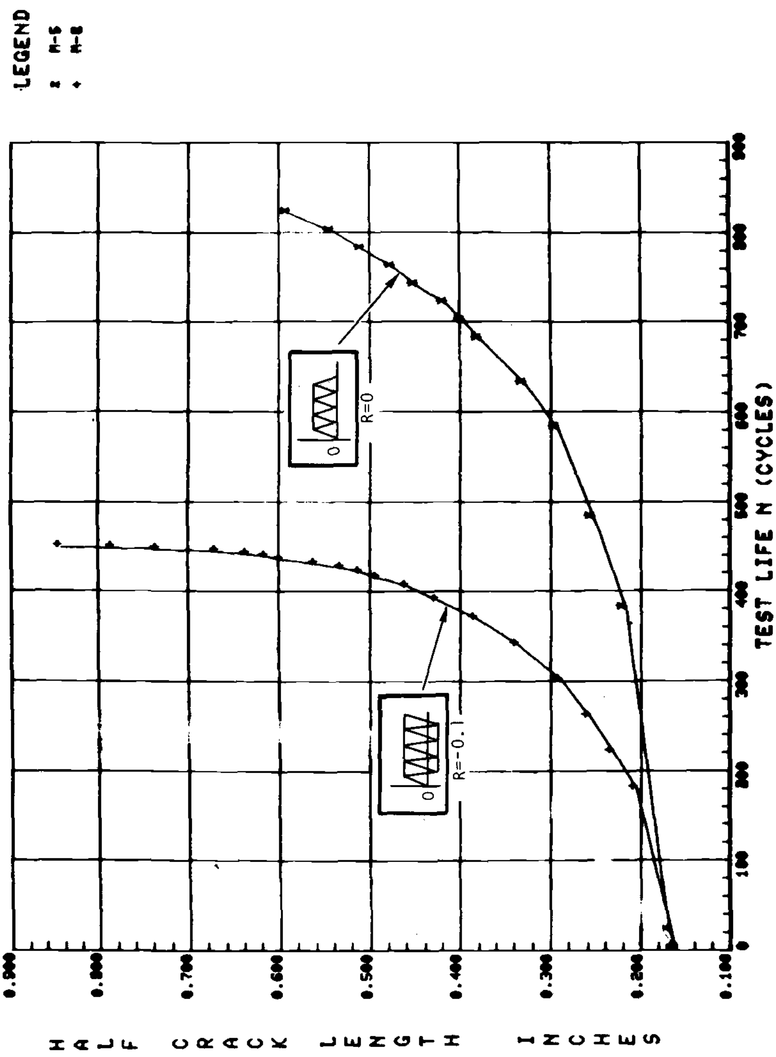

FIG. 3—*Negative-stress-ratio effects on crack growth life,* σ_{max} = *275.8 MPa (40 ksi).*

cycles ($R = 0$ and -0.3) with either an overload or an underload applied a single time or periodically. Figures 4 and 5 show the single and periodic overload effects on crack growth at different overload ratios ($R_{ol} = 1.5$ and 2.25). These figures show that at $R_{ol} = 1.5$ the crack growth rate was retarded approximately 20 percent, while at $R_{ol} = 2.25$ it was retarded as much as 275 percent. The combined overload retardation and compression load acceleration effect can be seen in Figs. 6 and 7. The figures indicate that the tensile overload retardation effect was reduced by the compression load immediately following the overload. Reversing the sequence (applying the compression load first and then the tensile overload) resulted in a 10 to 15 percent increase of total life.

Multiple Overload/Underload Tests

A total of 30 multiple over/underload tests was conducted, as shown in Table 4, in order to investigate the retardation and acceleration effects due to

TABLE 3—*Single or periodic overload/underload test descriptions and crack growth data correlations.*

	Test condition							$(C_i - C_f)$	Analytical predictions			
	Applied base load			Over-/Under-load				Test life	EFFGRO with Vroman/Chang model		CRACKS IV with Willenborg model	
Test	Loading profile	σ_{Max} (ksi)	σ_{Min} (ksi)	σ_{Max} (ksi)	σ_{Min} (ksi)	N_I (cycle)	N_{II} (cycle)	N_{Test} (cycle)	N_{pred} (cycle)	ϵ	N_{pred} (cycle)	ϵ
M-11		20	0	30	0	2,500	To failure	0.148-C_{CR} 15,182	13,180	0.87	14,501	0.96
M-12		20	0	30	0	2,500	2,500	0.149-C_{CR} 16,623	13,590	0.82	21,608	1.30
M-13		20	0	45	0	2,500	2,500	0.147-0.84 49,600	32,500	0.66	>250,100	>5
M-14		20	6	40	6	2,500	2,500	0.155-C_{CR} 225,090	175,000	0.78	>500,200	>2
M-15		30	21	40	21	2,500	2,500	0.156-C 125,050	117,500	0.94	45,017	0.36
M-16		20	0	20	-6	2,500	2,500	0.151-C_{CR} 11,370	12,700	1.12	12,820	1.13
M-17	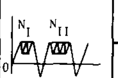	20	6	20	-6	2,500	2,500	0.152-C_{CR} 20,810	>23,500	>1	27,510	1.32
M-18		40	28	40	-12	2,500	2,500	0.145-C_{CR} 11,600	13,000	1.12	13,005	1.12
M-19		20	0	30	-6	2,500	To failure	0.145-C_{CR} 13,460	13,454	1.0	14,751	1.1
M-20	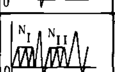	20	0	30	-6	2,500	2,500	0.150-C_{CR} 36,083	13,414	0.37	19,757	0.55

Note: $\epsilon = \frac{N_{pred}}{N_{test}}$

TABLE 3—*Continued.*

Test	Test condition							$(C_i\text{-}C_f)$	Analytical predictions			
	Applied base load			Over-/Under load				Test life	EFFGRO with Vroman/Chang model		CRACKS IV with Willenborg model	
	Loading profile	σ_{Max} (ksi)	σ_{Min} (ksi)	σ_{Max} (ksi)	σ_{Min} (ksi)	N_I (cycle)	N_{II} (cycle)	N_{Test} (cycle)	N_{pred} (cycle)	ϵ	N_{pred} (cycle)	ϵ
M-21	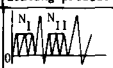	20	0	40	-12	2,500	2,500	0.160-C_{CR} 22,850	15,000	0.66	>75,030	>3
M-22	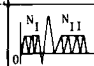	20	0	30	-6	2,500	To failure	0.158-C_{CR} 13,948	12,334	0.88	13,502	0.97
M-23		20	0	30	-6	2,500	2,500	0.151-C_{CR} 17,200	13,319	0.77	19,514	1.14
M-24		20	-6	30	-6	2,500	2,500	0.220-C_{CR} 10,950	6,430	0.59	12,504	1.14
M-25		20	-6	40	-6	2,500	2,500	0.151-C_{CR} 22,512	9,513	0.42	>75,030	>3
M-26		8	-2.4	8	-16	2,500	To failure	0.151-C_{CR} 269,840	270,102	1.00	359,500	1.33
M-27	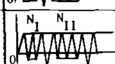	8	-2.4	8	-16	2,500	2,500	0.178-C_{CR} 194,723	229,644	1.18	>304,120	>1.5
M-28	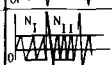	20	-6	30	-15	2,500	2,500	0.233-C_{CR} 10,003	6,050	0.6	10,003	1.00
M-29	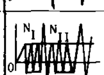	20	-6	40	-15	2,500	2,500	0.160-C_{CR} 15,005	8,960	0.6	>75,030	>5
M-30	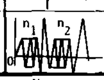	20	-6	40	-15	2,500	2,500	0.145-C_{CR} 20,007	9,912	0.5	>75,030	>3

Note: $\epsilon = \dfrac{N_{pred}}{N_{test}}$

the application of a block of high or low load cycles. The overload retardation effect can be best demonstrated by the drastic slowing down of the crack growth of the M-44 specimen shown in Fig. 8. In this test case, the overload ratio was $R_{ol} = 2$. The underload acceleration (sharpening) effect can be clearly seen in Fig. 9. The step jump of the crack growth curve of the M-34 specimen indicated that the crack growth accelerated for a short period of time immediately following the application of a block of underloads (low tensile load cycles).

The application of 5000 compression-compression load cycles did not seem to affect the crack growth of those load cycles immediately following the compression-compression cycles.

Crack Growth Data Correlations

Fatigue crack growth data from the aforementioned test program were correlated with analytical predictions made by the modified EFFGRO computer

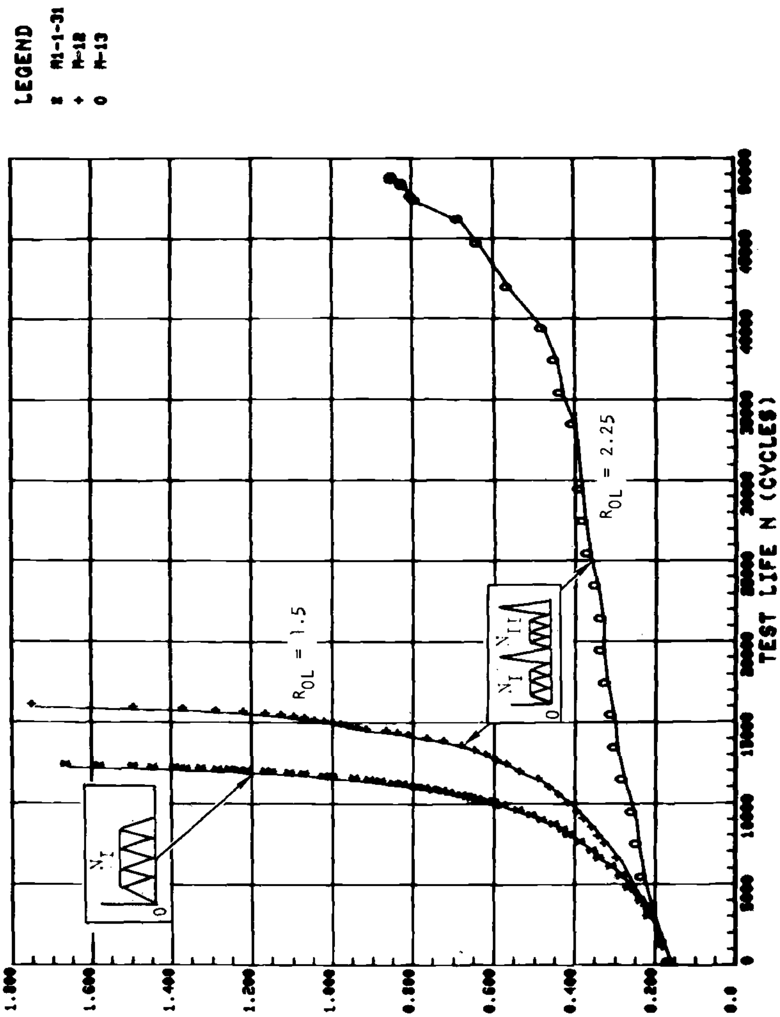

FIG. 4—*Periodic overload retardation effect on tension-zero cycles on crack growth life,* $R_{ol} = 1.5$ *and* 2.25.

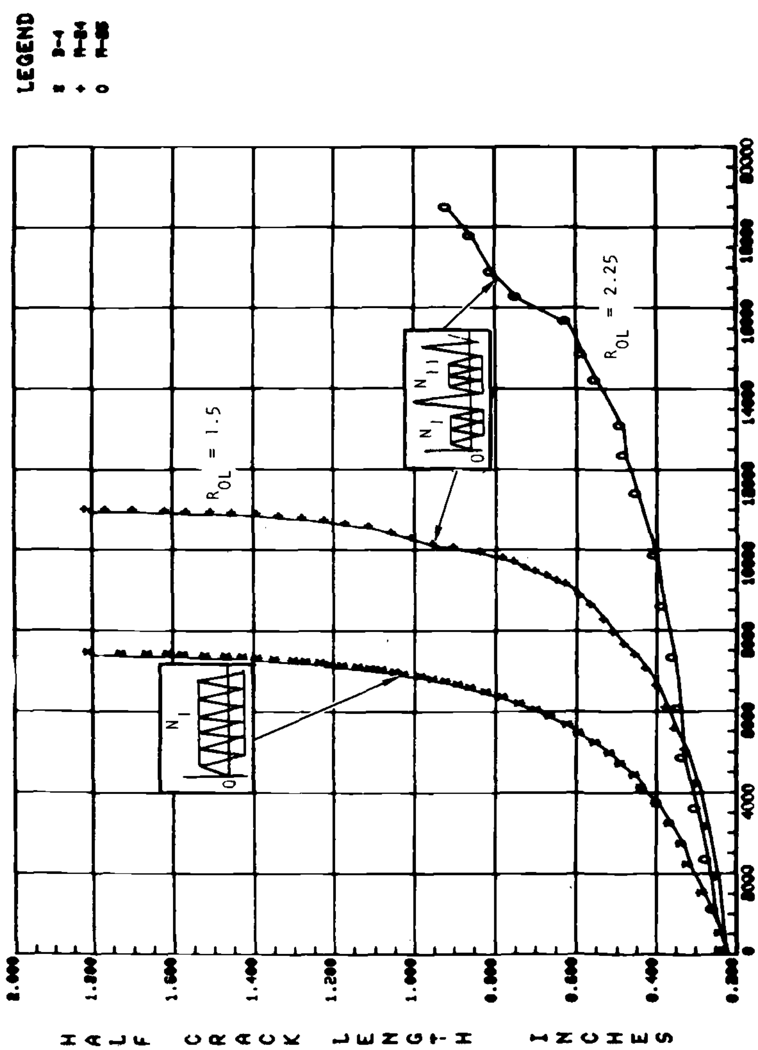

FIG. 5—*Periodic overload retardation effect on tension-compression cycles on crack growth life,* $R_{ol} = 1.5$ *and* 2.25.

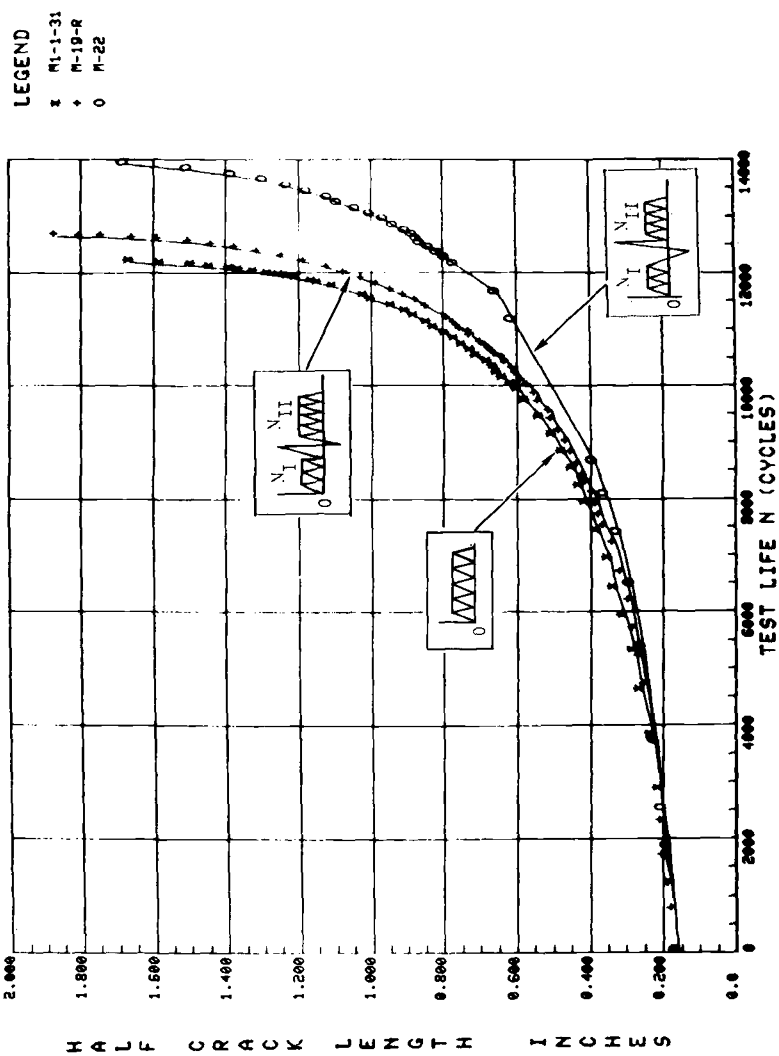

FIG. 6—*Combined overload retardation and compressive load acceleration effect on crack growth life.*

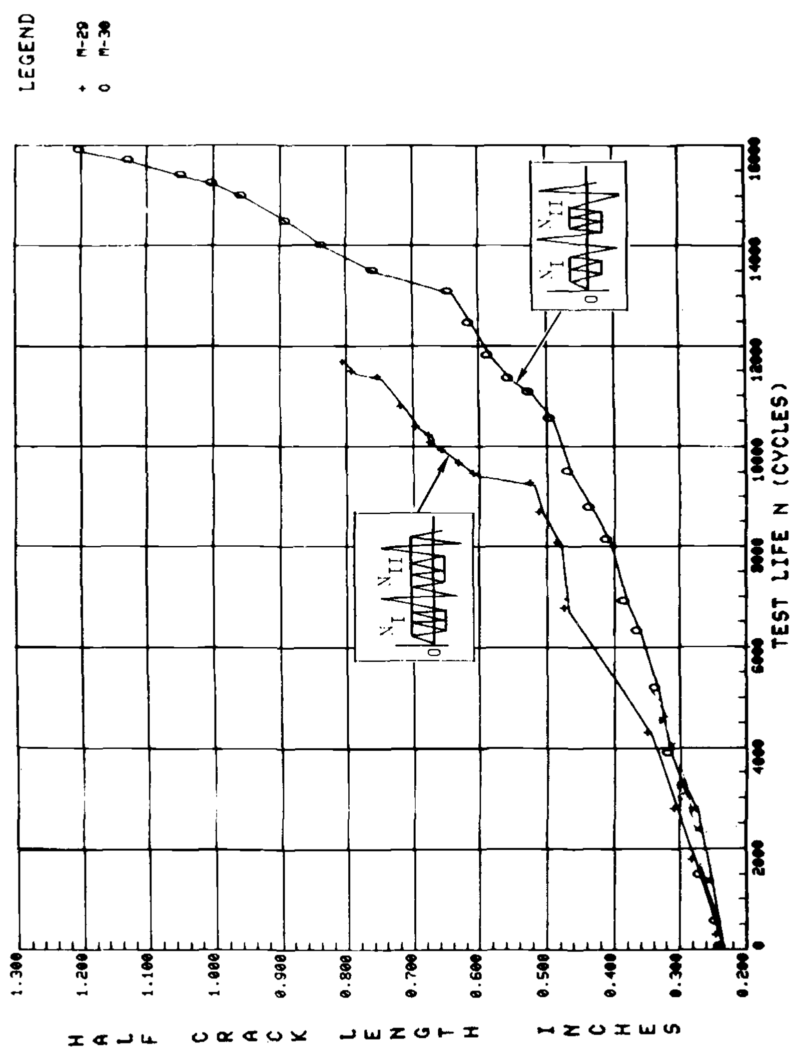

FIG. 7—*Combined overload retardation and compressive load acceleration effect on crack growth life.*

program, which is a crack growth analysis program developed in-house at Rockwell International Corp. The original research version of EFFGRO provided options to the user for selecting fatigue crack growth rate equations which include the Paris et al [*17*], Walker [*18*], Forman et al [*19*], and Collipriest (Sigmoidal) [*20*] equations. It also provided the options for choosing one of the three retardation models built in the program. They are the Willenborg [*12*], Elber (closure) [*13*], and Vroman [*14*] models.

The original EFFGRO program set the stress level to zero for a compression load cycle. Extensive experimental data generated in recent years have shown that crack growth rates at negative stress ratios are generally higher than their $R = 0$ counterparts [*4*]. Hence, it is important that the effects of the negative stress ratios be properly accounted for in the crack growth predictions. Chang's acceleration scheme [*15*] was adapted in the modified EFFGRO program to account for the compressive load acceleration effect to the fatigue crack growth.

TABLE 4—*Multiple overload/underload test descriptions and crack growth data correlation.*

	Test condition								$a(C_i-C_f)$	Analytical predictions			
	Applied base load			Over-load / Under-load					Test life	LEFGRO with Vroman/Chang model		CRACKS IV with Willenborg model	
Test	Loading profile	σ_{Max} (ksi)	σ_{Min} (ksi)	σ_{Max} (ksi)	σ_{Min} (ksi)	N_I (cycle)	N_{II} (cycle)	N_{Test} (cycle)	N_{pred} (cycle)	ϵ	N_{pred} (cycle)	ϵ
M-31	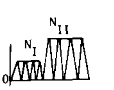	8	0	20	0	10,000	To failure	0.150-C_{CR} 22,430	22,443	1.0	23,000	1.03
M-32		20	0	40	0	5,000	To failure	0.155-C_{CR} 5,275	5,476	1.04	5,500	1.04
M-33	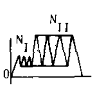	8	2.4	20	2.4	10,000	To failure	0.148-C_{CR} 27,000	26,990	1.00	27,000	1.00
M-34		20	6	40	12	5,000	To failure	0.150-C_{CR} 6,884	6,584	0.96	7,000	1.02
M-35	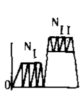	8	0	20	14	10,000	To failure	0.143-C_{CR} 178,838	191,845	1.07	192,500	1.08
M-36		20	0	40	28	5,000	To failure	0.150-C_{CR} 9,346	12,051	1.29	12,000	1.28
M-37	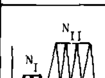	8	-2.4	20	0	10,000	To failure	0.155-C_{CR} 24,200	21,904	0.91	23,000	0.95
M-38		20	-6	40	0	5,000	To failure	0.150-C_{CR} 5,197	5,376	1.03	5,600	1.08
M-39	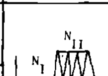	0	-6	20	0	5,000	To failure	0.150-C_{CR} 19,300	17,796	0.92	18,000	0.93
M-40		0	-12	40	0	5,000	To failure	0.150-C_{CR} 5,653	5,910	1.04	6,000	1.06

Note: $\epsilon = \frac{N_{pred}}{N_{test}}$

TABLE 4—*Continued.*

Test	Test condition: Applied base load: Loading profile	Applied base load: S_{Max} (ksi)	Applied base load: S_{Min} (ksi)	Over-/Under-load: S_{Max} (ksi)	Over-/Under-load: S_{Min} (ksi)	N_I (cycle)	N_{II} (cycle)	(C_i-C_f) Test life N_{Test} (cycle)	Analytical predictions: EFFGRO with Vroman/Chang model: N_{pred} (cycle)	EFFGRO with Vroman/Chang model: ϵ	CRACKS IV with Willenborg model: N_{pred} (cycle)	CRACKS IV with Willenborg model: ϵ
M-41	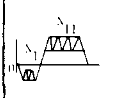	-3	-6	20	10	5,000	To failure	0.150-C_{CR} 67,400	63,150	0.94	63,500	0.94
M-42		-3	-12	20	10	5,000	To failure	0.155-C_{CR} 57,842	61,255	1.06	61,500	1.06
M-43		30	0	20	0	500	To failure	0.158-C_{CR} 17,813	10,676	0.6	12,500	0.70
M-44		40	0	20	0	500	To failure	0.153-C_{CR} 50,470	7,407	0.15	29,250	0.58
M-45	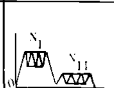	30	9	20	6	3,370	To failure	0.145-C_{CR} 23,624	18,030	0.76	18,120	0.77
M-46		40	12	20	6	500	To failure	0.150-C_{CR} 133,260	28,453	0.21	50,500	0.38
M-47	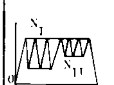	20	6	20	14	500	To failure	0.153-0.697 203,526	144,590	0.71	170,000	0.83
M-48		40	12	40	28	500	To failure	0.158-C_{CR} 10,489	9,256	0.88	9,500	0.91
M-49	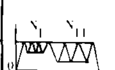	20	14	20	6	500	To failure	0.155-C_{CR} 25,675	27,401	1.07	27,500	1.07
M-50		40	28	40	12	500	To failure	0.155-C_{CR} 2,270	2,332	1.03	2,500	1.10

Note: $\epsilon = \frac{N_{pred}}{N_{test}}$

Analytical predictions on all the test cases shown in Tables 2, 3 and 4 were performed by selecting the Walker equation as the baseline crack growth rate equation. The Vroman model was selected to account for the tensile overload retardation effect, which was combined with the Chang acceleration scheme to account for the compressive load acceleration effect. This methodology is identified as the Vroman/Chang load interaction model. The following paragraphs briefly describe this model and the corresponding constants used in the model for performing the analytical predictions.

For tension-tension cyclic loading ($R \geq 0$) cases, the Walker equation is adapted; that is

$$da/dN = C[(1 - R)^{m-1}\Delta K_{eff}]^n, \qquad R > R_{cut}^+, \qquad R = R_{cut}^+ \tag{2}$$

where R_{cut}^+ is the cutoff value of the positive stress ratios. It is assumed that above this value, no stress ratio layer occurs in the da/dN versus ΔK curve.

TABLE 4—*Continued.*

Test	Test condition							$(C_i$-$C_f)$	Analytical predictions			
	Applied base load			Over-/Under-load				Test life	EFFGRO with Vroman/Chang model		CRACKS IV with Willenborg model	
	Loading profile	σ_{Max} (ksi)	σ_{Min} (ksi)	σ_{Max} (ksi)	σ_{Min} (ksi)	N_I (cycle)	N_{II} (cycle)	N_{Test} (cycle)	N_{pred} (cycle)	ϵ	N_{pred} (cycle)	ϵ
M-51	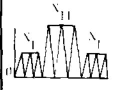	8	0	20	0	2,500	500	0.153-C_{CR} 86,600	74,718	0.86	75,000	0.87
M-52		20	0	40	0	500	50	0.150-C_{CR} 8,238	8,217	1.00	10,950	1.33
M-53	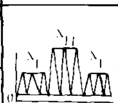	8	2.4	20	2.4	2,500	500	0.145-C_{CR} 113,570	104,871	0.92	105,000	0.92
M-54		20	0	40	0	500	50	0.150-C_{CR} 9,316	13,700	1.47	15,350	1.65
M-55	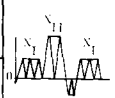	8	0	20	0	2,500	50	0.156-0.977 551,050	502,000	0.91	211,000	0.38
				0	-6		50					
M-56		20	0	40	0	2,500	50	0.154-C_{CR} 18,130	12,904	0.71	10,300	0.57
				0	-12		50					
M-57	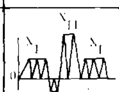	20	0	0	-12	2,500	50	0.145-C_{CR} 20,760	12,960	0.62	41,600	2.04
				40	0		50					
M-58	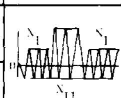	20	-6	40	-6	2,500	500	0.153-C_{CR} 2,774	4,500	1.6	5,750	2.08
M-59		8	-2.4	30	-2.4	5,000	2,500	0.158-C_{CR} 7,402	7,413	1.0	13,750	1.86
M-60	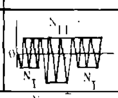	8	-2.4	8	-16	2,500	2,500	0.150-0.6 123,197	170,500	1.38	>250,000	>2

Note: $\epsilon = \dfrac{N_{pred}}{N_{test}}$

The ΔK_{eff} term in Eq 2 was proposed by Vroman in the following form

$$\Delta K_{eff} = \frac{4}{3}\left[K_{max} - \frac{3}{4}(K_{min}) + \frac{1}{3}K_{max_{ol}}\sqrt{(a_{ol} + r_{y_{ol}} - a)/r_{y_{ol}}}\right] \tag{3}$$

where K_{max} and K_{min} are the maximum and minimum values of the stress-intensity factors corresponding to the maximum and minimum stress of the applied load cycle; a_{ol} and $K_{max_{ol}}$ are the crack size and the stress-intensity factor value corresponding to the previously applied tensile overload. $r_{y_{ol}}$ is the radius of the plastic zone produced by the tensile overload. It is determined from

$$r_y = \frac{1}{\beta\pi}(K_{max})/\sigma_y)^2 \tag{4}$$

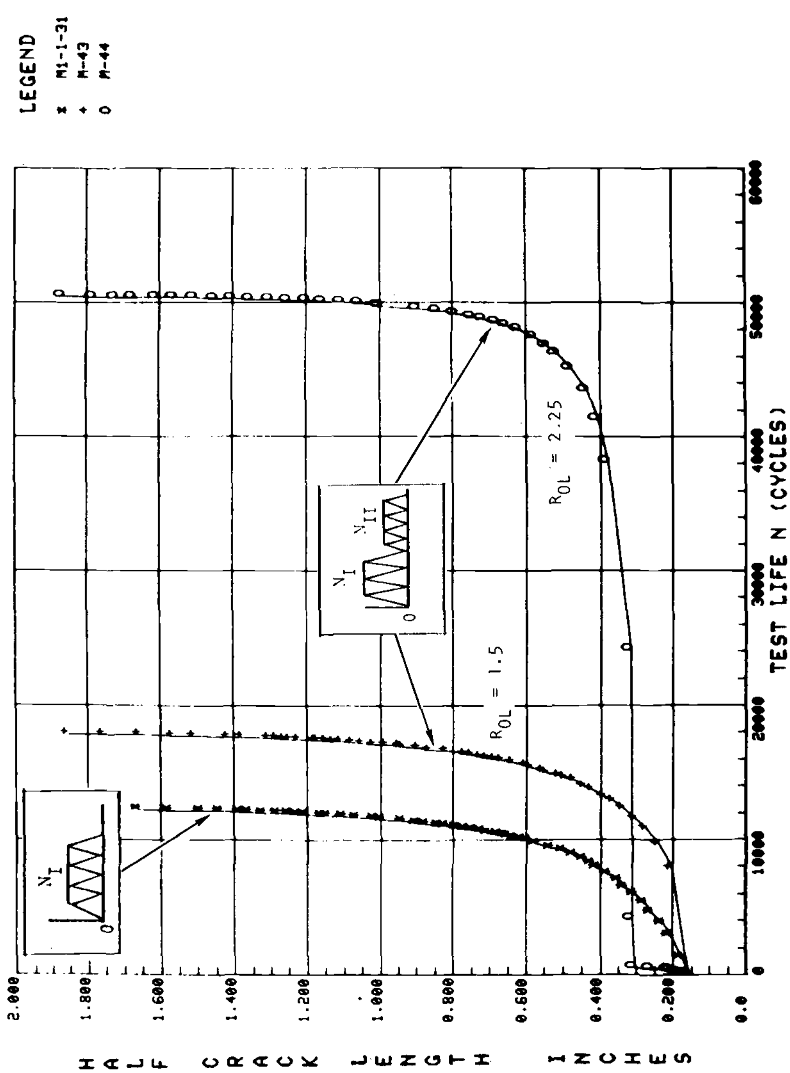

FIG. 8—*Multiple overload retardation effect on crack growth life.*

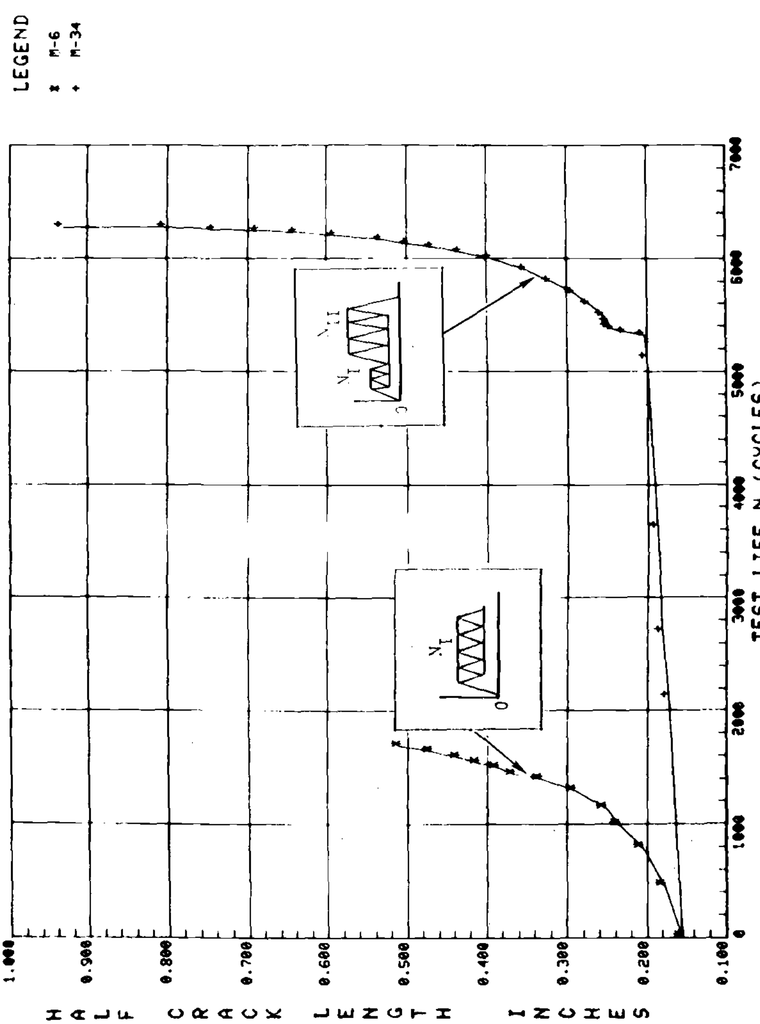

FIG. 9—*Low-to-high multiple-load acceleration effect on crack growth life.*

where σ_y is the material tensile yield strength and β the plane stress/plane strain coefficient: $\beta = 2$ for plane stress, and $\beta = 6$ for plane strain.

The effective stress-intensity factor range ΔK_{eff} in the Vroman model (Eq 3), can be reformulated as

$$\Delta K_{eff} = (K_{max} - K_{min}) - \frac{1}{3}\left[\left(\sqrt{(a_{ol} + r_{yol} - a)/r_{yol}}\right) - K_{max}\right] \quad (5)$$

It can be seen from Eq 5 that the numerical value of ΔK_{eff} is always less than $\Delta K = K_{max} - K_{min}$ when the overload is existing; hence, the corresponding value of the fatigue crack growth rate is smaller than its constant-amplitude loading counterpart, resulting in crack growth retardation.

For tension-compression cyclic load ($R < 0$) cases, the following rate model is adopted

$$da/dN = C[(1 - R)^q K_{max}]^n, \qquad R < R_{cut}^-, \qquad R = R_{cut}^- \quad (6)$$

where R_{cut}^- is the cutoff value of the negative stress ratio.

Equation 6 is very similar to Eq 2 in the mathematical form, yet the exponent q is considered as the acceleration index as proposed by Chang [*21*], which does not act as the collapsing factor as the exponent m does in the Walker equation. For a specific negative stress ratio ($R < 0$), q is determined by

$$q = [ln(\alpha)/ln(1 - R)]/n, \qquad R < 0 \quad (7)$$

where α is the ratio of the crack growth rate at a specific negative stress ratio to its $R = 0$ counterpart, and n is the fatigue crack growth rate exponent determined from the $R = 0$ crack growth data.

Fatigue crack growth rate constants, the fracture and material properties, and other parameters used in the analytical predictions for 2219-T851 aluminum were as follows. The fatigue crack growth rate constants were determined by least-square-fit for *da/dN* in the 2.54×10^{-8} m/cycle (1×10^{-6} in./cycle) to 2.54×10^{-5} m/cycle (1×10^{-3} in./cycle) range through the use of PLOTRATE

$$C = 8.367 \times 10^{-10}, \qquad n = 3.64, \qquad m = 0.6, \qquad q = 0.3$$

$$R_{cut}^+ = 0.75, \qquad R_{cut}^- = -0.99, \qquad \Delta K_{th} = 1.65 \text{ MPa}\sqrt{\text{m}}\ (1.5 \text{ ksi}\sqrt{\text{in.}})$$

$$\sigma_y = 330.96 \text{ MPa (48 ksi)}, \qquad (K_c = 71.5 \text{ MPa}\sqrt{\text{m}}\ (65 \text{ ksi}\sqrt{\text{in.}})$$

Analytical crack growth predictions made by EFFGRO were correlated with experimental data. The results of the correlations were summarized and are presented in Tables 2, 3, and 4. Included in these tables is the ratio of the predicted life to the test life, ϵ, of each test case. The crack life is defined as the total cycles to grow from an initial crack size (half length) c_i to a final size c_f. In the experimental testing, unless it was stated otherwise, the test specimens were tested to failure. Consequently, the corresponding analytical predictions were carried out until the critical crack size c_{cr} was reached. It can be seen that, with few exceptions, the analytical predictions correlated with the test data very well.

For the sake of comparison, crack growth predictions were also made by using the CRACKS-IV computer program [22] developed by the U.S. Air Force. The generalized Willenborg model [23] was selected to account for the tensile overload retardation effects on the crack growth. This generalized Willenborg model, proposed by Gallagher, closely resembles the Vroman retardation model. The only difference is that the generalized Willenborg model operates on the effective stress-intensity factor K_{eff} instead of the effective stress-intensity range ΔK_{eff}. The effective maximum and minimum stress intensity factors in the generalized Willenborg model are defined as

$$K_{max_{eff}} = K_{max} - \Phi[K_{max_{ol}}(1 - \Delta a/r_{y_{ol}})^{1/2} - K_{max}] \tag{8}$$

$$K_{min_{eff}} = K_{min} - \Phi[K_{max_{ol}}(1 - \Delta a/r_{y_{ol}})^{1/2} - K_{max}] \tag{9}$$

where Φ is a proportional constant which can be obtained from the form in terms of the overload shutoff ratio S_{so}

$$\Phi = [1 - (K_{max})_{th}/K_{max_{ol}}]/(S_{so} - 1) \tag{10}$$

The effective stress intensity factor range and effective stress ratio are then determined from:

$$\Delta K_{eff} = K_{max_{eff}} - K_{min_{eff}} = \Delta K \tag{11}$$

$$R_{eff} = K_{min_{eff}}/K_{max_{eff}} \tag{12}$$

The effective stress ratio will be set to zero if the calculated value is less than zero.

The fatigue crack growth rate equation used in CRACKS predictions was also the Walker equation which is formulated in terms of the effective stress-intensity factor, $K_{max_{eff}}$, and the effective stress ratio, R_{eff}, as

$$da/dN = C[(1 - R_{eff})^m K_{max_{eff}}]^n, \qquad R_{eff} \geq 0$$

The corresponding rate constants and other parameters used in the analytical predictions performed by the CRACKS program were

$$C = 8.367 \times 10^{-10}, \qquad n = 3.64 \qquad m = 0.6,$$

$$K_{th} = 1.65 \text{ MPa}\sqrt{\text{m}} \text{ (1.5 ksi} \sqrt{\text{in.}}), \qquad S_{so} = 3,$$

$$\sigma_y = 330.96 \text{ MPa (48 ksi)} \qquad K_c = 71.5 \text{ MPa}\sqrt{\text{m}} \text{ (65 ksi} \sqrt{\text{in.}})$$

The analytical predictions made by the CRACKS program through using the generalized Willenborg model were also correlated with the test data as summarized in Tables 2, 3, and 4. It can be seen that in most cases, especially for loading cycles containing compressive stresses, such as M-3, M-4, M-26, M-27, M-29, and M-30, the Vroman/Chang model provided apparently better predictions. Figures 10 and 11 are typical plots of the measured crack growth data, with analytical predictions by the Vroman/Chang and the generalized Willenborg models.

Conclusions

The primary parameters which affect the fatigue crack growth rates and various retardation and acceleration effects resulting from the application of overload and underload on the 2219-T851 aluminum alloy were investigated. The following conclusions can be drawn, applicable mostly for 2219-T851 aluminum:

1. Both the positive and negative stress ratio affect the crack growth behavior.

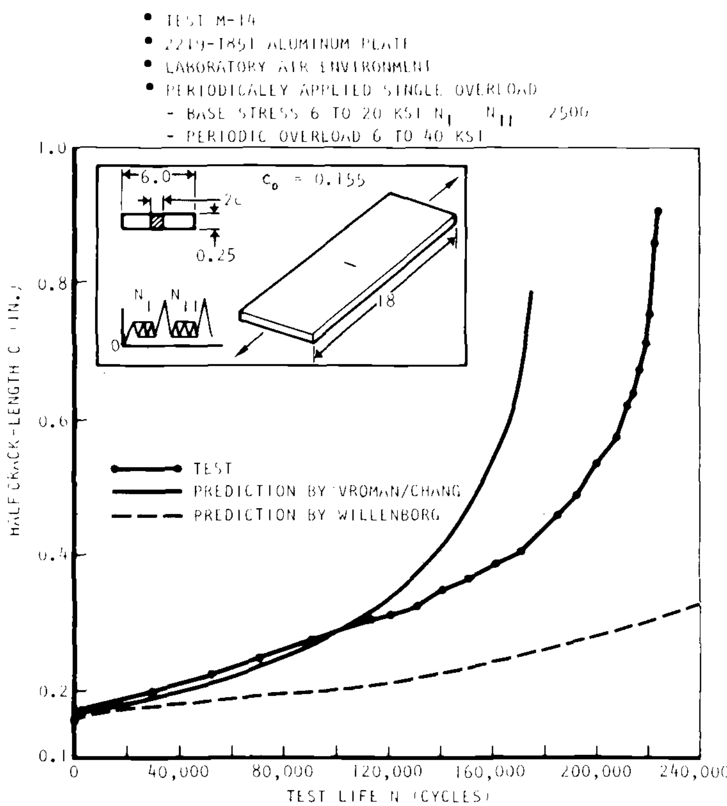

FIG. 10—*Crack growth curve and predictions for Test M-14.*

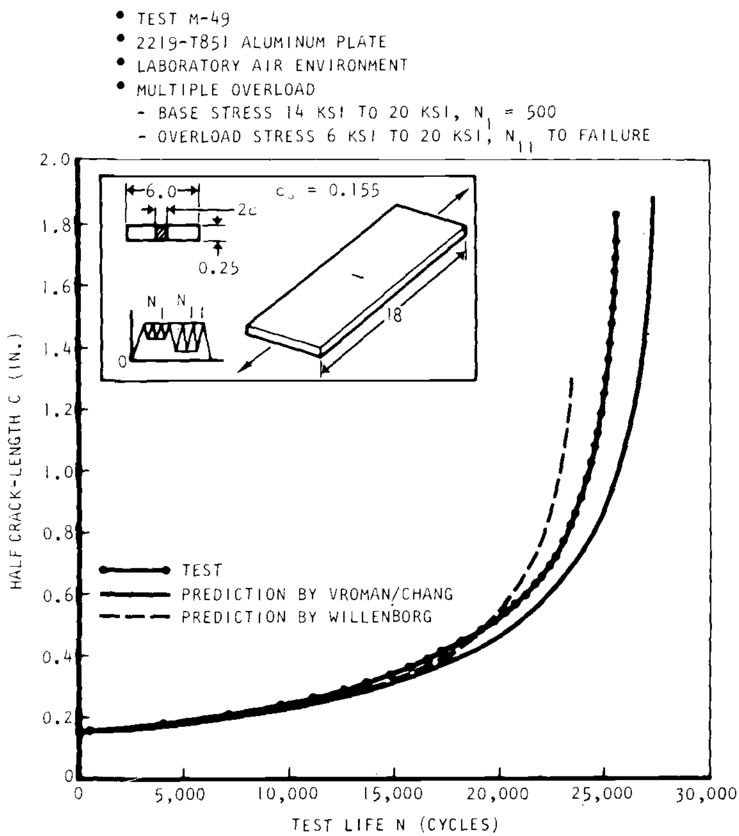

FIG. 11—*Crack growth curve and predictions for Test M-49.*

2. Application of the tensile overload cycle causes retardation of crack growth for positive and negative stress ratios. The degree of retardation depends largely on the overload ratio. Increasing the number of overload cycles also increases the degree of retardation.

3. Application of a compression load cycle accelerates the crack growth rates of those load cycles immediately following the compression load by only a slight amount. However, the compressive load reduces the effect of the tensile overload retardation effect rather drastically.

4. A block of underload (low load level) cycles accelerates the crack growth rate of the positive load cycles immediately following the underload cycles. A step jump of the growth rates often appears in the first few cycles after the low-high load transition.

5. In order to accurately predict crack growth behavior under variable-amplitude loadings similar to those applied in the test program, a load in-

teraction model which is able to predict retardation and acceleration effects is needed. Results of the test data correlation indicate that the proposed Vroman/Chang load interaction model is adequate for engineering applications.

Acknowledgments

This report is based on part of the results of a study performed on Contract F33615-77-C-3121, sponsored by the U.S. Air Force, Air Force Wright Aeronautical Laboratory, Flight Dynamics Laboratory, Wright-Patterson Air Force Base, Ohio.

The authors wish to express their thanks to L. Burnham for supervising the test program. M. Szamossi for coding the load interaction model into the computer program, EFFGRO, and K-W. Liu for assisting in the analytical predictions.

References

[1] Hudson, C. M. and Hardrath, H. F., "Investigation of the Effects of Variable-Amplitude Loadings on Fatigue Crack Propagation Patterns," NASA TND-1803, National Aeronautics and Space Administration, Washington, D.C., 1963.
[2] Schijve, J., "The Accumulation of Fatigue Damage in Aircraft Materials and Structures," AGARDograph 157, 1972.
[3] Von Euw, E. F. J., Hertzberg, R. W., and Roberts, R. in *Stress Analysis and Growth of Cracks, ASTM STP 513*. American Society for Testing and Materials, 1972, pp. 230-259.
[4] Crooker, T. W., *Transactions*, American Society of Mechanical Engineers, *Journal of Engineering for Industry*, 1971.
[5] Hsu, T. M. and Lassiter, L. W., "Effect of Compressive Overload on Fatigue Crack Growth," AIAA Paper 74-365, American Institute of Aeronautics and Astronautics, Washington, D.C., 1974.
[6] Stephens, R. I., McBarney, G. W., and Oliphant, L. J., *International Journal of Fracture*, Vol. 10, No. 4, 1974.
[7] Stephens, R. I., Chen, D. K., and Aom, B. W. in *Fatigue Crack Growth Under Spectrum Loads. ASTM STP 595*, American Society for Testing and Materials, 1976.
[8] Dill, H. D. and Saff, C. R. in *Cyclic Stress-Strain and Plastic Deformation Aspects of Fatigue Crack Growth, ASTM STP 637*, American Society for Testing and Materials, 1977.
[9] McMillan, J. C. and Pelloux, R. M. N. in *Fatigue Crack Propagation, ASTM STP 415*, American Society for Testing and Materials, 1967, pp. 505-535.
[10] Trebules, V. W., Roberts, R., and Hertzberg, R. W. in *Progress in Flaw Growth and Fracture Toughness Testing, ASTM STP 536*, American Society for Testing and Materials, 1973, pp. 115-146.
[11] Wheeler, O. E., *Transactions*, American Society of Mechanical Engineers, *Journal of Basic Engineering*, 1972.
[12] Willenborg, J., Engle, R. M., and Wood, H. A., "A Crack Growth Retardation Model Using Effective Stress Concept," AFFDL-TR-71-1, Air Force Flight Dynamics Laboratory, Wright-Patterson AFB, Ohio, 1971.
[13] Elber, W. in *Damage Tolerance in Aircraft Structures, ASTM STP 486*, American Society for Testing and Materials, 1971, 230-242.
[14] Vroman, G. A., "Analytical Prediction of Crack Growth Retardation Using a Residual Stress Concept," Briefing Charts, Rockwell International, B-1 Division, Los Angeles, Calif., 1971.
[15] Chang, J. B., Stolpestad, J. H., Sinozuka, M., and Vaicaitis, R., "Improved Method for Predicting Spectrum Loading Effects—Phase I Report, Volume I—Results and Discus-

sions," AFFDL-TR-79-3036, Air Force Flight Dynamics Laboratory, Wright-Patterson AFB, Ohio, 1979.

[*16*] Chang, J. B., Klein, E. J., and Cheng, J. S., "Automated Procedures for Fatigue Crack Growth Test Data Processing and Presentation (PLOTRATE Users Guide)" NA-78-860, Rockwell International, North American Aircraft Division, Los Angeles, Calif., 1979.

[*17*] Paris, P. C., Gomez, M. P., and Anderson, W. E., *The Trend in Engineering*, Vol. 13, No. 1, 1961.

[*18*] Walker, K. in *Effects of Environment and Complex Load History on Fatigue Life, ASTM STP 462*, American Society for Testing and Materials, 1970.

[*19*] Forman, R. G., Kearney, V. E., and Engle, R. M., *Transactions*, American Society of Mechanical Engineers, *Journal of Basic Engineering*, Vol. 89, 1967.

[*20*] Collipriest, J. E. and Ehret, R. M., "Computer Modeling of Part-Through-Crack Growth," SD72-CE-15, Rockwell International, Space Division, Downey, Calif., 1972.

[*21*] Chang, J. B., "Fifth Quarterly Interim Report, Improved Methods for Predicting Spectrum Loading Effects," NA-78-491-5, Rockwell International, North American Aircraft Division, Los Angeles, Calif., 1979.

[*22*] Engle, R. M., "CRACKS IV User's Manual," AFFDL-TM-74-173, Air Force Flight Dynamics Laboratory, Wright-Patterson AFB, Ohio, 1974.

[*23*] Gallagher, J. P., "A Generalized Development of Yield-Zone Models," AFFDL-TM-74-27, Air Force Flight Dynamics Laboratory, Wright-Patterson AFB, Ohio, 1974.

R. J. Bucci[1]

Effect of Residual Stress on Fatigue Crack Growth Rate Measurement

REFERENCE: Bucci, R. J., "**Effect of Residual Stress on Fatigue Crack Growth Rate Measurement,**" *Fracture Mechanics: Thirteenth Conference, ASTM STP 743,* Richard Roberts, Ed., American Society for Testing and Materials, 1981, pp. 28–47.

ABSTRACT: Examples are given where influence of residual stress leads to erroneous interpretation of fatigue crack growth rate measurements made in accordance with ASTM Method E 647-78T. The experimental data presented form a basis for modification of applicable ASTM documents to give recognition to problems caused by residual stress, and to suggest guidelines for minimization of their effect on fracture property measurement.

KEY WORDS: residual stress, fracture mechanics, fatigue, fatigue crack growth, test methods (metals), mechanical properties (metals)

Recognizing the influence of residual stress on fracture property measurement is important when fracture mechanics-type specimens are removed from parent metal where complete stress relief is impractical. This is particularly true when test specimens are removed from weldments, complex forged or extruded shapes, or from metallurgical coupons which have been heat-treated without subsequent stress relief.

An example of the latter case is indicated by crack propagation results obtained from laboratory-scale, nonstress-relieved extruded rod, Fig. 1. Rapid quenching after solution heat treatment produces a core of residual tension at the center and compression at the surface of the cylinder.[2] This residual stress distribution is largely responsible for the different propagation rates observed when crack starter notches are located in different regions of indentically fabricated extruded rods. In the center crack tension (CCT) specimen the crack initiated in a field of tension and propagated at a faster rate than

[1]Technical specialist, Engineering Properties and Design Division, Alcoa Laboratories, Alcoa Center, Pa. 15069.

[2]Barker, R. S. and Sutton, J. G., *Aluminum, Vol. III: Fabricating and Finishing,* American Society of Metals, Metals Park, Ohio, 1967, Chapter 10.

(SI Conversion: 1 in. = 25.4 mm, 1 ksi $\sqrt{\text{in.}}$ = 1.1 MPa $\sqrt{\text{m}}$)

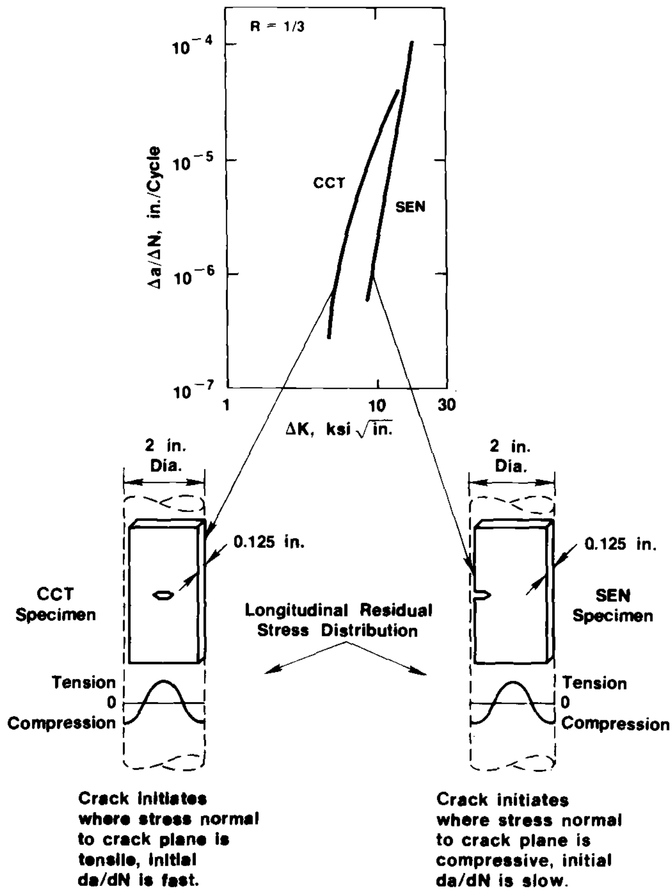

FIG. 1—*Effect of specimen type on fatigue crack growth rates established from nonstress-relieved high-strength 7XXX aluminum alloy extruded rod.*

the initial crack in the single-edge notch (SEN) specimen at comparable applied ΔK, but embedded in a field of compression.

In another research program experimental data suggested that certain fabrication and metallurgical variants were responsible for high fatigue crack growth resistance within a class of experimental high-strength 7XXX-type aluminum alloys. The alloy product form evaluated was a powder metallurgy hand forging from which compact tension specimens were removed for growth rate testing. Crack growth rate information established in this work was completely valid according to the ASTM Test for Constant-Load-Amplitude Fatigue Crack Growth Rates Above 10^{-8} m/Cycles (E 647-78T).[3] Valid fatigue crack growth rates in these materials were reproduced by a second laboratory employing identical specimens removed from remnants of the same hand forgings.

Second-generation hand forgings of the same material were prepared to better establish interrelationships between fabricating practices and microstructure on fatigue crack growth resistance. Crack growth experiments on the second-generation materials, however, failed to reproduce the dramatic improvements observed in earlier work. Because of the observed discrepancies, test procedures employed in the more recent work were reexamined and found to be satisfactory. However, detailed reevaluation of the fabrication practices revealed that first-generation hand forgings had not been stress-relieved following quenching, whereas a compressive stress relief operation was applied to second-generation forgings.

Because of potential confounding of crack growth rate measurement arising from the influence of residual stress, the superior crack growth resistance observed on first-generation materials could not be confirmed or refuted. In the following, results are reported from an investigation conducted with the goal of (1) reproducing the slow crack growth rates observed in early work on the subject material, and (2) evaluating the effect of residual stress on fatigue crack growth measurement. Additional background and experimental details of this investigation are reported in Part III of a report by Sanders et al.[4]

Experimentation

The experiment was designed to two alloys, both laboratory fabricated to a 10 by 15 by 51-cm (4 by 6 by 20.4 in.) hand forgings. The two alloys had similar 7XXX-type aluminum alloy chemical composition; however, the subject material (designated here-on as Alloy A) was forged from powder metallurgy produced billet, while the control material (Alloy B) was forged from laboratory cast ingot. The basic microstructural characteristics of Alloys A and B were, therefore, drastically different because of their respective process histories (footnote 4). Prior to solution heat treatment (SHT) two 3.8-cm-thick (1.52 in.) slabs were removed from each forging at the short transverse-longitudinal (S-L) plane, as shown in Fig. 2. After SHT and quench one of the two pieces was compressively stress-relieved by 3 to 5 percent permanent reduction in the shortest dimension [3.8 cm (1.52 in.)] of the slab. Each slab was then aged to the final temper. With the exception of the stress relief, this pro-

[3]An exception to this was noted on several test specimens where the fracture path deviated by an angle greater than 5 deg from the plane of the machined starter slot. When this occurred the crack length was generally more than half way through the specimen.

[4]Sanders, R. E., Otto, W. L., Jr., and Bucci, R. J., "Fatigue Resistant Aluminum P/M Alloy Development," Technical Report AFML-TR-79-4131, Air Force Materials Laboratory, Wright-Patterson Air Force Base, Ohio, Sept. 1979.

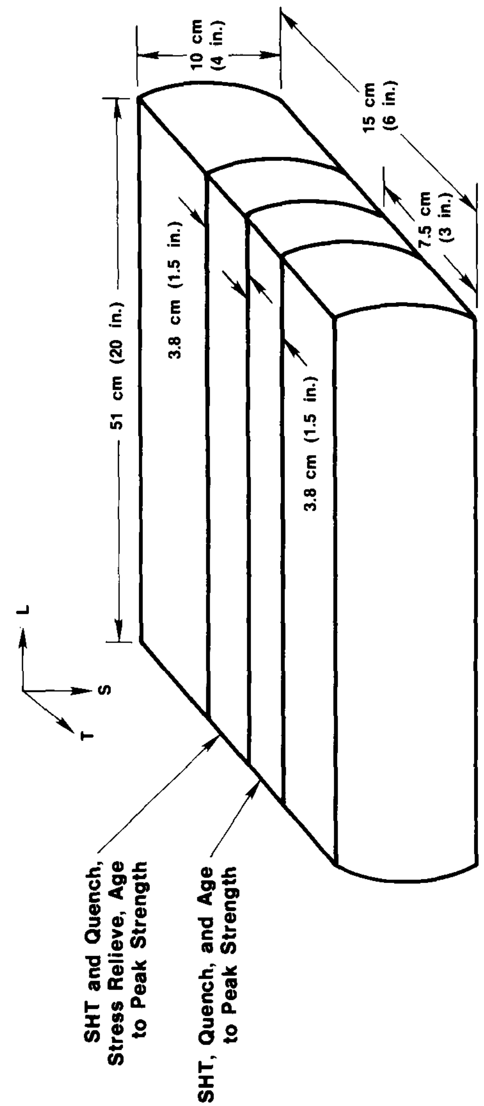

FIG. 2—*Slabs removed from original hand forging for subsequent heat treatment and mechanical testing.*

cedure reproduced the fabrication history of the subject material which demonstrated high fatigue crack growth performance in the early work.

Residual stress and mechanical properties were determined for the four material conditions, namely, Alloys A and B with and without stress relief. Table 1 gives, for each condition, the tests conducted according to the designated ASTM standard test method. Specimen locations are shown in Fig. 3. The fatigue crack growth tests were conducted in dry air (relative humidity < 10 percent) at a stress ratio (R) equal to 1/3. All other mechanical tests were conducted in ambient air. Crack growth specimens were removed from material at the mid-thickness ($T/2$) plane and both surfaces of the parent slab.

To better quantify the effect of residual stress on crack growth, residual stresses in the S and L direction were measured prior to test by X-ray and layer removal methods in both the parent slab and crack growth specimens. Additional detail on these measurements, their precision, and method of analysis is provided by Sanders et al (footnote 4).

Crack propagation rates (da/dN) were determined from visual crack

TABLE 1—*Test particulars.*

Quantity	Type of Test	Specimen Type	ASTM Practice
2	tension	6.35-mm (1/4 in.) diameter	E-8
2	notch tension	12.7-mm (1/2 in.) diameter	E 602-76T
1	fracture toughness	CT specimen 38.1 mm thick (1 1/2 in.)	E 399
3	fatigue crack growth	CT specimen 6.35 mm thick (1/4 in.)	E 647-78T

(SI Conversion: 1 in. = 25.4 mm)

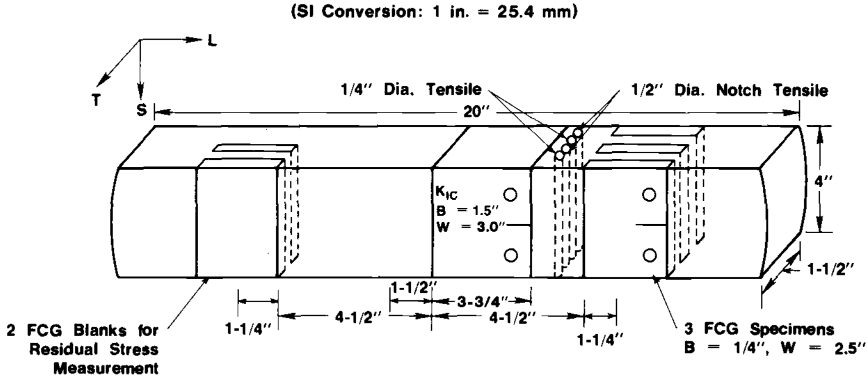

FIG. 3—*Location of test specimens within parent metal slab.*

length measurements. A crack-opening displacement (COD) gage was used to monitor compliance change with crack extension in specimens removed from the $T/2$ and one surface plane of each material condition. A crack-opening load (P_{op}) was estimated from the load-COD trace obtained in the instrumented tests, as in Fig. 4. The opening load is required to offset compression at the crack tip caused by the superposition of clamping forces attributed to residual stress in the bulk material and forces caused by wedging action of residual deformation left in the wake of the propagating crack, as described by Elber.[5] The residual stress influence on da/dN could, therefore, be evaluated using the concept of effective cyclic stress-intensity factor (ΔK_{EFF}), which assumes that propagation occurs only when the crack is completely open. For a constant applied cyclic load (ΔP), any internal force system which increases P_{op} above the minimum cyclic load would decrease ΔK_{EFF}, and thus decrease da/dN.

Two rectangular blanks, having identical thickness and plan size as the crack growth specimens, were removed from Alloy B at locations comparable to the instrumented crack growth tests, but from the opposite end of the parent slab, as indicated in Fig. 3. The redistribution of residual stresses following progressive sawcuts, simulating a growing crack, was determined from displacements measured at the three locations indicated in Fig. 5.

Results

Residual Stress Measurements

The following conclusions were determined from statistical analysis of residual stress measurements made on the parent slab and crack growth specimens removed from parent metal.

1. Residual stress magnitudes were consistently larger in nonstress-relieved materials.
2. The residual stress magnitude in both stress-relieved and nonstress-relieved crack growth specimens was significantly different from zero.
3. Neither a main nor interaction effect of material (Materials A versus B) on residual stress magnitude was detected in test specimens or parent metal.
4. In both the parent metal and test specimens, the stress relief operation generally produced greater changes to stress in the S-direction than in the L-direction.
5. Within parent metal the effect of through-the-thickness specimen location on residual stress magnitudes was greatest in nonstress-relieved materials.

[5]Elber, W. in *Damage Tolerance in Aircraft Structures, ASTM STP 486,* American Society for Testing and Materials, 1971, p. 230.

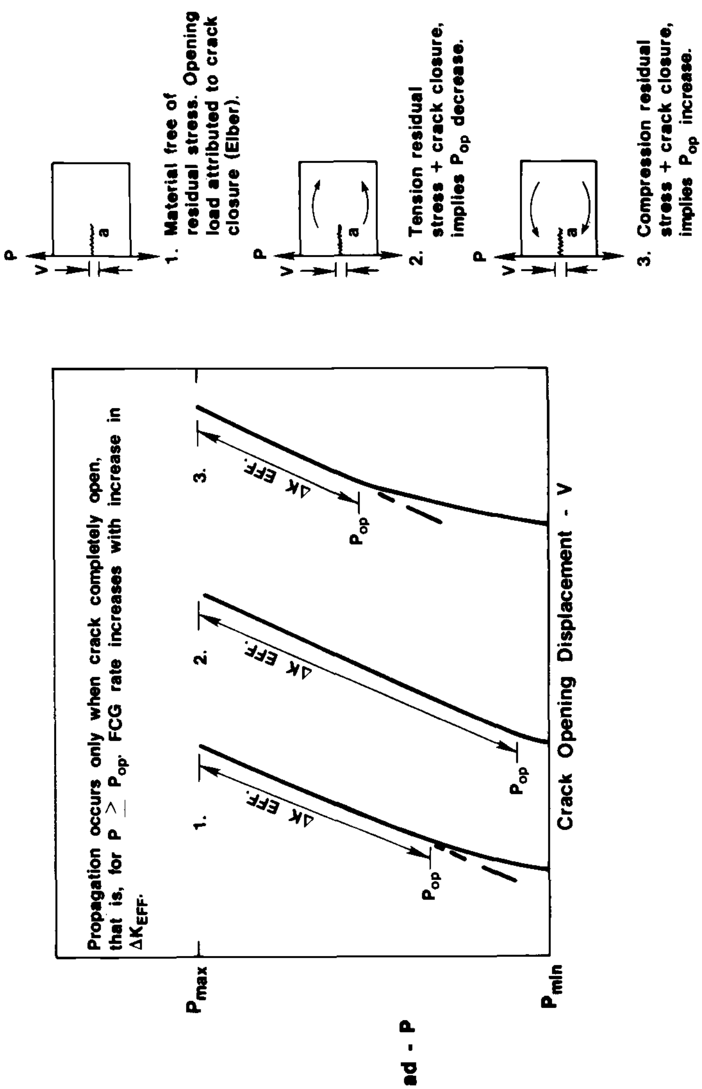

FIG. 4—*Effect of residual stresses on load-COD trace in bulk material surrounding the crack tip.*

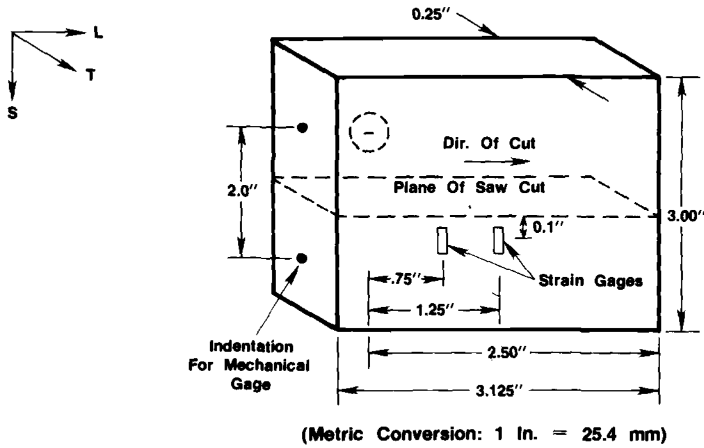

FIG. 5—*Location of displacement measurements in CT specimen blanks simulating fatigue crack growth by progressive sawcuts.*

Mechanical Properties

Tensile and fracture toughness properties of Materials A and B are given in Table 2. Valid fracture toughness (K_{Ic}) numbers were established for stress-relieved materials, while results of nonstress-relieved materials were invalid due to excessive fatigue precrack curvature caused by the residual stress-distribution indicated in Fig. 6.

Fatigue Crack Growth

The comparison of stress-relieved versus nonstress-relieved crack growth behavior (da/dN versus ΔK) is shown for Alloys A and B, respectively, in Figs. 7 and 8. Data from triplicate tests of identical stress-relieved material were in good agreement. For identical applied ΔK, the growth rates in nonstress-relieved material were significantly slower than rates in stress-relieved material, particularly at low ΔK. In nonstress-relieved material, the measured response depended upon specimen location within the parent slab, for example, Fig. 7, while in stress-relieved material, specimen location was not a factor.

The crack growth results of nonstress-relieved materials indicate that significant internal stresses altered the crack-tip stress intensity factor, thereby causing the disagreement with behavior of stress-relieved materials. The recommended standard test method (ASTM E 647-78T) assumes internal stresses to be zero, and uses external loads only to compute ΔK. Hence, though growth rates from nonstress-relieved materials are completely accurate and valid according to ASTM practice, the data should not be considered representative of the true material behavior.

TABLE 2—*Short-transverse mechanical properties of aluminum alloy hand forgings.*

Material	Stress Relief?	Tensile Strength ksi (MPa)	Yield Strength, ksi (MPa)	Elongation in 25 mm (10 in.), %	Reduction in Area, %	Notch Tensile Strength/Yield Strength	K_Q, K_{Ic}, MPa$\sqrt{m}$
A	yes	73.9 (509.5)	70.1 (483)	2.0	2.0	0.86	20.2
A	no	69.5 (479)	66.8 (>460.5#)	1.0	1.5	<0.81[a]	22.3[b]
B	yes	69.6 (480)	63.4 (437)	2.5	2.5	1.32	40.5
B	no	76.2 (525)	72.1 (497)	1.0	1.5	1.10	24.0[b]

NOTES:

Tensile and notched tensile properties are average values from duplicate tests.

K_Q-values are single test values only.

[a] Second tension test failed before 0.2% offset at higher stress than yield strength recorded for initial test.

[b] ASTM E 399 not satisfied because of excessive crack curvature. These values are not valid K_{Ic} measurements.

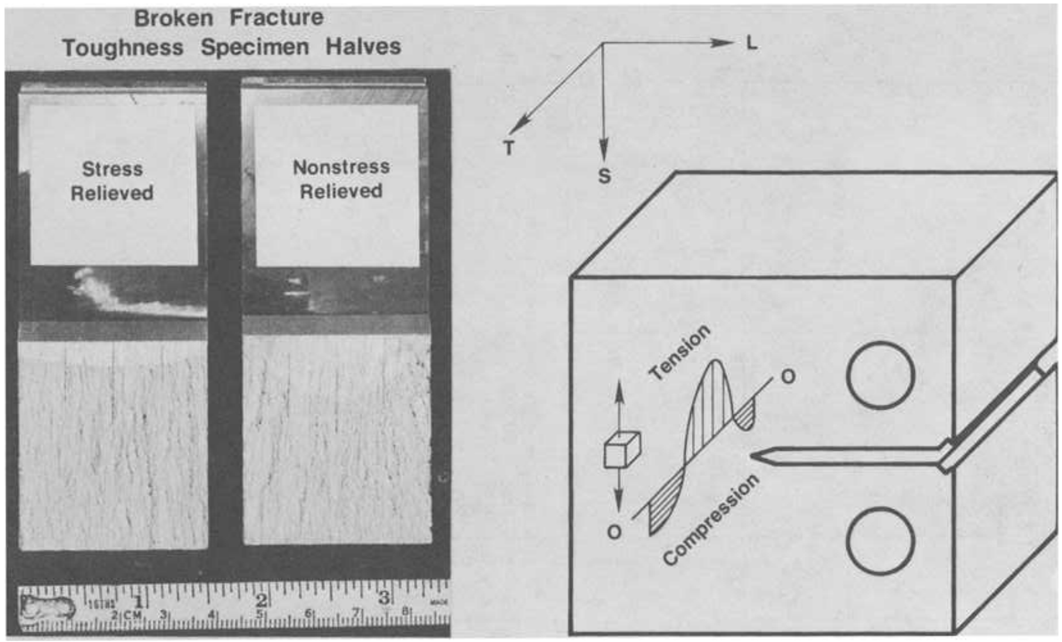

FIG. 6—*Through-thickness residual stress distribution normal to plane of the notch. This stress causes excessive crack curvature in nonstress-relieved fracture toughness specimens.*

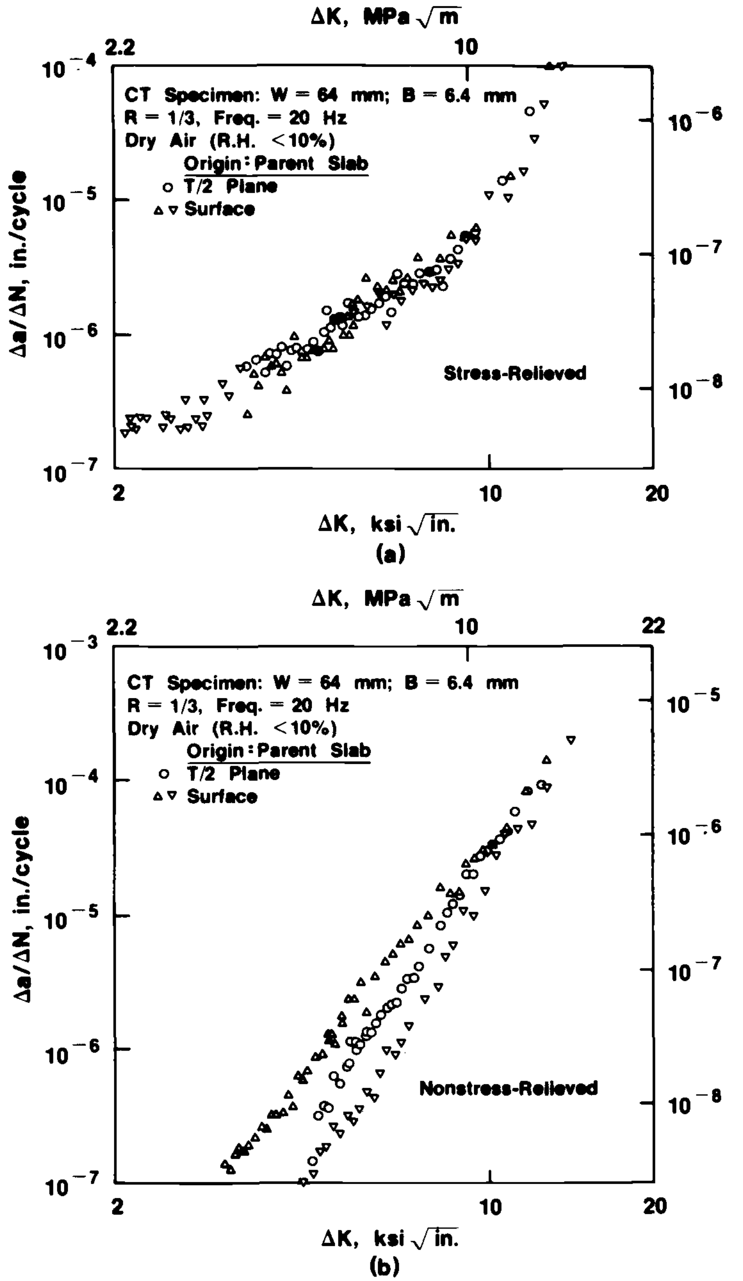

FIG. 7—*Effect of stress relief on fatigue crack growth rate measurement in Material A (*a*) stress-relieved and (*b*) nonstress-relieved.*

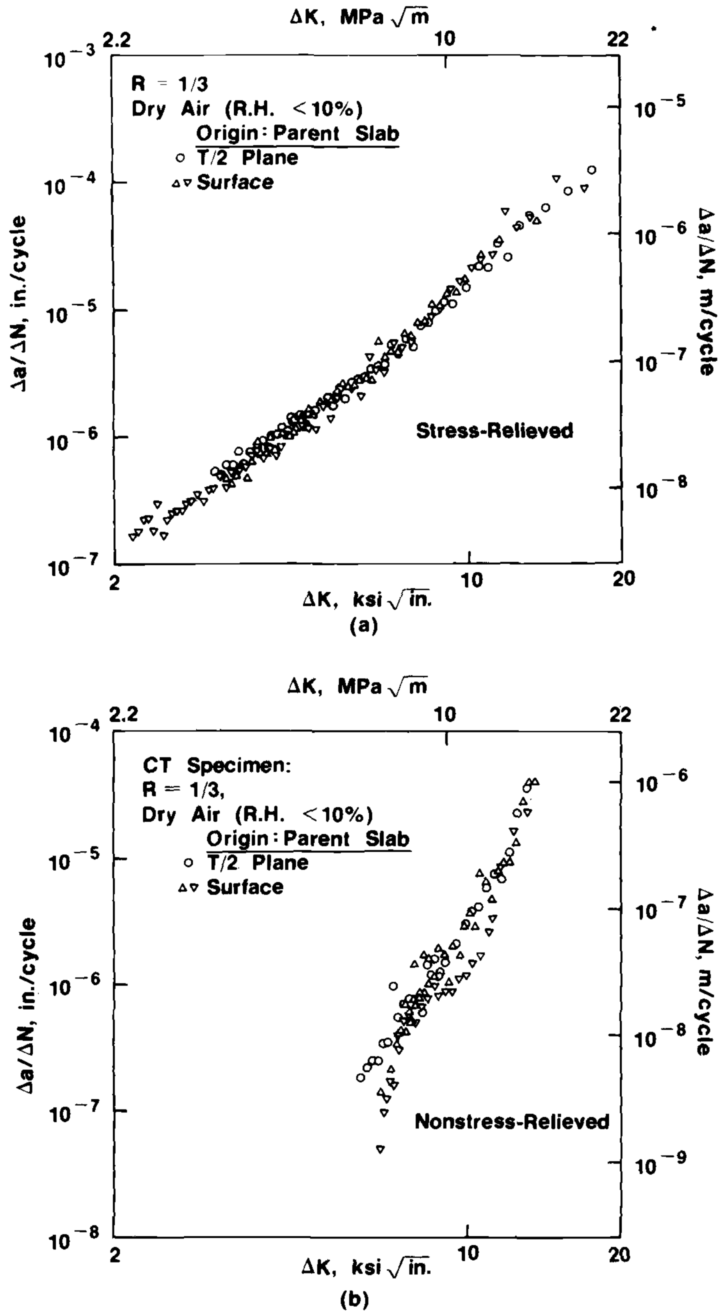

FIG. 8—*Effect of stress relief on fatigue crack growth rate measurement in Material B (a) stress-relieved and (b) nonstress-relieved.*

Discussion

Residual stresses are produced during quenching by deformation associated with shrinkage during cooling. Generally the first portion of the specimen to cool is left in residual compression, while the last portion to cool is left in residual tension. This is true of the cylinder indicated in Fig. 1 where residual compression along the outer surface is balanced by a core of residual tension at the center. Using the foregoing rationale, the principle of equilibrium, and the boundary condition that stresses normal to a free surface must be zero, the distribution of residual stresses in the S- and L-directions for a nonstress-relieved rectangular cross section would be similar to those illustrated in Fig. 9. This typical distribution was verified by X-ray measurements on the nonstress-relieved parent slabs. Longitudinal surface compression is greatest at the corners, since these locations are the first to cool.

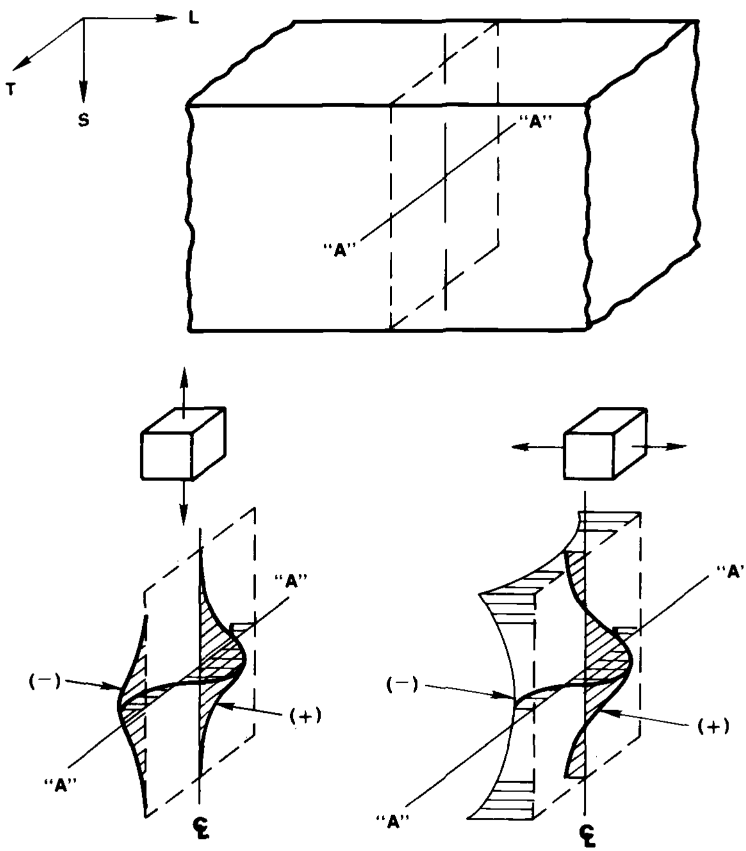

FIG. 9—*Typical residual stress distribution from quenching on rectangular section "A-A".*

Full section thickness fracture toughness specimens indicate that compressive stresses in the S-direction of nonstress-relieved material caused the precrack to grow slower at the surface than at the T/2 plane, where the S residual stress was tensile. Machining crack growth specimens to a thickness of 6.35 mm (0.25 in.) sufficiently reduces the S stress variation through the thickness such that excessive crack front curvature is no longer a problem in nonstress-relieved specimens having comparable plan size to the toughness specimens.

Residual stress in the L-direction had the greatest effect on measurement of crack growth resistance in nonstress-relieved compact specimens. Figure 10 illustrates that crack-tip compression results from a clamping moment caused by the stress unbalance which develops upon introduction of the crack starter slot. This force system is relatively uniform through the specimen thickness and, therefore, its occurrence cannot be detected by excessive curvature in the propagating fatigue crack. That is, by failing to recognize the effect of residual stresses acting parallel to the propagation direction, one would likely interpret the resultant crack growth measurement as valid according to ASTM Method E 647-78T.

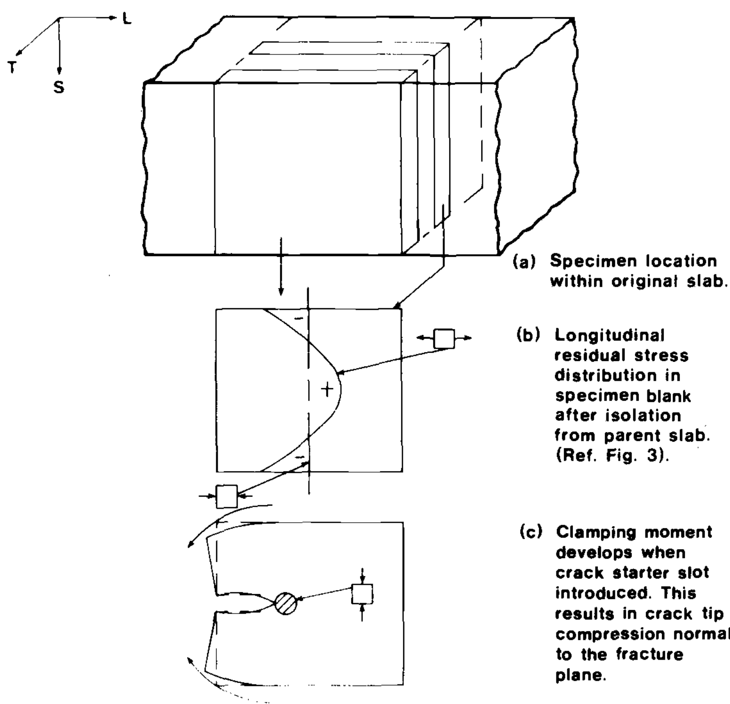

FIG. 10—*Effect of residual stress parallel to notch plane on fatigue crack growth rate measurement in CT specimen taken from nonstress-relieved materials.*

A simple technique to determine where a clamping moment exists is to measure surface displacement before and after the introduction of the machined starter notch. For example, following a sawcut simulating the crack starter slot in the compact specimen blank of Fig. 5, mechanical gage marks initially spaced 51 mm (2.0 in.) apart closed, respectively, by about 0.20 mm (0.008 in.) in blanks removed from the $T/2$ and surface plane of the parent nonstress-relieved slabs. Comparable measurements made on stress-relieved blanks indicated that the initial gage locations on average spread apart by about 0.05 mm (0.002 in.) at both the $T/2$ and surface locations. The latter observation suggests that growth rates established in stress-relieved specimens might actually be greater than those expected in residual stress-free material, because of tension mean stress at the crack tip.

Stress redistribution in compact specimen blanks, Fig. 5, following a series of progressive sawcuts simulating a growing crack, was measured by strain gages mounted just below the sawcut plane in Alloy B. The blanks were removed from the parent slab at locations symetrically opposite the crack growth specimens, Fig. 3. Residual stresses in the parent metal were equivalent at the corresponding location. Measurements made in nonstress-relieved blanks indicated significant compression stress in material at and ahead of the tip of the sawcut simulating a propagating crack, Fig. 11. In nonstress-relieved specimens crack propagation would, therefore, be retarded by clamping forces which close the crack. Stresses ahead and at the simulated crack tip in stress-relieved material were either slightly positive at short crack

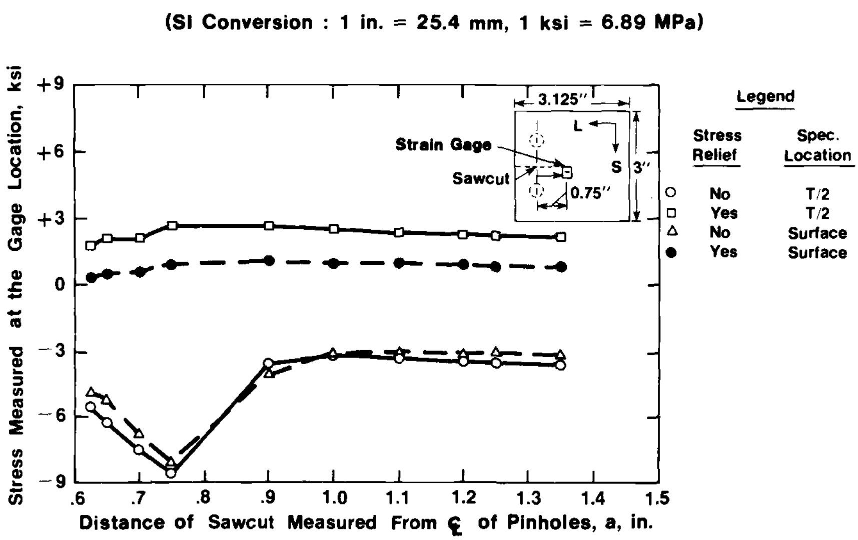

FIG. 11*a*—*Stress redistribution at Gage Location 1 following sawcuts to simulate a propagating crack in a compact tension specimen.*

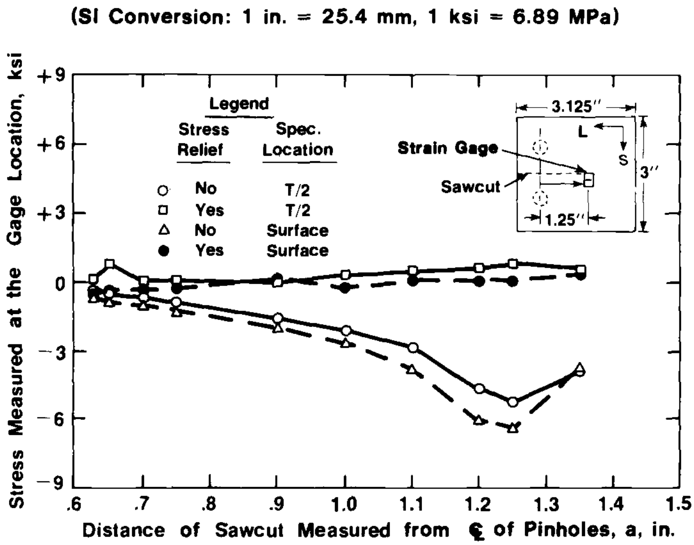

FIG. 11*b*—*Stress redistribution at Gage Location 2 following sawcuts to simulate a propagating crack in a compact tension specimen.*

length or zero at longer crack lengths. Crack growth may, therefore, be either accelerated or unaffected by the residual stress system in the original stress-relieved blank.

Clear differences were observed in the load-COD traces established in instrumented crack growth tests of stress-relieved versus nonstress-relieved specimens. Typical test records for Alloy B specimens removed from the $T/2$ plane are indicated in Fig. 12. Comparable test records were reproduced in Alloy A specimens removed from the $T/2$ location and in both materials from specimens taken from the surface location. For simplicity, the crack-opening load, P_{op}, was determined at the intersection of two traces which divide the test record into linear segments. At relatively short crack length, P_{op} in nonstress-relieved material was of the order of the maximum applied load, P_{max}, in tests of stress-relieved material. This explains why nonstress-relieved specimens required P_{max} about double that in stress-relieved specimens to propagate a crack at equivalent rates early in the test. In nonstress-relieved specimens, P_{op} decreased with stress relief during crack extension. This explains the near equivalence of da/dN versus ΔK data in both stress-relieved and nonstress-relieved specimens at high ΔK (long crack length).

Nonstress-relieved propagation rates were corrected using the effective ΔK concept of Fig. 4. The adjusted results from nonstress-relieved material agreed reasonably well with data established in the stress-relieved specimens, for example, Figs. 13 and 14. Thus it is concluded that residual stresses were

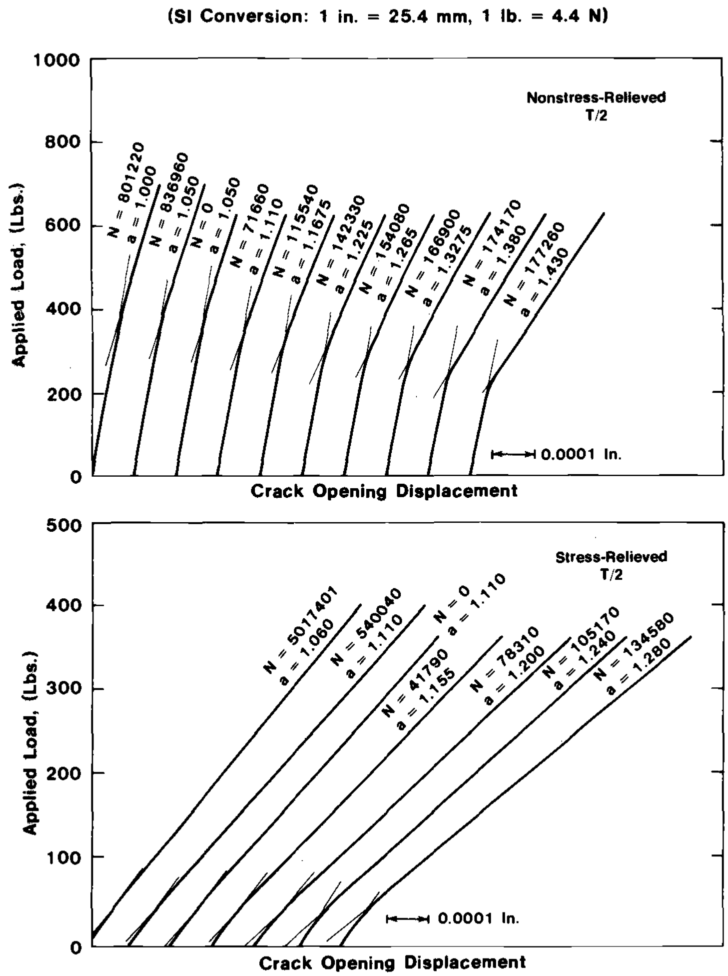

FIG. 12—*Characteristic load-COD traces established on stress-relieved and nonstress-relieved fatigue crack growth specimens of Material B.*

largely responsible for the extremely low propagation rates observed in the original investigation on the subject material.

Summary

Accurate fracture property measurement requires caution that determined properties are not an artifact of residual stress remaining in the test coupon. The problem develops in that stress-intensity factors are generally reproduced in fracture mechanics-type specimens with relatively small applied

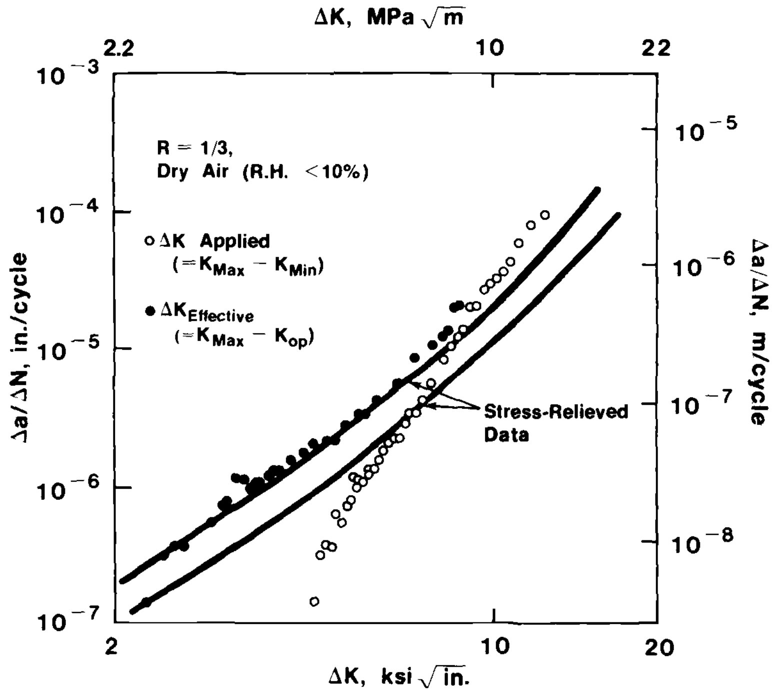

FIG. 13—*Corrected fatigue crack growth rates in nonstress-relieved hand forgings of Material A.*

stresses and large cracks. In engineering structure, however, the same stress-intensity factor is often produced by large stresses and small cracks. Therefore, residual stresses perceived to be small in the engineering sense can affect growth rate measurement when the ratio of residual stress to applied stress in the test coupon is significant. Under this premise low ΔK (near-threshold) fatigue crack growth rates represent the fracture mechanics property likely to be most seriously affected by residual stress influences.

Examples given show where failure to recognize influence of residual stress results in erroneous interpretation of fatigue crack growth rate measurements that could be perceived as valid according to ASTM Method E 647-78T. The affected growth rates and ΔK-values in the illustrated examples were drastically different from those typically associated with near-threshold behavior. Though not explicitly shown, it follows that the confounding influence of residual stress extends also to stress corrosion cracking (K_{Iscc}) and fracture toughness (K_{Ic}) property determinations.

The following guidelines are suggested for the purpose of recognizing and minimizing the effects of residual stress on measurement of fracture properties established from specimens where complete stress relief is impractical. It

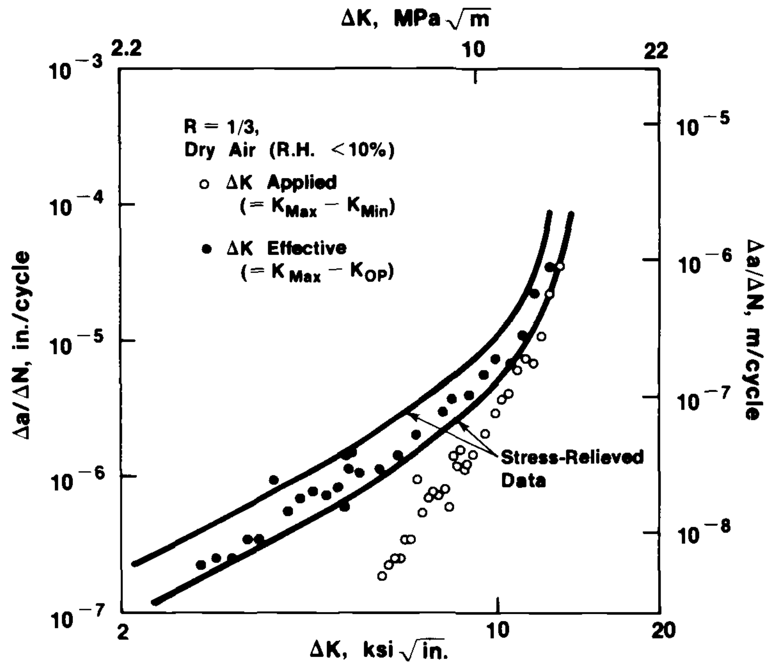

FIG. 14—*Corrected fatigue crack growth rates in nonstress-relieved hand forgings of Material B.*

is recommended that these guidelines be given consideration to the applicable ASTM fracture test method documents.

1. Excessive crack front curvature or irregular crack growth (that is, out of plane fracture) is a tip-off to the likelihood that test results are confounded by residual stress influence.

2. When residual stresses are suspect, local displacement measurements made before and after the machining of the crack starter slot (for example, at the mechanical gage locations in Fig. 5) are useful for detecting the severity of the effect.

3. Residual stresses both parallel and normal to the specimen fracture plane may influence fracture property measurement.

(*a*) Effects of residual stresses normal to the fracture plane can be minimized by selecting the specimen width to plan size ratio (*B/W*) to be small.

(*b*) Effects of residual stress parallel to the fracture plane may produce clamping (or opening) moments which affect the crack-tip stress-intensity factor. The effect of these moments can be minimized by selecting symetrical specimen configurations (for example, selecting the CCT over the CT configuration).

4. Autographic load versus COD traces are useful for the reduction of confounding residual stress influences on fatigue crack growth rate comparisons between materials. These comparisons might best be made on the basis of effective stress-intensity factor range (ΔK_{EFF}) rather than applied ΔK.

Acknowledgments

The support of the U.S. Air Force Materials Laboratory is acknowledged. Contributions to this work by the following collegues are also gratefully acknowledged: R. A. Kelsey and R. S. Barker for sharing their experiences on residual stress measurement in aluminum alloys and products; L. N. Mueller for assistance in statistical interpretation of residual stress measurements; and P. H. Jacobus for his assistance in the test work and data presentation.

J. H. Underwood[1] *and J. A. Kapp*[1]

Benefits of Overload for Fatigue Cracking at a Notch

REFERENCE: Underwood, J. H. and Kapp, J. A., "**Benefits of Overload for Fatigue Cracking at a Notch,**" *Fracture Mechanics: Thirteenth Conference, ASTM STP 743,* Richard Roberts, Ed., American Society for Testing and Materials, 1981, pp. 48–62.

ABSTRACT: Tests are described which measure the effect of compression overload on fatigue crack initiation and growth from a 0.1-mm-radius notch in alloy steel K_{Ic} specimens.

Other tests are described which measure the effect of tension overload on fatigue crack initiation and growth from a 3.4-mm-root-radius notch in similar specimens.

The effect of overload on the number of cycles required for crack growth is described for both types of tests in relation to a residual stress model.

KEY WORDS: overload, fatigue cracking, residual stress, notch, fracture mechanics

Nomenclature

a	Crack depth
Δa	Average crack growth from three points on crack front
Δa_{min}	Minimum value of crack growth at specimen surface
B	Specimen thickness
K	Opening mode stress-intensity factor
K_{Ic}	Plane-strain fracture toughness
K_{max}	Maximum value of K during fatigue loading
K_{min}	Minimum value of K during fatigue loading
N_{i-C}	Number of cycles to Δa = 0.25 mm in compression overload tests
N_{f-C}	Number of cycles to final Δa in compression overload tests
N_{i-T}	Number of cycles to $2c$ = 2.0 mm in tension overload tests
N_{f-T}	Number of cycles to $2c$ = 10.0 mm in tension overload tests
p	Probability that mean values represent same population of data
W	Specimen depth

[1]Materials engineers, U.S. Army Armament Research and Development Command, Large Caliber Weapon Systems Laboratory, Benet Weapons Laboratory, Watervliet, N.Y. 12189.

σ_{max} Maximum stress at notch root due to applied K
ρ Root radius of notch
μ Mean value
σ Standard deviation

There are situations in which a fatigue crack at a notch is required and others in which a fatigue crack is to be avoided. In either case the application of an overload to the structure or specimen containing the notch can be of benefit. When a fatigue crack is required, such as when precracking the specimens used in some fracture tests, a compression overload applied to the notched specimen can result in faster formation of a crack at the root of the notch. Faster precracking is particularly important in testing of brittle materials, because the maximum allowed K-value for precracking is not much above the fatigue threshold, ΔK_{th}, for some brittle materials. One of the objectives of this paper is to describe compression overload tests performed with some fracture toughness specimens and show the effect of overload on fatigue crack initiation and growth from the notch.

When initiation and growth of a fatigue crack should be avoided, such as at a fillet or corner in a loaded structural component, a tensile stress overload applied in the vicinity of the fillet or corner can serve to prevent or delay the initiation and growth of a crack. The second objective here is to describe and analyze laboratory tests which simulate a component with a notch subjected to a tensile stress overload.

Overload to Induce Cracks

A few laboratories apply compression overloads to fracture test specimens in order to save time in fatigue precracking. But the overload procedure and the effect on precracking have not been described in the literature, and the overload procedure is not generally used. This lack of information and use of overloads prompted this effort.

Test Procedure

The general test procedure was the compression overload procedure commonly used in our laboratory when precracking plane-strain fracture toughness, K_{Ic}, specimens. In brief, the procedure is a single compression load applied to the notched K_{Ic} specimen using twice the maximum load to be used in precracking. Details will follow. A total of 30 K_{Ic} specimens was tested. The specimens were the C-shaped geometry described in the ASTM Test for Plane-Strain Fracture Toughness of Metallic Materials (E 399-78) and shown in Fig. 1. The specimens were taken from cylindrical steel cannon forgings of 44-mm inner radius, 85- or 120-mm outer radius.

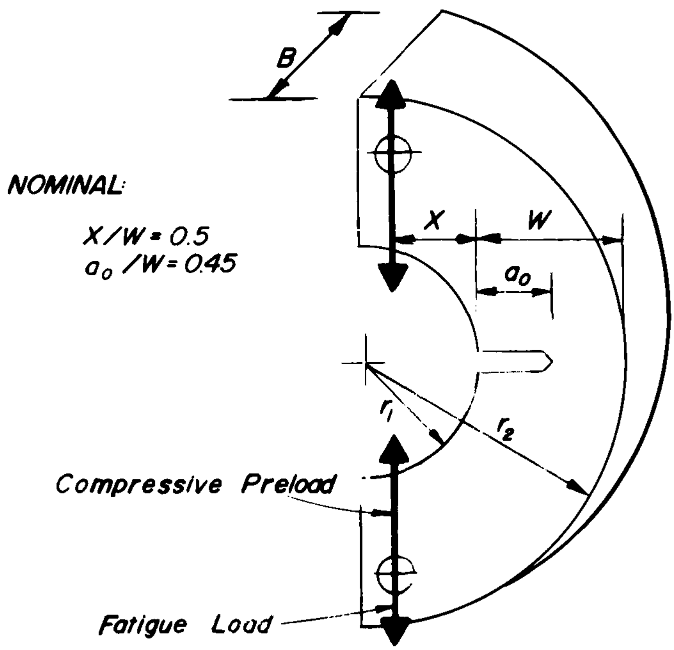

FIG. 1—*Compression overload test specimen.*

The steel is a nickel-chromium-molybdenum-vanadium composition similar to A1S1 4335, heat-treated to a yield strength range of 1150 to 1200 MPa. Table 1 lists some additional test conditions.

Three groups of 10 specimens were tested, as indicated in Table 1. The Group 1 specimens are of thickness B = 25.4 mm and nominal depth W = 42 mm; they were taken in pairs from five forgings. The Groups 2 and 3 specimens are of B = 38.1 mm and nominal W = 74 mm, and they were taken one per forging from 20 forgings. All specimens were tested with as-forged inner and outer diameters, so dimensions vary somewhat. The variation can be noted in the W-values listed in Table 1. Details of the notch tip configuration are a 90-deg included angle with a 0.13-mm root radius as measured on a sampling of specimens using an optical comparitor.

In each group of 10 specimens, five were overloaded, five were not. Using nominal specimen dimensions and the overloads listed in Table 1, the K-values corresponding to the overloads are 86 MPa$\sqrt{\text{m}}$ for Groups 1 and 2 specimens and 66 MPa$\sqrt{\text{m}}$ for Group 3 specimens. Although at the time of the overload there is no crack present and therefore no K-value as strictly defined, we still choose to use K to describe the overloads. We believe it is the best simple description of both the loading and the geometry of a notch overload. The K-values were calculated using the following expression for the C-shaped specimen [1][2]

$$K = \frac{P}{B(W)^{1/2}}[3\,X/W + 1.9 + 1.1\,a/W]$$

$$\times\ [1 + 0.25(1 - a/W)^2(1 - r_1/r_2)]F(a/w) \quad (1)$$

where

$$F(a/W) = \frac{(a/W)^{1/2}}{(1 - a/W)^{3/2}}(3.74 - 6.30\,a/W + 6.32(a/W)^2$$

$$- 2.43(a/W)^3)$$

which applies for $0.2 \leq a/W \leq 1$, $0 \leq X/W \leq 1$, $0 \leq r_1/r_2 \leq 1$. See Fig. 1 for definition of terms. The maximum tension load in fatigue was always one half of the overload, so at the start of the fatigue loading the nominal K_{max} was 43 MPa$\sqrt{m}$ for Groups 1 and 2 and 33 MPa$\sqrt{m}$ for Group 3. The specific values of K_{max} at the start of fatigue loading, including the effects of variations in W, relative loading hole position, X/W, and notch length, a/W, were calculated using Eq 1 and are listed in Table 1. As can be determined from Table 1, W varies by as much as ± 3 percent; the quantities X/W and a/W vary by like amounts. This leads to a variation in K_{max} at the start of fatigue loading of as much as ± 8 percent. For all tests K_{min} was one tenth of K_{max}. Fatigue loading was continued until about 3 mm of crack growth had occurred.

In summary, the tests provide for the determination of the effect of compression overload on fatigue crack initiation from a notch in a K_{Ic} specimen, considering two different specimen sizes and two different levels of overload and fatigue loading. In addition, the effect of overload on the subsequently measured K_{Ic} can be determined.

Results

The results from the compression overload tests are presented in Table 2. For each of the 30 tests, crack growth data, number of fatigue cycles required for growth, and the measured K_{Ic} are listed. The crack growth datum is, first, Δa, the average amount of fatigue crack growth beyond the notch tip, as described in ASTM Method E 399-78. Three measurements, at locations corresponding to ¼, ½, and ¾ B, were made on the fracture surface after the K_{Ic} test and averaged to obtain Δa. Values of Δa vary

[2]The italic numbers in brackets refer to the list of references appended to this paper.

TABLE 1—*Test conditions for compression overload specimens.*

	Specimen No.	Specimen Depth, W, mm	Compression Overload, kN	Starting Fatigue Load, K_{max}, MPa$\sqrt{m}$
Group 1:	42A	42.4	35.0	43.2
	42B	42.4	0	43.7
	34A	41.9	35.0	45.1
	34B	42.4	0	45.2
	25A	42.7	35.0	45.8
	25B	42.4	0	45.1
	43A	43.2	35.0	45.0
	43B	42.1	0	44.7
	28A	42.7	35.0	46.7
	28B	43.2	0	43.9
Group 2:	734	73.9	67.6	43.4
	807	74.9	0	42.4
	839	74.9	67.6	43.2
	842	75.7	0	42.4
	703	74.9	67.6	41.5
	818	74.4	0	42.1
	810	72.4	67.6	44.5
	822	72.4	0	44.5
	875	75.7	67.6	40.4
	931	74.4	0	42.6
Group 3:	851	72.4	51.6	34.7
	865	73.2	0	33.9
	852	74.2	51.6	32.3
	847	72.9	0	33.0
	004	72.4	51.6	35.4
	005	72.4	0	35.4
	943	74.9	51.6	33.8
	663	74.9	0	32.7
	846	74.9	51.6	31.8
	850	76.2	0	30.4

between 2.1 and 3.5 mm. The smaller of the two surface crack growth measurements also was made, divided by Δa, and listed as $\Delta a_{min}/\Delta a$. This ratio provides a quantitative measure of the crack front symmetry; because Δa_{min} is normalized by Δa, the ratio includes little or no effect of the variation in Δa noted in the foregoing. A value of $\Delta a_{min}/\Delta a$ near one corresponds to a relatively straight, symmetrical crack front with no more curvature than the normally observed lagging of the crack front at both specimen surfaces. A lower value of this ratio indicates that the crack front lags more than normal at one surface. In Groups 1 and 2, the specimens with higher K_{max} in fatigue, there appears to be no significant effect of overload on crack front symmetry as measured by $\Delta a_{min}/\Delta a$. In Group 3, the lower K_{max} specimens, there is indeed an effect of overload on symmetry. Without overload, the crack front is much more likely to lag sig-

nificantly at one surface, which causes nonsymmetry and a potentially poor fracture test.

The number of fatigue cycles, N_{i-C}, required to grow the crack to an average Δa of 0.25 mm determined from the two surface measurements and the number of cycles, N_{f-C}, required to grow the crack to the final Δa are listed in Table 2. Note that the difference between these two numbers, $N_{f-C} - N_{i-C}$, is approximately constant for all tests. This means that the test conditions do not greatly affect crack growth from $\Delta a = 0.25$ to the final value, about 3 mm; the effects of the test conditions are apparently on the initiation and early growth of the crack. Considering the N_{f-C} data in Table 2, all three groups of specimens show a significant decrease in N_{f-C} when overload is applied compared with the tests with no overload. This is particularly so for the Group 3 tests at lower K_{max}. The last column of data in Table 2 is the results from K_{Ic} tests; there appears to be no significant effect of overload on K_{Ic}.

Statistical Analysis

To give a quantitative measure of the observed results, some statistical analysis was performed. The effect of overload on three parameters was analyzed; namely, the number of fatigue cycles to initiate and grow the crack to $\Delta a = 3$ mm, N_{f-C}, the crack front shape as measured by $\Delta a_{min}/\Delta a$, and the fracture toughness, K_{Ic}. For each group of specimens the mean, μ, and standard deviation, σ, were determined for specimens with and without overload. These data are given in Table 3. Once the μ and σ are known for the two test conditions in each group, a test statistic can then be calculated which is used to determine the probability that the two means represent the same population of data. To do this it is first necessary to determine if the measured data are normally distributed. The Kolmogorov-Smirnov test [2] was applied to each subgroup of data to test for normality. This test compares the observed distribution with the theoretical normal distribution with the same μ and σ. If the maximum difference between the observed distribution and the theoretical distribution is less than a specified amount for the given specimen size, then it can be stated with a 99 percent confidence level that the observed data are normally distributed. All six subgroups of data met the Kolmogorov-Smirnov criterion.

The test statistic necessary to compare the two means is

$$d = \frac{|\mu_{\text{overload}} - \mu_{\text{no overload}}|}{\sqrt{\sigma^2_{\text{overload}} + \sigma^2_{\text{no overload}}}} \tag{2}$$

where the subscripts correspond to the two test conditions compared. Once d is known we are able to determine the probability with a 99 percent confidence level that the means represent the same population of data through

TABLE 2—*Results of compression overload tests.*

Test Conditions	Specimen No.	Δa Final, mm	$\Delta a_{min}/\Delta a$	N_{i-C}, $\Delta a = 0.25$ mm, kilocycles	N_{f-C}, Final Δa, kilocycles	K_{Ic}, MPa$\sqrt{m}$
Group 1: $W = 42$ *mm*						
$K_{max} = 43$ MPa$\sqrt{m}$						
	42A	3.3	0.57	7	14	159
	34A	3.4	0.68	5	14	148
$K_{overload} = 86$ MPa$\sqrt{m}$	25A	2.3	0.78	5	12	165
	43A	2.1	0.72	5	12	163
	28A	2.2	0.80	6	12	134
	42B	2.8	0.54	11	20	152
	34B	2.8	0.73	11	19	158
$K_{overload} = 0$	25B	2.5	0.82	11	18	149
	43B	3.0	0.85	10	20	148
	28B	3.1	0.73	8	15	137

Group 2: $W = 74$ mm						
$K_{max} = 43$ MPa$\sqrt{m}$						
	734	2.5	0.52	4	11	138
	839	2.7	0.56	4	14	138
$K_{overload} = 86$ MPa$\sqrt{m}$	703	2.6	0.58	4	12	140
	810	2.7	0.47	4	11	141
	875	2.4	0.32	4	13	144
	807	2.5	0.62	8	15	134
	842	2.4	0.32	8	15	154
$K_{overload} = 0$	818	2.6	0.29	8	14	153
	822	3.0	0.60	10	16	136
	931	2.6	0.49	11	16	147
Group 3: $W = 74$ mm						
$K_{max} = 33$ MPa$\sqrt{m}$						
	851	3.0	0.42	10	23	123
	858	2.7	0.47	10	24	133
$K_{overload} = 66$ MPa$\sqrt{m}$	004	2.5	0.52	9	21	126
	943	2.7	0.37	10	24	134
	846	2.4	0.54	11	25	135
	865	2.5	0.10	27	35	141
	847	3.2	0.31	59	66	151
$K_{overload} = 0$	005	3.0	0.04	31	38	137
	663	3.3	0.23	31	42	131
	850	3.5	0.18	70	78	139

TABLE 3—*Summary and statistical analysis of compression overload tests.*

Group	Overload, MPa$\sqrt{m}$	Fatigue, MPa$\sqrt{m}$	Crack Growth $\Delta a_{min}/\Delta a$			Fatigue Cycles N_{f-C} kilocycles			Fracture Toughness, K_{Ic}, MPa$\sqrt{m}$		
			μ	σ	p_a %	μ	σ	p_N %	μ	σ	p_K %
1	86	43	0.71	0.09	98	12.8	1.1	<5	154	13	95
	0	43	0.73	0.12		18.4	2.1		149	8	
2	86	43	0.49	0.10	97	12.2	1.3	<5	140	3	93
	0	43	0.46	0.15		15.2	0.8		145	9	
3	66	33	0.46	0.07	5	23.4	1.5	21	130	5	55
	0	33	0.17	0.11		51.8	19.1		140	7	

the use of "Operating Characteristic Curves" available in the literature [3]. These probabilities are given in Table 3 as p_a, p_N, and p_K, the probabilities related to crack growth, fatigue cycles, and K_{Ic} data, respectively. They indicate that the overload data are a significantly different population and thus overload has a significant effect in regard to (1) crack front shape for the low K_{max} tests, Group 3, and (2) number of fatigue cycles to initiate and grow a crack for all tests. For both of these situations, overload is a benefit, because for (1) overload leads to a more uniform crack front shape, and for (2) it leads to fewer fatigue cycles to grow the crack. In regard to the measured K_{Ic}, for the low K_{max} tests the probability that the overload data and no-overload data are the same population, and thus the probability that overload has no effect on K_{Ic}, is 55 percent. No conclusion is made from this result. However, considering that the mean K_{Ic}-values are different by less than 10 percent, which variation is not uncommon with K_{Ic} tests, this 55 percent probability should cause no alarm.

Overload to Prevent Cracks

A tensile stress overload to the area of the notch in order to prevent the growth of fatigue cracks is, like the compression overload, not generally used. The overpressure of cylindrical pressure vessels in order to prevent crack growth is commonly done and has been studied in our laboratory [4,5]. This process, called autofrettage, involves plastic deformation near the inner radius of the cylinder which results in compressive residual stress at the inner radius. This prevents the growth of fatigue cracks. Our experience with autofrettage led us to the work here with tension overloads applied to notches.

Test Procedure

Four specimens similar to the compact fracture toughness specimen described in ASTM Method E 399-78 were made as shown in Fig. 2. The specimens were taken from a cannon forging similar to that described earlier, except with a yield strength of 1040 MPa. The test procedure was, first, the application to two of the specimens of a tension overload, then the fatigue loading of all specimens at a maximum load of 15.6 kN. This would correspond to a K_{max} of 56 $\text{MPa}\sqrt{\text{m}}$ if a crack were present in the specimen rather than a notch. We choose to use K to describe the loading in the tests because K includes the effect of notch length in addition to the effect of load level; the full meaning of a K-value is not intended since there is no sharp crack present at the start of the tests. The value of K_{min} during fatigue loading was always one tenth of K_{max}. The initiation and growth of a fatigue crack at the notch root was monitored using a magnetic particle inspection procedure and a 10-power telescope. Crack length along

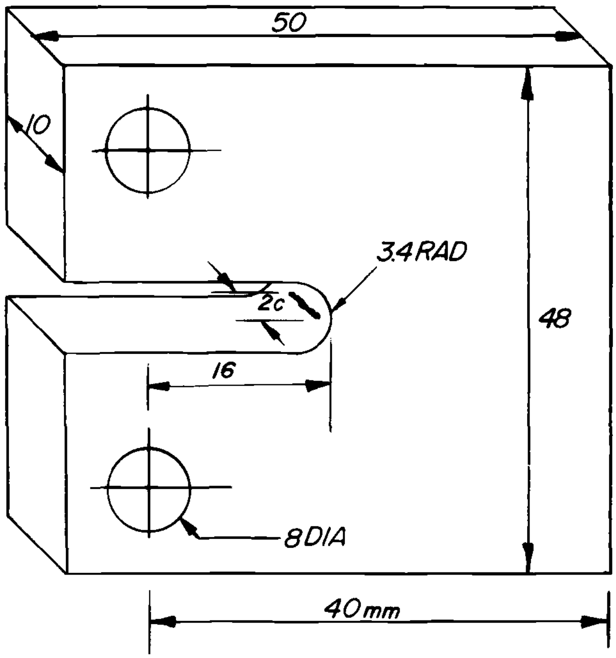

FIG. 2—*Tension overload test specimen.*

the notch root, $2c$, was measured, as indicated in Fig. 2; measurements of and changes in $2c$ as small as 0.5 mm could be detected.

Results

Table 4 gives the results of the tension overload tests. Specimens 11-1 and 11-2 had no overload, that is, an overload ratio of one. With no overload, 65 000 cycles were required to initiate and grow a fatigue crack to a $2c$ length of 2 mm, and an average of 18 000 additional cycles was required to grow the crack across the entire 10-mm thickness of the specimen.

With an overload of 1.5 times the K_{max} used in fatigue, the number of fatigue cycles required for the same amount of crack growth is increased by about a factor of 2.5. More significantly, with an overload ratio of 2.0, the fatigue life may be extended indefinitely; the test was stopped after 1 000 000 cycles with no indication of crack initiation.

Even though only four specimens were tested, the large difference in the test results clearly leads to the conclusion that, at least for the type of material and geometry tested, tension overload of large enough magnitude can produce manyfold increases in the fatigue life of notched components.

TABLE 4—*Results of tension overload tests.*

Specimen No.	$K_{overload}$, MPa$\sqrt{m}$	$K_{overload}/K_{max}$	N_{i-T}, for $2c = 2$ mm, kilocycles	N_{f-T}, for $2c = 10$ mm, kilocycles
11-1	56	1.0	65	84
11-2	56	1.0	65	82
11-3	84	1.5	194	214
11-4	112	2.0	>1000	>1000

Analysis

Analysis of the effect of overload on crack growth from a notch can serve to identify the basic source of the effect. The following may help to accomplish this.

It is known that the primary effect of overpressure on fatigue crack growth from the inner radius of cylinders is the effect of residual stress referred to earlier. It is our contention that residual stress is the basic source of overload effects on fatigue crack growth from a notch. To test this belief, the maximum stress at the notch root during fatigue loading is calculated, modified to account for residual stress, and used to estimate N_f for comparison with measured N_f.

Paris and Sih [*6*] give a useful relation for calculating the maximum stress, σ_{max}, at the root of a notch with radius ρ. The relation is exact only for $\rho \rightarrow 0$, but it can be used to estimate σ_{max} over a range of ρ, and it is in terms of the applied K as determined from overall specimen dimensions and loading

$$\sigma_{max} = \frac{2\,K_{app}}{\sqrt{\pi\rho}} \tag{3}$$

Values of K_{max} in fatigue, ρ, and the calculated σ_{max} from some of the tests are given in Table 5. For the compression tests the values of σ_{max} are very high due to the small ρ. However, this estimate of σ_{max} is still useful as a comparative estimate of the stress at the notch, including as it does both global and local information, K_{app} and ρ, respectively.

The estimate given in Table 5 of residual stress due to overload, σ_R, is simply 0.7 times the yield stress for all cases except Specimen 11-3. The rationale for this is that there is sufficient overload to produce a residual stress approaching the yield strength; the 0.7 factor is due to variations in the yield behavior known to occur in the type of steel used here, such as the Bauschinger effect [7], which is a lowering of the yield strength following yielding in the opposite sense. For Specimen 11-3, which had a smaller

TABLE 5—*Comparison of overload tests with analysis.*

	K_{max} MPa$\sqrt{m}$	ρ mm	σ_{max} MPa	σ_R MPa	$\left[\frac{\sigma_{max} + \sigma_R}{\sigma_{max}}\right]^3$	$\frac{N_f \text{ no overload}}{N_f \text{ overload}}$
Compression overload:						
Groups 1,2	43	0.13	+4260	+820	1.70	1.34
Group 3	33	0.13	+3270	+820	1.96	2.21
Tension overload:						
Specimen 11-3	56	3.4	+1090	−420	0.23	0.39
Specimen 11-4	56	3.4	+1090	−730	0.04	<0.08

overload ratio of 1.5, the σ_R-value shown is 0.7 times the difference between the overload stress, 1640 MPa, and the yield strength, 1040 MPa.

A hypothetical sketch of the applied and residual stress distributions near the notch is shown in Fig. 3. As is shown, the amount of crack growth is considered small relative to the depth of the stress distributions. So the maximum values of stress, that is, σ_{max} plus σ_R, are used to analyze the effect of overload on N_f. Since N_f in the tests was in the range of 10^4 to 10^5 cycles, the Paris-type expression for this material in this da/dN range [5] can be used

$$da/dN = 6.52 \times 10^{-12} \Delta K^3$$

with da/dN in m/cycle and K in MPa$\sqrt{m}$. Based on this cubic relation, a stress parameter is calculated for comparison with the ratio of N_f with no overload to N_f with overload. This stress parameter, the cube of the inverse ratio of σ_{max} with no overload to σ_{max} with overload, is compared in Table 5 with the N_f ratio measured in the tests. The rationale of this comparison is that N should vary inversely with the third power of σ, provided that the effects of overload are included in both the calculation of σ and the measurement of N. The comparison in Table 5 of the σ and N_f parameters is good, considering the inherent variation in fatigue data. This supports our contention that it is the residual stress due to overload which controls the fatigue crack growth from a notch.

Applications and Concluding Remarks

The compression overload tests showed that when a crack is required, an overload before fatigue loading is of clear benefit, both in reducing the number of cycles required to grow a crack and reducing the variation in crack front shape. To obtain these beneficial effects, the overload-to-maximum fatigue load ratio must be high enough that the overload residual

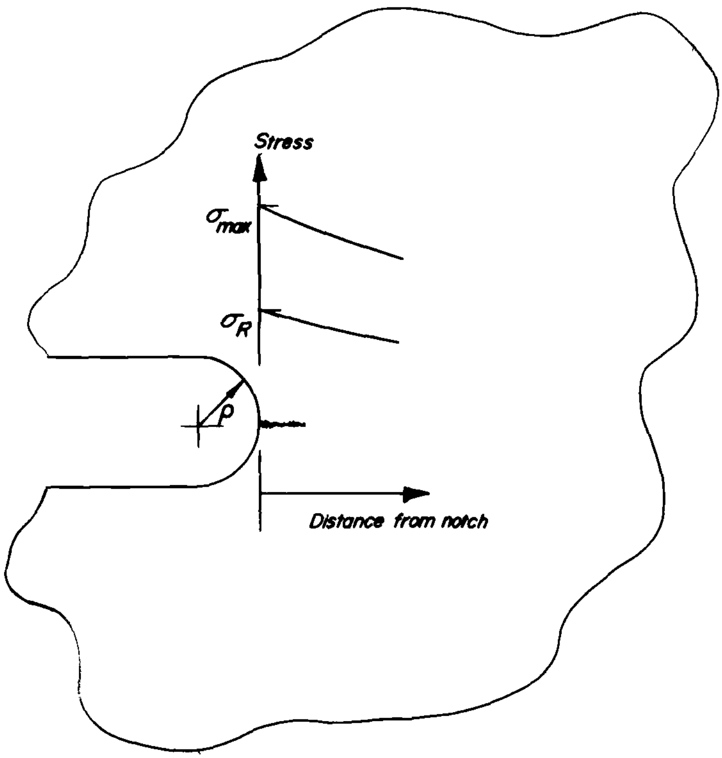

FIG. 3—*Sketch of stresses near a notch.*

stress is not overwhelmed by the applied stress on the first fatigue load cycle. An overload ratio of 2.0 was adequate for the tests here. A related concern is that the overload is not too large. Calculation of the plastic zone size using Irwin's formula

$$r_y = \frac{1}{6\pi}\left[\frac{K_{\text{overload}}}{\sigma_{\text{yield}}}\right]^2 \tag{4}$$

can check for an excessive overload by comparing r_y with the amount of crack growth following overload. In the tests here, for example, the largest r_y was 0.3 mm, compared with 3-mm crack growth, so the overloads were not too large.

The tension overload tests showed the clear benefit of overload in increasing the fatigue life of a notched specimen. A factor of 2.5 increase in life was seen with an overload-to-maximum fatigue load ratio of 1.5, and a factor of more than 12 increase in life was seen with an overload ratio of

2.0. In the use of tension overloads the analysis and results here indicate that two conditions may be necessary for a significant increase in fatigue life: an overload of at least twice the maximum fatigue load and an overload which produces an indicated tension stress at the notch root of at least twice the material yield strength. The concern of an excessive tension overload can be met by observing the load-deflection behavior of the specimen during overload or by calculating the bending limit load of the remaining section of the specimen ahead of the notch.

Acknowledgments

We are pleased to acknowledge the help of R. T. Abbott, F. A. Heiser, and J. J. Zalinka in accomplishing this work.

References

[*1*] Kapp, J. A., Newman, J. C., and Underwood, J. H., *Journal of Testing and Evaluation*, Vol. 8, No. 6, Nov. 1980, pp. 314-317.
[*2*] Bowker, A. H. and Lieberman, G. J., *Engineering Statistics*, Prentice-Hall, Inc., Englewood Cliffs, N.J. 1972, pp. 454-458.
[*3*] Bowker, A H. and Lieberman, G. J., *Engineering Statistics*. Prentice-Hall, Englewood Cliffs, N.J., 1972, pp. 225-228.
[*4*] Davidson, T. E., Kendall, D. P., and Reiner, A. N., *Experimental Mechanics*, Vol. 3, Nov. 1963, pp. 253-262.
[*5*] Underwood, J. H. and Throop, J. F. in *Part Through Crack Fatigue Life Prediction, ASTM STP 687*, J. B. Chang, Ed., American Society for Testing and Materials, 1979, pp. 195-210.
[*6*] Paris, P. C. and Sih, G. C. in *Fracture Toughness Testing and Its Applications, ASTM STP 381*, American Society for Testing and Materials, 1965, p. 34.
[*7*] Milligan, R. V., Koo, W. H., and Davidson, T. E., *Journal of Basic Engineering*, Vol. 88, June 1966, pp. 480-488.

A. U. de Koning[1]

A Simple Crack Closure Model for Prediction of Fatigue Crack Growth Rates Under Variable-Amplitude Loading

REFERENCE: de Koning, A. U., "**A Simple Crack Closure Model for Prediction of Fatigue Crack Growth Rates Under Variable-Amplitude Loading,**" *Fracture Mechanics: Thirteenth Conference, ASTM STP 743*, Richard Roberts, Ed., American Society for Testing and Materials, 1981, pp. 63–85.

ABSTRACT: A model for the prediction of growth rates of fatigue cracks in aluminium alloys is presented. The model is based on an approximate description of the crack closure behavior and can be used to predict effects of crack growth acceleration and retardation observed experimentally under variable-amplitude loading.

A computer program was developed for analysis of fatigue crack growth. It was used to analyze the effect of certain parameter variations in a flight simulation load spectrum on the crack growth rate. For 7075-T6 thin sheet material the results are compared with experimental data.

KEY WORDS: fatigue crack growth, flight simulation loading, TWIST, variable-amplitude loading, delay effects, crack growth model, crack closure, crack opening, delay switcher, plane-strain/plane-stress transition

Aircraft structures have to satisfy certain requirements with regard to strength, stiffness and weight. These requirements have led to relatively high design stress levels in structures made of high-strength aluminium alloys. In view of the loading conditions and the increasing lifetimes, fatigue damage cannot always be prevented at all locations. In general, a limited fatigue life of some structural components has to be accepted. In these circumstances there is an urgent need for analytical models that allow a prediction of growth rates of cracks in structures subjected to service loading conditions and, hence, of an assessment of the structural fatigue life.

[1]Research engineer, Structures and Materials Division, National Aerospace Laboratory, NLR, The Netherlands.

It is known from the theory of linear fracture mechanics that the state of stress and deformation near a crack tip can be characterized by the stress-intensity factor K. In the mid-1960's fracture mechanics principles were introduced in the analysis of fatigue crack growth by relating the crack growth rate da/dn to the stress-intensity range ΔK. Careful measurements of growth rates have revealed that da/dn not only depends on ΔK but also on the stress ratio, $R = \sigma_{min}/\sigma_{max}$. Several crack growth laws were proposed to account for the effect of R. Using these laws crack growth rates can be predicted accurately for some simple crack configurations in specimens subjected to constant-amplitude loading. However, for more complex loading sequences such as flight simulation loading, the results are conservative by a factor 3 to 10 or more. Nowadays, it is known that these disappointing experiences were a result of ignoring plastic deformations near the crack surface and near the crack tip. Analytical models [*1-4*],[2] finite-element [*5,6*], and experimental techniques [*7,8*] were used to demonstrate that permanent deformations near the crack tip can give rise to a considerable reduction of the part of the load cycle during which the crack is effectively open. Thus, the crack is physically present only for loads higher than the crack opening level. Crack growth models have been developed that accounted for the plasticity effects by considering crack opening behavior corresponding to different modified versions of the Dugdale strip yield model [*9*]. In view of the shape of the plastic zone, application of these models to aluminium sheet materials seems to be less obvious than it is for some steel alloys. Nevertheless, the results obtained by Dill and Saff [*4*], Hardrath et al [*10*], and Führing [*11*] indicate that crack growth rates predicted using these models can be quite accurate even for aluminium alloys.

However, in the application to thin sheet material subjected to rather extensive flight simulation loading histories the strip yield approach has some disadvantages. In the first place, a model for the plane-strain/plane-stress transition (which has to be modeled in an application to thin sheet materials) is not yet available. Further, in a cycle-by-cycle analysis of extensive loading sequences, the computer load becomes so excessive that the analysis must be restricted to a computation of average values for the crack growth rate at a limited number of crack lengths. Then the risk of overlooking some interaction effects occurring at crack lengths not considered in the analysis cannot be ignored. For these reasons a new and relatively simple model accounting for load interaction effects as well as for the plane strain to plane stress transition was developed at the National Aerospace Laboratory (NLR) in The Netherlands. The model has been used successfully in an analysis of fatigue crack growth in centrally cracked sheet specimens cut from 7075-T6 sheet material. The sheet thickness is 2 mm. For this configuration the effect of some parameter variations in the load spectrum on the crack growth rate was studied. The results are compared

[2]The italic numbers in brackets refer to the list of references appended to this paper.

with experimental data obtained previously [16] for the same configuration and material. It is to be noted that the model is still under development. Applications to different configurations and materials are planned for the near future. The results presented in the present paper were obtained for one configuration in 7075-T6 material and it is not known whether the conclusions can be generalized to cover other materials as well.

Fatigue Crack Growth Model

The growth model is based on a cycle-by-cycle analysis of crack growth, that is

$$a = a_0 + \sum_i \Delta a_i \tag{1}$$

where Δa_i is the amount of crack growth associated with the load increment $\sigma^{i+1} - \sigma^i$. It is assumed that crack growth occurs only in the upward part of the load cycles. Moreover, the principles of fracture mechanics are adopted, and crack growth is related to the variation of the effective stress-intensity factor $\Delta K_{\text{eff}}{}^i$. These assumptions can be written as

$$\Delta a_i = 0 \quad \text{if } \Delta\sigma^i \leq 0$$

and

$$\Delta a_i = f(\Delta K_{\text{eff}}{}^i) \quad \text{if } \Delta\sigma^i > 0 \tag{2}$$

where, $\Delta\sigma^i = \sigma^{i+1} - \sigma^i$. The crack is assumed not to grow during the downward part of the load cycle. However, in an analysis of the deformations near the crack tip, this part of the cycle plays an important role, as will be shown later. The growth function relates the increment of crack growth to the range of the effective stress-intensity factor. This relation is assumed to be a material law. The form assumed for f is not essential for the model. The material law adopted for the 7075-T6 material is specified in a later section. According to the theory of linear fracture mechanics the stress-intensity range is related to the load range. For the part of the load cycle during which the crack is open, this yields

$$\Delta K_{\text{eff}}{}^i = \alpha \Delta\sigma_{\text{eff}}{}^i \sqrt{\pi a} \tag{3}$$

where α accounts for the effect of free edges. The effective load range $\Delta\sigma_{\text{eff}}{}^i$, that is, the part of the upward part of the cycle for which the crack is open, needs further specification. By definition

$$\begin{aligned}
&\Delta\sigma_{\text{eff}}{}^i = \sigma^{i+1} - \sigma^i \quad \text{if } \sigma_{\text{op}} \leq \sigma^i \\
&\Delta\sigma_{\text{eff}}{}^i = \sigma^{i+1} - \sigma_{\text{op}} \quad \text{if } \sigma^i < \sigma_{\text{op}} < \sigma^{i+1} \\
&\Delta\sigma_{\text{eff}}{}^i = 0 \quad \text{if } \sigma_{\text{op}} \geq \sigma^{i+1}
\end{aligned} \tag{4}$$

where σ_{op} stands for the crack opening stress. It is evident that in the present model the crack opening stress governs the effective part of the stress range. In particular, it is possible that no growth at all occurs during a cycle, namely, when $\sigma_{op} \geq \sigma^{i+1}$. To determine the crack opening stress level a model for crack opening must be formulated. As mentioned in the Introduction, plasticity effects play a dominant role in crack closure and crack opening. In the next section two plasticity effects are discussed, namely

1. in front of the crack tip, and
2. in the wake of the growing fatigue crack.

Using the results of this discussion a crack opening model is formulated.

Effects of Plastic Deformation on Crack Opening Behavior

In this section two aspects of plastic deformation near the crack tip are discussed in a qualitative way. First, the effect of plastic deformations in front of the crack tip are studied. It is noted that linear elastic fracture mechanics (LEFM) predicts stress and strain fields that are singular at a sharp crack tip. However, the yield strength of the material is limited and, therefore, a yield zone is present near the tip of a loaded crack. On the basis of this concept, any change of the state of loading will lead to additional plastic deformations near the tip. For the sake of convenience the presence of a fictitious initial fatigue crack is assumed in this analysis. This crack has grown at a mean stress level and load amplitude that left negligible plastic deformations along the crack surface behind the tip.

To the initial situation sketched in Fig. 1 a spike load is applied. As a result a zone of plastically deformed material is created at the crack tip and inside this zone the material is loaded from the initial state to the yield limit. With respect to additional loading of material that has been loaded to the yield limit the incremental stiffness is smaller than the stiffness of material that is behaving purely elastically. For this reason the crack opening displacements (COD's) near the tip are larger than predicted by LEFM theory. This result is shown in Fig. 1.

Upon subsequent unloading a zone of material, yielding in reverse is

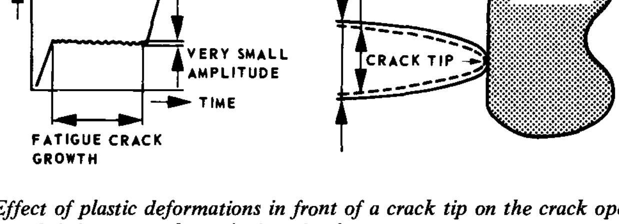

FIG. 1—*Effect of plastic deformations in front of a crack tip on the crack opening displacements. The crack is loaded to the spike load level.*

created. Inside this zone the material is loaded additionally from the positive yield limit at the spike load level to the negative yield limit. This implies that with respect to reversed plastic flow the material can carry approximately twice the load increment observed for plastic flow in virgin material. Therefore the zone of reversed plastic flow is much smaller than the primary plastic zone and in the unloaded state the crack is still open near the tip [*17*]. In Fig. 2 this effect is illustrated. For this state compressive loads have to be applied to close the crack. Thus, after application of the spike load the crack closure stress has decreased from zero to a negative value. Further loading of the closed crack will not noticeably change the state of plastic deformation, and the stress level at which in a next-load cycle the crack is opened is essentially similar to the crack closure stress. *In general, it can be concluded that plastic deformations in front of the crack tip tend to increase the crack opening displacements. A reduction of the crack opening stress occurs.*

As a second important aspect, the effect of plastic deformations left in the wake of a growing fatigue crack is considered. This is done in the following way. After application of the overload-underload combination the fictitions low-amplitude fatigue test is continued. Additional plastic deformations associated with the fatigue loading sequence can be kept small by varying the mean load level according to the crack opening stress. The precise load levels are selected in such a way that the additional plastic deformations associated with fatigue crack growth can be safely ignored. It is seen that the spike load plastic zone is situated at a fixed position. Its location can be characterized by the position of the crack tip at the time the spike load was applied, that is, at a distance, a^n, measured from the center of the crack. As a result of the fatigue loads the crack grows into the plastic zone, and after crack growth over a distance equal to the primary plastic zone size, D^n, the crack tip is situated at the boundary of this zone. After further continuation of the test the crack tip is advancing in virgin material again.

As shown in Fig. 3, at this stage the plastic deformations associated with the spike load have become visible in the form of a hump located a distance a^n from the center of the crack. The width of the hump corresponds to the

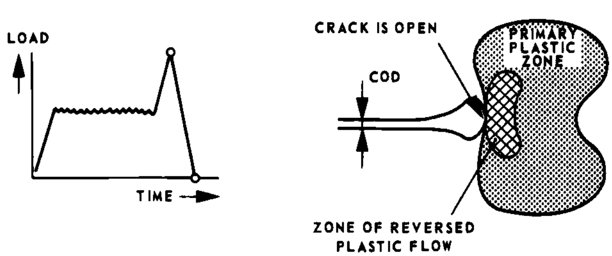

FIG. 2—*Effect of plastic deformations in front of the crack tip on the crack opening displacements. Unloading the spike load level.*

primary plastic zone size, D^n. Moreover, reversed plastic flow due to unloading the spike load has caused a reduction of the hump. It was demonstrated by finite-element computations [12] that the area affected is of the same order of magnitude as the zone of reversed plastic flow. It is seen that the presence of the hump has locally decreased the COD's. Thus, the hump opening stress is larger than the crack opening stress in the case of purely elastic material behavior. *Clearly, plastic deformations left in the wake of a growing fatigue crack tend to increase the crack opening load.*

From the foregoing considerations it follows that plastic deformations in front of the crack tip tend to increase the COD's whereas permanent deformations left in the wake of a growing crack tend to reduce them. With respect to the crack opening stress level the opposite tendency is observed.

The extreme situations discussed in the foregoing are fictitious. In general, plastic deformations are observed in front of the crack tip as well as in the wake of an advancing crack tip. Thus the crack closure level will be a result of competition between the two plasticity effects. Using experimental and finite-element techniques the combined effect was investigated for a single spike load-underload combination. On the basis of these results and the insights obtained from the qualitative considerations presented in the preceding, a crack opening model is formulated in the next section.

Crack Opening Model

Introduction

It was shown that fatigue crack growth after application of a spike load will reveal a hump on the crack surface. The hump is blunted by reversed plastic flow due to application of an underload. In order to quantify the effect of hump formation on the behavior of the crack opening stress, the loading sequence used in the previous section was analyzed also by means of the finite-element method [12]. Again, plastic deformations are introduced by application of a spike load-underload combination. In Fig. 4 the loading sequence and the crack-tip situation are shown. Subsequent fatigue crack growth, $a > a^n$, was analyzed by disconnecting finite elements at the crack tip. During growth of the crack the load level was varied in such a way that no additional plastic deformation was observed.

At different crack lengths the hump opening stress was calculated. The results are presented schematically in Fig. 5. Initially, the stress level at which the set of humps breaks contact is nearly constant. After some growth the crack tip intersects the boundary of the plastic zone: then $a = a^n + D^n$. In this situation the opening stress level is still 70 percent of the initial value at $a = a^n$. With regard to further growth of the crack the opening stress level decreases more sharply. The finite-element results tend to zero for larger crack sizes.

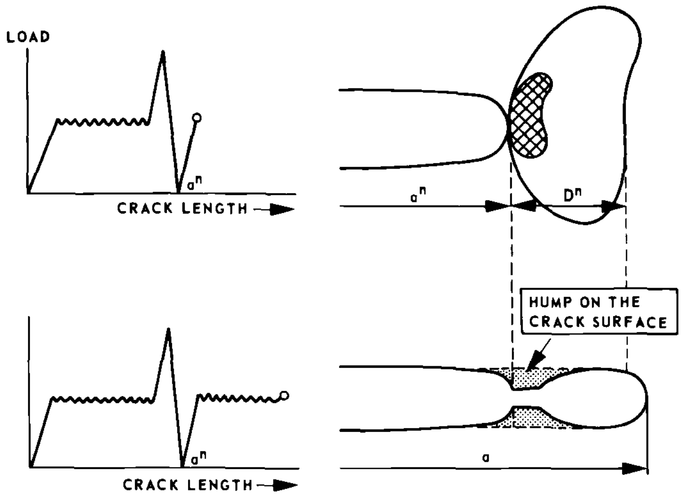

FIG. 3—*Effect of plastic deformation left in the wake of a growing fatigue crack.*

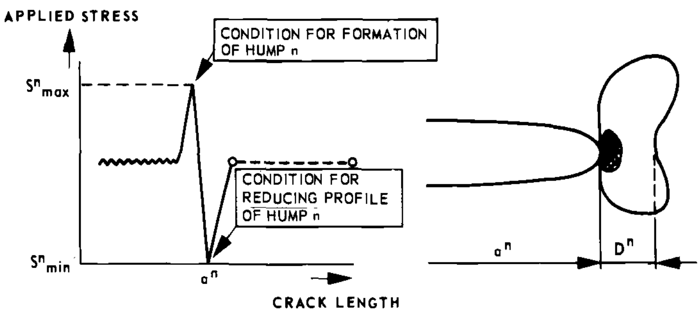

FIG. 4—*Loading sequence used to analyze the behavior of the hump opening stress and the crack tip situation after application of a spike load-underload combination.*

A similar crack opening behavior was observed experimentally by Schijve et al [*8*]. It is clear that in these experiments plastic deformations resulting from the fatigue load cycles have some effect. Nevertheless, for crack sizes smaller than $a^n + D^n$ the same tendencies were observed.

Model for a Description of the Hump Opening Behavior

In the model the hump opening behavior, sketched in Fig. 5, is approximated using a "delay" switch. The switch is set *on* after application of a spike load and set *off* if the crack has grown through the spike load plastic zone. In this way the opening stress is switched from zero to a positive value $S_{op}{}^n$ if a

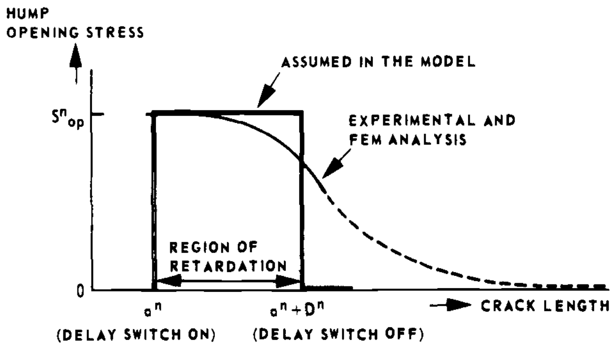

FIG. 5—*Illustration of the hump opening behavior as observed experimentally and by the finite-element method. The behavior assumed in the model is indicated also.*

spike load $S_{max}{}^n$ of level n is applied. Further, it is assumed that the opening stress level $S_{op}{}^n$ depends on the load $S_{max}{}^n$ applied to create the hump and on the minimum stress $S_{min}{}^n$ experienced by that hump afterwards, that is

$$S_{op}{}^n = g\,(S_{max}{}^n, S_{min}{}^n) \quad \text{if } a^n < a < a^n + D^n \tag{5a}$$

$$S_{op}{}^n = 0 \quad \text{if } a > a^n + D^n \tag{5b}$$

where g is the hump opening function. As crack closure and crack opening depend on the plastic deformation behavior of the material, the function g in principle will be different for different materials. With regard to the functional behavior of $S_{op}{}^n$ the following observations can be made:

1. When a $S_{min}{}^n$ is encountered of a lower level than met before, the hump is flattened further and, consequently, it opens at a lower stress, so $S_{op}{}^n$ decreases with $S_{min}{}^n$, that is

$$\partial S_{op}{}^n / \partial S_{min}{}^n > 0$$

2. The size of the hump increases with the load level $S_{max}{}^n$ that created the hump. The same goes for the opening stress $S_{op}{}^n$. It follows that

$$\partial S_{op}{}^n / \partial S_{max}{}^n > 0$$

To describe the behavior of the 7075-T6 material a form similar to Elber's [*13*] function was determined empirically from constant-amplitude and simple spike load test data. The specimens and material are the same as described in a later section.

For different overload-underload combinations the delays in subsequent constant-amplitude fatigue crack growth were measured. The present model predicts that crack arrest (defined by $\Delta N \geq 200$ kc) occurs if the maximum load in the constant-amplitude load sequence is smaller than the hump opening stress level. Using an extrapolation technique the maximum underload that causes crack arrest was determined for some given overloads and constant-amplitude fatigue load sequences. Then, for these particular overload-underload combinations the hump opening stress simply follows from the maximum stress applied in the constant-amplitude test.

The polynomial function adopted for this study is given by

$$g(S_{max}{}^n, S_{min}{}^n) = S_{max}{}^n\,(-0.4R^4 + 0.9R^3 - 0.15R^2 + 0.2R + 0.45) \quad \text{if } R > 0$$

and

$$g(S_{max}{}^n, S_{min}{}^n) = S_{max}{}^n\,(0.2R + 0.45) \quad \text{if } -0.5 \leq R \leq 0 \tag{6}$$

where R denotes the load or stress ratio $S_{min}{}^n/S_{max}{}^n$. The relation between $S_{op}{}^n/S_{max}{}^n$ and R is plotted in Fig. 6. In the same figure the condition for no crack closure is indicated by the dotted line $\sigma_{op} = \sigma_{min}$.

Effect of Application of Underloads on the Hump Opening Stress

It was stated that a hump n can be reduced by application of underloads and in Eq 5*a* it was assumed that $S_{min}{}^n$ is the minimum stress experienced by the hump. Clearly, application of a more severe underload causes a further flattening of the hump and thus the hump opening stress has changed. This effect is illustrated in Fig. 7. As a result of application of $S_{max}{}^n$ a hump n is created. The hump opening stress is determined by the value of the underload $S_{min,1}{}^n$. According to Eq 5*a* it follows that

$$S_{op}{}^n = g\,(S_{max}{}^n, S_{min,1}{}^n)$$

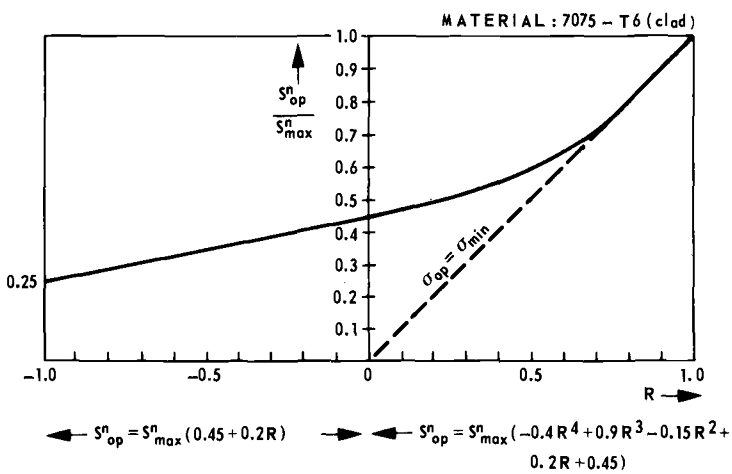

FIG. 6—*Hump opening stress plotted in relation to the stress ratio* $R = S_{min}{}^n/S_{max}{}^n$.

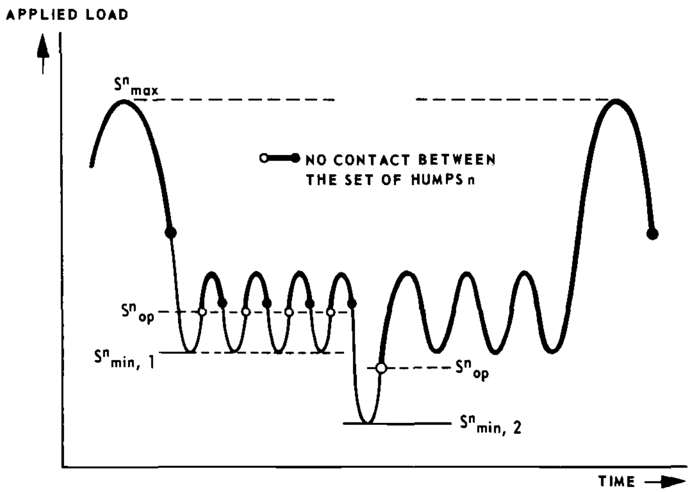

FIG. 7—*Effect of underloads on the hump opening behavior. The hump is created at* $S_{max}{}^{n}$, *flattened by application of* $S_{min,1}{}^{n}$, *and, later on, flattened by* $S_{min,2}{}^{n}$.

This level is constant provided that the "delay" switch is not set *off* and no "more severe" underload is applied. Thus, application of underload $S_{\min,2}{}^{n}$ ($<S_{\min,1}{}^{n}$) changes this state. According to Eq 5*a* the new value of the opening level is given by

$$S_{\rm op}{}^{n} = g\ (S_{\max}{}^{n},\ S_{\min,2}{}^{n})$$

This illustrates the limited memory of the material: as a result of application of $S_{\min,2}{}^{n}$ the value of $S_{\min,1}{}^{n}$ is erased from the memory of the material.

Definition of the Crack Opening Stress

So far, the considerations have been restricted to the opening behavior observed after application of a single spike load-underload combination. Variable-amplitude loading can be considered as a sequence of such combinations. In general, the number of load levels in the spectrum is limited. Application of the present model implies that one delay switch per load level is introduced. Each switch n accounts for the opening behavior of one set of humps created by application of that particular load level.

The crack is assumed to be closed as long as one or more of the humps is in contact with its counterpart on the opposite crack surface. Then the crack is not completely closed physically but the effective crack length at the crack tip is relatively small. The stress-intensity ranges associated with this effective crack length can be ignored when compared with the stress-intensity range calculated for the opened crack at a positive load excursion.

The crack is opened if all humps have lost contact. The hump that last lost contact determines the crack opening stress σ_{op}, that is

$$\sigma_{op} = \max (S_{op}{}^n) \tag{7}$$

where $S_{op}{}^n$ is the opening stress level at which hump n breaks contact. Obviously, to determine σ_{op}, the hump opening stresses must be known for all significant humps. In Fig. 8 the crack opening behavior is demonstrated. In this example, it is assumed that three humps are significant. One after another, the humps are opened. Hump 3 is the last to lose contact and, therefore, the crack opening stress σ_{op} equals $S_{op}{}^3$.

"Limited Memory" Properties of the Model

The introduction of delay switches already demonstrates some of the "limited memory" properties of the present model. Using the loading sequence presented in Fig. 9 some other properties are discussed hereafter.

To indicate parts of load cycles for which the crack is open and propagating, the load sequence is also plotted versus the crack length. From this sequence it is seen that the first hump is created by application of $S_{max}{}^1$ and, subsequently, flattened by $S_{min}{}^1$. The opening stress $S_{op}{}^1$ of this hump is given by Eq 5. It follows that

$$S_{op}{}^1 = g\,(S_{max}{}^1, S_{min}{}^1)$$

Then the effective stress range $\Delta\sigma$ for the next cycle is given by

$$\Delta\sigma_{eff}{}^1 = S_{max}{}^2 - S_{op}{}^1$$

The second hump is created by application of $S_{max}{}^2$. This hump has not experienced $S_{min}{}^1$, but in the next cycle it is flattened by $S_{min}{}^2$. Thus the opening stress of this hump is given by

$$S_{op}{}^2 = g\,(S_{max}{}^2, S_{min}{}^2)$$

The first hump has experienced a minimum stress $S_{min}{}^1$. Application of $S_{min}{}^2$ will not produce a further reduction of this hump provided that $S_{min}{}^2 \geq S_{min}{}^1$.

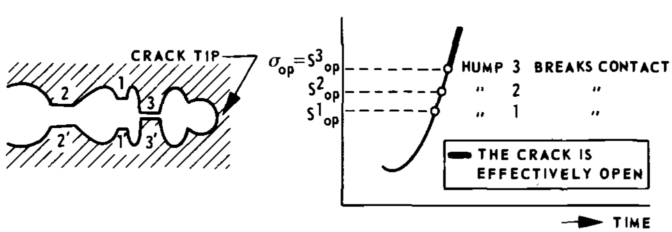

FIG. 8—*Opening behavior of a crack tip in the case of three significant humps on the crack surface.*

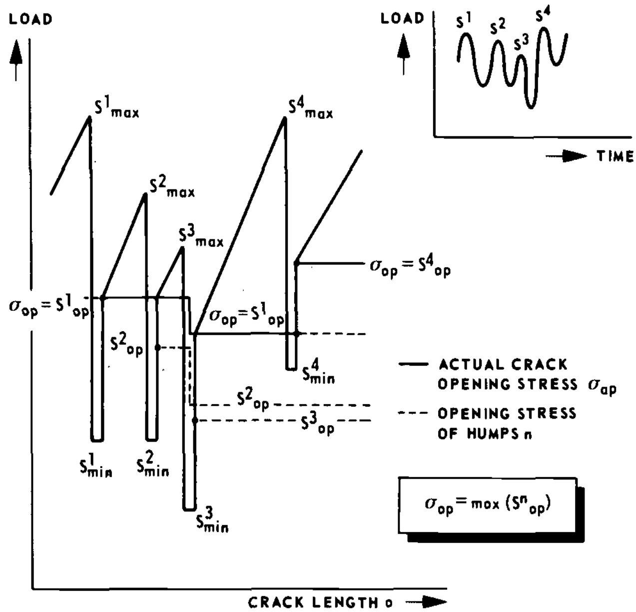

FIG. 9—*Examples of hump and crack opening behavior.*

Therefore the opening stress of the first hump, denoted by $S_{op}{}^1$, is the same in the second cycle. According to the definition of the crack opening stress (Eq 7) both humps (and also the crack surfaces) break contact if the applied load is greater than $S_{op}{}^1$. It follows that $\sigma = S_{op}{}^1$. The effective stress increment in the second cycle is given by

$$\Delta\sigma_{eff}{}^2 = S_{max}{}^3 - \sigma_{op} = S_{max}{}^3 - S_{op}{}^1$$

A third hump is created by application of $S_{max}{}^3$. The subsequent negative load increment $S_{max}{}^3 - S_{min}{}^3$ flattens all three humps because $S_{min}{}^3 < S_{min}{}^2$, and $S_{min}{}^3 < S_{min}{}^1$. The hump opening stresses for the next positive load increment, $S_{max}{}^4 - S_{min}{}^3$, are, respectively,

$$S_{op}{}^1 = g\,(S_{max}{}^1, S_{min}{}^3) \qquad \text{(update } S_{op}{}^1\text{)}$$

$$S_{op}{}^2 = g\,(S_{max}{}^2, S_{min}{}^3) \qquad \text{(update } S_{op}{}^2\text{)}$$

$$S_{op}{}^3 = g\,(S_{max}{}^3, S_{min}{}^3)$$

and according to Eq 7, the crack is fully opened at a level corresponding to the new value of $S_{op}{}^1$, this being the highest opening stress level. It is concluded that the hump created first is still dominant, that is, $\sigma_{op} = S_{op}{}^1$

Suppose that the maximum load applied in the next cycle $S_{max}{}^4$ is greater than all maximum loads $S_{max}{}^1$, $S_{max}{}^2$, and $S_{max}{}^3$ applied previously. It will be shown that the hump created by application of S_{max}^4 dominates the effect of Humps 1, 2, and 3. Therefore, two subsequent negative load steps will be analyzed. In the first place $S_{min}^4 \geq S_{min}^3$ gives $S_{op}^4 \geq S_{op}^1$ and, according to Eq 7, Hump 4 becomes dominant. On the other hand, if $S_{min}^4 < S_{min}^3$, then Humps 1, 2, and 3 experience a minimum load more severe than the previous minimum S_{min}^3. For the updated values of the hump opening stress, it follows that $S_{op}^4 \geq S_{op}^1 > S_{op}^2 > S_{op}^3$. It is seen that after application of any negative load increment, Hump 4 governs the crack opening behavior. In general, it can be concluded that the effect of a previous hump, j, on the crack opening behavior is overruled by application of a more severe maximum load S_{max}^n, that is, $S_{max}^n \geq S_{max}^j$. In this way application of a relatively high load level erases part of the memory effect.

In the foregoing, it was assumed that a hump can actively influence the crack opening behavior as long as the crack tip is situated in the plastic zone associated with that hump. It follows that the effect of Hump j is also erased permanently if $a \geq a^j + D^j$. In both cases the delay switch associated with Hump j must be turned *off*.

Estimate of Plastic Zone Sizes

In the model, crack growth retardation effects depend on the crack opening stress and, via the delay switches, also on the plastic zone size D^j at the time the humps under consideration were created. Clearly, the procedure used to estimate the plastic zone sizes has an effect on the accuracy of the predicted crack growth retardations. It is known that the size of the plastic zone strongly depends on the state of stress near the crack tip. Two extreme situations are the states of plane strain and plane stress. Using an Irwin [*14*] type of approach in reference [*15*] a formula was derived for the size of a crack-tip plastic zone extending in virgin material. The applicability is restricted to the centrally cracked sheet specimen used in this study. For other geometries the corrections for finite specimen dimensions and high loads will be different. For a primary plastic zone the following relations were obtained, for plane-stress conditions

$$D_s^n = \frac{a^n}{1.32}\left(\frac{S^n}{\bar{\sigma}}\right)[1 + (a/b)^2 + (S^n/\bar{\sigma})^2/1.32] \tag{8}$$

and for plane-strain

$$D_n^n = \frac{a^n}{9.0}\left(\frac{S^n}{\bar{\sigma}}\right)^2[1 + (a/b)^2 + (S^n/\bar{\sigma})^2/9.0] \tag{9}$$

where $\bar{\sigma}$ denotes the uniaxial yield limit and a/b is the crack aspect ratio. In these equations the factors 1.32 and 9.0 account for differences in the state of stress. Further, the last factor on the right-handside accounts for finite width of the specimen and for the effect of relatively high load levels. The latter correction was derived [15] from the contribution of nonsingular terms in the Westergaard Solution to the stress distribution in the net section of an infinite sheet specimen. Equations 8 and 9 are valid in the extreme situations of plane stress and plane strain, respectively. In general, the state of stress near the front of a through crack in sheet material is more or less plane stress near the free surfaces and, if the sheet thickness is large enough, plane strain in the middle of the sheet. These three-dimensional aspects of crack closure and the development of yield zones are very complicated. For engineering purposes this problem will be simplified by considering a plane-stress plastic zone of size D_s^n and thickness βD_s^n near the surface of the sheet and a plane strain plastic zone in the midsection. The model is shown in detail in Fig. 10. The presence of plane-stress plastic zones is accounted for by introduction of an average plastic zone size D^n.

The growth rate factor β will be specified later on. On the basis of surface areas covered by the two types of plastic zones, it can be concluded that

$$\begin{aligned} D^n &= D_n^n + 2\beta D_s^n (D_s^n - D_n^n)/t \quad \text{if } \beta D_s^n < t/2 \\ D^n &= D_s^n \quad \text{if } \beta D_s^n \geq t/2 \end{aligned} \tag{10}$$

where t is the sheet thickness and D^n denotes the average plastic zone size. At first glance the assumption of β being constant is appealing in this rather

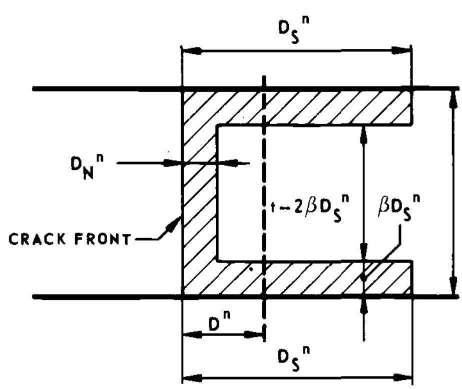

D_S^n =PLANE STRESS PLASTIC ZONE SIZE
D_N^n =PLANE STRAIN PLASTIC ZONE SIZE
D^n =AVERAGE PLASTIC ZONE SIZE
βD_S^n =THICKNESS OF THE PLANE STRESS LAYER
t =SHEET THICKNESS

FIG. 10—*Model adopted for a description of the effect of free surfaces on the plastic zone size.*

crude engineering model. However, it was observed from the results that the transition to pure plane stress ($\beta D_s^n \geq t/2$) is less gradual than predicted. Probably this is due to interaction effects between both plane-stress plastic zones. Using the empirical relation

$$\beta = 16 (D_s^n/t)^4 \tag{11}$$

the results were improved. For $D_s^n = t/2$, Eq 11 yields $\beta = 1$. Then $\beta D_s^n = t/2$ and, according to Eq 10, the state is fully plane stress. Equations 10 and 11 were adopted for the present study.

Reversed plastic flow is assumed to develop under plane-strain conditions. Delay effects depend mainly on the primary plastic zone sizes. The formula selected for a computation of sizes of zones of reversed plastic flow does not affect the results very much. According to the Irwin model it is assumed that reversed plastic zones are given by

$$D_n^n = \frac{a^n}{36}\left(\frac{\Delta\sigma_{\text{eff}}}{\sigma}\right)^2 \tag{12}$$

In this expression no corrections for finite width or high loads are introduced.

Failure Analyses

In an application of the crack growth model to a practical problem the computations must be ended when final failure occurs. For this purpose two criteria were selected: a test on net section yield (NSY) and on fracture of the specimen. The condition for net section yield was formulated as

$$\text{NSY, if } \sigma_{\max}{}^n \geq \bar{\sigma}(1 - a/b) \tag{13}$$

where $\bar{\sigma}$ denotes the yield limit and a/b is the crack aspect ratio. The test on fracture yields

$$\text{Fracture, if } K = \alpha\sigma_{\max}{}^n \sqrt{\pi a^n} \geq K_{1c} \tag{14}$$

where α is a correction on the effect of finite specimen width and K_{1c} is the fracture toughness of the material under consideration. The applied stress $\sigma_{\max}{}^n$ is defined by the user or automatically selected as the maximum stress from the loading sequence.

Application of the Model to Crack Growth Under Flight Simulation Loading

Specimen and Material

The specimens selected for a verification of the model were cut from 2-mm Alclad 7075-T6 sheet material. The width was 160 mm. All specimens were provided with a central hole and two sawcuts simulating a central initial crack of total length 7 mm. The loading direction was parallel to the rolling direction. The fatigue crack growth properties of the material were determined in a series of constant-amplitude fatigue tests executed at stress ratios R of 0.03, 0.04, 0.052 and 0.9, respectively. In Fig. 11 the results have been plotted in relation to the effective stress-intensity range. For a calculation of these values the crack opening function (Eq 6) was adopted. The crack

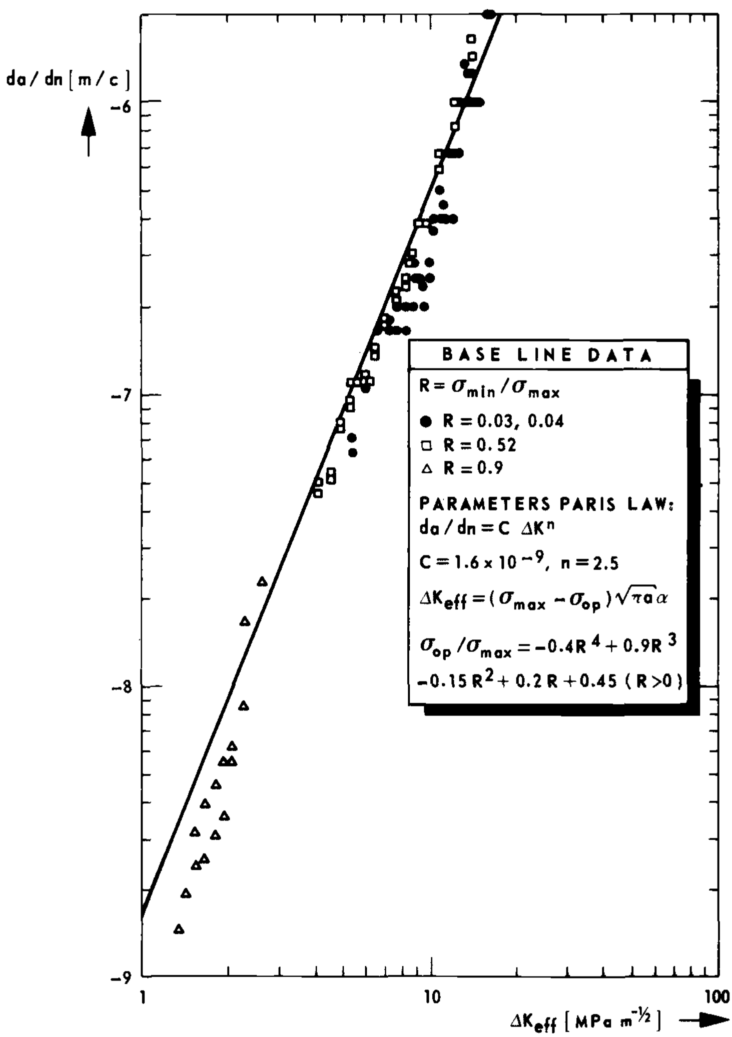

FIG. 11—*Constant-amplitude calibration curves* da/dn *versus* ΔK_{eff}.

growth behavior is approximated by selecting $C = 1.6 \times 10^{-9}$ and $n = 2.5$ in the Paris law. The approximation is shown in the same figure. Other material properties adopted for the present application are

$$\bar{\sigma} = 500 \text{ MPa}$$

$$K_{1c} = 70 \text{ MPa m}^{1/2}$$

Load Spectrum

The specimens were subjected to loading sequences that are representative for the lower wing skin of a transport aircraft. Typical details are indicated in Fig. 12. Basically the loading sequence consists of ground-to-air cycles (GTAC) and gust cycles.

The main features of the loading program can be summarized as follows:

1. The loading sequence consists of a series of identical blocks of 2500 flights (approximately 30 000 load cycles per block).
2. In a block, nine different flight types are distinguished ranging from "good weather" to "severe weather" conditions.
3. The ground loads and the mean stress in flight are constant. Taxi loads are ignored.

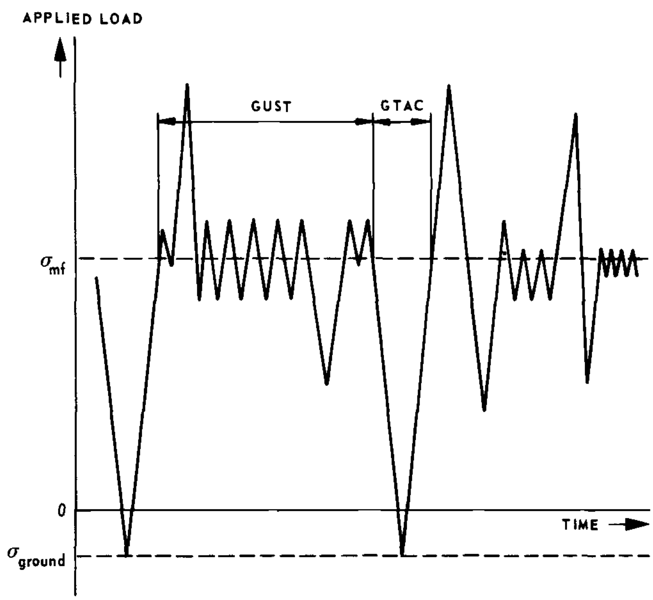

FIG. 12—*Typical loading sequence for flight simulation loading of a lower wing skin.*

4. The sequence of flights and the sequence of the loads are randomly selected once and for all; after application of a block of 2500 flights, exactly the same block is applied again, and so on.
5. A detailed description of the contents of a block can be found in Ref *16*.

The basic test load spectrum refers to a specific aircraft usage and a specific wing station. Different usage patterns may result in a different gust load experience. Moreover, the severity of the GTAC depends on the distribution of masses and on the location under consideration [*16*]. In this circumstance, it is of interest to have information about the effects of variations of ground load and gust severity on the growth rates of cracks.

Comparison of Predicted and Experimental Results

Using the specimen described in the foregoing the effect of variations of gust and ground loads was investigated. In Ref *16* the results are presented. In this study the crack growth rates will be reproduced numerically.

Three gust variations and three ground load levels ranging from "light" to "severe" were selected. In Ref *16* these variations are specified in detail. For the three gust variations the calculated effect of variations of the ground level on the crack growth rate are given, respectively, in Figs. 13, 14, and 15. The experimental results are also indicated. It is concluded that the agreement is good.

Finally, the predicted life was compared with the experimental results. In Fig. 16 the results are plotted. The dashed curves indicate the type of gust variation. It is seen that the fatigue lives associated with the extreme variations are different by a factor of 3. Again, the agreement between predicted and experimental results is excellent.

Conclusions

1. A model for prediction of fatigue crack propagation under variable-amplitude loading is based on a simple approximation of the crack opening behavior.
2. A simple model for the plane-strain/plane-stress transition is presented.
3. Crack growth rates are predicted for a centrally cracked sheet specimen subjected to flight simulation loading.
4. The predicted growth rates are in agreement with experimental results presented earlier.
5. The effects of crack tip blunting, stable crack growth, and multiple overloads on the crack opening behavior are not covered by the present model. Further research in this field is being undertaken.

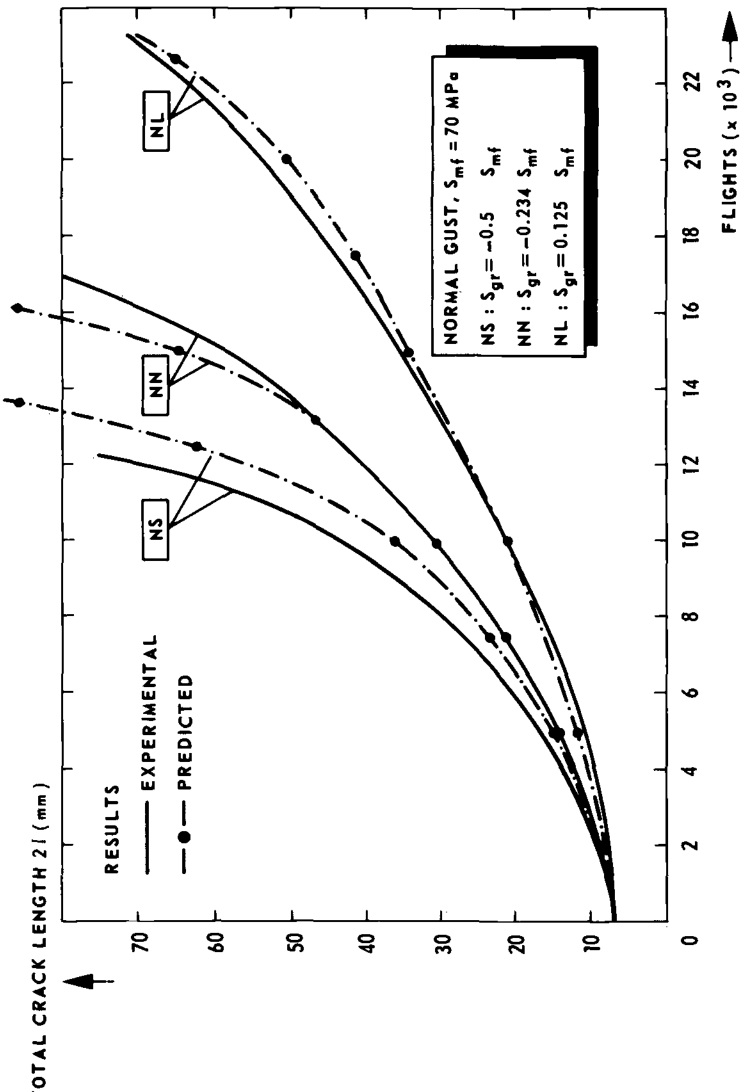

FIG. 13—*Average of experimental crack propagation curves compared with predicted result:* NORMAL GUST.

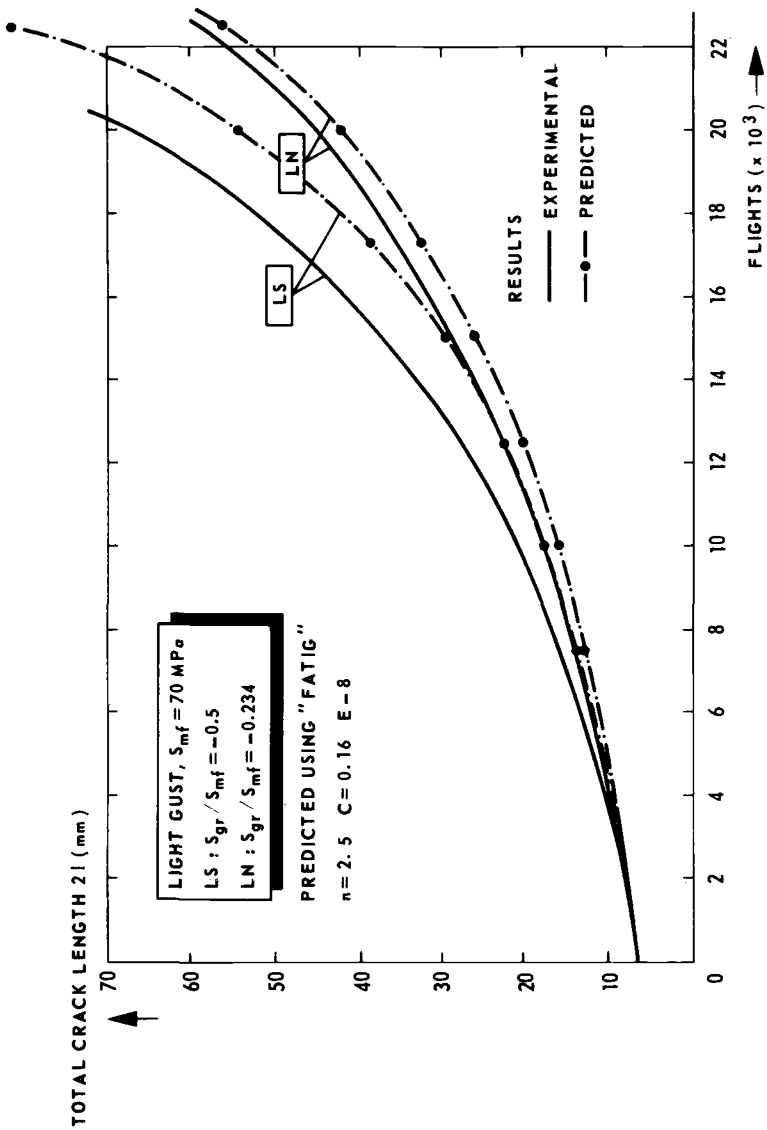

FIG. 14—*Average of experimental crack propagation curves compared with predicted results:* LIGHT GUST.

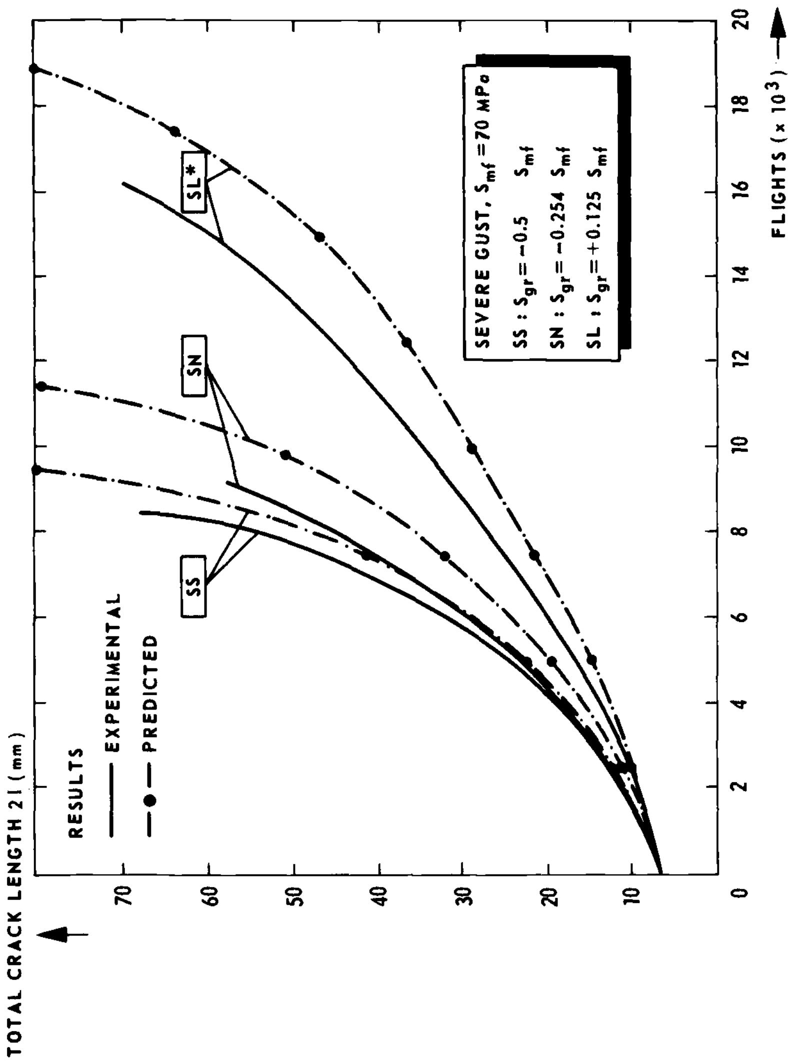

FIG. 15—*Average of experimental crack propagation curves compared with predicted results:* SEVERE GUST.

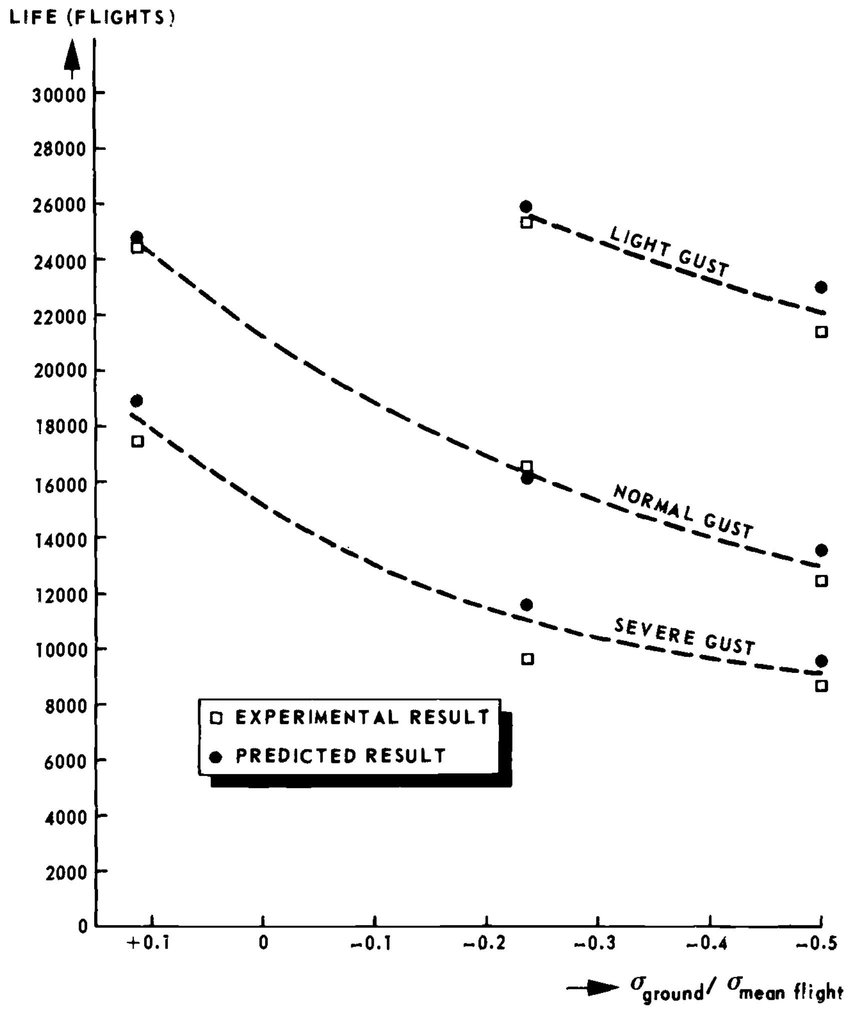

FIG. 16—*Effect of variations of ground load and gust severity on the life of a centrally cracked sheet specimen subjected to flight simulation loading.*

Acknowledgments

This investigation was performed under contract with The Netherlands Agency for Aerospace Programs (NIVR) (Contract No. 1777)

References

[1] Budiansky, B. and Hutchinson, J. W., *Journal of Applied Mechanics,* Vol. 45, June 1978, pp. 267-276.

[2] Hanel, J. J., "Riß Fortschreitung in ein- und mehrstufig schwing belasteten Scheiben," *Veröffentlichungen*, Heft 27, Institut für Statik und Stahlbau der THD, Darmstadt, Germany, 1975.
[3] Führing, H., "Berechnung von elastisch-plastischen Beanspruchungsabläufen in Dugdale-Riszscheiben mit Riszuferkontakt auf der Grundlage nichtlinearen Swingbruchmechanik," *Veröffentlichungen*, Heft 30, Institut für Statik und Stahlbau der THD, Darmstadt, Germany, 1977.
[4] Dill, H. D. and Saff, C. R. in *Fatigue Crack Growth Under Spectrum Loads, ASTM STP 595*, American Society for Testing and Materials, 1976, pp. 306-319.
[5] Newman, J. C., Jr. in *Cyclic Stress-Strain and Plastic Deformation Aspects of Fatigue Crack Growth, ASTM STP 637*, American Society for Testing and Materials, 1977, pp. 56-78.
[6] Ohji, K., Ogura, K., and Ohkubo, Y., *Engineering Fracture Mechanics*, Vol. 7, 1975, pp. 457-464.
[7] Elber, W. in *Fatigue Crack Growth Under Spectrum Loads, ASTM STP 595*, American Society for Testing and Materials, 1976, pp. 236-247.
[8] Schijve, J. in *Fatigue Crack Growth Under Spectrum Loads, ASTM STP 595*, American Society for Testing and Materials, 1976, pp. 3-23.
[9] Dugdale, P. S., *Journal of Mechanics and Physics of Solids*, Vol. 8, 1960, pp. 100-104.
[10] Hardrath, H. F. et al, *Fracture Mechanics*, N. Perrone et al, Eds., University Press of Virginia, 1978.
[11] Führing, H., *Numerical Methods in Fracture Mechanics II*, A. R. Luxmoore et al, Eds., Swansea, U.K., 1980.
[12] de Koning, A. U., *Fracture 1977*, D. M. R. Taplin, Ed., University of Waterloo Press, Waterloo, Canada, Vol. 3, 1977, pp. 25-31.
[13] Elber, W., *Damage Tolerance in Aircraft Structures, ASTM STP 486*, American Society for Testing and Materials, 1971, pp. 230-242.
[14] Irwin, G. R. in *Handbuch der Physik*, Springer-Verlag, Berlin, Vol. 6, 1958, pp. 551-590.
[15] de Koning, A. U., "A Simple Analytical Model for Computation of Specimen Compliance and Effective Crack Extension Force in a Centrally Cracked Strip, Including Effects of Yielding," NLR TR 79062, National Aerospace Laboratory, The Netherlands, 1977.
[16] de Jonge, J. B. et al, "Effect of Flight Load Spectrum Variations on Fatigue Life of Riveted Specimens and Crack Propagation in Sheet Made of Alclad 7075-T6," NLR TR 78071, National Aerospace Laboratory, The Netherlands, 1978.
[17] Rice, J. R. in *Proceedings*, First International Conference on Fracture, Sendai, Japan, 1965, pp. 283-308.

A. Saxena,[1] *R. S. Williams,*[1] *and T. T. Shih*[1]

A Model for Representing and Predicting the Influence of Hold Time on Fatigue Crack Growth Behavior at Elevated Temperature

REFERENCE: Saxena, A., Williams, R. S., and Shih, T. T., **"A Model for Representing and Predicting the Influence of Hold Time on Fatigue Crack Growth Behavior at Elevated Temperature,"** *Fracture Mechanics: Thirteenth Conference. ASTM STP 743.* Richard Roberts, Ed., American Society for Testing and Materials, 1981, pp. 86–99.

ABSTRACT: An analytical model is developed to represent and predict the influence of hold time on fatigue crack growth behavior at elevated temperature where creep deformation is significant. This model was formulated by considering the relaxation of stress in the crack-tip region due to creep deformation and its influence on the crack-growth behavior during the hold time.

Fatigue crack growth rate data at various hold times were obtained for ASTM A470 Class 8 (chromium-molybdenum-vanadium) steel at 538°C (1000°F) to evaluate the model. Based on these results and the data taken from the literature on Inconel alloy 718, it was concluded that the proposed model is capable of accurately representing and predicting the effect of hold time on the fatigue crack growth behavior at elevated temperature. This model represents a significant improvement over the linear damage summation model used previously. Some limitations of the model are also discussed.

KEY WORDS: creep, fatigue, fracture mechanics, stresses, intensity, Inconel 718, cracks, parameters, chromium-molybdenum-vanadium steel

Many structural components of rotating machinery, such as steam turbines, jet engines, or land-based combustion turbines, operate in the elevated temperature regime where creep deformation becomes a significant consideration. These components experience a static loading under normal operation and occasional fluctuating loads during startup and shutdown of the equipment. Hence, a fatigue cycle consists of a period of rising stress, a hold time, and a period of decreasing stress: Regions I, II, and III, respectively, in Fig. 1.

[1]Senior engineers, Structural Behavior of Materials Department, Westinghouse R&D Center, Pittsburgh, Pa. 15235.

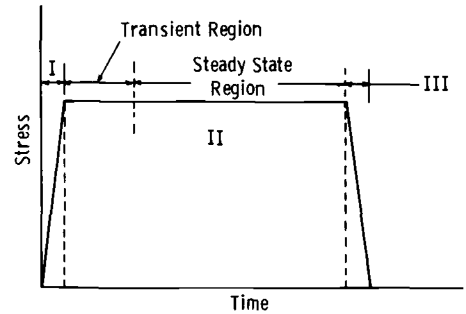

FIG. 1—*Schematic of the load (or stress) history experienced by a turbine rotor.*

The growth of a crack or cracklike defect in these components is expected to be influenced by the hold time. Hence, a model is needed to account for the effect of hold time on the fatigue crack growth behavior at elevated temperature.

In this paper, a model is proposed to mathematically represent as well as predict the effect of hold time on the fatigue crack growth behavior at elevated temperature. Fatigue crack growth rate data were generated at various hold times for A470 Class 8 steel for verifying the model. The model is also evaluated using similar data in Inconel alloy 718 taken from the work of Shahinian and Sadananda [*1*].[2]

Model Development

In this section, a model to account for hold time effects is proposed. This model is based upon parameters that characterize the stress in the crack-tip region in the presence of creep deformation. Hence, prior to describing the model, the analysis of stress in the crack-tip region at elevated temperature is reviewed.

When a cracked body is loaded at elevated temperature, the stress and strain distribution in the crack-tip region for a stationary crack is given by the following equations derived by Riedel and Rice [*2*]

$$\sigma \propto \left(\frac{K^2}{Ert}\right)^{1/k+1} \tag{1a}$$

$$\epsilon \propto \left(\frac{K^2}{Er}\right)^{k/k+1} (t)^{1/k+1} \tag{1b}$$

[2]The italic numbers in brackets refer to the list of references appended to this paper.

where

σ = stress,
ϵ = strain,
E = elastic modulus,
t = elapsed time,
r = distance from crack tip, and
k = exponent in secondary creep hardening law

$$\dot{\epsilon} = A(\sigma)^k \tag{2}$$

where $\dot{\epsilon}$ is the strain rate and A the material constant. Equations *1a* and *1b* characterize the crack-tip conditions when secondary creep deformation is localized, such as in the transient portion of the hold time shown in Fig. 1.

When the secondary creep deformation is widespread, the stress and strain rate at the crack tip is given by the energy rate line integral, C^* [*2-5*]

$$\sigma \propto \left(\frac{C^*}{r}\right)^{1/k+1} \tag{3a}$$

$$\dot{\epsilon} \propto \left(\frac{C^*}{r}\right)^{k/k+1} \tag{3b}$$

For a detailed discussion on the C^* integral, see Refs *2* and *4-6*. Equations *3a* and *3b* characterize the crack-tip conditions during the steady-state portion of the hold time.

The model described in the following discussion is based upon the foregoing stress analysis. As presented here, the model is applicable only for hold times that are in the transient region where K characterizes the crack-tip conditions. In a later section, some modifications to the model will be suggested which enable it to be extended to account for longer hold times. A quantitative method for determining the cutoff point between the short and long hold time will also be discussed.

The Model

In Equation *1a*, it is noted that K^2/t characterizes the time dependence of stress in the crack-tip region at a fixed distance from the crack tip. Thus, it is proposed that this parameter also characterizes da/dt during the hold time according to

$$\frac{da}{dt} = b\left(\frac{K^2}{t}\right)^p \tag{4}$$

where b and p are material constants.

If the crack growth rate during hold time, Region II in Fig. 1, is given by Eq 4, the total crack growth rate per cycle, $(da/dN)_h$ (including all three regions), can be given by superposition, that is

$$\left(\frac{da}{dN}\right)_h = \left(\frac{da}{dN}\right)_0 + \int_0^{t_h} \left(\frac{da}{dt}\right) dt \tag{5}$$

where t_h is the hold time, and $(da/dN)_0$ the crack growth rate for the same loading/unloading rates but no hold time, and which may be represented by

$$\left(\frac{da}{dN}\right)_0 = C(\Delta K)^n \tag{6}$$

Substituting Eq 4 into Eq 5, we obtain

$$\left(\frac{da}{dN}\right)_h = \left(\frac{da}{dN}\right)_0 + \int_0^{t_h} b\left(\frac{K^2}{t}\right)^p dt$$

or

$$\left(\frac{da}{dN}\right)_h = C(\Delta K)^n + A'(\Delta K)^{2p} \cdot t_h^{(1-p)} \tag{7}$$

where

$$A' = \frac{b}{1-p} \cdot \frac{1}{(1-R)^{2p}} \left[\left(\text{note, } K_{\max} = \left(\frac{\Delta K}{1-R}\right)\right)\right]$$

and $K_{\max}$ is the value of K during hold time.

For slow loading/unloading rates, Eq 6 may not always be adequate for representing the contribution of the cyclic load, $(da/dN)_0$, to the overall fatigue crack growth rate, $(da/dN)_h$. In such situations, an alternative more complex mathematical descriptions of $(da/dN)_0$, given in a previous paper [7], can be used. It is also recognized that introducing the hold time may result in different crack-tip stress and strain histories during the unloading portion of the cycle compared with continuous cycling. However, this influence is expected to be small and has been ignored in this paper.

To evaluate the constants in Eq 7, the da/dN versus ΔK behavior for no hold time and for at least one hold time must be characterized. The no-hold-time data yield the constants c and n. From the data at a given hold time, the constants A' and p can be obtained from the plot of log $[(da/dN)_h - (da/dN)_0]$ as a function of log (ΔK), Step 2 in Fig. 2. A' is obtained from the intercept and p from the slope of the plot.

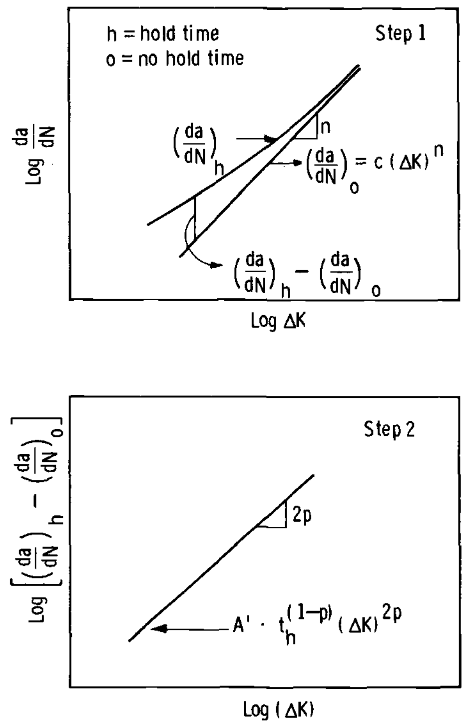

FIG. 2—*Schematic representation of the steps involved in determining constants* A', c, n, *and* p.

Experimental Procedure

Standard 2.54-cm-thick (1 in.) and 5.08-cm-wide (2 in.) compact-type (CT) specimens [ASTM Test for Plane-Strain Fracture Toughness of Metallic Materials (E 399-78)] were machined from a large cylindrical forging manufactured to the ASTM Specification for Vacuum-Treated Carbon and Alloy Steel Forgings for Turbine Rotors and Shafts (A 470-74), Class 8. The notches in the specimens were oriented along the radial direction of the forging. The chemical composition and the tensile properties of the test material are given in Tables 1 and 2, respectively.

The fatigue crack growth tests were conducted on servohydraulic test systems equipped with resistance furnaces for heating the specimens to the

TABLE 1—*Chemical composition of the test material (weight %).*

C	Mn	Si	Cr	Mo	V	Ni	P	S	Sn	As	Al	Cu	Fe
0.32	0.78	0.28	1.20	1.18	0.23	0.13	0.012	0.011	0.01	0.008	0.005	0.05	Bal.

TABLE 2—*Tensile properties of ASTM A470, Class 8 (chromium-molybdenum-vanadium) steel at various temperatures.*

Test Temperature		0.2% Yield Strength		Ultimate Strength		% Elongation	
°C	°F	MPa	ksi	MPa	ksi	5 cm gage length	Reduction in Area, %
24	75	623	90.4	776	112.5	14.2	39
427	800	516	74.8	625	90.6	14.2	53
538	1000	464	67.3	523	75.8	17.5	75

test temperature, 538°C (1000°F). These tests were conducted on a 24-h basis with minimum interruptions. Two types of tests, described in the following, were conducted to obtain the data.

Constant-Load-Amplitude (CLA) Tests

These tests were conducted in accordance with the ASTM Test for Constant-Load-Amplitude Fatigue Crack Growth Rates Above 10^{-8}m/Cycle (E 647-78T). The crack length in these tests was monitored visually. To minimize oxidation and thus facilitate crack length measurements, the specimens were electroplated with a thin coating of nickel.

Deflection Control (DC)-ΔJ Tests

These tests were conducted under deflection control, in which the deflection range was continuously increased with the aid of a digital computer as the crack length increased. This procedure was similar to the one used by Dowling and Begley [*8, 9*] to obtain fatigue crack growth rate data at high growth rates using small specimens.

The deflection on the specimen was measured continuously at a point 4.44 cm (1.75 in.) from the load line using a linear variable differential transformer. The amplitude of deflection, ΔV, was controlled according to Eq 8 so that ΔK increased linearly with crack length

$$\left(\frac{E}{W^{1/2}}\right)\Delta V = \Delta K_0[1 + 3(a - a_0)]\,F\left(\frac{a}{W}\right) \tag{8}$$

where

E = elastic modulus,
W = specimen width,
a = crack length,
a_0 = length of machine notch measured from load line,
ΔK_0 = initial stress-intensity range at $a = a_0$, and

$F(a/W)$ is given in

$$\frac{\Delta V}{\Delta K}\left(\frac{E}{W^{1/2}}\right) = F\left(\frac{a}{W}\right) = 2.15 \times 10^3 - 2.0 \times 10^4 \left(\frac{a}{W}\right) + 7.81 \times 10^4 \left(\frac{a}{W}\right)^2 - 1.60 \times 10^5 \left(\frac{a}{W}\right)^3 + 1.83 \times 10^5 \left(\frac{a}{W}\right)^4 - 1.11 \times 10^5 \left(\frac{a}{W}\right)^5 + 2.78 \times 10^4 \left(\frac{a}{W}\right)^6 \quad (9)$$

Equation 9 was derived from curve-fitting the ratio of compliance (BEV/P, where B = specimen thickness) and the K calibration $[(K/P)/BW^{1/2}]$ expressions at various crack lengths taken from Ref *10*. The ratio of minimum to maximum deflection was maintained constant at 0.1. The crack length was continuously monitored by using the appropriate compliance versus crack length expression derived from the method outlined in Ref *10*. Only the linear portion of the loading segment of the load-deflection plot was used to calculate compliance. The crack length thus obtained was substituted back into Eq 8 to calculate the deflection range and complete the control loop.

The crack length versus number of fatigue cycles and the corresponding load deflection plot were stored in the computer for every 0.5 mm (0.02 in.) of crack extension. These data were reduced using procedures described in the following.

Data Reduction

The crack length versus cycles (a versus N) data from the CLA tests were reduced using the seven-point incremental polynomial technique (ASTM E 647-78T) in the tests that yielded 20 or more a-versus-N points. In some tests, due to experimental difficulties, only limited data could be obtained. For those tests, the crack growth rates, da/dN, were calculated by the secant method. Since both methods have been shown to yield similar mean trends [*10*], no attempt was made to distinguish between the data from the two methods.

The a-versus-N data from the deflection control tests were reduced to the da/dN form by the seven-point incremental polynomial method. The corresponding cyclic J-integral, ΔJ, was calculated using the following expression [*11*]

$$\Delta J = \left(\frac{1-\alpha}{1-\alpha^2}\right)\frac{2A}{B(W-a)} \quad (10)$$

where A is the area under the loading portion of the load-deflection curve from the maximum load to the higher of the minimum load or the estimated closure load using the procedure outlined by Dowling and Begley [8,9] and α is given by

$$\alpha = 2\left[\left(\frac{a}{W-a}\right)^2 + \left(\frac{a}{W-a}\right) + \frac{1}{2}\right]^{1/2} - 2\left[\frac{a}{W-a} + \frac{1}{2}\right] \quad (11)$$

For the majority of the data, there was negligible nonlinearity in the load-deflection behavior; hence, the minimum load was used to calculate ΔJ. The load-line deflection was estimated by multiplying the measured deflection by $a/(a + 4.44)$, where 4.44 cm (1.75 in.) was the distance between the point of deflection measurement and the load line.

Results and Discussion

Figure 3 shows the fatigue crack growth rate data at various hold times for ASTM A470 Class 8 steel at 538°C (1000°F). The crack growth rate, da/dN, is plotted as a function of ΔK for the constant-load-amplitude tests. For the deflection control tests, the da/dN was plotted as a function of $\sqrt{E\Delta J}$, where E is the elastic modulus and ΔJ the cyclic J-integral proposed by Dowling and Begley [8,9] for characterizing da/dN under elastic-plastic and fully plastic loading. The data obtained from the two techniques are plotted in Fig. 3 using different symbols.

Under linear elastic conditions, $\sqrt{E\Delta J}$ and ΔK are equivalent forms [8,9]. Also, when small specimens are loaded under elastic-plastic or fully plastic conditions under deflection control, it has been demonstrated [8,9] that crack growth rate data expressed as a function of $\sqrt{E\Delta J}$ are identical to the data generated using large specimens that were tested under predominantly linear elastic conditions. The data shown in Fig. 3 also show that the deflection-controlled ΔJ tests and linear elastic load control tests yield identical results (within experimental scatter) where the data from the two techniques overlap.

The deflection control tests enabled data to be obtained at ΔK levels higher than those for which valid data could be obtained using CLA tests with same size specimens. The level of ΔK for which data can be obtained using CLA tests is restricted by the size requirement of ASTM Method E 647-78T. This size requirement becomes even more restrictive when testing at elevated temperatures.

Evaluation of the Model

In Fig. 3, it is observed that the crack growth rate increases significantly with hold time. The data at zero hold time (continuous cycling) and at 50-s

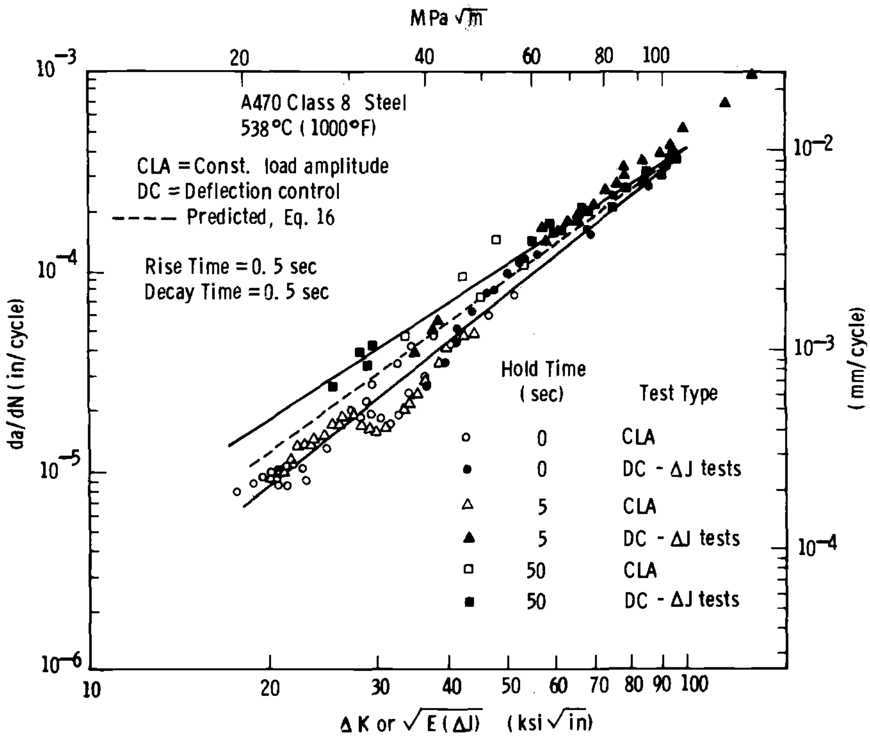

FIG. 3—*Fatigue crack growth rate data for A470, Class 8 steel at 538°C for various hold times.*

hold time were used to compute the constants in Eq 7 following the procedure described earlier. Thus, the equation describing the influence of hold time on the fatigue crack growth behavior of A470 Class 8 steel at 538°C (1000°F) for a 0.5-s rise and decay time is

$$\frac{da}{dN} = 1.49 \times 10^{-7} (\Delta K)^{2.35} + 1.18 \times 10^{-6} (\Delta K)^{1.27} \cdot t_h{}^{0.365} \qquad (12)$$

In Eq 12, da/dN is expressed in mm/cycle, ΔK in MPa$\sqrt{\text{m}}$, and t_h in seconds. Note, that this equation is derived only for a rise and decay time of 0.5 s each. Equation 12 was used to compute crack growth rates for a hold time of 5 s. The predicted crack growth rates are compared with experimental data in Fig. 3. In general, there is good correlation between the predicted and observed behavior. There are some unusual kinks in the da/dN-ΔK data that merit some discussion.

During elevated-temperature fatigue crack growth testing, nonsteady-state behavior is expected in the beginning of the test and following any unusual event such as temperature excursion, interruption, or a load spike. The material approaching the crack tip immediately following such an event will have a strain or thermal history or both which is time dependent and thus transient crack growth behavior may be obtained. When testing at slow frequencies for which tests last for several weeks, the occurrence of such abnormal behavior becomes more probable, resulting in larger data scatter than encountered in conventional fatigue crack growth testing. The unusual kinks in the data of Fig. 3 are considered a manifestation of such phenomena and should not be considered significant in judging the proposed model.

Additional crack growth rate data for Inconel alloy 718 at 538°C (1000°F) for hold times of 0, 6, and 60 s were taken from the work of Shahinian and Sadananda [1] to further verify this model, Fig. 4. The zero and 6-s hold time data were used to compute the constants in Eq 7. The final equation was

$$\frac{da}{dN} = 5.58 \times 10^{-8} (\Delta K)^{2.6} + 3.82 \times 10^{-6} (\Delta K)^{0.738} t_h^{0.631} \tag{13}$$

In Eq 13, ΔK is expressed in MPa$\sqrt{\text{m}}$, da/dN in mm/cycle, and t_h in seconds.

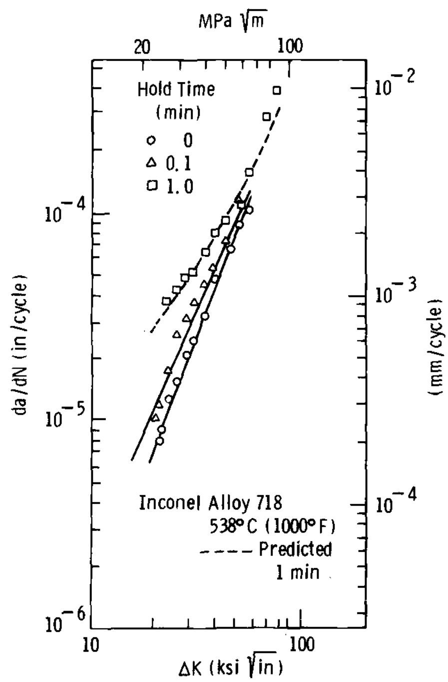

FIG. 4—*Comparison between predicted and experimental crack growth rate data for fatigue with hold time. The data are taken from the work of Shahinian and Sadananda.*

The crack growth rates for 60-s hold time were computed at several ΔK-values using Eq 13 and are compared with the experimental data in Fig. 4. Excellent correlation between the predicted and observed growth rates was obtained. It appears that the model can provide accurate descriptions of the influence of hold time on the fatigue crack growth behavior at elevated temperature, at least for limited hold times.

The proposed model is substantially different from the linear damage summation model [1]. In the latter model, steady-state creep crack growth behavior, da/dt, is substituted into Eq 5 for calculating da/dN. However, it should be recognized that a transient region, in which the crack-tip stress changes with time, follows the start of the hold time period, Fig. 1. During this region, da/dt does not acquire a steady-state value. In the proposed model, the change in da/dt with time is accounted for in Eq 4 and the constants in Eq 7 are determined from the data at a given hold time. Hence, this model represents a significant improvement over the simple linear damage summation model.

Limitations of the Proposed Model

The following limitations apply to the proposed model:

1. There may be conditions under which Eq 4 may not be adequate for characterizing the crack growth rates, da/dt. For example, in the temperature regime where no significant time-dependent deformation occurs (not even in the crack-tip region), Eq 4 does not apply. Also, when environmental cracking becomes significant, Equation 4 may not be valid in all situations. Other factors such as electrochemical reactions or diffusion processes occurring at the crack tip become more significant in determining the crack growth rate than the crack-tip stress. Additional terms to account for these contributions to the crack driving force will be needed in Eq 4 to achieve satisfactory results.
2. An unqualified attempt to use the model to account for wave shape effects may not be successful. For example, if it were required to compare the da/dN-values for a triangular waveform with a square waveform of equal frequency, Eq 4 could be integrated to analytically predict the results. It should be borne in mind, however, that for a triangular waveform creep (time dependent) and plastic (time independent) deformations will be occurring simultaneously at the crack tip. On the other hand, for a square waveform the creep and plastic deformations will, for a large part, occur separately. This could result in different crack growth micromechanisms for the two waveforms and yield a different set of constants in Eq 7 and thus, should be recognized in rationalizing wave shape effects.
3. This model describes hold time effects only in the situations where significant time-dependent deformation is localized in the crack-tip region. For very long hold-time periods, significant creep deformation can become

widespread and this model in its present form may no longer be valid. A quantitative criterion for determining the maximum hold time for which the model is valid and some modifications to the model to account for longer hold times are discussed next.

Extension of the Model for Longer Hold Times

Before discussing modifications to the model to account for long hold times, a quantitative criterion to determine the maximum hold time for which the proposed model will be valid is discussed.

The time for invalidating the K-controlled stress and strain fields, Eqs 1*a* and 1*b*, has been derived by Riedel and Rice [*2*] for stationary cracks. This has been termed as the transition time, t_1, and is given by

$$t_1 = \frac{K^2(1 - \nu^2)}{E(1 + k)C^*} \tag{14}$$

where K is calculated assuming linear elastic conditions, ν is Poisson's ratio, E the elastic modulus, k is defined in Eq 2. C^* is the energy rate line integral which is calculated assuming dominant secondary-state creep conditions in the structure. Methods for estimating C^* for these conditions are discussed elsewhere [*2,6,12*].

The transition time, t_1, may be used as an estimate of the maximum hold time for using this model. Figures 5 and 6 show the calculated values of t_1 from Eq 14 as a function of initially applied K-value for bend and tension geometries, respectively, for A470 steel at 538°C (1000°F). The specimen width used in the preceding calculations was 5.08 cm (2 in.) and the calculations were performed for various crack lengths. Depending on the various factors, this time is between a few minutes to several thousands of hours.

For hold times longer than t_1, the crack-tip stress, strain rate, and da/dt are characterized by the energy rate line integral, C^* [*2,8*]. The da/dt is given by

$$da/dt = C'(C^*)^q \tag{15}$$

where C' and q are constants determined from the experimental data. Hence, for hold times longer than t_1, Eq 15 can be integrated in the time limits between t_1 and t_h to estimate the crack growth. This can be added to the crack growth predicted by Eq 7; thus $(da/dN)_h$ will be given by

$$\left(\frac{da}{dN}\right)_h = C(\Delta K)^n + A'(\Delta K)^{2p}\cdot(t_1)^{1-p} + C'(C^*)^q(t_h - t_1) \tag{16}$$

Experimental data in support of Eq 16 are not yet available.

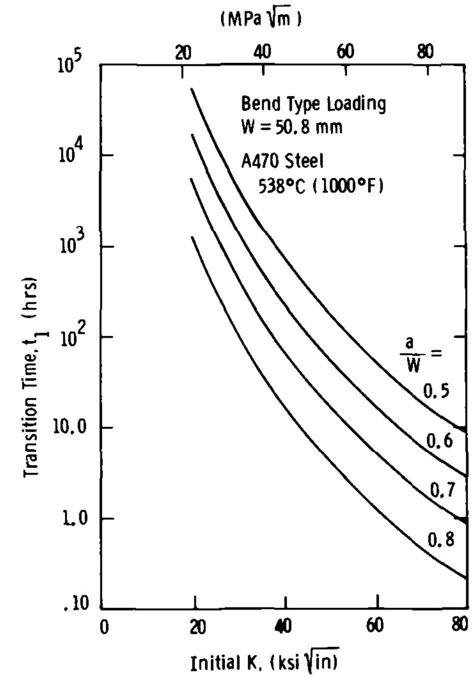

FIG. 5—*Transition time for* K-*controlled to* C*-*controlled crack-tip conditions for bend-type loading.*

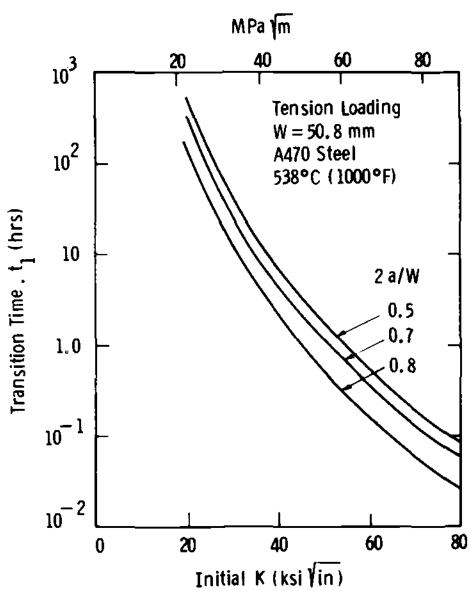

FIG. 6—*Transition time for* K-*controlled to* C*-*dominated crack-tip conditions for tension-type loading.*

Summary and Conclusions

An analytical model is developed for representing and predicting the influence of hold time on fatigue crack growth behavior at elevated temperature where creep deformation becomes significant. Fatigue crack growth rate data with hold times of 0, 5, and 50 s were developed for A470 Class 8 steel at 538°C (1000°F) to evaluate the model. Additional data on Inconel alloy 718, also at 538°C (1000°F), were taken from the literature to evaluate the model. It was concluded that the model is capable of accurately representing and predicting the hold time effects on fatigue crack growth behavior at elevated temperature. Limitations of the model and some potential approaches for alleviating these limitations are discussed.

Acknowledgments

We wish to acknowledge the financial support of the Technical Operating Division-Turbine Development of Westinghouse Electric Co. and contributions of W. H. Halligan, M. G. Peck, R. B. Hewlett, and W. H. Pryle to the experimental phase of the program. Discussions with N. E. Dowling and V. P. Swaminathan of Westinghouse Electric Co. and Herman Riedel of Max Plank Institute, West Germany, were also helpful.

References

[1] Shahinian, P. and Sadananda, K., "Crack Growth Behavior Under Creep-Fatigue Conditions in Alloy 718," ASME-MPC Symposium on Creep-Fatigue Interaction, MPC-3, R. M. Curren, Ed., American Society of Mechanical Engineers, Dec. 1976, pp. 365-390.
[2] Riedel, H. and Rice, J. R. in *Fracture Mechanics ASTM STP 700*, American Society for Testing and Materials, 1980, pp. 112-130.
[3] Goldman, N. L. and Hutchinson, J. W., *International Journal of Solids and Structures*, Vol. 11, 1975, pp. 575-591.
[4] Landes, J. D. and Begley, J. A. in *Mechanics of Crack Growth, ASTM STP 590*, American Society for Testing and Materials, 1976, pp. 128-148.
[5] Nikbin, K. M., Webster, G. A., and Turner, C. E. in *Cracks and Fracture, ASTM STP 601*, American Society for Testing and Materials, 1976, pp. 47-62.
[6] Saxena, A. in *Fracture Mechanics, ASTM STP 700*, American Society for Testing and Materials, 1980, pp. 131-151.
[7] Saxena, A., "A Model for Predicting the Effect of Frequency on Fatigue Crack Growth Behavior at Elevated Temperature," Scientific Paper 79-1D3-EVFLA-P3, Westinghouse R&D Center, Pittsburgh, Pa., 1979, submitted to *Fatigue of Engineering Materials and Structures*.
[8] Dowling, N. E. and Begley, J. A. in *Mechanics of Crack Growth, ASTM STP 590*, American Society for Testing and Materials, 1976, pp. 82-103.
[9] Dowling, N. E. in *Cracks and Fracture, ASTM STP 601*, American Society for Testing and Materials, 1976, pp. 19-32.
[10] Clark, W. G. and Hudak, S. J., *Journal of Testing and Evaluation*, Vol. 3, No. 6, 1975, pp. 454-476.
[11] Landes, J. D., Walker, H., and Clarke, G. A. in *Elastic-Plastic Fracture, ASTM STP 668*, American Society for Testing and Materials, 1979, pp. 266-287.
[12] Hutchinson, J. W., Needleman, A., and Shih, C. F., "Fully Plastic Crack Problems in Bending and Tension," MECH-6, Division of Applied Sciences, Harvard University, Cambridge, Mass., May 1978.

B. N. Leis[1] *and T. P. Forte*[1]

Fatigue Growth of Initially Physically Short Cracks in Notched Aluminum and Steel Plates

REFERENCE: Leis, B. N. and Forte, T. P., **"Fatigue Growth of Initially Physically Short Cracks in Notched Aluminum and Steel Plates,"** *Fracture Mechanics: Thirteenth Conference, ASTM STP 743,* Richard Roberts, Ed., American Society for Testing and Materials, 1981, pp. 100–124.

ABSTRACT: Much of the fatigue life of engineering structures is spent initiating cracks at a notch and propagating one (or more) of these cracks into and through the notch stress field. Experimental results and empirical analysis suggest that early in this process the physically small crack sometimes propagates in a manner inconsistent with analysis based on linear elastic fracture mechanics (LEFM). Available empirical adjustments for this apparent aberration postulate that the data can be made consistent with LEFM by the addition of a constant, with length dimensions, to the current crack length, resulting in a pseudo-crack.

The present paper introduces and analyzes an extensive data set pertinent to this so-called short-crack problem. Included are results for notched plates made from two aluminum alloys and a steel. These plates, which contain either circular or one of two different elliptical notches, have been tested under load or displacement control and encompass both confined flow and gross-section yield. Results for crack lengths as small as 20 μm (0.0008 in.) are reported.

Data presented and analyzed do indeed show trends which differ from those of LEFM analysis of so-called long cracks. More significantly, they show that the so-called short-crack behavior does not occur only for physically short cracks. Results presented indicate that cracks as large as 2.5 mm (0.1 in.) in the aluminum alloys and 1.25 cm (0.5 in.) in the steel also exhibit aberrations in their behavior as compared with longer-crack trends. Also, the results presented suggest that the data cannot be made consistent with the LEFM trend through the addition of a constant pseudo-crack length to the current crack size as has been suggested in one of the currently popular empirical models. It is postulated that the aberrations observed are a consequence of the failure of the LEFM-based analyses to recognize that crack growth in the plastic field of the notch is dominantly displacement-controlled local to the crack tip. Other relevant aspects of the problem are also discussed.

KEY WORDS: fatigue crack initiation, fatigue crack propagation, short cracks, notches, stress concentration, stress-intensity factor, control condition

[1]Senior research scientist and research scientist, respectively, Battelle Columbus Laboratories, Columbus, Ohio 43201.

Most of the life in many engineering structures is spent initiating cracks at a notch root and propagating one dominant crack through the highly stressed field of the notch. A variety of approaches has been advanced to deal with the analysis of this problem. Early work suggested that the problem be approached in terms of a total life prediction using S-N concepts (for example, [*1*][2]). More recently, however, S-N analysis has been replaced by the so-called local stress-strain concept, approaches to which have been reviewed in Ref *2*. Typically, these approaches have been identified with only the prediction of the formation of a crack of engineering size. [Definitions in the literature range from lengths of about 125 to about 2.54 μm (0.005 to 0.0001 in.).] A number of authors have coupled this nonlinear analysis with linear elastic fracture mechanics (LEFM) analysis to make complete life predictions (for example, see Ref *3*). Others have used LEFM concepts (for example, see Ref *4*) to predict both initiation and growth. Such approaches work well for constant-amplitude loading but break down under general variable-amplitude cycling [*5,6*]. Still others assume the initial presence of defects means the total life is spent in crack growth (for example, see Ref *7*). In the latter case, LEFM is used exclusively, an obvious extension of which is to modify the initial crack size such that the analysis inherently includes the initiation period. Termed the equivalent initial flaw-size (EIFS) concept, this approach has been found to be moderately effective except for generalized variable-amplitude loading. But, unfortunately, the value of the EIFS is found to be a function of the loading (for example, see Ref *8*).

One of the major problems with the schemes noted in the foregoing is that they fail to directly address the transition regime where the just-initiated fatigue crack grows through the elastic-plastic field of the notch root. Because typically there is confined flow at notches, this transition regime is associated with physically small or "short" cracks. The so-called short-crack problem exists because available data developed since the early 70's suggest that in this regime the growth rate is apparently higher than for load-controlled long-crack data when analyzed in terms of LEFM. Results developed by Broek [*9*] showed such an effect at intermediate growth rates in circularly notched 2024-T3 aluminum sheets when the data are analyzed using LEFM. Subsequent work by Gowda, Topper, and Leis [*10*], who modified the Bowie solution [*11*] after Neuber [*12*] to account for inelastic action, showed a correlation of crack propagation rates in inelastically strained circularly notched steel plates but noted that the correlation was no longer linear on logarithmic coordinates of growth rate and stress intensity. Thereafter, Pearson [*13*], Dowling [*14*], El Haddad et al (for example, Ref *15*), and others also noted such an effect for problems of confined flow. El Haddad et al have also presented a model which appears to consolidate the short-crack behavior, but the model is based on purely empirical arguments. During this same era, a great deal of

[2]The italic numbers in brackets refer to the list of references appended to this paper.

crack-growth data have been developed for naturally initiating short fatigue cracks in a steel and two aluminum alloys, a part of which has been reported [*10,16*]. Curiously, based on the results of limited analysis of a portion of this physically short crack [*16*], these data did not appear to exhibit the accelerated growth rate of short cracks as compared with long cracks as has been more recently observed. That analysis did, however, serve to demonstrate the influence of the initial notch geometry on fatigue crack growth rate.

The purpose of this paper is to present the complete set of the just-noted short-crack fatigue growth rate data within the historical framework in which they were developed. The analysis of these data will then focus on the currently popular notion that physically short cracks grow more rapidly than do long ones. The paper also considers critical issues pertinent to (1) defining crack initiation in a manner consistent with both crack initiation and growth analyses, (2) achieving similitude between the damage rate processes being compared in predicting crack initiation and growth, and (3) determining when and why physically short cracks will fail to behave in accordance with LEFM.

Experimental Aspects

Historical Perspective

The data to be presented have been developed in the context of a program whose purpose was to develop and verify an approach to predict crack initiation in notched coupons [*17*][3] and subsequently in notched components and real structures [*18*][3] subjected to variable-amplitude loading. The desire was to achieve this using only smooth-specimen data and the results of appropriate mechanics analysis. For the reasons discussed in the following, initiation was defined in this program as a crack 125 μm (0.005 in.) long. Consequently, observations to determine when "initiation" occurred included the measurement of crack growth with cycles at lengths smaller than or on the order of 125 μm (0.005 in.). These data remained in part unpublished in that limited analysis [*16*] indicated they followed the then already extensive long-crack trends available in the literature. Reexamination of these data became of interest with the apparent aberrations in the behavior of physically short cracks.

Since it was recognized early on that once the crack initiated it propagated in a gradient, a very short crack length was adopted as a definition of initiation in an attempt to ensure similitude between the early growth rates at notch roots and in smooth specimens. At the same time, the length chosen had to be large enough to be reliably detectable. Using then-available stress-intensity factor solutions and considering the problems of measurement, a crack length of 125 μm (0.005 in.) was selected. This single length was proposed for use with

[3]See Ref *19* and *20*, respectively, for a review of the details and more extensive reference material.

a range of notch root radii. While it was used, it was not considered philosophically appropriate, as evident in the quote "to match damage rate processes at the tip of a crack in a notch root using reference smooth specimen data to a given level of accuracy, the maximum allowable crack length will decrease with decreasing notch radius" [*21*]. It was also emphasized then that the initiation length should be consistent with the assumptions inherent in the analysis used to grow the initiated crack to failure [*21*]. Dowling [*22*] independently recognized this. In his extensive related work [*23*], he has shown that, to a reasonable approximation, the length for the initiation/propagation transition is on the order of one tenth of the notch root radius. Such a result compares reasonably well with the constant value of 125 μm for the circular and elliptical notch data to be discussed herein. Finally, it should be noted that a 125-μm (0.005 in.) length compares very well with the transition from long- to short-crack behavior being exhibited by the recently generated data [*24-26*]. Thus by adopting the postulate stated in the foregoing to predict the total life of a structure (initiation plus growth), one may approximately account for the complex short-crack behavior in that it is inherent in the crack initiation life of the smooth specimen.

Experimental Details, Techniques, and Program

Optical methods involving essentially continuous observation at $\times 30$ via a traveling microscope with a least count of 12.5 μm (0.0005 in.) were used to detect and monitor the growth of small cracks. Included were initial crack lengths as small as 20 μm (0.0008 in.). These data were used to estimate the cycle number at which a crack of length 125 μm (0.005 in.) developed via interpolation (or limited extrapolation). These tests made use of both circular and elliptical notch configurations and include K_t-values of 2.68, 4.60, and 6.40. The studies covered stress and edge strain (displacement) controlled testing of mild steel, and 2024 and 7075 aluminum alloys. Data were developed under fully reversed constant-amplitude cycling at levels which generated conditions at the notch root (or short crack tip) ranging from confined flow to that well beyond net section yield. Details can be found in Refs *17* and *18*.

Now since the purpose here is to examine the growth of physically small cracks, it is appropriate to discuss the accuracy of the measured crack length in the short-crack domain. There are at least three sources of error: locating the crack tip, determining the absolute length of the crack, and determining the relative advance of the crack.

The first significant point relates to the repeatability in locating a tight crack tip that lies in a region of significant cyclic plasticity. Note that in this context one presumes that a single tip exists as it does in the long-crack case. However, it is not unusual to observe many short cracks [$\sim$25 μm (0.001 in.)], all of which may grow significantly [100 μm (0.004 in.)] before a dominant crack develops. After that crack develops, its growth often involves branching to lengths almost beyond the domain heretofore associated with so-called short-crack effects, as shown for example in Fig. 1. Even at ×50 magnification where a crack 25 μm (0.001 in.) long appears to be 1250 μm (0.05 in.), there may be difficulty identifying such crack tips. Errors in this resolution while small in an absolute sense are large in a relative sense. Uncertainties of 10 percent are not unreasonable. A second significant source of error enters through the resolution of the microscope vernier. In this and other comparable studies the resolution is about 12.5 μm (0.0005 in.)—about one half of the length of the crack being measured. Clearly then an uncertainty of 50 percent is possible

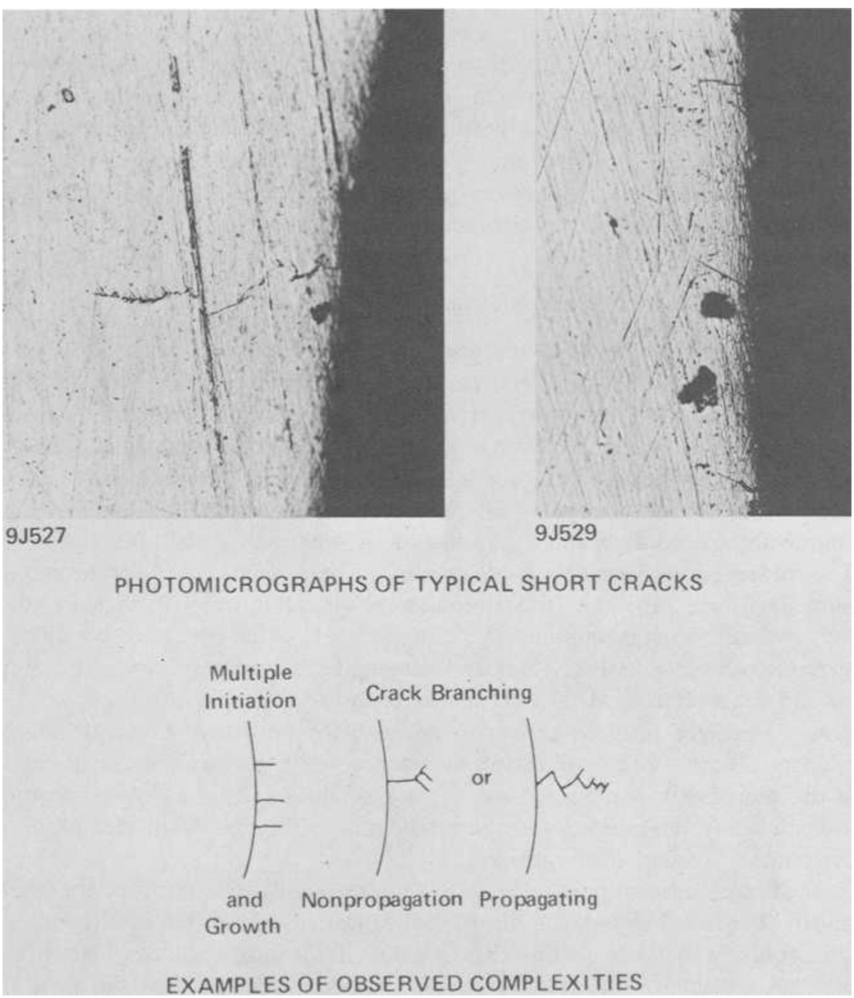

FIG. 1—*Observations on the growth of physically short cracks:* (top) *micrographs* (×200) *of branching and multiple initiation:* (bottom) *complexities in growth.*

in a worst-case sense. Finally, there is at least one further source of uncertainty which arises in the context of crack extension. Say the short crack domain is on the order of 125 μm (0.005 in.). If one chooses to make five readings in this domain, then one would seek to measure increments of 25 μm (0.001 in.), just twice the resolution of the vernier. Again, on a worst-case basis the uncertainty is on the order of 50 percent. Thus, in a worst-case sense the most probable error in absolute length is $(0.1^2 + 0.5^2)^{1/2} \simeq 50$ percent for either the absolute length or the increment in crack growth. Caution, therefore, must be used in interpreting the data that will be presented both here and in papers using comparable techniques. Such care should be taken even if the uncertainty is less than that for this crude worst-case analysis.

Experimental Results

Raw Data

Data generated in fatigue crack growth studies give rise to plots of crack length as a function of applied cycles. Raw data to be examined in this paper are presented in Figs. 2 and 3 on logarithmic coordinates of crack length and cycles.

It is appropriate here to comment on crack length in the context of short cracks. The short cracks of concern here were all surface-connected. Invariably the crack aspect ratio shown schematically in Fig. 4 changed as the crack grew so that a single linear dimension does not necessarily adequately characterize the growth. Nevertheless, these results will be presented in the context of a single surface measurement as this is the approach popularized in other relevant papers. Note from Fig. 5 that crack length plotted in these figures is the length of the crack growing out of the notch root. These figures plot the average of the average readings from both front and back sides of the plate at each notch root. The only data considered are that for which the growth has been symmetric.

In virtually all cases there were a number of initiation sites through the thickness. If the crack initiated at an intermetallic particle, its initial shape was typically almost semicircular. Similar observations were made for cracks that initiated in the bulk. Only limited corner cracking was observed. Once the microcrack had formed, its growth was largely along the free surface of the notch root because the driving force for growth in the depth direction decreases with the strain gradient as the crack traverses the net section. This decrease is also coupled with increased restraint to flow with depth, a consequence of increased constraint due to grain-to-grain compatibility requirements. Clearly, then, the raw data shown in Figs. 2 and 3 cannot be considered representative of the true complex two-dimensional growth behavior of physically short cracks. At this scale, crack growth is not planar—it is truly three-dimensional. Furthermore, the growth may involve Mode II in addition

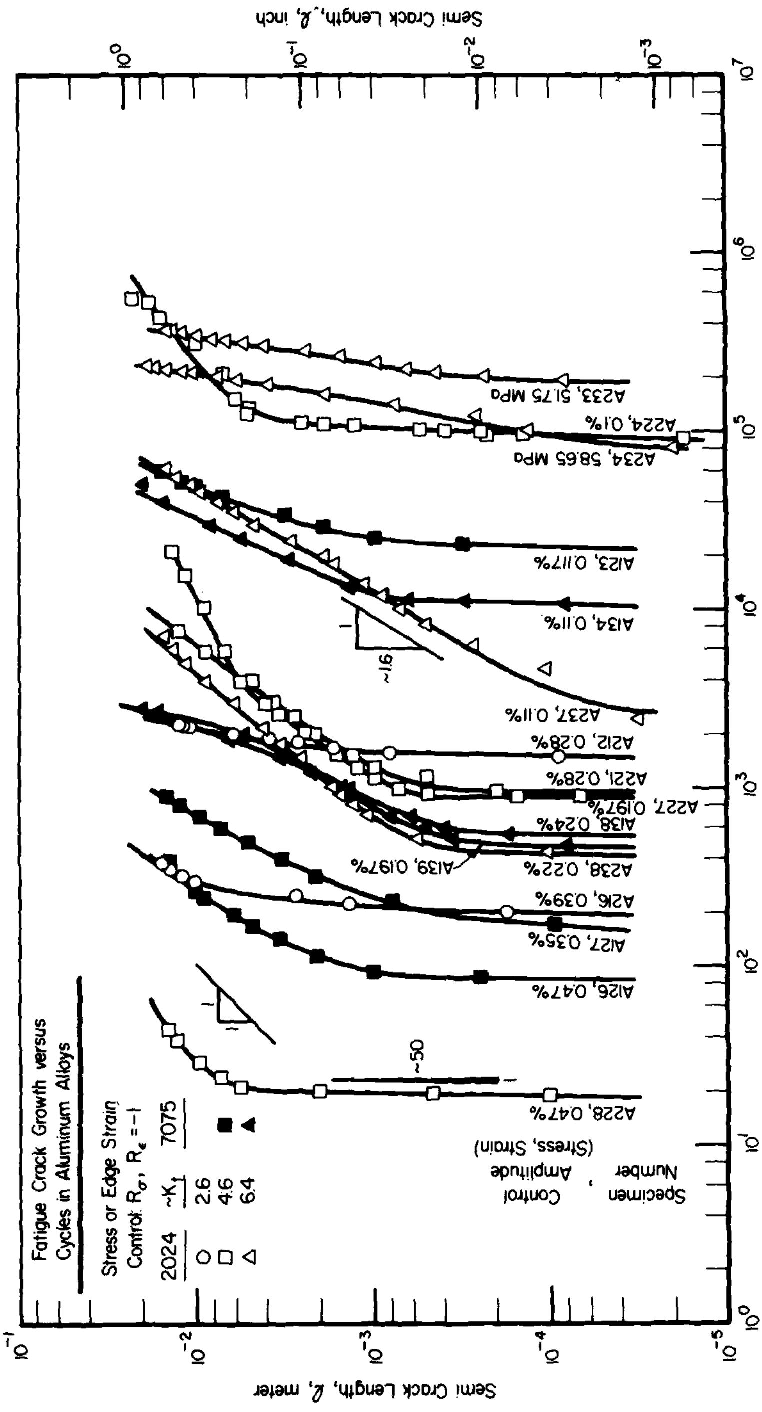

FIG. 2—Growth of initially physically short cracks in notched aluminum plates.

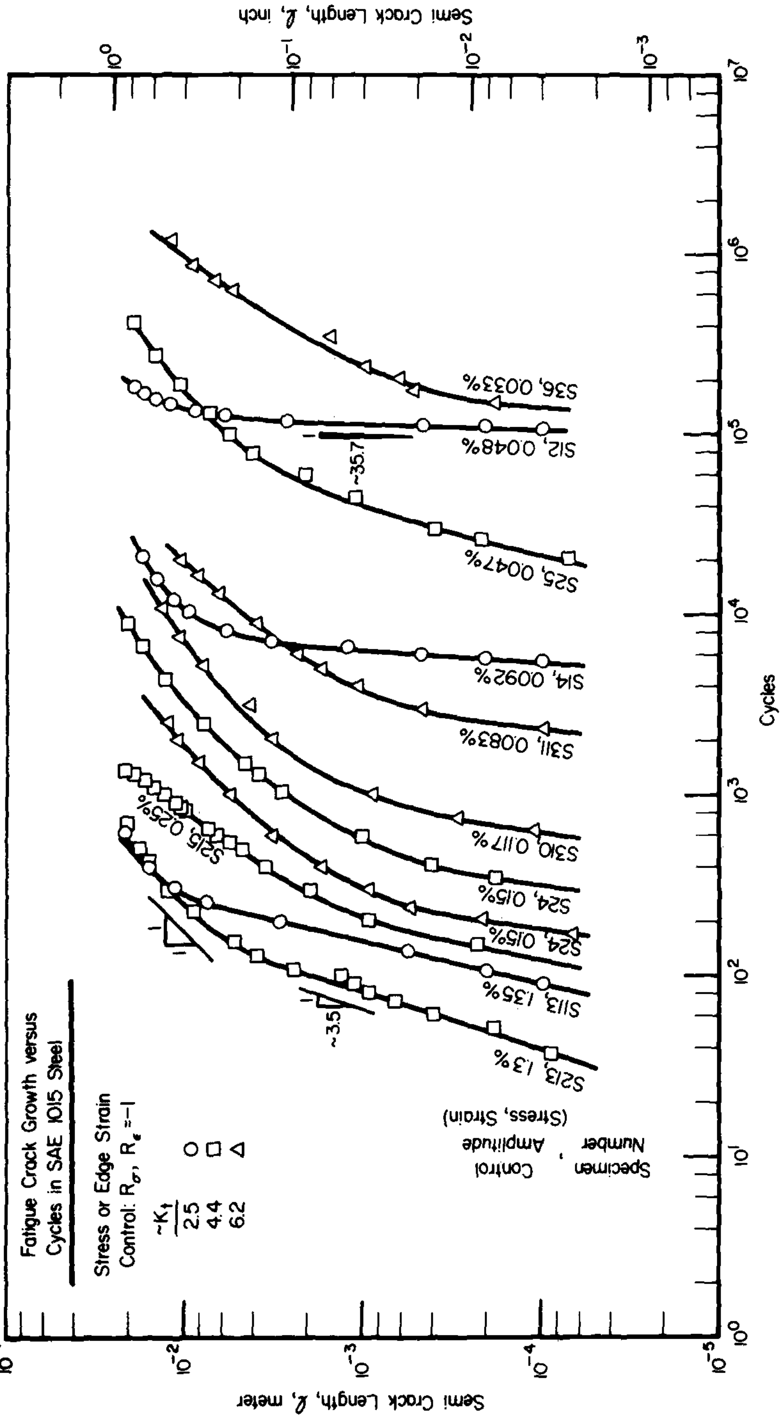

FIG. 3—Growth of initially physically short cracks in notched steel plates.

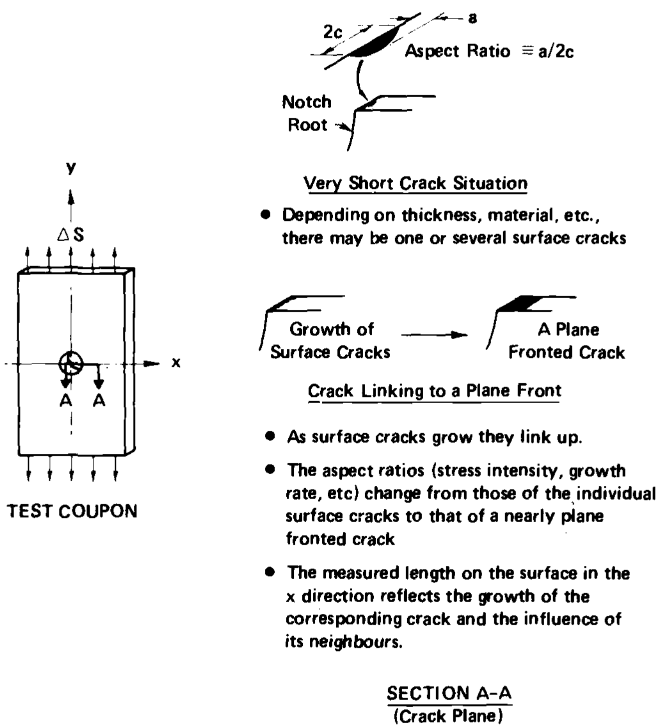

FIG. 4—*Changes in crack aspect ratio in the growth of physically short cracks (schematic).*

to Mode I, which dominates long crack growth. Such figures will nevertheless be used as a vehicle for discussion in that this approach has been used in all previous papers.

With reference to Figs. 2 and 3, note that for comparable conditions the 2024-T3 aluminum has the highest growth rate whereas the SAE 1015 steel has the lowest, at least at the shorter crack lengths. Note too that, for the scales used, the growth rate of the shorter cracks appears essentially constant with increasing length (that is, length is a power-law function of cycles). For the aluminum alloys, these curves are generally quite steep. Just slightly higher rates would be approaching an almost unbounded condition. Clearly then, such data can be extrapolated to shorter lengths without much fear of bias to lower than actual rates for shorter cracks, especially since these trends hold to lengths as short as 20 μm (0.0008 in.). This is due to the fact that, for such cases, the steep log l-log N curves suggest that the errors in measured length discussed earlier do not significantly impact on the growth rate. With regard to the mild steel data, some of the results show the same steep, constant-rate behavior exhibited by the aluminum. The majority of the data, however, show a concave-down trend so that extrapolation is neither recommended nor used.

(a) NOTCH AND CRACK NOMENCLATURE

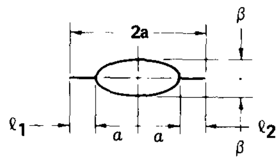

Notch: Semi major axis; a

Semi minor axis; β

Aquity ratio; a/β

Crack: Length; $\ell = \dfrac{\ell_1 + \ell_2}{2}$

ℓ_1, ℓ_2 are averages of readings from both sides of the plate

(b) SPECIMEN NUMBERING

First Designation – Material: A1; 7075-T6 Aluminum Alloy
A2; 2024-T3 (51) Aluminum Alloy
S; SAE 1015 steel (normalized)

Second Designation – Notch Aquity: 1 → a/β = 1; $K_t \doteq 2.6$
2 → a/β = 2; $K_t \doteq 4.6$
3 → a/β = 3; $K_t \doteq 6.4$

Third Designation – Sample Number

Example: A1314 → 7075-T6, $K_t \doteq 6.4$, sample 14

FIG. 5—*Definitions of notch geometry and specimen numbering scheme: (*a*) notch geometry; (*b*) numbering scheme.*

For the most part, all data in the short- and intermediate-crack domain follow continuous trends so that interpolation is not deemed to introduce significant bias or uncertainty and is therefore used.

Consider now the implications of a power-law relationship between semi-crack length, l, and cycles, N, for the short-crack domain:

$$l = aN^b \tag{1}$$

Differentiating Eq 1 gives

$$\frac{dl}{dN} = abN^{b-1}$$

which, with substitution of Eq 1 gives rise to

$$\frac{dl}{dN} = ab\left(\frac{l}{a}\right)^{1-1/b} \tag{2}$$

With reference to Figs. 2 and 3, note that the value of b for shorter cracks ranges from about 2 to 50. At the longer crack lengths it takes on a value of about 1 for displacement control data and a somewhat larger value for the load control data. Consequently, except when $b = 1$, Eq 2 suggests that the crack growth rates will be a function of the crack length and not simply related to the behavior of longer cracks, and that for values of $b \geq 1$ the growth rate will increase with crack length.

Note that sharp breaks in the log l-log N trends are apparent at various lengths and nominal stress (strain) levels. These are a consequence of the change in the driving force for crack growth under either edge strain or load control. Note too that for the most part the more blunt notches have a higher growth rate over longer crack lengths under comparable control conditions (control type and imposed magnitude). This is an apparent consequence of the fact that the field of the more blunt notch extends farther into the specimen as compared with the steeper gradient of the sharper notches. This feature is somewhat more apparent when these data are plotted in terms of growth rate and crack length.

Growth Rate as a Function of Crack Length

Before crack-growth rate can be pursued as a function of crack length, scheme(s) to compute growth rates from discrete data must be selected. A simple slope (point-to-point) scheme could be used. Alternatively, a three-point divided-difference scheme or an incremental polynomial that is fit to some larger number of data points could also be used. But, if indeed there are significant changes in the growth rate as the crack extends, including a large number of points in the analysis may mask such a trend. Consequently, only the simple slope and three-point schemes have been considered. Superimposed on the so-computed raw growth rate data is the growth rate behavior estimated using the trends shown in Figs. 2 and 3. This will include the trend extrapolated to shorter crack lengths but still within the limit of the shortest crack measured.

Data analyzed this way are plotted in Figs. 6 and 7 for the three-point scheme. Results for the simple slope scheme are comparable so that, in the interest of brevity, only one set is reported. But, in the interest of extending the results to the shortest crack length measured, the first point plotted for each data set is taken from the results developed using the two-point scheme at the corresponding crack length. Based on the trends exhibited in Figs. 2 and 3, this is not considered to be inappropriate. Notice by comparing the trends for A22-4 and A23-4, for example, that the difference between displacement and load control, respectively, is apparent in the increasing and then decreasing to constant growth rate versus crack length for displacement control as compared with a steadily increasing rate for load control.

Now consider the growth rate behavior for shorter cracks for data sets for which the longer crack-growth rates are comparable, that is, cases for which the LEFM long-crack stress intensities are comparable. As suggested in the context of Figs. 2 and 3, the growth rates for the more blunt notches continue to increase over longer crack lengths as compared with those for the sharper notches. As noted previously, this is considered to be an indication of the influence of the initial notch geometry [*16*]. Under comparable control conditions blunt notches have a larger zone of influence (and plastic zone) compared with sharper notches. Most importantly, observe in Figs. 6 and 7 that, for these data which cover the range from confined to unconfined flow at both blunt and sharp notches, there is no apparently anomalous behavior in the initial growth rates of physically short fatigue cracks. That is, the growth rate increases with crack length, at least initially. In no case is there clear-cut evidence that the growth rate initially decreases and then increases with crack length as is often shown in evidence for the existence of a physically short-crack effect (for example, Ref *15*). Physically short in this context includes lengths as small as 20 μm (0.0008 in.). Decreases in rate are, of course, observed in the displacement control data at longer crack lengths, a consequence of the decreasing stress intensity for this control condition as discussed in the next section.

Stress-Intensity Factor Analyses

Data from three basic notched geometries subjected to either load or displacement control have been examined thus far. To put these data into a common format for comparison requires that the growth rates be presented as a function of some universal measure of the driving force for crack growth. For long cracks the LEFM stress-intensity factor, K, [*27*] serves as such a parameter. Since at present there are no generally accepted comparable parameters for short cracks, it will be used.

In a simple functional form, K is defined for Mode I cracking as

$$K = \beta(l)S\sqrt{\pi l}; \tag{3}$$

where

S = far-field stress,
l = semicrack length, and
$\beta(l)$ = function of geometry and crack length.

It has been postulated [*28,29*] that the fatigue crack growth rate is a unique function of K and other constant parameters that pertain to the loading, specifically the ratio of the minimum to maximum stress, R; that is

$$\frac{dl}{dN} = g(\Delta K, R) \tag{4}$$

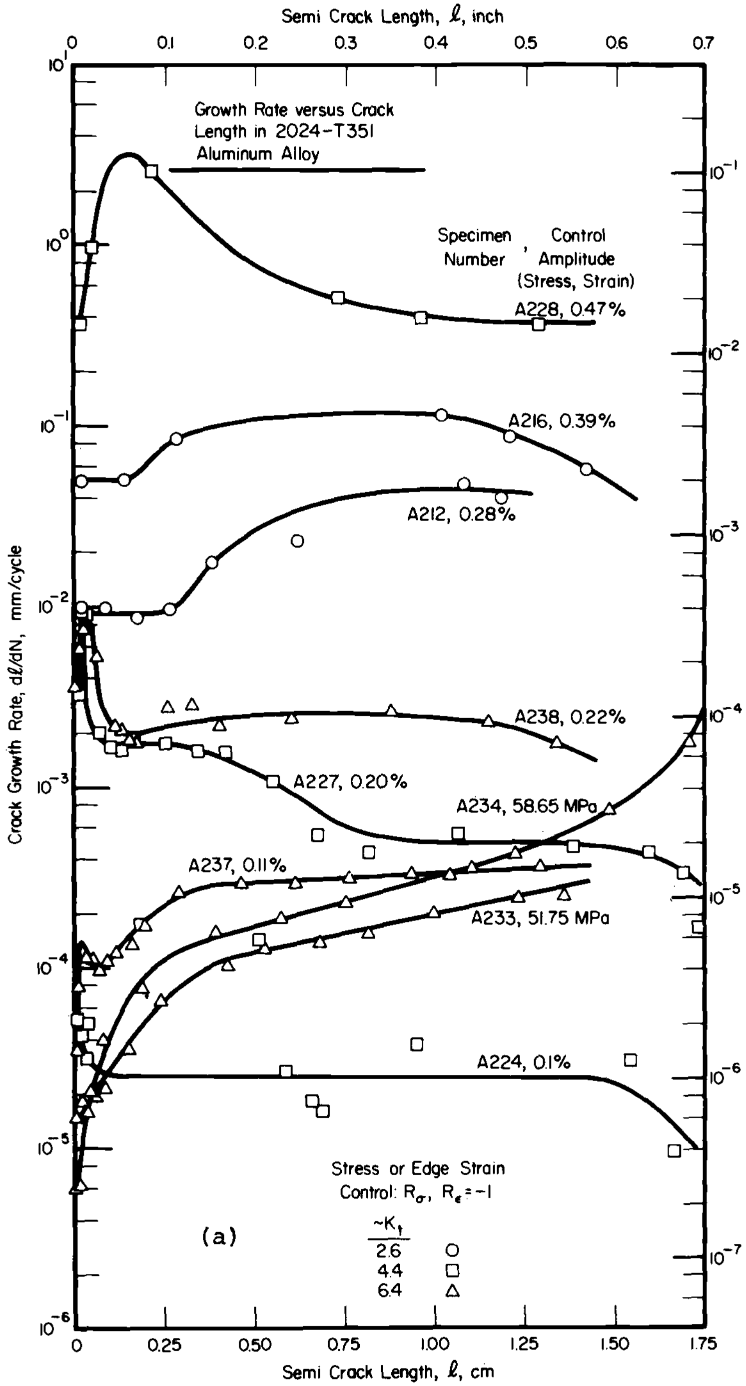

Semi Crack Length, ℓ, inch
0 0.1 0.2 0.3 0.4 0.5 0.6 0.7
Growth Rate versus Crack Length in 2024-T351 Aluminum Alloy
Specimen Number, Control Amplitude (Stress, Strain)
A228, 0.47%
A216, 0.39%
A212, 0.28%
A238, 0.22%
A227, 0.20%
A234, 58.65 MPa
A237, 0.11%
A233, 51.75 MPa
A224, 0.1%
Stress or Edge Strain Control: R_σ, R_ϵ = −1
(a)
~K_t
2.6 ○
4.4 □
6.4 △
Crack Growth Rate, dℓ/dN, mm/cycle
Crack Growth Rate, dℓ/dN, inches/cycle
10^1 10^0 10^{-1} 10^{-2} 10^{-3} 10^{-4} 10^{-5} 10^{-6}
10^{-1} 10^{-2} 10^{-3} 10^{-4} 10^{-5} 10^{-6} 10^{-7}
0 0.25 0.50 0.75 1.00 1.25 1.50 1.75
Semi Crack Length, ℓ, cm

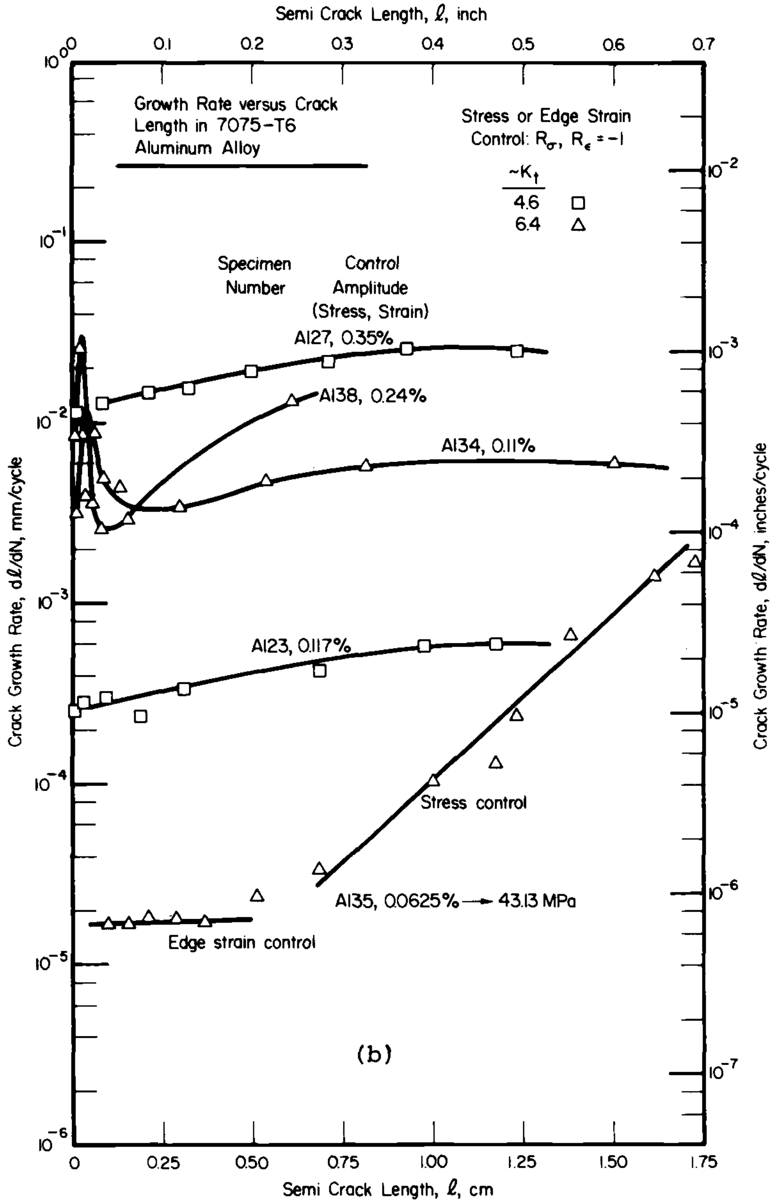

FIG. 6—*Dependence of fatigue crack growth rate on crack length for aluminum alloys: (*a*) 2024-T351 aluminum alloy; (*b*) 7075-T6 aluminum alloy.*

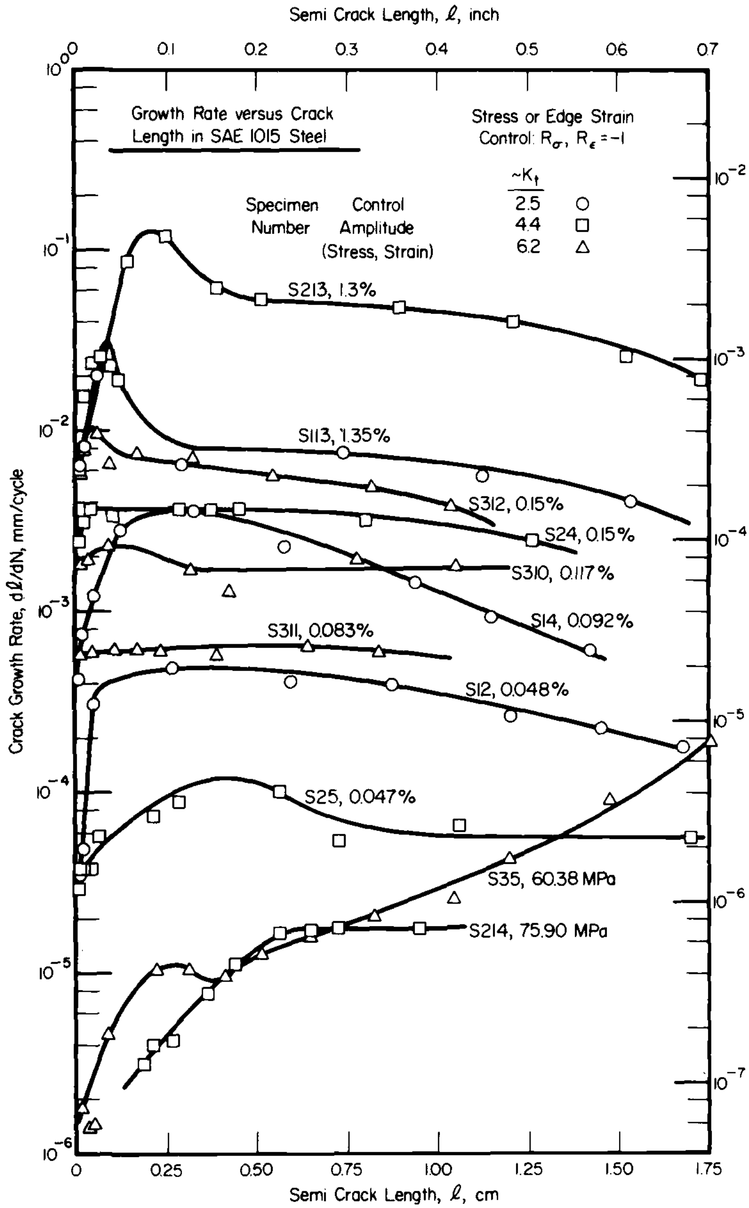

FIG. 7—*Dependence of fatigue crack growth rate on crack length for SAE 1015 steel.*

In this equation, ΔK is defined from the cyclic range of stress, ΔS, inserted into Eq 3. It should be emphasized that in LEFM the confined crack-tip plastic zone size, r_p, is a unique function of K; that is

$$r_p \propto K^2 \tag{5}$$

Consequently, care must be exercised in interpreting data from histories where r_p is history-dependent and not uniquely related to the current value of ΔK (or K_{max}). Likewise, a significant limitation to the utility of LEFM in the present context is that it is valid only so long as the plastic zone is small compared with crack length. Although it is recognized that this limitation can cause difficulties in using Eq 4 [*10*], the LEFM ΔK will nevertheless be used in that no rigorously developed alternatives exist. It should be emphasized in this context that data for the steel include gross-section yield. Under such circumstances ΔK may not provide a unique measure for the crack driving force [*10*]; it is used only in lieu of a rigorous alternative.[4]

From Eq 3 it follows that six stress-intensity factor solutions are required—one for each combination of control condition and geometry. These are presented in Fig. 8 on coordinates of normalized stress-intensity factor versus semicrack length. Note that the vaule of $\beta(l)$ in Eq 3 can be extracted by comparing these solutions with that for the corresponding center-cracked panel.

The stress-intensity solutions for load-controlled geometries designated as A1, A2, and S have been developed by coupling a finite-width correction (secant) with that for the notch field derived from handbook solutions [*32*]. Solutions for the displacement-controlled geometries have been developed using the load-controlled solutions in conjunction with a load shedding function calibrated using the experimentally measured data.

Crack-Growth Rate as a Function of Stress-Intensity Factor

Eliminating the common parameter, crack length, between Figs. 6 and 7 and Fig. 8 leads to plots of growth rate as a function of ΔK or K_{max}. Of course, the uncertainty noted earlier in "l" carries through this process. The uncertainty in the stress-intensity factor may be found from that in the crack length using Eq 3.

Results are shown in Figs. 9 and 10 for the three-point divided-difference scheme plotted as a function of K_{max}. Here K_{max} is computed using Eq 3 and the maximum stress in the cycle. Note that, on this coordinate scheme, data for a given specimen tend to cluster for displacement control at longer crack lengths where $\beta = 1$ whereas those for load control trace the trend from low to high K_{max}. This is a consequence of the K versus crack length behaviors ex-

[4]In an attempt to assess the influence of errors introduced by using ΔK in situations of unconfined flow (large plastic zones or $r_p \gg l$), inelastic measures of the crack driving force were also evaluated. Two schemes were employed: one based on J-integral [*30*] and one based on a modified Bowie [*11*] solution [*10*]. The results are detailed in Ref *31* and discussed later in this paper.

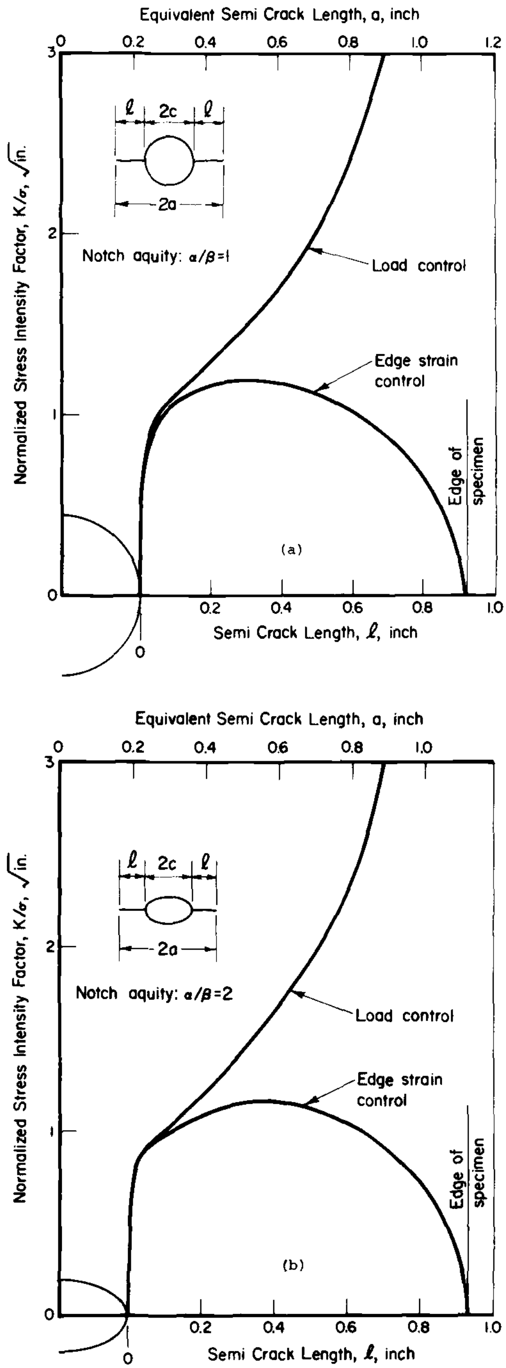

FIG. 8—*Normalized stress intensity as a function of crack length.*

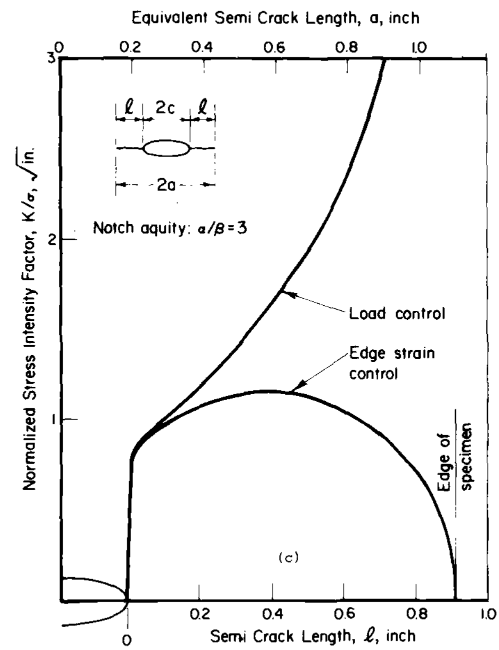

FIG. 8—*Continued.*

hibited in Fig. 8. Where independently developed data exist, there is very little difference between much of the "long crack" data of this investigation and that observed for other long cracks.

If $\Delta K/2$ rather than K_{max} is used as a measure of the crack driving force and the results presented are restricted to nominally the same R_σ-ratio $R_\sigma = R_\epsilon = -1$ for both displacement and load control, the trend of Figs. 9 and 10 remains the same. If on the other hand data for increasingly negative R-ratios from displacement control tests with load shedding are admitted, the data groups shown in Figs. 9 and 10 show a trend of decreasing growth rates as evident, for example, in Fig. 11. Here the data represent R_σ-values of $-1 \leq R_\sigma \leq -5$. It is important to note that the load shedding is very gradual. Nevertheless, the decrease in rate cannot be entirely attributed to a decrease in K in that the crack must grow through the plastic field created by prior cycling—see Eq 5. It is unlikely that the effects of prior plasticity are very significant, however, in that on a K_{max} basis, ascending and descending rates are well consolidated. It is also significant to note that this same trend exists for more positive R-ratios under constant R_σ testing. That is, for the same range in K the growth rate decreases from $R_\sigma \rightarrow 1$ through $R_\sigma = 0$ to $R_\sigma = -1$.

In contrast to the trends of Figs. 2 and 3, Figs. 9 and 10 present strong evidence that there is anomalous behavior in the growth of physically short

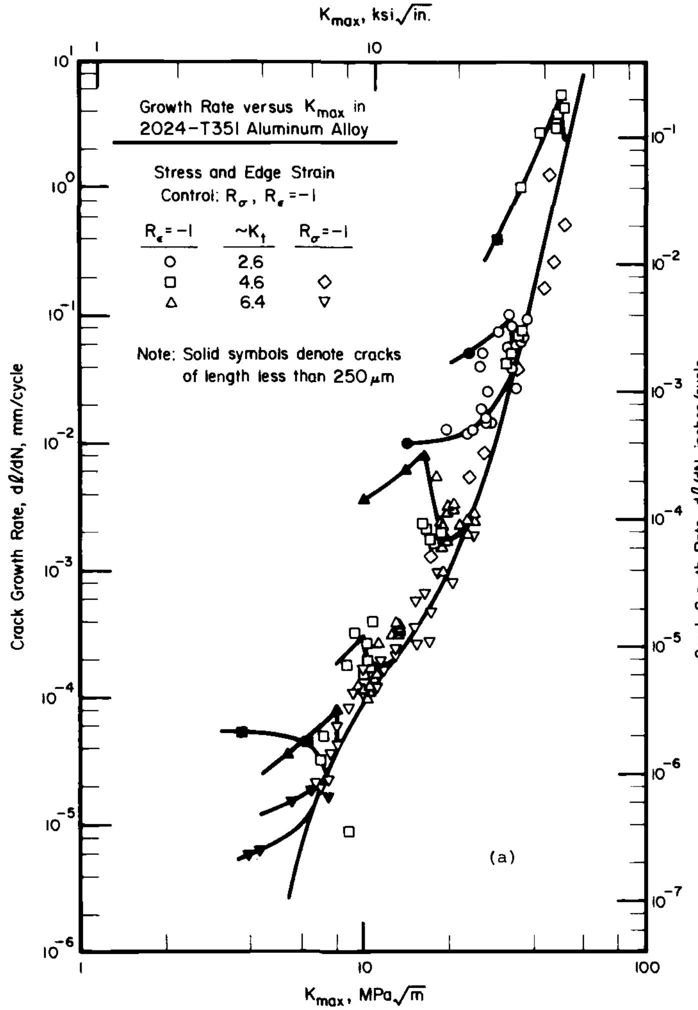

FIG. 9—*Dependence of fatigue crack growth rate on maximum stress intensity for aluminum alloys: (*a*) 2024-T351 aluminum alloy; (*b*) 7075-T6 aluminum alloy.*

cracks. More significantly it shows that the sometimes observed anomalous behavior of short cracks also occurs for cracks which are physically very long. That is, the effect is not necessarily a consequence of the crack's physical length. Possible explanations for why a short-crack effect is sometimes observed and other times is not, and why it occurs for long cracks as well, are discussed in the next section. Note that this discussion does not focus on the influence of errors introduced by using ΔK instead of an inelastic measure of the crack driving force. This is because, as detailed in Ref *31*, the trends and conclusions are not altered significantly.

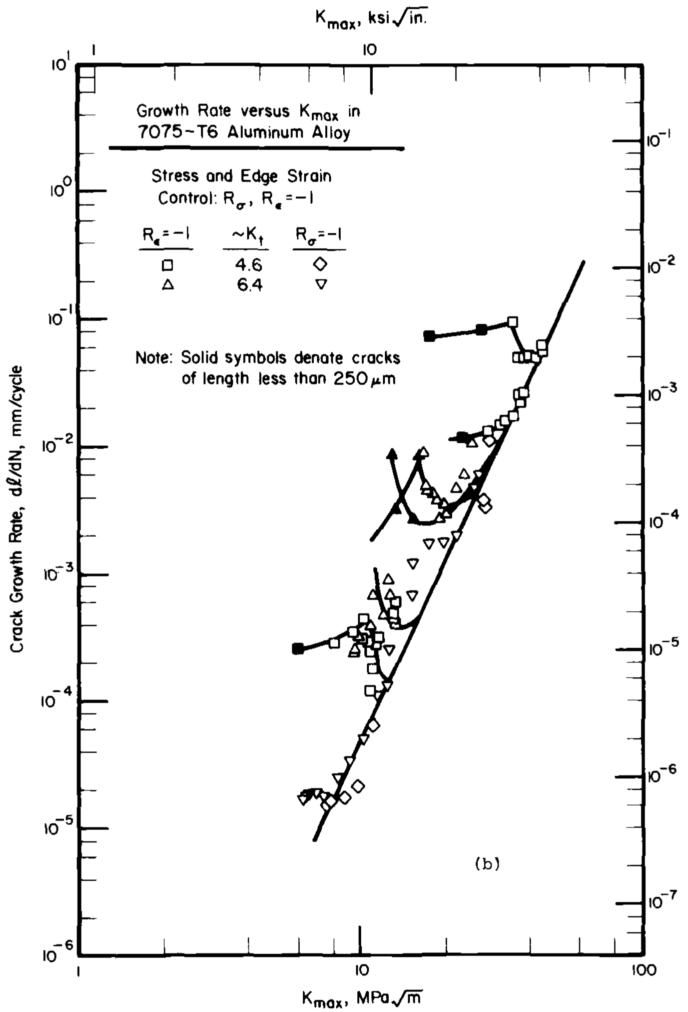

FIG. 9—*Continued.*

Discussion

While Figs. 2 and 3 and Figs. 6 and 7 failed to indicate possible discrepancies between long and short cracks, Figs. 9 and 10 do show differences. But contrary to previous papers which dealt with these differences in the context of physically short cracks, the present investigation shows that cracks need not be physically short to exhibit a behavior inconsistent with that associated with a LEFM portrayal of growth rate. Nor for that matter must the crack-tip plastic zone to crack length ratio be very large, thereby violating the basic premise of LEFM, to observe aberrations in the growth rate behavior. With reference to

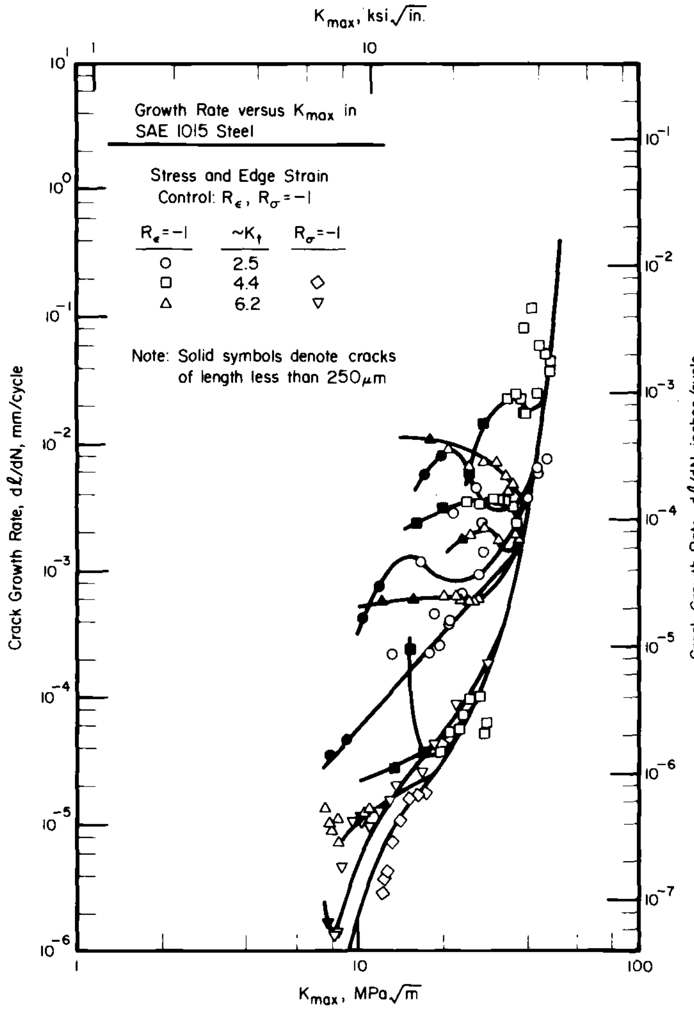

FIG. 10—*Dependence of fatigue crack growth rate on maximum stress intensity for SAE 1015 steel.*

these figures, note that crack lengths greater than 2.5 mm (0.1 in.) in the aluminum alloys and 1.25 cm (0.5 in.) in the steel plates are observed to behave in a manner previously associated only with physically short cracks. Furthermore, note that the data cannot be made to be consistent with the so-called long-crack LEFM trend by an empirical adjustment such as adding a constant with length dimensions to the crack length. As such, the hypothesis of El Haddad et al [*15*] that the so-called short crack can be made to grow *à la* LEFM through the addition of some constant, l_0, to the current crack length cannot be ascribed any generality.

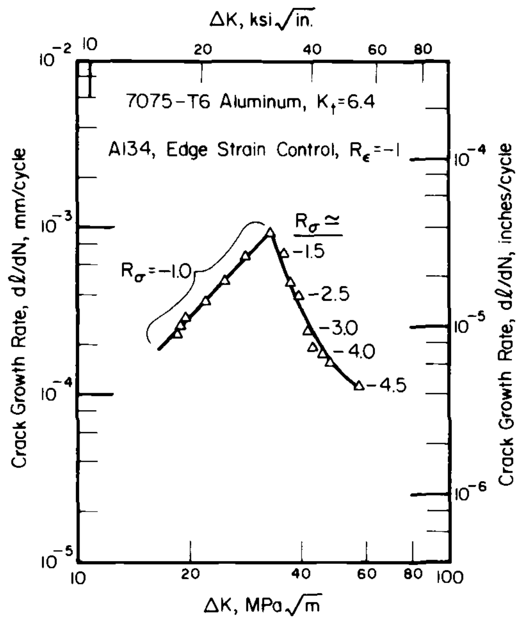

FIG. 11—*Dependence of fatigue crack growth rate on range of stress intensity.*

One obvious postulate for the anomalous short-crack behavior follows from some of the aforementioned trends. It develops in contrast to the current LEFM scheme for dealing with notches, which is first briefly reviewed. Long cracks have typically been studied under load-controlled conditions. Similitude is invoked in the growth rates through the LEFM K, which for equal values means equal plastic zones at crack tips. This is true so long as these crack tips exist in load-controlled domains as they do in the reference data base geometries. But when examining short cracks which grow out of notches, the notch stress field must be accounted for. In the context of LEFM this is tantamount to including the notch gradient in K through $\beta(l)$ in Eq 3, an approach which has been used for some time. What is missed in such a formulation is the fact that the crack may exist in a plastic zone which is largely displacement-controlled by the surrounding elastic field. This displacement control leads to a constant or possibly decreasing driving force for growth until the crack nears the elastic-plastic boundary of the notch field. At this point, there is a gradual shift from predominantly displacement control to load control. Thereafter, the crack behaves as the so-called long crack in that it grows in a load-controlled field, the same as other long crack data. One physical consequence of the postulate is that the size of the notch plastic field should correlate with the transition from displacement-controlled to load-controlled growth. That is, with regard to Figs. 9 and 10, the crack length at the transition from the growth rates not consolidated by LEFM to those that are consolidated should correlate with the notch plastic field. Results presented in Ref *31*, which details the development of this postulate,[5] do indeed show such a correspondence.

The essence of the just-noted postulate is that the crack growth rate depends on a measure of the driving force that is local to the crack tip and also reflects the local control condition. It suggests that the transition of control conditions occurs at or near the elastic-plastic boundary of the notch. Thus from a practical viewpoint, analysis of component lifetime must entail crack initiation, growth through the elastic-plastic notch field, and finally LEFM-based analysis of the remaining growth. When the elastic-plastic field is small, the behavior of crack growth in a smooth specimen with a similar stress-strain field (except for the gradient) may reflect that at a notch. As such the "short crack" (displacement-controlled) effect may be embedded in the strain-controlled smooth specimen results. The corresponding definition of initiation would be the depth of the notch elastic-plastic field. For such cases, approaches discussed earlier to define initiation and predict total life (for example, Refs *21* and *22*) are likely to yield reasonable predictions. At longer crack lengths such an approach becomes increasingly approximate and nonconservative (it ignores the gradient). Fatigue life analysis therefore becomes more complex in that the transition between nucleation and elastic-plastic displacement-controlled growth must be consistently defined. In addition, a rigorous treatment of the growth process must be developed. In these cases the just-noted approach is unlikely to yield consistently accurate predictions. Note in this context that this postulate suggests that a local value of effective stress intensity, K_{eff}, which maps the decrease in stress-intensity range and R-value and reflects the displacement control of the plastic field, would correlate short-crack data which appear to be anomalous when compared with "long crack" data as a consequence of displacement-controlled plastic action. Note too, then, that inelastic analysis may be required to estimate such a K_{eff}.

The preceding postulate tends to explain why in this study, which presents primarily displacement-controlled data, with sometimes large inelastic notch fields, a significant short-crack effect has been observed for physically long cracks. But it is an overly simplistic characterization of the general problem. A number of other important issues must ultimately be addressed before constant-amplitude fatigue microcrack and macrocrack growth can be adequately predicted. These include (1) the role of metallurgical features such as grain size, martensite packet size, etc. (that is, factors which pertain to the breakdown of continuum concepts); (2) the apparent coupling of Mode I and Mode II microcracking; (3) the predamaging of material ahead of the crack in the notch field due to cyclic inelastic action changing hardness, etc.; (4) the branching of microcracks and its influence on stress intensity; (5) the

[5]One obvious test of the postulate is to examine the so-called short crack behavior of a physically large specimen.

multiplicity of initiation sites and the complex behavior of the surface crack as compared with the plane fronted crack; (6) the influence of the free surface on both the stress state and restraint to plastic flow; (7) the accuracy of handbook solutions for infinite domains in applications to finite domains where boundary proximity effects are significant, and (8) the accuracy of crack length measurements. Certainly not all of these issues are critical in every problem, but until their role is resolved there will be uncertainty in life predictions, particularly in the area of microcrack propagation. Several of these issues are pursued at length elsewhere [*33,34*].

Conclusions

A number of conclusions may be drawn from the data presented in this paper:

1. Physically long as well as physically short cracks may behave in a manner inconsistent with LEFM.
2. The control condition which is local to the crack tip controls the growth-rate process. Whereas at inelastically strained notch roots this process is displacement-controlled, a steady or a decreasing growth rate may be observed followed by an increasing rate once the crack grows into the load-controlled domain. The length over which this steady or decreasing rate occurs increases with nominal stress (strain) and decreasing notch severity. It appears to correlate with the plastic field at the notch and physically may be quite large.
3. Decreasing growth rates in the displacement-controlled notch plastic field should be resolved by using an effective measure of stress intensity which embodies local closure effects and the local control condition.

Acknowledgments

Financial support for this study was provided by Battelle's Columbus Laboratories. Helpful discussions with the authors' colleagues—Drs. A. Zahoor and D. Broek—as well as the support of others on the technical staff are gratefully acknowledged.

References

[*1*] *Fatigue Design Handbook*, SAE-AE4, Society of Automotive Engineers, J. A. Graham, Ed., 1968.
[*2*] Leis, B. N., *Journal of Design Engineering, Transactions*, American Society of Mechanical Engineers, Vol. 100, No. 1, Jan. 1978, pp. 2-9.
[*3*] Broek, D. and Leis, B. N. in *Fatigue Resistance Testing and Forecasting*, SP-448, Society of Automotive Engineers, Sept. 1979.
[*4*] Barson, J. M. and McNicol, R. C. in *Fracture Toughness and Slow-Stable Cracking, ASTM STP 559*, American Society for Testing and Materials, 1974, pp. 183-204.
[*5*] Leis, B. N. in *Proceedings*, Fourth International Conference on Structural Mechanics in Reactor Technology, Vol. L, Aug. 1977, pp. L3.3/1-13.

[6] Morrow, J. D., Wetzel, R. M., and Topper, T. H. in *Effects of Environment and Complex Load History on Fatigue Life, ASTM STP 462,* American Society for Testing and Materials, 1970, pp. 74-91.
[7] Wood, H. A. and Engle, R. M., "Damage Tolerant Design Handbook," AFFDL-TR-79-3021, Air Force Flight Dynamics Laboratory, Wright-Patterson Air Base, Ohio, 1979.
[8] Noronha, P. J. et al, "Fastener Hole Quality," AFFDL-TR-78-206, Air Force Flight Dynamics Laboratory, Wright-Patterson Air Base, Ohio, Vol. 1, 1978.
[9] Broek, D., "The Propagation of Fatigue Cracks Emanating for Holes," NLR TR 72134 U, National Aerospace Laboratories, The Netherlands, Nov. 1972.
[10] Gowda, C. V. B., Topper, T. H., and Leis, B. N. in *Proceedings,* International Conference on Mechanical Behavior of Materials, Kyoto, Japan, Vol. 2, 1972, pp. 187-198.
[11] Bowie, O. L., *Journal of Mathematics and Physics.* Vol. 35, 1956.
[12] Neuber, H., *Journal of the Mechanics and Physics of Solids,* Aug. 1968, pp. 289-294.
[13] Pearson, S., *Engineering Fracture Mechanics,* Vol. 7, 1975, pp. 235-247.
[14] Dowling, N. E., "Crack Growth During Low Cycle Fatigue of Smooth Axial Specimens," Westinghouse Research Laboratories Paper 76-1E7-PALFA-P2, Pittsburgh, Pa., 16 June 1976.
[15] El Haddad, M. H., Topper, T. H., and Topper, T. N. in *Methods of Predicting Fatigue Life,* American Society of Mechanical Engineers, 1979, pp. 41-56.
[16] Gowda, C. V. B., Leis, B. N., Charlton, R. G., and Manherz, D. W. in *Proceedings,* 3rd International Conference on Fracture, Munich, West Germany, April 1973.
[17] Leis, B. N., "Cyclic Inelastic Deformation Behavior of Thin Notched Plates," M.Sc. Thesis, University of Waterloo, Waterloo, Ont. Canada, March 1972.
[18] Leis, B. N., "Fatigue Analysis to Assess Crack Initiation Life for Notched Coupons and Complex Components," Ph.D. Thesis, University of Waterloo, Waterloo, Ont., Canada, Sept. 1976.
[19] Leis, B. N. in *Methods of Predicting Fatigue Life,* American Society of Mechanical Engineers, 1979, pp. 57-76.
[20] Leis, B. N., *Journal of Testing and Evaluation,* Vol. 5, No. 4, July 1977, pp. 215-221.
[21] Leis, B. N. in *Proceedings,* 9th International Committee on Aeronautical Fatigue, ICAF Document 960, Laboratorium fur Betriebsfestigeit, Darmstadt, Germany, May 1977, pp. 3.4/1-47.
[22] Dowling, N. E., Brose, W. R., and Wilson, W. K., "Notched Member Fatigue Life Predictions by the Local Strain Approach," SAE-AE6, Society of Automotive Engineers, R. M. Wetzel, Ed., 1977.
[23] Dowling, N. E. in *Fracture Mechanics, ASTM STP 677,* American Society for Testing and Materials, 1979, pp. 243-273.
[24] Usami, S. and Shida, S., *Fatigue of Engineering Materials and Structures,* Vol. 1, No. 4, 1979, pp. 471-481.
[25] El Haddad, M. H., Smith, K. N., and Topper, T. H. in *Fracture Mechanics, ASTM STP 677,* American Society for Testing and Materials, 1979, pp. 274-289.
[26] Tanaka, K., private communication, Jan. 1980.
[27] Irwin, G. R., *Journal of Applied Mechanics, Transactions,* American Society of Mechanical Engineers, 1957.
[28] Paris, P. C., Gomez, M. P., and Anderson, W. E., *The Trend in Engineering,* Vol. 13, 1961, pp. 9-14.
[29] Broek, D. and Schijve, J., "The Influence of the Mean Stress on the Propagation of Fatigue Cracks in Aluminum Alloy Sheets," National Aerospace Institute, Amsterdam, TR-M-2111, 1963.
[30] Rice, J. R., *Journal of Applied Mechanics,* Vol. 35, 1968, pp. 379-386.
[31] Leis, B. N., "Displacement Controlled Fatigue Crack Growth in Elastic-Plastic Notch Fields and the Short Crack Effect," *Engineering Fracture Mechanics,* to appear.
[32] Rooke, D. P. and Cartwright, D. J., *Stress Intensity Factors,* Her Majesty's Stationery Office, London, 1976.
[33] Leis, B. N. and Galliher, R. D., "Growth of Physically Short Corner Cracks at Circular Notches," *Low Cycle Fatigue and Life Prediction, ASTM STP,* to appear.
[34] Leis, B. N. and Broek, D., "The Role of Similitude in Fatigue Damage Analyses at Notches," *Shock and Vibration,* to appear.

J. Janiszewski,[1] *R. W. Hertzberg,*[2] *and J. A. Manson*[2]

Fatigue Fracture Micromechanisms in Poly(Methyl Methacrylate) of Broad Molecular Weight Distribution

REFERENCE: Janiszewski, J., Hertzberg, R. W., and Manson, J. A., "**Fatigue Fracture Micromechanisms in Poly(Methyl Methacrylate) of Broad Molecular Weight Distribution,**" *Fracture Mechanics: Thirteenth Conference, ASTM STP 743,* Richard Roberts, Ed., American Society for Testing and Materials, 1981, pp. 125–146.

ABSTRACT: Scanning electron microscopy was used to examine the fatigue fracture surfaces of poly(methyl methacrylate) of varying molecular weight (MW) and molecular weight distribution. The specimens had been synthesized to incorporate various porportions of high- and low-MW tails in high, medium, and low-MW matrixes. In specimens with a high-MW matrix, increased proportions of low-MW additions resulted in higher fatigue crack growth rates and a gradual shift in the appearance of the fracture surface toward that of a low-MW matrix specimen with a small addition of a high-MW specie. Crack advance was continuous, with fatigue striation widths corresponding to the macroscopically measured growth increment associated with each loading cycle. In low-MW matrixes, addition of medium- and high-MW species resulted in attenuated crack growth rates and resulting longer life. With less than 2 percent of the medium- and high-MW species, crack advance was by a discontinuous mode with each growth increment equal to the size of the plastic zone at the crack tip. At high ΔK levels, discontinuous growth bands took on a scalloped appearance while maintaining a second power dependence between bandwidth and ΔK.

KEY WORDS: poly(methyl methacrylate), fatigue crack propagation, fatigue striations, discontinuous growth bands, polymer fatigue, fracture mechanics, fractography

Microscopic examination of fatigue fracture surfaces in several polymer systems [*1-6*][3] has revealed the existence of two distinct crack growth mechanisms. One mechanism leads to fatigue striations whose spacings correspond to the location of the crack front after each loading cycle. The spacing between these markings, therefore, reflects the local fatigue crack propagation rate in the material.

[1]Metallurgical consultant, Mohnton, Pa. 19540.

[2]Professors of metallurgy and chemistry, respectively, Lehigh University, Bethlehem, Pa. 18015.

[3]The italic numbers in brackets refer to the list of references appended to this paper.

Several polymer systems, however, reveal a second type of crack growth pattern. The surfaces of such specimens reveal a set of parallel bands whose sizes are up to several orders of magnitude larger than the increment of crack growth corresponding to one load cycle at the crack length concerned [*4-7*]. These bands exhibit an internal structure of voids [*4*] whose size gradually decreases across the band in the direction of crack growth. The size of these fracture bands has been found to be approximately equal to the size of the plastic zone r at the tip of the crack as calculated by the Dugdale plastic strip model [*8*]

$$r \cong \frac{\pi}{8}\left(\frac{K}{\sigma_{ys}}\right)^2 \qquad (1)$$

where K is the stress-intensity factor and σ_{ys} the yield strength. Yield strengths of polymers calculated by using this model have been found [*4*] to agree with crazing strengths measured from tension tests.

These large bands develop in two distinct stages [*4*]. First, a craze enlarges continuously in front of the stationary crack tip with each successive loading cycle. Then, when the craze reaches some limiting size, the crack extends abruptly through the craze during the next loading cycle and terminates at the craze tip. Crack growth occurs again in discontinuous fashion only after development of a new craze.

It has been proposed [*5*] that the applied loads are transmitted across the craze ahead of the crack tip by molecular entanglement networks contained within craze fibrils. Under long-term static or cyclic loading conditions, the entanglement networks must eventually undergo disentanglement, and weaker fibrils fail, thus shifting an increasing proportion of load to the remaining intact components of the network. Within the craze, then, sudden crack advance will take place when the applied load exceeds the collective load-bearing capacity of the remaining craze-spanning fibrils. As the crack advances through the craze, the remaining craze fibrils are ruptured (in some combination of bond rupture and plastic flow); eventually the crack is arrested as it reaches the undeformed material ahead of the original damaged zone.

Discontinuous growth is more likely to occur under conditions of (1) low stress-intensity factor range, (2) high test frequency, and (3) relatively low molecular weight [*1-4, 7*]. All three factors tend to favor development of a single craze as opposed to multiple crazes. Detailed examination of molecular weight effects on discontinuous crack growth reveals a complex behavioral pattern. No discontinuous growth bands have been found in poly(methyl methacrylate) (PMMA) specimens with $M_w > \sim 2 \times 10^5$ weight-average molecular weight, or in poly(vinyl chloride) (PVC) with $M_w < \sim 60\,000$ [*7*]. Extending an earlier idea by Berry [*9*], Kausch [*10*] has proposed that molecules having lengths greater than a certain critical value are necessary to form entanglement networks that can span a developing craze. It follows that specimens of higher average molecular weight will develop a greater number of entanglements per molecule and thus lead to more stable crazes. On the other hand, craze stability at low M_w is too low to permit the development of craze zones that can withstand repeated loadings without rupture. Thus, as with static fracture [*11,12*], measurable strength requires that a critical value of molecular weight, M_0, must be exceeded.

In the previous discussion it was assumed implicitly that the molecular weight distribution was similar for all molecular weights. In fact, increased craze stability should be made possible by broadening the molecular weight distribution in the direction of higher molecular weight (MW). Indeed, Kim et al clearly demonstrated that high-MW fractions lead directly to significant, and often remarkable, increases in the resistance to fatigue crack propagation [*8*].

In the previous study, the molecular weight distribution of PMMA was broadened by the separate addition of small amounts of high- or low-molecular-weight polymer to a matrix of greatly differing molecular weight. For this paper fatigue specimens were prepared from this material and tested to fracture. Resulting fracture surfaces were examined to identify the fatigue crack growth micromechanisms as a function of the prevailing stress-intensity level and the polymer's molecular weight distribution.

Experimental Procedure

In order to ensure the closest possible control of material composition and behavior, specimens for studying the molecular weight distribution of poly(methyl methacrylate) were prepared in our laboratory by a two-step process. First, the polymer constituting the minor species of the specimen was synthesized to obtain the value of MW desired; both low-MW and high-MW species were prepared. This "tail" was then dissolved in monomer which was then polymerized under controlled conditions to produce a polymer with a desired bimodal distribution. With one series, the polymerization of both the minor and major constituents of each polymer was effected thermocatalytically. With the second series, which contained low-MW species in a high-MW matrix, polymerization was effected photochemically. (For details, see Kim et al [*13*]).

Characterization of molecular weight and dynamic mechanical properties was done by Kim [*13*] for both the minor additions (prior to addition to monomer) and the final specimens. Viscosity-average molecular weight, M_v, was measured in benzene using standard techniques [*13*]; the number-average and weight-average molecular weights, M_n and M_w, were measured with a Waters Model 6000A Gel Permeation Chromatograph. Dynamic mechanical properties were measured with a Rheovibron unit, Model DDV-II. Characteristics of the bimodal-distribution PMMA specimens are summarized in Table 1.

All materials were machined into standard-geometry compact tension specimens using a standard [ASTM Test for Plane-Strain Fracture Toughness of Metallic Materials (E399-78A)] height/width ratio of 0.6. Fatigue tests were performed using a closed-loop electro-hydraulic testing machine, with a 9-kN load frame. Specimens were precracked at 100 Hz until a stable crack front was established, and the actual crack growth data were then recorded at 10 Hz. All testing was conducted with a minimum/maximum load ratio (R-value) of 0.1. Successive crack positions were monitored with a Gaertner traveling microscope with 0.1 to 0.3-mm measurement intervals. In this manner, several discontinuous cracking events would occur between readings, if discontinuous growth bands were to form under a given set of experimental conditions.

Stress-intensity factors were calculated using the formula

$$\Delta K = Y \Delta \sigma \sqrt{a}$$

where

$\Delta\sigma$ = stress range = $\Delta P/tw$,
ΔP = load range,
t = specimen thickness,
w = specimen width,
a = crack length, and
Y = geometric correction factor, $f(a/w)$ [11].

The crack growth rate at a particular point was calculated to be the average crack growth rate from the previous to the succeeding point; that is

$$(da/dN)_n = \frac{a_{n+1} - a_{n-1}}{N_{n+1} - N_{n-1}}$$

where a is the crack length and N the total number of cycles at the time of each crack-tip reading.

Following the calculation of ΔK and da/dN for all points, a least-squares fit was mathematically performed to obtain values for A and m in the general Paris power law relationship [14].

$$\frac{da}{dN} = A \, \Delta K^m$$

An apparent fracture toughness K_{cf} was calculated based on the value of ΔK associated with the last data point by use of the relation

$$K_{cf} = \frac{\Delta K_f}{1 - R}$$

TABLE 1—*Summary of broad-distribution PMMA specimens*

Series[a]	Method of Polymerization of Matrix	M_n Matrix	M_n Addition	Weight % Addition
H-L	thermal	$(1.6 \text{ to } 5.1) \times 10^5$	2.9×10^4	0,1,5,10 30
H-LU	ultraviolet	$(1.1 \text{ to } 5.2) \times 10^5$	1.4×10^4	0,2,5,10,20
L-H	thermal	$(1.1 \text{ to } 2.3) \times 10^{4(b)}$	4.2×10^5	0.5,
L-M	thermal	$(1.1 \text{ to } 2.3) \times 10^{4(b)}$	3.1×10^5	0.5,1,2

[a]H-L = high-MW matrix + low-MW addition.
L-H = low-MW matrix + high-MW addition.
L-M = low-MW matrix + medium-MW addition.
[b]Specimens having $M_n < 3 \times 10^4$ were found to be too brittle to test.
[c]0.5% specimen used for fractography only.
[d]For details of actual M_w and M_n, see Table 2.

Fractographic studies were performed on an ETEC Autoscan Scanning Electron Microscope. Prior to examination, specimens were coated with gold and carbon to prevent charge buildup on the surface. Since these specimens were found to be susceptible to electron beam damage (Fig. 1), accelerating potential of the electron beam was limited to 5 kV.

Results and Discussion

Characterization

The molecular weights and polydispersity indexes, M_w/M_n, for the broad-molecular-weight-distribution specimens are given in Table 2.

Molecular weight characterizations indicate that the desired results were achieved. Addition of low-M fractions to high-M materials tended to lower all molecular weight averages, and addition of a high-M component to raise them. As expected, the M_w/M_n ratio, an indication of the breadth of the distribution of chain lengths, is larger for the two-component specimens than for the single distribution (matrix only) specimens.

The gel permeation chromatography (GPC) curves were also analyzed to determine $w_{<300}$, the weight-percent of material having a number-average degree of polymerization less than 300 [300 corresponding approximately to a molecular weight of 3×10^4, the critical value (M_0) required for development of tensile strength]. The mole fraction of added tail, n_{tail}, is also given.

FCP Testing

Results of fatigue crack propagation (FCP) testing are summarized in Table 3. The column headings "lower portion" and "upper portion" refer to

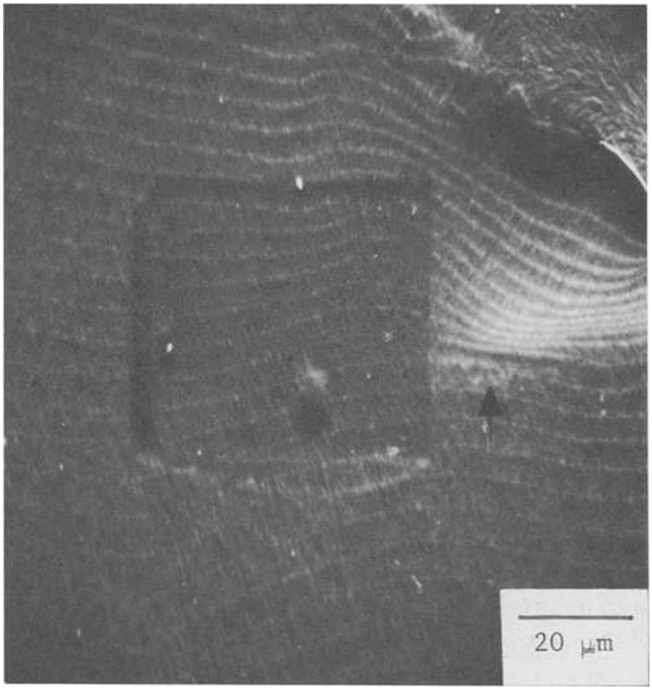

FIG. 1—*Electron beam-induced specimen damage (square zone). Arrow indicates crack direction normal to fatigue striations.*

TABLE 2—*Detailed MW characterization of broad-MWD PMMA.*

Specimen	M_n	M_w	M_w/M_n	$w_{<300}$	n_{tail}
H	4.2×10^5	1.3×10^6	3.1	0.52	...
M	3.1×10^5	1.0×10^6	3.3	0.87	...
L	2.9×10^4	6.9×10^4	2.4	22.5	...
H1L	2.4×10^5	1.8×10^6	7.4	1.52	0.08
H5L	2.8×10^5	1.6×10^6	5.5	1.22	0.41
H10L	1.1×10^5	6.6×10^5	5.7	5.4	0.38
H30L	2.3×10^4	1.1×10^5	4.7	8.2	0.24
L1H	1.4×10^4	5.8×10^4	4.1	44.2	0.33×10^{-3}
L2H	2.1×10^4	7.5×10^4	3.5	33.2	1.0×10^{-3}
L.5M	2.3×10^4	6.7×10^4	2.9	31.4	0.37×10^{-3}
L1M	1.1×10^4	4.7×10^4	4.4	54.4	0.35×10^{-3}
L2M	1.7×10^4	5.4×10^4	3.3	36.4	0.11×10^{-3}

the observation that the da/dN versus ΔK plots exhibited two separate straight-line regions, each with its characteristic parameters (A and m) for the relationship [14] $da/dN = A \, \Delta \, K^m$. In the high-MW-matrix specimens, the ΔK level associated with the slope transition also marked the point where the macroscopic fracture surface topography changed from a rough to a smooth appearance with fatigue striations being associated only with the smooth region. In the low-MW-matrix specimens, no change in fracture surface appearance was observed at the point of slope transition.

From Fig. 2*a*, it can be observed that the addition of increasing amounts of low-MW PMMA to a high-MW matrix tended to result in lowered resistance to fatigue crack propagation and lowered fracture toughness (Table 3). Addition of high- or medium-MW PMMA to a low-M matrix, on the other hand, increased FCP resistance and K_{cf} (Figs. 2*b* and 2*c* and Table 3).

It is interesting to note that without the addition of M or H fractions, the L-M and L-H series (Table 1) would have been at best on the borderline of machinability, and in some cases unable to be machined at all (see also Ref *13*).

Fractographic Results

High-MW Matrix—Scanning electron microscopy (SEM) examination of selected high-MW-matrix specimens (H1L, H10L, and H30L) revealed two types of fracture surface micromorphology at low values of ΔK. With specimens H1L and H10L, surfaces were very smooth in texture with the exception of classic river patterns which pointed in the direction of crack growth (Fig. 3). However, as the proportion of low-MW addition increased to 30 percent, the surface began to lose its flat appearance and exhibited a "blocky" struc-

TABLE 3—*Summary of FCP results.*

Specimen	Lower Portion		Transition	Upper Portion			No. of Specimens
	A	m	ΔK	A	m	K_{cf}	
H1L	3.2×10^{-4}	4.3	0.96	4.7×10^{-4}	13.7	1.40	1
H5L	8.4×10^{-4}	6.8	0.81	2.3×10^{-3}	11.5	1.20	2
H10L	6.4×10^{-4}	5.7	0.90	8×10^{-3}	29.7	1.09	2
H30L	1.8×10^{-3}	5.7	0.81	1.3×10^{-2}	14.8	1.12	2
H-U	3.7×10^{-4}	9.0	0.90	9×10^{-4}	17.3	1.30	1
H2LU	6×10^{-4}	5.9	0.82	7×10^{-3}	19.4	1.02	1
H5LU	8.1×10^{-4}	5.5	...	...	...	0.98	1
H10LU	8.1×10^{-4}	5.5	0.85	5.9×10^{-2}	34.0	1.13	1
H20LU	1.2×10^{-3}	4.2	0.69	2×10^{-1}	19.8	1.05	1
L1H	1.2×10^{-3}	3.0	0.58	6×10^{-3}	6.1	0.79	1
L2H	6.4×10^{-4}	2.6	0.70	5×10^{-3}	8.4	1.0	1
L.5M	3.5×10^{-3}	3.9	0.53	2.7×10^{-2}	7.1	0.95	1
L1M	2.8×10^{-3}	3.7	0.76	5×10^{-2}	14.2	1.09	2
L2M[a]	4.4×10^{-3}	4.8	0.62	3.5×10^{-2}	9.1	0.84[a]	1
L	1.1×10^{-2}	4.8	0.51	5.6×10^{-1}	10.6	0.78	1
M	2.65×10^{-4}	4.9	0.85	2.9×10^{-3}	19.5	1.04	1
H	1.4×10^{-4}	6.0	0.97	1.7×10^{-4}	12.0	1.54	1

[a]Specimen failed at unexpectedly low ΔK level—probable production defect.

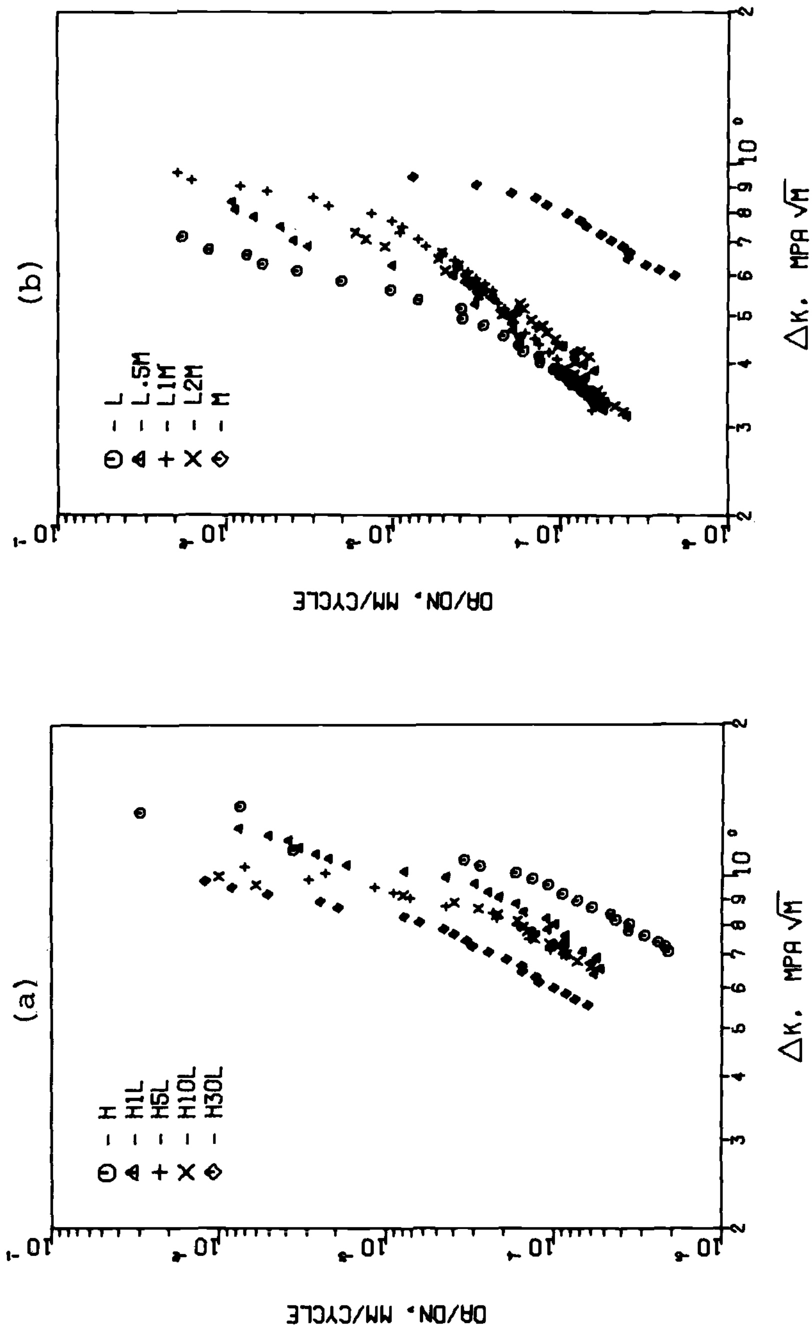
(b)
L
L.5M
L1M
L2M
M
(a)
H
H1L
H5L
H10L
H30L
DA/DN, MM/CYCLE
ΔK, MPA √M

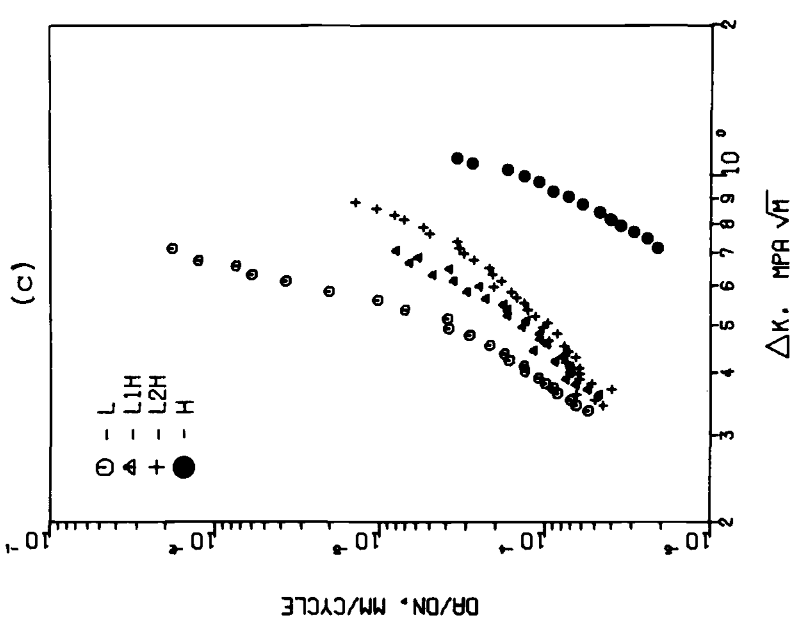

FIG. 2—*Fatigue crack propagation data in broad MWD PMMA: (a) high-MW matrix containing 1, 5, 10, and 30 weight percent low-MW species; (b) low-MW matrix containing 0.5, 1, and 2 weight percent medium-MW species; (c) low-MW matrix containing 1 and 2 weight percent high-MW species.*

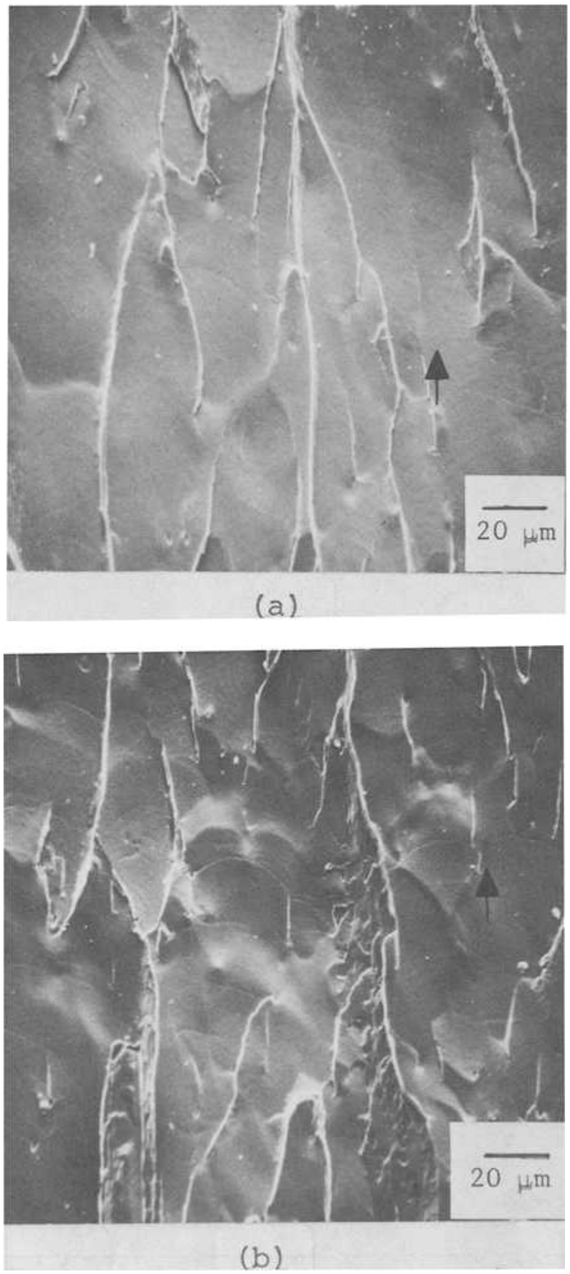

FIG. 3—*Fracture surface appearance in high-MW matrix at* $\Delta K = 0.66$ *MPa* $\sqrt{m}$. *(a) Specimen H1L; (b) Specimen H10L. Arrow indicates crack propagation direction.*

ture (Fig. 4*a*). A similar fracture surface appearance was noted in a low-MW-matrix specimen, L2H, that contained 2 percent of a high-MW addition (Fig. 4*b*). Examination of these fracture surfaces reveals a striking similarity that parallels the FCP response of these two materials (Fig. 5). It would appear that the fatigue response of the high-MW-matrix specimens begins to be controlled by the large number of short chains introduced when 30 percent low-MW material is added. This is so even though the number of low-MW chains is smaller than in Specimen L2H (Table 2).

Distinct fatigue striations such as those shown in Fig. 1 were visible in all specimens (except H30L) at higher values of ΔK above the slope transition. Agreement between striation spacing widths and macroscopic growth increments was found as shown in Fig. 6 for Specimens H10L and H10LU. (At lower ΔK-values associated with lower FCP rates, striation formation may have occurred but could not be confirmed due to the tendency for electron beam-induced specimen damage associated with surface examination at higher magnifications.)

Specimen H30L revealed a somewhat different fracture surface appearance at high ΔK levels (Fig. 7*a*). An array of coarse bands of relatively constant spacing was seen over much of the fracture surface in this high-ΔK regime. When this pattern was examined in greater detail (Fig. 7*b*) regions containing voids were observed, indicative of failure through a craze. The flat patchy areas suggest, in turn, that the crack had proceeded along the boundary between crazed and undeformed material with the patches being formed when the crack jumped from one boundary to the other. This phenomenon has previously been seen to occur during fast fracture in polystyrene [*15,16*].

The significance of these fracture bands is not clear at this time. Bandwidths have proven to be erratic and no clear relationship has been established between band spacing and the stress-intensity level. Nonetheless, one may speculate that these irregular bands represent the first evidence of discontinuous crack extension in the high-MW-matrix polymer, this mode being possible only after large additions of a low-MW species.

Low-MW Matrix—At low ΔK, the fracture surfaces of all low-MW-matrix specimens exhibited a blocky structure similar to that seen in Fig. 4. Specimens with small amounts of additions (L.5M, L1M, L1H) showed a distinct discontinuous growth band (DGB) structure superimposed on the overall blocky surface (Fig. 8*a*). When viewed at a higher magnification (Fig. 8*b*), each DGB revealed classic evidence of the discontinuous growth process—each band contained many microvoids which decreased in size in the direction of crack growth.

DGB sizes were measured for Specimens L1H, L.5M, and L1M and found to follow the predicted second-power dependence with ΔK (Fig. 9). Yield strengths were computed based on the Dugdale plastic strip model [*8*], by equating the band size to the plastic zone size. Results of this calculation are given in Table 4.

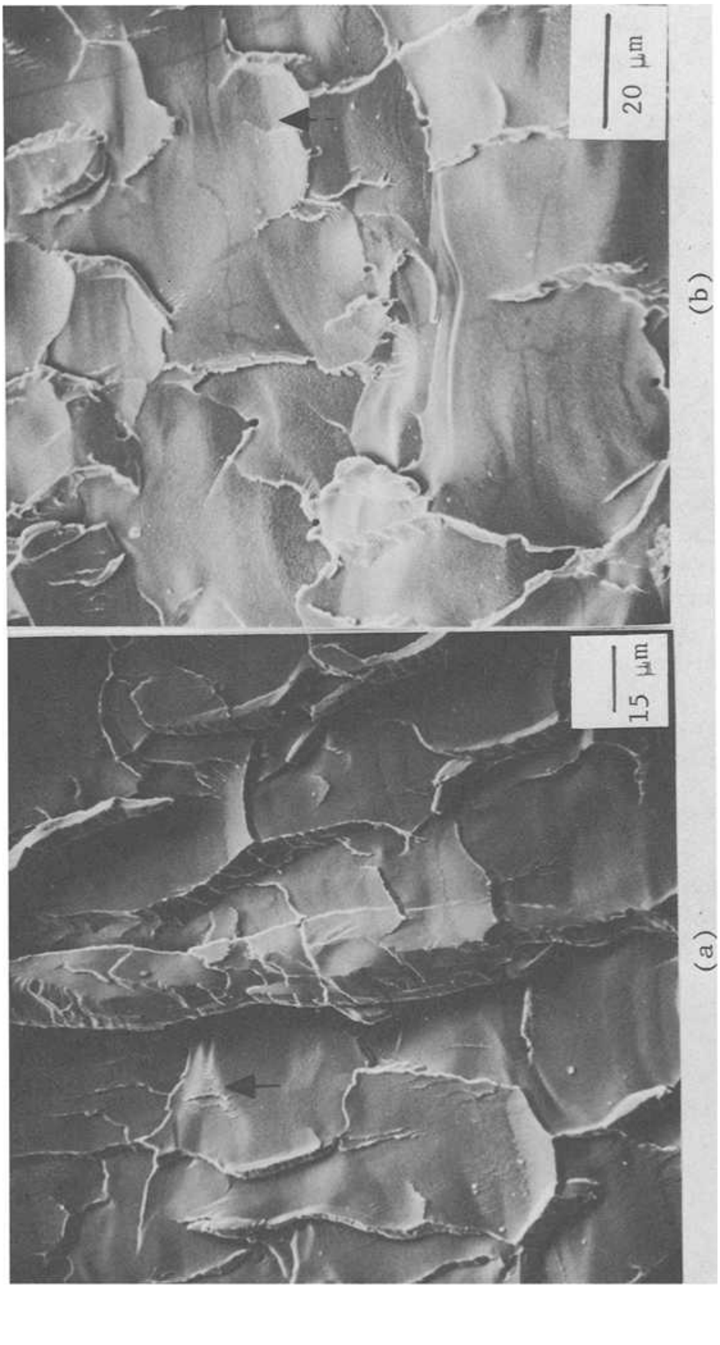

20 μm
(b)
15 μm
(a)

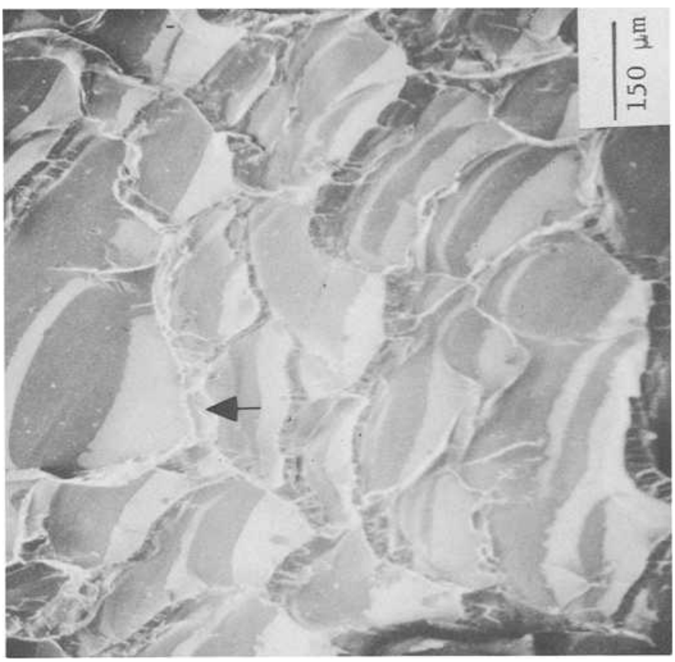

FIG. 4—"Blocky" fracture appearance. (a) Specimen H30L, $\Delta K = 0.56$ MPa $\sqrt{m}$; (b) Specimen L2H; $\Delta K = 0.35$ MPa $\sqrt{m}$; (c) Specimen L2M, $\Delta K = 0.45$ MPa $\sqrt{m}$. Arrow indicates crack propagation direction.

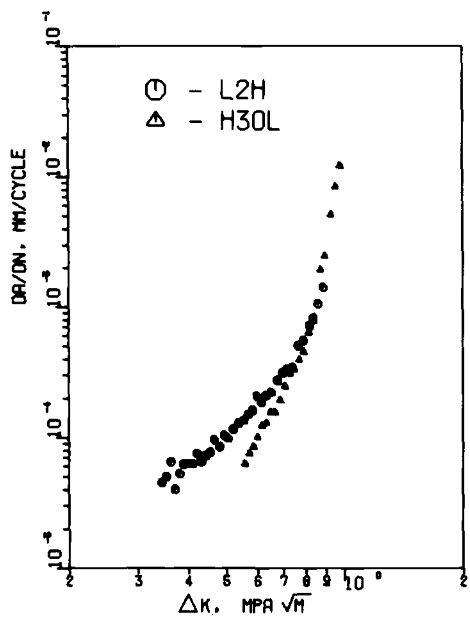

FIG. 5—*Similarity in FCP response between Specimens L2H and H30L.*

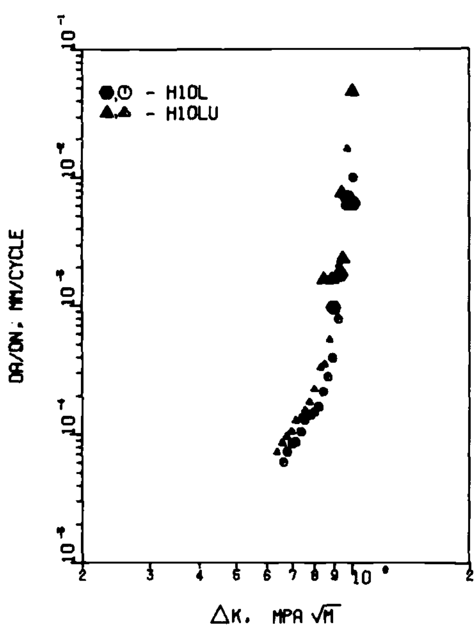

FIG. 6—*Correlation between macroscopic and microscopic FCP rates in Specimens H10LU and H10L. Closed data points correspond to fatigue striation measurements.*

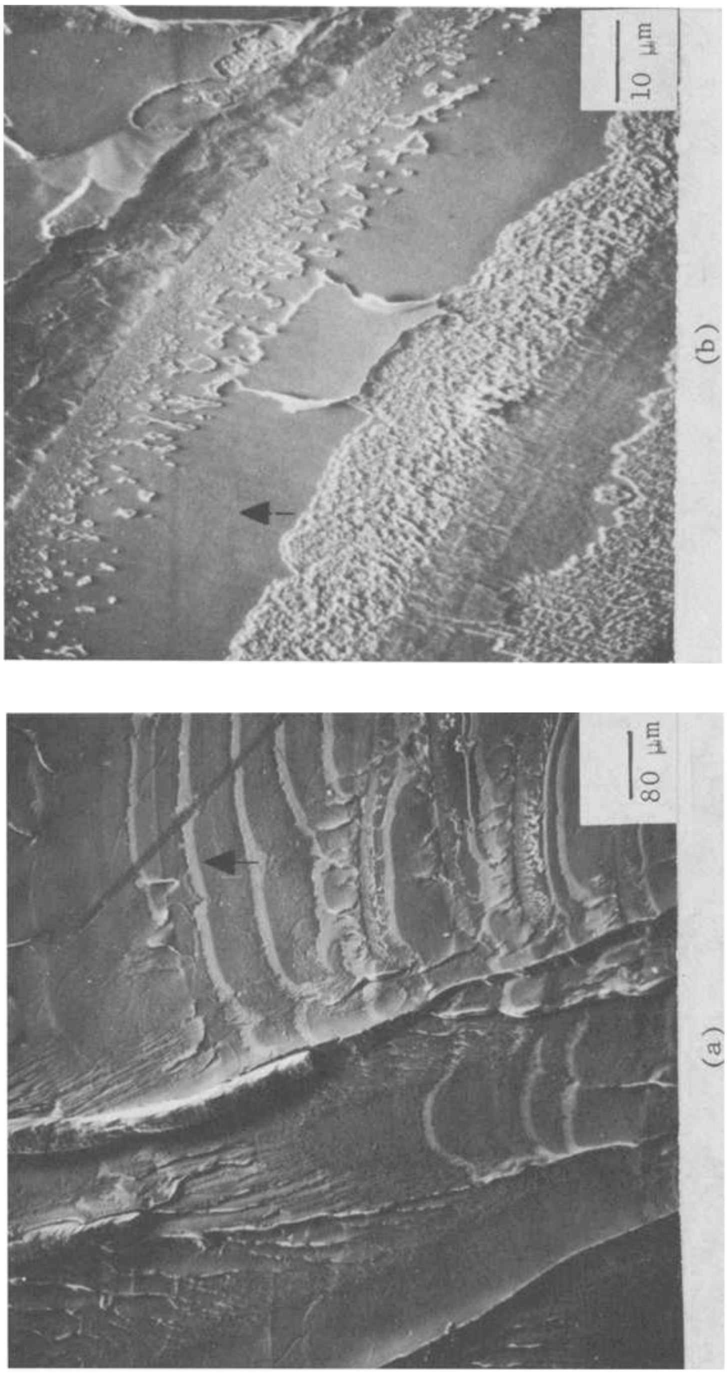

FIG. 7—*Coarse fracture bands in H30L which may represent early stage of discontinuous growth band formation. (a) ΔK = 0.87 MPa $\sqrt{m}$; (b) ΔK = 0.91 MPa $\sqrt{m}$. Arrow indicates crack propagation direction.*

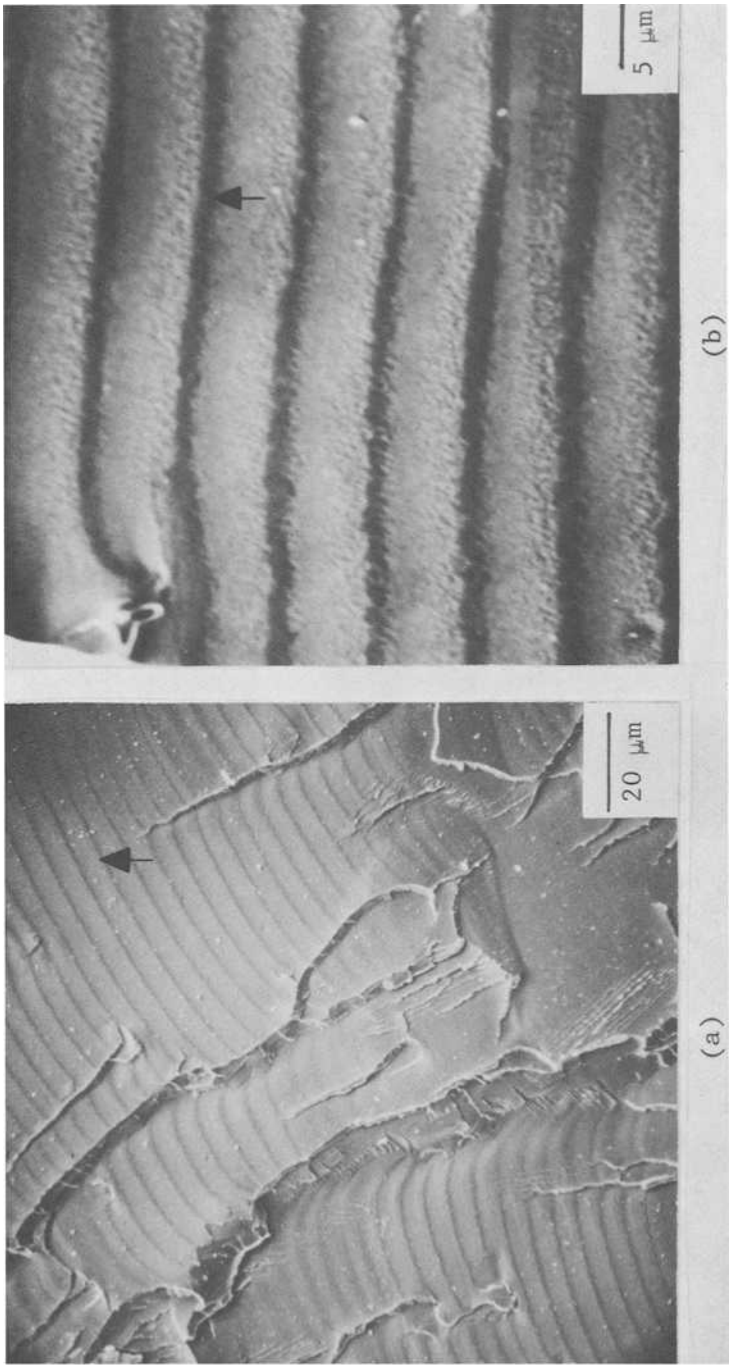

FIG. 8—*Discontinuous growth bands corresponding to the size of the crack-tip plastic zone. (a) Specimen L.5H, ΔK = 0.32 MPa $\sqrt{m}$; (b) Specimen L1H, ΔK = 0.36 MPa $\sqrt{m}$. Arrow indicates crack propagation direction.*

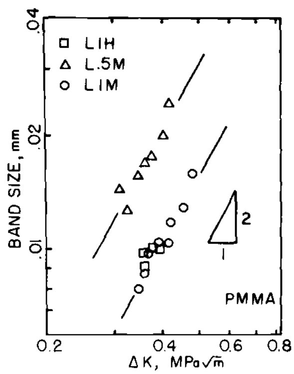

FIG. 9—*Discontinuous growth band width versus ΔK in low-MW-matrix PMMA containing 0.5 M, 1 M, and 1 H additions.*

TABLE 4—*Calculated yield strengths based on Dugdale model.*

Specimen	$w_{<300}$	Calculated σ_{ys},MPa	$w_{tail} \times M_{tail}$[a] ($\times 10^{-3}$)	M_n	$n_{tail} \times 10^3$
L.5M	0.31	60.8	5	2.3×10^4	0.37
L1M	0.54	86.2	8	1.1×10^4	0.35
L1H	0.44	83.6	10	1.4×10^4	0.34

[a]Weight-average MW.

The computed yield strengths for L1M and L1H agreed closely with the value of yield strength of 83 MPa reported by Morgan and Ward [*17*], while that for the L.5M specimen was considerably lower. At first glance this finding seems not to fit in with the general experience with single-distribution polymers in that σ_{ys} increases with MW. Also, no correlation with the proportion of low-MW or high-MW components exists ($w_{<300}$ and n_{tail}). However, if one calculates a weighted fraction of the tail added (weight fraction times MW), one finds that the weighted effect of the tail is much less for L.5M than L1M and L1H. This is not at all surprising, for the weight-average molecular weight may well be expected to dominate yielding. Since the matrixes of the three polymers all have very low values of MW (Table 1), the weight-average contribution of the tail should be most important (Table 4). In other words, with these bimodal distributions of MW, use of the *average* MW for correlations may be misleading.

Molecular weight also affects craze stability. An indication of the stability of the craze and its resultant discontinuous growth band may be gained by dividing the band size by the overall crack growth rate to compute the number of cycles represented by each band. Figure 10 shows the results of band stability calculations for specimens L.5M, L1M, and L1H. The fracture

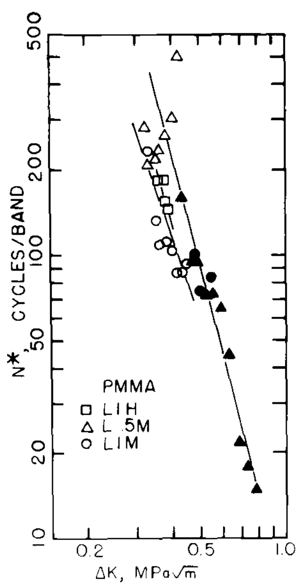

FIG. 10—*Discontinuous growth band cyclic stability versus* ΔK *in PMMA broad-MWD specimens.*

bands observed in these specimens exhibited the lowest cyclic stabilities as compared with data from other engineering plastics [*4*]; this finding is consistent with the fact that the FCP rates at a given ΔK level in Specimens L.5, L1M, and L1H are generally higher than those recorded in other polymers that exhibited discontinuous cracking. It is interesting to note, however, that the cyclic stabilities of bands from Specimen L.5M exceeded those computed from Specimen L1M and L1H even though the FCP rates in the latter two were lower (see Figs. 2*b* and 2*c*). This curious behavior is attributed to differences in the material's respective yield strengths (Table 4). That is, the lower yield strength associated with Specimen L.5M will generate a larger DGB that would require more loading cycles to break down.

In low-M-matrix specimens containing 2 percent of high- or medium-MW additions, no distinct discontinuous growth band pattern was seen. The disapperance of discontinuous growth bands associated with 2 percent by weight of high-MW additions to a low-MW matrix suggests that even this small percentage addition of long chains is sufficient to increase craze stability to the point where multiple crazing begins and discontinuous growth no longer provides the preferred method of crack advance. No appreciable change in overall fracture surface appearance of Specimens L2M and L2H was noted when going from low to high ΔK levels. The blocky surface seen at low ΔK values (Fig. 4*b*) persisted at high ΔK values, but in addition more pronounced, though irregularly spaced, surface relief markings appeared (Fig. 4*c*).

The contrasting results from specimens L.5M and L2H strongly suggest that DGB formation takes place only when certain molecular weight requirements are met within a particular range of MW. When there are too few long-chain molecules to create an entanglement network stable enough to stabilize a craze in a given polymer during cyclic loading, DGB formation will not occur. This was found to be the case in FCP studies of low-MW PVC [7]. Alternately, when a particular polymer contains more than some critical number of long-chain molecules, cycle-induced craze breakdown is suppressed to the point where discontinuous crack extension is precluded. The latter was observed in PMMA having a common unimodal distribution of MW ($M_v > 2 \times 10^5$) and in the results for Specimen L2H described herein. Finally, the micromorphology of DGB's was seen to break down progressively with increasing MW in PVC [7].

At higher ΔK, in those specimens previously found to exhibit discontinuous growth, the distinct DG bands began to lose their crisp lineage. Under these conditions, the crack front appears to be heavily segmented with the banded structure taking on a scalloped appearance (Fig. 11*a*). Closer examination (Fig. 11*b*) reveals different morphological features; there is a central region containing voids, in which all the voids are essentially the same size, and two almost flat areas, with occasional sharp changes in elevation, which give the appearance of patches of material having been torn out. This appearance again suggests, as in the case of the H30L specimen at high ΔK (recall Fig. 7*b*), that crack advance had occurred by means of two concurrent processes—growth through the middle of the craze, revealed by voids on the fracture surfaces, and growth along the craze boundary, resulting in flat areas. The observed elevation changes are interpreted to be the result of crack growth changing from one mode to the other or from one craze-matrix boundary to the other. The lack of an observed void-size gradient probably indicates that the craze had developed and fractured in a relatively few number of loading cycles [15 to 150 cycles (see Fig. 10)].

Measurement of these high-ΔK band sizes revealed that they too followed a second-power dependence (Fig. 12). This does not mean that the micromechanism of the crack growth process remained the same. In fact, the gross and detailed band structures were considerably different between low- and high-ΔK areas. The second-power dependence does, however, imply that these surface features were phenomenologically similar in that they were both related to the size of the plastic zone.

The similarity of these bands to those seen at high ΔK on the H30L specimen (Fig. 7*b*) suggests that the behavior of the H30L specimen was governed more by the low-MW addition then by the high-MW matrix. This is not surprising, since most of the chains in the H30L specimen are short.

These high ΔK bands on both H30L and the low-MW-matrix, low percent

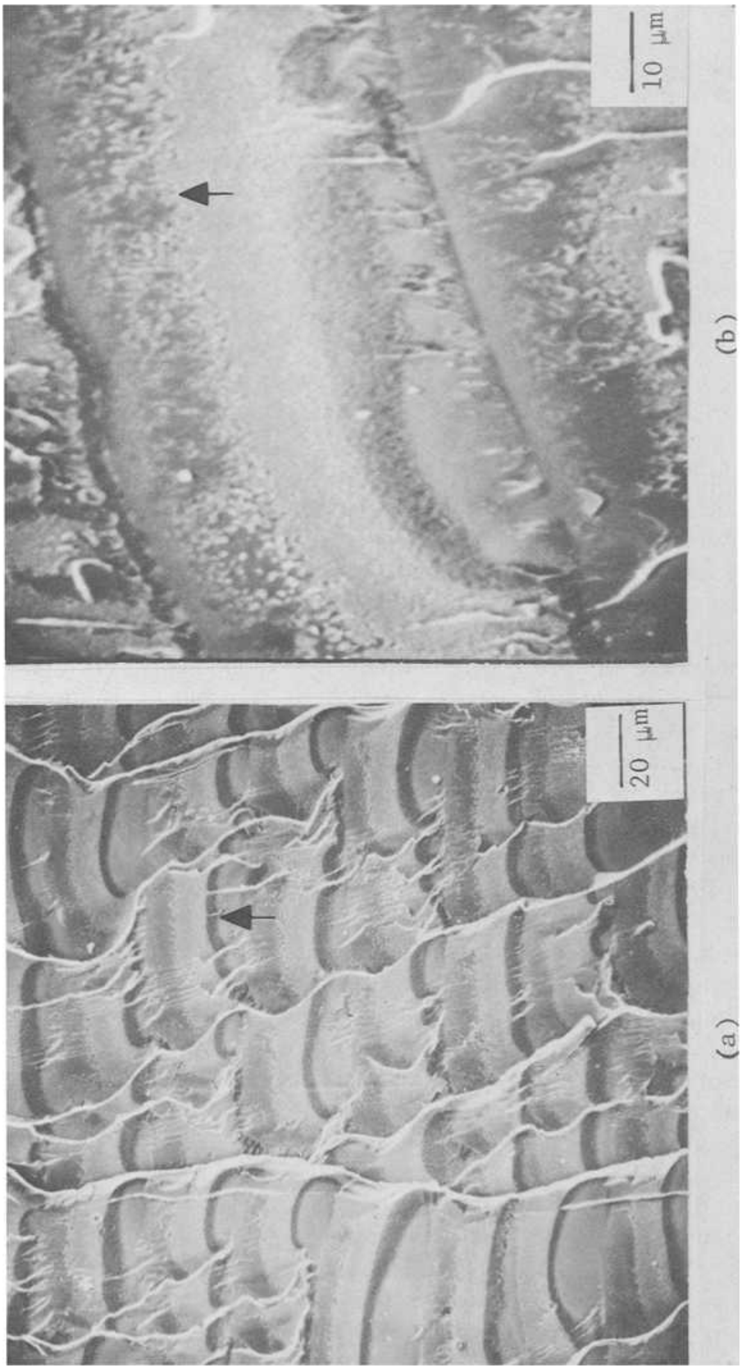

FIG. 11—"Scalloped" band structure in Specimen L.5H at $\Delta K = 0.41$ MPa $\sqrt{m}$. Arrow indicates crack propagation direction.

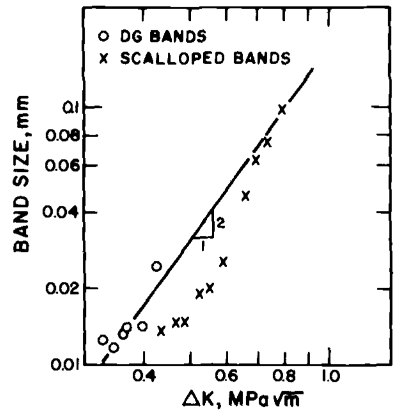

(a)

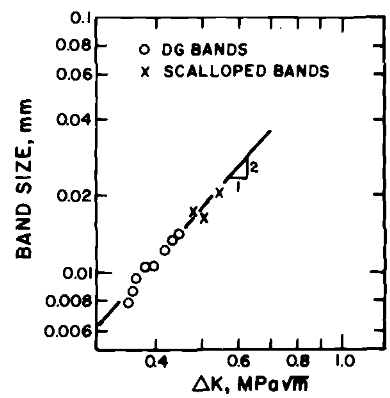

(b)

FIG. 12—*Relationship between discontinuous growth band and "scalloped" band spacing versus* ΔK. *(a) Specimen L.5M; (b) Specimen L1M. Arrow indicates crack propagation direction.*

addition specimens bear a strong resemblance to the "scalloped striations" reported previously in PMMA by Johnson [*18*] and Feltner [*19*]. Since no crack propagation data were obtained in either of these studies, it is quite possible that these reported "striations" were *not* the result of single crack advance steps (that is, classical fatigue striations), but rather discontinuous growth bands as observed in this study.

Conclusions

1. The fracture surface micromorphology of PMMA is seen to depend on both the character of the polymer molecular weight distribution and the magnitude of the stress-intensity factor range.

2. Up to 10 percent additions of low-MW polymer to a high-MW matrix in poly(methyl methacrylate) has a minimal effect on the fatigue fracture mechanism. With a larger fraction of low-MW molecules, the fatigue fracture surface changes and resembles that of a low-MW-matrix PMMA that contains 2 percent of a high-MW addition.

3. Small additions (0.5 and 1.0 percent) of medium- and high-MW-polymer to low-MW PMMA greatly improves fatigue crack propagation resistance and allows for the formation of discontinuous growth bands.

Acknowledgments

The earlier experimental phase of this investigation was supported by the Army Research Office-Durham (Grant No. DAAG29-76-G0036). Subsequent analysis and interpretation of these data received partial support from the National Research Foundation, Grant No. DMR 77-10063.

References

[1] Skibo, M. D., Hertzberg, R. W., and Manson, J. A., *Journal of Materials Science*, Vol. 11, 1976, pp. 479-490.
[2] Skibo, M., Manson, J. A., Hertzberg, R. W., and Collins, E. A., *Journal of Macromolecular Science and Physics*, Vol. B14, No. 4, 1977, pp. 525-543.
[3] Skibo, M. D., Janiszewski, J., Hertzberg, R. W., and Manson, J. A., *Toughening of Plastic*, Plastics and Rubber Institute, London, July 1978, pp. 25.1-25.8.
[4] Skibo, M. D., Hertzberg, R. W., Manson, J. A., and Kim, S. L., *Journal of Materials Science*, Vol. 12, 1977, pp. 531-542.
[5] Hertzberg, R. W., Skibo, M. D., and Manson, J. A. in *Fatigue Mechanisms, ASTM STP 675*, American Society for Testing and Materials, 1979, pp. 471-500.
[6] Elinck, J. P., Bauwens, J. C., and Homes, G., *International Journal of Fracture Mechanics*, Vol. 7, No. 3, 1971, p. 227.
[7] Rimnac, C. M., Hertzberg, R. W., and Manson, J. A. in *Fractography and Materials Science, ASTM STP 733*, American Society for Testing and Materials, 1981, p. 291-313.
[8] Dugdale, D. S., *Journal of the Mechanics and Physics of Solids*, Vol. 8, 1960, p. 100.
[9] Berry, J. P., *Journal of Polymer Science, A*, Vol. 2, 1964, p. 4069.
[10] Kausch, H. H., *Kunstoffe, 65*, Vol. 8, 1976, p. 1.
[11] Fellers, J. F. and Kee, B. F., *Journal of Applied Polymer Science*, Vol. 18, 1974, p. 2355.
[12] Gent, A. N. and Thomas, A. G., *Journal of Polymer Science, A-2*, Vol. 10, 1972, p. 571.
[13] Kim, S. L., Janiszewski, J., Skibo, M. D., Manson, J. A., and Hertzberg, R. W., *Polymer Engineering and Science*, Vol. 19, 1979, p. 145.
[14] Paris, P. C. in *Proceedings*, 10th Sagamore Conference, Fatigue—An Interdisciplinary Approach, Syracuse, N.Y., 1964, p. 107.
[15] Murray, J. and Hull, D., *Journal of Materials Science*, Vol. 6, 1971, p. 1277.
[16] Murray, J. and Hull, D., *Journal of Polymer Science, A2*, Vol. 8, 1970, p. 583.
[17] Morgan, G. P. and Ward, I. M., *Polymer*, Vol. 18, 1977, p. 87.
[18] Johnson, T. A., *Journal of Applied Physics*, Vol. 43, 1972, p. 1311.
[19] Feltner, C. E., *Journal of Applied Physics*, Vol. 38, 1967, p. 3576.

Günter Marci[1]

Fatigue Crack Growth Rates as a Function of Temperature

REFERENCE: Marci, Günter, **"Fatigue Crack Growth Rates as a Function of Temperature,"** *Fracture Mechanics: Thirteenth Conference, ASTM STP 743*, Richard Roberts, Ed., American Society for Testing and Materials, 1981, pp. 147–166.

ABSTRACT: The equation

$$\frac{da}{dN} = C[(K_I^G - K_{\mathrm{Imin}}) + \Delta K^T][(K_{\mathrm{Imax}} - K_I^G) - \Delta K^T]^2$$

had been proposed by the author to predict fatigue crack growth rates. By adopting this functional relation and setting $K_I^G = 0.5\,K_{\mathrm{Imax}}$ ($K_I^G \sim K_{\mathrm{Iopen}}$ under constant-amplitude cyclic loading), there are the two parameters, C and ΔK^I, left to be determined from experimental data.

The parameters C and ΔK^T for several structural alloys as a function of temperature between room temperature and 811 K had been analyzed. It was found that the "fatigue tolerance range" ΔK^T decreased linearly with increasing temperature. Initially, the parameter C increases nearly linearly with increasing temperature and then increases steeply at higher temperatures. In the present work, this temperature dependence is shown to be found between 4 and 911 K by analyzing low-temperature as well as additional high-temperature data for Inconel 718 and Inconel X-750. By assuming the observed qualitative temperature dependence of C and ΔK^T as being correct, available fatigue crack growth rates for Type 304 stainless steel obtained at temperatures ranging from 4 to 922 K were analyzed with respect to C and ΔK^T.

KEY WORDS: fatigue, crack growth rates, Inconel 718, Inconel X-750, Type 304 stainless steel, temperature effect, material parameters

Nomenclature

K_{Imax} Maximum stress-intensity factor
K_{Imin} Minimum stress-intensity factor
K_I^G Limit value of true stress-intensity range
ΔK^T Fatigue tolerance range
ΔK_{th} Threshold stress-intensity range

[1]Babcock Brown Boveri Reaktor Gmbh, Mannheim, F.R.G.: presently, DFVLR—German Aerospace Establishment, Institut für Werkstoff-Forschung, Cologne, F.R.G.

K_{Iopen} Crack opening stress-intensity factor
R K_{Imin}/K_{Imax}
e Total equivalent plastic strain
$\Delta\epsilon_c$ Effective compressive strain range
$\Delta\epsilon_T$ Effective tensile strain range
$\Delta\sigma_c$ Effective compressive stress range
$\Delta\sigma_T$ Effective tensile stress range

The goal of fatigue research is to predict failure of structural parts subject to fluctuating service loads and thereby design parts or limit service life such that structural failure is reliably prevented. Since most structural parts contain flaws due to manufacture, initiation of such flaws does not determine the service life, but rather the growth of the—mostly minute—flaws already present at the start of structural service. That is the main reason for the success of fracture mechanics in safe-life analysis.

Initially, the capability of fracture mechanics as a tool for safe-life predictions was demonstrated for relatively simple service environments and mechanical loading conditions. Yet, the initial success prompted the ongoing effort to extend the fracture mechanics analysis capability into more complex service environments. This work tries to show that temperature, as one of the service conditions, does not affect the basic functional relationship between growth rates and cyclic loading conditions. It should be remarked that this is true only as long as no temperature-induced phase transformation occurs. The material parameters characterizing the material's resistance to fatigue crack growth (FCG) are temperature-dependent.

The investigation relies on a model of FCG previously presented [*1*][2] and extends the initial work [*2*] related to the effect of temperature on the material parameters governing fatigue. In order to make this publication "self-contained," a short review of the FCG-model presented in Ref *1* is given in the following.

Model of Fatigue Crack Growth

Figure 1 shows schematically the cyclic stress-strain curves that material elements at the different positions ahead of the crack front inside the plastic zone experience during a loading cycle. Use was made of the fact that at the elastic-plastic boundary ahead of the crack the stresses and strains have to stay in the tensile range while at the crack front they can be compressive during the lower part of a loading cycle between K_{Imax} and $K_{Imin} = 0$. By plotting the cyclic stress-strain state corresponding to K_{Imax} for each such material element, one obtains an upper-bound curve (Curve X in Fig. 2) for the cyclic stresses and strains under that loading condition. Similarly, by

[2]The italic numbers in brackets refer to the list of references appended to this paper.

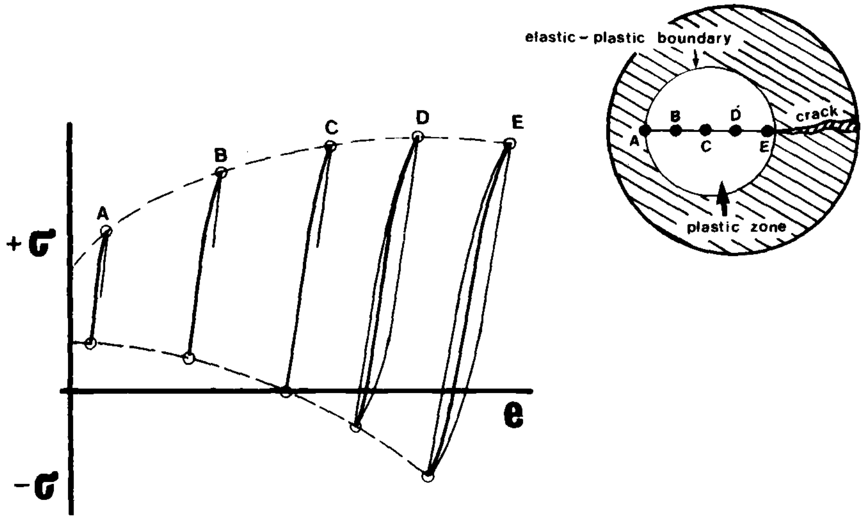

FIG. 1—*Stress-strain conditions at certain points inside the active plastic zone.*

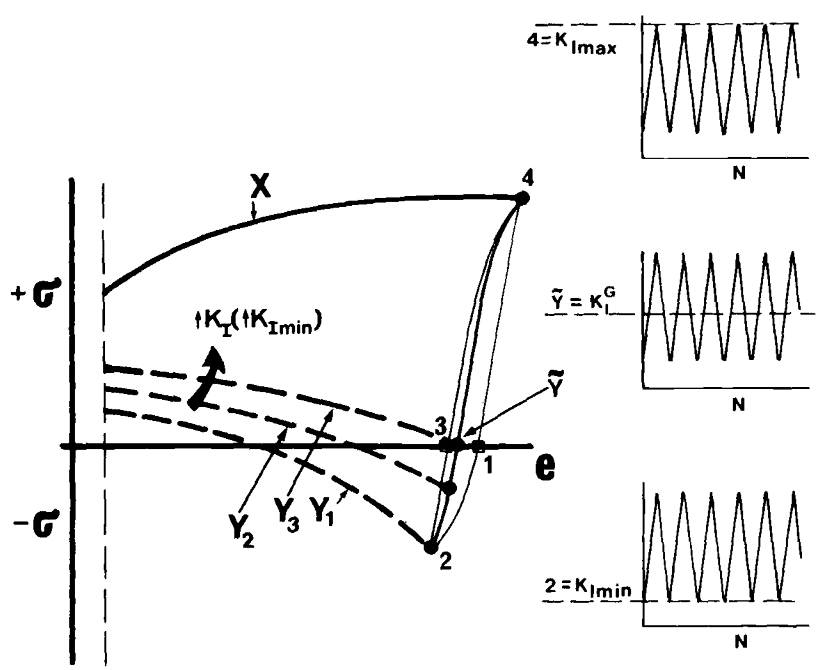

FIG. 2—*Stress-strain bounding curves for the state of stress and strain inside the active plastic zone.*

plotting the cyclic stresses and strains of such material elements corresponding to K_{Imin}, one obtains a lower-bound curve (Curve Y_1 in Fig. 2) for the cyclic stresses and strains.

The dependence of the active plastic zone size on K_{Imax} [3] and the independence of the R-ratio effect from prior K_{Imin} loading conditions [4,5] suggests that the upper-bound (Curve X) as well as the lower-bound (Curve Y_1) curve in Fig. 2 is uniquely dependent on K_{Imax} during constant-amplitude fatigue cycling with constant K_{Imax}. If this is correct, then there must be a stress-intensity factor between $K_{\mathrm{Imin}} = 0$ and K_{Imax} which causes the near region of the crack front to be free of stresses. Let point $\tilde{Y}$ in Fig. 2 represent this condition for material elements ahead of the crack front; then curve Y_3 would represent that stress-intensity factor, this stress intensity factor, denoted as $K_I{}^G$, should be uniquely related to K_{Imax}, that is

$$K_{\mathrm{I}}{}^G = \alpha K_{\mathrm{Imax}} \tag{1}$$

The stress-intensity factor at which the transition from compressive stresses and strains to tensile stresses and strains occurs in the material elements ahead of the crack front is defined as the "limit value" of the true stress-intensity range transmitted to the active plastic zone. This limit value $K_{\mathrm{I}}{}^G$ was measured to be 0.5 K_{Imax} for the alloy 2024-T3. Low-cycle fatigue behavior suggests that the total plastic strain e (e = equivalent strain), as shown in Fig. 2, is not very influential with respect to fatigue damage. The excursion of strains and the respective stresses should be more important. But the excursion of strains in the near region of the crack front is exactly what is characterized by partitioning of the transmitted stress-intensity range via $K_{\mathrm{I}}{}^G$. For clarification, the excursion of strains and respective stresses is defined as follows

$\Delta\epsilon_c$ = effective compressive strain range (Position 1 to 2)

$\Delta\sigma_c$ = effective compressive stress range (Position 1 to 2)

$\Delta\epsilon_T$ = effective tensile strain range (Position 3 to 4)

$\Delta\sigma_T$ = effective tensile stress range (Position 3 to 4)

The foregoing positions relate to Fig. 2. Accordingly, equations predicting "Stage II" fatigue crack growth rates (FCGR) (see Appendix for definition) should contain at least the two elements $\Delta\epsilon_c$ and $\Delta\epsilon_T$

$$\frac{da}{dN} = f(\Delta\epsilon_c, \Delta\epsilon_T) \tag{2}$$

Since

$$\Delta\epsilon_c \propto K_{\mathrm{I}}{}^G - K_{\mathrm{Imin}} \tag{3a}$$

$$\Delta\epsilon_T \propto K_{\mathrm{Imax}} - K_{\mathrm{I}}{}^G \tag{3b}$$

Eq 2 becomes

$$\frac{da}{dN} = g\ [(K_I{}^G - K_{\text{Imin}}), (K_{\text{Imax}} - K_I{}^G)] \tag{4}$$

where f and g are some functions. Stage II FCG can occur only if the near region of the crack front experiences excursions in effective tensile stresses $\Delta\sigma_T$ and strains $\Delta\epsilon_T$. In fracture mechanics terminology this condition means

$$K_{\text{Imax}} - K_I{}^G > 0 \tag{5}$$

Figure 3 shows that loading conditions which do not comply with relation (5) do not result in crack growth. Since excursions in effective compressive stresses do not produce crack growth, it makes no sense to define a threshold stress-intensity range which includes part or the total effective compressive stress range. Therefore, if a threshold stress-intensity range exists, it has to characterize a certain excursion in the effective tensile stress range $\Delta\sigma_T$ which does not produce crack growth. The threshold stress intensity range so defined (see Appendix for further definition of ΔK^T) is subsequently denoted

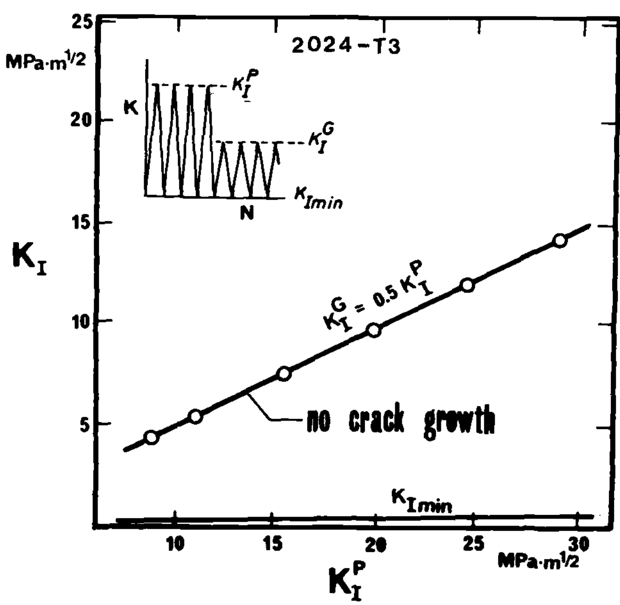

FIG. 3—*No fatigue crack growth under loading conditions producing only excursions in effective compressive stress* $\Delta\sigma_c$.

as "fatigue tolerance range" ΔK^T. The measured fatigue tolerance range for the alloy 2024-T3 is shown in Fig. 4 [*1*].

The findings concerning the fatigue tolerance range ΔK^T require that the FCGR equation, Eq 4, has to be modified. Since excursions of effective tensile stresses and strains have to exceed a range equivalent to ΔK^T before any crack growth occurs, ΔK^T has to be subtracted out of the total effective stress and strain range, that is

$$(K_{\mathrm{Imax}} - K_{\mathrm{I}}{}^{G}) - \Delta K^T \tag{6}$$

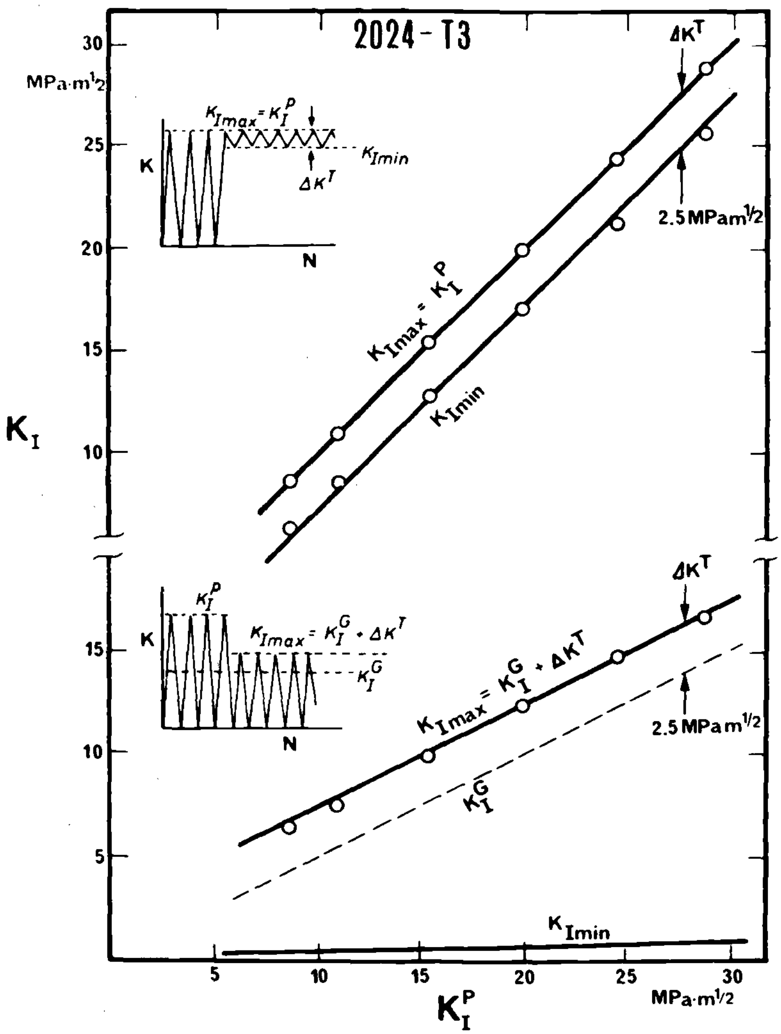

FIG. 4—*Conditions and results of the fatigue tolerance range* ΔK^T *determination.*

and Eq 4 is modified to

$$\frac{da}{dN} = h\ [(K_I{}^G - K_{\mathrm{Imin}}), \Delta K^T, (K_{\mathrm{Imax}} - K_I{}^G) - \Delta K^T] \tag{7}$$

where h is some function. The three elements contained in Eq 7 should enter any FCGR equation explicitly. The following equation had been proposed (for details, see Ref *1*)

$$\frac{da}{dN} = C\ [(K_I{}^G - K_{\mathrm{Imin}}) + (\Delta K^T)^m]\ [(K_{\mathrm{Imax}} - K_I{}^G) - \Delta K^T]^n \tag{8}$$

The R-ratio dependence of FCGR suggested that the term $(K_I{}^G - K_{\mathrm{Imin}})$ should enter linearly into Eq 8. It can be argued that ΔK^T can cause the same or less fatigue damage (not crack growth) as $(K_I{}^G - K_{\mathrm{Imin}})$ does, if they have equal magnitude. As an upper-bound value, $m = 1$ was chosen. With this assumption, n and C were determined by fitting Eq 8 to experimental data. ΔK^T was fixed by the experimental data themselves. It was shown in Refs *1* and *2* that for all materials analyzed (aluminum, titanium, and nickel-based alloys and ferritic steel) excellent agreement between predicted and experimentally measured FCGR was achieved with exponent $n = 2$. Under the assumption that $n = 2$ and $m = 1$ can be generalized, Eq 8 can be written

$$\frac{da}{dN} = C\ [(K_I{}^G - K_{\mathrm{Imin}}) + \Delta K^T]\ [(K_{\mathrm{Imax}} - K_I{}^G) - \Delta K^T]^2 \tag{9}$$

Equation 9 forms the basis for the following analysis of the effect of temperature on FCGR.

Method of Analysis

The value $n = 2$ in Eq 9 can be interpreted to mean that FCGR's are related to the fatigue damage accumulated in the path of the crack inside the active plastic zone. If the generalization concerning $n = 2$ and $m = 1$ is incorrect, then it would certainly show up as an inability to predict the experimentally observed FCGR for some of the materials.

The loading conditions enter Eq 9 directly via K_{Imax} and K_{Imin}. Thus, there remain three parameters unknown in Eq 9, namely $K_I{}^G$, ΔK^T, and C. Of these, $K_I{}^G$ is a material parameter which varies with varying loading history; that is, $K_I{}^G$ is already fixed at the beginning of a loading cycle by the previous loading conditions. Under constant-amplitude fatigue cycling with either constant maximum load or constant K_{Imax} the value of $K_I{}^G$ is equal to αK_{Imax}. It can be assumed, based on crack opening measurements, that for most structural materials α is in the range between 0.4 and 0.6 with maximum density at $\alpha = 0.5$. Small variations of the value $K_I{}^G$, say ± 0.03

K_{Imax}, have negligible influence on the predicted FCGR. As a starting point for checking the predictive capability of Eq 9, $K_I{}^G = 0.5\,K_{\mathrm{Imax}}$ was assumed (under certain restrictions $K_I{}^G = K_{\mathrm{Iopen}}$).

The remaining parameters ΔK^T and C must characterize the response of an individual material to cyclic loading. They must be an inherent property of the subject material which can be extracted by analysis of experimentally measured FCGR only. Generally the experimentally measured FCGR's are produced under constant-amplitude cycling with either constant maximum load or K_{Imax} and are therefore compatible with the assumption of $K_I{}^G = 0.5\,K_{\mathrm{Imax}}$. The way in which the parameters ΔK^T and C were extracted from experimentally measured FCGR is as follows.

Fatigue Tolerance Range ΔK^T

According to Eq 9, FCGR should become zero as the excursions in effective tensile stresses and strains decrease to or below the magnitude of excursions corresponding to ΔK^T, that is

$$\frac{da}{dN} \rightarrow 0 \text{ as } (K_{\mathrm{Imax}} - K_I{}^G) \rightarrow \Delta K^T \tag{10}$$

For R-ratios equal or greater than 0.5 the relation (10) takes on the form

$$\frac{da}{dN} \rightarrow 0 \text{ as } (K_{\mathrm{Imax}} - K_{\mathrm{Imin}}) = \Delta K \rightarrow \Delta K^T \tag{11}$$

Therefore, the fatigue tolerance range ΔK^T can be determined directly from a log da/dN versus log ΔK plot from FCGR with R-ratios equal or greater than 0.5 as that stress-intensity range ΔK^* at which FCGR approaches $\sim 3 \cdot 10^{-10}$ m/cycle

$$\Delta K^* = \Delta K^T \tag{12}$$

For FCGR with R-ratio between 0 and 0.5 the ΔK^* is measured at which FCGR approaches $\sim 3 \cdot 10^{-10}$ m/cycle and the respective K^*_{Imax} is determined

$$K^*_{\mathrm{Imax}} = \frac{\Delta K^*}{1 - R} \tag{13}$$

Since the conditions of relation (10) are fulfilled, the fatigue tolerance range is determined as follows

$$\Delta K^T = K^*_{\mathrm{Imax}} - K_I{}^G \tag{14a}$$

$$= K^*_{\mathrm{Imax}} - 0.5\,K^*_{\mathrm{Imax}} \tag{14b}$$

The model of FCG represented by Eq 9 is based on unique dependence of FCGR on the excursion of stresses and strains in the near region of the crack front during each individual loading cycle. If the FCGR cannot any more be uniquely related to each loading cycle, as it must be for FCGR smaller than the lattice parameter ($\sim 3 \cdot 10^{-10}$m), then the model ceases to apply; the same is true for ΔK^T. Actually, FCGR's down to $\sim 3 \cdot 10^{-10}$ m/cycle are not available in general. In such a case the trend line of FCGR was extrapolated down to this low FCGR and values on or to either side of the trend line assumed. The ΔK-value which gave the best fit through the experimental data was taken as ΔK^T and is the one shown in the following figures.

Material Parameter C

The values of the material parameter C was determined from FCGR in the range between $5 \cdot 10^{-7}$ and $5 \cdot 10^{-8}$ m/cycle. In that range the FCGR are plotting nearly linear on a log-log scale. FCGR greater than $5 \cdot 10^{-7}$ m/cycle might contain some contribution from a tearing mechanism due to high K_{Imax}; Eq 9 cannot account for that. Consequently, the predictions of Eq. 9 for FCGR greater than $5 \cdot 10^{-7}$ m/cycle should fall at or below the experimental data. Below $5 \cdot 10^{-8}$ m/cycle, FCGR's become very sensitive to the value of ΔK^T. Setting that lower limit of FCGR with respect to the determination of C insures that the value of C is only little affected by the particular choice of ΔK^T.

Results and Discussion

Figure 5 shows experimentally measured FCGR for Inconel 718 [*6*] for different R-ratios and different temperatures. An analysis of the data according to the methods described in the foregoing section was performed with respect to ΔK^T and C. The predictions of Eq 9 based on the empirically determined values ΔK^T and C are shown in Fig. 5 as curves through the data points. In Fig. 6, the parameters ΔK^T and C for the FCGR in Fig. 5 are plotted as a function of temperature. The thin vertical lines in Fig. 6 with data markings on the upper end indicate that the data marks coincide with the data marks already positioned on the curves. Figure 7 shows the values for ΔK^T and C as a function of temperature for Inconel X-750 [*7–9*] obtained by the same kind of analysis. Figures 6 and 7 had been published in similar form. The curves for ΔK^T and C had been extrapolated to lower temperatures and compared with additional data [*10–12*]. Figure 7 was augmented by some data sets from Ref *9*. The same qualitative temperature dependence of the parameters ΔK^T and C, as shown in Figs. 6 and 7, was obtained for Inconel 600 [*13*], Hastelloy X-280 [*14,15*], and SA 387 Grade C [*16*] in Ref 2.

Starting with this kind of temperature dependence of ΔK^T and C, it was the intention to analyze a widely used structural alloy with the anticipation

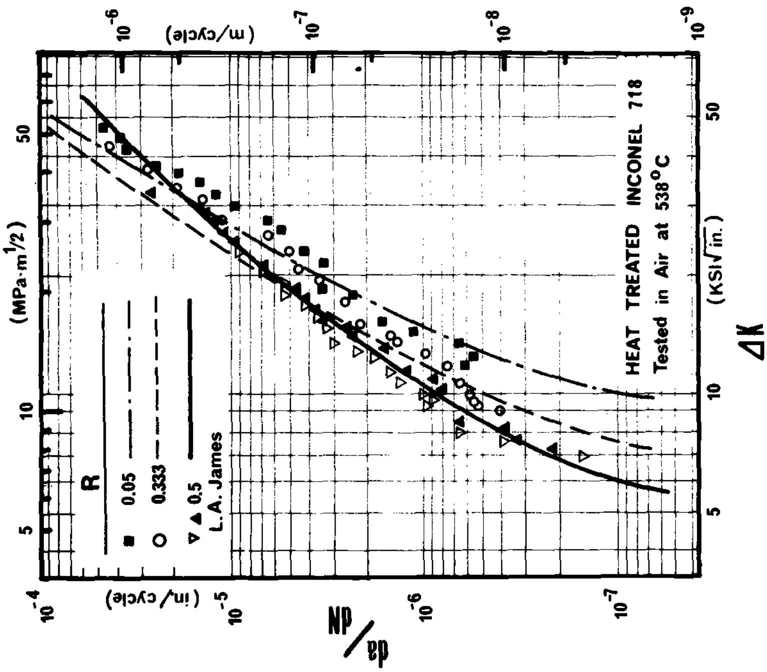
HEAT TREATED INCONEL 718
Tested in Air at 538°C
R
■ 0.05
○ 0.333
▽ ▲ 0.5
L.A. James
(MPa·m^1/2)
(KSI√in.)
ΔK
da/dN
(m/cycle)
(in./cycle)

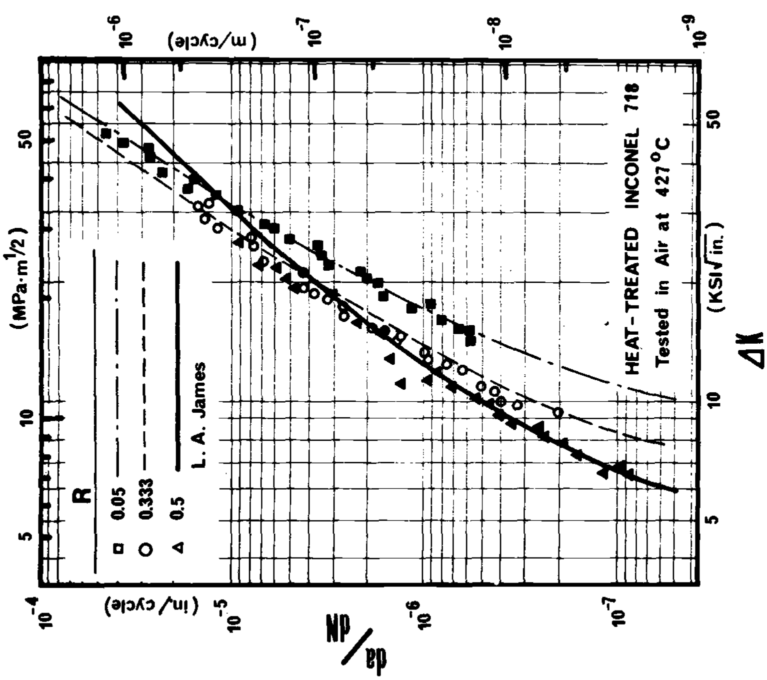
HEAT-TREATED INCONEL 718
Tested in Air at 427°C
R
□ 0.05
○ 0.333
△ 0.5
L. A. James
(MPa·m^1/2)
(KSI√in.)
ΔK
da/dN
(m/cycle)
(in./cycle)

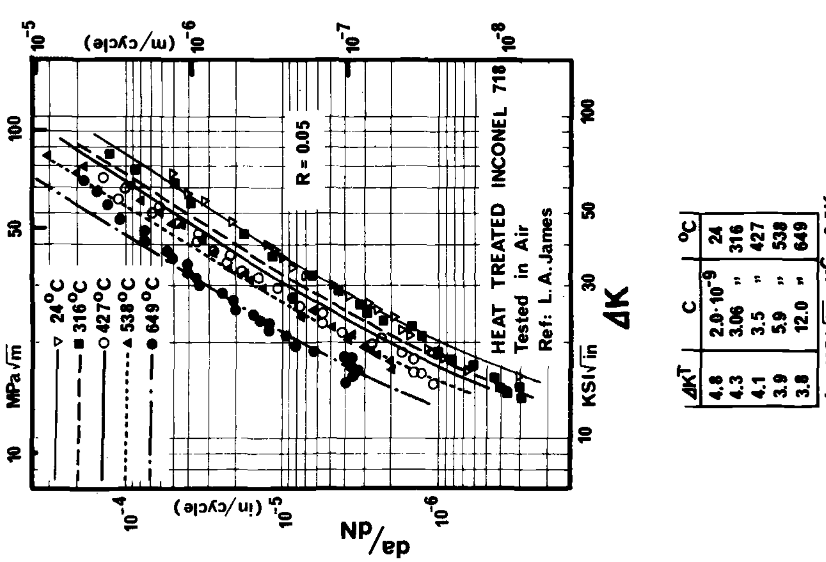

ΔK^T	C	°C
4.8	$2.0 \cdot 10^{-9}$	24
4.3	3.06 "	316
4.1	3.5 "	427
3.9	5.9 "	538
3.8	12.0 "	649

FIG. 5—*Experimental FCGR's and their predictions by the proposed equation for Inconel 718.*

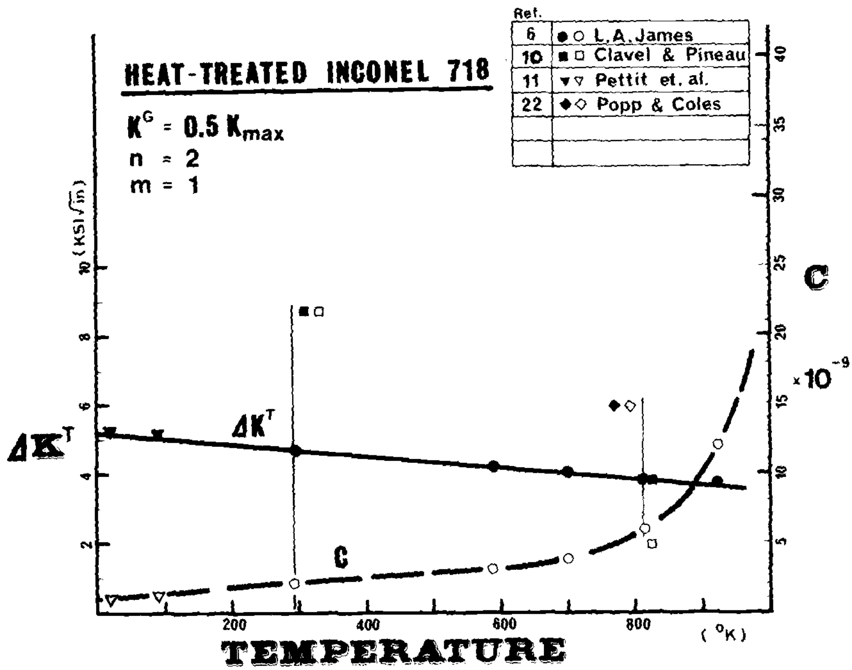

FIG. 6—*Temperature dependence of the fatigue parameters* C *and* ΔK^T *for Inconel 718.*

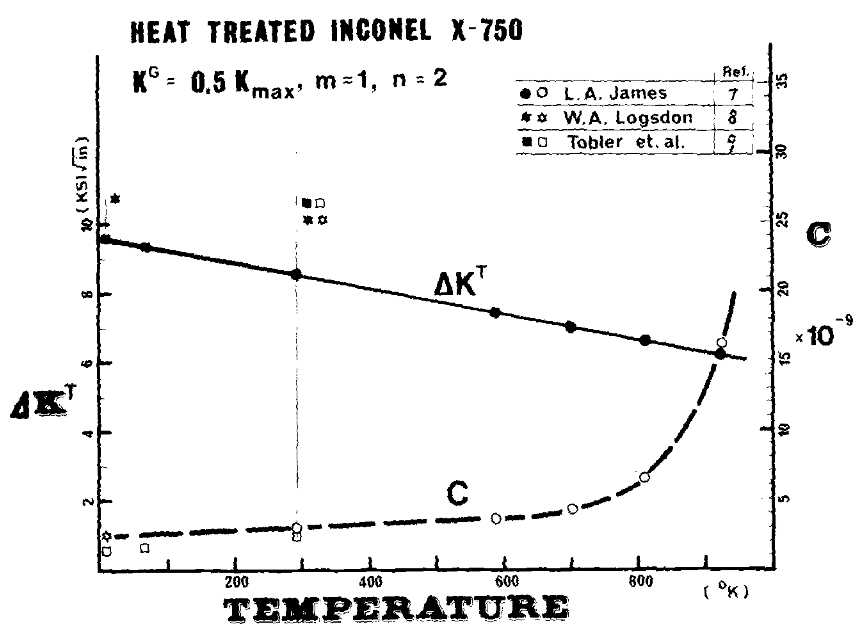

FIG. 7—*Temperature dependence of the fatigue parameters* C *and* ΔK^T *for Inconel X-750.*

that many FCGR data were available. The only requirement was that ΔK^T of the material should be high in order to establish the temperature effect on that parameter. A high ΔK^T-value causes a greater spread of FCGR at low ΔK-values for different R-ratios. Type 304 stainless steel was selected. The product form was limited to plates and forged materials. In Figs. 8 through 11, FCGR for Type 304 stainless steel [*17-21*] were analyzed by the method outlined previously. The parameters ΔK^T and C so obtained are plotted as a function of temperature in Fig. 12. As can be seen from Fig. 12, identical qualitative temperature dependence was obtained for ΔK^T and C as was found for the other alloys investigated.

In two aspects the chosen alloy did not fulfill the expectation. First, there were not as many FCGR data in the open literature as was hoped for. Second, the FCGR for different R-ratios and FCGR down to $5 \cdot 10^{-9}$ m/cycle were scanty.[3] Only data in Fig. 11 come close to this requirement. Therefore,

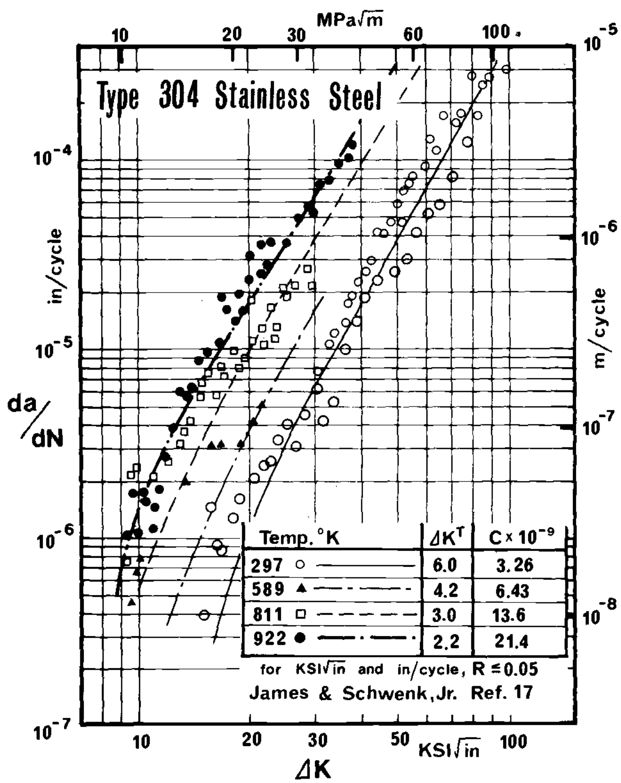

FIG. 8—*Experimental FCGR for Type 304 stainless steel and theoretical predictions based on Eq 9 for temperatures between 4 and 866 K.*

[3]In the author's opinion, FCGR down to $5 \cdot 10^{-9}$ m/cycle for two distinctly different R-ratios, say R = 0.1 and R = 0.4, allows a reasonable estimate of ΔK^T.

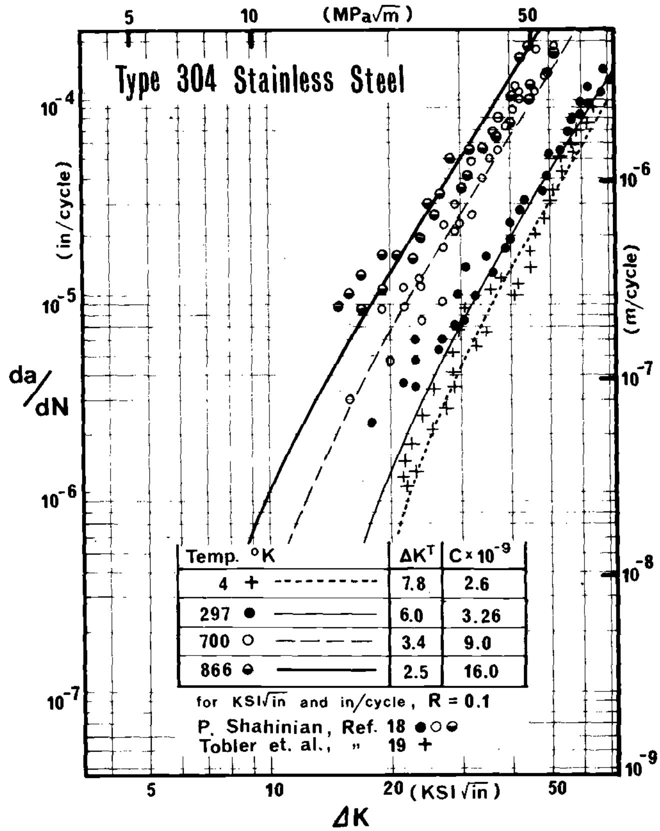

FIG. 9—*Experimental FCGR for Type 304 stainless steel and theoretical predictions based on Eq 9 for temperatures between 297 and 922 K.*

ΔK^T in Fig. 12 was most reliably estimated at 811 K. For FCGR at other temperatures, ΔK^T was obtained to give the best fit for *all* the data under the proposition that ΔK^T varies linearly with temperature. As can be seen in Figs. 8-11, a reasonable agreement between predicted and experimental FCGR was achieved based on the estimated values of ΔK^T and C. It has to be realized that the values for ΔK^T are only an estimate and could be in error. Any error in the value of ΔK^T would entail an error in C too. But the error would only cause a corresponding shift in the curves for ΔK^T and C and not alter the qualitative temperature dependence.

Figures 6, 7, and 12 exhibit identical qualitative temperature dependence of the parameters ΔK^T and C. The fatigue tolerance range ΔK^T decreases linearly with increasing temperature. The parameter C increases nearly linearly with increasing temperature up to relatively high temperatures,

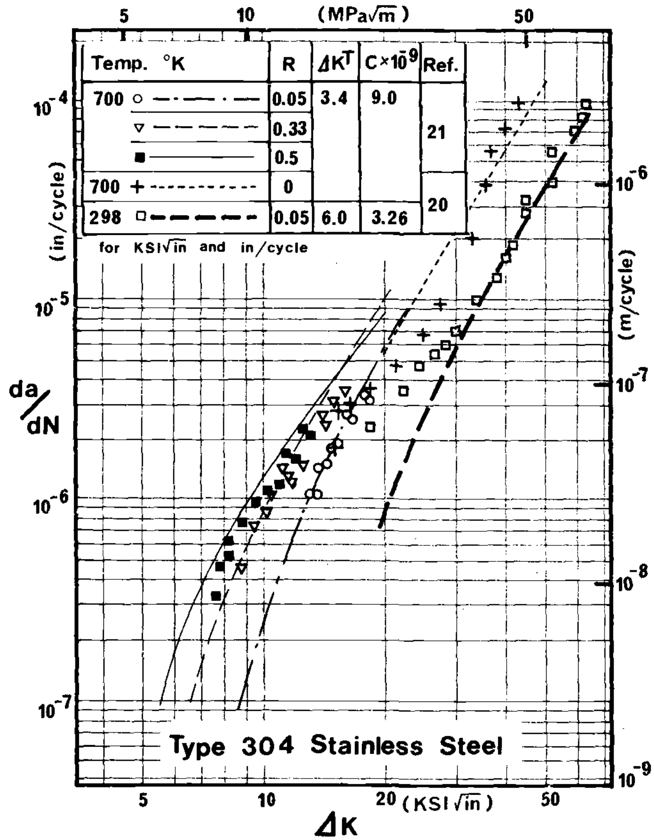

FIG. 10—*Experimental FCGR for Type 304 stainless steel at different* R*-ratios and their theoretical predictions.*

where it then increases very rapidly in a temperature range of 200 K. The temperature range in which C increases rapidly depends on the subject material.

Since ΔK^T and C are continuous functions of temperature between certain limits (temperature-induced phase transformations), the FCGR should be uniquely related to the excursions in effective stresses and strains in that temperature range; Eq 9 seems to be a quite accurate description of this unique relation.

One has to realize that low and high temperatures are difficult test environments. In the light of these environmental conditions, the scatter in the individual FCGR sets can be considered quite reasonable. The same is true for the agreement between predicted and measured FCGR. Furthermore, Type 304 stainless steel FCGR were measured on different types of specimen

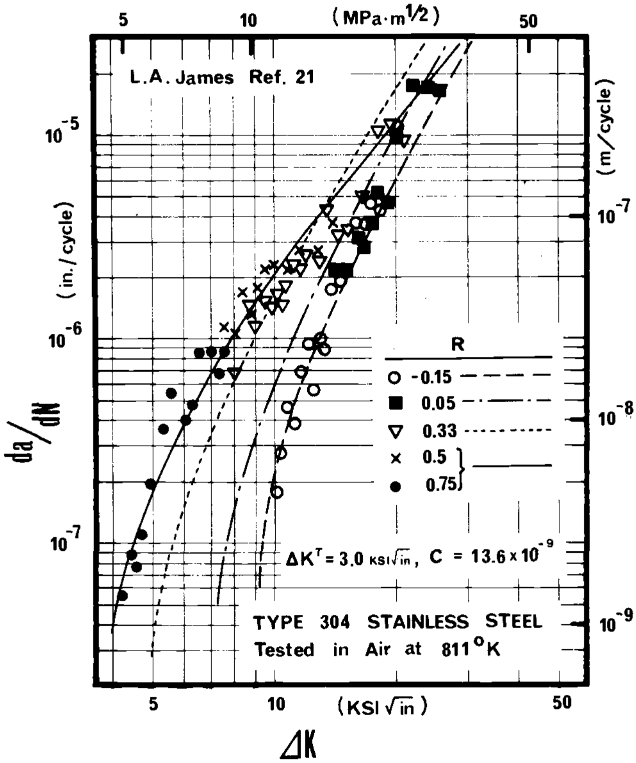

FIG. 11—*Experimental FCGR for Type 304 stainless steel at different* R*-ratios and their theoretical predictions.*

produced from many different heats of material which individually obtained different heat treatments. The test frequency varied widely too.

In Fig. 8, the experimentally measured FCGR at 589 K shows a kind of knee-shape; this kind of propagation behavior has been observed on individual specimens of Inconel X-750 [*7*] and Inconel 718 [*10*]. It seems to be associated with the experimental setup used at elevated temperatures. All FCGR data obtained at room and higher temperatures are from tests conducted in air. The fatigue tests at cryogenic temperature were conducted in a particular liquefied gas environment. It could be argued that liquefied gases constitute environments which lie in aggressiveness somewhere between vacuum and air environment. Thus, one would expect that FCGR's are somewhat lower in the liquefied gas environment than that predicted by extrapolating air environmental data to lower temperatures. This might be the reason why the values of C for Inconel X-750 lie below the extrapolated curve in Fig. 7.

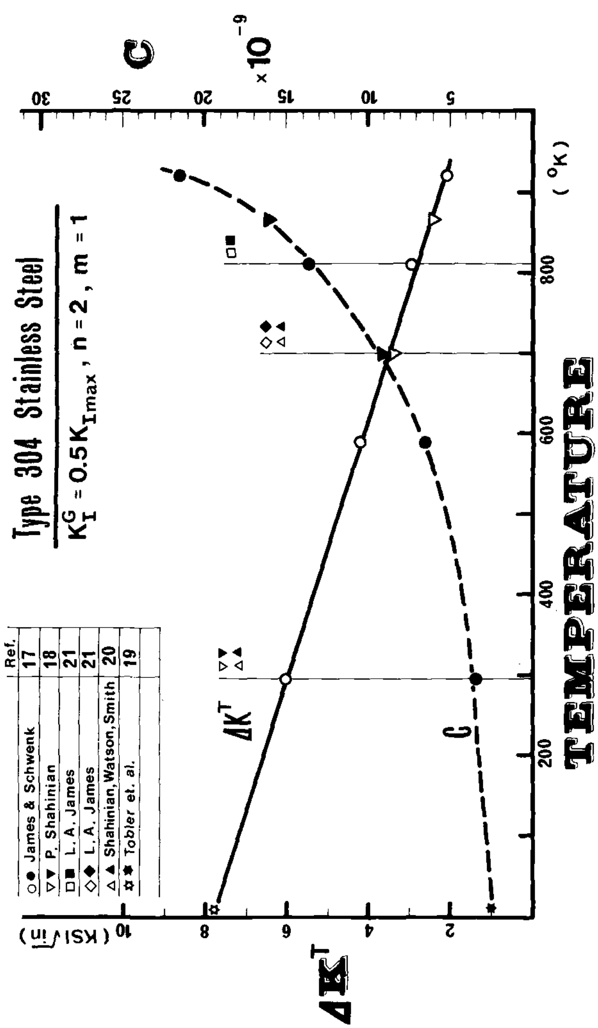

FIG. 12—*Values of C and ΔK^T extracted from FCGR in Figs. 8 through 11 plotted as a function of temperature.*

Due to the lack of FCGR data with higher R-ratios and FCGR down to $5 \cdot 10^{-9}$ m/cycle for Type 304 stainless steel, no conclusive proof for the qualitative temperature dependence of the parameters ΔK^T and C could be furnished. Yet, one more structural material seems to have the same temperature dependence of the parameters ΔK^T and C as was noticed for Inconel 718 and Inconel X-750 in the temperature range between 4 and 920 K. It does not seem appropriate to push the analysis any further. The investigation of Type 304 stainless steel clearly shows the importance of FCGR tests with high R-ratios and FCGR starting with $3\text{-}5 \cdot 10^{-9}$ m/cycle.

Conclusion

The analysis of FCGR data available in the open literature for Inconel 718, Inconel X-750, and Type 304 stainless steel strongly suggests that the material parameters ΔK^T and C obey identical qualitative temperature dependence in the temperature range between 4 and 920 K. The fatigue tolerance range ΔK^T decreases linearly with increasing temperature. The material parameter C increases nearly linearly with increasing temperatures up to relatively high temperatures (depending on the material) and then increases rapidly over a temperature range of 200 K.

APPENDIX

Originally, "Stage II fatigue" was defined as that portion of a log da/dN versus log ΔK plot which is approximately linear. This linear portion was subsequently associated with striation-producing crack propagation mechanism. At present there is enough evidence that the association of the nearly linear portion of the log da/dN versus log ΔK curve with a particular fracture morphology cannot be maintained to justify a distinction. On the other hand, the following partition of the "life" of structural parts is useful from a scientific and engineering standpoint

Stage I—crack initiation
Stage II—subcritical crack growth
Stage III—fracturing

A unique correlation between each load cycle and each increment of crack growth is only possible if the FCGR's are greater then the lattice parameters of the subject material ($\sim 3 \cdot 10^{-10}$ m/cycle). One could define "Stage II" as that regime on a log da/dN versus log ΔK curve for which a unique correlation between a load cycle (in whatever form) and crack propagation is possible, namely, FCGR above $\sim 3 \cdot 10^{-10}$ m/cycle. This would be a plausible argument for partitioning the total fatigue life, but not necessarily a useful one.

If Eq 7 is correct, namely, that FCGR's above $3 \cdot 10^{-10}$ m/cycle are a unique function of the three parameters

$$(K_{\mathrm{Imax}} - K_{\mathrm{I}}{}^{G}) - \Delta K^T$$

$$\Delta K^T$$

$$(K_{\mathrm{I}}{}^{G} - K_{\mathrm{Imin}})$$

then defining Stage II as that part of the total fatigue life between FCGR's greater than $\sim 3 \cdot 10^{-10}$ m/cycle and the beginning of fracture is plausible and useful too.

This paper together with Refs *1* and *2* tried to prove that fatigue crack growth is the unique response to the change of stresses and strains in the near region of the crack tip for FCGR's greater $\sim 3 \cdot 10^{-10}$ m/cycle. Therefore, Stage II was defined as that part of the total fatigue life between FCGR's greater than $\sim 3 \cdot 10^{-10}$ m/cycle and the beginning of fracture.

The foregoing implies that the fatigue tolerance range ΔK^T is only defined for FCGR's greater than $3 \cdot 10^{-10}$ m/cycle. One should note the difference between ΔK^T and the threshold stress-intensity range ΔK_{th}. The latter defines ΔK below which no FCG is produced with no restriction on the FCGR. In contrast, ΔK^T defines ΔK below which crack growth with each loading cycle does not occur any more.

References

[*1*] Marci, G. in *Fracture Mechanics, ASTM STP 677*, American Society for Testing and Materials, 1979, pp. 168–186.

[*2*] Marci, G., *Zeitschrift für Werkstofftechnik* (Materials Technology and Testing), Vol. 10, 1979, pp. 158–166.

[*3*] Marci, G., Packman, P. F., and Jones, J. W. in *Proceedings*, 2nd International Conference on Mechanical Behavior of Materials, Boston, 16–20 Aug. 1976, pp. 583–589.

[*4*] McMillan, J. C. and Pelloux, R. M. N. in *Fatigue Crack Propagation, ASTM STP 415*, American Society for Testing and Materials, 1967, p. 505.

[*5*] Marci, G., Ph.D. Thesis, Vanderbilt University, Nashville, Tenn., 1976.

[*6*] James, L. A., "Fatigue-Crack Propagation Behavior of Inconel 718," Report HEDL-TME 75-80, Hanford Engineering Development Laboratory, Richland, Wash., Sept. 1975.

[*7*] James, L. A., "The Effect of Temperature upon the Fatigue-Crack Propagation Behavior of Inconel X-750," Report HEDL-TME 76-39, Hanford Engineering Development Laboratory, Richland, Wash., 1976.

[*8*] Logsdon, W. A., "Cryogenic Fracture Mechanics Properties of Several Manufacturing Process/Heat Treatment Combinations of Inconel X-750," Scientific Paper 75-1E7-CRYMT-P1, Westinghouse Laboratory, Pittsburgh, Pa., May 1975.

[*9*] Tobler, R. L., Mikesell, R. P., Durcholz, R. L., and Reed, R. P., "Fatigue and Fracture Toughness Testing at Cryogenic Temperatures," National Bureau of Standards, Report NBSIR 74-393, Washington, D.C., Oct. 1974, pp. 57–121.

[*10*] Clavel, M. and Pineau, A., *Metallurgical Transactions A*, Vol. 9A, 1978, pp. 471–480.

[*11*] Pettit, D. E., Feddersen, C. E., and Mindlin, H., "Flaw Growth Behavior of Inconel 718 at Room and Cryogenic Temperatures," NASA CR-101942, National Aeronautics and Space Administration, Washington, D.C., 1969.

[*12*] James. L. A., *Welding Research Supplement*, 1978, pp. 17s–23s.

[*13*] James, L. A., "Fatigue-Crack Propagation Behavior of Inconel 600," Report HEDL-TME 76-43, Hanford Engineering Development Laboratory, Richland, Wash., May 1976.

[*14*] James, L. A., "The Effect of Temperature upon the Fatigue-Crack Propagation Behavior of Hastelloy X-280," Report HEDL-TME 76-40, Hanford Engineering Development Laboratory, Richland, Wash., 1976.

[*15*] Brinkman, C. R., Rittenhouse, P. L., Corwin, W. R., Strizak, J. P., Lystrup, A., and DiStefano, J. R., "Application of Hastelloy X in Gas-Cooled Reactor Systems," ORNL/TM-5405, Oak Ridge National Laboratory, Oak Ridge, Tenn., Oct. 1976.

[*16*] James, L. A., *Welding Research Supplement*, Dec. 1977.

[*17*] James, L. A. and Schwenk, E. B., *Metallurgical Transactions*, Vol. 2, Feb. 1971, pp. 491–496.

[*18*] Shahinian, P., *Nuclear Technology*, Vol. 30, Sept. 1976, pp. 390–397.

[*19*] Tobler, R. L. and Reed, R. P. in *Advances in Cryogenic Engineering*, Plenum Press, New York, 1977, pp. 35–46.

[*20*] Shahinian, P., Watson, H. E., and Smith, H. H., *Journal of Materials*, Vol. 7, No. 4, 1972, pp. 527–535.

[21] James, L. A., "The Effect of Stress Ratio upon the Elevated Temperature Fatigue Crack Growth Behavior of Several Reactor Structural Materials," Report HEDL-TME 75-20, Hanford Engineering Development Laboratory, Richland, Wash., 1975.
[22] Popp, H. G. and Coles, A. in *Proceedings*, Air Force Conference on Fatigue and Fracture of Aircraft Structures and Materials, Air Force Flight Dynamics Laboratory Report TR 70-144, Wright-Patterson Air Force Base, Ohio, 1970, pp. 71-86.

P. Balladon,[1] *J. Freycenon,*[1] *and J. Heritier*[1]

A Fracture Mechanics Study of Stress-Corrosion Cracking of Some Austenitic and Austeno-Ferritic Stainless Steels

REFERENCE: Balladon, P., Freycenon, J., and Heritier, J., "**A Fracture Mechanics Study of Stress-Corrosion Cracking of Some Austenitic and Austeno-Ferritic Stainless Steels,**" *Fracture Mechanics: Thirteenth Conference, ASTM STP 743,* Richard Roberts, Ed., American Society for Testing and Materials, 1981, pp. 167–185.

ABSTRACT: Crack propagation and plane-strain rupture by stress-corrosion cracking (SCC) have been studied on austenitic stainless steels Grades 304, 316, 316L and a austeno-ferritic steel. Tests were carried out in 45 $MgCl_2$ at 154°C at constant load on fatigue precracked constant tension specimens. These tests show that the presence of macrocrack branching is related to the size of the cyclic plastic zone generated at the fatigue crack tip. A crack propagation threshold K_{Iscc} (for a life of 500 h) has been determined. We have noticed the particularly good behavior of the austeno-ferritic steel. The crack propagation rates have been determined for different steel grades and, in the case of the 304 and 316 steels, compared with the rates of anodic dissolution. Fractographic studies have elucidated the crack propagation modes: Up to the end of a region of constant propagation rate, transgranular cracking occurs, and at higher propagation rates, mixed and intergranular cracking is observed. In conclusion, the difficulties of applying fracture mechanics concepts to SCC of austenitic and austeno-ferritic stainless steels (difficulties due to the problem of macrocrack branching) have been overcome by eliminating the plastic zone at the fatigue crack tip (by annealing) such that planar crack propagation is favored.

KEY WORDS: fracture properties, stainless steels, stress-corrosion cracking, K_{Iscc}-factor, crack propagation, compact tension specimen, anodic dissolution, magnesium chloride

Nomenclature

- a Crack length
- a_i Initial crack length
- a_f Crack extension due to corrosion

[1] Research engineers, Department of Mechanics, Creusot-Loire, Centre de Recherches d'Unieux, 42701 Firminy, France.

B	Specimen thickness
B^*	Actual thickness after side grooving
B'	Corrected thickness $B' = \sqrt{B.B^*}$
E	Young's modulus
K_I	Stress-intensity factor
K_{If}	Maximum value of K_I at the end of precracking
K_{Ii}	Initial value of K_I during the stress-corrosion cracking test
K_{Iscc}	Nonpropagation threshold value of K_I
P	Load
V	Total mouth opening displacement (load line)
V_i	Initial mouth opening displacement (load line)
V_f	Mouth opening displacement (load line) due to crack extension
V_o	Load displacement due to backlash and creep effects
V_t	Total load displacement
W	Specimen width
da/dt	Crack growth rate
dV/dt	Mouth opening displacement rate
d	Dissolving metal density
F	Faraday's constant
ja	Anodic dissolution current density
M	Dissolving metal atomic mass
n	Dissolving metal ion valency
v_{diss}	Anodic dissolution rate

Crack initiation and propagation by stress-corrosion cracking (SCC) take place under the combined influence of mechanical stress and the chemical environment. This crack propagation can lead to the fracture of metallic components which undergo this type of damage.

Although the crack initiation stage has already been investigated [*1*],[2] the crack growth stage has not so far been examined in detail. One way of looking at this problem is to use precracked specimens of the type used in fracture mechanics. Such a method has been used with success on high-strength steels [*2,4*] and allows the determination of both a stress-intensity factor corresponding to the nonpropagation threshold in Mode I (K_{Iscc}), and the crack growth rate da/dt as a function of K_I.

The application of the concepts of fracture mechanics to the study of SCC of austenitic stainless steels has only been reported in a few publications [*5–8*]. The problem is not easy due to the appearance of branching cracks which make any determination of K_{Iscc} and da/dt very difficult. Preliminary tests, carried out on a 304 stainless steel in boiling $MgCl_2$ at 154°C have shown that it is possible, by annealing at high-temperature fatigue-precracked constant-tension (CT) specimens, to obtain planar crack propagation.

[2]The italic numbers in brackets refer to the list of references appended to this paper.

These results have lead us to work in the following three directions:

1. development of an SCC test in plane strain for austenitic and austeno-ferritic stainless steels which enables the determination of the K_{Iscc} and of the crack propagation rate da/dt,
2. determination of K_{Iscc} and da/dt for the steel grades AISI 304, AISI 316, and the austeno-ferritic alloy, and
3. comparison of da/dt with the anodic dissolution rate in the active state to evaluate the importance of the dissolution rate during SCC.

All the tests were performed in boiling $MgCl_2$ at 154°C (a 45 weight percent solution), that is, in a frequently used reference environment.

Materials, and Experimental Techniques

Materials

Tests have been performed on Grades 304, 316, 316L, and an austeno-ferritic stainless steel (50 percent ferrite). The steel products tested came from industrial melts made in either an induction furnace or an arc furnace.

Tables 1-3 give, respectively, for each grade, the type of product used, the chemical analysis, and the mechanical properties at room temperature and 150°C.

TABLE 1—*Product type.*

Steel	Product	Heat-Treatment
304	bar ⌀ 80 mm	1100°C 1 h, WQ
316	bar ⌀ 80 mm	1100°C 1 h, WQ
316L	sheet e = 41 mm	1070°C 1 h, WQ
Austeno-ferritic	flat ⌀ 100 × 35	1150°C 1 h, WQ

WQ = water-quenched.

TABLE 2—*Chemical analysis.*

Steel	C	Mn	Si	S	P	Ni	Cr	Mo	Cu	Ti
304	0.054	1.82	0.61	0.021	0.028	8.90	18.70	0.16	0.13	...
316	0.042	1.90	0.59	0.028	0.024	10.60	17.00	2.03	0.095	...
316L	0.022	2.00	0.47	0.006	0.030	12.29	17.56	2.41	0.20	...
Austeno-ferritic	0.020	1.56	0.51	0.014	0.018	6.80	21.23	2.34	1.38	0.092

TABLE 3—*Mechanical properties.*

Steel	Tensile Properties at 20°C				Tensile Properties at 150°C				Impact Properties at 20°C		Impact Properties at 150°C	
	Yield Strength, MPa	Tensile Strength, MPa	Elongation, %	Reduction of Area, %	Yield Strength, MPa	Tensile Strength, MPa	Elongation, %	Reduction of Area, %	CVN (Length), J	CVN (Transverse), J	CVN (Length), J	CVN (Transverse), J
304	274	597	65	78	194	485	53	77	257	108	273	106
316	269	558	66	78	182	474	48	76	230	109	254	104
316L	263[a]	579[a]	56[a]	...	...	...	...	...	...	206	...	...
Austeno-ferritic	456	629	31	75	353	543	29	74	181	87	217	90

[a]Transverse properties.
CVN = Charpy V-notch.

Experimental Techniques

Choice of Test Method—Previous tests using the "imposed opening" method on modified wedge opening loading (WOL)-type specimens had enabled us, despite difficulties in analyzing the results, to evaluate the level of K_{Iscc} between 10 and 20 MPa$\sqrt{m}$ for the 304 and 316 grades in boiling $MgCl_2$ at 154°C. This method was abandoned in favor of the "constant load" method using fatigue precracked CT specimens. The specimen dimensions were such as to fulfill the validity conditions for plane-strain $B \geq 2.5\ (K_I/\sigma_y)^2$ for stress intensity factors up to 20 MPa$\sqrt{m}$ for the austenitic grades, that is, for the maximum likely value of K_{Iscc} for these steels. This led to the choice, given the 150°C yield strength of these steels, to a specimen width of 30 mm (CT 30). Guiding grooves were machined along the specimen faces to try and facilitate planar crack propagation (Fig. 1).

Experimental Apparatus—The test machine was a modified vertical creep machine. The specimen opening displacements were taken along the loading axis, and amplified by means of a mechanical lever.

The displacements of this lever were measured by a dial gage and recorded graphically. The corrosion cell is made of Hastelloy and heated by electrical resistance. A schematic diagram of the apparatus is shown in Fig. 2.

Basic Concepts—

Measurement of K_{Iscc}—The principle of the constant-load test is as follows: A load is applied to the specimen such that the initial value of the stress-intensity factor K_{Ii} is higher or lower than that of K_{Iscc}.

If $K_{Ii} > K_{Iscc}$ the initial crack grows, K_I increases, and the propagation continues until specimen failure.

If $K_{Ii} < K_{Iscc}$ the initial crack does not propagate.

The applied load P is defined by the required value of K_{Ii} and the initial

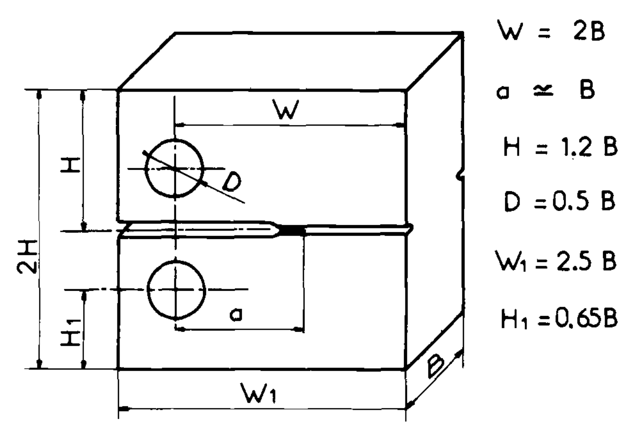

FIG. 1—*Modified CT specimen (the longitudinal grooves are semicircular with a radius of 1 mm and depth of 0.5 mm).*

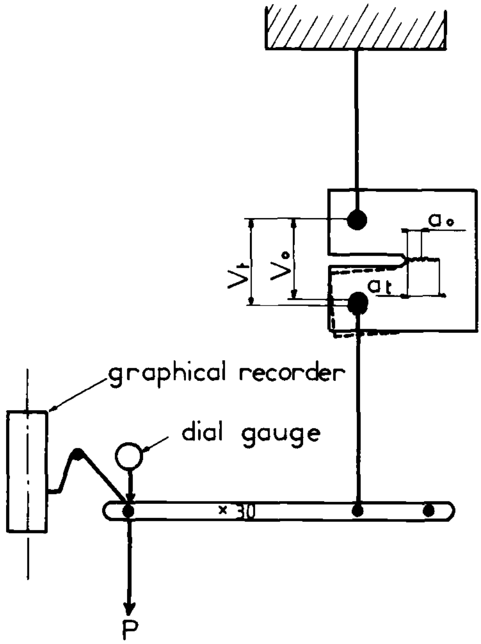

FIG. 2—*Apparatus (schematic).*

crack length measured along the specimen side face. After testing, the real value of the initial crack length is determined, according to the ASTM Test for Plane-Strain Fracture Toughness of Metallic Materials (E 399-74), and hence the real value of K_{Ii}. Several values of K_{Ii} are tried to determine K_{Iscc} by successive approaches.

This method defines limits to the value of K_{Iscc}. The K_{Iscc} values determined in this way correspond in fact to the threshold for nonpropagation in 500 h.

Determination of the crack growth rate da/dt—The measurements taken during a test allow one to trace curves giving the specimen opening displacements V_{total} as a function of time, t. These curves have the general form shown in Fig. 2*a* and can be separated into three stages:

Stage I, where dV/dt decreases rapidly with time
Stage II, where dV/dt is practically constant
Stage III, where dV/dt increases rapidly with time

The measured value of V is divided into several parts resulting from

backlash in the apparatus,
creep of the Zircaloy loading rods,
possible creep of the specimen, and
crack growth.

The opening V_i due to the elastic deformation during initial loading is allowed for by setting the dial gage reading to zero immediately after loading.

The first stage always exists even for low values of K_{Ii} for which $dV/dt = 0$ during the second stage. In such a case, the absence of crack growth during Stage I was established on other steel grades by micrographic examination of the crack during Stage II. These results led us to assume that the first part of the curve (Stage I) corresponds essentially to backlash and creep effects, which have practically no influence when Stage II is reached.

To separate parasite effects from the opening displacement due to crack propagation, the real value due to cracking is taken as $V_t - V_0$ where V_0 is the point of intersection of the extrapolation of the second stage ($dV/dt \simeq$ constant) to the ordinate (Fig. 3*a*). The validity of this hypothesis will be discussed later.

The crack length, a, and the opening displacement, V, are related by the elastic compliance which has been determined by the Institut de Recherches de la Siderurgie for a CT specimen [9]. This relation is

$$\frac{EB'V}{P} = \exp\left[0.75 + 9.3\frac{a}{w} - 11.6\left(\frac{a}{w}\right)^2 + 9.5\left(\frac{a}{w}\right)^3\right] \quad 0.4 \leq \frac{a}{w} \leq 0.8$$

$$B' = \sqrt{BB^*}$$

where B^* is the reduced thickness between the grooves. The values obtained for $EB'V/P$ are from 6 to 10 percent higher than the values given by the working document of ASTM Subcommittee E24.08 entitled "The Determination of J_{Ic}, a Measure of Fracture Toughness" (31 Jan. 1980).

The value of a_i (initial crack length) allows the determination of V_i (initial opening displacement due to the elastic deformation) and $V = V_i + V_f$ then gives a total $= a_i + a_f$ (a_f is the crack extension due to corrosion). One can then construct graphs giving a as a function of time and hence da/dt, the instantaneous crack propagation rate as a function of K_I.

These curves are then plotted out in the form of log(da/dt) as a function of K_I. Figure 3 summarizes the operations involved.

Metallographic study of the cracks—The metallographic examination of the cracked specimens was carried out in the following way:

1. A macrographic examination of the specimen surfaces (the two halves of the specimen being brought together) to determine if crack branching occurs.
2. A macrographic examination of the fracture surface.
3. A micrographic examination to check for microbranching.
4. A micrographic examination of the fracture surface to determine the crack propagation mode.
5. A check by X-rays for the presence of martensite α' or ϵ at the fatigue crack tip and on the rupture surface.

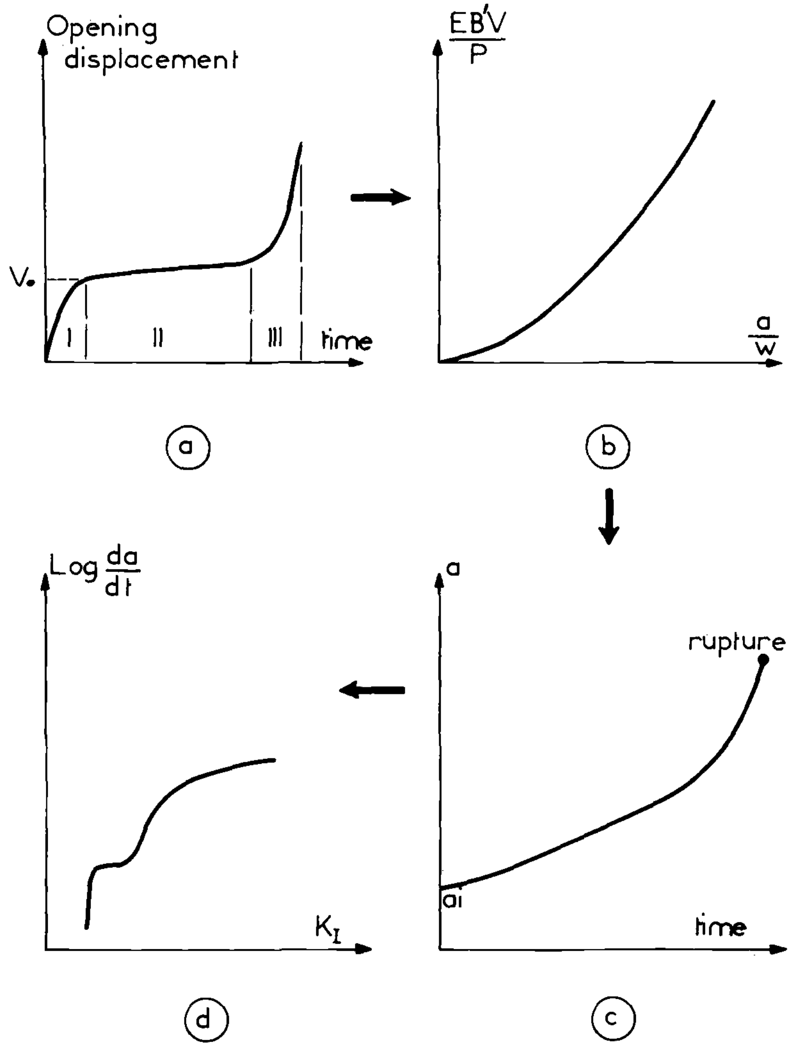

FIG. 3—*Analysis of the experimental results.*

Determination of the anodic dissolution current densities in the active state—Tension tests were carried out at a constant strain rate higher than the critical strain rate for depassivation (in order to avoid localized dissolution).

During the test the free corrosion potential obtained after 15-h immersion is imposed. The dissolution current is measured at the instant corresponding to the ultimate tensile strength. At this instant the specimen is completely depassivated and all the surface is attacked. This dissolution is thought to be relatively slight and the current density is calculated supposing constant volume. These tests were performed at a crosshead displacement speed of 0.3 mm/s on cylindrical specimens (diameter 2 mm, gage length 22 mm) in an aerated solution of $MgCl_2$ at 154°C. The specimens were taken from the same material as used for the CT 30 specimens.

Results

Determination of K_{Iscc}

The results of the determination of K_{Iscc} are given in Table 4. The austenitic stainless steel tests were performed both on specimens directly after precracking and on specimens that were annealed after precracking.

Influence of Plastic Zone at Fatigue Crack Tip—The size of the cyclic plastic zone at the fatigue crack tip is related to the value of K_{If} (the maximum value of K_I obtained at the end of precracking).

The tests on the austeno-ferritic grade show that in the absence of a second anneal, crack propagation is practically planar when K_{Ii} (defined as the value of K_I on loading) is close to K_{If} (see Fig. 4). On the other hand, as can be seen on the nontreated austenitic grades, extensive crack branching occurs when K_{Ii} is significantly lower than K_{If}. In this case, one cannot determine K_{Iscc} correctly since crack initiation may occur on the sides of the fatigue crack or even on the as-machined notch.

In all cases, we have verified that the postfatigue crack anneal (that is, elimination of the cyclic plastic zone size) leads to planar crack propagation (Fig. 5).

Influence of Alloy Composition—

Austenitic steels—One observes a favorable influence of molybdenum, which significantly increases the level of K_{Iscc}. This result can be related to the beneficial influence of this alloying element on the resistance to depassivation.

TABLE 4—*Results of the* K_{Iscc} *measurements.*

Grade	No. of Specimens	Heat Treatment Before Testing	K_{Iscc} (MPa$\sqrt{m}$)	Observations
304	9	as precracked	$9.4 \leq K_{Iscc} \leq 10.7$	crack branching
	9	reannealed 1100°C ½ h, WQ[a]	$11.4 \leq K_{Iscc} \leq 12.0$	planar crack
316	6	as precracked	$10.1 \leq K_{Iscc} \leq 11.3$	crack branching
	9	reannealed 1100°C ½ h, WQ	$13.6 \leq K_{Iscc} \leq 13.8$	planar crack
Austeno-ferritic	5	as precracked	$31.3 \leq K_{Iscc} \leq 32.8$	practically planar crack
316L	1	reannealed 1070°C ½ h, WQ	K_I applied = 13.8	life 534 h

[a] WQ = water-quenched.

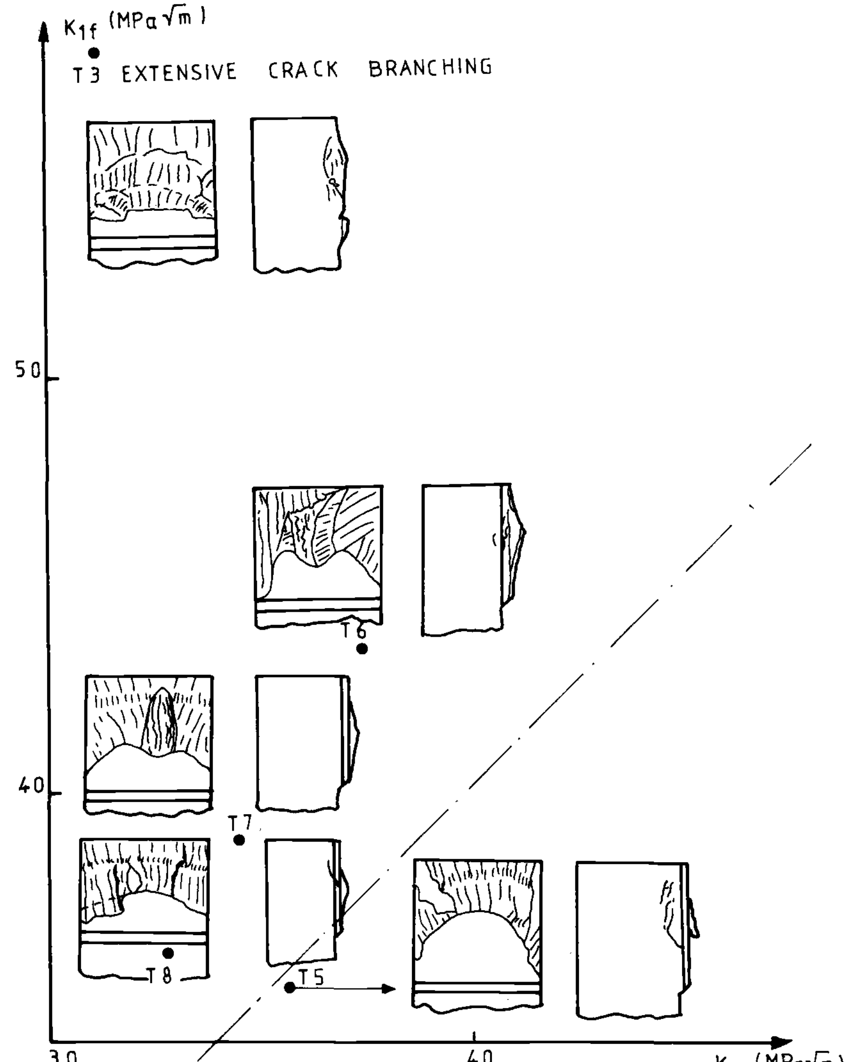

FIG. 4—K_{If} *influence on branching (austeno-ferritic steel).*

Insufficient tests were performed on the low-carbon grade steel to specify the influence of carbon.

Austeno-ferritic steel—The value of K_{Iscc} of the austeno-ferritic steel is clearly higher than the values obtained for the austenitic steels. However, the results obtained on this grade should be treated with a certain degree of caution since relatively few tests have been carried out and the real value of K_{Ii} is not easy to calculate.

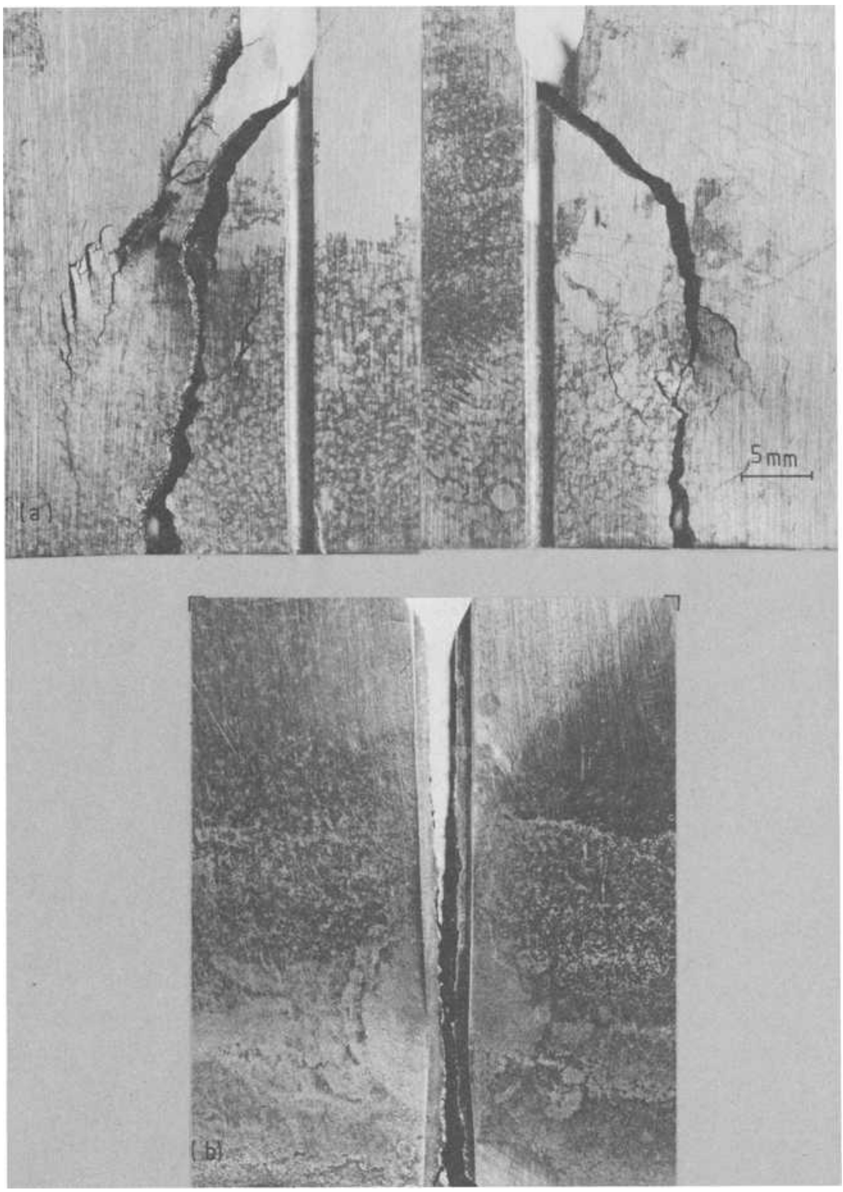

FIG. 5—*(a) branching crack (304 specimen without anneal after precracking); (b) plane crack (304 specimen with anneal after precracking).*

In opposition to the behavior of the austenitic alloys for which the fatigue crack front is relatively linear, the fatigue crack fronts observed on the austeno-ferritic steels after failure were found very much curved, showing that the fatigue crack depth at the specimen center was two or three times that observed on the edges. In this case, the calculation of K_{Ii}, with the conventional formulas used, is not strictly valid.

Comparison with Previous Results—The only available comparable results are those obtained by Speidel [*6*] on a 304L steel in 42 $MgCl_2$ at 130°C and those obtained by Russell [*10*] on a 316 steel in 45 $MgCl_2$ at 154°C. The values of K_{Iscc} determined by these authors are 8 MPa$\sqrt{m}$ for the 304L and 12 MPa$\sqrt{m}$ for the 316 steel. The experimental conditions were, however, quite different from those of the present study.

Determination of Crack Propagation Rate.

Results—This study was essentially limited to the 304 and 316 grades on specimens that had been annealed after the fatigue precracking. The application of the compliance relation to calculate the crack length is, in fact, meaningless when crack branching occurs or when the crack front is strongly curved (the austeno-ferritic steel).

Figure 6 shows, for the 304 and 316 grades, the variation of da/dt as a function of K_I in a semilogarithmetic plot. The curves exhibit two plateaus which correspond to regions where the crack propagation rate is constant and independent of K_I. Table 5 indicates, for both steel grades, the range of values of the propagation rate da/dt and K_I corresponding to these two plateaus.

Influence of Composition—Molybdenum has relatively little influence on the propagation rate corresponding to the first plateau: 0.104 mm/h on average for the molybdenum-containing steel compared with 0.168 mm/h for the steel without molybdenum. This element has, however, a large influence both on the rate corresponding to the second plateau (the presence of molybdenum reduces the average propagation rate by a factor of 4) and on the values of K_I corresponding to the end of the first plateau and the beginning of the second (markedly higher K_I-values for the molybdenum steel).

Comparison with Previous Results—Robinson and Scully during their work on stress-corrosion cracking of the 304 steel in $MgCl_2$ [*5*] have also shown the presence of two plateaus in the graphs of the propagation rate as a function of the stress-intensity factor. At 160°C they obtained the following values:

1st plateau da/dt	0.232 mm/h	K_I max = 19 MPa$\sqrt{m}$
2nd plateau da/dt	1.62 mm/h	K_I min = 26 MPa$\sqrt{m}$

These values are very close to those obtained in the present study on the 304 grade. On the other hand, Speidel [*6*] in tests of the 304L steel in $MgCl_2$ at 130°C, and Russell and Tromans [*10*] for the 316 steel in $MgCl_2$ at 154°C, found only one plateau for which the corresponding crack propagation rate

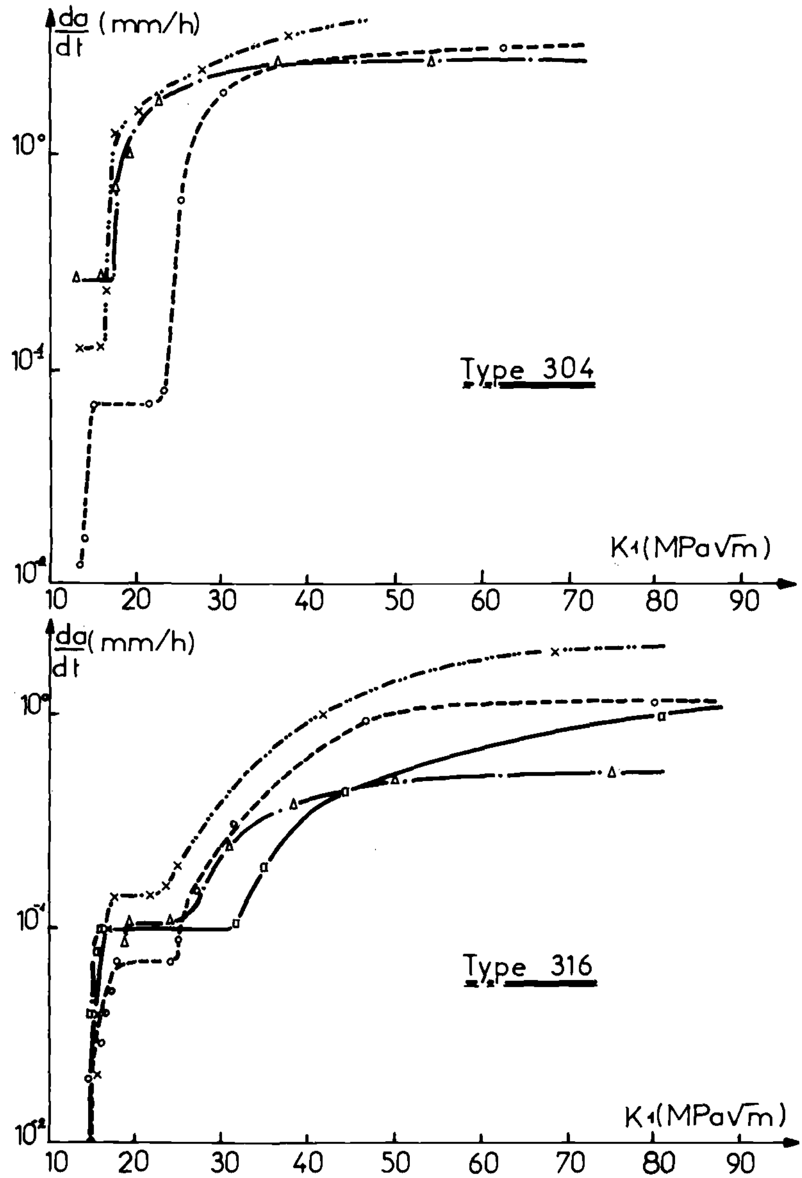

FIG. 6—*Crack propagation rate for 304 and 316.*

TABLE 5—*Results of crack propagation rate measurements.*

Grade	1st Plateau		2nd Plateau	
...	$\left(\frac{da}{dt}\right)_1$ (mm/h)	K_I max (MPa$\sqrt{m}$)	$\left(\frac{da}{dt}\right)_2$ (mm/h)	K_I min (MPa$\sqrt{m}$)
304	0.071/0.266	15.7/21	2.66/4.8	25/40
316	0.073/0.135	23.20/32	0.5/1.2	50/65

was about 0.16 mm/h for the 304L steel and 1.44 mm/h for the 316 steel. This latter value is close to that we obtained for the second plateau on the 316 grade. Desestret [*11*] using a constant-strain-rate tension test obtained, on the same 304 steel as this study, a propagation rate at the plateau of 0.15 mm/h.

Microfractographic Observations

The rupture surface appearance was studied by scanning electron microscope as a function of the crack length. The crack aspect can be related via the plots $a = f(t)$ to the propagation rate da/dt and to the stress-intensity factor K_I.

Figure 6 describes the observations made on the 304 grade (on specimens annealed after the fatigue precracking). Two propagation modes are observed—transgranular and intergranular—both being clearly related to the measured propagation rates:

1. For the regions corresponding to the first plateau on the $\log(da/dt) = f(K_I)$ plots and during the incubation period, propagation is transgranular. The characteristic "fanlike" appearance of the crack surface is similar to that described in the literature [*12*].
2. For the transition regions [the knee of the $a = f(t)$ plots], the region between the 1st and 2nd plateaus on the $\log da/dt = f(K_I)$ plots, some intergranular crack propagation can be observed.
3. For the region corresponding to the 2nd plateau of the $\log da/dt = f(K_I)$ plots, propagation is almost completely intergranular. One can occasionally observe the occurrence of intergranular crack microbranching.

Similar observations were made on the 316 grade steel. One can note, in Fig. 7, that the micrographs were taken from regions closer to the edge than to the specimen center.

A systematic check of the rupture surface along directions parallel to the fatigue crack showed that there was little difference between the center of the specimen and the regions from which the micrographs were taken.

These results are not quite in agreement with those of Russell and Tromans [*10*], who on a 316 steel observed, on the $\log(da/dt) = f(K_I)$ plot, only one plateau close to our 2nd plateau and a transintergranular transition which occurred in the plateau region.

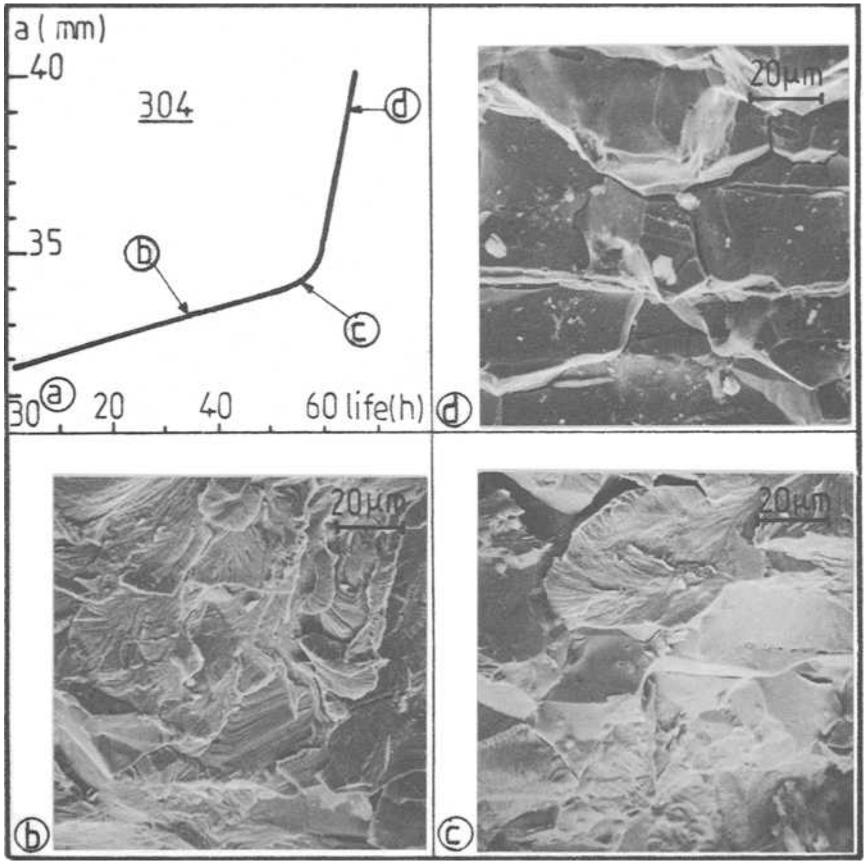

FIG. 7—*(a) Evolution of crack length with time; (b) transgranular propagation; (c) trans/intergranular propagation; (d) intergranular propagation.*

The fanlike transgranular fracture appearance is related to the coalescence of several cracks propagating on parallel planes which then join up by ductile shear failure, thus creating the steps. The initiation of corrosion cracks as well as their propagation could, in this case, be related to the slip planes created by deformation at the crack tip.

Intergranular cracking is associated with the separation of grain boundaries which could be provoked by localized chemical attack.

Anodic Dissolution Current Density Measurements in the Active State

The values of the dissolution rates, calculated from the anodic dissolution current density measurements using Faraday's law in the form v_{diss} =

ja/(*M*/*nFd*) [*13*], assuming the solvated ions are Fe^{++}, vary within the following limits:

0.065 to 0.085 mm/h for the 304 steel
0.065 to 0.10 mm/h for the 316 steel

In the case of compact specimens in $MgCl_2$ the pH of which is very low, we can assume that there is not an important variation of the pH at the crack tip, where it also remains very low and about the same as in the bulk solution. Moreover, the tests on compact specimens are carried out at free corrosion potential and the part of the specimen in the passive state is much larger than the crack tip surface. The resisitivity of the solution is very low so that the potential drop is negligible and the crack tip potential remains very close to the free corrosion potential [*14*].

Comparing the upper values with the crack propagation rates obtained in the 1st plateau region during tests on CT 30 specimens, one notices that the measured anodic dissolution rates roughly correspond to the lower end of the range of crack propagation rates. These results indicate that one can apply the anodic dissolution control model of SCC to crack propagation of austenitic stainless steels in $MgCl_2$ at 154°C for the K_I-values corresponding to the 1st plateau of the $\log(da/dt) = f(K_I)$ curves determined during this study.

Discussion

The K_{Iscc}-values obtained for the 304 and 316 grades are close to those cited in the literature and confirm the beneficial effect of molybdenum additions. This latter point indicates a crack propagation mechanism which involves mechanical depassivation at the crack tip; the beneficial influence of molybdenum on resisting depassivation and accelerating repassivation is a well-established fact [*15*].

Comparison of the propagation rates (corresponding to the 1st plateau) with the anodic dissolution rates (calculated using Faraday's law and the measured anodic dissolution current densities) seems to indicate that the mechanism of anodic dissolution by microdeformation and rupture of the passive film can be applied in the present case. The relationship between the $a(t)$ plots and the observed fracture surface appearance suggests the following mechanism of crack propagation:

1. For K_{Ii}-values slightly higher than K_{Iscc}, plastic deformation at the fatigue crack tip leads to the emergence of a number of slipbands which become preferential sites for crack formation by anodic dissolution. These cracks coalesce by mechanical rupture of the connecting ligaments, thus developing the fanlike appearance of the fracture surface. The increase of K_I due to crack propagation may then lead to an increase in the number of evolving dissolution sites up to an equilibrium value reached when K_I attains K_{I_2}

[the value of K_I corresponding to the start of the 1st plateau on the log(da/dt) $= f(K_I)$ plots].

2. For the K_I-values corresponding to the 1st plateau of the log(da/dt) $= f(K_I)$ curves, crack progression is mainly controlled by anodic dissolution, the mechanical contribution to rupture being relatively small and limited to the ligaments between the microcracks due to the dissolution process. The number of evolving sites remains constant until K_I attains K_{I_3}, the value of K_I corresponding to the end of the first plateau.

3. For the K_I-values higher than K_{I_3}, the appearance of intergranular cracking may be due to a mechanical depassivation of the grain boundaries provoked by localized deformation of the boundaries producing preferential dissolution. A similar mechanism has already been proposed by Baeslack et al [*16*]. The mechanical contribution to the crack propagation mechanism seems to be greater in this case than for transgranular crack propagation.

These considerations emphasize the role of anodic dissolution and mechanical depassivation in the fracture mechanisms in $MgCl_2$ at 154°C.

The results show that such a mechanism may operate but they do not allow one to completely exclude the theories proposed by some authors based on the crucial role of embrittlement by hydrogen [*17*]. The present study has essentially examined the problem from a mechanical point of view and should be completed from an electrochemical point of view. The good agreement between our results and those obtained by Desestret [*11*] using very different tests (constant-strain-rate tension test) is particularly encouraging.

Conclusion

We have developed an apparatus for studying SCC of stainless steels in 45 $MgCl_2$ at 154°C using fracture mechanics-type CT specimens according to the constant-load method. The tests carried out on austenitic (304, 316, 316L) and austeno-ferritic grades have given a certain number of results concerning the phenomenon of macrocrack branching, the existence of a crack propagation threshold K_{Iscc}, the crack propagation rates, and the mechanisms which control crack propagation. The principal results are as follows:

1. The presence of macrocrack branching is related to the size of the plastic zone at the crack tip created during precracking. Crack propagation is practically planar when the maximum stress-intensity factor at the end of precracking K_{If} is less than or equal to the stress-intensity factor on loading K_{Ii} during the stress corrosion test. A high temperature anneal after precracking always produces plane propagation.

2. A propagation threshold K_{Iscc} (for a life of 500 h) has been determined for the 304 and 316 grades. Complementary measurements would be necessary to specify the K_{Iscc} values for the 316L and austeno-ferritic grades. A beneficial influence of molybdenum on resistance to SCC is observed. Furthermore,

despite the difficulties of determining the K-factor for the austeno-ferritic steel, it is quite clear that this latter steel exhibits much better behavior than the other grades. The results that we have obtained also confirm the results previously published in the literature.

3. Determination of the crack propagation rates using the elastic compliance method, in spite of experimental difficulties due to the backlash and creep of the loading bars, has shown the existence of two plateaus in the curves $\log(da/dt) = f(K_I)$ for the 304 and 316 grades. The propagation rates corresponding to the 1st plateau are very close to the rates of anodic dissolution determined from measurements of the dissolution current density using Faraday's law. The crack propagation mode is in this case transgranular and the appearance of the rupture surface is identical to that previously observed by other authors. The propagation rates corresponding to the 2nd plateau are very much higher and the propagation mode becomes essentially intergranular.

The results show that the model of crack propagation by rupture of the passive film and anodic dissolution may operate in the case of these steels.

The overall results show that it is possible to utilize the concepts of fracture mechanics to study SCC of austenitic stainless steels. These results, obtained in a particular environment (45 $MgCl_2$ at 154°C), should not, however, be extrapolated to other environments without further tests.

Acknowledgments

The authors wish to thank the French "Delegation Générale à la Recherche Scientifique et Technique" for its help and contribution to this work.

We also thank A. Desestret (Creusot-Loire, Centre de Recherches d'Unieux), R. Labbens (Creusot-Loire Paris), and R. Oltra (University of Dijon) for our discussions about the results.

References

[1] Petit, M. C., Desjardins, D., and Darrieutort, B., *Mémoires Scientifiques de la Revue de Métallurgie*, Vol. 73, No. 4, April 1976, pp. 241-255.

[2] Smith, H. R. and Piper, D. E. in *Stress Corrosion Cracking in High Strength Steels and in Titanium and Aluminum Alloys*, B. F. Brown, Ed., Naval Research Laboratory, Washington, D.C., 1972, pp. 17-77.

[3] Speidel, M. O. and Hyatt, M. V. in *Advances in Corrosion Science and Technology*, M. G. Fontana and R. W. Staehle, Eds., Plenum Press, N.Y., Vol. 2, 1972, pp. 115-335.

[4] Hyatt, M. V. and Speidel, M. O. in *Stress Corrosion Cracking in High Strength Steels and in Titanium and Aluminium Alloys*, B. F. Brown, Ed., Naval Research Laboratory, Washington, D.C., 1972, pp. 147-244.

[5] Robinson, M. J. and Scully, J. C. in *Proceedings*, 1973 Firminy Conference—Stress Corrosion Cracking and Hydrogen Embrittlement of Iron Base Alloys, R. W. Staehle, J. Hochmann, R. D. McCright, and J. E. Slater, Eds., National Association of Corrosion Engineers, Houston, Tex., 1977, pp. 1095-1103.

[6] Speidel, M. O., *Transactions*, National Association of Corrosion Engineers, Vol. 33, No. 6, . June 1977, pp. 199-203.
[7] Speidel, M. O., *Blech—Rohre—Profile 25*, Vol. 1, 1978, pp. 14-18.
[8] Scully, J. C., *Metal Science*, June 1978, pp. 290-300.
[9] Charbonnier, J. C., Marandet, B., and Sanz, G., Institut de Recherches de la Siderurgie Report RI 394, Sept. 1973.
[10] Russell, A. J. and Tromans, D., *Metallurgical Transactions A*, Vol. 10A, Sept. 1979, pp. 1229-1238.
[11] Desestret, A., Creusot-Loire, Internal Report, 1979.
[12] Scully, J. C. in *The Theory of Stress Corrosion in Alloys*, North Atlantic Treaty Organization, Brussels, Belgium, 1971, pp. 127-166.
[13] Parkins, R. N., *British Corrosion Journal*, Vol. 14, No. 1, 1979, pp. 5-14.
[14] Oltra, R., Thesis, University of Dijon, Dijon, France, 1980, to be published.
[15] Desjardins, D., Daret, J., and Petit, M. C., *Mémoires Scientifiques de la Revue de Métallurgie*, Nov. 1978, pp. 657-669.
[16] Baeslack, W. A. et al, *Metallurgical Transactions*, Vol. 10A, Oct. 1979, pp. 1429-1435.
[17] Eliezer, D. et al, *Metallurgical Transactions*, Vol. 10A, July 1979, pp. 935-941.

R. C. Donath,[1] *T. Nicholas,*[1] *and L. S. Fu*[2]

An Experimental Investigation of Creep Crack Growth in IN100

REFERENCE: Donath, R. C., Nicholas, T., and Fu, L. S., **"An Experimental Investigation of Creep Crack Growth in IN100,"** *Fracture Mechanics: Thirteenth Conference, ASTM STP 743,* Richard Roberts, Ed., American Society for Testing and Materials, 1981, pp. 186–206.

ABSTRACT: Sustained load crack growth in IN100 at 732°C (1350°F) is studied using two specimen geometries, a standard compact tension specimen, and a radially crack ring loaded in tension. The effects of specimen thickness on the growth rate are investigated covering a range from 5.6 mm to 18.3 mm (0.22 to 0.72 in.) in thickness. Only the thinnest specimens show a crack growth rate which is lower than that obtained from all of the other thickness specimens. Stress-intensity factor, net section stress, and the C*-integral were investigated as possible crack growth rate correlating parameters. The concept of an "effective" crack length determined from specimen compliance measurements is introduced as a measure of crack length for severely tunneled crack front geometries. Neither net section stress nor C^* is found to be acceptable as a crack growth parameter based on data from both test geometries. Although K provides fair correlation, the phenomenology of creep crack growth prevents its description adequately with only a single parameter. In particular, the crack growth rate is observed to decrease from an initially higher value to a "steady state" rate for constant values for any of the correlating parameters investigated.

KEY WORDS: creep crack growth, crack propagation, compliance testing, linear elastic fracture mechanics, C*-integral, nickel-based alloy, temperature

Nomenclature

a	Crack length
B	Specimen thickness
C	Compliance
C^*	C*-integral
e_{mn}	Strain components
E	Young's modulus of elasticity

[1]Materials research engineer, AFWAL Materials Laboratory, Wright-Patterson Air Force Base, Ohio 45433.
[2]Department of Engineering Mechanics, Ohio State University, Columbus Ohio 43210.

K Stress intensity factor
P Load
R_i, R_o Inner, outer ring specimen radii
T_i Traction vector components
U Potential energy
v_i Displacement rate vector components
W Specimen width
W^* Strain energy density rate
α Crack length per unit width, a/W, for the compact tension (CT) specimen and $a/(R_o - R_i)$ for the ring specimen
Γ Path around a crack tip in the counterclockwise sense
δ Displacement
σ_{ij} Stress components
ν Poisson's ratio

In recent years, requirements in the use of high-strength nickel-based superalloys in turbojet engine applications has created the need for a clearer understanding of the fracture and fatigue behavior in these materials. Higher and higher temperatures produce increasingly hostile operating environments in the turbine end of aircraft engines. This places in question the direct applicability of linear elastic fracture mechanics (LEFM) as a tool for predicting life performance in engine components. Complexities arise in the determination of the material fracture toughness as well as in the characterization of fatigue crack growth at these temperatures.

Recent advances in understanding the crack growth behavior of turbine disk alloys have emphasized cyclic crack growth [*1*],[3] cycle-dependent growth with hold times at constant load [*2*] or with peak overloads [*3*]. The applicability of LEFM to high-temperature crack growth has been investigated [*4,5*] within the limitations on time-dependent behavior imposed by specimen geometry and loading conditions. One of the features of the load spectrum which is seen by turbine disk materials is the existence of sustained load for various periods of time. It therefore is important to have an understanding of the growth of cracks under sustained load in order to be able to accurately predict crack growth behavior in these materials.

Quasi-static crack growth in metals at elevated temperature has been reviewed by Fu [*6*], who observed that slow stable crack growth occurs at stress intensities well below a material's fracture toughness K_{Ic}. Cracks in the stable growth region may grow not only for conditions of cyclic loading, but also as a result of sustained load combined with exposure to high temperatures and corrosive environments. The interaction between fatigue-creep crack growth is found to be highly complex and is frequency dependent. The effect of temperature on creep crack growth behavior in Inconel 718 was

[3]The italic numbers in brackets refer to the list of references appended to this paper.

studied by Floreen [7]. Thickness is also a consideration in the phenomenon of crack growth in the stable region defined by plane-strain fracture toughness. Green and Knott [8] examined the effect of a range of specimen thicknesses on the critical value of crack opening displacement in a mild steel. They found that for a given constant applied load, the crack opening displacement (COD) below which failure will not occur is inversely proportional to thickness for specimen widths greater than 10 mm (0.4 in.), and that crack growth can occur above the COD limiting values. A detailed account of empirical results of creep crack growth and its microscopic and macroscopic descriptions is given in [6].

The following study was undertaken in an attempt to correlate sustained load crack growth behavior with one or more fracture mechanics parameters at elevated temperature. The material chosen was IN100, a nickel-based superalloy used as a turbine disk material in the F-100 engine. Two specific aspects of the growth rate behavior were addressed. One is the effect of creep strain on crack growth behavior under sustained load; the second is the possible effect of specimen thickness and the accompanying triaxial stress field on the growth rate.

Several parameters were investigated as correlating parameters for creep crack growth rate based on data obtained from two different specimen geometries covering a range of thicknesses. The two geometries provided cases of increasing and constant stress intensity and thus provided a wide range of test conditions. Compliance was used as a measure of effective crack length for all of the tests because of the inability of surface crack measurements to describe the actual three-dimensional crack shape. Fracture surfaces were examined and observations on the general phenomenology of creep crack growth for this material are presented.

Theoretical Considerations

Crack Growth Rate Parameters

Although the stress-intensity factor, K, was initially developed and used as a parameter which controls the onset of unstable crack growth, it was subsequently extended by Paris [9] and others [10,11] to characterize the growth rate of cracks under cyclic loading, even though the mechanisms of unstable crack growth and fatigue crack propagation are different, and considering that there is no fundamental reason why K should be able to predict fatigue crack growth rates [12]. Thus, it is not surprising that K can also be considered as a possible governing parameter for slow stable creep crack growth, even though the mechanisms here are different from either the case of unstable crack growth or fatigue crack growth.

Reidel [13] established that for a correlation to uniquely exist between the stress-intensity factor and creep crack growth rates, conditions of small-scale yielding are required as well as steady-state crack growth rates. However, as pointed out by Fu [*6*], in a survey article on creep crack growth, for slow stable creep crack growth, the LEFM parameter, K, may not be the appropriate parameter to correlate with experimental data. Failure of K to correlate in certain circumstances [*7,14,15*] has led to consideration of other parameters which may better correlate the steady-state crack growth rate. In addition to K, parameters which have been used include crack opening displacement [*15*], net section stress [*17*], the J-integral [*4,14*] and the C*-integral [*14,16*].

Landes and Begley [*16*] postulated that C^* may be a better descriptor of elevated temperature creep crack growth than the LEFM stress-intensity factor, K. They showed that crack growth rates in discaloy center-cracked panels and CT specimens tested in the creep range at 649°C (1200°F) could be correlated with the C*-integral through a power-law relation. Sadananda and Shahinian [*14*] found that the creep crack growth rate in CT specimens of Inconel 718 is not sensitive to C^* at 538°C (1000°F). Landes and Begley's data were obtained testing at a constant displacement rate whereas the results of the former [*14*] were obtained under constant load.

The C*-integral, or $\dot{J}$ as it is sometimes referred to, is obtained directly from the J-integral of Rice [*10*] by replacing the strain terms with strain rate terms, that is

$$C^* = \int_\Gamma \left[W^* dx_2 - T_i \left(\frac{dv_i}{dx_1} \right) ds \right] \tag{1}$$

where

$$W^* = \int_0^{\dot{e}_{mn}} \sigma_{ij} \, d\dot{e}_{ij} \tag{2}$$

is the strain energy density rate and $\dot{e}$ denotes strain rate. As in the case of the J-integral, the C*-integral is path independent, and thus single-valued, if, and only if

$$W^* = W^*(\dot{e}_{mn}) = \int_0^{\dot{e}_{mn}} \sigma_{ij} \, d\dot{e}_{ij} \tag{3}$$

The existence of a strain energy density rate requires a material constitutive law such that

$$\sigma_{ij} = \partial W^*(\dot{e}_{ij}) / \partial \dot{e}_{ij} \tag{4}$$

For computational purposes, the C*-integral can be interpreted as an energy rate release rate

$$C^* = -\left(\frac{1}{B}\frac{d\dot{U}}{da}\right) \tag{5}$$

where $\dot{U}$ is the potential energy rate and B the specimen thickness.

For the determination of C^* from displacement measurements in constant load crack growth rate tests, a scheme is developed similar to that employed by Landes and Begley [16] in constant displacement rate tests as outlined in Fig. 1. In Fig. 1*a*, $\dot{\delta}$ is plotted against P for a number of selected values of crack length from several tests at constant P. The points for a given value of crack length, a, are then connected. To obtain the values for zero displacement rate, separate tests were conducted at continually decreasing loads or K-values until a level was found at which no displacements occurred after several days. The threshold value for K was found to be $K = 8.8$ MPa-m$^{1/2}$ (8 ksi-in.$^{1/2}$) and corresponding load values were calculated for each value of a to establish the origin in Fig. 1*a*. Integration of the curves in Fig. 1*a* gives $\dot{U}$ as shown in Fig. 1*b*. The curves of Fig. 1*b* are replotted as $\dot{U}$ versus a in Fig. 1*c* for fixed values of $\dot{\delta}$. For sets of values of a and $\dot{\delta}$ in Fig. 1*c*, values of C^*

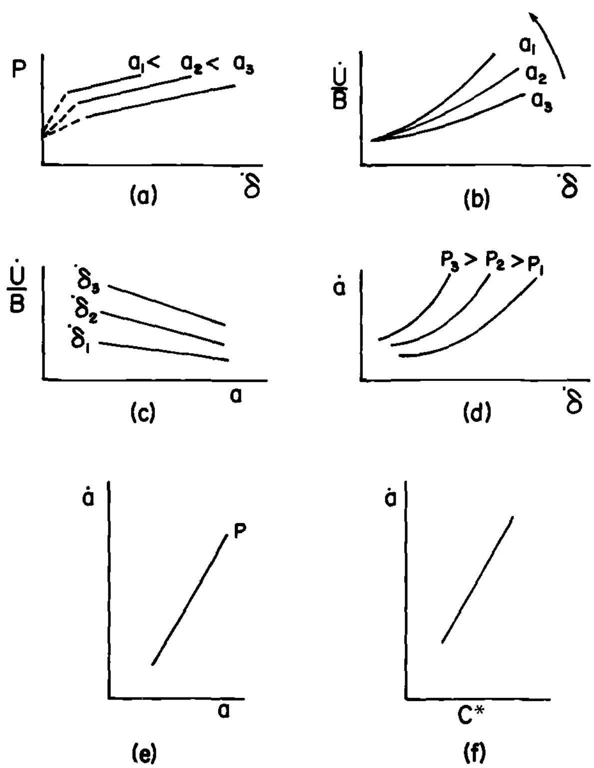

FIG. 1—*Scheme for obtaining* C* *from experimental data.*

can be computed by taking the slope of the appropriate curves at the various values of a. Hence C^* $(a, \dot{\delta})$ can be determined for any value of a and for the fixed values of $\dot{\delta}$ in Fig. 1*c*. The original data are replotted in Fig. 1*d* as $\dot{a}$ versus $\dot{\delta}$ for each test corresponding to fixed values of P. From this plot, values of $\dot{a}$ are obtained for values of $\dot{\delta}$ identical to those used in Fig. 1*c* corresponding to each fixed load level. Finally, a plot of $\dot{a}$ versus a for each load level, Fig. 1*e*, is used to obtain the corresponding value of a. Thus $\dot{a}$ $(\dot{\delta}, P)$ is transformed into $\dot{a}$ $(a, \dot{\delta})$. The tabulated quantities for $\dot{a}$ and C^* are plotted against each other in Fig. 1*f* to provide the final correlation.

Compliance and Effective Crack Length

Experimental observations of the crack front features under sustained load or creep crack growth in IN100 at 732°C (1350°F) and in other materials show a characteristic thumbnail shape. Thus, surface crack lengths are unreliable as a measure of the effect of any governing parameter which depends on crack growth behavior in the interior of the specimen, where the actual crack length is greater than on the surface. Since the parameters which are proposed to govern creep crack growth behavior depend on crack length, there is no way to evaluate or calculate these parameters because the internal crack length cannot be measured directly during an experiment.

In LEFM, K can be obtained from measurements or calculations of the strain energy release rate. From a global viewpoint this depends on determining the load-line displacements and applied load for different crack lengths. The slope of the load versus load-line displacement curve in the vicinity of the origin where nonlinear effects are nonexistent can be used as an alternative measure of crack length. For a crack that is not straight, as in the case of tunneling, the slope or its reciprocal, the specimen compliance, can be used as a measure of "effective" crack length. For the case of creep crack growth, this crack length will be larger than the measured length at the surface of the specimen because of the tunneling of the crack front as the deformation proceeds.

Compliance assumes linear elastic material behavior throughout the entire body in order to have any physical meaning; thus it has the same restrictions as LEFM. For a body containing a crack, the compliance can be related to the stress-intensity factor, K, associated with the geometry of the crack under certain conditions depending upon the dimensions of the crack, and the position and direction of the load [*18*]. Hence compliance changes with crack length as the specimen becomes less stiff as the crack grows. For a two-dimensional plane crack, the derivative of compliance with respect to crack length is related to K, in nondimensional form

$$\frac{d(EBC)}{d(a/W)} = \frac{2B^2\,WK^2}{P^2} = f(a/W) \tag{6}$$

where

E = "effective" modulus of elasticity,
B = specimen thickness, and
W = specimen width.

Integration yields

$$EBC = \frac{2B^2W}{P^2} \int_{a_0/W}^{a/W} K^2 d(a/W) = F(a/W) - F_0(a_0/W) \tag{7}$$

Although theoretical solutions exist for the CT specimen for K as a function of a/W in the range of interest, only the variation of compliance with crack length is determinable since $F_0(a_0/W)$ is not known. Furthermore, compliance is a measure of theoretical load-point displacement and does not take into account the actual method and distribution of applied load in actual experiments as well as the point where displacement is measured if different from the loading pins. It is important, therefore, to have solutions for displacements at the point where they are actually measured experimentally based on realistic models of the actual load application in solutions for C as a function of (a/W). For the case of the ring geometry, both K and C solutions are required.

Rudolphi [19] presented a method for the integral equation solution for a bounded two-dimensional elastic medium with an edge crack applicable to Mode I deformation. His formulation allows for the direct evaluation of displacements on a CT specimen as a function of crack length. A solution by Rudolphi [20] over the range $0.3 \leq (a/W) \leq 0.7$ is reproduced in Fig. 2 and compares mouth opening, crack opening load line, point load, and total height unit displacements as a function of crack extension. The load-line displacements used in this investigation corresponds to δ_4 in Fig. 2. The choice of measuring displacements off the specimen directly is considered superior to measuring off the pins because of the experimental problems associated with pin bending and rotation. From the relationship between displacement and crack length, Fig. 2, dimensionless compliance, *EBC*, was fitted to the polynominal

$$EBC = l + m\alpha^n \tag{8}$$

where $\alpha = a/W$. A best fit to the Rudolphi solution over the range used gives the coefficients over two segments

$$\begin{aligned} l &= 11.51, \quad m = 248.8, \quad n = 3.167, \quad 0.25 \leq \alpha \leq 0.50 \\ l &= 22.468, \quad m = 632.7, \quad n = 5.240, \quad 0.50 \leq \alpha \leq 0.65 \end{aligned} \tag{9}$$

where continuity up to the first derivative has been assured at $\alpha = 0.50$ for the two segments. The Rudolphi solution has been verified independently by

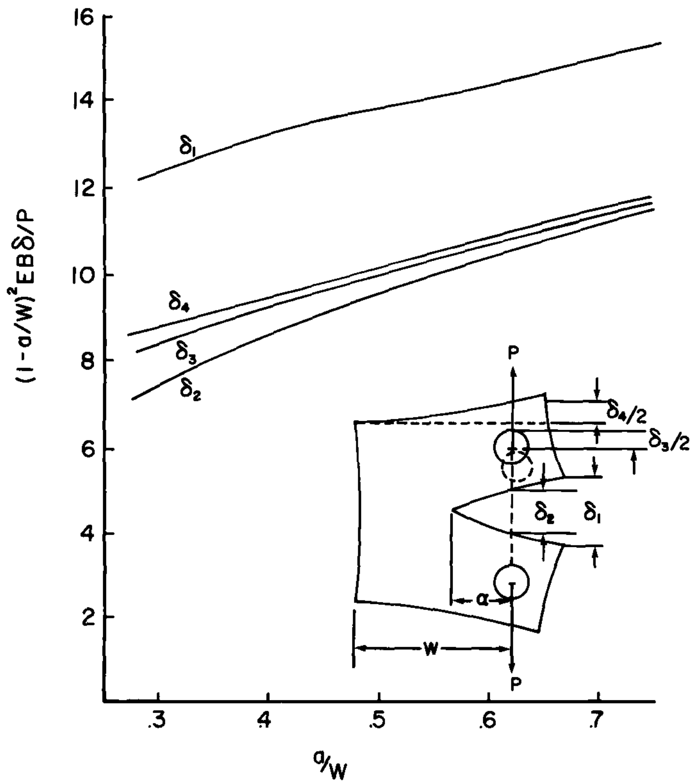

FIG. 2—*Displacements in CT specimen at several different points.*

Ahmad [22] using a finite-element method. From these equations, an "effective" crack length can be determined from experimental compliance measurements. Compliance measured experimentally at the start of the test provided an "effective" modulus of elasticity at 732.2°C (1350°F) based on three-point-averaged initial crack length [Test for Plane-Strain Fracture Toughness of Metallic Materials (E 399-78a)] measured directly on the fracture surface after test completion. Thus, neither plane-stress modulus, E, nor plane-strain modulus, $E/(1 - \nu^2)$, had to be assumed, but rather an "effective" modulus was obtained for each test specimen experimentally.

The use of a ring geometry for the study of crack growth at constant stress intensity was proposed by Grandt [21], who demonstrated the relative insensitivity of K for the radially cracked ring geometry loaded in remote compression over the midrange of crack lengths for specimens having an inner to outer radius ratio $R_i/R_0 = 0.5$. The ring was cracked radially from the inner diameter under the point of application of the compressive load. However, for this investigation, a ring loaded in tension was used. For the tensile loaded ring with a radial crack on the inner diameter at 90 deg to the points of loading, a situation of nearly constant K is again obtained. Solutions for remote tensile loading are presented by Ahmad [22] based on the finite-element method. Stress intensity is fitted to a polynomial in dimensionless crack length, α, where α is the crack length divided by $(R_o - R_i)$, in the form

$$K = \frac{P\sqrt{\pi\alpha}}{2B\sqrt{R_o - R_i}}(6.5481 - 14.428\alpha + 31.873\alpha^2 - 38.656\alpha^3 + 17.684\alpha^4) \quad (10)$$

K is found to be constant within ± 2.5 percent for $0.4 < \alpha < 0.8$. Corresponding solutions for displacements or compliance as measured at the loading pins are also obtained.

Experimental Procedure

The material for this investigation was Gatorized IN100, an advanced fine-grained powder metallurgy nickel-base alloy used as a turbine disk material in the F-100 turbofan engine. Typical chemistry and heat treatment are provided in Ref *1*. Twenty-two standard CT specimens were cut from one pancake of IN100 in the transverse plane (perpendicular to the flat face) such that some specimen crack planes lay in the circumferential direction and some in the radial. Five thicknesses were tested at four initial nominal stress intensities as summarized in Table 1. In addition, a second series of tests was conducted on rings of 76-mm (3.0 in.) outside diameter and 36-mm (1.5 in.) inside diameter with a radial crack emanating from the inner diameter, using specimens cut from a second pancake as summarized in Table 1. All specimens were fatigue precracked at room temperature at 20 Hz, $R = 0.1$, to initial crack lengths of approximately 16.5 mm (0.65 in.) in the CT specimens and 7.6 mm (0.3 in.) in the rings. Averaged quarter-point starter crack lengths, measured on the fracture surface after the tests were run, varied from surface-measured starter crack lengths by 2 to 8 percent. Surface crack lengths during the test were recorded at 5-min intervals from readings made through traveling microscopes on each side of the specimen and displayed on a digital readout. The microscopes were mounted outside a resistance-heated oven which housed the test specimen. Constant load was applied using dead-weight loading in a 44.5-KN-capacity (10 000 lb) creep test frame having a 20-to-1 loading ratio. Temperature variation from test mean of 732°C (1350°F) varied no more than 2.2 deg C ($\pm$4 deg F) in the vicinity of the crack tip.

Specimens were mounted in one-piece rigid clevises with IN-713 pins. The displacement of the CT specimen due to crack opening in the plane of load application (perpendicular to the crack plane) was measured using two E-shaped plates made of IN-718 rigidly attached to the top and bottom of the

TABLE 1—*Summary of test conditions.*

Specimen No.[a]	Type	Thickness, mm (in.)	Load, KN (lb.)	Nominal Ki MPa-$M^{1/2}$ (ksi-in.$^{1/2}$)	Initial a mm (in.)	Final a mm (in.)
7-1	CT	5.41 (0.213)	7.84 (1762)	38.5 (35)	16.81 (0.662)	[b]
7-2		5.46 (0.215)	6.78 (1524)	33.0 (30)	16.87 (0.664)	32.5 (1.281)
7-3		5.46 (0.215)	9.05 (2034)	44.0 (40)	16.87 (0.664)	30.9 (1.218)
7-4		5.46 (0.215)	10.14 (2280)	49.4 (45)	16.84 (0.663)	27.3 (1.075)
11-2		8.53 (0.336)	14.09 (3168)	44.0 (40)	17.07 (0.672)	30.4 (1.197)
11-3		8.53 (0.336)	14.10 (3170)	44.0 (40)	17.02 (0.670)	23.0 (0.904)
11-4		8.59 (0.338)	12.40 (2788)	38.5 (35)	17.09 (0.673)	[b]
11-5		8.61 (0.339)	10.70 (2406)	33.0 (30)	17.07 (0.672)	[b]
11-6		8.61 (0.339)	16.05 (3608)	49.4 (45)	17.04 (0.671)	32.5 (1.278)
15-2		11.73 (0.462)	16.83 (3784)	38.5 (35)	17.93 (0.706)	[b]
15-6		11.86 (0.467)	14.70 (3304)	33.0 (30)	17.42 (0.686)	37.3 (1.469)
15-7		11.84 (0.466)	19.54 (4394)	44.0 (40)	17.30 (0.681)	28.0 (1.102)
15-8		11.84 (0.466)	21.98 (4942)	49.4 (45)	17.27 (0.680)	28.0 (1.101)
19-1		14.96 (0.589)	21.71 (4880)	38.5 (35)	17.53 (0.690)	[b]
19-2		14.83 (0.584)	18.41 (4138)	33.0 (30)	17.45 (0.687)	[b]
19-3		15.04 (0.592)	18.77 (4220)	33.0 (30)	17.48 (0.688)	34.9 (1.375)
19-4		15.06 (0.593)	23.70 (5328)	44.0 (40)	17.20 (0.677)	30.4 (1.197)
19-6		15.06 (0.593)	28.18 (6336)	49.4 (45)	17.35 (0.683)	29.0 (1.142)
23-1		18.08 (0.712)	26.18 (5886)	38.5 (35)	17.88 (0.704)	[b]
23-2		18.21 (0.717)	22.54 (5067)	33.0 (30)	17.63 (0.694)	38.7 (1.525)
23-3		18.24 (0.718)	33.14 (7450)	49.4 (45)	18.34 (0.722)	30.8 (1.213)
23-4		18.24 (0.718)	34.52 (7760)	49.4 (45)	17.35 (0.683)	27.7 (1.091)
8-1	Ring	6.12 (0.241)	19.37 (4354)	49.4 (45)	8.00 (0.315)	17.12 (0.674)
8-A		6.27 (0.247)	17.61 (3960)	44.0 (40)	8.05 (0.317)	17.65 (0.695)
8-3		6.25 (0.246)	13.21 (2970)	33.0 (30)	8.10 (0.319)	15.54 (0.612)
8-4		6.10 (0.240)	9.90 (2226)	25.3 (23)	8.15 (0.321)	15.72 (0.619)
4-1		3.10 (0.122)	9.76 (2194)	49.4 (45)	7.80 (0.307)	15.32 (0.603)
4-2		2.97 (0.117)	4.82 (1084)	25.3 (23)	7.92 (0.312)	14.50 (0.571)
4-3		3.07 (0.121)	6.47 (1454)	38.5 (30)	7.82 (0.308)	14.81 (0.583)

[a]First number is nominal thickness in 1/32's in.
[b]No measurements.

specimen. The use of a similar rigid fixture was demonstrated by Mills et al [*23*]. The E-plates, which translated the load-line displacement outside and around the loading clevises on either side of the specimen, each contained two small pins in the plane of the load line which supported two stainless steel rod-in-sleeve (concentric tubing) extension arms, one on either side of the specimen. These arms protruded down through the oven wall and were attached to two linear variable differential transformers (LVDT's). The LVDT signal output provided load-line displacement measurements which were tape punch recorded at 5-min intervals. For the ring tests, displacement measurements could not be made directly off the specimen. The extension arms for the LVDT's were thus attached directly to pins on the loading clevises for these tests.

Pretest compliance at room temperature was recorded on all specimens. The results were used to calculate initial crack length with which to establish load levels for selected values of initial K. Specimens were then soaked for 1 h at test temperature and compliance again measured for one to two load-unload cycles and for the initial test loading. These values, averaged, provided the data for calculating an "effective" modulus of elasticity for each specimen based on post-test actual initial crack measurements. During the test, compliance was measured at 30-min intervals shedding 0.445 to 0.89 KN (100 to 200 lb) of load incrementally up to 15 to 25 percent of total load. Loading and unloading curves were essentially parallel, indicating that no substantial creep or crack growth occurred during this procedure. Their average value was used to obtain compliance.

Those specimens in Table 1 for which final surface crack measurements are recorded were not allowed to fail catastrophically. Their fracture surfaces were heat-tinted by stopping the tests before the cracks grew into the unstable crack growth region. Photographs of the fractured specimens were used to make final crack length measurements.

At the completion of each test and after cooling to room temperature, a final compliance was recorded. These results, using the room temperature modulus of elasticity of 217 GPa (31×10^6 psi), provided the values of "effective" final crack length tabulated in Table 1 for comparison with actual surface crack lengths as measured on the fractured specimens.

Results and Discussion

Experimentally determined compliance and load-line deflection data were plotted for each CT test and replotted for all tests in Fig. 3, which is normalized for unit specimen thickness. Within the range of experimental scatter, a straight line provides a good fit for a PC-δ relation. In reducing the data for each individual test, the best straight line for each test was used. The data for δ versus t, smoothed using a 7-point averaging method, were used along with the C-δ relation to determine effective crack length, a, and all other necessary

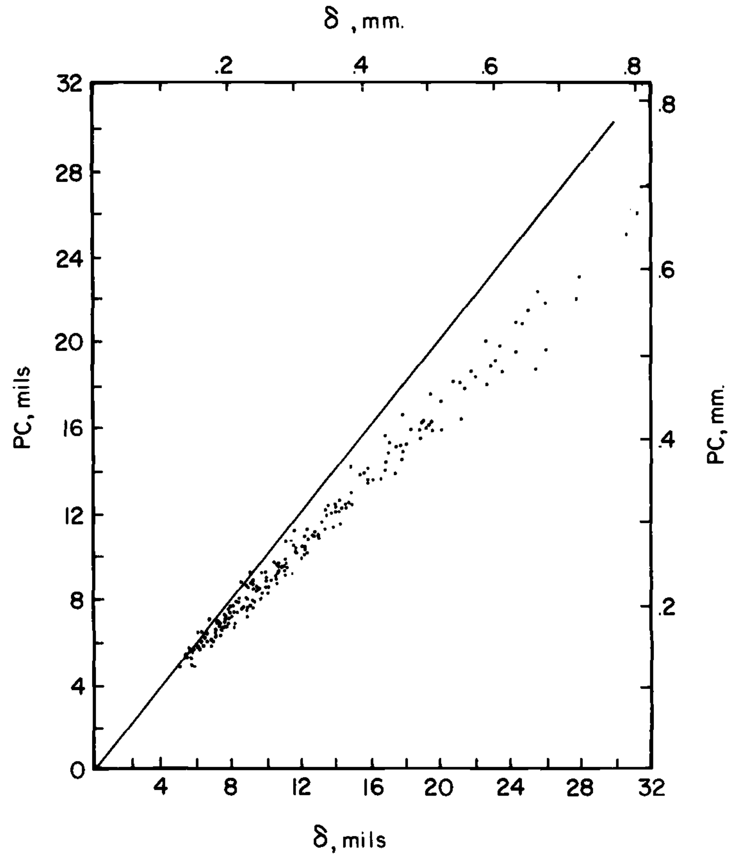

FIG. 3—*Compliance versus load-line displacement for all CT tests normalized for unit thickness.*

quantities. Two significant features appeared in the C-δ plots. The first was the experimental observation in nearly all the tests of a slight decrease in compliance during the initial stages of creep crack growth. This would correspond, physically, to a decrease in crack length. It is interesting to note that this same decrease in compliance was also observed in tests of aluminum and polycarbonate specimens conducted in the same laboratory. One possible physical explanation for this apparent decrease might be a blunting phenomenon combined with some complex three-dimensional stress redistribution. Noting, however, that the magnitude of this compliance decrease is only a few percent, the phenomenon may be solely due to experimental accuracy. The second significant feature of the normalized PC-δ plots is the fact that the slope is less than 1. For purely elastic deformation, the points would follow the unity slope line. In our case, however, there is a continuous accumulation of inelastic or nonrecoverable load-line displacement. Thus, for every increment in crack extension there is an increment of elastic or recoverable displacement due to change in compliance with crack length and an additional inelastic or nonrecoverable increment. The linear nature of the data points implies that the increments of inelastic displacement are proportional to the elastic increments for all tests for all thicknesses and all crack lengths.

Comparisons were made between the effective crack length calculated from the experimental compliance measurements and the actual shape of the final crack length as seen on the broken specimens. A photograph of a typical broken specimen is presented in Fig. 4, in which the effective crack length is also shown. The observed surface crack lengths are also indicated. Considering the severe tunneling, and noting the formation of "fingers" ahead of the crack zone as well as ridges and valleys on the fracture surface parallel to the direction of crack growth, the effective crack length appears to be a better physical measure of crack length than the observed surface crack length, which lags far behind the remainder of the crack. For all of the data reported

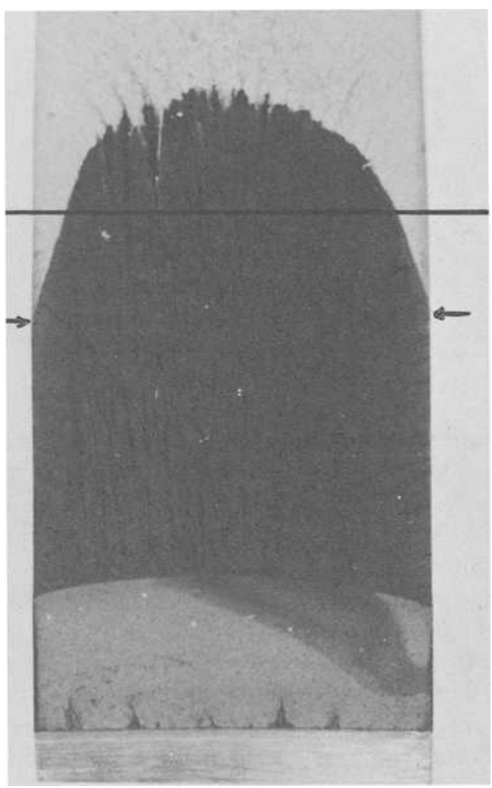

FIG. 4—*Typical fracture surface, Specimen 11-2.*

herein, crack lengths refer to effective crack lengths as calculated from compliance.

Crack growth rates as a function of K were plotted for all tests and then replotted for groups of specimens of identical thickness. A typical plot is shown in Fig. 5, which presents the data from four specimens of 5.6-mm (7/32 in.) thickness. A single curve was drawn through each set of data for each thickness as shown in Fig. 5 for the 5.6-mm-thick (7/32 in.) specimens and each of these curves is reproduced in Fig. 6 to represent the data for all thicknesses. Note that with the exception of the thinnest specimens, all of the data appear to fit a single curve or scatterband representing thicknesses from 8.7 mm up to 18.3 mm (11/32 to 23/32 in.) It appears that plane-strain conditions for creep crack growth have been effectively achieved for thicknesses above approximately 7.6 mm (0.3 in.). This is fairly consistent with the observations of Wallace et al [1], who noted, for the same material IN100 at 649 and 732°C (1200 and 1350°F), that the thickness required to assure plane strain at the crack tip increased from 1.5 mm (0.060 in.) for cyclic tests to 6.4

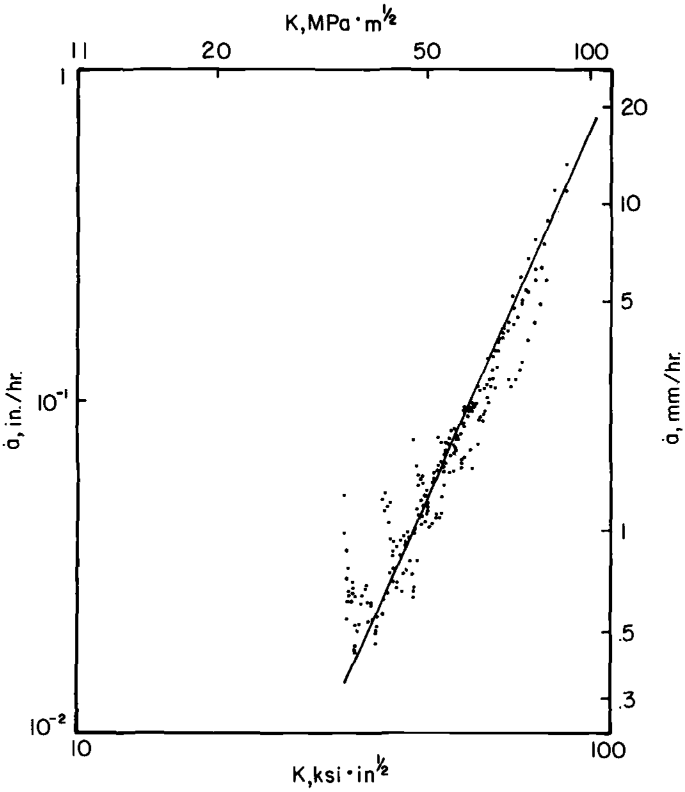

FIG. 5—ȧ-K *for 5.6-mm-thick (7/32 in.) CT specimens.*

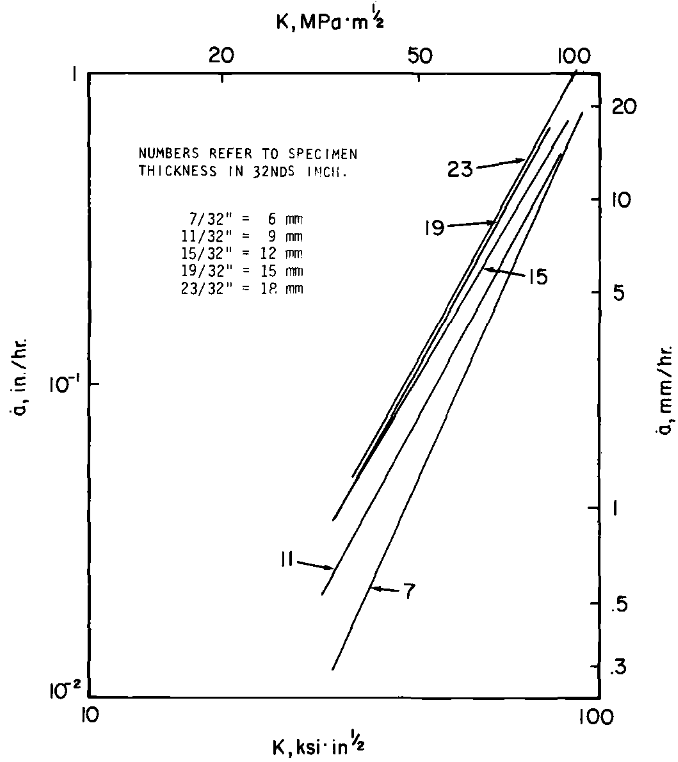

FIG. 6—ȧ-K *for all-thickness CT specimens.*

mm (0.25 in.) for tests containing short time dwells of 5 min or less to 12.7 mm (0.5 in.) for sustained load subcritical crack propagation. They attributed this behavior to environmental influences on crack-tip inelasticity (oxidation).

One characteristic feature which was noted on nearly all of the individual *ȧ-K* plots was an apparent high initial growth rate which shows as a characteristic checkmark shape on each *ȧ-K* plot as can be seen by a careful inspection of Fig. 5. Unpublished data using short hold time periods on the same material at the same temperature confirm this observation of an initially higher growth rate decreasing to a "steady state" creep crack growth rate which depends on *K* or some other governing parameter. The magnitude of this initial growth rate is about double the "steady state" rate, thus accounting for the apparent tails on the *ȧ-K* plots.

Net section stress was also examined as a possible correlating parameter. The data for the various-thickness CT specimens are presented in Fig. 7. Data points for only one thickness, 5.6 mm (7/32 in.), are presented along with a single curve which best represents each group of data. The data of Fig.

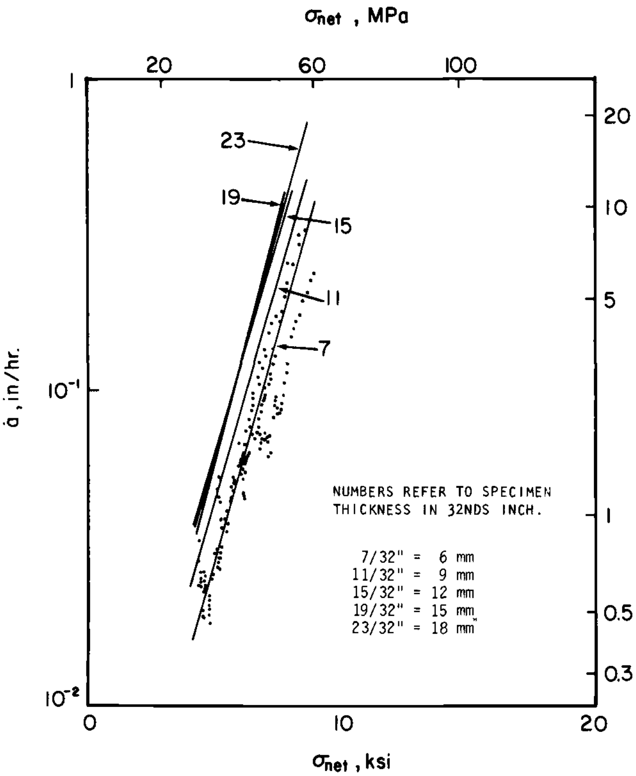

FIG. 7—*ȧ-σ net for all-thickness CT specimens [data points are shown only for 5.6-mm-thick (7/32 in.) specimens].*

7 show no variation with specimen thickness except for the thinnest, 5.6 mm (7/32 in.), specimens, which show a lower crack growth rate. This is consistent with the results presented in the form of $\dot{a}$-K plots.

The parameter C^* was calculated using the scheme outlined previously. Note that C^* calculations require the use of data from several different tests such that experimental scatter from test to test influences the calculations. Thus, one single test may tend to bias the data unfairly although many smoothing operations are performed in plotting, replotting, and cross-plotting the data to extract C^*. The results of the C^* calculations for each thickness group of CT specimens are presented in Fig. 8. The data points for only the 5.6-mm-thick (7/32 in.) specimens are shown to indicate the typical amount of variability for each group of data represented by a single curve. There appears to be no statistically significant variation of crack growth rate with thickness from Fig. 8.

To further evaluate the ability of a given parameter to correlate creep crack growth behavior, data obtained from radially cracked ring specimens

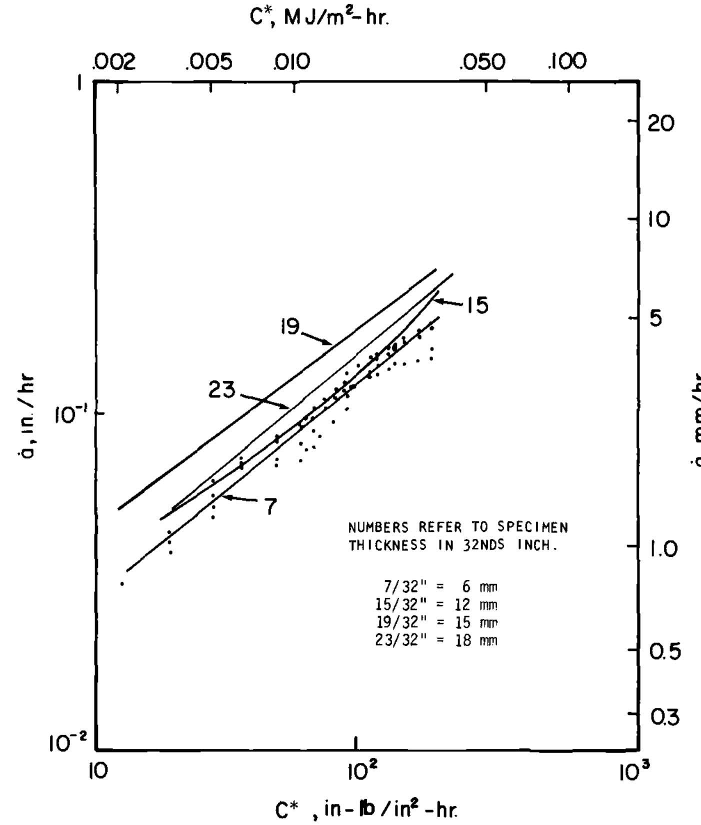

FIG. 8—$\dot{a}$-C* *for all-thickness CT specimens [data points are shown only for 5.6-mm-thick (7/32 in.) specimens].*

were also examined. For the ring specimens, the compliance values were considerably lower than those for the CT specimens for equivalent ranges of K or $\dot{a}$. Thus, it was extremely difficult to obtain reliable and accurate compliance measurements although load-line displacement readings provided good data. The experimental setup for the ring tests necessitated taking displacement measurements not directly on the specimen. Thus, although displacement measurements made at constant load were reliable because any other extraneous displacements did not change, compliance measurements involved changing load levels and thus possible changes in displacements due to other than specimen compliance were difficult to analyze. To circumvent this problem, the known values of compliance based on measured initial and final crack lengths were used along with a linear plot of PC versus δ as obtained in the CT specimens. Careful examination of all of the experimental data indicated that the linear relation for PC versus δ was as good a representation of the data as any other, considering the amount of uncertainty in the experimental compliance measurements.

The test data from seven rings of two thicknesses, 3.2 mm and 6.4 mm (0.125 and 0.250 in.), are presented in Fig. 9 as $\dot{a}$ versus K. Also shown is the best-fit curve for the thinnest CT specimens. The data from each ring appear as a nearly vertical line because the stress-intensity factor is essentially independent of crack length in the ring geometry. The vertical curves proceed from top to bottom with increasing crack length or time. Thus, a given K provides a range of (decreasing) crack growth rates. Again, the phenomenon of an initial higher creep crack growth rate is observed. If the bottom portion of each line is thought of as the more or less "steady state" creep crack growth rate in the ring tests, then one can see a fair correlation with the CT specimen data considering the variation in rates between specimens. Note also that the ring specimens were obtained from a separate forging than that used for the CT specimens.

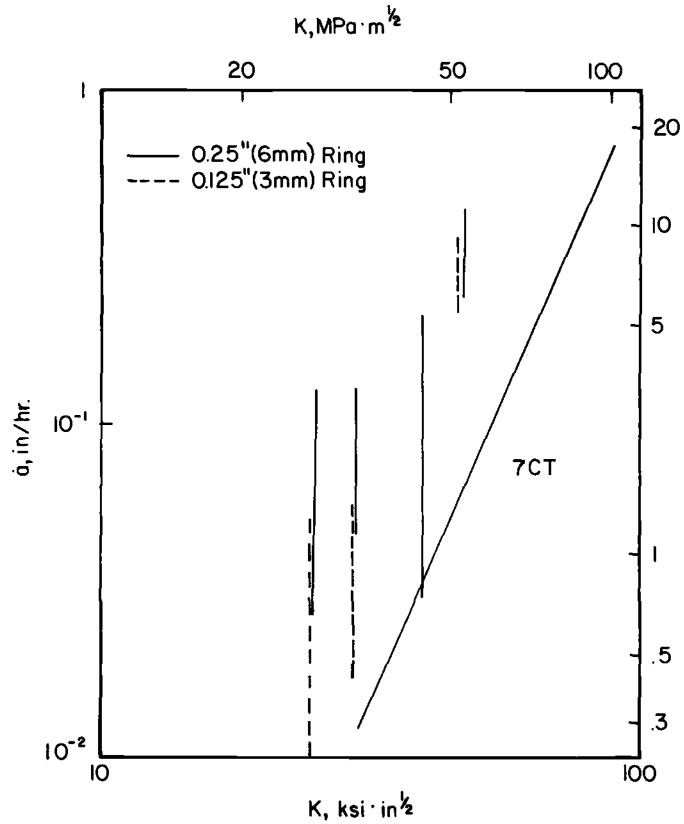

FIG. 9—$\dot{a}$-K *for all ring tests [6-mm (7/32 in.) CT data are shown for comparison].*

If one next considers net section stress as a correlating parameter, the application to the cracked ring geometry poses a dilemma. The ring can be thought of as a statically indeterminate structure or two half rings in parallel which carry a fraction of the load depending inversely on compliance. The compliance of the cracked half continually increases, thereby transferring load to the other half, since total load remains constant. It is this feature which results in a value of K which is essentially independent of crack length over a substantial range of crack lengths. Nonetheless, if one used either the entire net cross section area of the two halves of the ring or the area of the cracked portion in calculations, net section stress would be an increasing function of crack length. In experiments, crack growth rate was found to be a decreasing function of crack length. It is apparent, then, that net section stress is not a good parameter for correlating creep crack growth rate for the ring geometry data. Furthermore, net section stress does not have any significant physical meaning for the ring geometry unless a calculation is made of the actual stresses in the cracked half of the ring.

Finally, the data from the ring tests were used to calculate C^*. Following the scheme outlined in Fig. 1, one immediately concludes that C^*-values will be negative for the ring tests data. Since displacement rates are a decreasing function of time or crack length, calculations of $d\dot{U}/da$ produce negative values of C^*. Thus, C^* does not provide a means of correlating creep crack growth rate data as obtained from the cracked ring geometry. Since the analytical derivation of C^* is based on a creeping solid and does not consider elastic strains or strain rates in the body, a structure such as a cracked ring which is quite stiff is poorly represented by such a model. Thus the C^* parameter cannot be expected to provide a measure of creep crack growth rate when it is obtained experimentally from load-line displacements in a relatively rigid and statically indeterminate structural configuration.

Conclusions

Sustained load crack growth in IN100 at 732°C (1350°F) is a highly complex three-dimensional phenomenon characterized by initially high growth rates, severe tunneling, and the degree of constraints on the fracture surface. The concept of an effective crack length based on compliance appears to be a reasonable method of measuring crack extension and, furthermore, seems to have a physical basis as a measure of average crack length for severely tunneled cracks.

Crack growth rate was essentially independent of specimen thickness for thicknesses above 8.7 mm (0.34 in.) but slightly lower for specimens of 5.6-mm (0.22 in.) thickness. The plane-strain condition for creep crack growth is reached for specimens considerably thicker than those for cyclic fatigue crack growth, yet much thinner than those required for plane-strain fracture toughness testing.

The use of only one test specimen geometry such as a CT specimen with different loads and crack lengths provides experimental data which show crack growth rate to be controlled equally well with K, σ_{net}, or C^*. If, however, a second geometry specimen is introduced, σ_{net} and C^* do not provide good correlation with growth rate for all of the data. For any of the correlating parameters, the initial values of growth rate in any test appear to be higher than those obtained after the crack has been growing for the same value of the correlating parameter.

C^* as a correlating parameter does not predict the creep crack growth rate from the data on two distinct specimen geometries. C^* was calculated from experimental load line or far-field measurements using constant-load experiments. The analytical derivation of C^* requires the material to be a creeping solid throughout with no contributing elastic strains. Since this assumption does not appear to be valid, especially for the ring geometry, the path independence of the integral is not maintained. Thus, the C^*-integral as a governing parameter for creep crack growth would appear to be feasible only if the integral were taken along a path very close to the crack tip.

Acknowledgments

The work reported herein was conducted at the AFWAL Materials Laboratory under Project 2307P102. The authors gratefully acknowledge the cooperation of Dr. N. Ashbaugh, Systems Research Laboratories, for his many helpful technical discussions and to Mr. R. Klinger for his invaluable assistance in the experimental portion of the program.

References

[1] Wallace, R. M., Annis, C. G., and Sims, D. L., "Application of Fracture Mechanics at Elevated Temperatures," AFML-TR-76-176, Part 2, Air Force Materials Laboratory, Wright-Patterson Air Force Base, Ohio, 1977.

[2] Macha, D. E., Grandt, A. F., and Wicks, B. J. in *Effect of Load Spectrum Variables on Fatigue Crack Initiation and Propagation, ASTM STP 714,* American Society for Testing and Materials, 1980, pp. 108-127.

[3] Macha, D. E., *Journal of Engineering Fracture Mechanics,* Vol. 12, 1979, pp. 1-11.

[4] Sadananda, K. and Shahinian, P. in *Fracture Mechanics,* N. Perrone, et al, Eds., University Press of Virginia, 1978, pp. 685-703.

[5] Nikbin, K. M., Webster, G. A., and Turner, C. E. in *Cracks and Fracture, ASTM STP 601,* American Society for Testing and Materials, 1976, pp. 47-62.

[6] Fu, L. S., *Journal of Engineering Fracture Mechanics,* Vol. 13, 1980, pp. 307-330.

[7] Floreen, S., *Metallurgical Transactions, A,* Vol. 6A, 1975, pp. 1741-1749.

[8] Green, G. and Knott, J. F., *Journal of the Mechanics and Physics of Solids,* Vol. 23, 1975, pp. 167-183.

[9] Paris, P. C. in *Fatigue, An Interdisciplinary Approach,* Syracuse University, Syracuse, N.Y., 1964, pp. 107-132.

[10] Rice, J. R. in *Fracture,* Vol. 2, H. Liebowitz, Ed., Academic Press, New York, 1968, pp. 191-311.

[11] Paris, P. C. and Sih, G. C. in *Fracture Toughness Testing and Its Applications, ASTM STP 381,* American Society for Testing and Materials, 1965, pp. 30-81.

[12] Freudenthal, A. M., "Fatigue and Fracture Mechanics," Technical Report No. 11, Institute for the Study of Fatigue, Fracture and Structural Reliability, George Washington University, 1972.
[13] Reidel, H., *Materials Science and Engineering*, Vol. 30, 1977, pp. 187-196.
[14] Sadananda, K., and Shahinian, P., *Metallurgical Transactions, A*, Vol. 8A, 1977, pp. 439-449.
[15] Haigh, J. R., *Materials Science and Engineering*, Vol. 20, 1975, pp. 213-223 and 225-235.
[16] Landes, J. D. and Begley, J. A. in *Mechanics of Crack Growth, ASTM STP 590*, American Society for Testing and Materials, 1976, pp. 128-148.
[17] Harrison, C. G. and Sandor, G. N., *Journal of Engineering Fracture Mechanics*, Vol. 3, 1971, pp. 403-420.
[18] Bubsey, R. T., Fisher, D. M., Jones, M. H., and Srawley, J. E. in *Experimental Techniques in Fracture Mechanics*, SESA Monograph No. 1, Society for Experimental Stress Analysis, 1973, pp. 76-95.
[19] Rudolphi, T. J., "An Integral Equation Solution for a Bounded Elastic Body with an Edge Crack: Mode I Deformations," AFML-TR-78-113, Air Force Materials Laboratory, Wright-Patterson Air Force Base, Ohio, 1978.
[20] Rudolphi, T. J., unpublished data.
[21] Grandt, A. F., Jr. in *Fracture Mechanics and Technology: Vol I*, G. C. Sih and C. L. Chow, Eds., Sijthoff and Noordhoff, The Netherlands, 1977, pp. 89-98.
[22] Ahmad, J., unpublished data.
[23] Mills, W. J., James, L. A., and Williams, J. A., *Journal of Testing and Evaluation*, Vol. 5, 1977, pp. 446-451.

D. M. Norris,[1] *J. E. Reaugh,*[2] *and W. L. Server*[3]

A Fracture-Toughness Correlation Based on Charpy Initiation Energy

REFERENCE: Norris, D. M., Reaugh, J. E., and Server, W. L., **"A Fracture-Toughness Correlation Based on Charpy Initiation Energy,"** *Fracture Mechanics: Thirteenth Conference, ASTM STP 743,* Richard Roberts, Ed., American Society for Testing and Materials, 1981, pp. 207-217.

ABSTRACT: An upper-shelf correlation between fracture toughness and the energy required to initiate cracking (CVN_i) in the Charpy V-notch specimen is presented. The correlation is obtained using data on 23 steels with variations in yield strength of 447 to 1696 MPa, fracture toughness of 40 to 353 kN/m, and Charpy toughness (CVN) of 22 to 192. The toughness correlation based on all the data using either CVN_i or CVN is about the same and is also about equal to that of the Rolfe-Novak-Barsom (RNB) correlation. If only those data with fracture toughness less than 200 kN (1140 psi-in.) are used, the CVN_i correlation is better than that obtained by RNB or one based on CVN data alone.

KEY WORDS: fracture toughness, Charpy correlation

Observations of Charpy V-notch tests using a multispecimen, controlled-deflection method with SA533B-1 steel at 100°C showed that only 10 percent of the fracture energy is associated with crack initiation. It seemed to us that an improved correlation between fracture toughness and Charpy energy might be obtained if the Charpy energy associated only with the initiation event was used. An earlier upper-shelf correlation was given by Rolfe and Novak [*1*][4] and Barsom and Rolfe [*2*], who used the total Charpy fracture energy CVN. We refer to their work as RNB in this paper.

The ratio of static initiation energy to total dynamic Charpy energy was available from our tests on three steels and, in addition, these tests suggested a relation between this ratio and the material yield strength so that a correlation could be attempted using the fracture toughness-total Charpy energy data of others. Although both dynamic and slow-bend initiation tests were

[1]Technical manager, Electric Power Research Institute, Palo Alto, Calif. 94303; formerly with Lawrence Livermore Laboratory, Livermore, Calif.
[2]Division manager, Science Applications, Inc., Albuquerque, N. Mex., 87102.
[3]Vice president, Fracture Control Corp., Goleta, Calif. 93017.
[4]The italic numbers in brackets refer to the list of references appended to this paper.

performed [3], we chose to use the slow-bend data only. As a result, our correlation relates fracture toughness, measured by quasi-static tests, with a quasi-static initiation energy. The correlation we developed, using our data and that of others, showed marginal improvement over the RNB correlation.

The Charpy tests described here supplemented other multispecimen experiments required to calibrate a computer model of ductile fracture described elsewhere [3,4].

Materials

Charpy tests were performed on SA533B-1 steel and on two other quenched-and-tempered states of this steel. Specimens were made from a nozzle cutout from a nuclear reactor pressure vessel. The cutout was designated Heat CDB by Marston et al [5] and currently as 1bE in the Electric Power Research Institute data base [6]. The material was named M1, M1.5, or M2, corresponding to the heat treatment (see Table 1) chosen to raise the yield strength and lower the toughness. All tests were conducted in the short-transverse orientation (S-L) with respect to the plate; the Charpy specimen's crack plane was typically from the one-fourth thickness location in the plate stock. The plate was 267 mm thick.

Tests and Results

Static Charpy V-notch tests (slow bend at a ramp rate of 61.1×10^{-4} mm/s) were performed using a closed-loop hydraulic machine under ram-displacement control. Specimens were taken to various displacements chosen to span the crack initiation event, then heat-tinted at 288°C for 15 min and later broken dynamically at −196°C. A tup-anvil arrangement meeting standard Charpy requirements was used for the static loading, with a clip gage across the mouth of the specimen for most of the tests. Both load-versus-ram

TABLE 1—*Heat treatments for the materials investigated in this study. The basic material, designated M1, was SA533B-1 steel plate subjected to heat treatments involved in manufacturing and fabricating it into a nuclear-reactor pressure vessel.*

Material	Heat Treatment
M1	SA533B-1 steel heat-treated during manufacture and fabrication as follows: austenitized at 871 ± 14°C for 4 h and water-quenched; tempered at 663 ± 14°C for 4 h; postweld heat-treated at 621 ± 14°C for 25 h
M1.5	M1 condition; heat-treated at 871 ± 12°C for 1 h in a neutral atmosphere and water-quenched; tempered at 204 ± 12°C for 4 h and water-quenched; second heat treatment at 871 ± 12°C for 1 h in a neutral atmosphere and water-quenched; tempered at 621 ± 12°C for 4 h and water-quenched
M2	M1 condition; heat-treated at 871 ± 12°C for 1 h in a neutral atmosphere and water-quenched; tempered at 537 ± 12°C for 4 h and water-quenched

displacement and load-versus-clip gage response were recorded. The load-versus-ram displacement (P-versus-Δ) results were corrected for machine compliance. All tests were conducted at 100°C.

The crack distribution in the heat-tinted specimen was measured optically using a ×50 traveling-stage microscope. Data were obtained as the fraction of the specimen thickness (normal to the ligament) that cracked as a function of striker displacement, the deepest crack penetration, and the nine-point average crack penetration. The results are presented in Tables 2, 3 and 4.

TABLE 2—*Static interrupted Charpy bend data M1-100°C.*

Specimen No.	Deflection, mm	E,[a] J	% of Notch Cracked	Maximum Crack Depth, mm	$\bar{a}$,[b] mm
2758	0.394	3.10	0	...	2.03
2780	0.630	5.83	0	...	2.06
2753	0.764	7.27	4.7	0.2	2.06
2773	0.780	7.52	0	...	2.08
2776	0.886	8.94	0	...	2.08
2769	1.01	10.4	0	...	2.16
2751	1.11	11.5	18.5	0.254	2.13
2783	1.14	12.3	30.2	0.457	2.13
2782	1.26	13.7	22.6	0.178	2.13
2784	1.41	15.8	79.3	0.406	2.21
2746	1.48	16.4	75.0	0.635	2.26
2777	1.53	17.4	100.0	0.432	2.24

[a] Deformation energy corrected for machine compliance.
[b] Average distance from notch-side surface to crack tip, nine measurements.

TABLE 3—*Static interrupted Charpy bend data M1.5-100°C.*[a]

Specimen No.	Deflection, mm	E, J	% of Notch Cracked	Maximum Crack Depth, mm	$\bar{a}$, mm
A28	0.510	6.92	0	0	2.06
A4	0.551	7.74	35	1.4	2.26
A16	0.556	7.80	10	0.71	2.06
A22	0.625	8.94	8	0.30	2.08
A11	0.640	9.24	20	0.71	2.16
A18	0.691	10.4	10	0.41	2.11
A19	0.742	11.2	0	0	2.08
A31	0.770	11.8	45	1.1	2.26
A36	0.864	13.2	70	0.99	2.34
A43	1.14	18.5	70	2.0	2.77
A7	1.32	20.8	82	3.10	3.35
A46	1.41	22.2	100	3.00	3.48

[a] See footnotes on Table 2.

TABLE 4—*Static interrupted Charpy bend data M2-100°C.*[a]

Specimen No.	Deflection, mm	E, J	% of Notch Cracked	Maximum Crack Depth, mm	$\bar{a}$, mm
B6	0.396	5.88	0	0	2.0
B18	0.472	7.29	40	1.5	...
B23	0.503	8.35	12	0.51	2.1
B35	0.464	9.66	30	0.79	2.1
B21	0.732	12.8	85	3.00	2.87
B1	0.932	16.1	80	4.19	4.01

[a] See footnotes on Table 2.

We found the initiation energy from this data by plotting the fraction of the specimen thickness (normal to the ligament) cracked versus striker displacement and forming a regression line to extrapolate the deflection for zero cracking (see Fig. 1). The specimen energy versus deflection data (shown in Fig. 2) may then be used to find the initiation Charpy energy CVN_i. The results are given in Table 5.

The J_{Ic} data of Table 5 were obtained with 25-mm-thick compact specimens using the heat-tint method. Three specimens of each material were tested with resulting crack extensions between 0.05 and 0.6 mm [3].

A Correlation Based on Initiation Energy

The data of Table 5 provide the relationship between J_{IC} and CVN_i (and CVN) for the three steels of our test program. To improve the correlation for

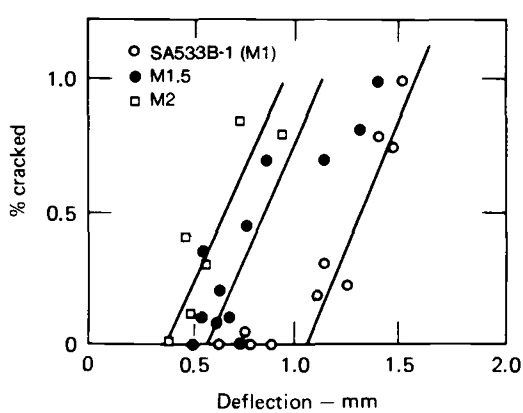

FIG. 1—*Determination of static Charpy V-notch specimen deflection at crack initiation. The basis is the percent of specimen thickness (normal to the ligament) cracked.*

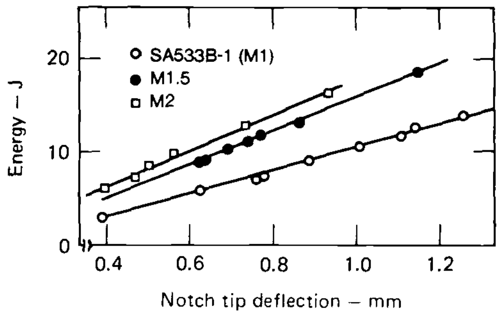

FIG. 2—*Charpy-specimen internal energy versus deflection, static data from interrupted deflection tests.*

TABLE 5—*Correlation data for three steels,* T = *100°C.*

Steel	Yield Stress, MPa	CVN, J	CVN_i J	CVN_i / CVN	Static CVN, J	J_{Ic}, kN/m
SA533B-1 (M1)	458	110	11.3	0.103	81	140
M1.5	788	70	8.5	.121	56	110
M2	895	45	5.6	0.124	37	77

wider data base, it was necessary to obtain initiation energy from results that provide only total Charpy energy.

We obtained this relationship by assuming that the ratio of CVN_i to CVN is a universal function of yield stress. For our three steels, the ratio is approximately linear at 100°C over the range of yield strengths we have tested (see Fig. 3). We would expect the ratio to increase even more in materials with higher yield strengths. The simple dependency of the ratio on yield strength at upper-shelf temperature is probably an oversimplification and requires further verification, but it appears to have merit, as we shall demonstrate.

Quality

Our correlation resulted in reduced scatter in the data when compared with displaying J_{Ic}[5] versus CVN directly. The error measure using CVN_i for the correlation is 25 percent and is 29 percent if CVN is used. The distribution of the data is given in Figs. 4 and 5 for the two cases.

Our error measure is determined by the root-mean-squared fractional er-

[5]We have converted K to J by the relation $EJ_{Ic} = (1 - \nu^2) K_{Ic}^2$.

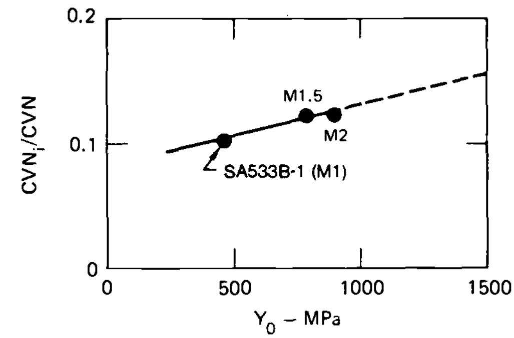

FIG. 3—*Ratio of Charpy V-notch initiation energy to total fracture energy as a function of yield stress for SA533B-1 steel and two additional heat treatments, 100°C.*

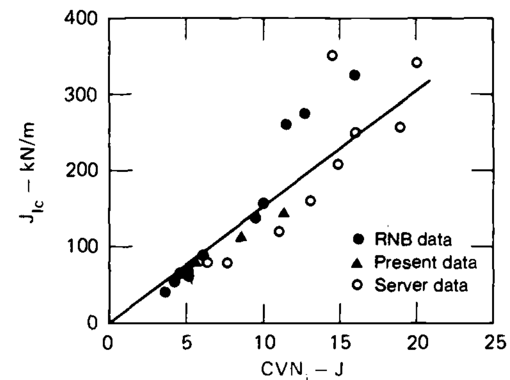

FIG. 4—*Experimental fracture toughness versus Charpy initiation energy. Data are reduced using Fig. 3. The straight line minimizes the mean-squared fractional error.*

ror. Given a value $f(x_i)$ calculated from the least-squares straight-line fit and a measured value f_i of the ith data point, this error measure, e, is given by

$$e = \left[\frac{1}{N}\sum_{i=1}^{N}\left\{\frac{f(x_i) - f_i}{f(x_i)}\right\}^2\right]^{1/2} \tag{1}$$

The correlation used a data base of 23 steels consisting of our data, the RNB data (Table 6), and the data of Server [7] (Table 7). For the RNB and Server data we used Fig. 3 to obtain the ratio CVN_i/CVN from the yield stress and plotted J_{Ic} versus CVN_i in Fig. 4. Our correlation, found from a least-squares fit, is a linear relation given by

$$J_{Ic} = \alpha\, CVN_i \tag{2}$$

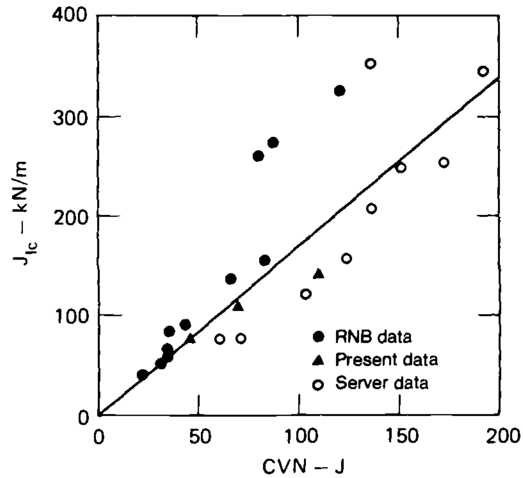

FIG. 5—*Experimental fracture toughness versus total Charpy energy to break the specimen. The straight line minimizes the mean-squared fractional error.*

where $\alpha = 15.1$ kN/Jm. Converting to CVN by substituting the linear relationship shown in Fig. 3 into Eq 2 gives[6]

$$J_{Ic} = \mathrm{CVN}\left(\frac{Y_o + 1600}{1300}\right) \tag{3}$$

where the units for CVN are joules and Y_o (the yield strength) in MPa for J_{Ic} in kN/m.

The RNB correlation is

$$J_{RN} = \frac{1 - \nu^2}{E} Y_o\left(5\,\mathrm{CVN} - \frac{Y_o}{4}\right) \tag{4}$$

where J_{RN} is in lb/in., Y_o is in ksi, and CVN is the Charpy energy in ft-lb. This upper-shelf K_{Ic}-CVN correlation was developed empirically from results obtained on the 11 steels of Table 6.

An error measure based on the RNB correlation may now be computed. Using the 23-point data base for CVN, Eq 4 provides J_{RN} that may be plotted versus the experimentally determined J_{Ic} (see Fig. 6). Equation 1 gives a

[6]Although expressed in terms of CVN, to avoid confusion with quality comparisons of J versus CVN, the reader should note that Eq 3 is a convenient form of Eq 2 and is based on initiation energy.

TABLE 6—*Upper-shelf correlation data for the RNB steels (*T = *27°C).*

Materials	Yield, MPa	CVN, J	$\frac{CVN_i^{a}}{CVN}$	CVN_i,[a] J	J_{Ic},[b] kN/m
A517FAM	758	84	0.119	10.0	155
4147AM	945	35	0.128	4.5	64
HT-130(T)AM	1027	121	0.132	16.0	324
4130AM	1089	31	0.134	4.2	53
12Ni5Cr3MoAM	1207	43	0.140	6.0	90
12Ni5Cr3MoVM	1262	81	0.142	11.5	259
12Ni5Cr3MoVM	1282	88	0.144	12.7	273
18Ni8Co3Mo (180 Grade AM)	1331	34	0.151	5.1	59
18Ni5Cr3Mo (180 Grade AM)	1310	34	0.150	5.1	67
18Ni8Co3Mo (180 Grade VM)	1289	66	0.144	9.5	137
18Ni8Co5Mo (250 Grade VM)	1696	22	0.162	3.6	40

[a] Estimated by present authors (see text).
[b] J_{Ic} calculated using measured K_{Ic}-values and the relation $J_{Ic} = K_{Ic}^2 (1 - \nu^2)/E$.

TABLE 7—*Correlation data for steels and weldments,* T = *177°C (Server [7]).*

Materials	Yield, MPa	CVN, J	$\frac{CVN_i^{g}}{CVN}$	CVN_i,[g] J	J_{Ic},[a] kN/m	J_{Ic},[a,f] kN/m
SA533B-1(M1)	486	125	0.106	13.2	125	159
SA508-2	488	152	0.106	16.1	226	249
SA302B	465	60	0.105	6.3	63	79
SA302B (special heat)	477	71	0.105	7.5	63	79
MMA[b] weld metal (A533B-1 base metal)	566	137	0.109	14.9	187	209
MMa weld metal (A508-2 base metal)	447	192	0.104	20.1	355	345[e]
SA[c] weld metal (A533B-1 base metal)	545	174	0.109	18.9	231	257
SA weld metal (A508-2 base metal)	490	104	0.106	11.0	103	120
SA533B-1 (HSSTO2)	481	137	0.106	14.5	288[d]	353[e]

[a] J_{Ic} calculated using measured K_{Ic}-values and the relation $J_{Ic} = K_{Ic}^2 (1 - \nu^2)/E$.
[b] Manual metal arc weld.
[c] Submerged arc weld.
[d] Tested at 71°C.
[e] Specimen did not satisfy ASTM size requirement.
[f] Merkle-Corten correction applied.
[g] Estimated by present authors (see text).

mean fractional error of 28 percent compared with the 25 percent error of our correlation.

Our results are summarized in Table 8. The scatter in the RNB correlation is slightly larger than ours. It is also instructive to examine only those data with fracture toughness less than 200 kN/m. This includes most heats of

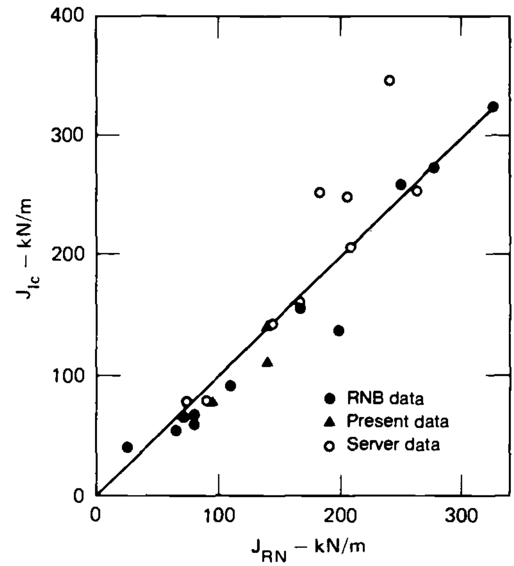

FIG. 6—*Experimental fracture toughness versus fracture toughness calculated from measured CVN using the RNB formula. The straight line minimizes the mean-squared fractional error.*

TABLE 8—*Comparison of fracture toughness correlations.*[a,c]

	$J_{Ic} = \alpha$ CVN, α	Fractional Error, %	$J_{Ic} = \alpha\ CVN_i$, α	Fractional Error, %	$J_{Ic} = \alpha\ J_{RN}$, α	Fractional Error, %
All data	1.97	29	15.1	25	1.03	28
$J_{Ic} \leq 200$ kN/m	1.6	19	12.6	12	0.93	24
			12.6[b]	10	0.83[b]	13

[a] Calculated to minimize the mean-squared fractional error [see Eq 1].
[b] Eliminated data point with maximum fractional error.
[c] Units of J_{Ic} are kN/m; units of CVN are in joules.

SA533B-1 steel, and all less-tough steel. Results of this subset of the data are also given in Table 8.

By the use of the standard statistical test for equality of variance (see, for example, Ref *8*), we find that when all the data are included, neither our correlation nor the RNB correlation is significantly better than a correlation using CVN data, uncorrected by Y_0, directly. Here a better correlation is one with a smaller error measure. If only those data points with fracture toughness less than 200 kN/m (1140 psi-in.) are used, our correlation is better than both the RNB correlation (at the 99 percent confidence level) and a correlation based on CVN data alone (at the 95 percent confidence level).

Discussion

It is remarkable that a correlation based on our three steels can give a correlation that is about as good as the RNB data, despite the necessity of extrapolating to nearly double the yield strength of our M2 material. It suggests that refining the CVN_i/CVN versus Y_0 curve by the addition of more data points could tighten the correlation.

Although the RNB correlation (and perhaps ours) is made more credible by its similar quality of fit, they are quite different correlations; a data point that seems anomalous in one correlation is in the mainstream of the other. It is unclear whether the reason for their similarity is accidental or has some fundamental basis.

Calculations by Norris [*9*] have shown that only 12 percent of the Charpy initiation energy is concentrated in the process volume at the notch tip. Using results from our computer simulations of the Charpy tests with the three different materials [*3*], we attempted two correlations for fracture toughness using strain-energy density extrapolated to the notch tip and the strain energy in a small volume (dimension 0.1 mm) at the notch tip. We had assumed that such localized measures of initiation energy in the Charpy test would provide better correlations. We found that (1) correlations using these local measures of initiation energy gave error measures for our three steels (25 percent) that were worse than the correlation based on CVN_i for these steels (14 percent), and (2) there was no apparent simple relationship among the local strain-energy measures, CVN, and Y_0. Thus, even had the correlation been excellent, there was no way of estimating the local strain-energy measures from data available for other steels.

A correlation of fracture toughness with the energy required to tear a ductile Charpy specimen appears tenuous because of the well-known differences in the stress-strain fields at a crack tip and that at a blunt notch. However, as shown in [*3*], in ductile materials sharp cracks blunt substantially before propagation and the resulting plastic-strain field decays exponentially from the blunted tip in the same manner as that at the 1/4-mm-radius notch of the Charpy specimen. Further, as shown in two- and three-dimensional calculations by Norris et al [*3*], a Charpy specimen is in a plane-strain state at crack initiation. For these reasons, it would be expected that some uppershelf correlation might be expected with the standard Charpy specimen. Even better results might be expected from a precracked specimen subject to some of the reservations discussed in [*9,10*] such as loading rate and amount of allowable crack growth.

We conclude that a correlation to obtain fracture toughness, J_{Ic}, from Charpy V-notch energy, CVN, may be obtained by considering only a portion of CVN absorbed by the specimen up to the time of initiation, CVN_i. We present a method of extracting CVN_i from interrupted, slow-bend tests of the Charpy specimen. We further demonstrate that the ratio CVN_i/CVN is a slowly varying function of yield strength for our three steels. Assuming this ratio to be a universal function of yield stress, we are able to correlate our data with data from materials with low fracture toughness extremely well, and with data from materials with high fracture toughness fairly well.

Acknowledgments

This work was done at the Lawrence Livermore Laboratory for the Electric Power Research Institute; T. U. Marston of the Institute was the project manager. The authors are pleased to acknowledge his encouragement and contributions to the program. We also thank B. Moran and D. F. Quiñones of the Lawrence Livermore Laboratory and J. W. Sheckherd of Fracture Control Corp. for their assistance in the research.

References

[1] Rolfe, S. T. and Novak, S. R. in *Review of Developments in Plane-Strain Fracture Toughness Testing, ASTM STP 436,* American Society for Testing and Materials, 1970, pp. 124-147.
[2] Barsom, J. M. and Rolfe, S. T. in *Impact Testing of Metals, ASTM STP 466,* American Society for Testing and Materials, 1970, pp. 281-302.
[3] Norris, D. M., Reaugh, J. E., Moran, B., and Quiñones, D. F., *Computer Model for Ductile Fracture: Applications to the Charpy V-Notch Test,* Electric Power Research Institute Report NP-961, Palo Alto, Calif., 1979.
[4] Norris, D. M., Jr., Reaugh, J. E., Moran, B., and Quiñones, D. F., *Journal of Engineering Materials and Technology,* Vol. 100, 1978, pp. 279-286.
[5] Marston, T. U., Borden, M. P., Fox, J. H., and Reardon, L. D., *Fracture Toughness of Ferritic Materials in Light Water Nuclear Vessels,* Electric Power Research Institute Report NP-232-2, Palo Alto, Calif., 1975.
[6] *Nuclear Pressure Vessel Steel Data Base,* Electric Power Research Institute Report NP-933, Palo Alto, Calif., 1978.
[7] Server, W. L. in *Elastic-Plastic Fracture, ASTM STP 668,* American Society for Testing and Materials, 1979, pp. 493-514.
[8] Chakravarti, I. H., Laha, R. G., and Roy, J., *Handbook of Methods of Applied Statistics,* Vol. 1, Wiley, N.Y., 1967, p. 327.
[9] Norris, Jr., D. M., *Engineering Fracture Mechanics,* Vol. 11, 1979, pp. 261-274.
[10] Norris, D. M., Jr., Quiñones, D. F., and Moran, B., "Computer Simulation of Plastic Deformation in the Charpy V-Notch Impact Test," Lawrence Livermore Laboratory Report UCRL 80868, Livermore, Calif., 1978; also in ASM Special Publication, *What Does the Charpy Test Really Tell Us,* American Society of Metals, Metals Park, Ohio, 1978, pp. 22-32.

K. P. Datta[1] *and W. E. Wood*[2]

Anomaly of Toughness Behavior with Notch-Root Radius

REFERENCE: Datta, K. P. and Wood, W. E., "**Anomaly of Toughness Behavior with Notch-Root Radius,**" *Fracture Mechanics: Thirteenth Conference, ASTM STP 743,* Richard Roberts, Ed., American Society for Testing and Materials, 1981, pp. 218–235.

ABSTRACT: The present investigation has studied the effects of notch-root radii on the Charpy apparent toughness of as-quenched and tempered 4340 steel as a function of (1) test temperature (liquid nitrogen and room temperature), (2) strain rate (high and slow strain rates corresponding to Charpy and plane-strain fracture toughness testing rates), and (3) grain size (25 and 250 μm). The toughness was evaluated by instrumented and slow-bend Charpy tests. Fracture surfaces were examined by scanning electron microscopy.

The results showed that initially the toughness increased as the notch-root radius increased, but that after a critical notch-root radius was reached, the toughness dropped. The loss in toughness was coincident with a change to an intergranular fracture mode initiation. Also, the critical root radius at which the drop in toughness occurred was temperature and strain-rate dependent. These results are not in agreement with other published results, which always show increasing toughness with increasing notch root radius beyond a limiting root radius. These results and the limitation of the current theories are presented and discussed in this paper. A physical process for the intergranular fracture mode initiation is also discussed.

KEY WORDS: toughness, notch-root radius, Charpy, critical root radius

The plane-strain fracture toughness test, K_{Ic}, in recent years is an often-required test to measure a material's resistance to fracture and in essence it determines the strain energy release rate [*1*][3] (which is related to the stress intensity factor [*2*]) as the crack advances. However, the conventional and still-popular method of measuring toughness of structural material is the Charpy method, according to the ASTM Notched Bar Impact Testing of Metallic Materials [E 23-72], Part 31, 1969, where a specimen of specified dimensions is broken under the hammering action of a swinging pendulum, and the energy

[1] Department of Metallurgical Engineering and Materials Science, University of Kentucky, Lexington, Ky. 40506.

[2] Oregon Graduate Center, Beaverton, Ore. 97006.

[3] The italic numbers in brackets refer to the list of references appended to this paper.

required to break the specimen is known as the toughness. Apart from many differences such as strain rate and specimen dimensions, one important difference in the aforementioned two tests is the notch-root radius; that is, the fracture toughness test contains a fatigue precrack, whereas in Charpy specimens the notch contains a root radius of 0.254 mm (0.010 in.). Any attempt to correlate the two tests implies therefore, at least partially, a knowledge of the variation of the toughness with notch-root radius, especially in the case of 4340 steel, where improvements in fracture toughness (K_{Ic}) by processing modifications do not necessarily result in improved Charpy values [3].

The variation of toughness with notch-root radius has been studied before [4-11]. It has been reported that the critical value of elastic strain energy release rate or toughness is relatively insensitive [4] to tip-root radius in the range from a mathematical "sharp" crack to macroscopic finite-root radii [up to 0.254 mm (0.010 in.)]. This is also expected from Irwin's formula [5]

$$K = \lim_{\rho \to 0} \frac{1}{2} \sigma_m (\pi\rho)^{1/2}$$

where σ_m is the maximum stress at the notch and ρ is the notch root radius. In this relationship K will become insensitive to root radius whenever σ_m is inversely proportional to $\rho^{1/2}$. However, experimental fracture data [6-11] show that this is not always the case. Fracture toughness values can be significantly lower for a fatigue-cracked specimen than for a small but finite-root-radius specimen. Malkin et al [6] found that the apparent toughness increases with the square root of the root radius for mild steel. Similar increases in toughness with increase of root radius have been observed by others, namely, Rack in unaged β-titanium alloy [7], Myers et al in monocrystalline silicon [8], and Ritchie et al in quenched-and-tempered 4340 steel [9,10]. A theoretical relationship of fracture toughness with notch root radius also predicts an increase in fracture toughness value with increase in root radius [11]. In this paper, an anomaly of toughness behavior of quenched-and-tempered 4340 steel with respect to notch-root radius (1) at liquid nitrogen temperature and high strain rate, (2) at room temperature and slow strain rate, (3) at room temperature and high strain rate, and (4) also at two grain sizes (25 and 250 μm) is reported.

Experimental Procedure

The material in the present study was AISI 4340 steel. The chemical composition of the steel in weight percent was

C	Mn	Si	Cr	Ni	Mo	Cu	S	P	V	Fe
0.40	0.60	0.32	0.69	1.87	0.20	0.16	0.015	0.015	...	balance

The room temperature longitudinal tensile properties were determined using 2.5-cm (1 in.) gage length, 0.625-cm-diameter (0.25 in.) round specimens. Machining was done prior to heat treatment. Testing was carried out at a loading rate of 0.1 cm/min (0.04 in./min).

Charpy specimens (10-mm thickness) were austenitized in a vertical tube in argon atmosphere at 870 and 1200°C for 1 h and directly quenched in an agitated oil. All tempering was done in a neutral salt bath for 1 h and then quenched in an agitated oil. A grinding wheel was used to produce specimens of variable root radii using coolant and light grinding passes. Specimens were heat-treated and then notched by grinding, and, prior to testing, the notch-root radius of each specimen was checked with a comparator. In addition to precracked and standard [0.254-mm (0.010 in.) root radius] Charpy specimens, specimens of root radii 0.102, 0.152, 0.508, 0.762, 1.016, 1.778, and 2.54 mm (0.004, 0.006, 0.020, 0.030, 0.040, 0.071, 0.101 in.) were prepared. The foregoing heat treatments and root radii were chosen to study the effects of root radii on the toughness of differently heat-treated 4340 steel in greater details than attempted before [*9*]. All specimens were tested in the longitudinal direction (L-TS) according to the ASTM Test for Plane-Strain Fracture Toughness of Metallic Materials (E 399-78a) procedures. The instrumented Charpy testing was done on a computerized test system at Effects Technology, Santa Barbara, Calif. A special fixture (Fig. 1) was made for a 3-point bend slow test in an Instron machine at a crosshead speed of 0.1 cm/min (0.04 in./min). Fracture morphology was studied in a JEOL scanning electron microscope (25-kV secondary electron voltage).

Results

The results are divided into two categories: mechanical testing results and scanning electron microscopy (SEM).

Mechanical Testing Results

The tensile properties of differently heat-treated 4340 steel at room temperature are given in Table 1.

The liquid nitrogen instrumented Charpy data having various root radii are shown in Fig. 2. Root radii varying from fatigue precrack (that is, root radius ≈ 0) to 1.016 mm (0.040 in.) were studied. Note that the toughness[4] increased with increasing root radius up to 0.152 mm (0.006 in.) root radius, after which further increasing the radius produced a drop in toughness, which then remained nearly constant as the root radius was further increased.

[4] The toughness is determined from the load displacement record according to ASTM Method E 399-78a. However, the toughness, thus determined, is known as the apparent toughness, since the specimen dimensions do not conform to those of fracture toughness specimens.

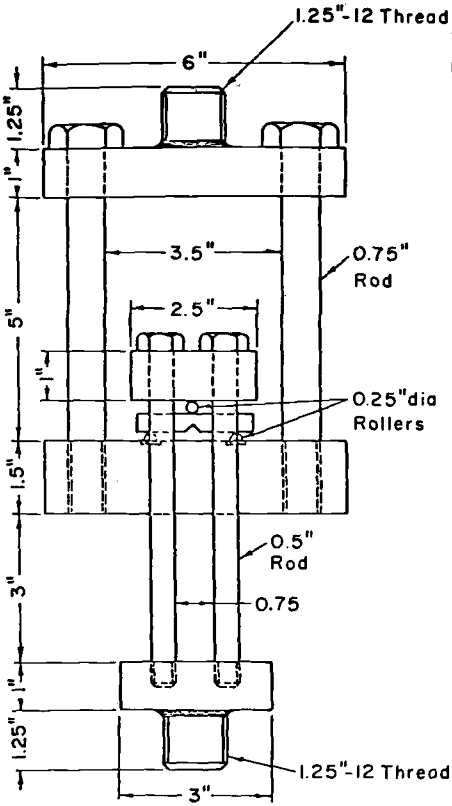

FIG. 1—*Testing fixture for slow-bend Charpy specimen (1 in. = 25.4 mm).*

TABLE 1—*Room temperature longitudinal tensile data for 4340 steel.*

Austenitizing Treatment, °C/1 h	Tempering Temperature, °C/1 h	Yield Strength ksi	Yield Strength MPa	Ultimate Tensile Strength ksi	Ultimate Tensile Strength MPa	% Elongation	% Reduction in Area
870	AQ	224	1544.5	302	2082.3	1.1	1.6
870	AQ	223	1537.6	293	2020.2	1.0	3.1
870	175	238	1641.0	288	1958.8	13.6	45.4
870	175	234	1613.4	284	1958.2	13.6	35.1
1200	AQ	213	1468.6	241	1661.70	1.2	3.2
1200	AQ	225	1551.4	245	1689.3	1.2	3.1
1200	175	225	1551.4	278	1916.8	3.4	4.7
1200	175	216	1489.3	268	1847.9	5.5	8.6

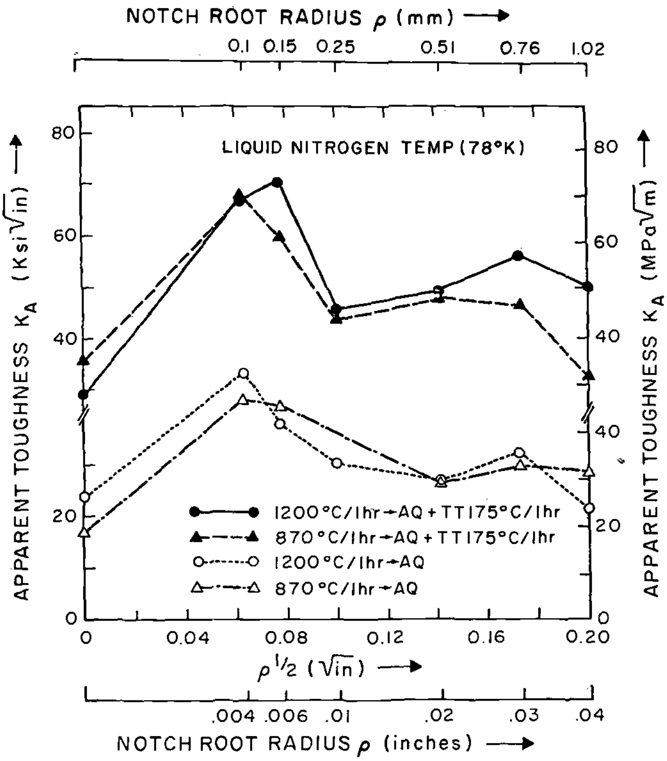

FIG. 2—*Effect of notch-root radius on the toughness of 4340 steel given different heat treatments by instrumented Charpy test at liquid nitrogen temperature (1 ksi = 6.8948 MPa; 1 in. = 25.4 mm).*

The room temperature slow-bend Charpy data as a function of root radius are shown in Fig. 3. Root radii varying from fatigue precrack (that is, root radius ≈0) to 1.016 mm (0.040 in.) were studied. For this test condition the toughness abruptly dropped when the root radius exceeded 0.254 mm (0.010 in.). For root radii less than 0.254 mm (0.010 in.) the toughness increased with increasing root radius.

The room temperature instrumented Charpy data as a function of root radii are shown in Fig. 4. Root radii varying from fatigue precrack (that is, root radius ≈0) to 2.54 mm (0.100 in.) were studied. For this case, toughness increased with increasing root radius up to 1.016 mm (0.04 in.) and beyond that radius the toughness remained almost constant for the 1200°C/175[5] heat treatment. On the other hand, the 1200°C/AQ[6] heat treatment exhibited a

[5] 1200°C/175 means austenitization at 1200°C followed by oil quenching and tempering at 175°C for 1 h.

[6] 1200°C/AQ means austenitization at 1200°C followed by oil quenching and testing in as-quenched condition.

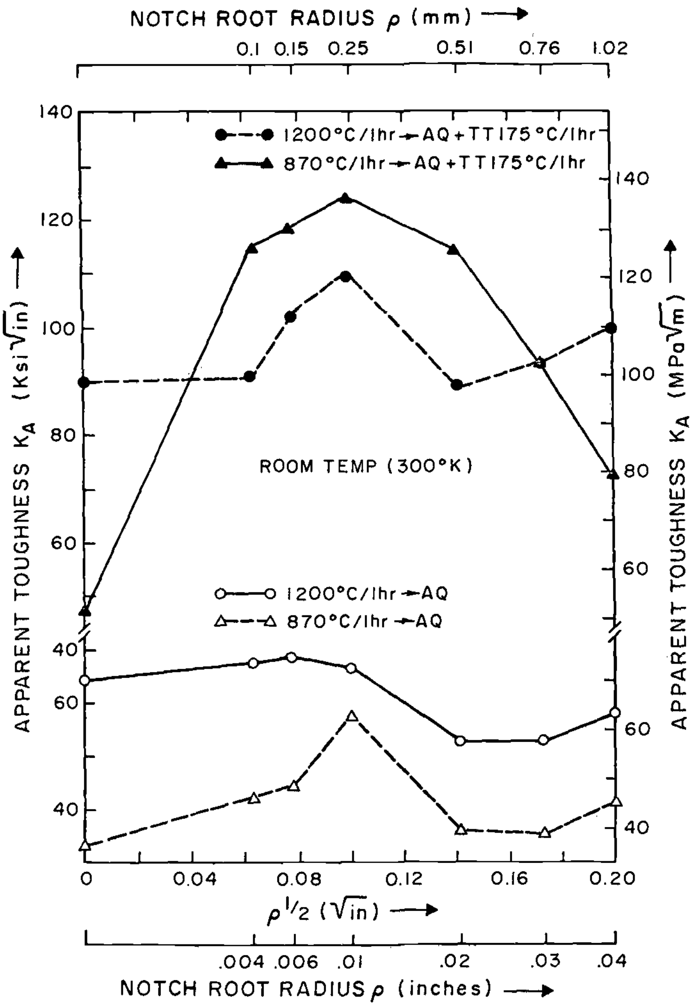

FIG. 3—*Effect of notch-root radius on the toughness of 4340 steel given different heat treatments by slow-bend Charpy test at room temperature (1 ksi = 6.8948 MPa; 1 in. = 25.4 mm).*

substantial drop in toughness at a critical root radius of 1.778 mm (0.070 in.). However, when the root radius was increased still further to 0.100 inch, the toughness again increased. These differences in toughness behavior may be explained by the fact that for 1200°C/175 treatment, general yielding occurred at a root radius of 1.016 mm (0.040 in.) and larger, whereas for 1200°C/AQ, general yielding took place at a root radius of 2.54 mm (0.100 in.).

In summary, the toughness increased initially with increasing notch root radius. However, after a critical root-radius was reached, the toughness

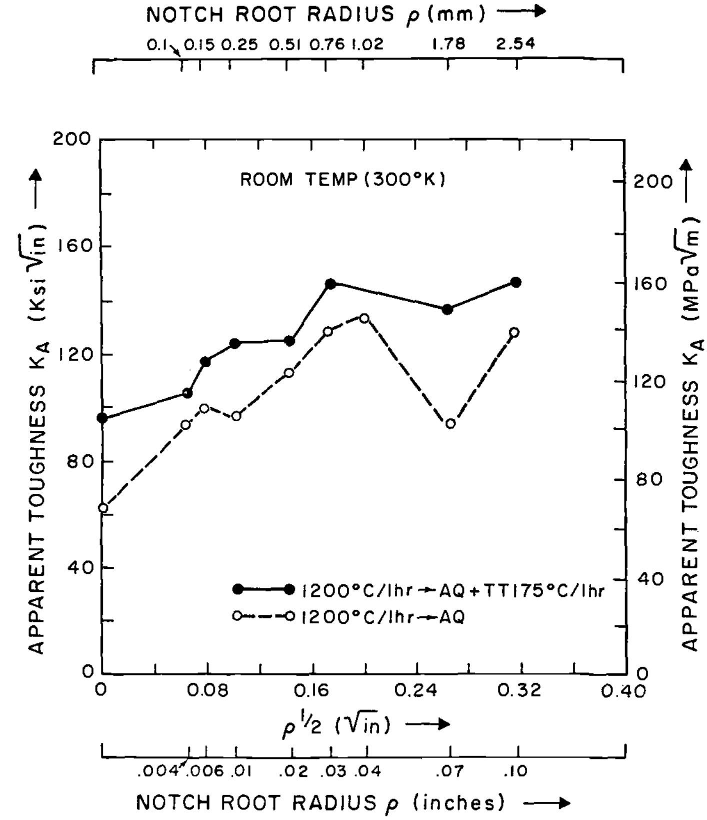

FIG. 4—*Effect of notch-root radius on the toughness of 4340 steel given different heat treatments by instrumented Charpy test at room temperature (1 ksi = 6.8948 MPa; 1 in. = 25.4 mm).*

dropped, in contrast to previously reported literature. Also, the "critical root radius" at which the toughness dropped was strongly temperature and strain-rate dependent.

Microscopy

Figures 5-7 show the fracture morphology of specimens with different notch-root radii. The effect of notch root radius on the toughness has been studied (1) at liquid nitrogen temperature and high strain rate, (2) at room temperature and slow strain rate, (3) at room temperature and high strain rate, and (4) also at two grain sizes (25 and 250 μm). The major portion of the fracture surface exhibited a quasi-cleavage fracture mode. However, the fracture initiation mode, which has a direct correspondence with the fracture

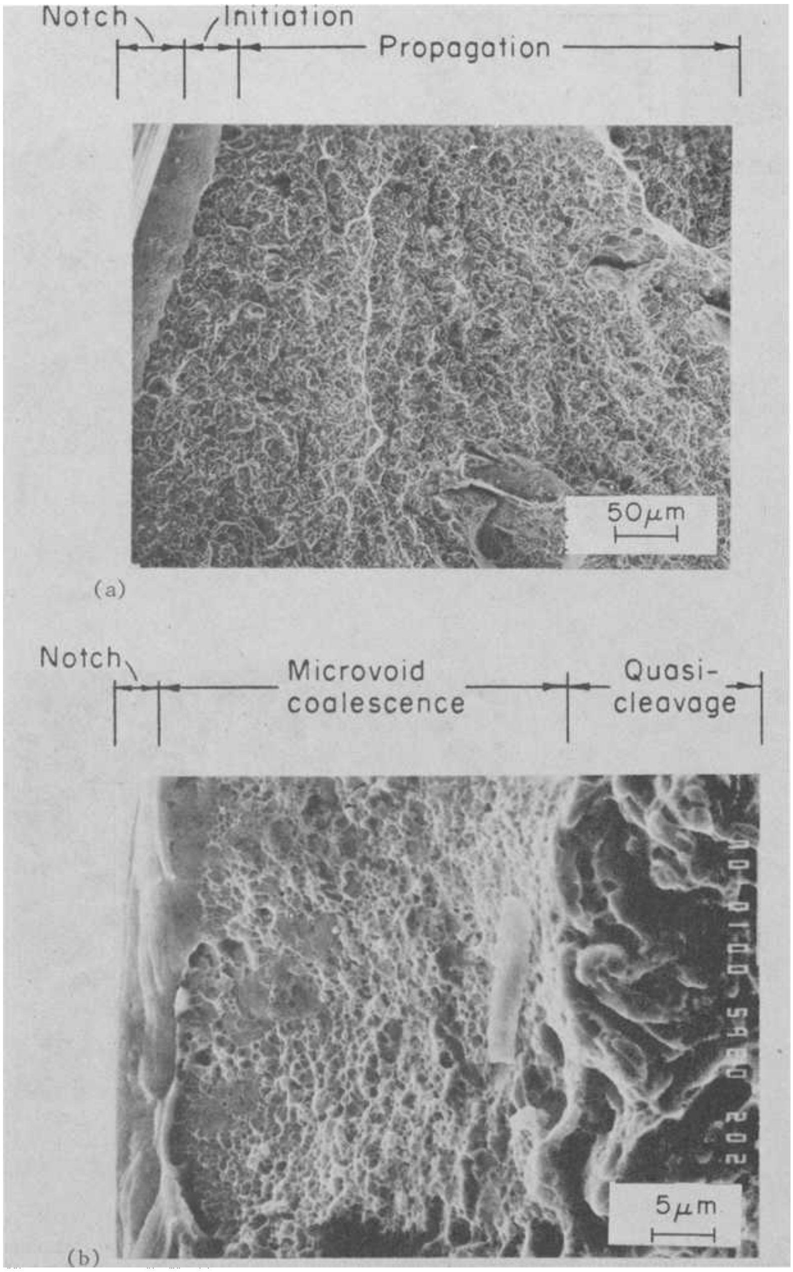

FIG. 5—*SEM micrographs of as-quenched specimen austenitized at 870°C. It is tested at liquid nitrogen temperature and by instrumented Charpy test.* (a) *It has a notch-root radius of 0.101 mm (0.004 in.).* (b) *It has a notch-root radius of 0.152 mm (0.006 in.). They show how microvoid zone (fracture initiation) changes to quasi-cleavage zone (fracture propagation) at low and high magnifications.*

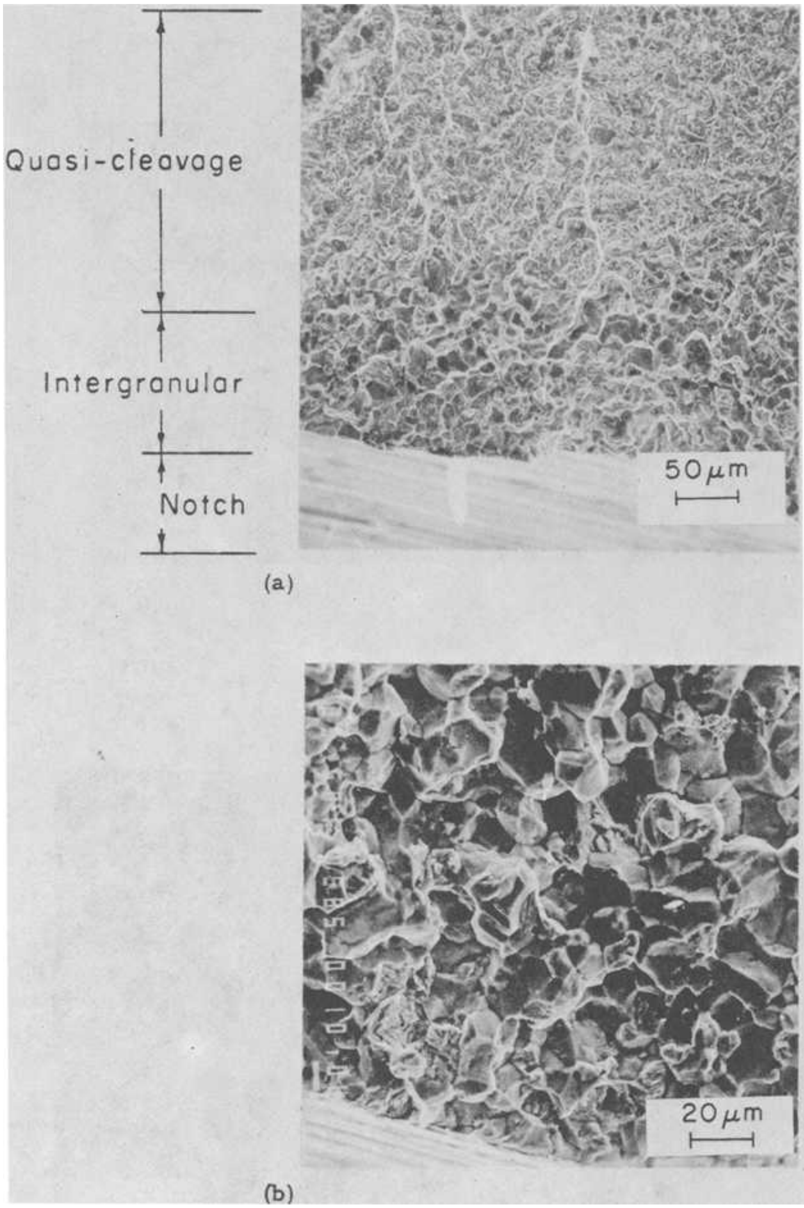

FIG. 6—*SEM micrographs of as-quenched specimen austenitized at 870°C. (a) It is tested at liquid nitrogen temperature (instrumented Charpy test) and it has a root radius of 0.508 mm (0.02 in.). It shows how intergranular zone (fracture initiation) changes into quasi-cleavage (fracture propagation). (b) It is tested at room temperature (slow-bend Charpy test) and it has a notch root radius of 0.762 mm (0.03 in.). It also shows intergranular fracture initiation mode. Thus the drop in toughness is associated with the intergranular fracture mode initiation.*

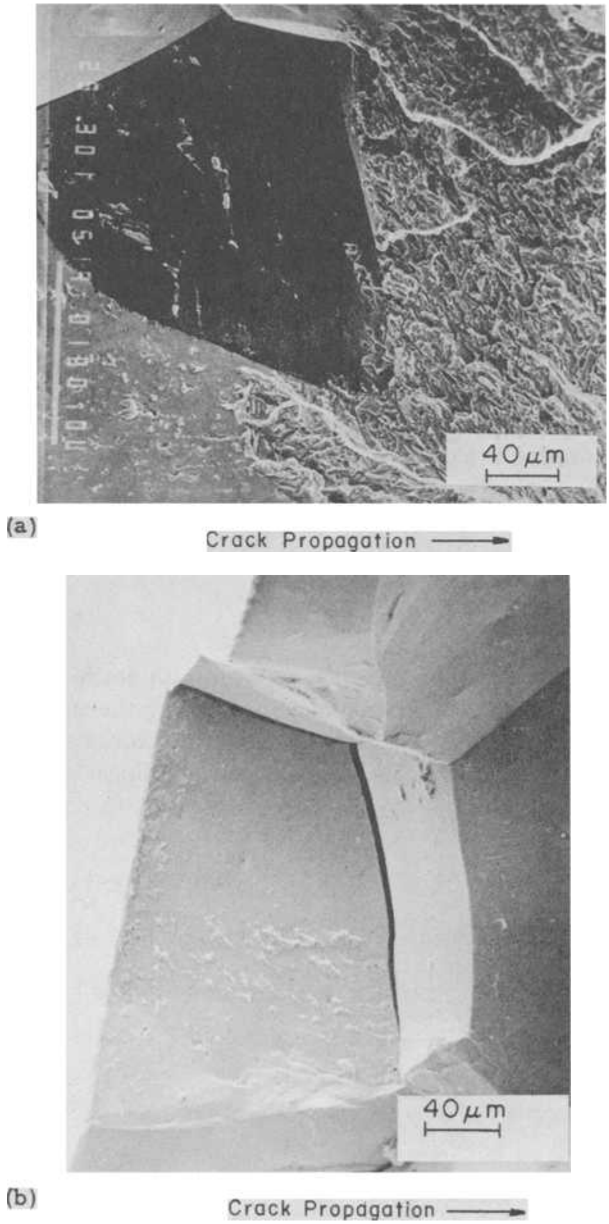

FIG. 7—*SEM micrographs of as-quenched specimen austenitized at 1200°C. (*a*) It is tested at liquid nitrogen temperature (instrumented Charpy) and it has a notch-root-radius of 0.508 mm (0.02 in.). It shows how intergranular zone (fracture initiation) changes into quasi-cleavage (fracture propagation). (*b*) It is tested at room temperature (slow-bend Charpy test) and it has a notch root radius of 1.016 mm (0.04 in.). Intergranular fracture initiation mode is evident. Thus, the grain size does not affect the notch-root radius when the drop in toughness is observed.*

toughness value, is different for different specimens. The results as depicted in Figs. 5-7 may be summarized schematically in the following cases:

Case 1: Toughness Increases with Increasing Notch-Root Radius—For this case a schematic fractographic representation was as shown in Fig. 8. In this case, the fracture initiation was always by microvoid coalescence which later changed to quasi-cleavage as the crack propagated. The microvoid region was about 40 μm for the instrumented Charpy test conducted at liquid nitrogen temperature and was apparently independent of prior austenitic grain size.

Case 2: Toughness Decreases as the Notch Root Radius is Increased Beyond a Critical Value—The schematic fractographic observation in this case looks like the sketch in Fig. 9. In this case, when the toughness drops, the mode of fracture initiation changed to intergranular mode, which later changed to quasi-cleavage as the crack propagated. However, this intergranular region was strongly heat-treatment dependent, that is, about 150 μm for the 870°C case (in other words 5 to 6 grains) compared with about 300 μm for 1200°C (for about 1 grain).

In essence, the fractographic observation is consistent with the toughness data.

Discussion

In order to analyze the variation of toughness with notch-root radius, it is worthwhile to examine the current models regarding the stress distribution ahead of a blunt notch [12,13]. Even though such theories assume idealized conditions, that is, plane strain, rigid plastic, or linear elastic material,

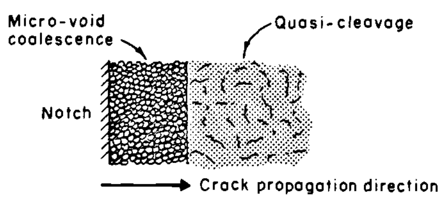

FIG. 8—*Case 1.*

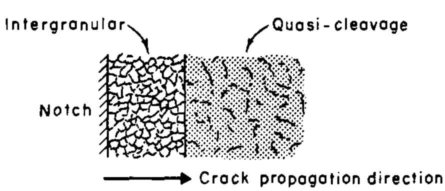

FIG. 9—*Case 2.*

ultrahigh-strength steel such as quenched-and-tempered 4340 steel closely resembles the foregoing conditions even in a small specimen such as Charpy.

The longitudinal stress distribution ahead of a blunt notch of radius ρ has been given by slipline field theory [12]

$$\sigma_{yy} = \sigma_y \left[1 + \ln\left(1 + \frac{R}{\rho}\right)\right] \tag{1}$$

where

σ_{yy} = longitudinal stress ahead of the notch,
σ_y = yield strength, and
R = distance from the notch.

The relative stress distribution ahead of blunt notches of different root radii are shown in Fig. 10. It is observed that stresses ahead of the notch are higher as the notch-root radius decreases.

Creager and Paris [13] have calculated the near-field notch tip stresses for a very slender elliptical crack having a "small" root radius; for a Mode I loading the stresses are

$$\begin{aligned}
\sigma_x &= -\frac{K_{\mathrm{I}}}{\sqrt{2\pi r}}\frac{\rho}{2r}\cos\frac{3\theta}{2} + \frac{K_{\mathrm{I}}}{\sqrt{2\pi r}}\cos\frac{\theta}{2}\left[1 - \sin\frac{\theta}{2}\sin\frac{3\theta}{2}\right] \\
\sigma_y &= \frac{K_{\mathrm{I}}}{\sqrt{2\pi r}}\frac{\rho}{2r}\cos\frac{3\theta}{2} + \frac{K_{\mathrm{I}}}{\sqrt{2\pi r}}\cos\frac{\theta}{2}\left[1 + \sin\frac{\theta}{2}\sin\frac{3\theta}{2}\right] \\
\tau_{xy} &= \frac{-K_{\mathrm{I}}}{\sqrt{2\pi r}}\frac{\rho}{2r}\sin\frac{3\theta}{2} + \frac{K_{\mathrm{I}}}{\sqrt{2\pi r}}\sin\frac{\theta}{2}\cos\frac{\theta}{2}\cos\frac{3\theta}{2}
\end{aligned} \tag{2}$$

For $\theta = 0$ the relative stress distribution for identical stress-intensity factors is plotted in Figs. 11 and 12 ahead of the notch tip for root radii ranging from 0.101 to 2.54 mm (0.004 to 0.100 in.). It is seen that the σ_y stresses ahead of the notch tip are quite similar beyond a distance of 0.127 mm (0.005 in.) for different notch-root radii. However, up to that distance from the notch tip, the stress increases as the notch root radius decreases. The σ_x stress distribution ahead of the notch root similarly increases, as the notch root radius decreases.

From the foregoing discussion, it is thus apparent that the toughness should increase as the notch radius increases, if a critical stress criterion applies for crack initiation. From a critical strain model also, it has been postulated by many investigators [6–8] that toughness follows a linear relation with the square root of the notch-root radius.

The results in this investigation, on the contrary, indicate that there exists a critical notch-root radius above which the toughness drops. Below that critical

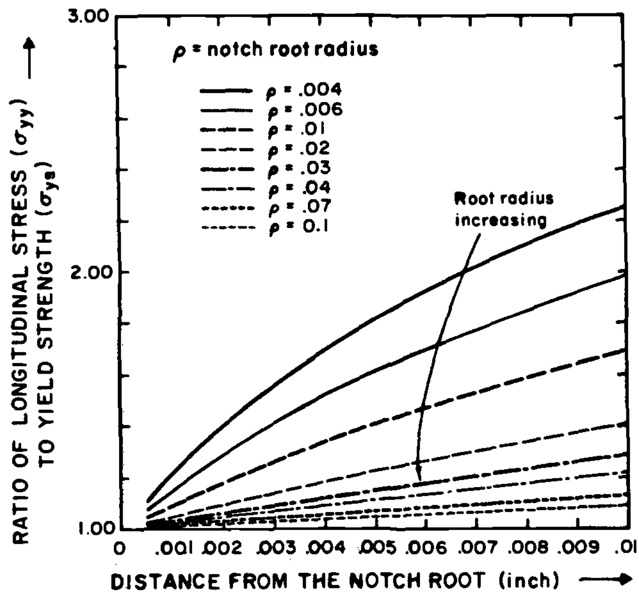

FIG. 10—*Stress distribution ahead of blunt notches of various root radii by slipline field theory (1 in. = 25.4 mm).*

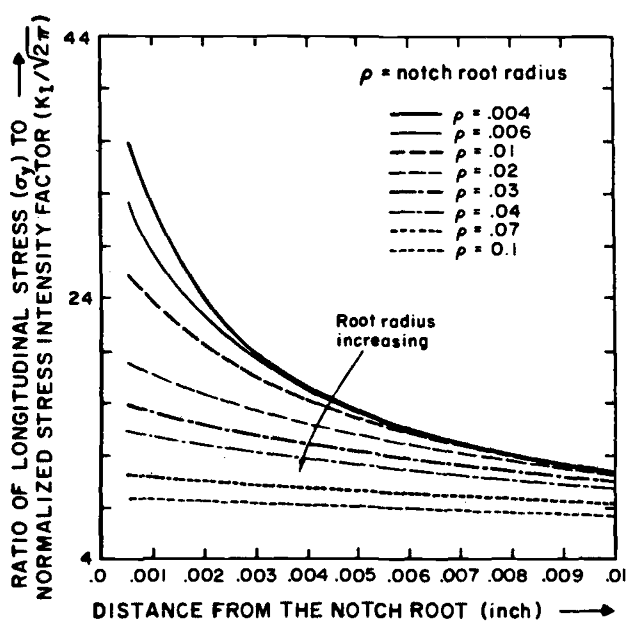

FIG. 11—*Variation of σ_y with distance from the notch root (θ = 0 deg) for different notch root radii for a Mode I stress intensity factor* K_I *(1 in. = 25.4 mm).*

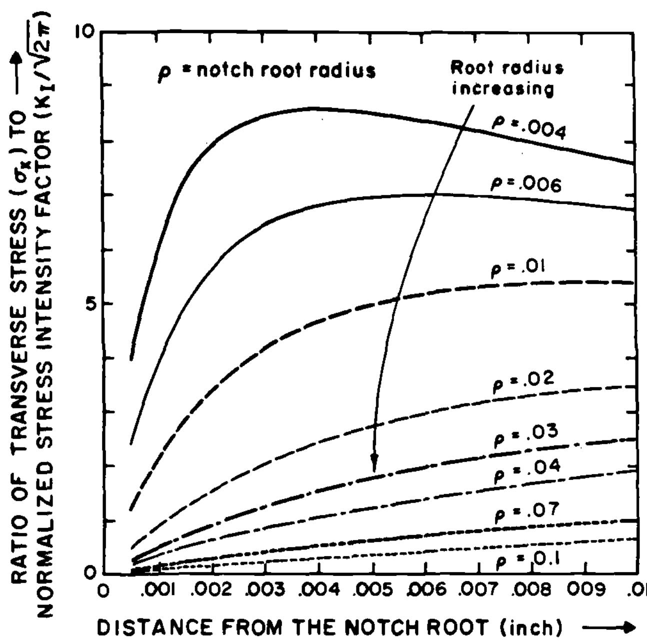

FIG. 12—*Variation of σ_x with distance from the notch root (θ= 0 deg) for different notch root radii for a Mode I stress intensity factor* K_I *(1 in. = 25.4 mm).*

root radius, however, the toughness increases with the increasing notch-root radius. The drop in toughness above the critical notch-root radius is also associated with an intergranular mode of fracture.

In considering possible mechanisms to account for this behavior, the relative size of the intergranular region with respect to plastic zone size is shown in Fig. 13. It is apparent that the size of the intergranular zone is only a fraction of the plastic zone size. Hence, the plastic zone size does not seem to play a role. Also, the root radius at which such a phenomenon occurs is independent of the grain size and hence grain size also does not seem to play a role in this anomalous behavior.

Recently Sih [*14*] proposed a strain-energy density theory for the initiation of a crack. Unlike other theories, this theory can predict the direction of crack propagation under combined loading. In this theory, the total strain energy density S is defined as

$$S = \frac{du}{dA} = \frac{1 - \nu^2}{2E}\left[\sigma_x{}^2 - \left(\frac{2\nu}{1 - \nu}\right)\sigma_x\sigma_y + \sigma_y{}^2 + \left(\frac{2}{1 - \nu}\right)\tau_{xy}{}^2\right] \quad (3)$$

According to this theory, fracture will occur when S assumes a critical value of S_c at $\theta = \theta_c$. It has also been demonstrated that for a Mode I loading $\theta_c = 0$ deg [*14*] and is independent of the notch root radius [*15*].

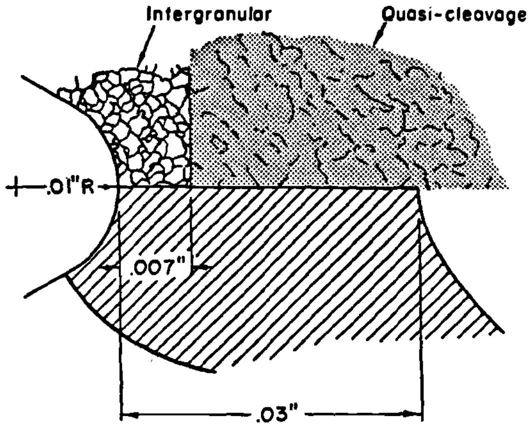

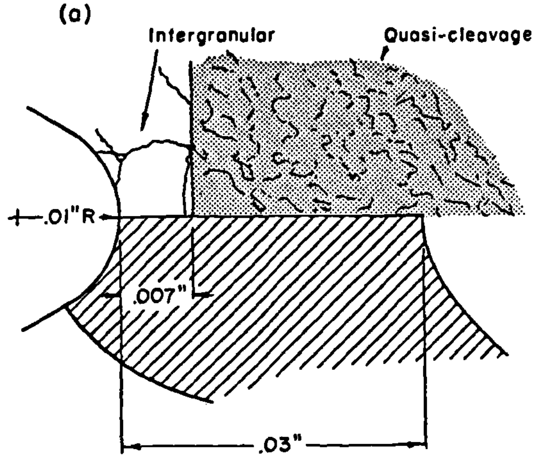

FIG. 13—*Relative fracture mode zones for a blunt notch of root radius 0.254 mm (0.01 in.). The plastic zone size is superimposed: (a) for low grain size material, (b) for high grain size material (1 in. = 25.4 mm).*

Creager and Paris's equations for a Mode I stress distribution for $\theta = 0$ deg were used for calculating the strain-energy density function for a constant K in the present investigation, and the relative strain-energy density as a function of the distance from the notch tip for different notch-root radii is shown in Fig. 14. To be noted in Fig. 14 is the fact that the *Sih* energy density function is plotted not directly ahead of the notch tip but from a finite distance ahead of the notch tip. It is seen that at any distance ahead of the notch, the strain-energy density for a constant K for larger root radius is much higher than that for smaller root radius. This is true irrespective of the value of core radius

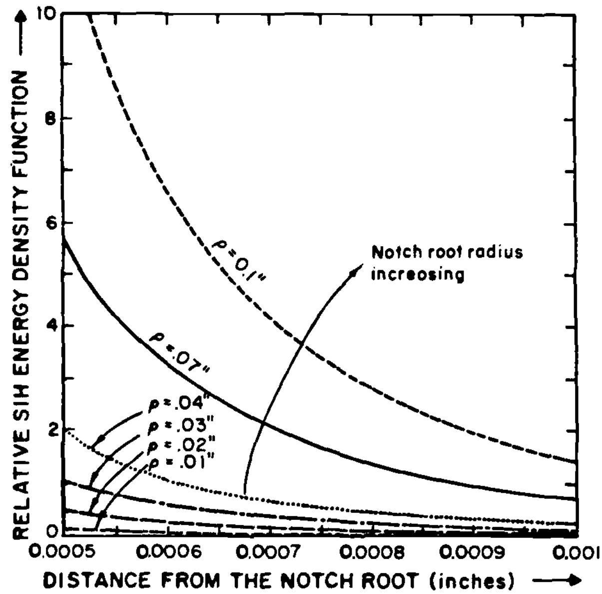

FIG. 14—*Variation of relative* Sih *energy-density function ahead of the notch for different notch root radii (1 in. = 25.4 mm).*

beyond which the *Sih* energy density [*14*] is applicable. In other words, if the critical strain-energy density is applied to the initiation of fracture, the toughness should decrease as the notch root radius increases.

Thus we have two competing situations. Both the critical stress and critical strain models predict higher toughness with larger root radii and the critical strain-energy density model predicts lower toughness with larger root radii. In this investigation, the critical stress model is proposed to operate initially until a critical root radius is reached. Above this critical root radius the strain-energy density activates fracture to initiate.

A further limitation in current models is that the foregoing theories are based on a continuum mechanics approach and do not consider microscopic aspects of fracture, and yet the change from microvoid to intergranular fracture initiation is the key to the existence of the critical root radius, above which the toughness drops.

In a recent paper Hondrous and McLean [*16*] tried to explain the grain boundary decohesion, which may be caused by impurity segregation, particle/matrix interactions, stress system, and stress magnification requirements. In the present investigation, the first two may be ruled out since the variable is purely a mechanical parameter, that is, notch root radius. Hence essentially the stress system is changed so as to cause the intergranular mode of fracture. In the foregoing model [*16*], it has been shown that a double slipband instead of a single slipband (schematically shown in Fig. 15) can potentially cause intergranular fracture because of stress intensification. The present investigation tends to support this microscopic model for the intergranular fracture. Hence it is proposed that at a critical root radius, the strain-energy density becomes large enough to induce double slipbands to operate, causing intergranular fracture. It may also be noted that dislocation movement is strongly temperature and strain-rate dependent. That is why the critical root radius at which the intergranular fracture and the drop in toughness occur is also strain-rate and temperature dependent.

Conclusions

1. The variation of toughness with notch root radius for 4340 steel given different heat treatments at different strain rates and temperatures showed that the toughness initially increased with increasing notch root radius. Thereafter, when a critical notch root radius was reached, toughness dropped with a further increase in notch root radius before general yielding. The critical root radius at which such phenomena occurred was strain-rate and temperature dependent.
2. The drop in toughness was associated with an intergranular fracture initiation mode.
3. The initial increase in toughness with increasing notch root radius up to the critical root radius is consistent with a critical stress or strain model; the critical strain energy-density fracture criterion is applicable beyond the critical notch root radius, when the toughness drops. The intergranular fracture mode may be possible due to double slipbands operating ahead of the notch root.

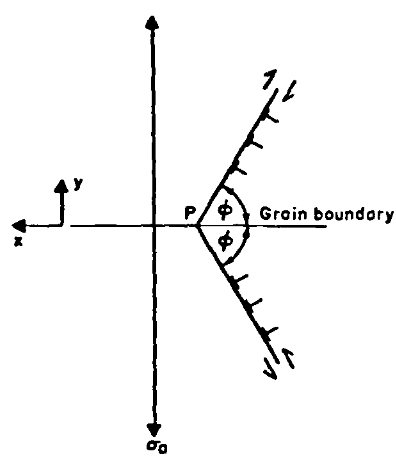

FIG. 15—*Schematic diagram of two slipbands meeting along a grain boundary at* P.

References

[1] Griffith, A. A., *Philosophical Transactions of the Royal Society of London,* Vol. A-221, 1920, p. 163.

[2] Irwin, G. R., *Applied Materials Research,* Vol. 3, 1964, p. 65.

[3] Lai, G. Y., Wood, W. E., Clark, R. A., Zackay, V. F., and Parker, E. R., *Metallurgical Transactions,* Vol. 5, 1974, p. 1663.

[4] Irwin, G. R., Kies, J. A., and Smith, H. L. in *Proceedings, American Society for Testing and Materials,* Vol. 58, 1958, p. 640.

[5] Irwin, G. R. in *Proceedings,* First Symposium on Naval Structure Mechanics, Pergamon Press, London and New York, 1960.

[6] Malkin, J. and Tetelman, A. S., *Engineering Fracture Mechanics,* Vol. 3, 1971, p. 151.

[7] Rack, H. J., *Materials Science and Engineering,* Vol. 24, 1976, p 165.

[8] Myers, L. J. and Hillberry, B. M. in *Proceedings,* Fracture 1977, 4th International Conference on Fracture, Waterloo, Ont., Canada, Vol. 3, June 1977, p. 19.

[9] Ritchie, R. O., Francis, B., and Server, W. L., *Metallurgical Transactions,* Vol. 7A, 1976, p. 831.

[10] Ritchie, R. O. and Horn, R. M., *Metallurgical Transactions, A,* Vol. 9A, March 1978, p. 331.

[11] Heald, P. T., Spink, G. M. and Worthington, P. J., *Materials Science and Engineering,* Vol. 10, 1972, p. 129.

[12] Hill, R., *Mathematical Theory of Plasticity,* Oxford Press, London, 1950.

[13] Creager, M. and Paris, P. C., *International Journal of Fracture Mechanics,* Vol. 3, 1967, p. 247.

[14] Sih, G. C. and Chen, E. P., *Journal of Composite Materials,* Vol. 7, 1973, p. 230.

[15] Francis, P. H. and Ko, W. L., *International Journal of Fracture,* Vol. 12, No. 2, April 1976, p. 243.

[16] Hondrous, E. D. and McLean, D., *Grain Boundary Structures and Properties,* G. E. Chadwick and D. A. Smith, Eds., Academic Press, London, 1976, p. 353.

M. P. Wnuk[1] *and S. Sedmak*[1]

Final Stretch Model of Ductile Fracture

REFERENCE: Wnuk, M. P. and Sedmak, S., "**Final Stretch Model of Ductile Fracture,**" *Fracture Mechanics: Thirteenth Conference, ASTM STP 743,* Richard Roberts, Ed., American Society for Testing and Materials, 1981, pp. 236–249.

ABSTRACT: The differential equations defining the material resistance developed during the early stages of a ductile fracture process are derived from the concept of "final stretch." The model suggests a certain near-tip distribution of displacements associated with a quasi-static Mode I crack such that the resulting strains are logarithmically singular at the crack tip.

The final results, which are illustrated by the diagrams of J-resistance curves, are equivalent to analogous data obtained by other researchers on the basis of the incremental plasticity theory. Similarities between the present results and the solutions due to Paris and co-workers as well as the most recent data obtained by Shih and co-workers are pointed out.

KEY WORDS: ductile fracture, stable crack growth, fracture criteria, stability, resistance curve, J-integral, crack-tip opening angle, tearing modulus, process zone, growth step

When a crack initiates near or after general yield within a ductile component, the material resistance to cracking continues to rise steeply with crack advance. Such variations of fracture toughness in ductile materials may be represented by either an R-curve or a J_R-curve, both representations being equivalent between each other. Even if the initiation parameters, R_i or J_{Ic}, are known from the observations made at the onset of crack growth, they alone are not sufficient means for predicting the instability which eventually terminates the process of slow stable cracking under fully plastic conditions. Therefore, it is necessary to devise a technique which would supply a more complete information regarding material response to propagation of ductile fracture.

[1] Visiting scholar and professor, respectively, Faculty of Technology and Metallurgy, University of Belgrade, Yugoslavia. Coauthor Wnuk is currently a visiting professor at the Department of Civil Engineering, The Technological Institute, Northwestern University, Evanston, Ill. 60201.

A model is suggested to describe a quasi-static crack extending in a stable manner through a ductile solid undergoing either small or large plastic deformations prior to and during the crack propagation (see Fig. 1). The mathematics of the model is based on the "final stretch" concept [*1-3*][2] which suggests that an incremental displacement is continually generated at the crack tip during the subcritical crack growth stage.

This study includes a detailed numerical investigation of the effects of the specimen size and the initial crack length on the shape of an R-curve which represents material resistance to cracking associated with the stable phase of fracture growth.

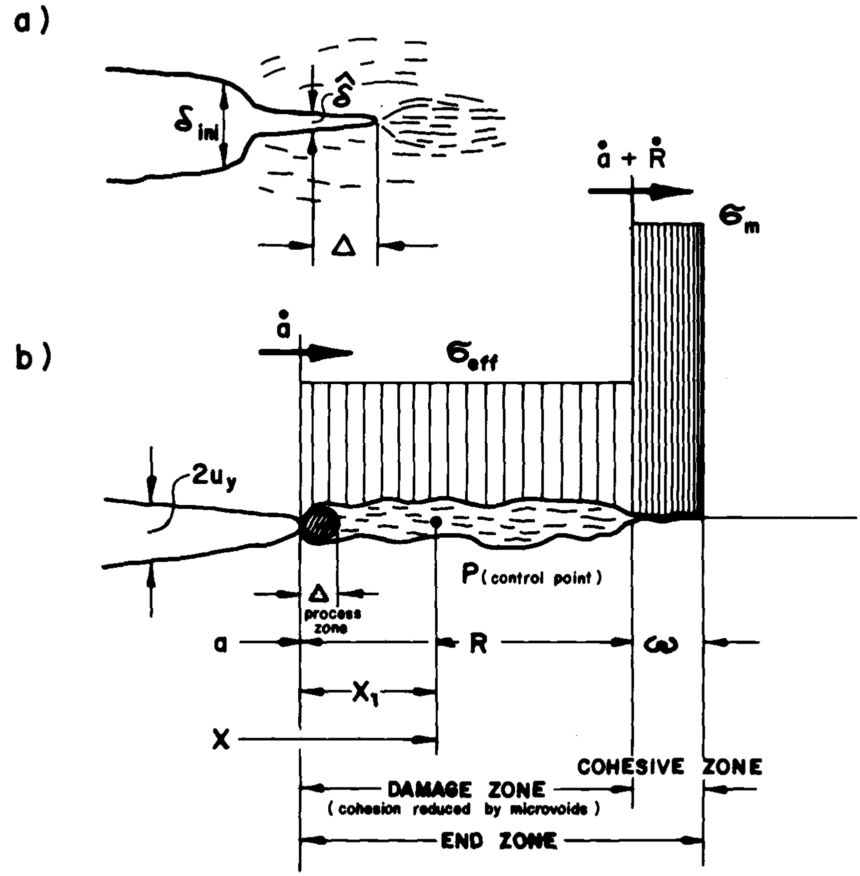

FIG. 1—*Structured end zone crack-tip model for a quasi-static crack penetrating a nonlinear material.*

[2]The italic numbers in brackets refer to the list of references appended to this paper.

Physical Model

A structured "end zone" located at the crack front is assumed to consist of three parts:

1. Cohesive zone, which is subjected to a high stress σ_m identified with the theoretical strength limit (in ductile metals this zone may be neglected).
2. Nonlinear or plastic deformation zone (sometimes referred to as a "damage" zone) in which an irreversible process of energy absorption takes place prior to fracture. Work is done against the yield stress, which is of much lower magnitude than the theoretical strength limit.
3. Process zone, which is identified with a small volume of material directly adjacent to the crack tip, and in which fracture is actively taking place. This is where the final breakdown of cohesion forces and separation of surfaces occur. The strains accumulated in this zone are continually redistributed to meet the critical level, sufficient for fracturing a material element of a finite dimension Δ.

The process of slow growth, therefore, is thought of as a sequence of stepwise crack extensions, each of the "growth steps" being of a constant magnitude equal to the process zone size Δ. Wnuk's criterion of final stretch is employed to set up a differential equation which relates the rate of crack growth (da/dt) to the rate of change of the material resistance to cracking, say dR/dt. Symbol R represents here a certain measure of apparent material toughness developed during the early phase of ductile fracture. This criterion requires that an incremental displacement $\hat{u}$ be continually generated at the control point P located at distance Δ from the crack tip, while this point is being traversed by the process zone, that is

$$\{u_y(0, a + \Delta) - u_y(\Delta, a)\}_{\text{at } P} = \hat{u} = \text{const.} \tag{1}$$

where $u_y = u_y(x_1, a)$ denotes displacement normal to the crack plane, evaluated at the distance x_1 from the crack tip and at the instant corresponding to the current crack length a. Note that the crack length is used here as a time-like parameter, and thus the real time can be entirely eliminated from the mathematical analysis of the problem.

To make the problem susceptible to a mathematical treatment a modified model of DBCS type is employed, but it should be emphasized that the basic physical concept underlying these considerations, that is, the constancy of the final stretch or, equivalently, the invariance of the crack-tip opening angle (CTOA) during slow crack growth, remains valid in a general sense, irrespective of a particular choice of the computational approach. It is not altogether surprising, therefore, that some of the end results of recent studies by Rice et al [4-6] concerned with a quasi-static plane-strain crack propagating in an elastic-plastic solid, but not exceeding the limits of contained yielding, turned out to be of an identical mathematical form as those predicted from the final stretch model in 1972; see Ref *1*.

This work suggests an extension of the early version of the final stretch model to other geometrical and loading configurations, while imposing no restrictions whatsoever on the amount of plasticity which precedes the onset of crack growth and accompanies the spread of stable ductile fracture up to the point of global failure.

Mathematical Considerations

Using Wnuk's [*7, 8*] expression for the near-tip displacement field associated with a quasi-static crack, one may set up the governing equation of the problem. This equation should relate an increment in the apparent material resistance to cracking, *dR*, to the accompanying amount of crack growth, *da*. The starting point of the mathematics involved here is to employ the expansion of the near-tip displacement suggested by our model in this form

$$u_y(\Delta, a) = \begin{cases} u_{\text{tip}}(a) - \Delta[\delta u_y/\delta x_1]_{x_1=\Delta} \\ u_{\text{tip}}(a) - \Delta C\Phi(\Delta, a) \end{cases} \tag{2}$$

Here, the constant C is roughly equal to the strain at yield point σ_Y, namely, $C = 4\sigma_Y/\pi E_1$. The modulus E_1 equals E for plane stress and $E(1 - \nu^2)^{-1}E$ for a plane-strain situation. The new derivative-like quotient $\delta u_y/\delta x_1$ has been defined as follows

$$\frac{\delta u_y}{\delta x_1} = \lim_{x_1 \to \Delta} \frac{u_y(0, a) - u_y(x_1, a)}{x_1} = C\Phi(\Delta, a) \tag{2a}$$

The dimensionless function $\Phi = \Phi(\Delta, a)$ can be evaluated for any particular crack geometry and a given loading configuration; see the discussion in the next section.

Combining Eqs 1 and 2 we have

$$u_{\text{tip}}(a + \Delta) - u_{\text{tip}}(a) + \Delta C\Phi(\Delta, a) = \hat{u} \tag{3}$$

Now, when the difference $u_{\text{tip}}(a + \Delta) - u_{\text{tip}}(a)$ is replaced by the first term of the appropriate Taylor expansion, $\Delta[du_{\text{tip}}(a)/da]$, one obtains the differential equation for the material toughness developed in the process of ductile tear, that is

$$\frac{du_{\text{tip}}}{da} = \frac{\hat{u}}{\Delta} - C\Phi(\Delta, a) \tag{4}$$

Multiplying both sides of this equation by $2n\sigma_Y$ (where n is an empirical coefficient whose value usually lies between 1 and 2.6) one obtains

$$\frac{dJ_R}{da} = n\sigma_Y(\hat{\delta}/\Delta) - (8n\sigma_Y{}^2/\pi E_1)\Phi(\Delta, a) \tag{5}$$

Note that in the notation of Eq 4 the amount of opening generated at the crack tip, u_{tip}, serves as a measure of material toughness, while in the equations which follow the Rice's integral is being used for the same purpose. For a plane-strain situation, Eq 5 can be cast into an alternative form

$$\frac{dJ_R}{da} = n(\sigma_Y{}^2/E)\left\{T_\delta - \frac{8(1-\nu^2)}{\pi}\Phi(\Delta, a)\right\} \tag{6}$$

where $T_\delta = (E/\sigma_Y)(\hat{\delta}/\Delta)$ corresponds to the tearing modulus suggested by Shih, $T_\delta = (E/\sigma_0)$ (CTOA), while the product $(\sigma_Y{}^2/E)T$ may be approximately identified with the initial slope of the J_R-curve. If the amount of stable growth is negligibly small versus the initial crack length and ligament size, then we may suggest that the modulus T_δ and the tearing modulus of Paris are equivalent, that is

$$nT_\delta \simeq T_J = (E/\sigma_Y{}^2)(dJ_R/da)_i \tag{7}$$

The function $\Phi(\Delta, a)$ is a geometry-dependent quantity, and it may be conveniently written for an arbitrary geometrical configuration in the following form

$$\Phi(\Delta, a) = \frac{1}{2}\log[\Lambda/\Delta] \tag{8}$$

in which the factor Λ depends only on geometry and loading configuration, just as the K-factor does. Λ may be usually expressed as a function of some measure of the external field intensity, such as the length of plastic zone R or the applied J-integral, and the current crack length, that is

$$\Lambda = \Lambda(J_A, a)$$

$$J_A = J_A(Q, a, \text{geometry})$$

The nondimensional loading parameter is denoted by Q.

An essential difference between this model and the Paris [*11-16*] constant T_J model can now be seen by a careful examination of Eq 6. According to this equation the slope of a J_R versus $a\Delta$ curve is *not* a constant quantity but is continually reduced as the crack progresses. When the current crack length increases, the second term in the right-hand side of

Eq 6 is augmented, and thus the content of the brace diminishes. One may find, however, that for a certain class of materials characterized by a low yield strength and high toughness, both models agree. It may be shown that when Paris's modulus equals at least 50, then $T_J \simeq T_\delta n =$ const., and if only a limited amount of slow crack growth precedes unstable fracture, then the second term in the brace of Eq 6 becomes negligible. In such a case both theories yield the same result

$$dJ_R/da = n(\sigma_Y{}^2/E)T_\delta = \text{const.} \tag{10}$$

Effect of Finite Width of a Center-Crack Specimen on the *J*-Resistance Curve; Fully Plastic Range

Extension of Wnuk's final stretch model for a finite-width panel containing a Mode I crack was made recently by Smith [9], who derived the following distribution of the near-tip displacement associated with a quasi-static crack in plane strain

$$[u(x_1, a)]_{x_1 \to 0} = u_{\text{tip}}(a) + \frac{4\sigma_Y(1 - \nu^2)x_1}{E}\frac{1}{2}\log\left(\frac{x_1}{\Lambda}\right) + \cdots \tag{11}$$

Here the geometrical factor Λ is a function of the panel width $2h$ and the crack length $2a$, that is

$$\Lambda = 2ea\frac{\sin^2\left[\dfrac{\pi(a+R)}{2h}\right] - \sin^2\left(\dfrac{\pi a}{2h}\right)}{\sin^2\left[\dfrac{\pi(a+R)}{2h}\right]} \cdot \frac{\tan\left(\dfrac{\pi a}{2h}\right)}{\left(\dfrac{\pi a}{2h}\right)} \tag{12}$$

At general yield we may assume $a + R = h$, and then the geometrical factor reduces considerably

$$\Lambda \simeq \frac{2eh}{\pi}\sin\left(\frac{\pi a}{h}\right) \tag{13}$$

It is a simple matter, now, to show that Eq 6, which defines the J-resistance curve, assumes this form

$$\frac{dJ_R}{da} = (\sigma_Y{}^2/E)\left\{T_\delta - \frac{4(1-\nu^2)}{\pi}\log\left[\frac{2eh}{\pi\Delta}\sin\left(\frac{\pi a}{h}\right)\right]\right\} \tag{14}$$

in which the symbol T_δ denotes the tearing modulus

$$T_\delta = (E/\sigma_Y)(\hat{\delta}/\Delta) \tag{15}$$

or

$$T_\delta = (E/\sigma_Y)(\mathrm{CTOA}) \tag{15a}$$

Equation 14 can be rewritten in a nondimensional form, more suitable for a numerical integration, that is

$$\begin{aligned}
\frac{dY}{dX} &= \left(\frac{a_0}{\delta_{\mathrm{Ic}}}\right)\left(\frac{\sigma_Y}{E}\right)\left\{T_\delta - \frac{4(1-\nu^2)}{\pi}\log(\Psi)\right\} \\
\Psi &= \left(\frac{2e}{\pi}\right)\left(\frac{h}{\Delta}\right)\sin(\pi p X), \qquad p = a_0/h \\
X &= a/a_0, \qquad Y = J_R/J_{\mathrm{Ic}}
\end{aligned} \tag{16}$$

Assuming the typical input data pertinent to the steels used in nuclear technology applications

$$\begin{aligned}
\hat{\delta} &\simeq 0.2\delta_{\mathrm{Ic}} = (0.2)(0.2*10^{-3}\mathrm{m}) = 4*10^{-5}\mathrm{m} \\
\mathrm{CTOA} &= (\hat{\delta}/\Delta) = 0.25
\end{aligned} \tag{17}$$

and considering the following initial crack sizes

$$a_0 = \begin{cases} 10\ \mathrm{mm} \\ 20\ \mathrm{mm} \\ 30\ \mathrm{mm} \\ 40\ \mathrm{mm} \end{cases} \tag{18}$$

at a constant value of the panel width, $h = 100$ mm, we have integrated the governing Eq 16 for three different values of the material tearing modulus T_δ, that is

$$T_\delta = \begin{cases} 5 \\ 25 \\ 50 \end{cases} \tag{19}$$

The results are shown in Fig. 2. It is seen that the increase in tearing modulus affects the slopes of the J-resistance curves; so does the initial crack length, a_0. The larger the tearing modulus and the longer the initial crack, the higher is the slope of the J-resistance curve. It should be noted, though, that the final instability point is determined by the condition

$$\begin{aligned}
J_A &= J_R \\
\left(\frac{\partial J_A}{\partial a}\right)_Q &= \frac{dJ_R}{da}
\end{aligned} \tag{20}$$

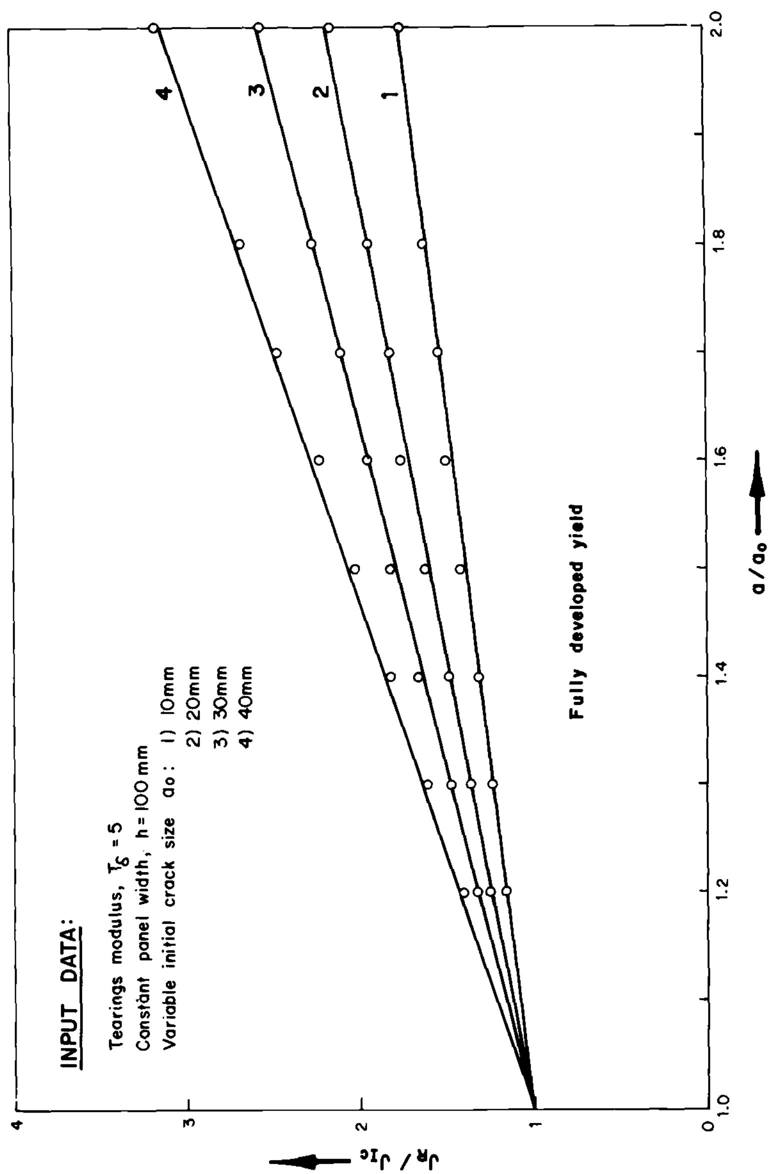

FIG. 2a—Integration results.

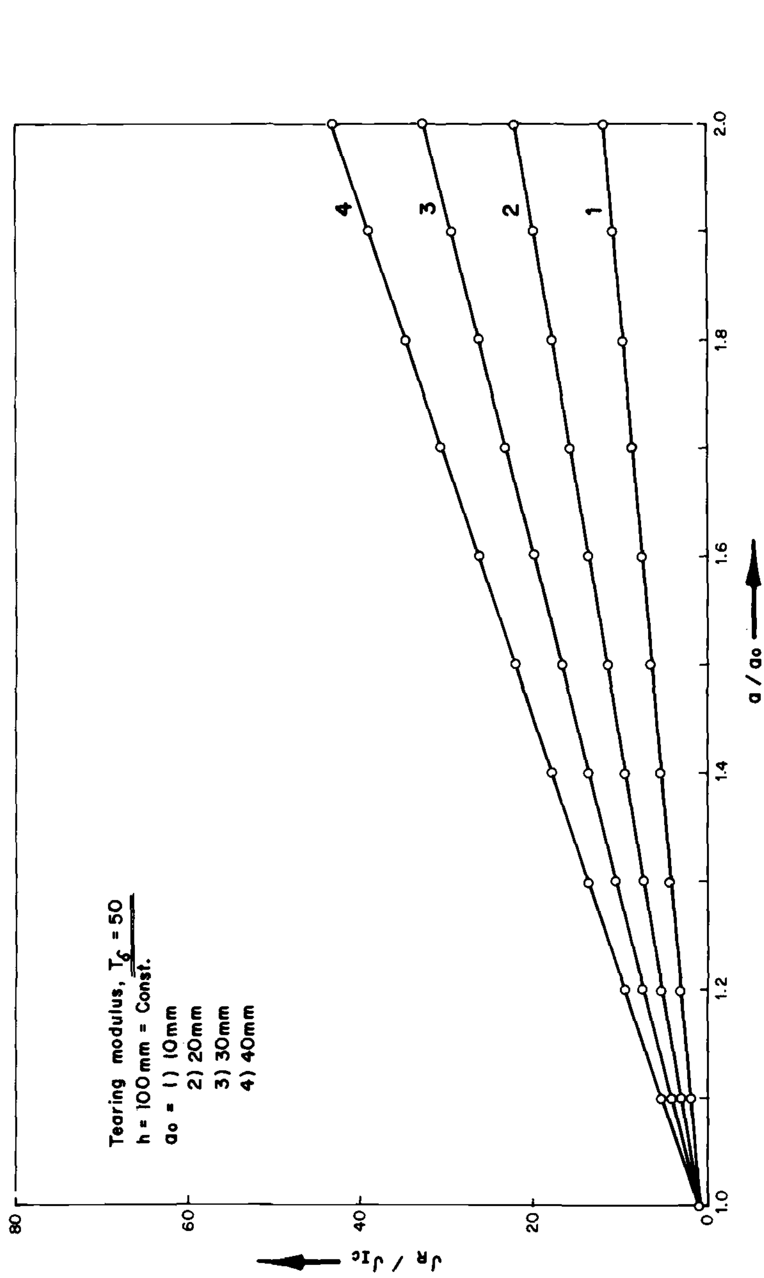

FIG. 2b—Despite a high value of tearing modulus the initial crack size has a pronounced effect on the slope of the J_R*-curve; compare with* Fig. 2a.

and it will be in general strongly dependent on the input data, involving the choice of the material ductility (defined by T_δ) and the ratio of the initial crack size a_0 to the panel half-width h. With the effective yield point to the Young's modulus ratio, σ_Y/E, being chosen as 0.005, and with Poisson's ratio $\nu = 0.3$, the equation governing the J-resistance curve reads

$$\frac{dY}{dX} = (0.025)a_0\{T_\delta - 1.16 \log \Psi_i\} \tag{21}$$

where a_0 is the initial crack length given in mm, while the dimensionless function Ψ_i is defined as follows

$$\Psi_i(X) = \begin{cases} 1000 \sin(0.1\pi X) \\ 1000 \sin(0.2\pi X) \\ 1000 \sin(0.3\pi X) \\ 1000 \sin(0.4\pi X) \end{cases} \quad (i = 1, 2, 3, 4) \tag{21a}$$

Another approach to the stability of the finite-width specimen is to apply the governing Eq 16 at a chosen (and constant) initial crack size, but at a variable panel width. This has been done; the initial crack size of 10 mm has been kept constant, while the panel half-width h was varied according to

$$h_i = \begin{cases} 100 \text{ mm} \\ 50 \text{ mm} \\ 33 \text{ mm} \\ 25 \text{ mm} \end{cases} \quad (i = 1, 2, 3, 4) \tag{22}$$

With the effective yield stress to the Young's modulus ratio, σ_Y/E, being chosen as 0.005, and with the Poisson's ratio $\nu = 0.3$, the equation governing the J-resistance curve (Eq 16) reads

$$\frac{dY}{dX} = 0.25\{T_\delta - 1.16 \log \bar{\Psi}_i\} \tag{23}$$

Here, the dimensionless function $\bar{\Psi}_i$ is defined as follows

$$\bar{\Psi}_i = \begin{cases} 1000 \sin(0.1\pi X) \\ 500 \sin(0.2\pi X) \\ 333 \sin(0.3\pi X) \\ 250 \sin(0.4\pi X) \end{cases} \tag{24}$$

The index $i = i$, 2, 3, 4 corresponds to the four values of the panel width given by Eq 12, and the coefficients 0.1, 0.2, 0.3, 0.4, appearing in the

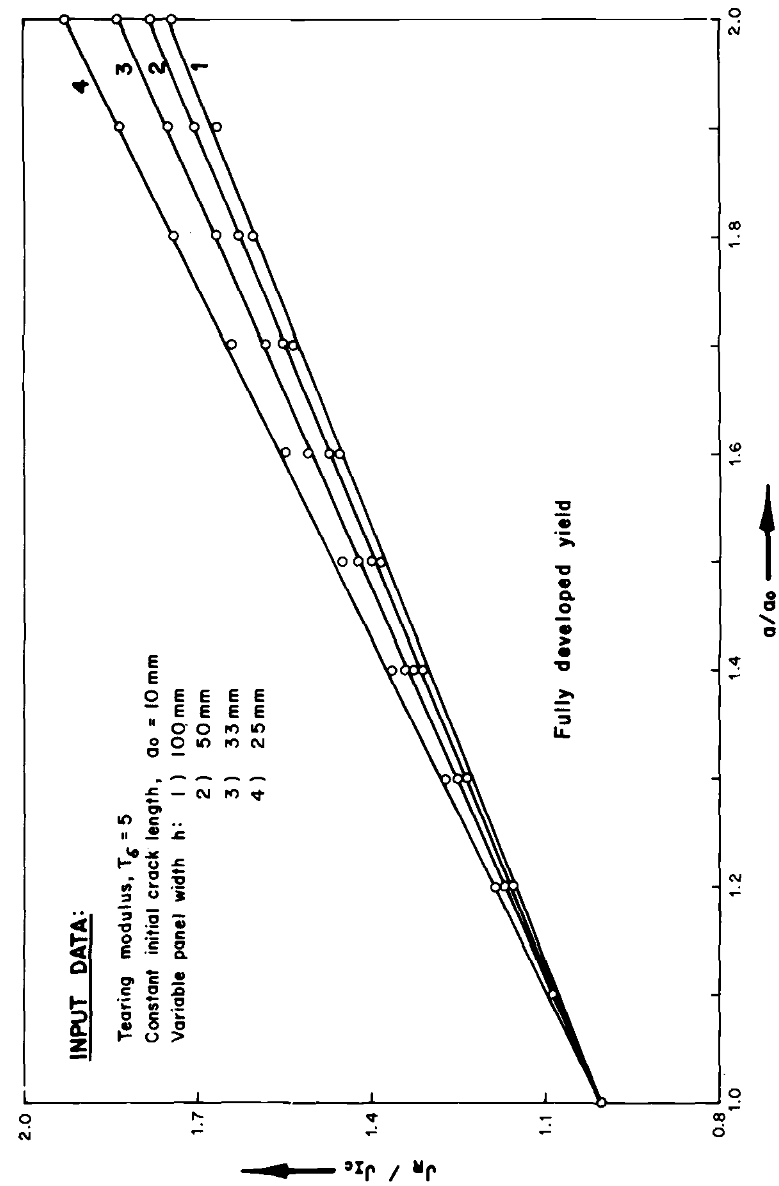

FIG. 3a—*Larger test specimen gives* lower *value of the tearing modulus (data so obtained is on the conservative side).*

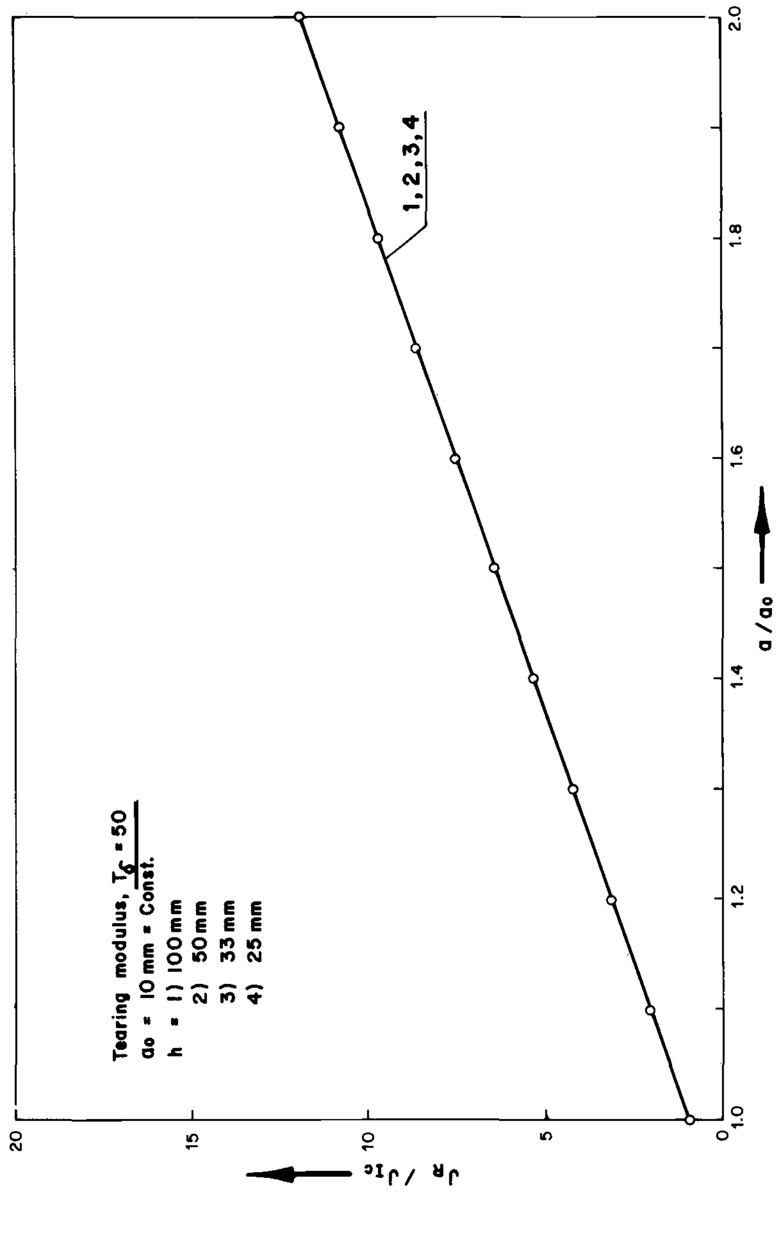

FIG. 3b—*At high values of the tearing modulus the effect of specimen* SIZE *is washed out and all four curves converge to one line;* COMPARE *with Fig. 3a.*

argument of the "sin" function in Eq 14, are the ratios of the initial crack size (fixed at 100 mm) to the panel width.

The integral curves resulting from the numerical integration of Eq 13 are shown in Fig. 3. It is seen that the size of the specimen, with all other pertinent parameters kept constant, does affect the slope of the J-resistance curve. An increasing value of the material tearing modulus appears to wash out the differences in the specimen response to the ductile tear test; however, it should be noted that an increasing size of the test specimen (at the same material ductility and the same initial crack dimension) leads to a more conservative prediction of the apparent material resistance associated with a slow tearing process occurring in the early stages of ductile fracture. An analogous observation was made recently by Shih et al. [9]. Their results are derived from a field plasticity solution for a quasi-static Mode I crack penetrating a compact tension specimen. All their results have been obtained through a numerical procedure, based on the finite-element approach to ductile fracture. The closed-form solutions derived from the final stretch model, as given in this paper, appear to substantiate the numerical data obtained from the field plasticity theories.

Conclusions

Numerical integration of Eq 14 performed at various input data leads us to conclusions which may be briefly stated as follows:

1. The slope of a particular J_R-curve is indeed a constant quantity, provided that the magnitude of the tearing modulus, which represents material sensitivity to ductile fracture, is sufficiently high.
2. Such constant slope, however, does depend rather strongly on the initial crack size and less strongly on the specimen size.

These concluding remarks are borne out by a direct inspection of Figs. *2a, 2b, 3a,* and *3b.*

Acknowledgment

One of the authors (MPW) wishes to express his gratitude to the National Academy of Sciences of Washington, D.C. and to the Serbian Academy of Sciences of Belgrade, Yugoslavia for contributing funds which have made this work possible.

References

[1] Wnuk, M. P., in *Proceedings*, International Conference on Dynamic Crack Propagation, Lehigh University, Bethlehem, Pa., 1972, pp. 273-280.

[2] Wnuk, M. P., in *Progress in Flaw Growth and Fracture Toughness Testing, ASTM STP 536*, American Society for Testing and Materials, 1973, pp. 64-75.

[3] Wnuk, M. P., *Journal of Applied Mechanics*, Vol. 41, 1974, pp. 234-242.
[4] Rice, J. R. and Sorensen, E. P., *Journal of the Mechanics and Physics of Solids*, Vol. 26, 1978, pp. 163-186.
[5] Rice, J. R., *The Mechanics of Quasi-Static Crack Growth*, Technical Report No. 63, Brown University, Providence, R.I., 1978.
[6] Rice, J. R., Drugan, W. J., and Sham, T. L., "Elastic Plastic Analysis of Growing Cracks," Technical Report No. 65, Brown University, Providence, R.I., presented at the 12th National Symposium on Fracture Mechanics at Washington University, St. Louis, Mo., May 1979.
[7] Wnuk, M. P., in *Proceedings*, ICM3, Third International Conference on Mechanical Behavior of Materials, Cambridge, England, Vol. 3, Aug. 1979, pp. 549-561.
[8] Wnuk, M. P., *International Journal of Fracture Mechanics*, Vol. 15, 1979, pp. 553-581.
[9] Smith, E., "The Invariance of the J versus Δc Curve for Plane Strain Crack Growth in Ductile Materials," to appear in *International Journal of Fracture Mechanics*.
[10] Shih, F. and Kumar, V., private communication, 1980.
[11] Paris, P. C., Tada, H., Zahoor, A., and Ernst, H., "A Treatment of the Subject of Teaning Instability," U.S. Nuclear Regulatory Commission Report NUREG-0311, 1977.
[12] Hutchinson, J. W. and Paris, P. C., in *Elastic-Plastic Fracture, ASTM STP 668*, American Society for Testing and Materials, 1979, pp. 37-64.

R. L. Tobler, [1] *D. T. Read,* [1] *and R. P. Reed* [1]

Strength/Toughness Relationship for Interstitially Strengthened AISI 304 Stainless Steels at 4 K Temperature

REFERENCE: Tobler, R. L., Read, D. T., and Reed, R. P., **"Strength/Toughness Relationship for Interstitially Strengthened AISI 304 Stainless Steels at 4 K Temperature,"** *Fracture Mechanics: Thirteenth Conference, ASTM STP 743,* Richard Roberts, Ed., American Society for Testing and Materials, 1981, pp. 250–268.

ABSTRACT: A study was conducted to determine the effects of carbon and nitrogen on the 4 K fracture properties of an Fe-18Cr-10Ni austenitic stainless steel having a base composition corresponding to AISI 304. J-integral fracture toughness tests using 24.5-mm-thick compact specimens (TL orientation) were performed in a liquid helium environment on nine steel heats having carbon plus nitrogen (C+N) contents between 0.067 and 0.325 weight percent. The fracture toughness decreased with increasing C+N content. The K_{Ic} estimates obtained at 4 K ranged from 337 to 123 MPa$\cdot$m$^{1/2}$, exhibiting an inverse dependence on tensile yield stress. A computer-aided J-integral test facility was implemented to conduct this study. This new facility improves measurement accuracy, conserves material specimens and testing time, and systematizes test procedures.

KEY WORDS: computer-aided mechanical tests, cryogenic mechanical properties, fracture (materials), fracture toughness, J-integral, low-temperature tests, stainless steels

Acceptance of the parameter J_{Ic} as a measure of the fracture resistance of metals has become widespread in recent years. A large volume of J-integral fracture toughness data on a variety of candidate materials for low-temperature applications has been accumulated. J-integral testing has the advantage of being applicable to smaller specimens (up to 100 times smaller) and tougher materials compared with the plane-strain fracture test (K_{Ic} test). A disadvantage of the J-integral technique has been its experimental difficulty. Previous test methods have required approximately five specimens and lengthy data reduction procedures [*1*].[2] Recently developed single-specimen J-integral test

[1]Metallurgists, National Bureau of Standards, Boulder, Colo. 80303.
[2]The italic numbers in brackets refer to the list of references appended to this paper.

techniques [2] eliminated the multiple-specimen requirement, but the data reduction procedure was still lengthy. In the computer-aided J-integral test, most of the data-reduction procedure is automated; the apparatus produces a plot of the J-integral value versus crack extension from which J_{Ic} can be quickly and simply extracted.

The AISI 300 series stainless steels are austenitic iron-chromium-nickel (Fe-Cr-Ni) alloys, offering relatively low strength but excellent cryogenic ductility and toughness [3]. By virtue of favorable mechanical properties, service history, and availability, AISI 304 is perhaps the most widely used cryogenic alloy in the world. The nitrogen-strengthened grades such as AISI 304 N or AISI 304 LN have attracted attention recently as possible substitutes for AISI 304 in applications demanding higher strength. Nitrogen is a relatively inexpensive and effective strengthener. Nitrogen also stabilizes the austenitic structure and reduces the probability of martensite transformation when stress is applied at cryogenic temperatures. Carbon has similar effects, but carbon contents in austenitic stainless steels must be held to low levels to prevent sensitization (chromium carbide precipitation) during thermal excursions.

Nitrogen-strengthened austenitic stainless steels are gaining popularity, but some applications are hindered by limited availability, limited service experience, lower fracture toughness, and lack of cryogenic design data. Most mechanical property studies conducted on these steels [4-18] are concerned only with room temperature behavior. In the present study, fracture toughness measurements for nine heats of an Fe-18Cr-10Ni stainless steel are reported at 4 K. The carbon and nitrogen contents of the nine heats were varied to enable a systematic study of interstitial concentration. The results can be used to predict the strength and toughness of commercial steels of given compositions, or to tailor the properties for a particular application by appropriate specification of the steel composition.

Materials

Nine stainless steel plates were procured from the research laboratories of a major steel manufacturer. These plates had a nominal base composition falling within the limits set by the ASTM Specification for Heat-Resisting Chromium and Chromium-Nickel Stainless Steel Plate, Sheet, and Strip for Fusion-Welded Unfired Pressure Vessels (A 240-78a) for AISI 304 stainless steel: Fe-18Cr-10Ni-1.5Mn-0.02P-0.02S-0.55Si-0.2Mo-0.2Cu. The carbon and nitrogen levels, however, varied with carbon at 0.03, 0.06, or 0.09 weight percent, and nitrogen at 0.04, 0.12, or 0.24 weight percent. The mill chemical analyses are listed in Table 1. The nine plates were produced from three 136-kg vacuum-induction-melted heats, split with respect to carbon level, and teemed into 76 by 200 by 360-cm hot-topped cast iron ingot molds. The ingots were then reheated and soaked at 1561 K, hot-rolled to 25.4-mm-thick plates, and

TABLE 1—*Stainless steel compositions (weight %), hardnesses, and grain sizes.*

Heat No.	Fe	Cr	Ni	Mn	P	S	Si	Mo	Cu	C	N	C + N	Hardness, Rockwell B	Average Grain Size, μm
1	balance	18.3	10.1	1.57	0.021	0.019	0.50	0.200	0.210	0.028	0.039	0.067	74	85
2	balance	18.3	10.1	1.57	0.021	0.019	0.50	0.200	0.210	0.058	0.039	0.097	76	78
3	balance	18.3	10.1	1.57	0.021	0.019	0.50	0.200	0.210	0.089	0.039	0.128	79	90
4	balance	18.0	9.91	1.50	0.022	0.017	0.57	0.205	0.197	0.037	0.120	0.157	79	105
5	balance	18.0	9.91	1.50	0.022	0.017	0.57	0.205	0.197	0.067	0.120	0.187	82	85
6	balance	18.0	9.91	1.50	0.022	0.017	0.57	0.205	0.197	0.094	0.120	0.214	82	78
7	balance	20.3	9.97	1.42	0.024	0.016	0.55	0.195	0.200	0.030	0.240	0.270	89	98
8	balance	20.3	9.97	1.42	0.024	0.016	0.55	0.195	0.200	0.057	0.240	0.297	89	82
9	balance	20.3	9.97	1.42	0.024	0.016	0.55	0.195	0.200	0.085	0.240	0.325	91	90

air-cooled. The plates were finally annealed at 1332 ± 7 K for 1 h and water-quenched. Hardness and grain size measurements are listed in Table 1.

Methods

Since elastic-plastic fracture was anticipated in the test materials, the J_{Ic} parameter was measured. The measurement problem in J_{Ic} testing is to obtain the required plot of J-integral, J, versus crack extension, Δa, from the directly measured quantities, which are the load, P, on the specimen and the relative displacement, δ, of two measurement points located on the specimen load line on opposite sides of the notch (Fig. 1). The J-value is proportional to the area under the (P, δ) curve (Fig. 2), and can be easily determined for any point along the curve. The shaded area in Fig. 2 is proportional to J at the point labeled "a". The principle used to measure Δa is that the crack length, a, is related to the slope of the specimen's (P, δ) curve for elastic conditions through the known specimen compliance function. The Δa measurement procedure is to partially (about 10 percent) unload the specimen while recording load displacement changes (Figs. 2 and 3). Subsequent unloadings at increasing crack extension values result in increased compliance. The crack extension at a given unloading is the difference between the crack length measured in that unloading minus the initial crack length, measured by an unloading carried out before crack extension.

The cryostat system that was used for computer-aided J-integral testing was

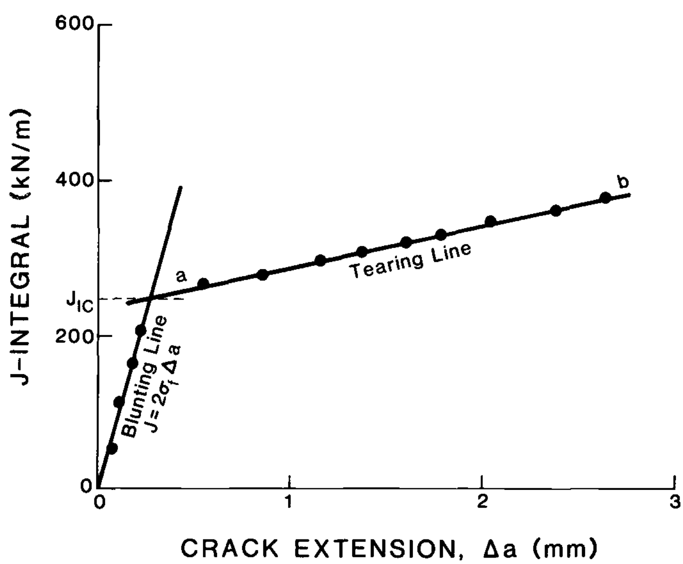

FIG. 1—*Typical J-integral versus crack extension curve.*

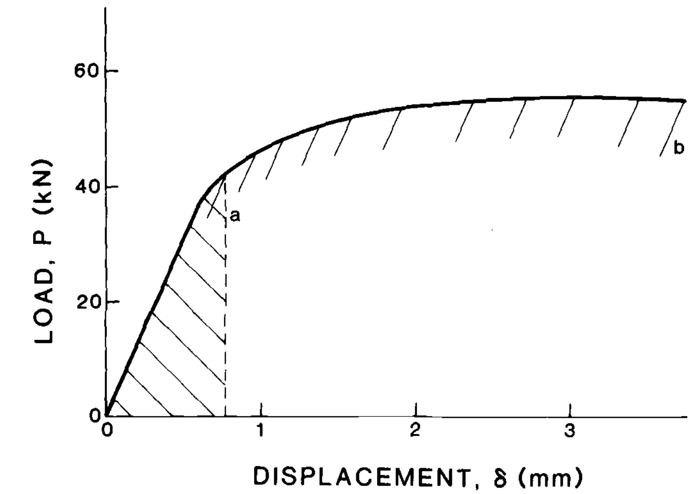

FIG. 2—*Typical load versus specimen displacement curve, indicating J-integral area for specimen at Point* a.

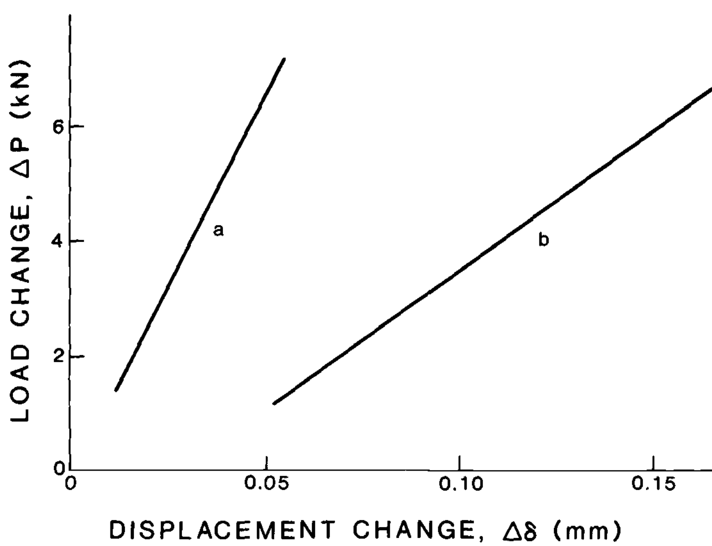

FIG. 3—*Calibration curve of load change versus displacement change.*

described previously by Fowlkes and Tobler [*19*]. The specimen loading is controlled in conventional fashion by the operator. The computer is used only in data acquisition and reduction. An analog ramp generator controlled by the operator applies a smoothly varying signal to the test machine control circuitry to allow unloading-reloading cycles as necessary. The additional equipment needed for computer-aided testing includes a multichannel analog-digital conversion system, the computer itself, a cathode ray tube (CRT) terminal, a dual floppy disk data storage unit and a digital plotter (Fig. 4).

Two signals are used to direct the operation of the data acquisition system. One is derived from the output of the ramp generator by which the operator initiates the unloading-reloading cycle. When the ramp generator is activated, a signal transmitted to the processor commands it to begin to acquire and store load and displacement change data during the unloading-reloading cycle. Data are stored until the load again reaches the value it had before the unloading. The test continues through as many unloading cycles as desired until the operator activates the quit signal, which directs the processor to await the operator's command, entered at the CRT terminal, to stop the data acquisition procedure and terminate the test.

During the incremental unloading required to measure Δa, displacement changes of the order of 0.05 mm and load changes of the order of 5 kN must be correlated accurately. These changes correspond to a change in the overall displacement signal of about 70 mV and a change in the load signal of about 1 V. Because the analog-to-digital converter used has only 16-bit resolution, the displacement signal cannot be converted directly to digital form with precision sufficient for accurate measurement of this displacement change. The measurement of the small displacement changes which occur during the unloading-reloading cycles is facilitated by regarding the overall displacement

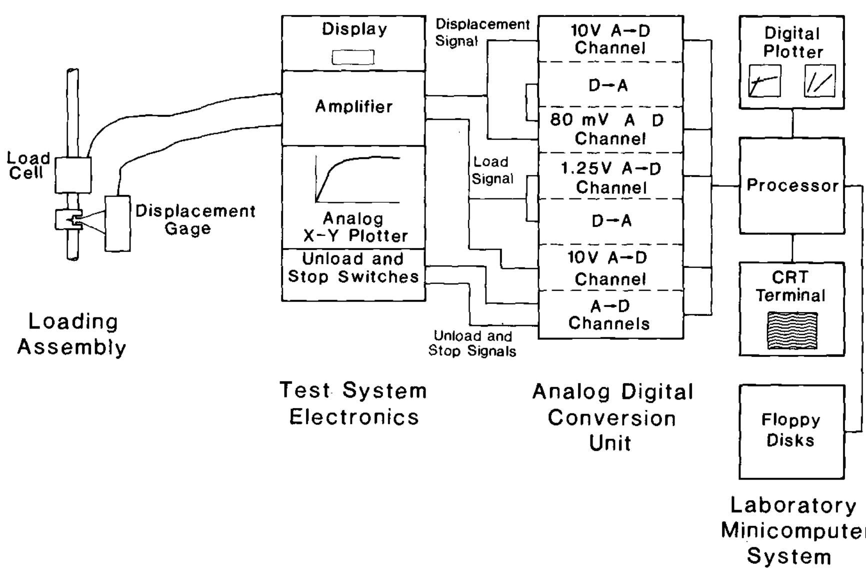

FIG. 4—*Flow chart of recording and analyses computer system for fracture testing.*

as consisting of small changing displacements superimposed on a large reference displacement value. The measurement is accomplished by canceling out the reference part, then converting the small displacement changes to digital form with high resolution. To achieve this cancelation, the overall displacement is converted to digital form at the beginning of each unloading-reloading cycle. This initial value is treated as the reference part. In order to cancel out this reference part of the displacement signal, a digital-to-analog converter with 14-bit resolution is used to apply a voltage equivalent to the reference part of the displacement signal to one terminal of a differential high-sensitivity analog-to-digital conversion channel. The overall displacement signal is applied to the other input terminal of this channel. This results in the analog-to-digital conversion of a voltage equal to the difference between the instantaneous value of the displacement signal and its value at the beginning of the unloading. This difference signal is the required change-of-displacement signal, and is converted to digital form with 16-bit resolution of its 80-mV range. The least significant bit represents about 2.5 μV, which is quite sufficient. The load change signal is produced in a similar manner using another digital-to-analog converted signal, and converted to digital form with 16-bit resolution at the 1.25-V level. Here the least-significant bit represents about 40 μV, which is again quite sufficient.

Approximately 80 load-change and displacement-change data points are obtained for each unloading-reloading cycle over a 30-s period. These data are plotted during the unloading-reloading cycle using a digital plotter, forming a plot like Fig. 3. From this plot the presence of excessive noise or other improper behavior in the signals can be easily observed. The load-change and displacement-change data are correlated using a least-squares fit. From the resulting slope the instantaneous crack length is calculated using the known expression for the compliance of the specimen.

Each (J, Δa) datum is plotted by the digital plotter as soon as it is available, forming a plot similar to Fig. 1. This plot allows convenient monitoring of the progress and quality of the test in real time. The values are also displayed on a CRT terminal for transcription. This step will be replaced by an automatic printout when facilities become available. The least-squares fit and data output procedure takes about 12 s.

The record of the completed test consists of the (J, Δa), (P, δ), and (ΔP, $\Delta\delta$) plots, the transcribed (J, Δa) data, and three files stored on a floppy disk during the test, one containing the (J, Δa) values and a few other key data, one containing all the (P, δ) data, and one containing all the (δP, $\Delta\delta$) data.

The National Bureau of Standards (NBS) computer-aided J-integral test facility is similar to that described by Joyce and Gudas [20]. The differences are in the specific types of equipment used and in the real-time outputs. Real time is used here to mean during the course of the test, as opposed to after the test is completed.

The procedure for extracting J and Δa from the directly measured load and displacement on a deeply notched compact tension specimen is as follows. The electrical signals from the load cell and displacement gage are amplified by the electronics supplied with the closed-loop servohydraulic apparatus used for the test. A plot of load versus displacement similar to Fig. 2 is produced by an x-y plotter throughout the course of the test. Either signal may be displayed on a digital readout. The plot and readout are used by the operator to monitor the progress of the test.

The amplified load and displacement signals are also introduced into an analog-to-digital conversion system to permit calculation of J and Δa. At this point, the overall levels of the signals range between 0 and 10 V. These signals are converted to digital form with a resolution of 16 bits; the least significant bit represents about 0.3 mV. The overall load and displacement values are used for calculating the instantaneous J-value, which is proportional to the area under the load-displacement curve. Stored overall-displacement points are separated by 2.5×10^3. Smaller observed overall-displacement increments are not stored. Computations of the instantaneous J-value are made when the overall displacement has increased sufficiently from the previously stored value.

The geometry of the Fe-Cr-Ni compact specimens tested in this study is shown in Fig. 5. The specimens were machined in the TL orientation as defined by ASTM Test for Plane-Strain Fracture Toughness of Metallic Materials (E 399-78a). The specimens were fatigue cracked at 4 K to a crack length between 28.8 and 36 mm ($a/W \simeq$ 0.57 to 0.71). The specimens were

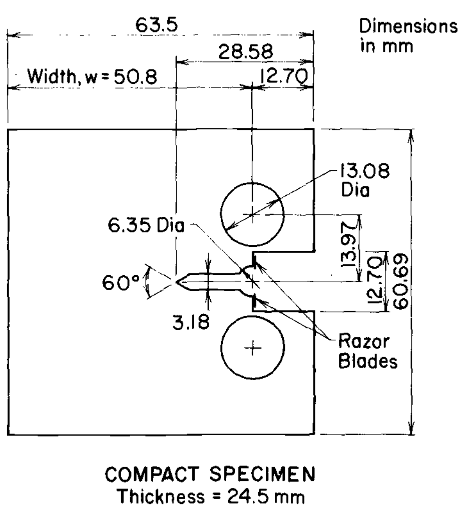

FIG. 5—*Specimen geometry used for fracture mechanics tests.*

then J-tested in displacement control, and partial unloadings were performed periodically. The J-value at each unloading point was calculated using the expression:

$$J = \frac{\lambda A}{Bb}$$

where

λ = Merkle-Corten factor dependent on crack length [21],
A = area under load-versus-deflection curve at unloading point
b = specimen ligament ($b = W - a$), and
B = specimen thickness.

J-resistance curves consisting of many sets of J and Δa points were generated, as shown by the example in Fig. 6.

The J_{Ic}-value for each steel was taken at the intersection of the J-resistance curve with the blunting line. The blunting line is given by $J = 2\sigma_f \Delta a$ where σ_f is the flow stress, which is the average of the yield and ultimate tensile stresses. As shown in Fig. 6, there is an artificial offset of the data from the theoretical blunting line, so a blunting line parallel to the theoretical blunting line but passing through the data was used. After the test, the Δa-values inferred from compliance data were found to be up to 50 percent lower than the actual values found by direct measurement from the fracture surfaces.

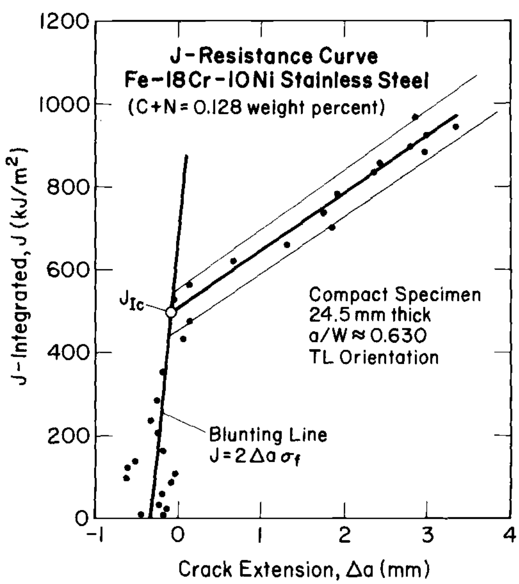

FIG. 6—*Typical J-resistance curve for an austenitic stainless steel tested at 4 K.*

The agreement is better at lower crack extension values. This causes a significant error in the resistance curve slopes, but has less effect on the J_{Ic}-values. Uncertainty in the J_{Ic}-values is estimated at about ± 12 percent.

The validity of J_{Ic} results was determined by the size criterion which requires that [1]

$$B, b, a \geq \frac{25 J_{Ic}}{\sigma_f}$$

In all low-temperature fracture tests, partial transformation of the paramagnetic austenite to ferromagnetic α' [body-centered cubic (bcc)] martensite was observed (for example, Ref 22). The extent of α'-transformation was estimated using a bar-magnet device [23]. Small amounts of ϵ (close-packed hexagonal) martensite may also have formed, but this was not measured.

Results and Discussion

At the time of writing, the computer-aided J-integral methods have been in use for nine months and have proved satisfactory. In comparison with the multiple specimen and non-computer-aided single-specimen techniques previously used, the new methodology has eliminated about 4 h of data reduction per test, and has provided a real-time readout of the test progress and quality. The cost of the complete data-acquisition system, including analog-to-digital converters, processor, digital plotter, and CRT terminal is estimated at about $25 000.

J_{Ic} results were obtained for seven of the austenitic stainless steels tested, but the data for the two lower strength heats with C+N (0.067 and 0.097 weight percent) were invalid. The maximum J-values in these tests exceeded the allowable limits for 24.5-mm-thick specimens. Moreover, the round-house curves obtained could not be analyzed according to conventional techniques because there was no obvious knee at the blunting line-resistance curve intersection. The J_{Ic} values for the seven steels at 4 K range from 63 to 499 kJ/m^2, while the yield stresses for the same materials at 4 K range from 329 to 1286 MPa (Table 2). Higher toughness is associated with lower interstitial C + N contents, and hence lower strength. All of the steels tested exhibited a ductile dimpled fracture mode at 4 K, as shown by the scanning electron fractographs of Figs. 7 and 8.

Estimates of the plane-strain fracture toughness parameter K_{Ic} which would be observed under linear-elastic conditions were obtained using the relationship

$$K_{Ic}(J) = \frac{J_{Ic} E}{(1 - \nu^2)}$$

TABLE 2—*Yield stress and J-integral toughness results for Fe-18Cr-10Ni steels at 4 K.*

Specimen	C + N Content, weight %	Yield Stress, σ_y, MPa	Flow Stress, σ_f, MPa	$\frac{25 J_{Ic}}{\sigma_f}$, mm	J_{Ic}, kJ/m^2	K_{Ic} (J),[a] MPa$^{1/2}$
1	0.067	329	892	NA	NA	NA
2	0.097	445	996	NA	NA	NA
3	0.128	530	1029	12.2	499	337
4	0.157	745	1158	6.7	312	266
5	0.187	876	1288	4.5	230	230
6-A	0.214	896	1264	4.3	218	222
6-B	0.214	896	1264	5.3	272	249
7	0.270	1186	1411	1.2	67	124
8-A	0.297	1178	1456	1.5	88	141
8-B	0.297	1178	1456	1.3	78	133
9	0.325	1286	1496	1.1	63	124

[a]Calculated from the expression $K_{Ic}{}^2 = J_{Ic} \cdot E/(1-\nu^2)$, assuming E = 206.8 GPa and ν = 0.3 at T = 4 K.

where

E = Young's modulus,
ν = Poisson's ratio, and
K_{Ic} (J) = an estimate of K_{Ic} from J_{Ic}.

The values of E and ν for the stainless steels at 4 K were estimated to be 206.8 GPa and 0.3 [*24*], respectively. The calculated K_{Ic} estimates are plotted versus C + N content in Fig. 9, and versus yield stress in Fig. 10. As shown, the K_{Ic} (J)-values decrease linearly with interstitial concentration, and are inversely related to yield stress. Therefore nitrogen, which is a particularly effective strengthener, also has a strong influence on fracture toughness at cryogenic temperatures. An expression governing the relationship between fracture toughness and yield stress was derived from Fig. 10.

$$K_{Ic}\,(J) = 500 - 0.3\,\sigma_y$$

The data scatter of K_{Ic} (J) from this expression is ± 20 MPa$\cdot$m$^{1/2}$.

The present results compare well with existing data, some of which are shown for comparison in Fig. 10. The AISI 304 N datum of Read and Reed [*5*] falls slightly below the present data, reflecting differences owing to metallurgy or measurement techniques. The Fe-Cr-Ni-Mn-N (Nitronic) steels tend to have higher nitrogen contents, higher 4 K strength, and lower toughness as compared with the Fe-Cr-Ni-N (AISI 304) steels [*4*]. Yet, the Fe-Cr-Ni-Mn-N steels in Fig. 10 appear to possess superior toughness than would be expected from the extrapolated trend for Fe-Cr-Ni-N steels. It is uncertain whether this is due to metallurgical effects, or whether the apparent superiority could be due to measurement bias since the Fe-Cr-Ni-Mn-N data were obtained by other methods, including the multispecimen technique, which have greater J_{Ic} uncertainty.

The inverse relationship of σ_y and K_{Ic} is well known for linear-elastic fracture toughness data. Now there is appreciable evidence that the inverse relationship holds in the elastic-plastic regime as well. Previous 4 K data for a variety of austenitic stainless steels and uncontrolled metallurgical conditions [5] indicated a linear trend of lesser slope than shown in Fig. 10. It is advantageous that the present data derive from a controlled alloy series in which strength was varied by interstitial content while other compositional and processing variables were constant.

The approximate amount of α' (bcc) martensite formed during fatigue and fracture at 4 K is plotted as a function of interstitial content in Fig. 11. These results provide only an approximate indication of the extent of phase transformation, because the measurements were taken directly from the compact specimen fracture surfaces, which are rough and unmachined. It is clear from Fig. 11 that some martensite forms in all of the steels during testing. The quantity of martensite that forms would be expected to increase with the plastic zone size. Referring to Fig. 11, more α' is detected in steel specimens of lower strength, higher toughness, and, presumably, larger plastic zone size. It is not clear at this time whether the formation of martensite plays a significant role in the fracture process of these metastable steels.

Summary and Conclusions

1. New computer-assisted J-integral test methods and facilities have been developed and applied to cryogenic fracture testing.

2. Fracture toughness measurements at 4 K are reported for Fe-18Cr-10Ni austenitic stainless steels having C + N contents ranging from 0.067 to 0.325 weight percent.

3. The fracture toughness at 4 K decreased with increasing C + N content, and the K_{Ic}-values estimated from J_{Ic} (ranging from 123 to 337 $MPa \cdot m^{1/2}$) were inversely related to yield stress.

4. Further improvements in our J-integral test procedure should be directed at reducing the blunting line offset and improving the accuracy of Δa-values inferred by compliance measurements.

Acknowledgments

This research was supported by the David W. Taylor Naval Ship Research and Development Center (J. Gudas, coordinator) and by the Office of Fusion Energy, Department of Energy (D. Beard, coordinator). T. Whipple, A. Castillo, D. Burkhalter, and D. Beekman assisted in performing the fracture tests.

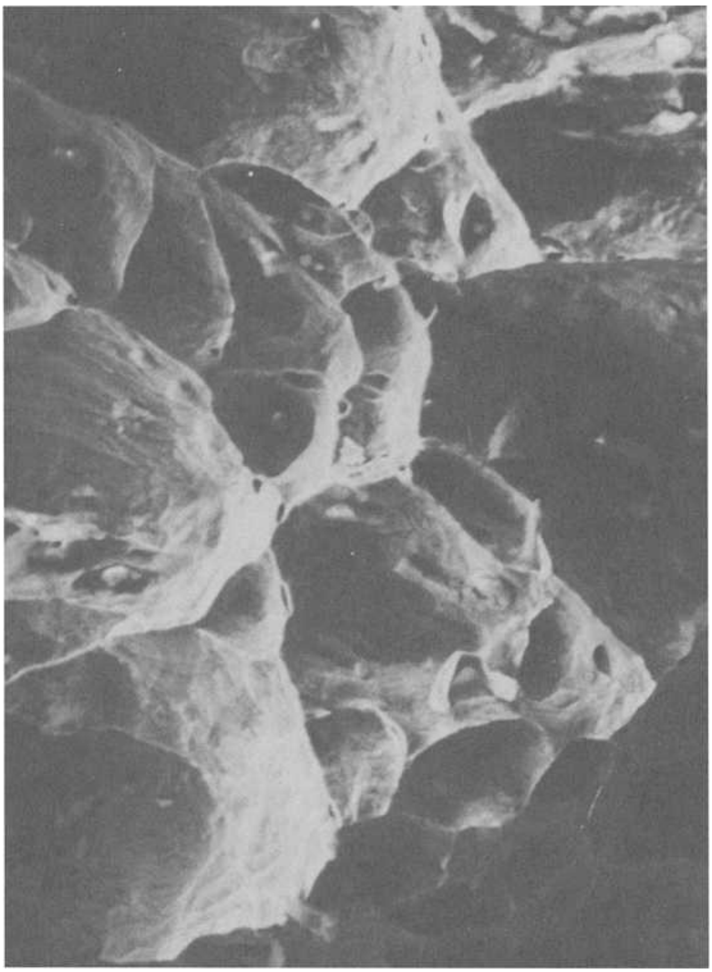

FIG. 7—*Scanning electron microscopy photograph of Fe-18Cr-10Ni, C + N = 0.325 weight percent, 4 K fracture surface at ×200 and ×1000.*

FIG. 8—Scanning electron microscopy photograph of Fe-18Cr-10Ni, C + N = 0.067 weight percent 4 K fracture surface at ×200 and ×1000.

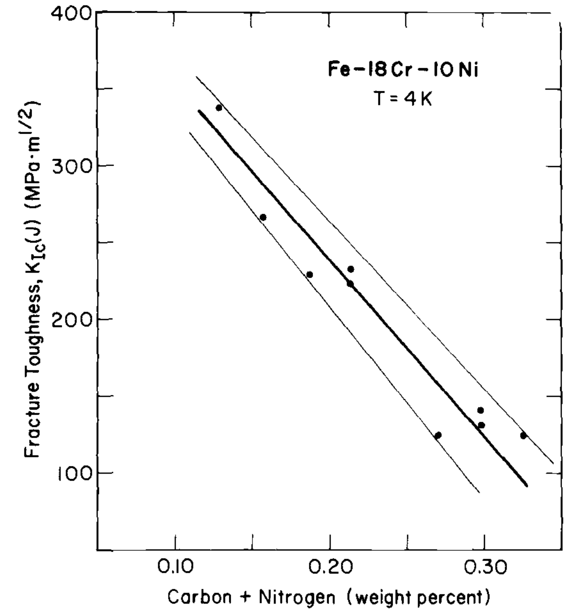

FIG. 9—*Dependence of* K_{Ic} *at 4 K on carbon and nitrogen content.*

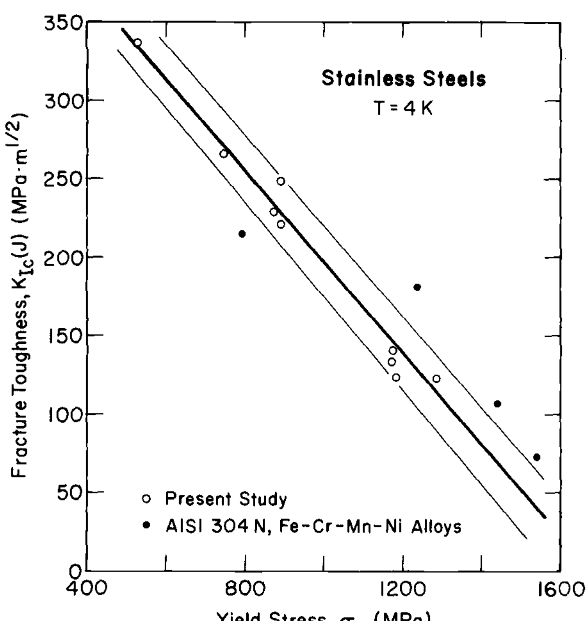

FIG. 10—*Inverse relationship between fracture toughness and yield stress for austenitic stainless steels at 4 K.*

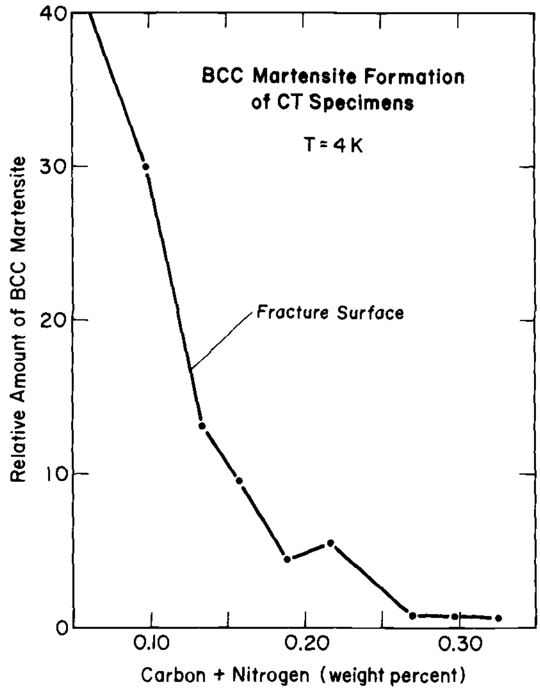

FIG. 11—*Relative amounts of α′ (bcc) martensite formed during tests of compact specimens at 4 K.*

References

[1] Landes, J. D., and Begley, J. A. in *Fracture Analysis, ASTM STP 560*, American Society for Testing and Materials, 1974, pp. 170-186.

[2] Clarke, G. A., Andrews, W. R., Paris, P. C., and Schmidt, D. W. in *Mechanics of Crack Growth, ASTM STP 590*, American Society for Testing and Materials, 1976, pp. 27-42.

[3] Reed, R. P., Fickett, F. R., Kasen, M. B., and McHenry, H. I. in *Materials Studies for Magnetic Fusion Energy Applications at Low Temperatures-I*, NBSIR 78-884, F. R. Fickett and R. P. Reed, Eds., National Bureau of Standards, Boulder, Colo., 1978, pp. 245-335.

[4] Read, D. T. and Reed, R. P. in *Materials Studies for Magnetic Fusion Energy Applications at Low Temperatures-I*, NBSIR 78-884, F. R. Fickett and R. P. Reed, Eds., National Bureau of Standards, Boulder, Colo. 1978, pp. 91-154.

[5] Read, D. T. and Reed, R. P. in *Materials Studies for Magnetic Fusion Energy Applications at Low Temperatures-II*, NBSIR 79-1609, F. R. Fickett and R. P. Reed, Eds., National Bureau of Standards, Boulder Colo. 1979, pp. 81-122.

[6] Read, D. T., Reed, R. P., and Schramm, R. E. in *Materials Studies for Magnetic Fusion Energy Applications at Low Temperatures-II*, NBSIR 79-1609, F. R. Fickett and R. P. Reed, Eds., National Bureau of Standards, Boulder, Colo., June 1979, pp. 151-172.

[7] Read, D. T. and Reed, R. P. in *Materials Studies for Magnetic Fusion Energy Applications at Low Temperatures-II*, NBSIR 79-1609, F. R. Fickett and R. P. Reed, Eds., National Bureau of Standards, Boulder, Colo. 1979, pp. 125-147.

[8] Tobler, R. L. and Reed, R. P. in *Elastic-Plastic Fracture, ASTM STP 668*, American Society for Testing and Materials, 1979, pp. 537-552.

[9] Dessau, P. P., "LN_2 and LH_2 Fracture Toughness of Armco Alloy 22-13-5," Report No. TID/SNA-2083, Aerojet Nuclear Systems Co., Sacramento, Calif., 1971.
[10] Larbalestier, D. C. and Evans, D. in *Proceedings*, Sixth International Cryogenic Engineering Conference, IPC Science and Technology Press Ltd., Surrey, England, 1976, pp. 345-347.
[11] Gunia, R. B. and Woodrow, G. R., *Journal of Materials* Vol. 5, 1970, pp. 413-430.
[12] Voyer, R. and Weil, L. in *Advances in Cryogenic Engineering*, Vol 11, K. D. Timmerhaus, Ed., Plenum, New York, 1965, pp. 447-452.
[13] Norström, L.-A., *Metal Science*, Vol. 11 1977, pp. 208-212.
[14] Booker, M. K. and Sikka, V. K., "Effects of Composition Variables on the Tensile Properties of Type 304 Stainless Steel," ORNL-5353, Oak Ridge National Laboratory, Oak Ridge, Tenn. 1977, p. 38.
[15] Soo, P. and Horton, W. H., "The Effect of Carbon and Nitrogen on the Short-term Tensile Behavior of Types 304 and 316 Stainless Steels," Ward NA 3045-2, Westinghouse Electric Corp., Madison, Pa., p. 48.
[16] Irvine, K. J., Lewellyn, D. T., and Pickering, F. B., *Journal of the Iron Steel Institute*, Vol. 199, 1961, pp. 153-175.
[17] Irvine, K. J., Gladman, T., and Pickering, F. B., *Journal of the Iron Steel Institute*, Vol. 207, 1969, pp. 1017-1028.
[18] Spaeder, C. E., Jr., and Domis, W. F., "Cryogenic and Elevated-Temperature Mechanical Properties of a High-Nitrogen Type 304 Stainless Steel," Report No. 44012-062-2, United States Steel Corp., Pittsburgh, Pa., 1969.
[19] Fowlkes, C. W. and Tobler, R. L., *Engineering Fracture Mechanics*, Vol. 8, 1976, pp. 487-500.
[20] Joyce, J. A. and Gudas, J. P. in *Elastic-Plastic Fracture, ASTM STP 668*, American Society for Testing and Materials, 1979, pp. 451-468.
[21] Merkle, J. G. and Corten, H. T., *Journal of Pressure Vessel Technology, Transactions American Society of Mechanical Engineers*, Vol. 6, 1974, pp. 1-7.
[22] Reed, R. P. and Guntner, C. J., *Transactions, Metallurgical Society of the American Institute of Mining, Metallurgical and Petroleum Engineers*, Vol. 230, 1964, pp. 1713-1720.
[23] Reed, R. P. and Mikesell, R. P. in *Advances in Cryogenic Engineering*, Vol. 4, K. D. Timmerhaus, Ed., Plenum, New York, 1960, pp. 84-100.
[24] Ledbetter, H. M., Frederick, N. V., and Austin, M. W., *Journal of Applied Physics*, Vol. 51, 1980, pp. 305-309.

W. G. Clark, Jr.[1]

Some Problems in the Application of Fracture Mechanics

REFERENCE: Clark, W. G., Jr., "**Some Problems in the Application of Fracture Mechanics,**" *Fracture Mechanics: Thirteenth Conference, ASTM STP 743,* Richard Roberts, Ed., American Society for Testing and Materials, 1981, pp. 269–287.

ABSTRACT: In addition to the widely recognized continuum mechanics restrictions associated with the use of fracture mechanics, there are a number of problems and areas of concern that en arise in the application of the technology to actual situations. These problems range from the development of adequate material properties data to the analytical and defect characterization aspects of the technology. Some of these problems are identified and discussed with regard to their potential impact on structural life predictions and quantitative risk analyses. Material characterization problems associated with data scatter, prior loading effects, and time-dependent behavior are included along with the consideration of the probability of flaw detection and the analysis of small defects and interacting flaws. Suggestions and recommendations for experimental work required to resolve these problems are included.

KEY WORDS: fracture, stresses, cracks, testing, growth, environment, strength, failures, fatigue, corrosion, toughness

In recent years, it has been clearly demonstrated that the concepts of cracked-body fracture mechanics provide significant advantages over the more traditional methods of material selection and design. Consequently, fracture mechanics has become the preferred and, in some cases, the required method of structural analysis for many critical components. The success of fracture mechanics in these and other applications has led to the wide acceptance and rapidly increasing use of the technology for a broad range of material characterization and structural integrity considerations. Despite this success, existing fracture mechanics methodology has several inherent limitations which must be considered in the rational application of the technique. For the most part, these limitations are generally well recognized and include problems such as the violation of continuum mechanics concepts, the characterization of elastic-plastic/plastic behavior, and the

[1]Manager, Materials Reliability Research, Structural Behavior of Materials Engineering Department, Westinghouse R&D Center, Pittsburgh, Pa. 15235.

development of adequate stress-intensity expressions for complex combined-mode loading situations. However, in addition to these widely recognized limitations, there are a number of other problems and areas of concern which often arise in the application of fracture mechanics. Such problems range from the availability of appropriate design data to questions regarding the applicability of the technology itself. Although important in the prevailing deterministic or "worst case" approach to the application of fracture mechanics, these problems become even more significant in the consideration of a probabilistic fracture mechanics approach to structural life predictions.

Recent work associated with the development and evaluation of reliability analysis techniques based on a probabilistic fracture mechanics approach has clearly demonstrated the potential value of this concept [*1,2*].[2] Specifically, such a methodology offers the ability to address structural reliability as a physical quantity which can be established as a design goal. Preliminary work has also revealed some of the major problems associated with the incorporation of probabilistic and statistical considerations into a fracture mechanics analysis. Unfortunately, much of the current effort in this area is aimed at improvements in the statistical characterization of the required input data. Although extremely important to the overall development of a rational probabilistic fracture mechanics methodology, overemphasis of the statistical aspects of the problem poses the danger of overshadowing some of the more fundamental limitations which can render even the most sophisticated probabilistic analysis useless. Clearly, an adequate approach to the development of a useful probabilistic fracture mechanics methodology requires a combined effort which addresses both the statistical as well as the more general problems.

This paper is intended to identify some of the most important problems and limitations encountered in the application of fracture mechanics technology to actual material selection and design considerations. Particular emphasis is placed on low visibility problems which must be addressed and resolved before a rational probabilistic fracture mechanics methodology can be developed. Discussion is limited primarily to linear elastic fracture mechanics (LEFM) considerations, and problems related to the inherent limitations of the technology (continuum mechanics restrictions) are not included. The problems of concern are addressed from the point of view of the three major areas of input required in the application of the technology: (1) material characterization, (2) nondestructive inspection or defect characterization, and (3) stress/stress-intensity analysis information. There is no attempt to prioritize the problem areas since the specific priority would depend upon the actual application being considered. Suggestions and recommendations for research and development programs to resolve these problems are included.

[2]The italic numbers in brackets refer to the list of references appended to this paper.

Material Characterization Problems

The successful application of fracture mechanics requires cracked-body material properties data that truly represent the component and intended service conditions of interest. It is generally well recognized that most fracture mechanics material properties (K_{Ic}, K_{Iscc}, da/dN, da/dt) are strongly dependent upon material, mechanical loading, and environmental variables. As a result, considerable attention is usually given to these variables in the development of material properties data for a fracture mechanics analysis of a given structure. However, there are several important aspects of the material characterization problem which have yet to be resolved with regard to their potential impact on structural integrity and life prediction. These areas of concern include considerations associated with data scatter, prior loading effects, and time-dependent behavior.

Data Scatter

It is widely recognized that the crack growth and fracture properties of structural alloys can be strongly dependent upon several inherent material variables, including strength level, alloy composition, microstructure, and crack orientation. This variability in fracture properties leads to a major problem associated with the state-of-the-art application of fracture mechanics, specifically, data scatter.

To date, a limited amount of effort has been directed at the characterization of data scatter associated with fracture mechanics material properties. Generally, instead of conducting a statistical evaluation of the available data (usually because of the lack of data), an extreme worst-case value is used to represent the behavior of concern. This approach was taken in the development of the reference fracture toughness curve for Section III, Appendix G of the American Society of Mechanical Engineers (ASME) Pressure Vessel Code (Fig. 1) [*3*]. Although satisfactory in a deterministic analysis, such a technique is not adequate in a probabilistic approach to structural integrity. A quantitative characterization of data scatter is required.

Most of the effort directed at the evaluation of data scatter in fracture properties has focused on fracture toughness considerations. Typically, it has been reported that scatter on the order of ± 10 to 15 percent of the average is encountered for K_{Ic} testing of high-quality materials.[3] Although such results appear adequate, very little information is currently available regarding the scatter likely to be encountered in other important properties such as K_{Iscc} and corrosion-fatigue crack growth rate data. In fact, the small amount of data which do exist in these areas are disturbing. Specifically, in one instance involving a single test procedure—more than a dozen replicate tests—specimens from the same forging and an extremely reproducible environ-

[3]The data in Fig. 1 represent several different steels and two different test methods and, as such, do not illustrate this low scatter.

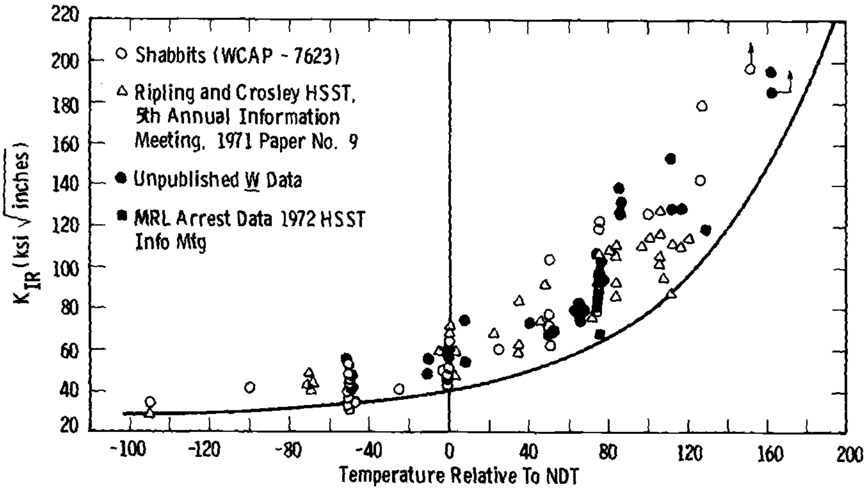

FIG. 1—*Derivation of curve of reference stress-intensity factor* (K_{IR}).

ment (H_2S gas), K_{Iscc} was found to vary by more than ± 20 percent of the average value [*4*]. In a round-robin investigation of K_{Iscc} performance currently being conducted by ASTM Committee E24.04.02, data scatter on the order of ± 30 percent has been observed [*5*]. These data represent results from 14 different laboratories with the same material and environment and a common specimen design. In view of such results it is hard to justify the current practice of duplicate tests to establish K_{Iscc}. Obviously two tests are not sufficient to characterize behavior that may involve as much as ± 30 percent scatter.

A systematic evaluation of scatter in corrosion-fatigue crack growth rate data has yet to be reported. However, such scatter can be expected to exceed the factor of 2 to 3 on growth rate, *da/dN*, typically encountered in inert environment tests [*6*].

In view of the magnitude of data scatter encountered in environment fracture properties, it is apparent that a significant effort is required to both define the variability that can be expected in such tests and to develop recommendations regarding minimum testing requirements. Only when this information is available will it be possible to properly incorporate such data into a rational probabilistic fracture mechanics methodology.

Prior Loading Effects

The potential problems associated with the characterization of data scatter can have a significant impact on the successful use of fracture mechanics. However, there are other areas of concern associated with material characterization that can be even more important. Most of these problems are related directly to questions regarding the applicability of conventional fracture mechanics material properties to actual service loading conditions. Of particular concern is the effect of prior mechanical loading on subsequent crack growth and fracture behavior.

The fracture toughness parameter, K_{Ic}, is intended to define the critical combination of applied stress and defect size required to cause fracture under linear-elastic, monotonic loading conditions involving a single application of load. The stress-corrosion threshold parameter, K_{Iscc}, defines the onset of environment-induced crack extension under static loading and, again, for one application of load. However, rarely do such tests represent actual service loading conditions. In general, we are much more likely to encounter some kind of prior loading ranging from a few periodic "start-stop" cycles to extensive high-cycle fatigue. Thus, a valid question regarding the use of such parameters involves the potential impact of prior loading on these properties.

Prestressing—Prestressing, for the purpose of this discussion, refers to limited periodic loading beyond the normal expected loading of the hardware. Virtually all engineering structures are likely to be subjected to prestressing or even overloading as the result of fabrication, shipping and handling, proof-testing, and transient loading is service. Such irregular loading is likely to have a very significant effect on the subsequent crack growth and fracture behavior of the material.

The effect of periodic load excursions and transients on fatigue crack growth rate behavior has been the subject of investigation for several years. Although a universally applicable predictive model has yet to be developed, it has been clearly demonstrated that such load fluctuations can significantly retard or even stop a growing fatigue crack [7].

However, very little quantitative information exists regarding the potential impact of prestressing on K_{Ic}, K_{Iscc}, or environment-induced static-load crack growth. Obviously, if prestressing can alter the fracture properties of a material, it is important to be able to characterize this behavior in a risk analysis.

The question of prestressing has been addressed to some extent in the development of the ASTM Test for Plan-Strain Fracture Toughness of Metallic Materials (E 399-78a) and it has been shown that prior loading at a sufficiently high stress level can significantly alter (increase) the apparent value of K_{Ic}. Thus, the recommended practice limits the magnitude of prior loading in K_{Ic} testing. Equivalent restrictions apply to other crack growth and fracture tests. However, these restrictions are somewhat arbitrary and it is not possible to quantitatively predict the impact of prior loading on subsequent fracture toughness performance.

Limited data exist which show that prestressing can significantly alter the environment-induced crack growth and fracture behavior of a material.

Carter has shown that prior tension loading in air can increase the measured value of K_{Iscc} (AISI 4340 steel in seawater) by at least a factor of 2 [*8*]. In addition, it has been shown that prestressing in air prior to loading in a detrimental environment can significantly alter the notched-body fracture behavior of high-strength steels [*9*]. Such observations indicate that prestressing can have a significant effect on fracture performance. Consequently, where applicable, this behavior must be addressed in a rational life-prediction analysis.

Cyclic Loading—Another area of concern related to prior loading effects involves the potential impact of cyclic loading on K_{Ic} or K_{Iscc} parameters. Specifically, does cyclic loading to failure or the onset of environmental cracking yield the same critical values of K_{Ic} and K_{Iscc} as the more conventional (monotonic or static) tests?

Again, this problem has been addressed in the development of the current ASTM specification for K_{Ic} testing (E 399-78a) and it has been shown that fatigue precracking at high stress levels (approximately 60 percent of K_{Ic} or higher) can significantly alter the value of K_{Ic}. Thus, the recommended practice limits the magnitude of the precracking conditions. More detailed studies of such behavior have indicated the potential severity of this problem.

Dowling has examined the impact of cyclic loading to failure on the K_{Ic} fracture toughness of several intermediate-strength steels (ASTM A533B, A469, and A470) and a high-strength aluminum alloy (7075-T651) [*10*]. For the case of the aluminum alloy and the A533B (manganese-molybdenum) and A469 (nickel-chromium-molybdenum-vanadium) steels, cyclic loading to failure resulted in a K_{Ic}-value essentially equal to that measured as the result of a conventional rising-load K_{Ic} test. The data developed for the 7075-T651 aluminum alloy are shown in Fig. 2. For the ASTM A470 (chromium-molybdenum-vanadium) steel, however, failure as the result of cyclic loading yields critical K_I-values about twice as high as those obtained from a standard K_{Ic} test. These data are shown in Fig. 3. Such results imply that cyclic loading to failure, at least in some materials, may significantly elevate the effective toughness. If this behavior occurs in a real structure, a problem obviously exists as to what critical toughness value should be used in a risk analysis. Perhaps an even more important question is, Can cyclic loading lead to failure below the established K_{Ic}-value? Limited data developed by Troshchenko et al show that such behavior can occur [*11*].

This case is illustrated in Fig. 4 for two low-strength [345 MPa (50 ksi) yield strength] structural steels tested at low temperature. Note the severe degradation in toughness associated with cyclic loading to failure. Such behavior can have a significant impact on structural performance. Consequently, additional effort is required to understand the mechanisms involved and to permit the incorporation of the appropriate critical toughness values into an accurate probabilistic life prediction. The concern for cyclic loading

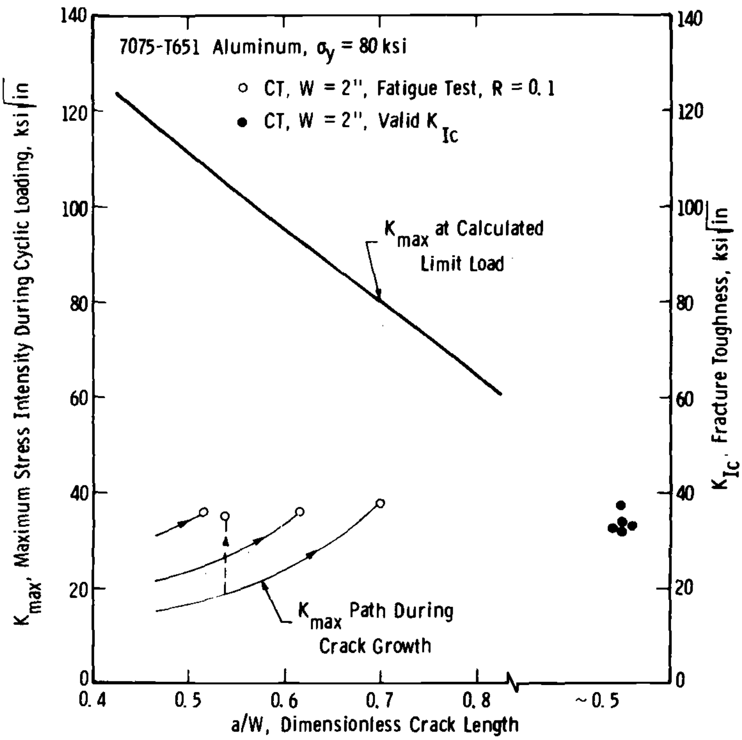

FIG. 2—*Fracture toughness failures terminating fatigue crack growth in 7075-T651 aluminum (Dowling).*

effects on K_{Ic} toughness is equally applicable to elastic-plastic fracture criteria; for example, J_{Ic} and J-resistance curves.

The potential effect of cyclic loading on toughness is obviously an important concern in a rational life prediction analysis. However, the problem may be even more significant for the case of environmental behavior where K_{Iscc} is used to establish the critical combination of applied stress and flaw size below which environment-induced cracking is not expected to occur under static loading conditions. Again we are faced with the problem of how well a conventional laboratory test represents actual service performance, which rarely, if ever, involves a single application of load or static loading.

It is well recognized that under cyclic loading, environment-accelerated fatigue crack growth behavior can occur at stress-intensity-range (ΔK) levels far below the K_{Iscc} established from a static load test. In addition, it is well known that both loading frequency and waveform can have a very significant effect on crack growth rate [12]. Specifically, for a given material-environment system there is a particular frequency at which the crack growth

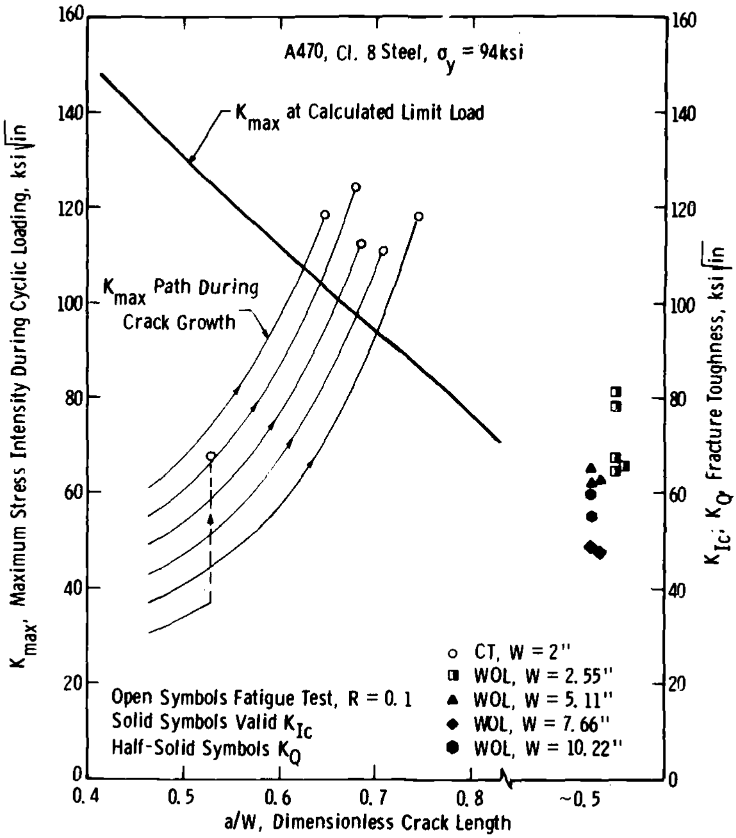

FIG. 3—*Unexpected fully plastic limit load failures following fatigue crack growth in A470 steel (Dowling).*

rate is maximized. A dramatic illustration of environment-assisted cracking below K_{Iscc} and the effect of loading frequency is provided in Fig. 5 [*13*]. In view of such observations related to corrosion-fatigue behavior, it is reasonable to question the use of the K_{Iscc} parameter to define the threshold for environment-induced cracking in real structures which experience periodic loading. Periodic or cyclic loading may significantly alter the K_{Iscc} threshold parameter. The basic question becomes: What constitutes cyclic loading and when does corrosion-fatigue behavior prevail over static loading predictions? In other words, when can we use K_{Iscc} as a meaningful design parameter? Does one "start-stop" loading cycle per day, month, etc. represent cyclic or static loading conditions, and what kind of information is required to make useful life predictions? Unfortunately, the data required to address this very important question do not exist. Very-low-frequency con-

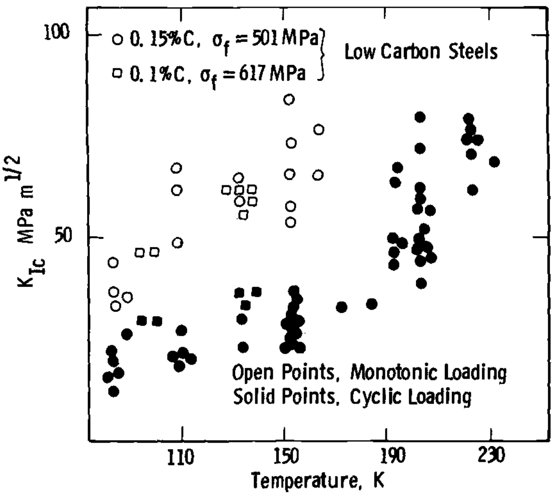

FIG. 4—*Effect of cyclic loading on apparent* K_{Ic} *(Troshchenko).*

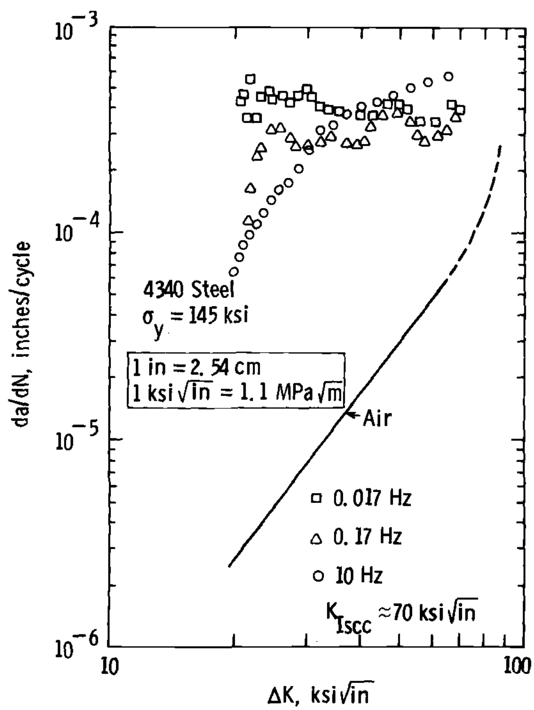

FIG. 5—*Fatigue crack growth rates in 345 kPa (50 psig)* H_2S *(Brose).*

trolled ramp corrosion-fatigue data must be developed and compared with conventional static loading K_{Iscc} data to validate the use of this design parameter.

Time-Dependent Behavior

Questions regarding the use of the K_{Iscc} parameter are not limited to concerns associated with mechanical loading interactions alone. Another extremely important area is time-dependent behavior. Environment-induced cracking is a time-dependent phenomenon controlled by the kinetics of the material-environment-stress reactions. Thus, parameters such as exposure time in the environment and nonsteady-state conditions can impact subsequent fracture behavior.

Exposure Time—Exposure time in the environment of concern is widely known to have an important effect on crack initiation and growth behavior. However, the question as to how much time is required to yield a satisfactory K_{Iscc} parameter has not been resolved. In addition, it appears that different material-environment systems require different amounts of exposure time to yield a valid K_{Iscc} [7].

Presently, the typical approach to the determination of a K_{Iscc}-value for design purposes involves exposure times of significantly less than 10 000 h. In addition, rarely is the testing time noted as an integral part of the material properties data. As a result, relatively short-time test data are often used to estimate very-long-time material performance. The potential impact of exposure time on K_{Iscc} data is given in Table 1. Note that in this test, 879 days (2.4 years) were required to develop a satisfactory estimate of K_{Iscc}. When

TABLE 1—*Results of accelerated versus long time* K_{Iscc} *testing.*

Material: 155 ksi[a] σ_{ys} Ni-Cr-Mo-V[b] Steel (ASTM A471)
Environment: 212°F[c] Steam + 40 ppm 0_2
Test: IT WOL Bolt Loaded (Decreasing K_I)

Exposure Time, h (days)	Crack Extension, cm. (in.)	Stress Intensity, MPa$\sqrt{m}$ (ksi$\sqrt{in.}$)
0	0	88 (80)
5 200 (217)	0.66 (0.26)	77 (70)
14 100 (587)	1.98 (0.78)	46 (42)
21 100 (879)	2.69 (1.06)	23 (21)

Rising Load K_{Iscc} Test 50 psig[d] H_2S
Time: 150-min Apparent K_{Iscc} 22.5 MPa$\sqrt{m}$ (20.5 ksi$\sqrt{in.}$)

[a] 155 ksi = 1062 MPa.
[b] Nickel-chromium-molybdenum-vanadium.
[c] 212°F = 100°C.
[d] 50 psig = 345 kPa.

crack extension does occur as noted in Table 1, confidence in the test is enhanced and the results are meaningful. However, when no cracking occurs after a given amount of exposure time, we are faced with an interpretation problem—either the test was not long enough or the material is resistant to the environment.

Problems with exposure time or crack incubation make the development of accelerated K_{Iscc} testing techniques very attractive. As shown in Table 1, procedures such as the rising-load hydrogen sulfide test can significantly reduce required testing time [*14*]. However, accelerated testing techniques, in themselves, give rise to other problems. Specifically, do the accelerated testing conditions truly represent the intended service conditions?

Based on the existing problems associated with the use of K_{Iscc} as a design parameter, it is obvious that further effort is required to qualify the validity of this parameter for use in a rational life-prediction analysis. A detailed evaluation of the impact of realistic loading variables on K_{Iscc} must be conducted. From the discussion presented here, it appears that some type of limited prior loading in the environment of concern may offer the potential to reduce the crack incubation time and, thus, yield a meaningful accelerated test.

Nonsteady-State Effects—Another important aspect of environment-induced cracking behavior which can have a direct influence on life-prediction accuracy involves the effect of nonsteady-state behavior on crack growth performance. The practical significance of this time-dependent behavior is that it can cause laboratory data to misrepresent crack growth rates which occur under service conditions.

A basic tenet associated with the use of fracture mechanics to characterize crack growth rate behavior is a unique geometry-independent relationship between the rate of crack growth and the crack tip stress-intensity factor, K. However, recent data developed on low-alloy steels exposed to aqueous environments under both static and cyclic loading indicate that the relationship between growth rate and stress intensity can be strongly affected by the initial test conditions, test interruptions, and changes in loading variables. Hudak and Wei have shown that these phenomena are caused by nonsteady-state environmental effects associated with the underlying kinetics of hydrogen embrittlement at the crack tip [*15*]. The potential significance of such behavior is illustrated in Fig. 6, where the static load crack growth rate behavior of an AISI 4340 steel exposed to water is plotted as a function of K_I. Note the strong dependence of da/dt on initial K-level. Similar results have been observed under cyclic loading where, in this case, the delayed behavior is often misinterpreted to reflect a fatigue threshold. Such transient growth rate phenomena can be important both in the evaluation of test data and in design life considerations. It is not yet possible, however, to adequately characterize such behavior for incorporation into reliability analyses despite the potential impact on life predictions.

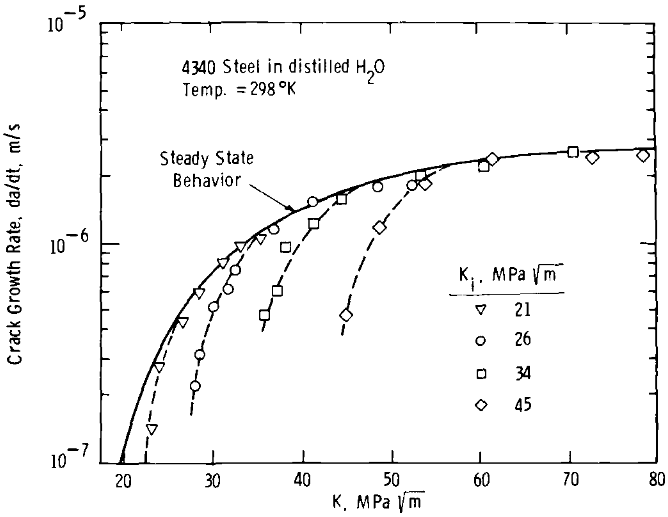

FIG. 6—*Dependence of static-load crack growth kinetics on initially applied stress-intensity factor,* K_i *(Hudak and Wei).*

Defect Characterization

Perhaps the weakest link in the successful application of fracture mechanics technology is the area of defect characterization or, more specifically, nondestructive inspection limitations. An adequate fracture mechanics analysis requires a detailed quantitative characterization of the type of defect or defects which exist or are likely to exist in the structure of concern. Not only defect size (length and depth), but information regarding shape, orientation location, and spacing must be available. Until very recently, the sensitivity, accuracy, and reliability of various nondestructive evaluation (NDE) techniques have been a matter of debate and extensive discussion. As the result, quantitative information regarding flaw detection capabilities were not available for incorporation into fracture mechanics analyses. At best, an estimate of minimum detectable defect size based on past experience was used in the life prediction considerations. Although adequate from a deterministic point of view, such an approach is not satisfactory for a probabilistic analysis. Improved methods for the characterization of flaw detectability are required.

Only recently has the subject of flaw detectability received the kind of attention required to provide rational guidelines for use in probabilistic life predictions. The bulk of this work has been sponsored by the U.S. Air Force and, consequently, the work has focused on the characterization of aircraft structures. An example of the type of data being developed is illustrated in Fig. 7. These data reflect the ability of various NDE methods to detect cir-

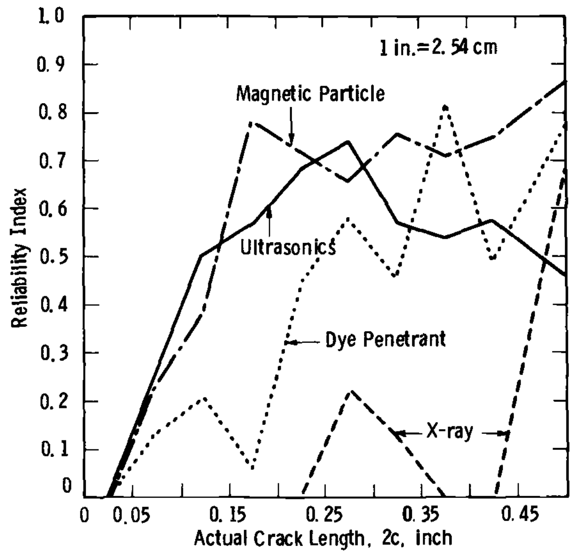

FIG. 7—*Comparison of four NDT techniques on reliability of flaw indications in steel cylinders (Packman et al).*

cumferential surface flaws (fatigue cracks) on the outside surface of a 7.62-cm-diameter, (3 in.) 0.635-cm-wall, (1/4 in.) steel cylinder [*16*].

The reliability index used to analyze the data includes consideration of: (1) sensitivity—the ability to detect the presence of a flaw (percent of flaws found); (2) size accuracy—the ability to establish defect length; and (3) location accuracy—axial and radial measurement of flaw location. The flaw depth is inferred from the length measurement assuming a fixed length-to-depth ratio. Among the important conclusions associated with this work is the fact that low reliability is due to the inability to accurately establish defect length. The poor sensitivity of the methods for detecting flaws smaller than 0.5 cm (0.200 in.) long is also important. Such data provide valuable insight into NDE capabilities and the complexities involved in the characterization of such information. However, the reliability index used in this work provides only a qualitative measure of performance.

More recent studies have addressed the statistical characterization of NDE capabilities [*17*]. An example of such data is shown in Fig. 8. In this case, various NDE inspection techniques were evaluated using controlled surface-flawed test specimens. Both flaw detection probability and the associated confidence levels were established. The probability of detection (POD) at the 95 percent confidence level is noted. These data mean that the NDE procedure will find POD × 100 percent of the flaws in the given size range, 95 percent of the time. Such attempts to quantify flaw detection capabilities

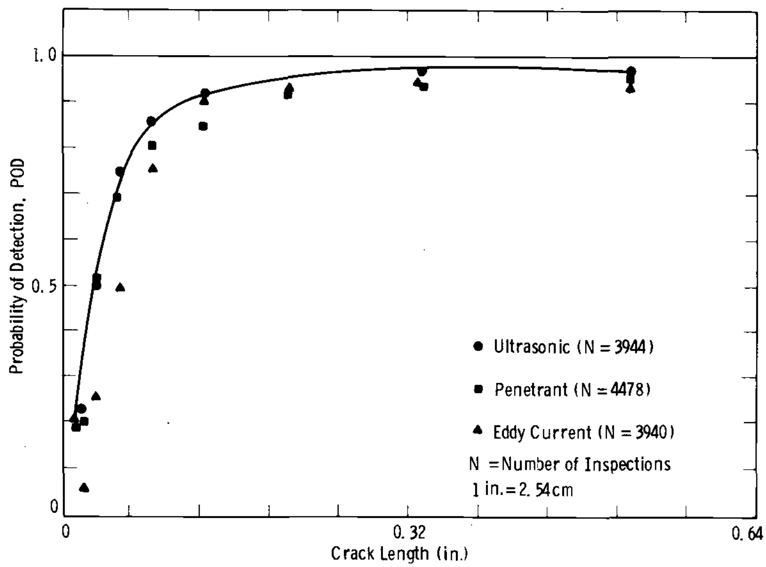

FIG. 8—*NDE methods sensitivity for flat plates by point estimate method (Chang et al).*

represent a very significant advancement in structural reliability considerations. However, these data are applicable only to the specific inspection procedure, detect type, and hardware involved. Considerably more work is required to develop information regarding the characterization of defect shape, multiple defects, subsurface defects, and other areas of concern involved in a fracture mechanics analysis. In view of the formidable problems and complexities associated with the nondestructive inspection aspects of life prediction, it appears that this area will remain a major limitation in the development of a probabilistic fracture mechanics approach to design.

Analytical Problems

Problems related to the analytical aspects of the application of existing fracture mechanics technology are essentially limited to the characterization of elastic-plastic behavior and the evaluation of very complicated loading configurations which require advanced three-dimensional stress analysis techniques. From the practical point of view, these limitations are less restrictive than the existing material characterization and nondestructive inspection problems. More specifically, the "state of the art" associated with the analytical aspects of applied fracture mechanics is far more advanced than the other areas of concern. However, there are a few problem areas which often develop in typical applications. For the most part these problems involve the analysis of specific defect configurations and include small-defect and multiple-defect considerations.

Small Defects

Existing requirements for state-of-the-art crack growth and fracture testing include very explicit criteria regarding the minimum crack length required to yield valid test results. Specifically, for a compact toughness specimen, the total crack length (crack starter notch plus fatigue crack as measured from the centerline of loading) must be sufficiently long to eliminate any undesirable interaction of the loading arrangement with the crack tip. In addition, the required fatigue precrack must be long enough to eliminate any influence of the crack starter notch on the crack tip. As a result of these criteria, a typical toughness test specimen has a relatively large preexisting crack [on the order of 2.54 cm (1 in.) long in a 2.54-cm-thick (1 in.) specimen]. In actual service considerations, rarely are we concerned with initial defects this large. Most often we must address the performance of initial defects on the order of the detection limit of the applicable NDE procedure. In view of the crack size requirements for fracture mechanics testing versus the type of defects most likely of concern in actual applications, it is reasonable to question the applicability of existing fracture mechanics concepts to small flaws. More specifically, is there a defect size below which conventional linear-elastic fracture mechanics concepts do not apply? If so, it is obvious that such a limitation must be recognized in any attempt to conduct a rational, quantitative life-prediction analysis.

Clark has addressed the small-defect problem for the case of high-strength steels and has reported that as long as the crack is at least 25 times larger than the associated crack-tip plastic zone size

$$\left[r_p = \frac{1}{6\pi} (K_I/\sigma_{ys})^2 \right]$$

linear elastic fracture mechanics concepts are directly applicable [*4*]. This requirement is about one-half that included in the ASTM Method E 399-78a

$$a = 2.5\,(K_I/\sigma_{ys})^2$$

However, even for the less-restrictive criterion, the applicability of fracture mechanics concepts to small defects can become an important question. Figure 9 shows a graphical presentation of the empirical plastic zone size to crack size criterion for the monotonic loading case as reported by Clark. Note that based on these results, the minimum-size surface flaw that could properly be analyzed in a 690-MPa (100 ksi) yield strength material at an applied stress intensity of 66 MPa$\sqrt{m}$ (60 ksi$\sqrt{in.}$) is about 1.27 cm (0.500 in.) deep. Obviously, the successful use of fracture mechanics requires that defects

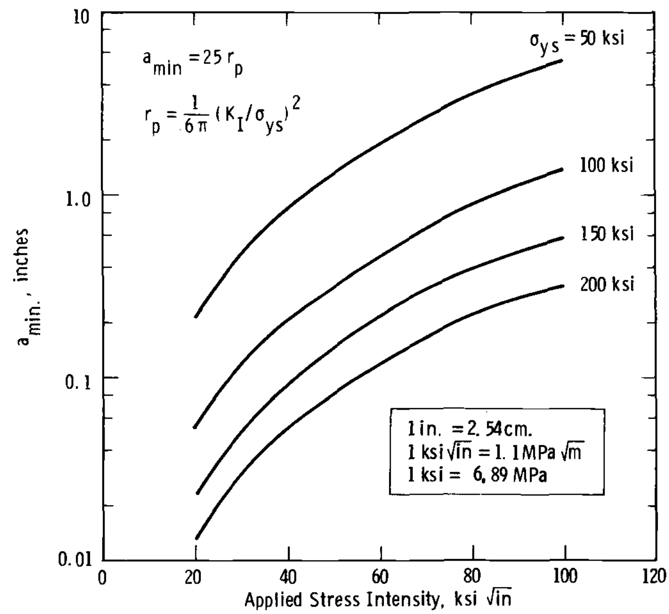

FIG. 9—*Graphical presentation of small-defect criteria;* a $\geq$ *25* r_p.

smaller than that predicted from Fig. 9 be capable of accurate analysis. Even for the case of cyclic loading where the prevailing plastic zone is likely to be smaller, questions exist regarding the analysis of small-defect performance. Unfortunately, adequate data do not exist which define the defect size below which LEFM analysis is no longer valid. In view of the typical defect sizes of concern in actual applications, it is apparent that the small-defect problem must be resolved in order to improve the risk analysis capability. In addition, concerns regarding small defects may even be more important in the area of elastic-plastic fracture behavior.

Interacting Defects

Another extremely important area of concern associated with the impact of analytical capability on life prediction involves the problem of multiple interacting defects (clouds and cluster-type discontinuities). Such defects are relatively common in heavy section and welded structures. However, the techniques required to properly analyze the effect of multiple defects on structural performance do not exist. The primary limitations include both the capability of existing nondestructive inspection techniques (typically, ultrasonic inspection) to adequately define multiple defects (size, number, shape, spacing, etc.) and when defined, the ability to incorporate the defect information into an adequate structural analysis. Presently, two different approaches are used to estimate the influence of multiple defects on fracture behavior. In one case, a grouping of multiple defects is handled as a single continuous flaw simply by constructing an envelope around the discontinuities and proceeding with a fracture mechanics analysis involving a single large defect. The other approach involves an attempt to establish the unflawed cross-sectional area of a plane through the defect (net section stress analysis) [*18*]. The applied stresses along this plane are then elevated in proportion to the reduction in net section area, and the behavior of the remaining sound material is predicted using the conventional mechanical properties of the alloy. Neither of these techniques has been verified as adequate and many questions remain regarding their usefulness in life predictions. A rational probabilistic approach to structural reliability requires that such analyses be quantified in terms of accuracy and applicability.

Very little data exist regarding the characterization of multiple defects and an extensive research and development effort is required in this area. Recent developments in the use of powder metallurgy materials containing preplaced artificial defects offer a potential technique for the investigation and evaluation of multiple discontinuities [*19*]. Both inspection capabilities and analytical methods can be characterized under well-controlled conditions. It is recommended that such a technique be used to develop an acceptable method for both the detection and analysis of multiple defects under various loading conditions.

Discussion and Summary

The success of cracked-body fracture mechanics as an important tool for improved structural integrity has been phenomenal. No other analytical technology offers the ability to characterize the interactions between the primary material, applied stress, and inspection considerations which subsequently control the crack growth and fracture properties of a component or system. In addition, the use of the technology as a research tool has done much to improve the understanding of material behavior and fracture mechanisms. Perhaps the greatest contributions of fracture mechanics concepts to structural integrity problems are associated with the current areas of research in the field: elastic-plastic fracture, notched body behavior, creep-fatigue-environmental interactions, and quantitative structural risk analysis. In view of the rapid growth in this relatively new technology and the tremendous potential offered by further advances, it is not surprising that a few problem areas such as those addressed in this paper remain to be resolved. However, because of the current high level of activity, it is also important to step back and review the state of the art with regard to areas of concern which may require further attention. This has been the approach taken in the development of this paper.

It has been noted that several potential problems exist in the application of fracture mechanics to structural integrity considerations. It was also noted that these problem areas became more important as the technology moves from the current deterministic approach to the more valuable probabilistic analysis. The pertinent areas of concern identified here relate to material characterization, flaw detection, and analytical considerations. With regard to material characterization, it has been shown that data scatter, prior loading effects, and time-dependent fracture performance require further investigation such that representative material properties data can be developed for use in design.

Problems associated with flaw detection and definition remain a major limitation in the successful use of fracture mechanics. However, the development of improved quantitative nondestructive inspection techniques and related probability-of-detection considerations do not appear to be receiving a degree of attention proportional to their impact on structural risk analysis.

The analytical aspects of fracture mechanics represent the most advanced area of the technology. Applied stress and stess-intensity information can be developed for all but the most complex structural configurations and loading situations. However, two analytical problems arise very often in the application of fracture mechanics. These areas of concern include the characterization of both relatively small defects and interacting defects. Although such situations can be approximated analytically, existing limitations in the procedures require further substantiation and verification of the predictions.

The potential problem areas addressed in this paper can have a significant impact on the successful application of fracture mechanics to structural integrity considerations. In each case, the area of concern can overshadow even the most advanced probabilistic life prediction techniques. Consequently, it is apparent that the advancement of fracture mechanics concepts into the area of quantitative risk assessment requires a combined effort which includes both the development of an appropriate statistical methodology and the resolution of the existing limitations.

References

[1] Jouris, G. M. and Shaffer, D. H., *International Journal of Pressure Vessels and Piping*, Vol. 6, 1978, pp. 3-21.

[2] Tetelman, A. S. and Besuner, P. M., Fracture 1977, 4th International Conference on Fracture, Waterloo, Ont., Canada, Vol. 1, 1977, p. 137-156.

[3] PVRC Ad Hoc Task Group, "PVRC Recommendations on Toughness Requirements for Ferritic Materials," Welding Research Council Bulletin No. 175, Aug. 1972.

[4] Clark, W. G., Jr. in *Cracks and Fracture, ASTM STP 601*, American Society for Testing and Materials, 1976, pp. 138-153.

[5] Wei, R. P., "Progress Report on ASTM Task Group E24.04.02 Round Robin," Presented at Atlanta, Ga., American Society for Testing and Materials, March 1979.

[6] Clark, W. G., Jr. and Hudak, S. J., Jr., *ASTM Journal of Testing and Evaluation*, American Society for Testing and Materials, Vol. 3, No. 6, 1975, pp. 454-476.

[7] Rolfe, S. T. and Barsom, J. M., *Fracture and Fatigue Control in Structures*, Prentice-Hall Inc., Englewood Cliffs, N.J., 1977.
[8] Carter, C. S., *Metallurgical Transactions*, Vol. 3, Feb. 1972, pp. 584-586.
[9] Clark, W. G., Jr., "Effect of Prestressing on Stress Corrosion Crack Initiation in High Strength Type 4340 Steel," presented at the 12th National Symposium on Fracture Mechanics, St. Louis, Mo., 21 May 1979, to be published.
[10] Dowling, N. E. in *Flaw Growth and Fracture, ASTM STP 631*, American Society for Testing and Materials, 1977, pp. 139-158.
[11] Troshchenko, V. T. et al, Fracture 1977, 4th International Conference on Fracture, Waterloo, Ont., Canada, Vol. 3 June 1977, pp. 683-686.
[12] Barsom, J. M., *Journal of Engineering Fracture Mechanics*, Vol. 3, No. 1, July 1971.
[13] Brose, W. R., unpublished Westinghouse R&D Center data.
[14] Clark, W. G., Jr. and Landes, J. D. in *Stress Corrosion—New Approaches, ASTM STP 610*, American Society for Testing and Materials, 1976, pp. 108-127.
[15] Hudak, S. J., Jr. and Wei, R. P. in *Proceedings*, 5th International Conference on Structural Mechanics in Reactor Technology, West Berlin, Germany, 13-17 Aug. 1979.
[16] Packman, P. F. et al, "The Applicability of a Fracture Mechanics Nondestructive Testing Design Criterion," U.S. Air Force Report AFML-TR-68-32, Air Force Materials Laboratory, Wright-Patterson AFB, Ohio, May 1968.
[17] Chang, F. H. et al., "Methods for the Determination of the Sensitivity of NDE Techniques," U.S. Air Force Report AFML-TR-76-246, Air Force Materials Laboratory, Wright-Patterson AFB, Ohio, Dec. 1976.
[18] Wells, C. H. and Gelhaus, F. E. in *Proceedings*, American Society of Mechanical Engineers Symposium on Structural Integrity, Washington, D.C., 9-11 May 1979.
[19] Clark, W. G., Jr., in *Fracture Mechanics, ASTM STP 677*, American Society for Testing and Materials, 1979, pp. 303-319.

A. G. Denyer[1]

Fracture Mechanics Technology Applied to Individual Aircraft Tracking

REFERENCE: Denyer, A. G., "**Fracture Mechanics Technology Applied to Individual Aircraft Tracking,**" *Fracture Mechanics: Thirteenth Conference, ASTM STP 743,* Richard Roberts, Ed., American Society for Testing and Materials, 1981, pp. 288–302.

ABSTRACT: The paper presents a crack growth analysis approach to individual aircraft tracking that will meet the intents and objectives of the U.S. Air Force requirements. The structural life definitions are discussed in terms of definitive crack sizes for both the durability and damage tolerance of the structure.

Instituting a tracking program for a specific aircraft fleet requires a background of data relating to baseline spectra, critical structural locations, and expected airplane usage. The sources of such data are outlined. The body of the paper presents a cost-effective crack growth integration technique which makes tracking for durability feasible even if the life is as much as 100 000 h. Closely linked with the crack growth analysis technique is the method of collecting the flight data. The presentation considers two distinct approaches, a pilot form system and a structural loads measuring system. The methodology is being incorporated into the overall tracking system for the USAF T-39 Utility Trainer which will be the first to use the crack growth principle for both durability and damage tolerance tracking. Some T-39 data are presented for explanatory and demonstration purposes.

KEY WORDS: fracture mechanics, crack growth, aircraft tracking, structural life tracking

An Individual Aircraft Tracking Program[2] is a requirement of the U.S. Air Force "Aircraft Structural Integrity Program" (ASIP). The objective of the Individual Aircraft Tracking Program (IATP) is to compute the rate at which the available structural life is being used. The computed life information establishes and adjusts inspection and repair intervals for each critical area of the airframe based on individual airplane usage data. In addition, the data enable planners to use the fleet in the most efficient manner by moving the more theoretically damaged aircraft to less severe duty.

[1]Member of the Technical Staff, Rockwell International, El Segundo, Calif. 90245.

[2]"Aircraft Structural Integrity Program, Airplane Requirements," MIL-STD 1530A (11), Department of the Air Force, 11 Dec. 1975.

The acceptance of fracture mechanics technology provides an attractive method for IAT, primarily because the direct output of the analysis is crack length, a definitive measure of the structural condition. In addition, the concept of crack growth is eminently suitable for prediction of damage tolerance life as well as the durability life. The structural life estimates are directly related to crack growth between specific limits. Formerly, the analytical durability estimates were based on conventional fatigue analysis wherein the structural damage was presented in the somewhat abstract terms of damage fractions (that is, percentage of life used assuming linearly accumulated damage).

The tracking program being prepared for the USAF T-39 Utility Trainer will be the first to use crack growth principles for both durability and damage tolerance life estimates. To date, most crack growth applications to IAT have been directed toward damage tolerance, wherein the initial crack size is the inspectable crack, as defined by the Air Force,[3] and computation of inspection intervals. To obtain estimates of the durability of the structure, however, it is necessary to perform crack growth analysis from small cracks representing the "as manufactured" condition. Extension of the crack growth analysis into the region of very slow growth necessitates development of more cost-effective crack growth schemes, which was accomplished for the T-39 IATP.

In summary, the tracking program consists of:

1. defining the structural life of aircraft and the crack growth limits relating thereto,
2. selecting the critical structural locations to be tracked,
3. collecting flight records from the aircraft fleet, and
4. performing crack growth analysis using the flight records to obtain the accumulated damage and an estimate of remaining life.

Structural Life Definitions

"Durability" is the crack growth life from the "equivalent initial flaw size" to the "economic repair limit." Durability is equivalent to fatigue life.

"Equivalent initial flaw size" represents the intrinsic crack-like defects in the aircraft structure at the time of initial fabrication.

"The economic repair limit" is the crack size which can be repaired without a prohibitively expensive modification of the structure.

"Damage Tolerance" is the crack growth from an "inspectable crack length" to the "critical crack length." Damage tolerance life is equivalent to fracture life.

An "inspectable crack length" is the minimum size detectable crack using nondestructive inspection (NDI) procedures such as Eddy Current devices.

[3] "Airplane Damage Tolerance Requirements," MIL-A-83444 (USAF), Department of the Air Force, 2 July 1974.

The "critical crack length" is the crack length at which rapid unstable crack growth commences.

"Inspection interval" is determined by the damage tolerance life divided by a factor. The factor is dependent on the inspectability of the component and is defined in the footnote 3 reference.

"Remaining life" is the durability minus the aircraft life to date. The relationship of the definitions within the crack growth life is shown in Fig. 1.

Background to the Tracking Program

For older aircraft it has been the practice to perform a durability and damage tolerance assessment (DADTA) before installing an IAT system. The DADTA is very important in providing baseline data for tracking, including the critical structural locations, crack length limits, material properties, and baseline spectra. Fatigue and fracture mechanics analyses and testing conducted during the design phases of the project will provide similar information for new aircraft.

Frequently some results of the Loads/Environmental Spectra Survey will be available to provide baseline spectra and an indication of fleet usage. The Loads Survey Program, described in the first reference (footnote 2), calls for instrumentation of 10 to 20 percent of the fleet in order to record flight parameters necessary for spectrum generation.

In the case of the USAF T-39 Utility Transport/Trainer, a multichannel load recording system was installed on 10 percent of the fleet. The measured parameters included VGH data (airspeed, acceleration, and altitude) as well as gross weight, roll rates, and strain-gage readings at selected structural locations. The complete system also includes mission descriptions.

Crack Growth Limits

The crack growth limits, both initial and final flaw size, are different for durability and damage tolerance analyses and will vary for each structural component as well as for each type of aircraft. The following definitions, which are being used on the T-39 Utility Trainer, are presented as typical examples.

The "equivalent" initial flaw size (EIFS) is used for durability analysis. It is determined statistically using laboratory and analytical procedures. In the case of the T-39, the mean value of EIFS was estimated during the DADTA program to be 0.063 mm (0.0025 in.). The procedures used to obtain this value included microscopic examination of full-scale test fracture surfaces in order to count the striations and determine the initiation of fatigue crack growth. The crack growth curves were then regressed analytically in order to ascertain the theoretical crack size at the beginning of the test (that is, the

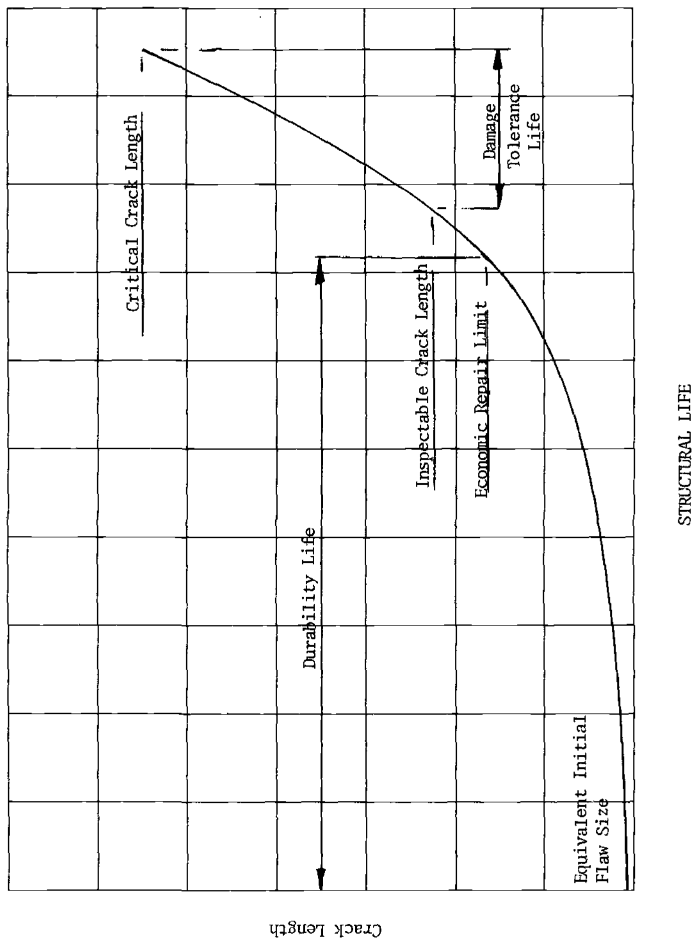

FIG. 1—*Structural life definitions.*

crack size which would result in the same crack growth life using pertinent analytical crack growth procedure).

The limiting flaw size for durability is the economic repair limit which is dependent upon the type of construction. Integrally stiffened machined wing skins, for example, are extremely difficult to repair if cracked. The skins for the most part cannot be patched, as not only would the doublers need to be machined to match the wing skin contours but the attachment holes necessary to assemble the doubler would cause stress concentrations in the unpadded machined pockets and at the doubler terminations, causing loss of fatigue life. Frequently, therefore, if replacement wing skins are considered an uneconomic repair, the limiting durability flaw size is a bolt hole crack of the size that can be reamed for an acceptable oversize bolt for which 0.762 mm (0.03 in.) is an approximation. Current design practices for fuselage structure of conventional skin, frame, and multiple riveted stringers make for relatively simple repairs. For such structure, the economic repair limit may be defined as a predetermined fraction of the critical crack length or a length which statistically can be related to extensive cracking at various locations in the component.

The initial flaw size for damage tolerance analysis is defined as the inspectable crack length (footnote 3). For the purposes of damage tolerance tracking at selected critical locations, the structure is treated as a slow crack growth structure whether or not the component is designed to have multiload paths. For the T-39, where the critical locations are attachment holes, an initial crack size of 1.27-mm (0.05 in.) corner crack at the bolt hole was assumed.

The allowable flaw size for damage tolerance analysis is the critical crack size computed with fracture mechanics principles using the maximum load derived from static design conditions or the maximum spectrum load from fatigue analysis or flight records, whichever is greater.

Crack Growth Calculation Methods

The cycle-by-cycle integration of crack growth characteristics, many versions of which are in industry use for detailed fracture mechanics analysis of airframes, is, generally speaking, too costly in computer time for IAT purposes. An indication of the magnitude of the IAT task can be obtained by considering the following desired output data. The calculation of "life used to date" as well as the remaining life estimate for durability and damage tolerance necessitates crack growth analysis from the EIFS to the critical crack length. These values may be in excess of 50 000 flights for a transport aircraft with each flight containing up to 100 cycles of significant loads. Typically, IAT crack growth calculations are reported twice a year at some 6 to 50 structural locations per aircraft for a fleet of 100 to 500 aircraft. In addition to cost considerations, the crack growth method should be suitable for whatever usage data collection system be incorporated, and must achieve acceptable technical quality. The method presented in this paper, and the technical quality assessment, was a comparison with the baseline crack growth analysis performed with the cycle-by-cycle integration method. The baseline cycle-by-cycle method described by Szamossi[4] and outlined in the next paragraph incorporates one of the most efficient crack growth integrations available and probably would be economically acceptable for damage tolerance tracking. However, additional economies were considered necessary for extension into the slower growth durability region for which a highly economical graphical integration method was developed.

Baseline Crack Growth Calculation Method (Cycle-by-Cycle)

The computer program EFFGRO (footnote 4) was developed for calculating crack growth in a cyclic loaded structure based on linear elastic fracture mechanics (LEFM) principles. Based on the LEFM concept, the stress state in the surrounding crack tip can be characterized by a single parameter, the crack-tip stress-intensity factor, K. Furthermore, the subcritical flaw growth can be characterized as a function of the cyclic range of the stress-intensity factor. The EFFGRO program computes the crack growth per cycle (da/dN) using a crack growth rate equation, fitted to material property subcritical flaw growth rate data, and performs the integration to obtain the complete crack growth curve (a versus flights).

Fatigue Crack Growth Rate Equation—Walker equation:

$$da/dN = C\,[(1 - R)^{m-1} \times \Delta K]^n \quad \text{if } R > 0$$

$$da/dN = C\,[(1 - R)^{q} \times K_{max}]^n \quad \text{if } R < 0$$

where

C, m, n, q = are material properties,
R = ratio of applied stress ($\sigma_{min}/\sigma_{max}$),
K_{max} = stress intensity due to σ_{max},
K_{min} = stress intensity due to σ_{min}, and
$\Delta K = K_{max} - K_{min}$.

*Stress-Intensity Factor Solution (*K)—EFFGRO has the capability of calculating stress-intensity factors of various cracked structural configurations. The stress-intensity factor (K) is a function of the remotely applied tension stress, the structural geometry, the local stress distribution, the crack location, size, and shape

$$K = (M_w \times M_f \times M_b \times M_g)\sqrt{\frac{\pi a}{Q}}$$

[4]Szamossi, M., "Crack Propagation Analysis by the Vroman Model—Computer Program EFFGRO," Rockwell International, Feb. 1972.

where

M_w = finite-width correction factor

$$= \left[1 = 0.025\left(\frac{2c}{W}\right)^2 + 0.06\left(\frac{2c}{W}\right)^4\right]\sqrt{\sec\frac{\pi c}{W}}$$

M_f = front face correction factor = $0.1 - 0.12\,(1 - a/2c)^2$
M_b = back face correction factor; see Table 1
M_g = geometric correction factor due to bolt hole; see Table 2
σ = remotely applied tensile stress
a = crack size (depth)
c = crack length on surface
W = plate width
t = plate thickness
r = bolt hole radius
Q = flaw shape correction factor
$= \Phi^2 - 0.212\,(\sigma/\sigma_y)^2$

$$\Phi = \int_a^{\pi/2} [1 - \{1 - 4(\sigma/2c)^2\}\sin^2\theta]\,d\theta$$

σ_y = yield stress

Load Interaction Model—EFFGRO provides a method to account for load interaction effects of overload retardation using the Vroman model.

TABLE 1—*Back face correction factor* (M_b).

$a/2c$ \ a/t	0.1	0.2	0.3	0.4	0.5	0.6	0.7	0.8	0.9	1.0
0.05	1.0	1.02	1.04	1.05	1.08	1.13	1.2	1.36	1.76	1.81
0.10	1.0	1.0	1.02	1.03	1.06	1.1	1.16	1.27	1.53	1.64
0.20	1.0	1.0	1.0	1.01	1.04	1.07	1.13	1.20	1.37	1.53
0.30	1.0	1.0	1.0	1.01	1.02	1.05	1.09	1.16	1.28	1.37
0.40	1.0	1.0	1.0	1.01	1.02	1.04	1.07	1.13	1.24	1.28
0.50	1.0	1.0	1.0	1.0	1.01	1.02	1.05	1.10	1.19	1.21

NOTE: a = crack depth; c = crack length on surface; t = plate thickness.

TABLE 2—*Geometric correction factor due to bolt hole* (M_g) *(Data for one crack from bolt hole).*

c/r	0.00	0.1	0.2	0.3	0.4	0.5	0.6	0.8	1.0	2.0	3.0	5.0	10.0
M_c	3.37	2.73	2.30	2.04	1.06	1.73	1.64	1.47	1.37	1.06	0.94	0.81	0.75

NOTE: r = bolt hole radius.

The effective K due to overload retardation is given by

$$\Delta K_{\text{eff}} = (K_{\max} - K_{\min}) - 0.33 \left[\left(\sqrt{\frac{a_{\text{ol}} + R_{Y_{\text{ol}}}{}^{-\text{a}}}{R_{Y_{\text{ol}}}}} \right) K_{\max\,\text{ol}} - K_{\max} \right]$$

where $K_{\max}$ and $K_{\min}$ are stress-intensity factors corresponding to the currently applied load cycle ($\sigma_{\max}$ and $\sigma_{\min}$) and a_{ol}, $Y_{Y_{\text{ol}}}$ and $K_{\max_{\text{ol}}}$ are the values corresponding to previously applied overload. The value of ΔK_{eff} is then used in the crack growth rate equation.

Integration Scheme—The EFFGRO program contains a specialized integration routine where an initial crack length is given and da/dN is integrated to yield a relationship between a and n for a given load spectrum. It is based on the fact that small changes in crack length have a minimal effect on the crack growth rate. The following paragraphs describe the integration procedure, which was originated by Vroman (footnote 4).

Step	Maximum Stress	Minimum Stress	Cycles/Flight
1	max 1	min 1	n 1
2	max 2	min 2	n 2
3	max 3	min 3	n 3
.	.	.	.
.	.	.	.
.	.	.	.
i	max i	min i	n i

The integration scheme proceeds by considering a load step (i) and using $\sigma_{\max\,i}$, $\sigma_{\min\,i}$ to calculate $K_{\max}$, $K_{\min}$, R, and da/dN.

The value of $0.01a/(da/dN)$ is then compared with n_i. If $0.01a/(da/dN)$ is greater than n_i, the crack growth for that load step is $a = n_i \times da/dN$. a is increased by Δa and the program proceeds to the next step.

If $0.01a/(da/dN)$ is less than, or equal to, n_i, the number of cycles to grow $0.01a$ is $0.01a/(da/dN)$. This value is subtracted from n_i, the crack size a is increased by $0.01a$, and the load step is reconsidered. This process continues with $0.01a(da/dN)$ being compared with the remaining cycles in the step.

When all the load steps in the flight are exhausted, the program proceeds to the next flight. The calculation ends when K_{limit} computed with the design limit load, or the maximum spectrum load, whichever is greater, exceeds the defined critical stress-intensity factor value K_{Ic} or K_{c}).

Graphical Integration Method

The graphical integration concept for generating individual aircraft crack growth curves within the tracking program was developed as a cost-effective alternative to the cycle-by-cycle EFFGRO program. The procedure is based upon the assumption that the usage for each aircraft in the fleet can be described in terms of a known sequence of a small number of mission profiles and that the incremental crack growth rate is dependent solely on the mission profile and the crack length and is not dependent on the load magnitude in previous flights. Substantiation of the foregoing assumption was based on an analytical study of wing strain records accumulated during the loads/environmental spectra survey. Crack growth analysis, using the cycle-by-cycle integration methodology, was performed on spectra created from strain traces of 100 individual flights. Variation of the sequence of flights resulted in less than 2 percent variation in the crack growth life. As previously stated, the technical acceptance of the graphical integration method was based on analytic comparison with an accepted cycle-by-cycle integration method. It thus follows that the crack growth curve (a versus flights) can be obtained by graphical integration of crack growth curves of the individual missions. The inputs to the graphical integration routine are the library of crack growth curves for the individual mission profiles and the aircraft mission sequence which may be described, if known, or random. Curves 1, 2, and 3 are the crack growth curves for mission types 1, 2, and 3, respectively, in Fig. 2, which depicts, for example purposes, a mission sequence of Profile 1 to Profile 3 to Profile 1.

For an initial crack length of a_i and a flight of Profile 1, Curve 1 will give the corresponding value of f_{1i}. The crack length at the end of the flight is a_{if} corresponding to F_{1f} where $F_{1f} = F_{1i} + 1$. a_{1f} is now the crack length at the beginning of the second mission (a_{2i}). Entering Curve 3 at a_{2i} will give an abscissa value of F_{2i}. F_{2f} equals $F_{2i} + 1$. The crack length at the end of Flight 2 is thus obtained as a_{2f}. The procedure continues for the actual crack mission sequence or until the crack length equals the critical crack length.

The crack growth curve library for individual missions can be generated by the aforementioned EFFGRO program. The computer cost for this task is small, requiring only a one-time crack growth analysis for a limited number of profiles at the beginning of the program. During the IAT operation additional crack growth curves can be added to the library if warranted by airplane usage changes. The scope of the crack growth curve library is discussed in the next section.

IAT Procedures

There are two basic approaches to aircraft tracking differentiated by the method of collecting flight data from the fleet.

Pilot Report Form (PRF)

In the Pilot Report Form System specific flight data are recorded for each flight by the pilot or his designated representative. In large transport aircraft

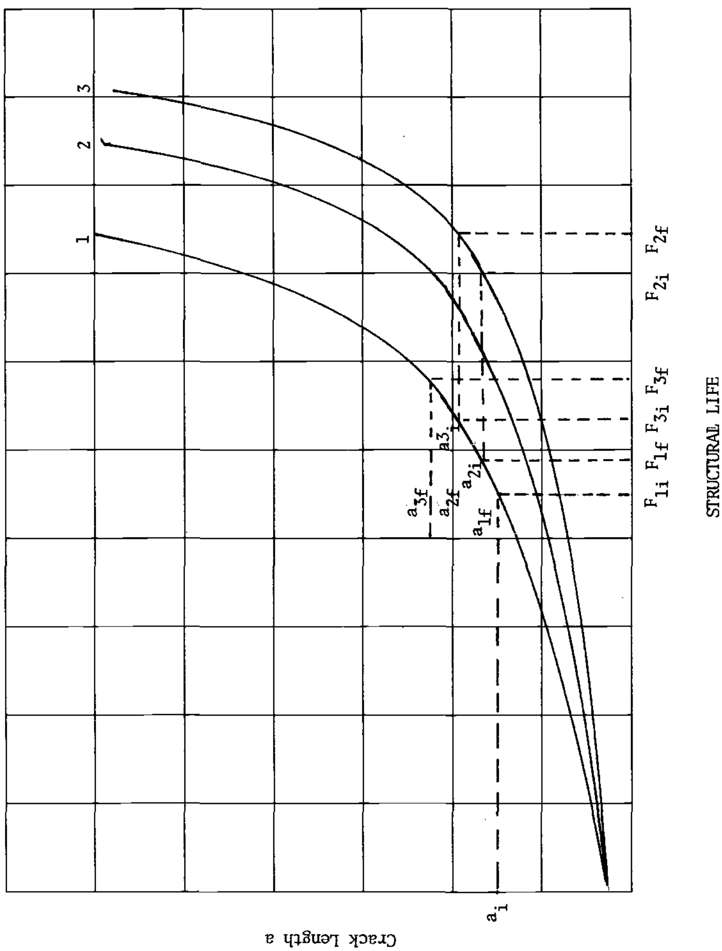

FIG. 2—*Graphical integration methodology.*

the pilot forms are written during the mission and may include a record of significant flight parameters at predetermined intervals or as required by profile events. Typical of the recorded parameters are gross weight, fuel weight, Mach number, altitude, flap position, and thrust. It is more common, however, for the pilot reports to be completed after the flight and such forms must, of necessity, be of a more general nature. The IAT System for the T-39 includes a simple pilot form containing mission description (cross-country transport or training, etc.) takeoff gross weight, maximum altitude, flight length, and number of touch-and-go landings. The data on a pilot form vary for aircraft types but must include sufficient key parameters to make a realistic "spectrum selection." The tracking computer program must contain an algorithm which relates the pilot form data to a preproduced spectra for which the crack growth curve has been derived. In the case of the T-39, the algorithm contains the terms mission description, flight length, takeoff weight, maximum altitude, and number of landings and was developed after studying 5000 h of data tapes from the loads/environmental spectra survey. The preproduced spectra represent typical flights of the pilot form description and must be obtained independently of the tracking program and are frequently based on the loads survey program results. The library of spectra generated from the load survey program and the subsequent computed crack growth curve library will be separated typically by mission description, flight length, number of landings, and any other data supplied by the pilot form.

The individual aircraft tracking analysis for the pilot reporting form system will use the graphical integration method where the sequence of missions flown is supplied by the pilot forms. The estimate of the remaining life for each aircraft assumes the past history of mixture of missions applied in random sequence.

PRF tracking cannot provide the loads to which an individual aircraft is subjected on each flight. The accuracy of the method is thus dependent upon the assumption that a comprehensive loads spectra survey will provide average spectra suitable for the lifetime use of the aircraft fleet. A continuing flight loads program for 10 percent of fleet will partially ensure continuing accuracy of the program. An alternative tracking method follows which will improve accuracy at an increased cost.

Loads Transducer

For more precise estimation of the rate of consuming the usable life of a fleet of aircraft, especially for types encountering considerable variability, load devices can be installed on each aircraft in the fleet. There are several types available: velocity, load factor, altitude (VGH) recorders, strain gages attached to a microprocessor, or mechanical strain recorders (MSR). This paper discusses the latter only as the MSR is being considered for use in the

T-39. The MSR records local strains on a metal strip which is transcribed to produce a sequenced trace of strain cycles. The MSR cannot be installed precisely at the fatigue critical location, thus requiring an analytically derived stress transfer function or a strain-gage calibration to compute the stress spectrum.

The local strain and corresponding stress history, as obtainable from the MSR, meets all the input requirements of cycle-by-cycle crack growth integration in that both load magnitudes and sequence are available. The EFFGRO program is particularly suitable for analysis of an MSR trace. The primary output of the crack growth tracking program is twofold: damage accumulation during the six-month tracking period involving from 200 to 500 flights and the remaining life calculation involving as much as 50 000 flights. Experience to date with an MRS indicates that some 20 cycles per flight are expected. Consequently, the crack growth for the tracking period can be economically calculated for the complete MSR trace with EFFGRO.

For the remaining life calculations, however, it is recommended, in the interest of economy, that a graphical integration method be used based on the aircraft mission mix from the pilot form as discussed under "Pilot Report Form." The crack growth curve library necessary for graphical integration may be generated from the load survey data at the beginning of the IAT program and replaced by curves based on MSR records as sufficient data become available.

Critical Structural Locations

In many IAT systems the analysis is based on a combination of data-collecting methods due to the distribution of critical structural locations in the airframe. In the T-39 system, for example, it is anticipated that an MSR will be fitted to the wing. The fuselage pressure shell analysis will make use of the recorded flight altitudes from the pilot form while empennage structure tracking will be based on pilot form data and library of spectra from loads survey program.

Summary

The crack growth approach to aircraft tracking described in this paper will be used for the USAF T-39 Utility Trainer fleet. A comprehensive computer program is being prepared to automate the procedures. During the early development of the T-39 IAT program, a study was undertaken to select the crack growth integration method. Some five methods were considered, including a linear crack growth approach and spectra simplification approach. All of the methods considered were studied primarily to find a cost-effective alternative to cycle-by-cycle crack growth integration. The selected approach of graphical integration proved to be very economical in computer time and

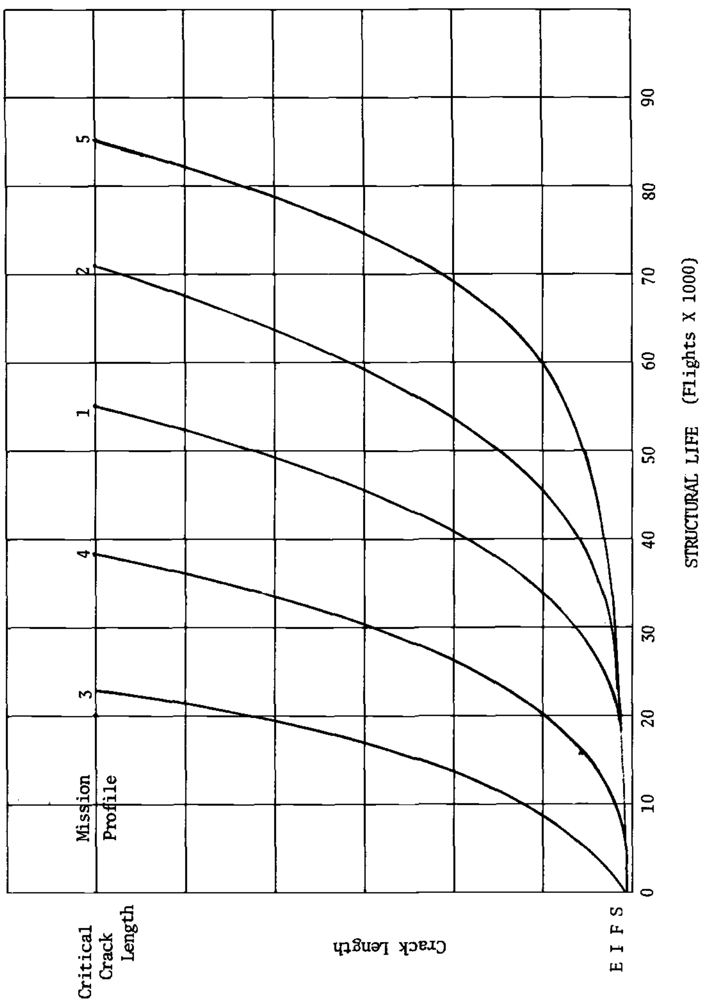

FIG. 3—*Crack growth curves for individual missions.*

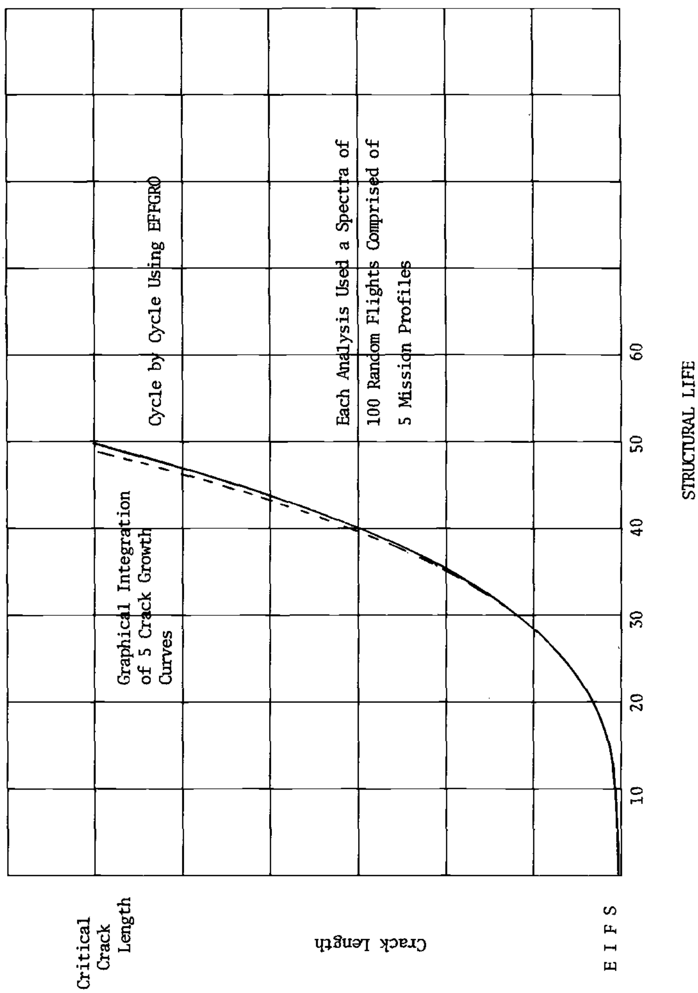

FIG. 4—*Comparison of graphical integration with cycle-by-cycle method.*

eminently suitable for the T-39, particularly for components where the flight data source is limited to simple pilot forms. Comparison of the graphical integration method with the cycle-by-cycle method was made with a wing skin analysis using a random sequence of 100 flight spectra from the T-39 loads survey program. The 100 flights were categorized into five distinct flight profiles. The mixture of missions were as follows:

Mission 1 (High-Altitude Cross-Country Flight)	40 percent
Mission 2 (Medium-Altitude Cross-Country Flight)	20 percent
Mission 3 (High-Altitude Training Flight)	10 percent
Mission 4 (Low-Altitude Training Flight)	20 percent
Mission 5 (Pilot Proficiency Flight)	10 percent

The crack growth curves for the five individual profiles are shown in Fig. 3. The graphically integrated curve for the mission mixture is shown in Fig. 4 as are the results of the EFFGRO program. The cost savings in terms of computer time by using the graphical integration method as against the cycle-by-cycle method was a factor of 15.

E. P. Kennedy[1] *and C. R. Kennedy*[2]

Dependence of Strength on Particle Size in Graphite

REFERENCE: Kennedy, E. P. and Kennedy, C. R., **"Dependence of Strength on Particle Size in Graphite,"** *Fracture Mechanics: Thirteenth Conference, ASTM STP 743,* Richard Roberts, Ed., American Society for Testing and Materials, 1981, pp. 303-315.

ABSTRACT: The strength-to-particle size relationship for specially fabricated graphites has been demonstrated and rationalized using fracture mechanics. In the past, similar studies have yielded empirical data using only commercially available material. Thus, experimental verification of these relationships has been difficult. However, the graphites of this study were fabricated by controlling the particle size ranges for a series of isotropic graphites. All graphites that were evaluated had a constant 1.85-g/cm^3 density. Thus, particle size was the only variable. The strength-to-particle size relationship revealed that the fracture strength was logarithmically related to initial defect size by an apparent $-1/3$ power. Application of Dugdale crack extension model with simple modifications accounting for nonspherical pores and variable defect concentrations explains the $-1/3$ power relationship. This study also considered the particle size effect on other physical properties: coefficient of thermal expansion, electrical resistivity, fracture strain, and Young's modulus.

KEY WORDS: graphite, particle size, strength, fracture mechanics, microcracking, Dugdale model, physical properties

The increased use of graphite for structural applications has warranted a better understanding of the relationships between strength and porosity and grain size. The understanding of these relationships are particularly important in the development of optimized microstructures for specific applications. However, it is difficult to confirm proposed relationships by testing poorly defined commercially available materials. The need to have a clear understanding of the structural morphology to define the critical defect has been emphasized by earlier investigators [*1,2*].[3] The purpose of this study is twofold: (1) to furnish unambiguous experimental information that compares

[1]Associate engineer, Westinghouse Electric Corp., Lester, Pa. 19113; formerly a student at Vanderbilt University, Nashville, Tenn.

[2]Research staff, Metals and Ceramics Division, Oak Ridge National Laboratory, Oak Ridge, Tenn. 37830 (operated by the Union Carbide Corp. for the Department of Energy).

[3]The italic numbers in brackets refer to the list of references appended to this paper.

the various strength-to-particle size relationships, and (2) to develop, through the aid of fundamental fracture mechanics theory, a correlation of the fracture process with microstructure.

The objectives are accomplished by testing graphites fabricated using a green isotropic filler of carefully controlled particle size ranges. The graphites were made to achieve the same final 1.85-g/cm^3 bulk density. Thus, by controlling the fabrication and density, particle size is the only variable. It was found that by controlling the particle size during fabrication, the initial defect size was approximately equal to the mean particle size after graphitization. However, the test results indicated that the final defect size was incrementally larger than the initial size. Further, in terms of fracture mechanics theory, this anomaly is approximated by an apparent $-1/3$ power law relating the fracture strength to initial defect size rather than the expected $-1/2$ power law relationship.

This phenomenon is explained by developing an understanding of the fracture process in conjunction with microstructural effects on the parameters of the crack theory. It will be shown that the inherent stress relief system of graphite causes an effective crack extension that can be explained by the Dugdale model [*3*]. This investigation also considers the particle size effect on other physical properties: the coefficient of thermal expansion (CTE), electrical resistivity, fracture strain, and Young's modulus.

Materials and Fabrication

The desired isotropy in the experimental graphites was achieved by using a green Robinson filler coke. This coke, made from an air-blown petroleum residuum, has a very solid, fine, randomized optical domain structure which is approximately 3 to 4 μm in diameter. Initially, the coke was pulverized and carefully screened to obtain the desired particle size range distributions. Table 1 gives the particle size ranges. The graphites were then made using an Oak Ridge National Laboratory (ORNL) process [*4*] to plasticize the outer surfaces of the green filler coke. This process is used to obtain highly efficient bindering with uniform packing of moldings with fillers of a very narrow size range. Coal tar pitch 30 M was used as the plasticizer. After application of the plasticizer, the filler particles were screened again to assure conformity with the specified particle size range distributions as shown in Fig. 1.

Four 40-mm-diameter moldings were made using A-240 petroleum pitch as the final binder and were baked under restraint. One molding was graphitized without impregnation and a second molding was impregnated with petroleum pitch before graphitization at 3000°C. The impregnation was to assure that the final graphite densities or porosities were over a common range. As shown in Table 1, a common density range was very successful, except for the two larger particle size ranges. The 430-μm material was improved significantly by a second impregnation; however, the larger 725-μm material was very resistant to

TABLE 1—*Particle size range and final bulk densities of fabricated graphites.*

Particle Size Range, μm	Mean Particle Size: As-Screened, μm	Mean Particle Size: Graphitized, μm	Bulk Density, g/cm³ Impregnation: Without	Bulk Density, g/cm³ Impregnation: With 1 Pitch
105 to 125	115	90	1.84	1.91
125 to 149	137	110	1.86	1.89
149 to 177	163	130	1.83	1.90
177 to 210	194	155	1.86	1.87
210 to 250	230	180	1.86	1.90
105 to 149	127	100	1.81	1.87
125 to 177	151	120	1.84	1.86
149 to 210	180	140	1.87	1.90
177 to 250	214	170	1.84	1.84
500 to 590	545	430	1.75	1.78 (1.86[a])
840 to 1000	920	725	1.69	1.71 (1.73[a])

[a]Impregnated twice.

densification. Also in this table, the shrinkage of the initial filler size in processing is calculated.

As a result of the process, the graphites exhibit a contiguous structure with no apparent particle boundaries. The pores are well rounded, having a length approximately the size of the filler particles as seen in Fig. 2.

Testing and Results

The graphites were evaluated by testing a minimum of three brittle ring specimens [5] (18-mm outside diameter, 10-mm inside diameter, and 6.4-mm thickness). From each molded block the properties of bend strength, Young's modulus, and fracture strain were obtained. The load-deflection curve was recorded, and the stresses were calculated considering the shift in neutral axis [6]. Two 6.4-mm-diameter and 25.4-mm-long specimens, both the across-grain and with-grain orientations, were made to determine the electrical resistivity and the 1000°C mean CTE. The porosity-dependent properties were either interpolated or extrapolated for each particle size range to obtain comparisons at a common 1.85-g/cm³ density. The properties measured are given in Table 2.

The fracture strength as a function of initial particle size is compared with the results of a acicular grade graphite in Fig. 3. It should be mentioned that agglomeration of particles in graphite does lead to structures having defect sizes greater than the particle size. We found that very fine green Robinson filler particles (that is, particle sizes less than 90 μm) did tend to agglomerate and could not be considered in this study. The agglomeration is a particular problem in considering commercial graphites and was one of the incentives to fabricate controlled graphites.

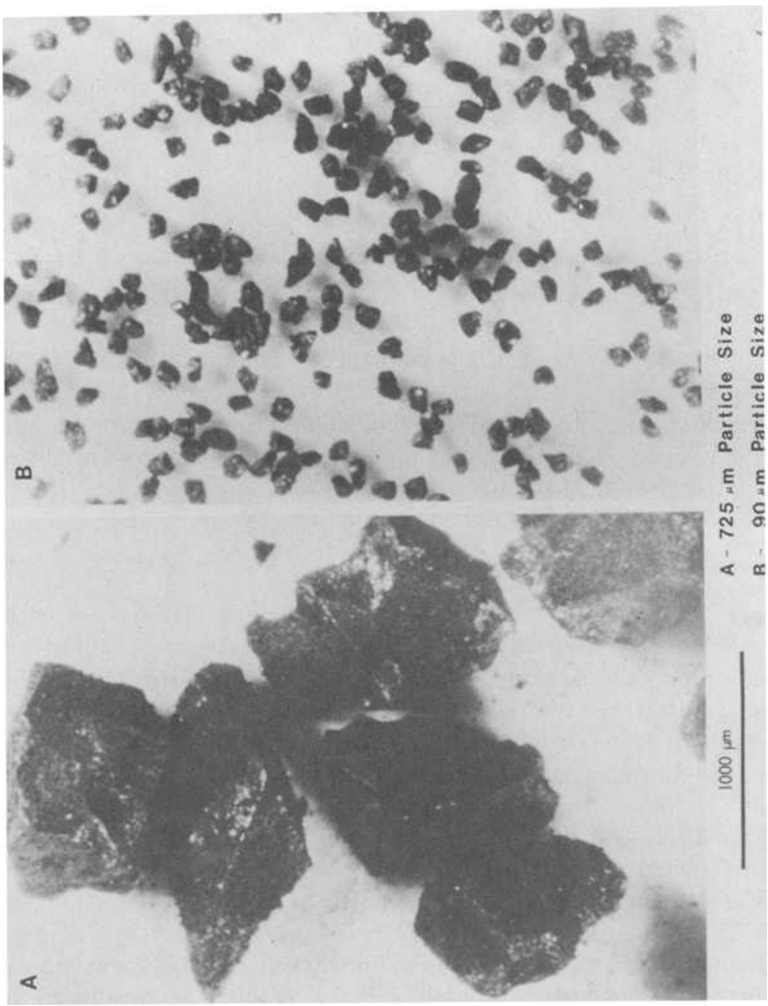

FIG. 1—*Particle size of the isotropic filler was carefully controlled.*

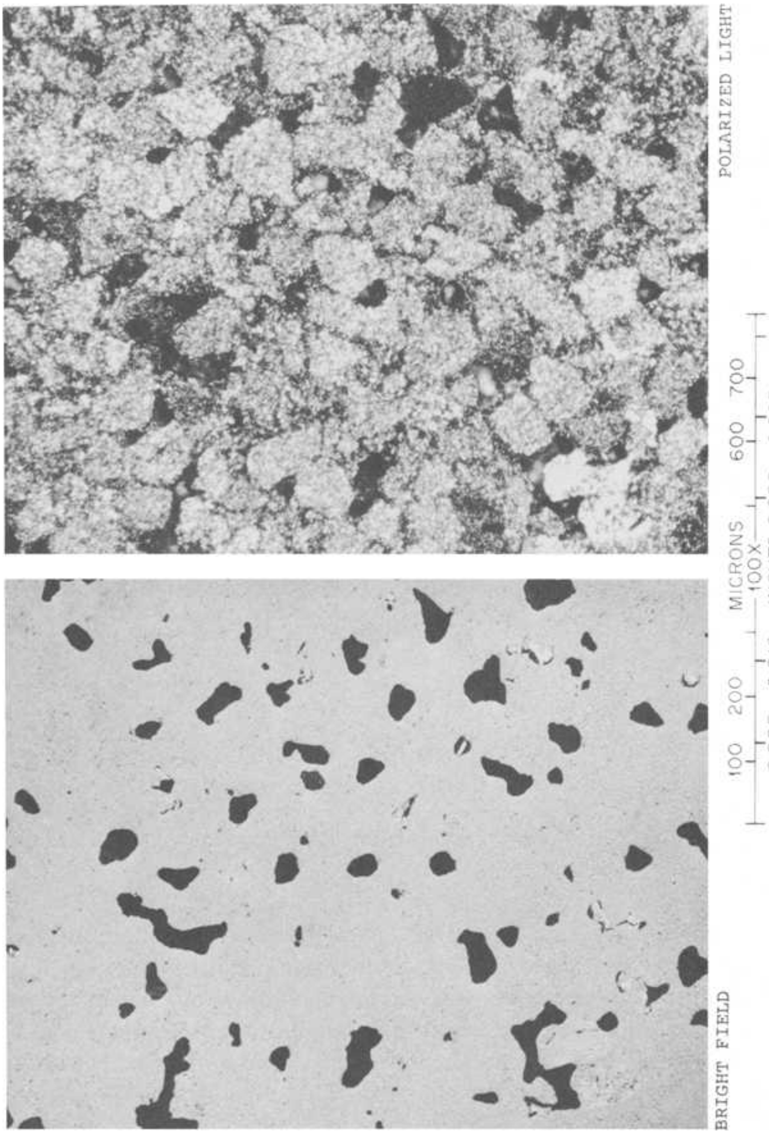

FIG. 2—Structure of the graphite is contiguous without apparent particle boundaries.

TABLE 2—*Properties of 1.85-g/cm³ graphites.*

Particle Size, μm	Fracture Strength, MPa	Fracture Strain, %	Modulus of Elasticity, GPa	Resistivity, μΩ-cm	1000°C CTE, $C^{-1} \times 10^{-6}$
725	46.2	0.68	10.3	850	6.35
430	52.4	0.71	11.3	880	6.50
180	68.3	0.75	12.3	1000	6.55
170	71.0	0.80	13.0	970	6.76
155	75.8	0.81	13.3	955	6.74
140	79.3	0.84	13.4	970	6.79
130	77.9	0.86	13.0	960	6.87
120	80.0	0.86	13.4	990	6.86
110	81.4	0.88	13.4	960	6.91
100	84.1	0.89	13.7	1000	6.93
90	86.9	0.91	13.4	950	6.75

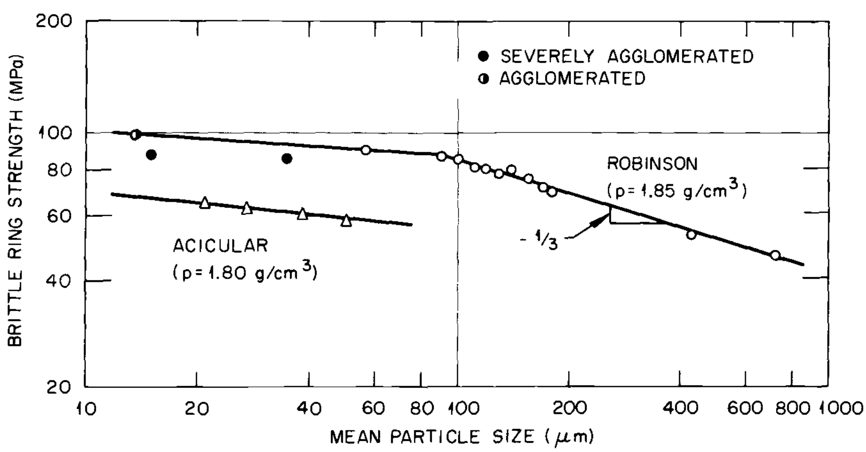

FIG. 3—*Brittle ring strength of Robinson graphites.*

Young's modulus was also measured. Figure 4 shows the modulus decreasing with increasing particle size. This result is significant because porosity is generally assumed spherically shaped, and the modulus would be independent of pore size. To account for this result a rationalization of Young's modulus must include the effects of nonspherical porosity, which would reduce the inherent spring constants within the structure. This effect can be considerably intensified in graphites with defective particles and with highly anisotropic structures with aligned porosity.

The degree of isotropy was evaluated by comparing the electrical resistivity and CTE in the with-grain and across-grain directions. In every block, both the electrical resistivity and the CTE in both directions were within 2 to 5 percent of each other, confirming the isotropic structure. In Fig. 5 the electrical resistivity is shown as a function of particle size for the 1.85-g/cm^3-dense material. The decreasing resistivity with increasing particle size is a result of reduced boundary resistance as the particle boundary area becomes smaller.

The CTE is compared with an anisotropic acicular grade in Fig. 6. In this figure, because of the anisotropy in the acicular grade, the volumetric CTE (sum of the three linear directions) is compared. For the Robinson grade only, the linear CTE is simply one third of the volumetric value. The CTE for both types of graphites apparently approaches the same value as the particle size is reduced. The CTE is affected by the defect concentration within the particle; therefore, as the particle size is reduced by breaking the particles through the defects, the defect concentration is reduced, and the CTE increases. For each curve in Fig. 6, the slope is a reasonable measure of the defect concentrations in a particular filler coke. As observed, the defect concentration within the Robinson filler particle is much less than in acicular filler cokes.

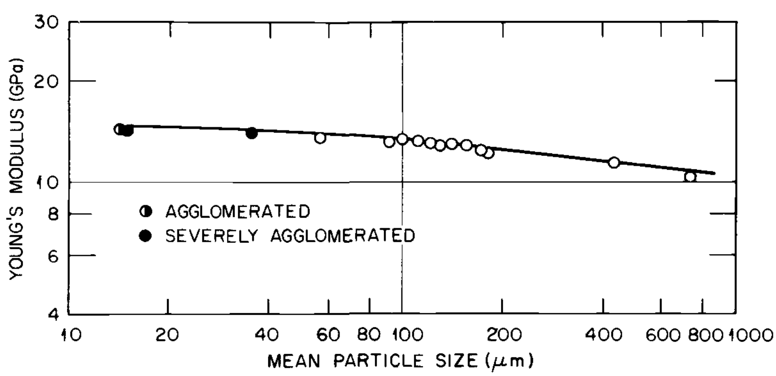

FIG. 4—*Modulus of elasticity decreases with increased particle size.*

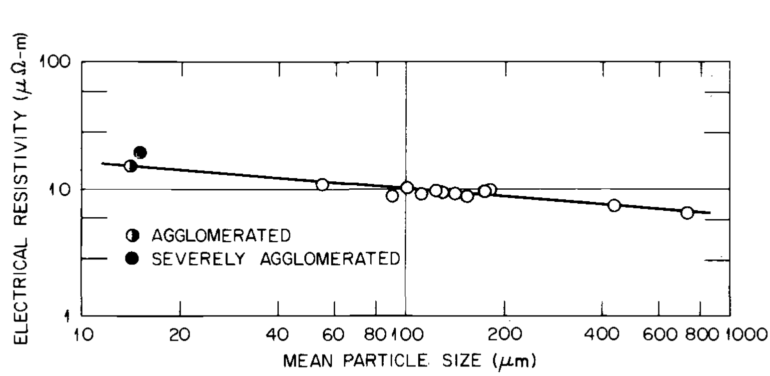

FIG. 5—*Electrical resistivity decreases with increased particle size.*

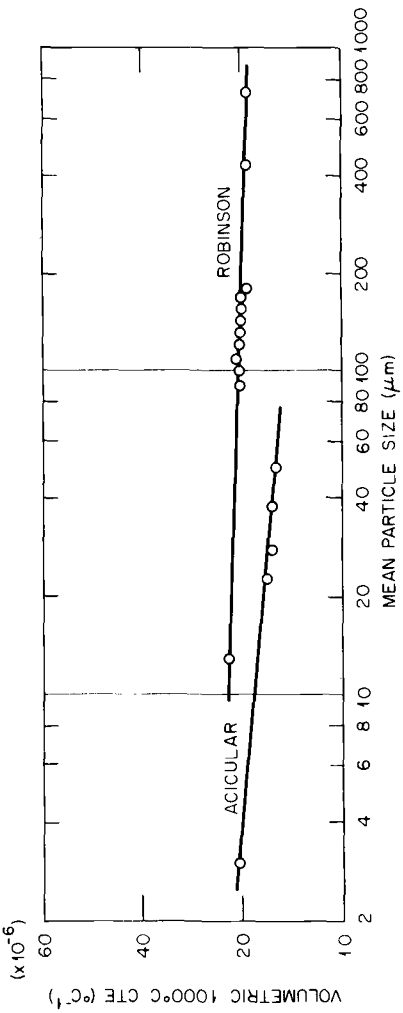

FIG. 6—*Coefficient of thermal expansion decreases with increased particle size for most graphite.*

The fracture strain obtained from testing these graphites is shown in Fig. 7. The stress-strain characteristic of graphite is nonlinear and the total strain (ϵ_t) to fracture can be separated into two components, the elastic strain (ϵ_e) and a nonlinear strain (ϵ_c) resulting from crack extension

$$\epsilon_t = \epsilon_e + \epsilon_c \tag{1}$$

The elastic strain can be calculated and subtracted from the total strain

$$\epsilon_t - \frac{\sigma_f}{E} = \epsilon_c \tag{2}$$

to give the nonlinear component of strain. Also given in Fig. 7 are the elastic and crack strains obtained from this test series. It is very significant to note that the crack strain did not vary with particle size.

Discussion

The accepted model of deformation, as discussed by Jenkins [7], describes the initial application of stress accommodated by interlamellar shearing and limited slip due to the inadequate number of slip systems. Simultaneously, the large macropores cause local strain concentrations in adjacent grains which open preexisting microcracks normal to the stress axis. These microcracks actually act as a stress relief mechanism much like the plastic zone of a ductile material. The size of this pseudo-plastic zone is determined by the stress concentrations at the macropores. The growth of the individual microcracks within the process zone may be obstructed by a boundary or by an obstacle such as a pore. The microcrack may then either terminate or deviate onto a less suitably oriented weakness plane where growth is discontinued.

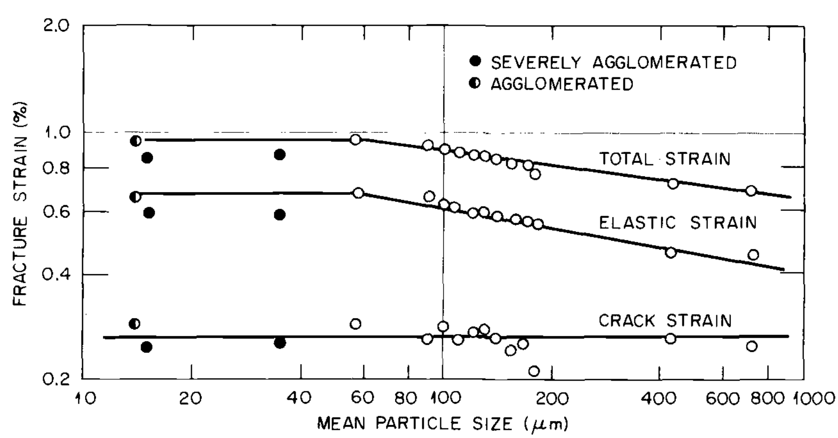

FIG. 7—*Decreasing the filler particle size increases the total fracture strain to the point of agglomeration. The crack strain is independent of particle size.*

Growth of the microcrack will continue only when the strain energy increases to allow the crack to pass either through or around the obstacle.

These coexisting stress relief mechanisms are indistinguishable at low stresses; however, at higher stress levels, the size of the microcrack process zone increases and becomes the dominant contributor to the deformation process. Eventually, coincidental alignment of this discontinuous array of microcracks causes them to link up, and macrocrack growth occurs. Ultimately, a critical effective crack length is reached, and catastrophic failure occurs.

The use of fracture mechanics is helpful in understanding the microstructural defect controlling fracture. Simply stated, the Griffith-Irwin [8, 9] crack theory for elastic materials describes the fracture criterion in terms of the applied stress, material properties, and inherent defects within the material

$$\sigma_f = \left[\frac{EG_{\mathrm{Ic}}}{\pi c(1 - \nu^2)}\right]^{1/2} \tag{3}$$

where

ν = Poisson's ratio, which varies from 0 to 0.30 depending on active void volume that will expand or decrease during loading. Poisson's ratio for Robinson graphite is 0.28, indicating a relatively defect-free material.

E = apparent Young's modulus, an average of the total microstructural effect, which is a function of micro- and macroporosity that occurs either within or between particles and the preferred orientation. These variables also determine the material's ability to absorb external strain primarily by allowing material expansion into the macrovoids. Therefore, the change in elastic modulus may be used as an indicator of the material's ability to concentrate strains at the crack tip.

G_{Ic} = strain-energy release rate, a measure of strain energy released per unit area of fracture surface (for example, twice the surface energy for elastic materials), which is the work to create new surface. This is constant at failure for a given type of filler particle and processing schedule. The material's resistance to crack propagation has been shown to be a function of all microstructural features except particle size [10].

c = half length of the inherent macrocrack before loading, which is a function of the size and distribution of the filler particles and packing efficiency. These large disparate voids will act as weak links and ultimately determine the fracture path.

The difficulty in applying any deformation model is that it must be consistent with the apparent $-1/3$ power shown in Fig. 3. The fracture mode in graphite actually excludes its implicit description as a linear elastic brittle material. Therefore, some consideration must be given to the crack growth and the microcracking to reduce the stress concentrations. This behavior can be modeled similarly to plastically induced failure by assuming that the pseudo-plastic zone at the crack tip effectively increases the crack length. The theoretical plastic zone adjustment for the general class of elastic-plastic materials is considered by Dugdale [3]. He approximates the size of the plastic zone and assumes that the presence of this limited process zone effectively increases the crack length

$$R = \left[\frac{\pi E}{8\sigma_y{}^2}\right] G_{\mathrm{Ic}} \tag{4}$$

where R is the plastic zone size at fracture and σ_y is the yield stress.

The extent of crack growth before failure is implied to be constant (that is, independent of particle size), as indicated by the experimentally determined constant crack strain (nonlinear strain component) at fracture as shown in Fig. 7. Also, as previously discussed, E is a measure of the structural compliance of the material and must be considered in the approximation of the Dugdale plastic zone size. This approximation is accomplished by simply using a geometric factor, δ, calculated by the ratio, E/E_0, where E is the modulus at failure and E_0 is the stabilized modulus measured (exhibited by the smaller particle size range). The approximation corrects for deviations due to nonspherical porosity and variable defect concentrations.

Applying this modification to the Griffith-Irwin equation, the relation becomes

$$\sigma_f = \left[\frac{EG_{\mathrm{Ic}}}{\pi(c + \delta\overline{R})(1 - \nu^2)}\right]^{1/2} \tag{5}$$

where the term $(c + \delta\overline{R})$ is the final defect size. G_{Ic} was experimentally determined using short-bar specimens to be 222 Pa·m [11].

In Table 3, the final defect sizes are calculated, $a = c + \delta\overline{R}$, and compared with the initial defect sizes from particle size considerations. The difference is found to be a constant $\delta\overline{R}$ equal to 98 $\pm$ 7 μm. This is the value of the modified mean pseudo-plastic zone size generated by the microcracking mechanism to reduce the defect stress concentration. The apparent yield stress of the material can be calculated from Eq 4 to give σ_y = 110 MPa, which is consistent with the fracture results. The use of constant plastic zone size to calculate the final defect size is illustrated in Fig. 8. This figure shows the comparison of the apparent $-1/3$ power relationship as given by the initial defect size with the calculated final defect size obtained by simply adding the constant plastic zone to the $-1/3$ power relationship yielding, the $-1/2$ power relationship. Obviously, as the defect size increases, the crack growth should become a small insignificant part of the overall strain. Therefore, there should exist a break in the initial defect size curve taking the slope of $-1/2$.

TABLE 3—*Calculation of the Dugdale plastic zone size.*

Particle Size, μm	Elastic Modulus, GPa	Half Initial Defect Size (c), μm	Calculated Half Final Defect Size (a),[a] μm	$R = a - c$, μm	δ^b	δR, μm
775	10.3	336	371	8	0.77	6[c]
430	11.3	215	316	101	0.84	85
180	12.3	90	203	113	0.92	104
170	13.0	85	198	113	0.97	110
155	13.3	78	178	100	0.99	99
140	13.4	70	164	94	1.00	94
130	13.0	65	165	100	0.97	97
120	13.4	60	161	101	1.00	101
110	13.4	55	155	100	1.00	100
100	13.7	50	149	99	1.02	101
90	13.4	45	136	91	1.00	91
						98 ± 7

[a]Calculated by Griffith-Irwin equation for plane strain, using measured fracture strengths.

$$a = \frac{EG_{Ic}}{\pi\sigma^2(1 - \nu^2)}$$

[b]$\delta = E/E_0$ where $E_0 = 13.4$ GPa.
[c]Not included in the mean value calculation.

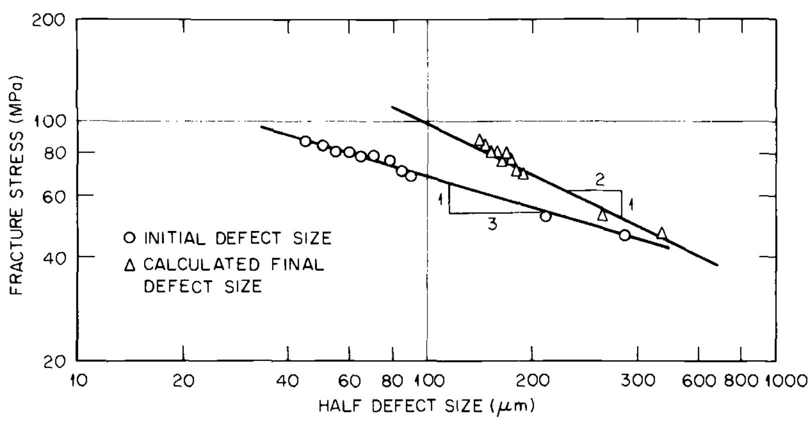

FIG. 8—*A comparison of the initial defect size with final defect size with a constant 98-μm crack growth.*

Conclusion

This study has provided graphites of the same basic structure in which the only fabrication variable was controlled particle size. Experimental data were generated which describe the dependence of physical properties on particle size. These results clearly describe a final defect size which is not equal to or linearly related to particle size but requires an addition of a crack growth size as suggested by Dugdale. It is also shown that while the total fracture strain increases with reduced particle size, the nonlinear or crack strain is constant for constant porosity. An unexpected feature is that both the modulus of elasticity and the electrical resistivity increased with decreasing particle size. The coefficient of thermal expansion also increased with decreasing particle size, but less than was expected.

These data emphasize the need to describe the structural morphology of graphite when defining the fracture mechanisms. Based on the Dugdale-modified Griffith-Irwin crack theory, the strength dependency of graphite on its microstructure was demonstrated. The fracture process was shown to exhibit a constant effective crack extension independent of particle size which occurred by the microcracking stress relief mechanism acting as a pseudoplastic zone. Because the effective crack growth and actual crack growth are indistinguishable, this model does not imply that crack extension completely consisted of effective extension. Presently, statistical analyses are being developed [*1,2,10*], based on the Griffith theory, in order to model the coincidental alignment of microcracks in the fracture process.

Acknowledgment

This research was supported, in part, by the Naval Surface Weapons Center under Contract No. N-60921. The authors also wish to acknowledge their appreciation of assistance from Fred Jeffers for his help in the laboratory and Dr. W. F. Flanagan for his stimulating comments and advice.

References

[*1*] Buch, J. D., *Properties Related to Fracture Toughness, ASTM STP 605*, American Society for Testing and Materials, 1976, pp. 124-144.
[2] Zimmer, J. E. and Meyer, R. A. in *Proceedings*, 12th Biennial Conference on Carbon, 1975, p. 95.
[*3*] Dugdale, D. S., *Journal of the Mechanics and Physics of Solids*, Vol. 8, 1960, p. 100.
[*4*] Kennedy, C. R. in *Proceedings*, 11th Biennial Conference on Carbon, 1973, pp. 304 and 973.
[5] Bortz, S. A. and Lund, H. H. in *Mechanical Properties of Engineering Ceramics*, Interscience, 1961, pp. 383-404.
[*6*] Timoshenko, S. and Goodin, J. N., *Theory of Elasticity*, 2nd ed., McGraw-Hill, New York, 1951, pp. 116-123.
[7] Jenkins, G. M., *Chemistry and Physics of Carbon*, Vol. 11, 1973, pp. 189-242.
[*8*] Griffith, A. A. in *Proceedings*, International Congress on Applied Mechanics, Vol. 55, 1924.
[*9*] Irwin, G. R., *Encyclopedia of Physics*, Vol. 6, Springer, Heidelberg, Germany, 1958.
[*10*] Anderson, C. A. and Salkovitz, E. I. in *Proceedings*, 11th Biennial Conference on Carbon, 1973, p. 273.
[*11*] Shipman, F. H., Resource Enterprizes, private communication.

T. T. Shih[1] *and W. A. Logsdon*[1]

Fracture Behavior of a Thick-Section Graphite/Epoxy Composite

REFERENCE: Shih, T. T. and Logsdon, W. A., "**Fracture Behavior of a Thick-Section Graphite/Epoxy Composite,**" *Fracture Mechanics: Thirteenth Conference, ASTM STP 743,* Richard Roberts, Ed., American Society for Testing and Materials, 1981, pp. 316-337.

ABSTRACT: In order to explore the possibility of utilizing composites as structural materials for generator retaining rings, the fracture behavior of an experimental thick-section [54 mm (2.125 in.)] graphite/epoxy composite was examined. Rectangular bend bar specimens of various cross-sectional dimensions were tested in three-point bending to determine the shear strength of the composite. Edge-notch-bend and center-notched-tension specimens with various notch depths were used to determine the fracture toughness of the composite. These tests served to permit an evaluation of the applicability of linear elastic fracture mechanics (LEFM) to composite materials in general and thick-section composites in particular. Results show that (1) LEFM is not directly applicable to thick-section composites with cracks perpendicular to the fiber orientation; (2) the test composite is insensitive to cracks in a plane perpendicular to the fibers, and the load-carrying capability can be calculated based on net section considerations; and (3) the failure mode of the test composite under three-point bending is interply shear failure. The interply shear strength equaled 24.6 MPa (3.5 ksi).

KEY WORDS: graphite, epoxy, composites, shear strength, fracture toughness

Retaining rings used on large electrical generators are highly reliable parts with excellent properties. However, the alloys used in retaining rings have almost reached a limit in tensile strength. Thus, much effort is being expended on alloy development to meet the need of future generator development.

As a parallel effort, the Electric Power Research Institute (EPRI) is sponsoring a development program at Westinghouse to explore the possibility of fabricating retaining rings from a composite material consisting of graphite fibers in an epoxy resin matrix. The graphite epoxy composite material was selected because it is nonmagnetic, has low density, and high tensile strength and modulus.

[1]Senior engineers, Structural Behavior of Materials Department, Westinghouse R&D Center, Pittsburgh, Pa. 15235.

This paper presents the results of a preliminary evaluation of the fracture properties of a thick-section, 54-mm (2.125 in.) graphite fiber-reinforced epoxy composite. The specific objectives of the work described here were to both develop preliminary material properties data required for initial design considerations and to explore the applicability of existing linear elastic fracture mechanics (LEFM) to thick-section composites.

Because manufacturing defects such as debonding and fiber breakup cannot be completely avoided in composite materials, it is imperative that an adequate technique be available to characterize the potential effect of such defects on the structural behavior of these materials. To date, considerable work has been done with regard to applying LEFM to composites [*1-19*].[2] While most of the results have been positive [*1-15*], some investigators have raised important questions [*16, 17*]. In view of this confusion plus the fact that nearly all work to date has been done with thin-section [less than 6.4 mm (0.250 in.)] material, it was deemed necessary to explore further the applicability of LEFM to thick-section composites.

In this study, both edge-cracked-bend and center-notched-tension specimens were used to evaluate the fracture properties and the applicability of LEFM to the test material. In addition, extensive work was done to determine the interply shear strength of the test material using three-point-bend tests of specimens of various dimensions.

Experimental Procedures

Material and Specimens

The graphite/epoxy composite material evaluated in this program was fabricated by Hercules Inc. for Westinghouse in 1973, using HMS graphite fibers and Hercules-designated 3501 epoxy resin. The test plate had a thickness of 54 mm (2.125 in.) and it contained 370 individual plies for a nominal per-ply thickness of 0.145 mm (0.0057 in.). This plate had a fiber volume of 55.06 percent and a resin volume of 44.94 percent. The layup summary for the plate is presented in Table 1. Note that the 90-deg fibers would lie in the hoop direction relative to a ring application. This is the first thick-section graphite/epoxy composite ever produced in the United States. Unfortunately, this plate contained microcracks, as shown in Fig. 1, which were produced during the manufacturing process. Ongoing research efforts have eliminated these microcracks via improved fiber surface treatment, by optimizing the fiber layup or by selecting the proper graphite-resin combination or both. Mechanical properties of a current thick-section graphite/epoxy composite will be developed and reported in the near future.

Unnotched-bend-bar specimens of various cross sections (Table 2) were

[2]The italic numbers in brackets refer to the list of references appended to this paper.

TABLE 1—*Layup summary of graphite/epoxy composite.*

	Ply Angle, deg	No. of Plies
Top	0	4
	90	16
	0	2
	90	16
	+45	1
	−45	1
	90	16
	0	2
	90	16
	+45	1
	−45	1
	90	16
	0	2
	90	16
	+45	1
	−45	1
	90	16
	0	2
	90	16
	+45	1
	−45	1
	90	16
	0	2
	90	16
	+45	1
	+45	1
	−45	1
Midplane		
	−45	1
	+45	1
	+45	1
	90	16
	0	2
	90	16
	−45	1
	+45	1
	90	16
	0	2
	90	16
	−45	1
	+45	1
	90	16
	0	2
	90	16
	−45	1
	+45	1
	90	16
	0	2
	90	16
	−45	1
	+45	1
	90	16
	0	12
	90	16
	0	4
Bottom		

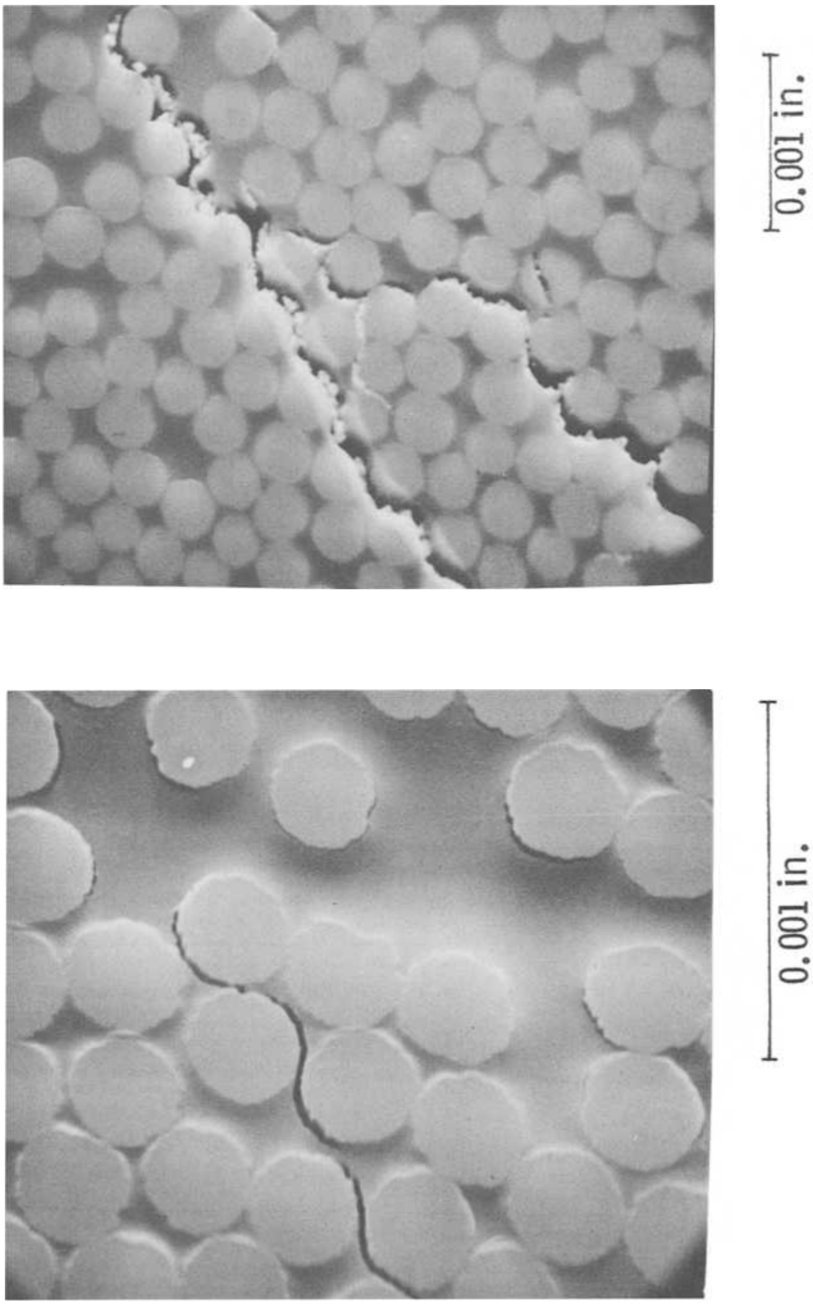

FIG. 1—*Microcracks observed in a thick-section [54 mm (2.125 in.)] graphite/epoxy composite.*

tested in three-point bending to determine the shear strength of the graphite epoxy composite. In all cases, the specimen depth (or height) corresponds to the thickness direction of the original plate. Edge-notched-bend specimens (Fig. 2) and center-notched-tension specimens (Fig. 3) with various notch depths were utilized to determine the fracture toughness of the graphite-epoxy composite and to evaluate the applicability of LEFM to this material. The orientation of the edge-notched and center-notched specimens in the original plate is noted in Figs. 2 and 3, respectively. This orientation corresponds to the C-R direction per the ASTM Test for Plane-Strain Fracture Toughness of Metallic Materials (E 399-78a). The notch-root radius used for both specimen geometries was 0.025 mm (0.001 in.). These specimens were not fatigue precracked since fatigue precracking can cause debonding at the crack tip rather than crack extension, thus yielding a more blunt crack than that obtained as the result of machining.

Shear Strength Tests

Shear strength tests were conducted in a room temperature air environment using the unnotched-bend specimens. The test specimens were loaded in three-point bending with a span S = 101.6 mm (4.0 in.) or S = 63.5 mm (2.5 in.), using a servo-hydraulic MTS machine operated in displacement control. Ramp displacement rates were selected to complete each test in approximately 5 min. Load-point displacement was continuously monitored and autographically recorded as a function of load.

TABLE 2—*Experimental results of unnotched-bend specimens.*

Specimen No.	Specimen Depth, W, in.	Specimen Width, B, in.	Support Span, S, in.	Load P_{max}, lb	Shear Stregth, τ, ksi	Flexural Strength, σ_f, ksi
2A	1.001	0.256	4	1270	3.81	15.23
2B	1.001	0.256	4	1185	3.46	13.83
3A	0.256	0.242	4	270	3.27	51.01
3B	0.251	0.236	4	245	3.12	49.68
3C	0.251	0.229	4	250	3.23	51.41
3D	0.501	0.223	4	540	3.62	28.90
3E	0.501	0.208	4	490	3.53	28.18
1C	0.995	0.503	2.5	2820	4.23	10.63
1D	1.003	0.503	2.5	2450	3.40	8.48
2C	1.001	0.251	2.5	1475	4.34	10.84
2D	0.989	0.251	2.5	1285	3.89	9.83
3F	0.251	0.238	2.5	285	3.56	35.42
3G	0.251	0.232	2.5	265	3.43	34.12
3H	0.251	0.228	2.5	260	3.42	34.04
3I	0.501	0.242	2.5	590	3.66	18.25
3J	0.501	0.233	2.5	480	3.10	15.46
					avg 3.57	

NOTE: 1 in. = 25.4 mm; 1 lb = 4.448 N; 1 ksi = 6.895 MPa.

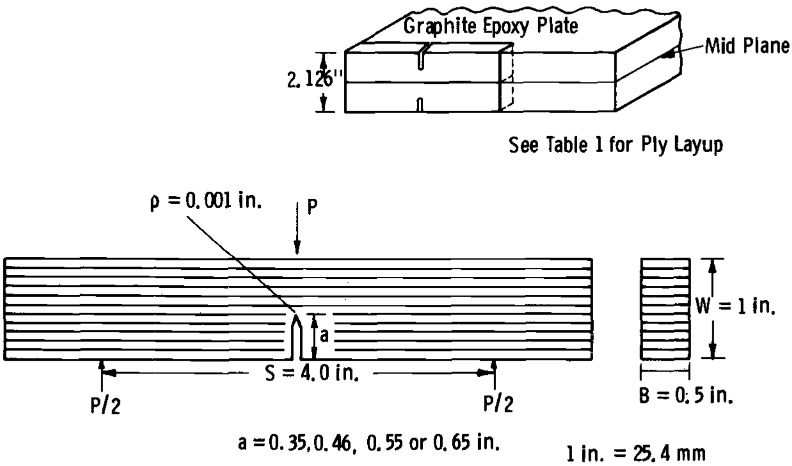

FIG. 2—*Single-edge-notched bend specimens.*

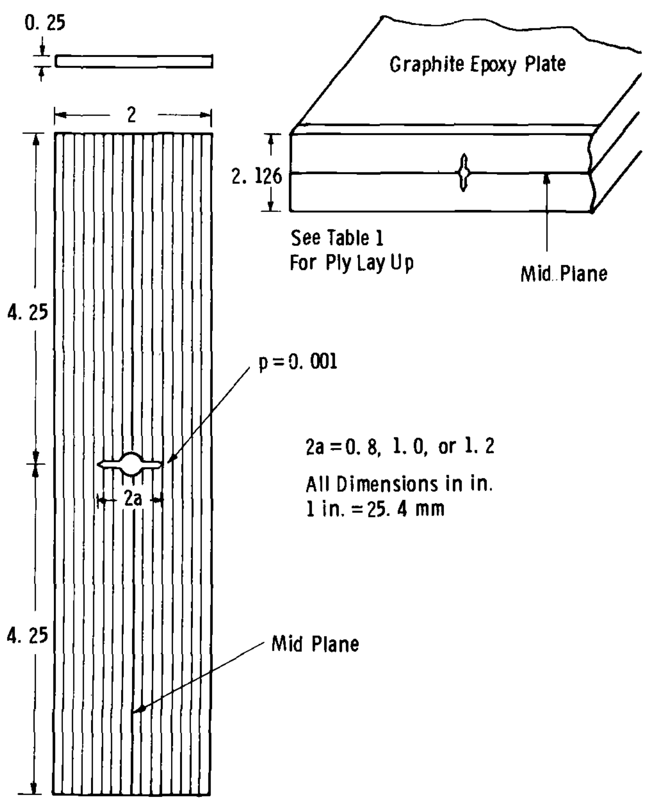

FIG. 3—*Center-notched tension specimen.*

Fracture Toughness Tests

Room temperature fracture toughness properties of this graphite/epoxy composite were determined utilizing both the edge-notched-bend and center-notched-tension specimens with various notch depths. Test procedures for these specimens are described separately.

Edge-Notched-Bend Specimens—The specimens were loaded in three-point bending with a span S = 101.6 mm (4.0 in.) (see Fig. 2), using a servo-hydraulic MTS machine operated in displacement control. The tests were performed with ramp displacement rates of 0.13, 0.25, 0.51, and 1.02 mm/min (0.005, 0.01, 0.02, and 0.04 in./min) for specimens with notch depths of 8.9, 11.7, 14.0, and 16.5 mm (0.35, 0.46, 0.55, and 0.65 in.), respectively. These displacement rates yielded a corresponding loading rate of approximately 2.2 kN/min (500 lb/min). Load-point displacement was continuously monitored and autographically recorded as a function of load. For specimens with notch depths of 8.9 and 11.7 mm (0.35 and 0.46 in.), the test was interrupted after a significant load drop was observed. The specimen was withdrawn from the machine and ultrasonically inspected, then reloaded using the identical test procedure until additional load drops were observed. For specimens with notch depths of 14.0 and 16.5 mm (0.55 and 0.65 in.), the test was not interrupted but was terminated after two or more load drops.

Center-Notched-Tension Specimen—The specimens were loaded via friction grips and tested in a Baldwin tension machine. The loading rate equaled approximately 4.45 kN/min (1000 lb/min). During each test, the applied load and the crack-opening displacement (COD) were monitored and continuously recorded. The COD was measured by a double-cantilever clip gage. This clip gage was attached to the tabs located 5.08 mm (0.2 in.) apart which were bonded to the specimen with epoxy cement.

Failure Mode and Fracture Behavior of Graphite/Epoxy Composite

Unnotched-Bend Specimens

Typical load versus load-point displacement records for the unnotched three-point-bend tests are shown in Fig. 4. There is an initial region of increasing slope during which slack in the load train is removed and bearing surfaces develop under the loading rollers. This is followed by a linear region in which the specimen deforms elastically. A third region of slight deviation from linearity was observed for specimens with depths of 25.4 mm (1.0 in.), Fig. 4*b*. After the applied load reached a maximum, a significant load drop occurred which indicated specimen failure. Visual inspection of the failed specimens revealed delamination as opposed to fiber breakup. This delamination occurred most often in the specimen midplane. Visual inspection of the 25.4-mm-deep (1.0 in.) specimens also revealed permanent deformation at the loading

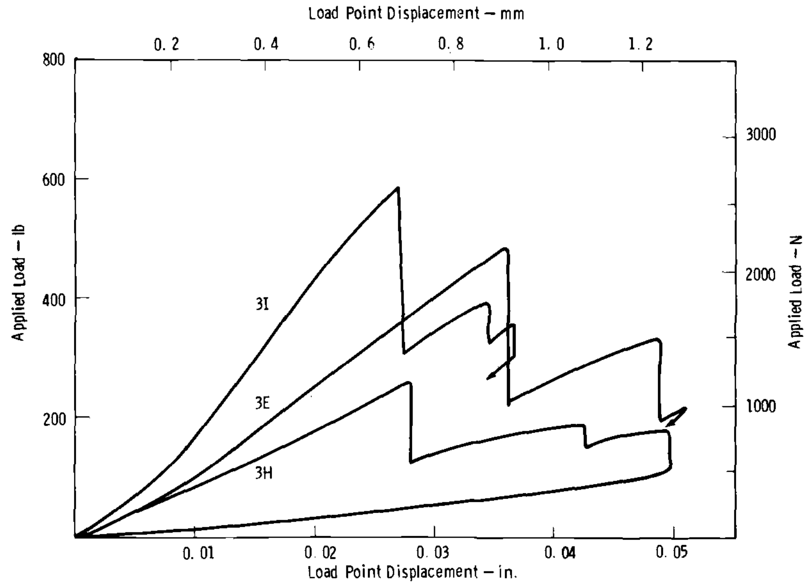

FIG. 4a—*Typical load versus load-point displacement records of three-point-bend test of unnotched specimens with W ≤ 12.7 mm (0.5 in.).*

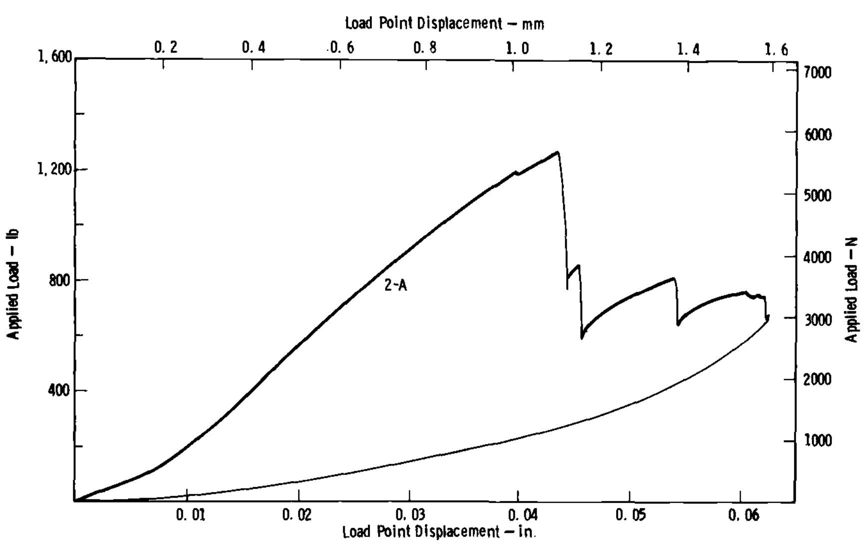

FIG. 4b—*Typical load versus load-point displacement records of three-point-bend test of unnotched specimens with W = 25.4 mm (1.0 in.).*

point. This permanent deformation, caused by the excessive compressive stresses under the loading knife, may account for the deviation from linearity demonstrated by the load-displacement record.

Notched-Bend Specimens

Typical load versus load-point displacement records for notched-bend specimens are illustrated in Fig. 5. These records are very similar to those of the 25.4-mm-deep (1.0 in.) unnotched-bend specimens. That is, there is always a region of slight deviation from linearity, probably caused by excessive compressive stress under the loading knife, before a sudden load drop, which indicates specimen failure.

Visual inspections of the specimens with initial notch depths of 8.9 and 11.7 mm (0.35 and 0.46 in.) were made immediately after the first significant load drop. This inspection showed that the crack did not extend in a self-similar fashion. Ultrasonic inspection revealed that the load drop was caused by the delamination of more than 25 mm (1.0 in.) at each side of the notch tip. This kind of fracture behavior whereby crack extension, actually delamination, occurs perpendicular to the original crack orientation has been previously reported [*18,19*].

Since the specimen did not break in half following the initial load drop, it could still support some load. After this first load drop (delamination at crack

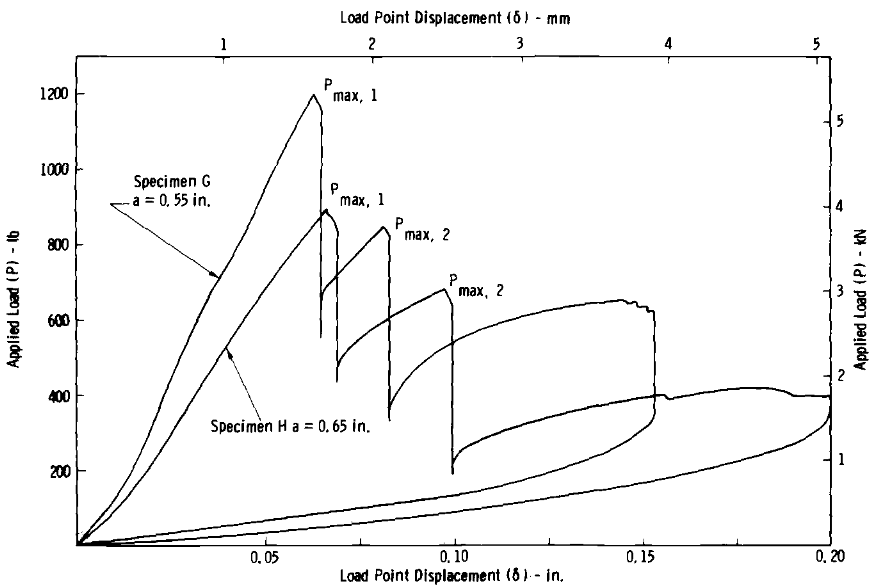

FIG. 5—*Typical load versus load-point displacement records for a three-point-bend, edge-notched graphite/epoxy composite specimen.*

tip), the load still increased with increasing load-point displacement until the next load drop occurred. These specimens could be subjected to a load-point displacement of more than 3.8 mm (0.15 in.) without breaking in half. A closeup of specimen K, which experienced three load drops while being subjected to a 2.7-kN (600 lb) load and a load-point displacement of 0.34 mm (0.0135 in.) is shown in Fig. 6. Note the visually detectable delamination (Fig. 6*b*) and the relative motion of the specimen ends (Figs. 6*a* and 6*c*). This delamination and relative motion suggest that the additional load drops which follow the initial load drop were also caused by delamination. This delamination would eliminate the shear stress on the longitudinal plane and cause excessive load-point displacement and the relative motion of the specimen ends. There are also indications of fiber rupture under the loading knife. This fiber rupture may be caused by the concentrated load and the excessive flexural stress which results from the delamination.

Center-Notched-Tension Specimens

Typical load-versus-COD records for center-notched-tension specimens are shown in Fig. 7. All the specimens initially behaved linear elastically. Load displacement records of specimens with notch lengths ($2a$) equal to 30.5 mm (1.2 in.) are similar to those typically demonstrated by brittle materials (Type II or Type III per ASTM Method E 399-78a). Visual inspection of the failed specimens showed that "pop-in" was caused by delamination which occurred perpendicular to the initial notch, as shown in Fig. 8. The excessive COD was attributed to the sliding of the broken halves of the specimen (see Fig. 8). On the other hand, load displacement records of specimens with shorter notch lengths, $2a$ equal to 20.3 and 25.4 mm (0.8 and 1.0 in.), are similar to those displayed by ductile materials (Type I per ASTM Method E 399-78a). Delamination at the crack tip caused the load-displacement records to deviate from linearity. The specimens could sustain additional loading after delamination without excessive displacement because the majority of the load was carried by the remaining ligament; see Fig. 8 [*16*].

Data Reduction

With knowledge of the fracture behavior of this graphite/epoxy composite material, the experimental results can now be properly interpreted as outlined in the following sections.

Unnotched-Bend Specimens

As shown previously, the unnotched-bend specimens failed by delamination caused by shear failure. The shear strength of this graphite/epoxy material was calculated as follows:

$$\tau = \frac{3}{4} \frac{P_{max}}{W \cdot B} \tag{1}$$

where

τ = shear strength,
P_{max} = load at which load drop occurred,
W = specimen depth, and
B = specimen thickness.

Notched-Bend Specimens

The fracture toughness of unidirectional laminated material (or laminated material with no fibers intersecting the direction of crack extension, such as the one tested) is strongly dependent upon the orientation of the crack relative to the fibers [*11*]. Also, the crack extension may or may not extend in the same direction as the original notch direction. Therefore, a notation system is proposed to denote the fracture toughness of unidirectional laminated material (or laminated material with the majority of the fibers oriented in a single direction). The notation system is such that the roman numeral within the parentheses indicates the mode of loading (per ASTM Method E 399-78a) and the number outside the parentheses indicates the angle of crack extension relative to the original crack (see Fig. 9).

Since the first load drop of the notched-bend specimens was caused by delamination at the notch tip, the LEFM approach was employed. In addition, since the deviation from linearity was attributed to plastic deformation under the loading point rather than plastic deformation at the notch-tip region, the *R*-curve technique was not used to determine the critical stress-intensity factor $(K_{Ic})_{90}$. The critical stress-intensity factor was simply calculated from the maximum load at the first load drop, $(P_{max,1})$. The *K*-calibration used was given by Wilson [*20*] for isotropic material. The stress-intensity factor for an edge-notched-bend specimen under pure bending can be expressed as

$$K_I = \frac{4M}{(W-a)^{3/2}B} \tag{2}$$

where

M = bending moment,
W = specimen depth,
B = specimen thickness, and
a = notch depth.

For the edge-notched-bend bar specimen tested in three-point bending, the fracture toughness is calculated via Eq 3 as

$$(K_{Ic})_{90} = 0.95 \frac{P_{max,1} \cdot S}{(W-a)^{3/2} \cdot B} \tag{3}$$

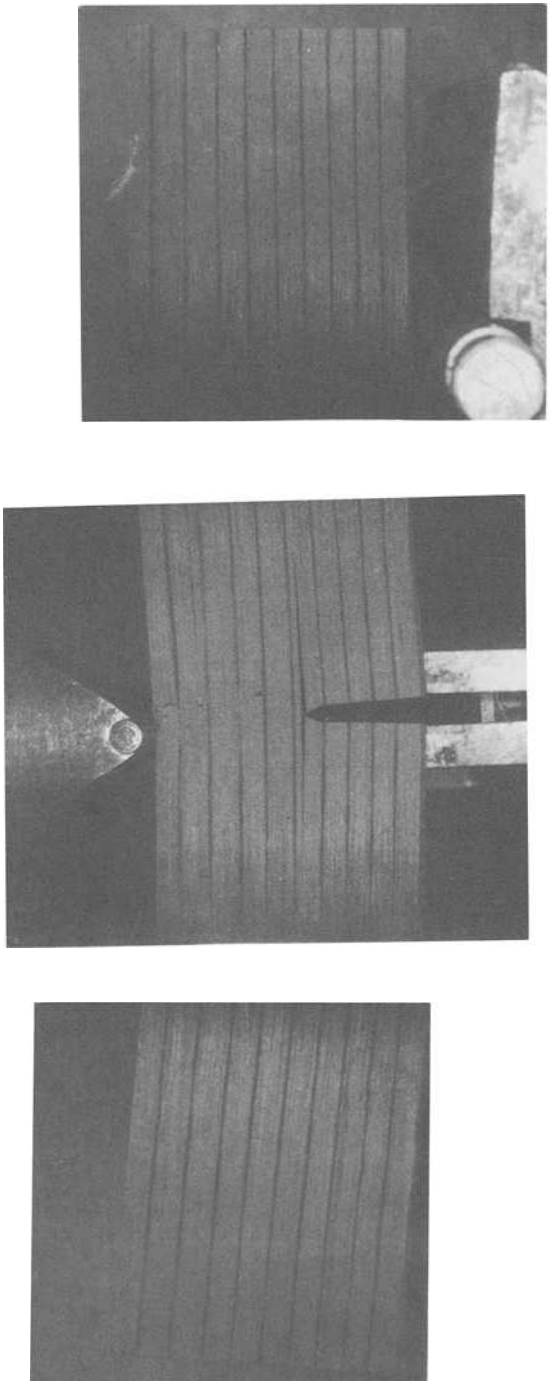

FIG. 6—*Closeup of a specimen* k *under a 2670-N (600 lb) load and a 3.4-mm (0.135 in.) displacement (after two load drops).*

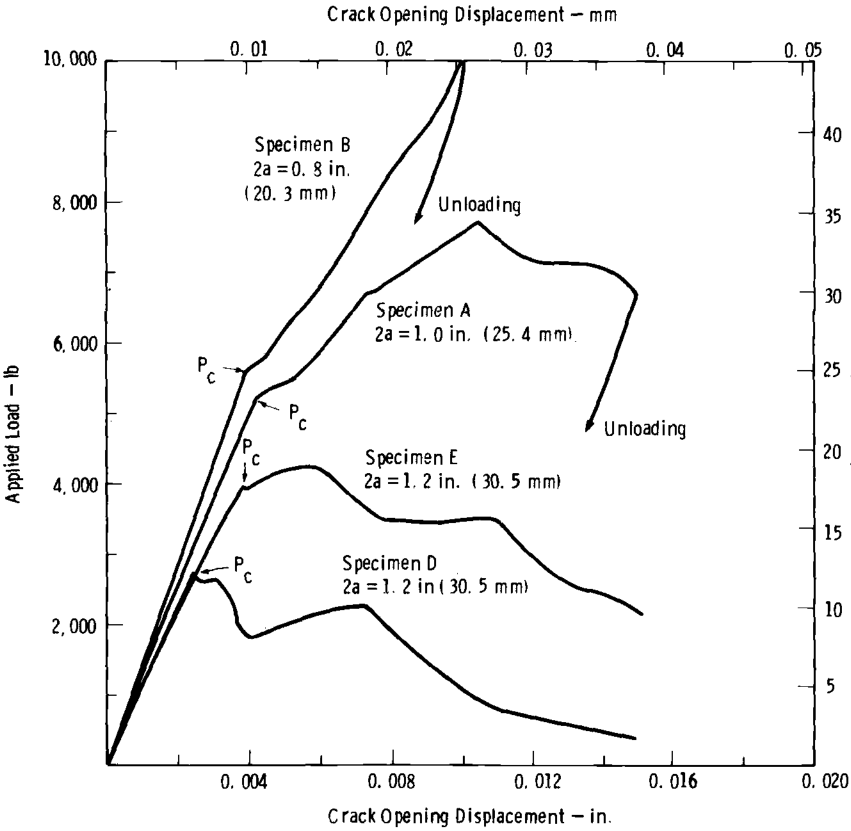

FIG. 7—*Load versus crack-opening displacement records for center-notched-tension specimens.*

The constant (0.95) accounts for the difference between three- and four-point bend loading [*21*].

Center-Notched-Tension Specimens

The critical stress-intensity factor for the center-notched-tension specimens was calculated via Eq 4 as given by Feddersen [*22*]

$$(K_{\mathrm{Ic}})_{90} = \frac{P_c}{WB}\sqrt{\pi a \sec\left(\frac{\pi a}{W}\right)} \tag{4}$$

where

P_c = critical load,
W = specimen width,
B = specimen thickness, and
$2a$ = crack length.

Experimental Results

The experimental results obtained from unnotched and notched specimens are presented separately.

Unnotched-Bend Specimens

The experimental results including the maximum loads, shear strength (τ), and flexural strengths (σ_f) are presented in Table 2 along with specimen dimensions (width W and thickness B) and support span (S). The shear strengths obtained from specimens of two different thicknesses and support

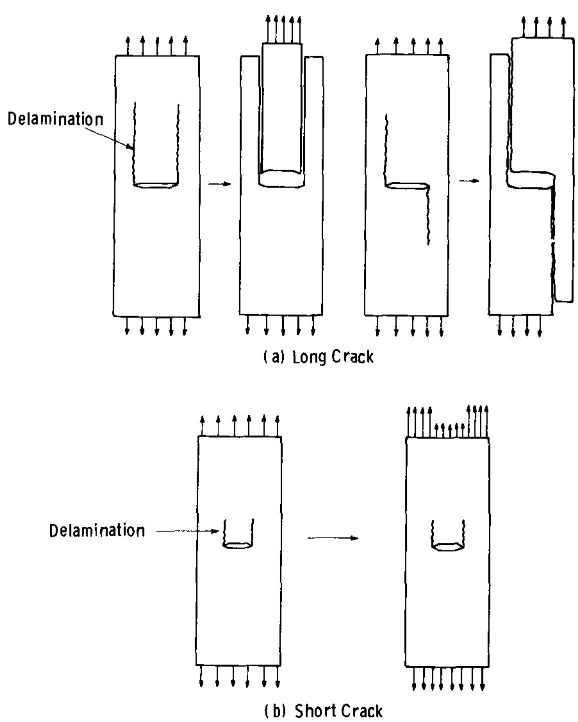

FIG. 8—*Failure mode of center-notched panels.*

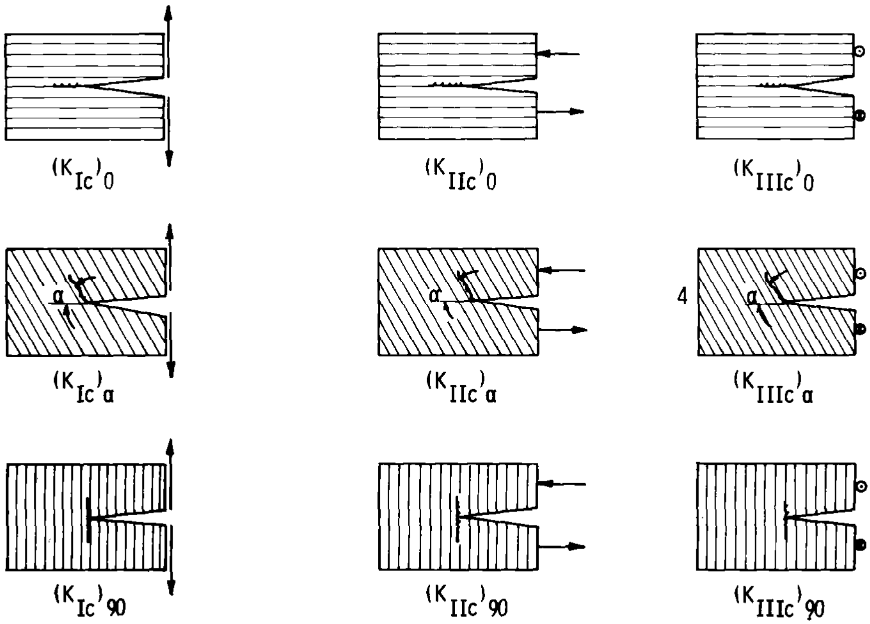

FIG. 9—*Proposed notation system for fracture toughness of anisotropic laminated materials.*

spans are plotted versus specimen depth in Fig. 10. Note that the shear strength of this graphite/epoxy composite is essentially independent of these testing variables. The average shear strength equals 24.6 MPa (3.57 ksi) with a scatterband of ±20 percent.

Notched-Bend and Center-Notched-Tension Specimens

Experimental results relative to the notched-bend specimens including $P_{max,1}$, $P_{max,2}$, $(K_{Ic})_{90}$, and τ are presented in Table 3. The critical stress-intensity factor $(K_{Ic})_{90}$ or fracture toughness of the graphite/epoxy composite is plotted as a function of crack length in Fig. 11. Note that apparent fracture toughness as determined via edge-notched-bend specimens increases with increasing crack length. A least-squares fit of the data shows that the relationship between $(K_{Ic})_{90}$ and crack length (a) can be expressed as

$$(K_{Ic})_{90} = 15.47 + 25.34\,(a)$$

with $(K_{Ic})_{90}$ in ksi$\sqrt{\text{in.}}$ and a in inches or

$$(K_{Ic})_{90} = 17.02 + 1.10\,(a)$$

with $(K_{Ic})_{90}$ in MPa$\sqrt{\text{m}}$ and a in mm. It should be mentioned that, if the two fracture toughness values for the shortest crack length (a) equal to 8.9 mm

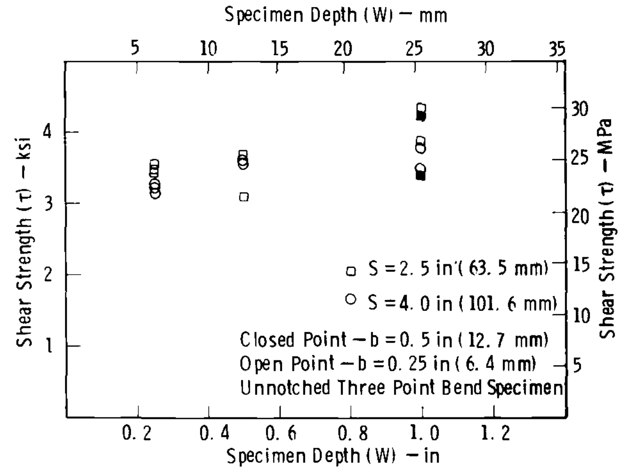

FIG. 10—*Shear strength versus specimen depth for a graphite/epoxy composite.*

TABLE 3—*Experimental results of notched-bend specimens.*

Specimen No.	Crack Length a, in.	$P_{max,1}$, lb	$(K_{Ic})_{90}$, ksi$\sqrt{in.}$	$W - a$, in.	$P_{max,2}$, lb	τ, ksi	σ_f, ksi
G	0.55	1164	29.27	0.45	840	2.80	49.77
H	0.65	900	33.05	0.35	680	2.91	66.61
I	0.46	1390	26.62	0.54	1170	3.25	48.15
J	0.46	1640	31.05	0.54	1120	3.11	46.09
K	0.46	1413	27.06	0.54	1120	3.11	46.09
L	0.65	810	29.74	0.35	680	2.91	66.61
M	0.35	1640	22.76	0.65	1105	2.65	32.66
N	0.35	1720	23.87	0.65	1050	2.42	29.82
			avg 27.91			avg 2.90	

NOTE: 1 in. = 25.4 mm; 1 lb = 4.48 N; 1 ksi = 6.895 MPa; 1 ksi $\sqrt{in.}$ = 1.099 MPa $\sqrt{m}$.

(0.35 in.) are neglected, the remaining data tends to render the fracture toughness independent of specimen crack length.

Fracture toughness values obtained via the four center-notched tension specimens are summarized in Table 4 and also included in Fig. 11. These fracture toughness values appear independent of crack length. This conclusion, however, is based on a very small data sampling.

Discussion

The shear strength of the graphite/epoxy composite is essentially independent of specimen size and support span (see Fig. 10). On the other hand, when

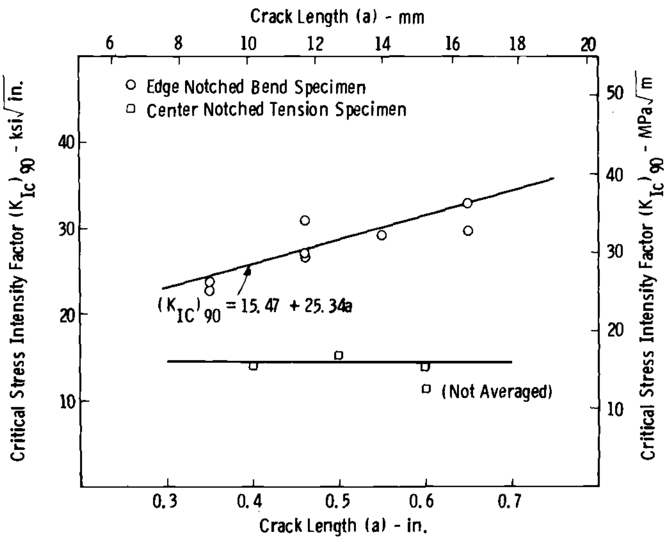

FIG. 11—*Fracture toughness* $(K_{Ic})_{90}$ *of graphite/epoxy composite obtained from edge-notched-bend and center-notched tension specimens.*

TABLE 4—*Experimental results of center-notched-tension specimens.*

Specimen No.	Crack Length, $2a$, in.	Critical Load, P_c, lb	Fracture Toughness, K_{Ic90}, ksi$\sqrt{\text{in.}}$
A	1.0	5250	15.5
B	0.8	5600	14.2
D	1.2	3200	11.5
E	1.2	3950	14.1

NOTE: 1 in. = 25.4 mm; 1 lb = 4.448 N; 1 ksi$\sqrt{\text{in.}}$ = 1.099 MPa$\sqrt{\text{m}}$.

the bend test results are interpreted and expressed as flexural strength versus specimen depth, Fig. 12, the "flexural strength" obtained from unnotched-bend specimens is dependent on the specimen dimensions and support span.[3] This dependent behavior is not unexpected since the failure mode of these bend specimens is delamination caused by shear failure rather than fiber breakup caused by excessive flexural stress. Thus, it is emphasized that, due to the nature of this anisotropic material, attention should be given to the failure mode in order to perform meaningful design calculations.

Fracture toughness values obtained for this graphite/epoxy composite via edge-notched-bend specimens fall between 25.04 and 36.35 MPa$\sqrt{\text{m}}$ (22.76 and 33.05 ksi$\sqrt{\text{in.}}$). These values are consistent with results presented by

[3]Bend tests are commonly used to establish the flexural strength of composites.

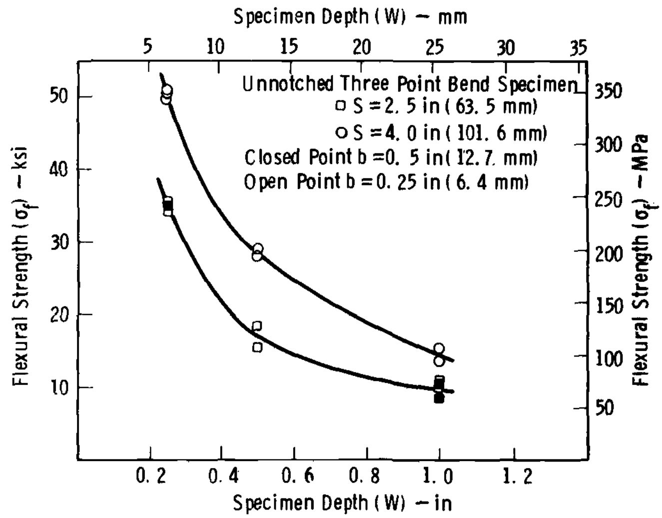

FIG. 12—*Flexural strength versus specimen depth for graphite/epoxy composite.*

others: (1) 35.86 MPa$\sqrt{\text{m}}$ ± 11 percent (32.6 ksi$\sqrt{\text{in}}$ ± 11 percent) obtained for a graphite/epoxy composite with 0-deg fiber orientation angle [*11*]; (2) 33 MPa$\sqrt{\text{m}}$ (30 ksi$\sqrt{\text{in.}}$) obtained for a $[0/\pm 45/90]_{ns}$ T300/5208 graphite/epoxy laminate [*13*]; and (3) 26.4 to 39.6 MPa$\sqrt{\text{m}}$ (24 to 36 ksi$\sqrt{\text{in.}}$) (depending on ply thickness) obtained for a (90/0/90/0/90) graphite/epoxy composite [*2*]. However, the present experimental results (Fig. 11) show that the fracture toughness of this graphite/epoxy composite increases with increasing crack length. Moreover, with the exception of a single low-fracture-toughness value, the fracture toughness values obtained from center-notched-tension specimens average 16.4 MPa$\sqrt{\text{m}}$ (14.9 ksi$\sqrt{\text{in.}}$) or almost exactly half of that obtained from the edge-notched-bend specimens. These results conflict with a basic premise of LEFM; that is, fracture toughness is an intrinsic material property and is geometry-independent. Thus, the applicability of fracture mechanics to laminated composites becomes questionable, as suggested by Hoover and Allred [*16*] plus Ellis and Harris [*17*].

In previous studies of T300/5208 graphite/epoxy material [*13,23*], the fracture of a notched specimen did not consist of a definite pop-in type behavior, which is often observed for metallic material and brittle material. As such, the resistance curve technique [*24*] was employed to determine fracture toughness. The nonlinearity for the $[0/\pm 45/90]_{ns}$ material tested was attributed to the damage zone at the crack tip developing slowly in the form of a number of small cracks within plies which are parallel to the fiber orientation in each ply, often accompanied by a local delamination between plies [*13*]. On the other hand, the graphite/epoxy material of the present study showed a definite pop-in type behavior. The difference in fracture behavior can be attributed to the fact that the graphite/epoxy material tested in this program is essentially a unidirectionally reinforced material.[4]

For a unidirectional reinforced material with a transverse crack subjected to Mode I (tensile) loading, such as the single-edge-notched-bend specimen, there is a shear stress concentration at the crack tip. This (shear) stress concentration will cause the material to split and delaminate from the crack tip along the plane of weakness (parallel to the fiber plane) rather than cracking normal to the applied load. It is unfortunate that fracture mechanics cannot be applied in this case to predict the load-carrying capacity. However, the delamination eliminates the stress concentration effect at the crack-tip region. Therefore, the edge-notched-bend specimen would behave like an unnotched bend bar with an effective specimen depth (W_{eff}) given by W-a; see Fig. 13. As can be seen from Table 3, the load necessary to cause delamination at the crack tip ($P_{max,1}$) is always higher than the load required to cause general shear failure ($P_{max,2}$). This suggests that the graphite/epoxy composite is not sensitive to cracks in a plane perpendicular to the plane of the fibers, and the loading-carrying capacity of such a cracked body can be calculated based on net section considerations; see Fig. 13. Similar conclusions were reached by Hoover and Allred [*16*].

The shear strengths corresponding to the second load drop ($P_{max,2}$), using the effective specimen depth concept, were determined from Eq 5 and are presented in Table 3 and Fig. 14

$$\tau = \frac{3}{4} \frac{P_{max,2}}{(W - a)\, B} \tag{5}$$

As expected, these shear strengths are essentially independent of effective specimen depth. The average shear strength equals 20 MPa (2.90 ksi) and is approximately 20 percent less than those obtained from unnotched-bend specimens. This discrepancy, however, may be attributed to the damage sus-

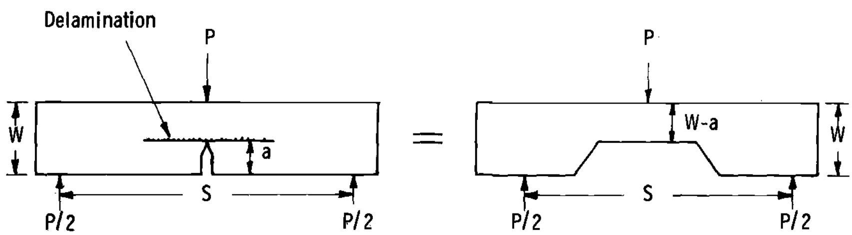

FIG. 13—*Effective specimen depth of a specimen with delamination from crack-tip region.*

[4]Although approximately 13.5 percent of the graphite fibers are not parallel to the (principal) flexural stress, they are on the same plane as the flexural stress.

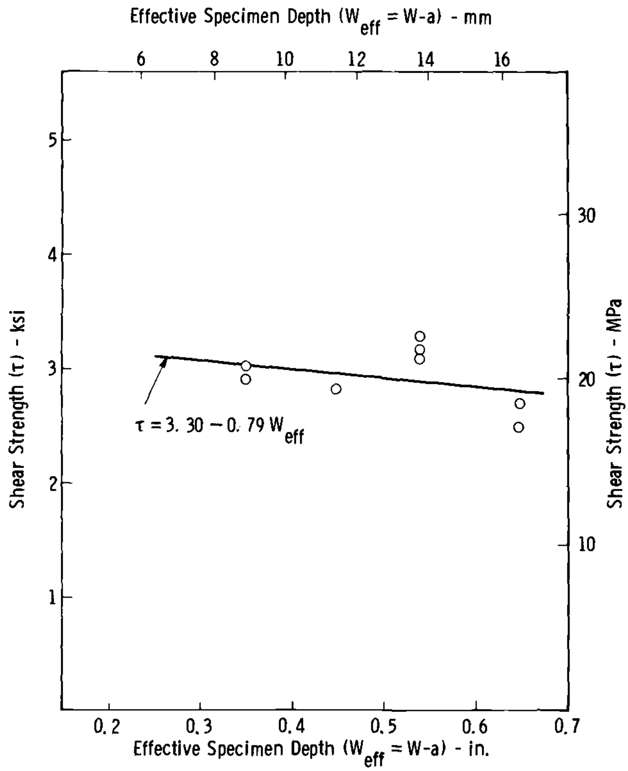

FIG. 14—*Shear strength of the graphite/epoxy composite determined from edge-notched-bend specimens.*

tained by these edge-notched-bend specimens at and prior to reaching $P_{max,1}$. The corresponding flexural strengths obtained from these notched-bend specimens are dependent on the effective specimen depth (see Fig. 15). This behavior is similar to that observed on the unnotched-bend specimens (see Fig. 12), where the flexural strengths were dependent on specimen dimensions and support span.

The interply shear strength of this thick-section [54 mm (2.125 in.)] graphite/epoxy composite is 24.6 MPa (3.57 ksi). This value is much lower than the 74.5 MPa (10.8 ksi) obtained for a 3.3-mm-thick (0.128 in.) graphite/epoxy material with similar fiber layup. This discrepancy can be attributed to the microcracks which exist in this vintage thick-section composite. These microcracks can be eliminated by improving the fiber surface treatment, by optimizing the fiber layup or by choosing the proper combination of fiber and resin. Eliminating these microcracks will significantly increase the interply shear strength of this material, thus moving the graphite/epoxy composite retaining ring one step closer to reality.

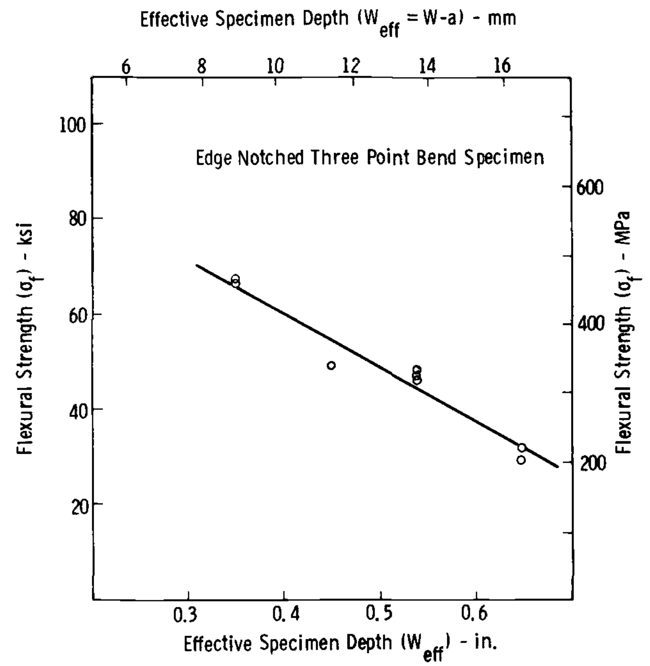

FIG. 15—*Flexural strength as a function of effective specimen depth.*

Conclusions

1. The failure mode of the test composite under three-point bending is interply shear failure. The interply shear strength of the test composite was 24.6 MPa (3.57 ksi).

2. The "flexural strength," determined from three-point bend tests, is dependent on specimen dimensions and support span and cannot be used for design calculation.

3. Apparent fracture toughness values obtained for a thick-section graphite/epoxy composite via edge-notched-bend specimens range between 25.04 and 36.35 MPa$\sqrt{m}$ (22.76 and 33.05 ksi$\sqrt{in.}$) and are dependent on notch depth.

4. Apparent fracture toughness values obtained for this graphite/epoxy composite via center-notched-tension specimens averaged 16.4 MPa$\sqrt{m}$ (14.9 ksi$\sqrt{in.}$) and are independent of notch length.

5. Due to the dependence of apparent fracture toughness values on specimen geometry and notch length, LEFM is not directly applicable to thick-section composites with cracks perpendicular to the fiber orientation.

6. The graphite/epoxy composite tested in this investigation was insensitive to cracks in a plane perpendicular to the fibers. The load-carrying capability can be calculated based on net section considerations.

References

[1] Dharan, C. K. H., *Journal of Engineering Materials and Technology*, Vol. 100, July 1978, pp. 233-247.
[2] Mandell, J. F., Wang, S. S. and McGarry, F. J., *Journal of Composite Materials*, Vol. 9, 1975, pp. 266-287.
[3] Hoover, W. R., *Journal of Composite Materials*, Vol. 10, April 1976, pp. 106-117.
[4] Phillips, D. C., *Journal of Composite Materials*, Vol. 8, April 1974, pp. 130-141.
[5] Holdsworth, A. W., Owen, M. J., and Morris, S., *Journal of Composite Materials*, Vol. 8, April 1974, pp. 117-129.
[6] Sun, C. T. and Prews, K. M., *Journal of Composite Materials*, Vol. 11, April 1977, pp. 164-175.
[7] Morris, D. H. and Hahn, H. T., *Journal of Composite Materials*, Vol. 11, April 1977, pp. 124-138.
[8] Wright, M. A. and Iannuzzi, F. A., *Journal of Composite Materials*, Vol. 7, Oct. 1973, pp. 430-447.
[9] Zimmer, J. E., *Journal of Materials*, Vol. 6, April 1972, p. 312.
[10] Guess, T. R. and Hoover, W. R., *Journal of Composite Materials*, Vol. 7, Jan. 1973, pp. 2-20.
[11] Konish, H. J., Jr., Swedlow, J. L., and Cruse, T. A., *Journal of Composite Materials*, Vol. 6, Jan. 1972, pp. 114-124.
[12] Mandell, J. F., McGarry, F. J., Wang, S. S., and Im, J., *Journal of Composite Materials*, Vol. 8, April 1974, pp. 106-116.
[13] Kim, R. Y., *Experimental Mechanics*, Feb. 1979, pp. 50-55.
[14] Morris, D. H. and Hahn, H. T. in *Composite Materials: Testing and Design, Fourth Conference, ASTM STP 617*, American Society for Testing and Materials, 1977, pp. 5-17.
[15] McKinney, J. M., *Journal of Composite Materials*, Vol. 6, Jan. 1972, pp. 164-167.
[16] Hoover, W. H. and Allred, R. E., *Journal of Composite Materials*, Vol. 8, Jan. 1974, pp. 55-64.
[17] Ellis, C. D. and Harris, B., *Journal of Composite Materials*, Vol. 7, Jan. 1973, pp. 76-80.
[18] Ueng, C. E. S., Aberson, J. A., and Lafitle, B. A., *Journal of Composite Materials*, Vol. 11, April 1977, pp. 222-234.
[19] Yeow, Y. T., Morris, D. H., and Brinson, H. F., *Experimental Mechanics*, Jan. 1979, pp. 1-8.
[20] Wilson, W. K., *Engineering Fracture Mechanics*, Vol. 2, 1970, pp. 169-171.
[21] Brown, W. F., Jr., and Srawley, J. E. in *Plane Strain Crack Toughness Testing of High-Strength Metallic Materials, ASTM STP 410*, American Society for Testing and Materials, 1967.
[22] Fedderson, C., Discussion to *Plane Strain Crack Toughness Testing of High-Strength Metallic Materials, ASTM STP 410*, American Society for Testing and Materials, 1967, pp. 77.
[23] Morris, D. H. and Hahn, H. T. in *Composite Materials: Testing and Design, Fourth Conference, ASTM STP 617*, American Society for Testing and Materials, 1977.
[24] *Fracture Toughness Evaluation by R-Curve Methods, ASTM STP 527*, American Society for Testing and Materials, 1973.

J. G. Avery,[1] *S. J. Bradley,*[1] *and K. M. King*[1]

Fracture Control in Ballistic-Damaged Graphite/Epoxy Wing Structure

REFERENCE: Avery, J. G., Bradley, S. J., and King, K. M., "**Fracture Control in Ballistic-Damaged Graphite/Epoxy Wing Structure,**" *Fracture Mechanics: Thirteenth Conference. ASTM STP 743,* Richard Roberts, Ed., American Society for Testing and Materials, 1981, pp. 338–359.

ABSTRACT: This paper describes the development of a graphite/epoxy wing skin configuration capable of sustaining limit load following damage from a 23-mm high-explosive (HE) projectile impact. The skin configuration incorporates information learned in sawcut and ballistic fracture testing, and consists of a ±45 graphite/epoxy laminate with integral spanwise and chordwise crack-arresting pads formed by adding 0-deg glass/epoxy between the plies of graphite/epoxy. The ±45-ply orientation provides enhanced battle damage tolerance because of its higher residual strain-to-fracture capability relative to quasi-isotropic 0/±45/90 laminates. This permits developing the full load-carrying capability of the spar chords before unstable crack propagation can occur in the damaged skin. The 0-deg glass/epoxy was added to further enhance this capability, and concentrated into pads to avoid undesirable ballistic damage augmentation caused by the glass fibers, and to provide a controlled failure mode under blast pressures. The optimum graphite-to-glass ratio and the required width of the crack-arresting pads were determined using a new analysis method for predicting fracture in laminates containing high-strength 0-deg fibers. The effectiveness of the damage tolerance concept was demonstrated by firing a 23-mm HEI projectile into the tension surface of a full-scale wing-box test component loaded in combined bending and torsion. Following damage, limit load was achieved as a result of successful crack arrestment.

KEY WORDS: cracking (fracturing), fracture (materials), advanced fiber composites, ballistic damage, impact strength, military aircraft, antiaircraft projectiles, high-explosive projectiles, tensile strength, fracture strength, ballistics, residual strength

Advanced fiber composites, chiefly graphite/epoxy, are being developed for increased use in the primary structure of combat airplanes. Since these airplanes operate in a hostile environment, research programs (for example, [*1*][2]) have been undertaken to establish the response of fiber composites to

[1]Manager, Survivability/Vulnerability, technical analyst, and senior specialist engineer, respectively, Boeing Military Airplane Co., Research and Engineering, Seattle, Wash. 98124.
[2]The italic numbers in brackets refer to the list of references appended to this paper.

projectile impact and to develop design approaches that improve battle damage tolerance. This work has shown that graphite/epoxy and boron/epoxy can be very intolerant of ballistic damage. 0/±45/90 graphite/epoxy for example is extremely notch-sensitive, comparable to 7178-T6 aluminum, one of the most notch-sensitive aluminum alloys. However, by varying the fiber orientation and hybridizing with other fiber types, the ballistic damage response and tolerance of graphite/epoxy structure can be controlled, providing a potential new dimension for achieving combat survivability.

The Battle Damage Tolerant Wing Structural Development Program [*2*] was initiated in 1974 to develop and demonstrate the technology for designing a graphite/epoxy wing box capable of meeting stringent battle damage tolerance criteria. These criteria required that the wing sustain limit load after being hit by a 23-mm high-explosive-incendiary (HEI) projectile under conditions causing worst-case damage. This projectile is an antiaircraft artillery round which detonates on contact, creating fragmentation and blast damage mechanisms. The entry damage from a superquick-fused 23-mm HEI projectile was represented as a 0.254-m (10 in.) sharp-edged crack for residual tensile strength assessment.

Figure 1 shows the final wing design with the major features highlighted. The battle-damage-tolerant design configuration consists of multiple high-stiffness spars and a low-stiffness skin having enhanced fracture resistance obtained by hybridization and geometric tailoring. This provides the required damage containment capability without significantly reducing the design strain level.

Development of the fracture resistant skin proceeded in five phases:

1. Evaluation of the relative fracture performance of candidate skin laminates, as measured by strain-to-failure.
2. Evaluation of fracture performance with ballistic damage, including the effects of the applied tension load at impact.
3. Development of an analysis method for detailed design optimization which provides fracture criteria in terms of laminate properties.
4. Definition of final design based on information from Phases 1-3.
5. Full-scale verification of the final design by impacting a loaded full-scale wing box with a superquick-fused 23-mm HEI projectile and demonstrating limit load capability with damage.

These five activities are addressed in the following paragraphs.

Fracture Response of Candidate Skin Materials

Analysis [*3*] indicated that good survivability to exploding projectiles could be achieved in a wing-box configuration using multiple spars containing uniaxial graphite/epoxy, and ±45 graphite/epoxy skins. Most of the spanwise bending loads are carried in the spar chords and the skin is sized primarily by

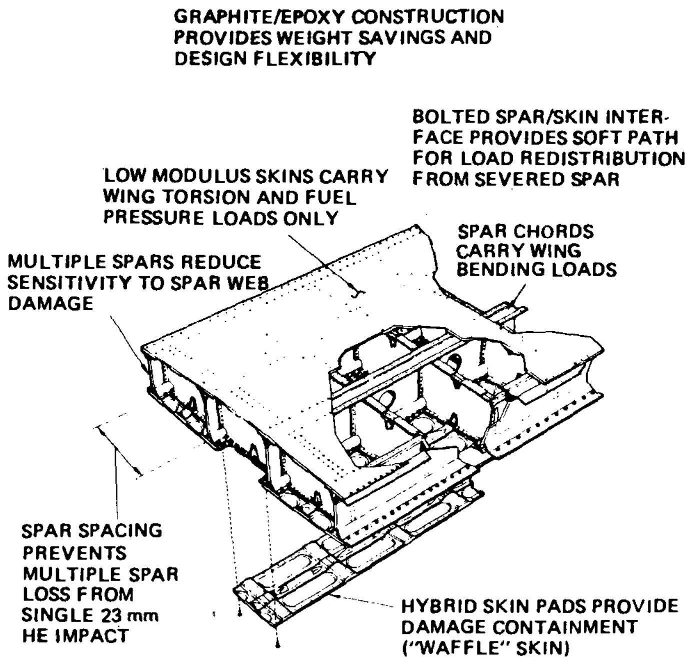

FIG. 1—*Battle-damage-tolerant wing final design.*

torsion and internal pressure due to fuel storage and delivery. Avoiding the use of 0-deg graphite fibers in the skin enhances residual strain-to-failure and fracture toughness following ballistic damage.

Having defined a general configuration, our next task was to conduct fracture testing to compare the fracture performance of candidate ± 45 fiber/resin systems for the skin panels. The following paragraphs describe the materials tested, test procedures, results, and conclusions.

Candidate Skin Laminates

The fracture performance of five ± 45 graphite/epoxy systems was evaluated: T300/934 and T300/5208 prepreg tape and fabric, and AS/3501 tape. ± 45 laminates of three nongraphite systems of potential interest were also tested: Kevlar 49/934 tape and fabric, and S-glass/1002 tape. Analytical predictions [*3*] indicated that interspersing plies of a high-strength material having a high strain-to-failure (such as glass or Kevlar) within ± 45 graphite/epoxy laminates would improve fracture resistance, particularly if oriented in the 0-deg direction. Therefore, several graphite-glass and graphite-Kevlar interply hybrid laminates were tested to determine the best combination and proportion of materials for meeting battle damage tolerance requirements while retaining the structural efficiency of the skin.

Test Procedure

Laminates were fabricated according to vendor recommendations, and test panels of each type were cut from the cured laminates. The panel sizes varied, and details are given in Ref *2*. Central through-cracks were machined according to the specifications shown in Fig. 2. Friction grips were designed and fabricated for gripping fiberglass end-pads bonded to the test panels. This reduced fabrication expense and the risk of grip failure associated with bolted attachments. Stress/strain data for the laminates were obtained from tensile coupons cut from the panels. For the sawcut panels, gross strain at failure was estimated from the stress/strain curves at the measured failure stress.

Test Results

Values of K_Q/F_{tu} (apparent critical stress-intensity factor/ultimate undamaged stress) were generally above 1.1 for all the graphites, and approached 1.5 for the Kevlar 49 and S-glass laminates fabricated from unidirectional tape. This compares with values of K_Q/F_{tu} averaging about 0.6 for laminates having 0-deg graphite/epoxy fibers [*1*]. As Figure 3 shows, on the basis of strain-to-failure, the AS/3501 tape and the T300/934 fabric exhibited the highest strain-to-failure of the ±45 graphite materials.

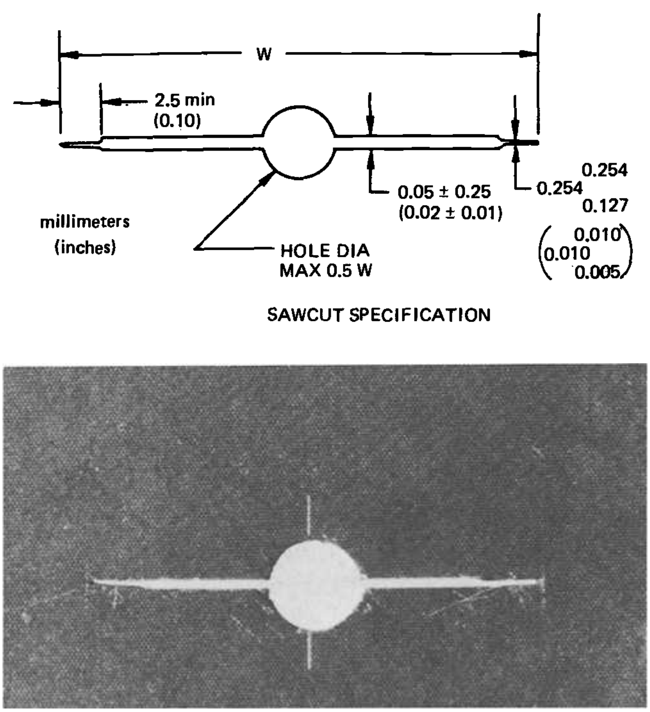

FIG. 2—*Photograph of sawcut used in fracture panels.*

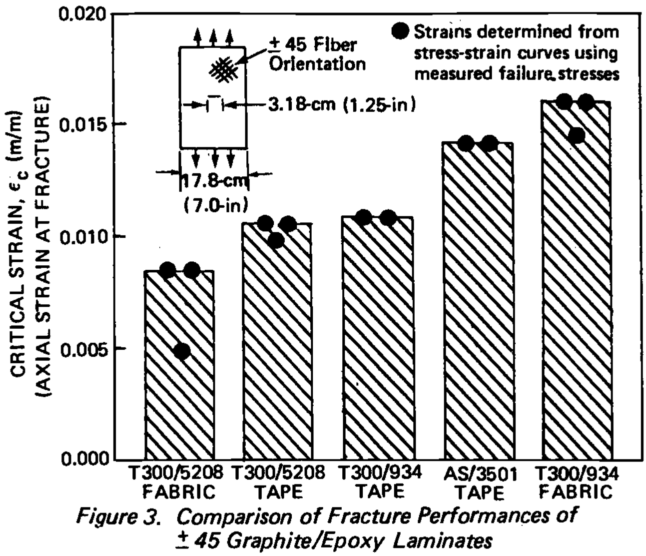

FIG. 3—*Comparison of fracture performances of* ±45 *graphite/epoxy laminates.*

Figure 4 shows photographs of some of the failed ±45 fracture panels. The failure surface was predominantly along the ±45 directions, except for the T300/934 fabric, the Kevlar 49/934 fabric, and the AS/3501 tape. Each of these latter configurations showed some transverse (self-similar) extension of the crack.

The test results for the interply hybrid systems containing 0-deg plies of S-glass/1002 (or Kevlar 49/934) interspersed with ±45 graphite/epoxy confirmed the analytical prediction of increased critical strain-to-failure and fracture toughness, as seen in Fig. 5. The curves shown in Fig. 5 relate critical crack length to the percentage of S-glass in the laminate, and were constructed using critical stress predictions (analysis method is described later) and stress/strain data obtained from undamaged graphite-glass hybrid laminates. The analysis predicted that a laminate with 35 percent S-glass could contain the 0.254-m (10 in.) crack simulating 23-mm HEI entry damage (superquick fuse) at the desired limit load strain.

Of the materials tested, AS/3501 graphite/epoxy reinforced with 0-deg S-glass/1002 glass/epoxy provided that best critical strain capability. However, T300/934 fabric with S-glass/1002 performed nearly as well and offered fabrication advantages for the application at hand. For these reasons the ±45 T300/934 fabric reinforced with 0-deg S-glass was selected for the wing skin. The strain-at-fracture and the ultimate strain of the graphite/Kevlar 49 hybrid panels were lower than the graphite/S-glass hybrids, and Kevlar 49 was not considered further for use as the hybridizing material.

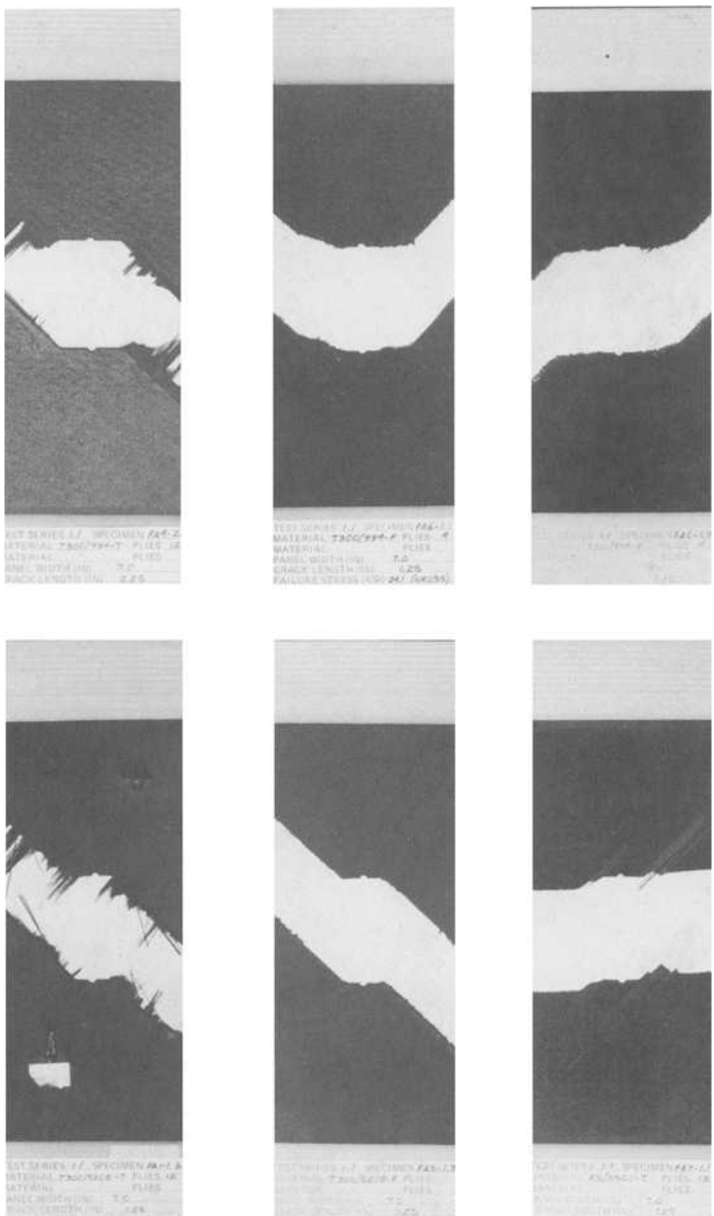

FIG. 4a—*Failure modes of center-cracked panels.*

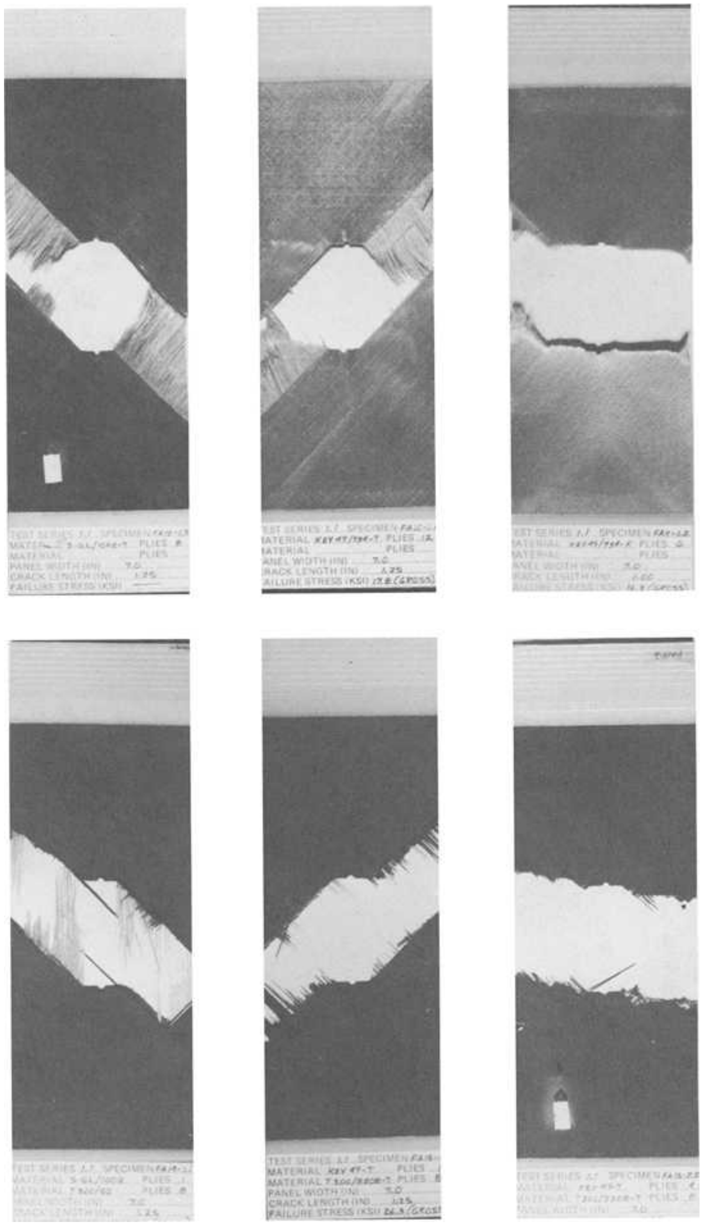

FIG. 4*b*—*Failure modes of center-cracked panels.*

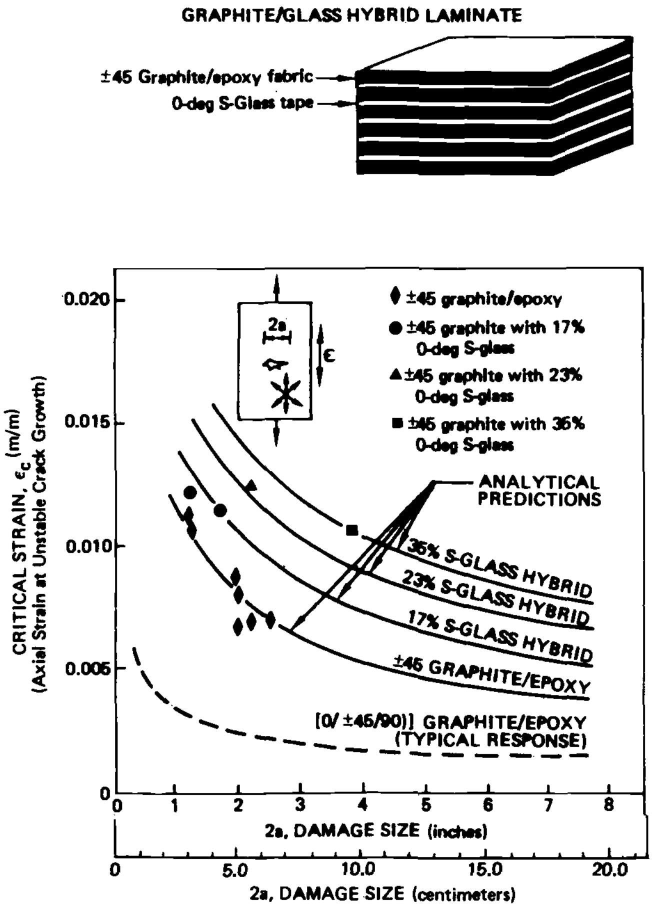

FIG. 5—*Damage containment improvement from adding 0-deg S-glass to ±45 graphite/epoxy.*

Fracture Response with Ballistic Damage

The sawcut fracture testing was valuable in determining the relative strain-to-failure and apparent fracture toughness of the candidate skin laminates, but did not provide sufficient information to fully define structural response to ballistic damage. The following paragraphs describe the work done to define this response, including ballistic impact tests to characterize damage, fracture testing of ballistic damaged panels, and ballistic impact tests of panels under tension load to assess the effect of applied load on damage and fracture.

Characterization of Ballistic Damage in Fiber Composite Laminates

Ballistic testing of graphite/epoxy and graphite-glass hybrid laminates was done with nonexplosive penetrators and high-explosive projectiles. The penetrator tests were conducted in an indoor ballistic test range consisting of a launcher, velocity measurement section, and test chamber. Within the test chamber, 0.127-cm (0.050 in.) test panels were mounted on a frame which could be rotated to establish the desired obliquity angle, and impacted with bullets or cubical fragments. The inflicted damages were examined visually and by ultrasonics, and four damage measures were defined as shown in Fig. 6.

1. *Maximum Perforation*—The maximum dimension of through-the-thickness material separation. This dimension corresponds approximately to a "see-through" capability.
2. *Maximum Perforation plus Through Delamination*—This dimension includes the preceding damage plus adjacent area that is delaminated through-the-thickness. This measure defines the extent of removed or completely degraded material from a structural standpoint.
3. *Maximum Transverse Perforation*—The maximum perforation transverse to the preceding Measurement 1.
4. *Maximum Extent of Visible Damage*—This dimension is the maximum extent of visual ballistic impact damage on the panel. In many cases this includes surface peeling that has little effect on structural performance.

Figure 7 shows an undesirable response of the interply graphite/S-glass hybrid laminates to ballistic impact. On the left is the entry face of a hybrid panel after penetration by a 2.54-cm (1 in.) steel cube traveling at approximately 305 m/s (1000 ft/s), resulting in perforation with little damage beyond the projectile impact region. This type of damage, indicating a shear-

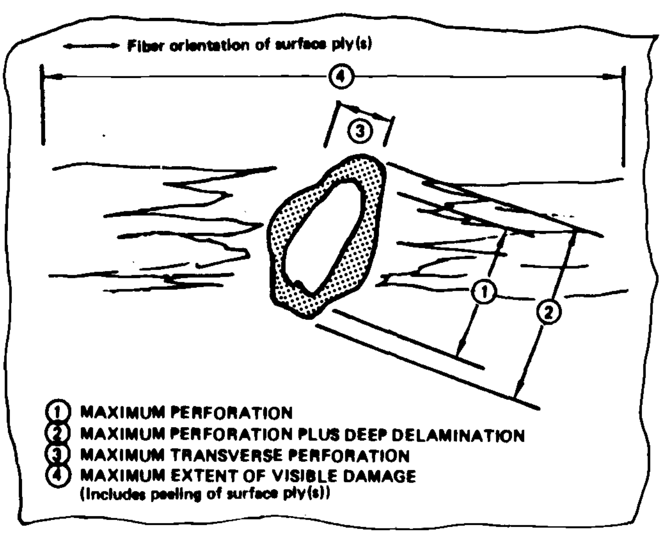

FIG. 6—*Representative measures of ballistic damage in composite materials.*

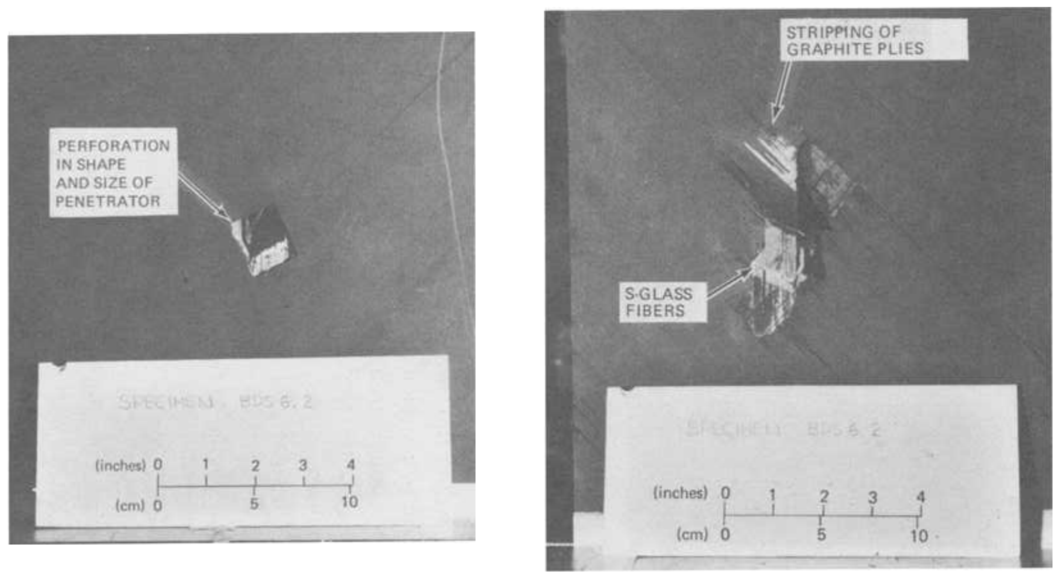

FIG. 7—*Typical entry and exit damage from ballistic penetration, ±45 graphite/epoxy reinforced with 0-deg S-glass.*

controlled or "plugging" penetration mode, is characteristic of both entry and exit surfaces for thin graphite/epoxy laminates. The exit surface of the hybrid laminate, however, has extensive damage in the direction of the 0-deg S-glass fibers. The tougher S-glass fibers resist penetration by elongation, thus bending the less-ductile graphite plies toward the exit surface, resulting in peeling and tearing much beyond the impact point. 23-mm HEI test firings into a replica wing-box test component clearly showed this undesirable damage augmentation, causing extension of damage spanwise into adjacent bays.

Strength Degradation of Ballistic-Damaged Composites

Having characterized the ballistic damage in the skin laminates, it remained to determine (1) the tensile strength degradation of ballistic damaged laminates, (2) the damage measures most influential in determining this strength degradation, and (3) the effect that applied load has on the extent of induced ballistic impact damage and residual strength.

The test procedure for determining these responses consisted of installing a test panel in the tension fixture, applying load, and firing a projectile through the stressed panel as indicated in Fig. 8. If fracture did not occur at impact, the applied load was removed and the ballistic damage was measured and photographed. Load was then reapplied until failure in order to determine residual strength. Past work (Refs *4* and *5*, for example) had demonstrated a threshold strength for a given impact condition, such that applied stresses exceeding the threshold strength result in immediate failure of the test panel upon penetration by the projectile. The threshold strength is often less than the residual strength (that is, the static strength) of panels damaged under the same impact conditions, indicating the potential significance of dynamic effects. When the applied stress is below the threshold strength, the panel will survive the impact with no apparent effect of applied load, and the residual strength of the damaged panel can be determined by subsequent loading to failure.

Olster and Roy [*5*] fired armor-piercing bullets into $0/\pm45$ and $0/\pm45/90$ graphite/epoxy laminates under preload and showed that the threshold strength was only slightly lower than the residual strength. The current work extends these conclusions to additional laminate configurations.

As shown in Fig. 9, ±45 graphite/epoxy laminates and interply hybrid laminates of ±45 graphite/epoxy reinforced with 0-deg S-glass/epoxy survived impacts even when the preload was just slightly less than the static residual strength level, indicating no significant strength degradation due to the dynamic conditions at impact. In other words, the threshold strength for applied load effects virtually equals the critical stress for residual strength.

Also indicated in Fig. 9, the residual strength of ±45 graphite/epoxy and graphite-glass hybrid panels with ballistic damage tends to correlate favorably with sawcut results using linear elastic fracture mechanics, taking

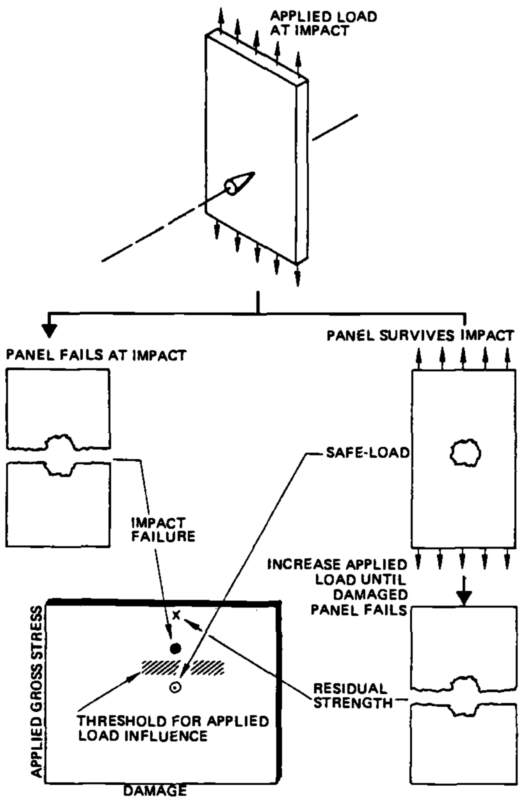

FIG. 8—*Strength degradation of tensile panels due to ballistic impact.*

the ballistic damage transverse to the applied load as the effective crack length. Best correlation is obtained with the damage defined as "maximum perforation plus through delamination" (Damage Measure 2). These results are consistent with conclusions from previous investigations addressing other laminate configurations [*1,6*]. Reference *6* reports a computational model for predicting this damage in graphite/epoxy laminates impacted by compact fragments and bullets, as shown in Fig. 10. The fracture test results indicate that the ballistic flaw is somewhat less severe than a sawcut of the same length. They are sufficiently close in effect, however, to justify using the sawcut results as a conservative estimation of the residual strength of ballistic damaged panels.

The graphite-glass hybrid panels exhibited substantial rear-surface ballistic damage as described previously, but this did not appear to have reduced the residual tensile strength. However, it may be significant in degrading shear and compression strength and causing the skin to separate from the substructure at attachments.

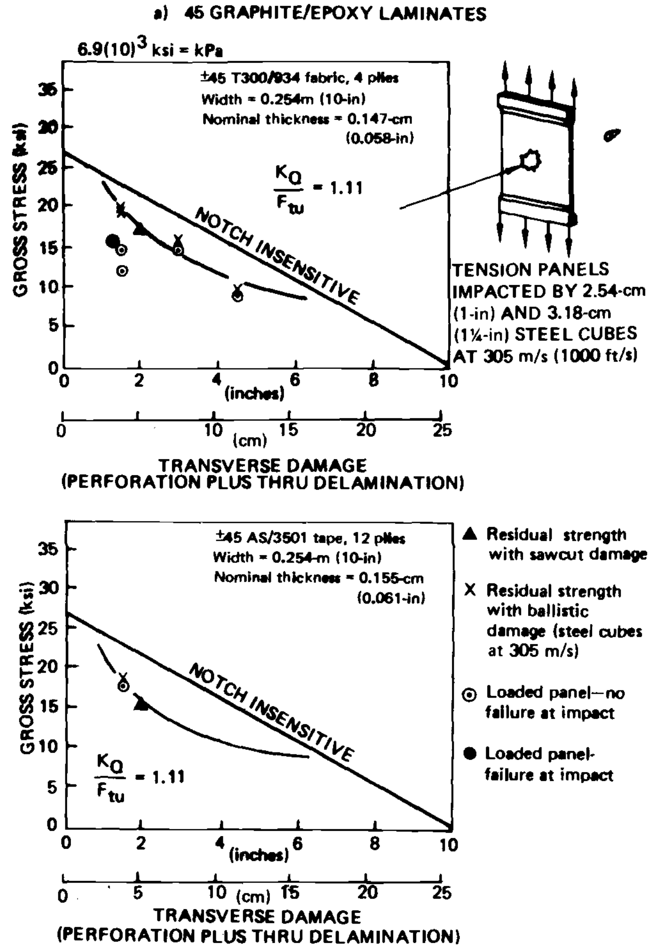

FIG. 9a—*Tensile strength degradation of ±45 laminates due to ballistic impact.*

Analysis Method for Predicting the Residual Strength of Fiber Composites

An analysis method was developed [3] for predicting the residual tension strength of fiber-controlled composite laminates containing projectile damage. The method is particularly useful for hybrid laminates, and was used to configure the "waffle" skin design with crack-arresting hybrid pads described later in this paper. In addition, the method provides the capability to predict critical fracture conditions directly from laminate properties, including ultimate tensile strength, shear modulus, and the tension modulus of the 0-deg constituent.

b) ±45 GRAPHITE/EPOXY HYBRIDIZED WITH 0-deg S-GLASS/EPOXY

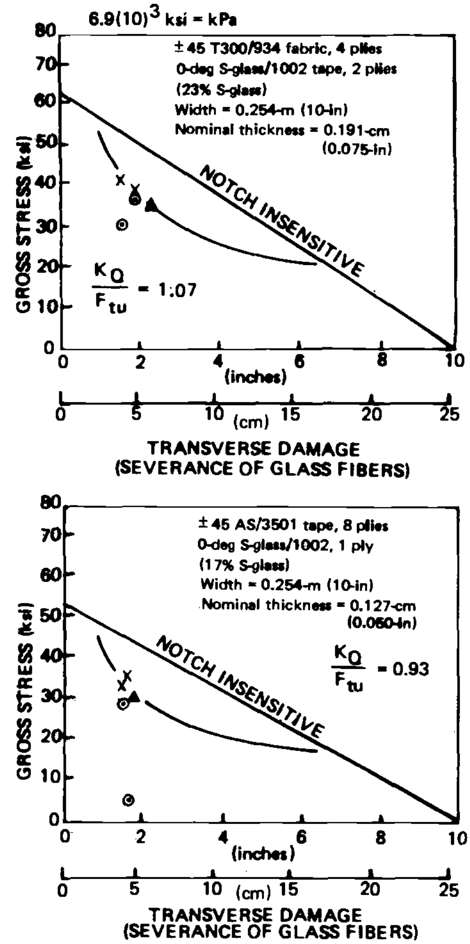

FIG. 9*b*—*Tensile strength degradation of* ±*45 laminates due to ballistic impact* (concluded).

The analysis method applies to layups containing 0-deg fibers that control the ultimate tensile strength of the laminate. A representation of the stress field near the tip of the crack is incorporated which presumes that all of the axial load interrupted by the crack is carried by the material near the tip, with ultimate stress at the tip when the gross stress equals the critical level for the flaw size. The local stress is assumed to decrease parabolically from ultimate to the gross stress at a distance Y from the crack tip.

The local stress distribution, including the distance Y, is assumed to de-

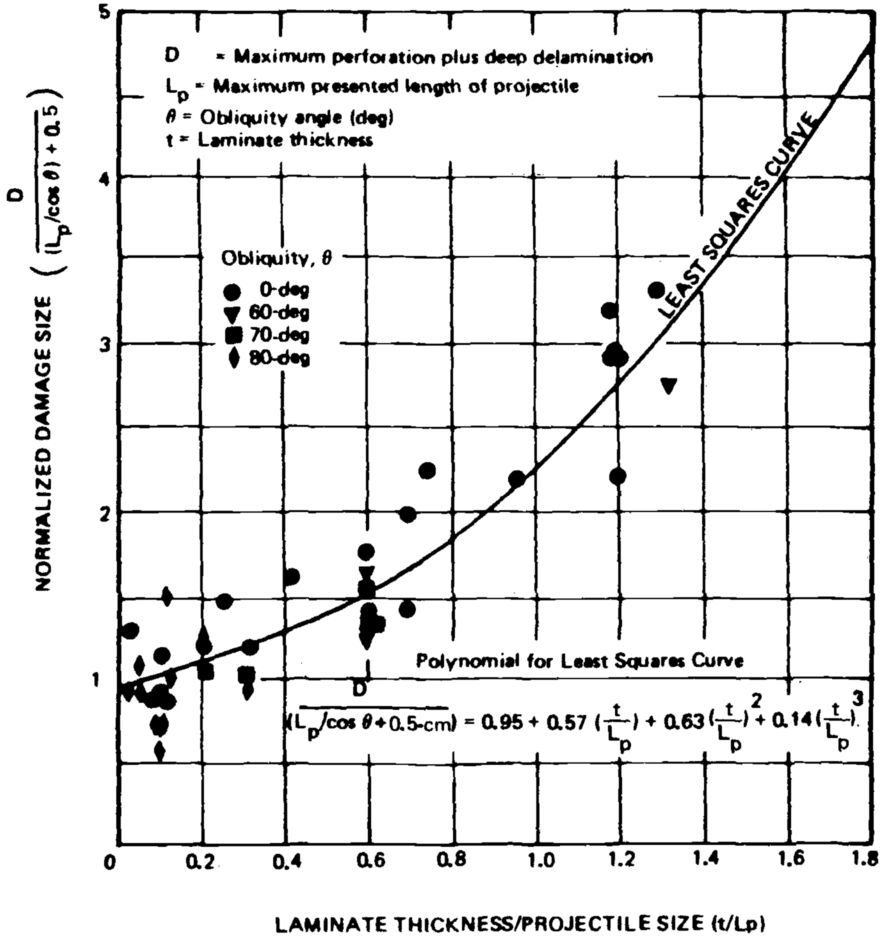

FIG. 10—*Damage size model for graphite/epoxy.*

pend on (1) the residual strength ratio, $R = \sigma_c/F_{tu}$; (2) the laminate shear modulus, G; and (3) the modulus of elasticity of a unidirectional laminate of the 0-deg constituent. Definition of these functional relationships was established empirically from available fracture test data for boron, graphite, E-glass, and graphite/S-glass hybrids, leading to the following relationship between critical crack size (in centimetres) and critical gross stress

$$a_c = 5\,\frac{G}{E_0}\left(\frac{1-R}{R}\right)^{1.5}$$ (use coefficient "2" instead of "5" to obtain a_c in units of inches)

where

a_c = critical crack half-length,
G = shear modulus of laminate,
E_0 = modulus of elasticity of a uniaxial laminate of the 0-deg material, and
R = σ_c/F_{tu} where σ_c is the critical tensile stress causing fracture and F_{tu} is the ultimate tensile strength of the undamaged laminate.

Figure 11 compares critical stress-intensity factors predicted using this equation with the results of fracture tests. There is good agreement between predicted and measured values.

The empirical constants defined in the preceding were evaluated from

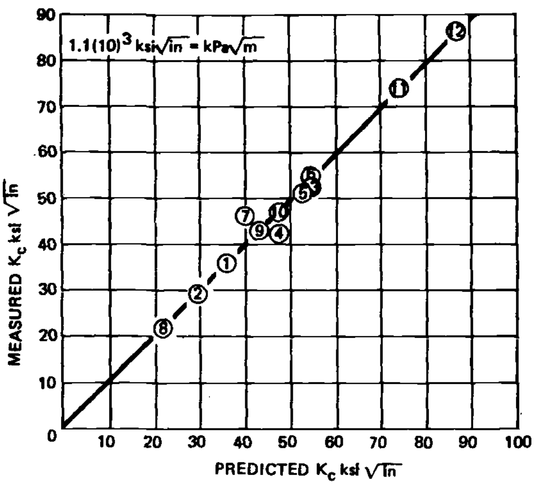

① $0_3/\pm45_2/90_2$ boron/epoxy
② $0_1/\pm45/90$ boron/epoxy
③ $0_2/\pm45$ boron/epoxy
④⑤⑥ $0_2/\pm45/90$ graphite/epoxy
⑦ $0/\pm45/90$ graphite/epoxy
⑧ $0/\pm45/90$ E-glass/epoxy
⑨ Hybrid 17.5% 0-deg SGL/ ±45 graphite/epoxy
⑩ Hybrid 17% 0-deg SGL/ ±45 graphite/epoxy
⑪ Hybrid 23% 0-deg SGL/ ±45 graphite/epoxy
⑫ Hybrid 35% 0-deg SGL/ ±45 graphite/epoxy

FIG. 11—*Correlation of test results with predictions from residual tensile strength analysis method.*

fracture test results of laminates havng 0, ±45, 90-ply orientations, and interply hybrid laminates of 0, ±45 orientation, where the ultimate strain of the 0-deg constituent did not greatly exceed that of the ±45 constituent. In addition, application is limited to self-similar crack extension transverse to the applied loads. The analysis method appears to accurately predict fracture levels for both large and small cracks within the limitations cited. Since the effect of the stress distribution near the crack is included, the analysis incorporates the parameters needed to configure crack-arresting pads or softening strips, and to predict the interaction between several cracks. Additional fracture toughness testing is needed to fully define the validity range of the analysis.

Design Approach for Battle-Damage-Tolerant Wing Skin

Three factors were evident from the testing and analysis of graphite/S-glass hybrid laminates:

1. For the wing-box configuration under development, graphite/S-glass interply hybrid skins with approximately 35 percent interspersed S-glass can contain 0.254-m (10 in.) ballistic damages at the selected limit load strain (0.0047 m/m), thus meeting the battle damage containment criteria.
2. The graphite/S-glass interply hybrid skins showed extensively augmented rear surface damage aligned in the direction of the S-glass fibers.
3. Internal blast pressures and impacting fragments from the 23-mm HEI projectile were capable of causing extensive skin detachment and delamination.

These factors guided the development of an improved skin design that greatly reduces inflicted ballistic damage while retaining the good damage tolerance of the graphite-glass hybrid. This design concept consists of placing the 0-deg S-glass only along the substructure interfaces, forming chordwise and spanwise crack-arresting pads of graphite-glass hybrid. The skin between the reinforced regions is ±45 graphite/epoxy, resulting in multithickness skin forming a "waffle" pattern as indicated in Fig. 12. The pad at the skin/rib interface contains 0/90 S-glass.

The damage tolerance design objective using these hybrid crack-arresting pads is to contain two-bay cracks between spanwise pads at limit load. This approach provides survivability to a worst-case damage introduction, that is, an impact causing severance of a spar cap with an associated equivalent sharp-edged crack of 0.254-m (10 in.). The thickness and width of the pads were sized by this requirement.

The damage resistance benefits resulting from the hybrid pad configuration are twofold: (1) Eliminating the S-glass from major portions of the skin and providing a rib pad eliminates the augmented rear surface damage and skin detachment associated with ballistic impacts into the interply hybrid de-

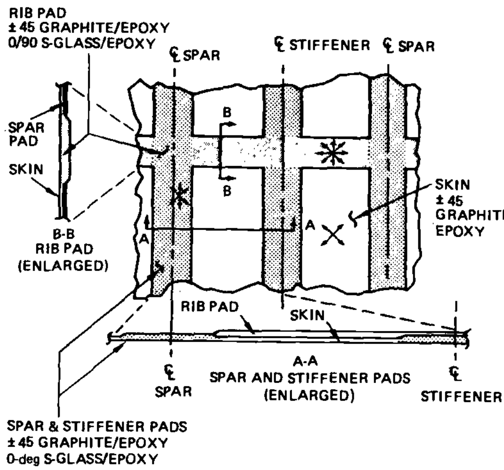

FIG. 12—*Hybrid pads for crack arrest and ballistic damage control.*

scribed previously. (2) The thinner sections of all-graphite skin bounded by the hybrid pads serve as "blowout" panels when subjected to intense pressures from the internal blast and fragments of the 23-mm HEI projectile. This action is achieved because skin failure occurs along the perimeter of the thinner all-graphite segment. The resulting failure line is relatively "clean," and the good fracture toughness of the hybrid pads prevents damage from propagating through the spar/skin or rib/skin attachments during subsequent loadings.

Full-Scale Verification of Ballistic Damage Tolerance and Control

A full-scale graphite/epoxy wing-box test component incorporating the damage tolerance concepts discussed was fabricated and tested. The three-spar test component was loaded in combined bending and torsion to a 4-*g* condition, and a 23-mm HEI round was fired into the center spar cap on the tension surface. The test component, loading fixture, and aim point are shown in Fig. 13. The loaded component survived the impact with no indication of structural failure. After the impact, the bending and torsion loads were increased to the 7.5-*g* design limit load. The damaged test component successfully sustained these loads. Ten cycles of two-thirds limit load were then applied, demonstrating 2-h cruise capability after damage. The component was then loaded to failure, which occurred on the compression spar cap at 8.6-*g*'s.

The photograph of the tension skin in Fig. 14 was taken following successful application of limit load. A crack can be seen in the upper right of the

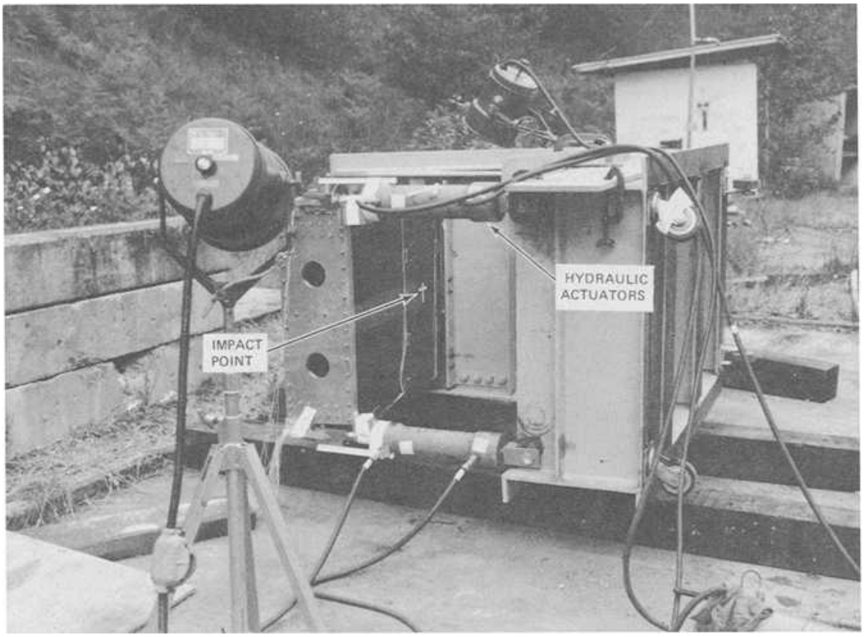

FIG. 13—*Full-scale wing-box component ready for 23-mm HEI impact.*

damaged region which propagated from the ballistic damage to the nearest hybrid crack-arresting pad and was successfully arrested. This verified the crack-arresting capability of the pads and the analysis methods for predicting the fracture response of graphite/epoxy and graphite-glass/epoxy hybrid laminates.

Damage to the compression skin is shown in Fig. 15. The raised segment of skin resulting from "blowout" of the thinner segment of ± 45 graphite/epoxy between the hybrid pads is evident. This response prevented attachment failure and extension of the damage beyond the impacted cell, and verified the effectiveness of the "waffle" skin configuration using graphite/glass hybrid laminates. Evidence of the wing-box final failure is also visible in Fig. 15. This occurred at the compression spar cap at 8.6-g's, when the skin buckled along the lower spar and above the central spar, with some skin detachment. The tension skin never failed.

Conclusions

The fracture control approach described in this paper was successfully demonstrated by a very severe test of a full-scale component subjected to impact by a high-explosive antiaircraft projectile. The work demonstrates the

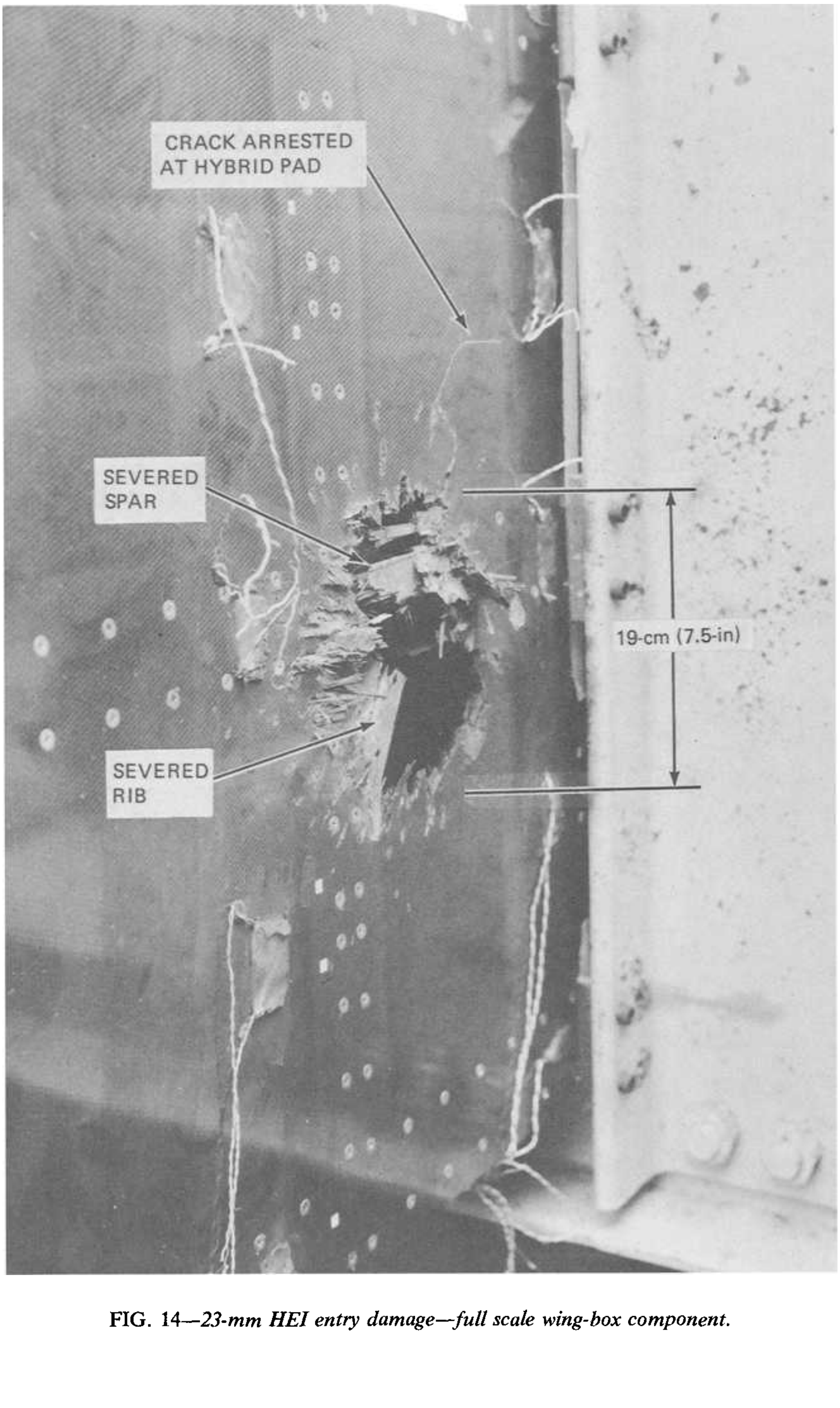

FIG. 14—*23-mm HEI entry damage—full scale wing-box component.*

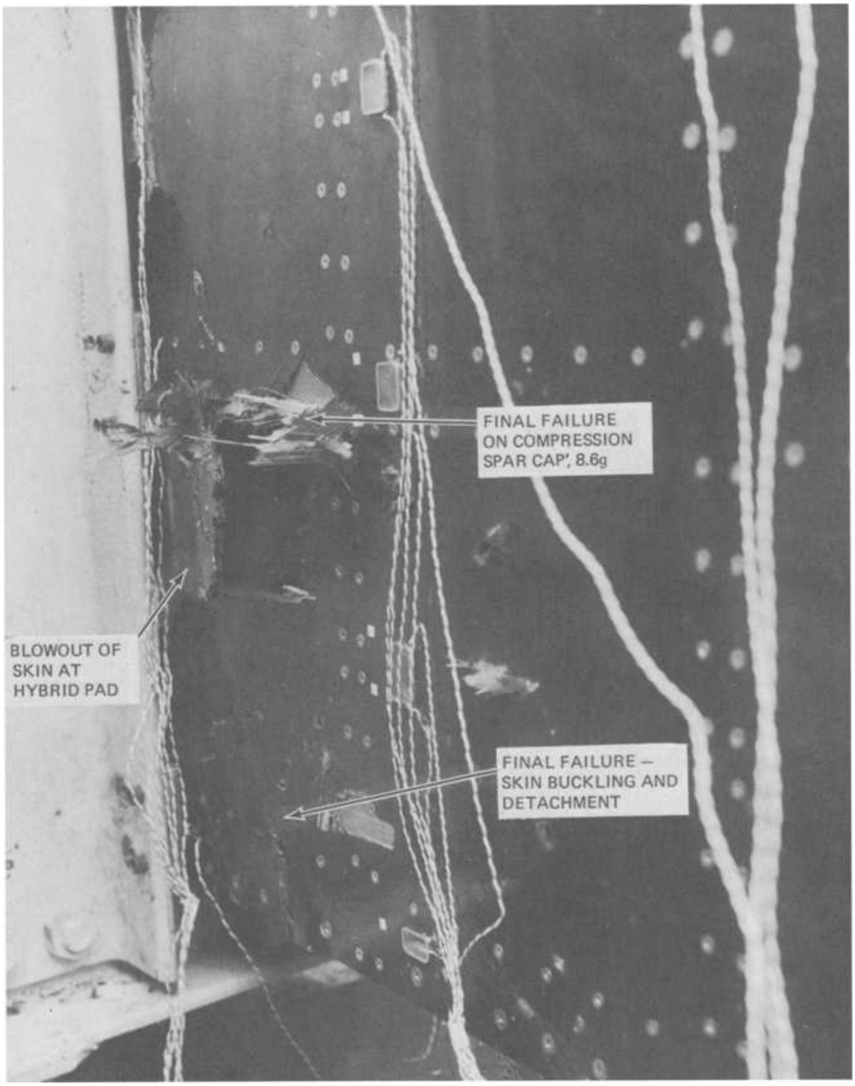

FIG. 15—*23-mm HEI damage in compression skin (photographed after final box failure).*

potential capability of advanced fiber composite structure for achieving battle damage tolerance as well as structural efficiency.

Acknowledgment

The authors wish to express their appreciation for the guidance, inspiration, and patience of the Navy project engineers for the Department of

Defense-sponsored research contract summarized in this paper: D. R. Mulville, A. Somoroff and A. Cowles of the Naval Air Systems Command, Washington, D. C.

References

[1] Avery, J. G. and Porter, T. R. in *Foreign Object Impact Damage to Composites, ASTM STP 568,* American Society for Testing and Materials, 1975.

[2] Avery, J. G., Bradley, S. J., and King, K. M., "Battle Damage Tolerant Wing Structural Development Program," Final Report, NASC Contract N00019-75-C-0178, Boeing Document D180-26069-1, and -2, The Boeing Co., Seattle, Wash., 1979.

[3] King, K. M., "Crack Extension in Fibrous Structural Materials," Boeing Document D180-25892-2, The Boeing Co., Seattle, Wash., March 1977.

[4] Avery, J. G., *Engineering Fracture Mechanics,* Vol. 4, 1972, pp. 749-763.

[5] Olster, E. F. and Roy, P. A. in *Composite Materials: Testing and Design (Third Conference), ASTM STP 546,* American Society for Testing and Materials, 1974, pp. 583-603.

[6] Avery, J. G., Bradley, S. J., and Bristow, R. J., "Survivable Composite Structure for Combat Aircraft," AFFDL-TR-79-3132, Air Force Flight Dynamics Laboratory, Wright Patterson AFB, Ohio, 1979.

J. C. Lewis[1] *and G. Sines*[2]

An R-Curve for a Surface Crack in Titanium

REFERENCE: Lewis, J. C. and Sines, G., "**An R-Curve for a Surface Crack in Titanium,**" *Fracture Mechanics: Thirteenth Conference, ASTM STP 743,* Richard Roberts, Ed., American Society for Testing and Materials, 1981, pp. 360–374.

ABSTRACT: R-curves for surface cracks in Ti-6A1-4V titanium alloy were generated for the purpose of studying the resistance of the alloy to their subcritical growth under a monotonically increasing load typical of a proof test. Another purpose was to evaluate Ehret's compliance calibration for measuring the instantaneous size of a surface crack using the unloading slope of a load-versus-clip-gage-opening curve. Another purpose was to study "leak-before-burst" during sustained load and during subcritical crack growth under rising load.

Clips were mechanically attached to either side of the surface crack on the face of the *specimen. A clip-gage extensometer was used to plot load-versus-clip-gage opening.* Slopes were taken periodically by unloading about 10 percent so that subcritical crack growth could be distinguished from crack-tip plastic deformation. The tests were run in accordance with the ASTM Recommended Practice for R-Curve Determination (E 561-78T) as much as possible.

KEY WORDS: R-curve, surface crack, titanium, stress-intensity factor, fracture toughness

With the advent of manned launch vehicles such as the Space Shuttle for launching satellites and interplanetary spacecraft, pressure vessel weight has become even more critical than with previous unmanned vehicles. In addition, as the pressure vessel wall thickness is decreased to minimize weight, the requirements for safety and reliability become more stringent for the safety of the crew [*1,2*].[3] All pressure vessels on spacecraft to be launched from the Space Shuttle must be proof-tested [*1,2*]. Therefore the subcritical crack growth behavior of surface cracks in thin metals under a monotonically

[1]Member, technical staff, TRW, Defense and Space Systems Group, Redondo Beach, Calif. 90278.

[2]Professor, School of Engineering and Applied Science, University of California at Los Angeles, Los Angeles, Calif. 90024.

[3]*The italic numbers in brackets refer to the list of references appended to this paper.*

increasing stress such as used in a proof test must be understood if safe, reliable vessels are to be designed.

A method for measuring subcritical crack growth as a function of applied stress is the R-curve method [*3*]. However, the ASTM Recommended Practice for R-Curve Determination (E 561-78T) applies only to through-cracks; no standard test method now exists for measuring R-curves of materials containing surface cracks. In a study of the effect of hydrogen in titanium on critical stress-intensity factors, several interesting aspects of the growth of surface cracks in thin sections were observed [*4*].

Previous investigations had constructed R-curves for surface cracks by periodically fatigue marking the fracture surface and correlating these marks to clip-gage data after the specimen was broken [*5-8*]. One purpose of this work was to use a clip gage as a direct measurement of instantaneous crack size using Ehret's compliance calibration [*9*]. This method and the data generated were then used to study the "leak-before-burst" phenomenon during sustained load and rising load.

Procedure

Materials

The metal tested was Ti-6A1-4V titanium alloy. The heat-treated forging specimens were from a 1.90-cm-thick (0.75 in.) propellant tank forging from TIMET Heat No. G-804. The 0.23- and 0.07-cm-thick (0.090 and 0.026 in.) annealed specimens were from plate, RMI Heat Nos. 892361 and 800432, respectively. Reference 4 gives the "as-received" chemical analyses.

Heat Treatment

The heat-treated specimens were solution-treated at 954 ± 8°C (1750 ± 15°F) for 1 h in a vacuum chamber at less than 1 × 10^{-5}-torr pressure, quenched in water at 20°C (68°F) from the vacuum chamber within 5 s and aged for 4 h at 510 ± 6°C (950 ± 10°F) in vacuum. This heat treatment was done while the material was 1.14 cm (0.45 in.) thick. After machining and notching these specimens were aged an additional 4 h at 510 ± 6°C (950 ± 10°F).

The annealed specimens were heated at 732 ± 14°C (1350 ± 25°F) for 2 h and cooled in air while the plate was 0.95 cm (0.375 in.) thick. The specimens were then machined.

Specimen Design

The surface-crack tension specimen was chosen for this study because it simulates cracks in pressure vessels and it is suited for testing thinner materials. The specimen meets the ASTM Test for Tension Testing of Metallic Materials (E 8-79). The specimens were prepared according to the ASTM Test for Surface-Crack Tension Specimens (E 740-80).

The approximate stress-intensity factor solution for the specimen used in this study is

$$K_I = \sigma M_K \sqrt{1.21\pi(a/Q)} \tag{1}$$

where

K_I = stress-intensity factor at the minor semi-axis of the crack front under pure tensile stress, ksi $\sqrt{\text{in.}}$ (MPa$\sqrt{\text{m}}$),

Q = Irwin's crack shape parameter [10]

$$= \Phi^2 - 0.212(\sigma/\sigma_{ys})^2 \tag{2}$$

a = minor semi-axis of an elliptical crack (crack depth), in. (m),

M_k = Master's magnification factor for cracks approaching the back-face free surface [11],

σ = remote gross uniaxial tensile stress, ksi (MPa),

Φ = elliptic integral of the second kind, and

σ_{ys} = 0.2 percent offset uniaxial tensile yield strength, ksi (MPa).

Specimen Preparation

The location and orientation of each specimen within the forging are shown in Ref *4*. This orientation corresponds to the L-S crack plane orientation of the ASTM Test for Plane-Strain Fracture Toughness of Metallic Materials (E 399-78a). Each segment was machined to a flat plate of 1.1-cm (0.45-in.) thickness before heat-treating. Blanks for the annealed specimens were cut from the plate with an orientation corresponding to the T-S orientation of ASTM Method E 399-78a.

For the heat-treated specimens, notches were cut into the specimens using electrial discharge machining (EDM) after final machining but before final aging. Each notch was a segment of a circle with an included angle between notch faces of 20 deg. Notch depths were approximately 0.18 cm (0.070 in) and 0.25 cm (0.100 in.). Corresponding notch widths were 0.71 and 1.07 cm (0.28 and 0.42 in.). A Cincinnati EDM machine was used with a silver-tungsten electrode. Cutting time was approximately 1 h using a 78-V, 2.5-A d-c signal pulsed at 400 Hz.

In the annealed specimens, the EDM notch was cut after annealing and final machining. The notch was 0.08 cm (0.030 in.) deep and 0.38 cm (0.15 in.) wide for the 0.23-cm-thick (0.90 in.) specimens and 0.02 cm (0.008 in.) deep and 0.10 cm (0.04 in.) wide for the 0.07-cm-thick (0.026 in.) specimens.

The heat-treated specimen, FM-2, was hydrogenated to 77 ppm [*4,12*]. This concentration of hydrogen gave a minimum in the K-values to start stable crack growth. Its cracking behavior was otherwise typical of that of the other concentrations of 25 to 115 ppm. Specimen FL-3 had 25 ppm of hydrogen. The annealed specimens were not specially hydrogenated to levels different from the "as-received" level of 59 ppm.

Standard round tension specimens from excess material on the specimen blanks were machined and tested per ASTM Method E 8-79. Reference *4* gives the results of these tests.

After hydrogenation, sharp cracks were started from the notches by cyclically loading the specimens to a maximum uniaxial tensile stress of +207 MPa (+30 ksi) and a minimum of +20.7 MPa (+3 ksi). This increased the crack depth approximately 20 percent without significantly increasing the crack length on the face of the specimen. Tables 1 and 2 give specimen and crack dimensions.

Clip Attachment

For the heat-treated specimens, aluminum clips for a clip-gage extensometer were attached to the face of each specimen above and below the crack surfaces using 0.10-cm-diameter (0.04 in.) steel pins. A small amount of epoxy adhesive was used on the pins to prevent rotation of the clips. The pinholes were drilled approximately 0.25 cm (0.1 in.) apart with the crack between them. Pinhole depth was 0.15 cm (0.06 in.).

For the annealed specimens, Invar clips were spot-welded in the same location as on the heat-treated specimens.

Clip-Gage Calibration

Ehret has derived a relationship between clip-gage opening (CGO) and crack depth for titanium alloys [*9*]. This relationship is:

$$\frac{\Delta \mathrm{CGO}}{\Delta P} = \left(\frac{G}{Etw}\right) \exp\left[16.5\,(a/\Phi^2)\exp\left(\frac{0.074}{t}\right)\right] \tag{3}$$

where

$\dfrac{\Delta \mathrm{CGO}}{\Delta P}$ = reciprocal of the unloading slope of the load-versus-CGO curve, in./lb (m/N),

E = Young's modulus, psi (Pa),

G = gage length between clip-gage attachment points, in. (m),

Φ = elliptic integral of the second kind,

a = minor semi-axis of elliptical crack (crack depth) in. (m),

t = specimen thickness, in. (m), and

w = specimen width, in. (m).

Instead of the measured gage length, an effective gage length was calibrated for each specimen by measuring the actual initial crack size

$(a/\Phi^2)_i$ after completion of testing. The initial slope of the compliance test record was then measured and G was calculated from Eq 3. This value of G was then used for all subsequent crack-size calculations for that particular specimen.

Equation 1 shows that K_I cannot be calculated without knowing the crack depth, a. Unfortunately, Eq 3 only permits calculation of a/Φ^2 and not a alone. To overcome this limitation Φ was assumed to remain unchanged during subcritical crack growth and therefore to be equal to that measured on the initial crack. The specific method was as follows:

1. At each unloading point, the slope was used to calculate a/Φ^2 from Eq 3.
2. The a/c ratio of the initial fatigue crack was used to calculate Φ.
3. a/Φ^2 from Step 1 was multiplied by Φ^2 from Step 2 to obtain a.
4. Equation 2 was used to calculate Q from Φ obtained in Step 2.
5. a from Step 3 was divided by Q from Step 4.

The validity of this assumption was checked on Specimens FM-2 and FL-3 by fatigue marking the crack after extensive growth on rising load. These marks can be seen clearly in Figs. 1 and 2. The calculated crack depth for FM-2 from Eq 3, assuming a constant value of ϕ, was 0.503 cm (0.198 in.) while the calculated crack length was 1.519 cm (0.598 in). The measured crack depth and length from the specimen were 0.505 cm (0.199 in.) and 1.620 cm (0.638 in.), respectively. For FL-3, the calculated crack depth was 0.439 cm (0.173 in.) and the calculated crack length was 1.178 cm (0.464 in.) while the measured crack depth and length were 0.442 cm (0.174 in.) and 1.326 cm (0.522 in.), respectively.

These calculated crack depths were then used to determine a/Q using Irwin's definition of Q in Eq 2 and to determine M_K from the ratio of crack-depth to thickness.

R-Curve Testing

The procedures of ASTM Method E 561-78T were used to generate the R-curves to the extent that the surface-crack geometry permitted. For example, the compliance test records for the surface-crack specimen will show

TABLE 1—*Cyclic load precracking data.*

Specimen No.	Width, cm (in.)	Thickness, cm (in.)	Max Load, kN (kips)	Min Load, kN (kips)	Kilo-cycles
FM-2	3.183 (1.253)	0.635 (0.250)	41.77 (9.39)	4.18 (0.94)	22
FL-3	3.812 (1.501)	0.635 (0.250)	50.04 (11.25)	5.00 (1.13)	25
A-3	2.667 (1.050)	0.236 (0.093)	12.72 (2.86)	1.29 (0.29)	32
A-4	2.667 (1.050)	0.066 (0.026)	3.56 (0.80)	0.76 (0.17)	20

TABLE 2—*Stress-intensity factors from compliance test records.*

Specimen No.[a]	Load		Crack Depth		Crack Length		Irwin's a/Q		Secant a/Q		M_k	K_I		Remarks
	kN	(kips)	cm	(in.)	cm	(in.)	cm	(in.)	cm	(in.)		MPa$\sqrt{m}$	(ksi $\sqrt{in.}$)	
FM-2 1	116	(26.0)	0.287	(0.113)	0.866	(0.341)	0.173	(0.068)	0.165	(0.065)	1.05	48.7	(44.3)	...
FM-2 2	160	(36.0)	0.297	(0.117)	0.897	(0.353)	0.183	(0.072)	0.170	(0.067)	1.06	70.0	(63.7)	...
FM-2 3	167	(37.6)	0.300	(0.118)	0.904	(0.356)	0.185	(0.073)	0.178	(0.070)	1.06	73.6	(67.0)	...
FM-2 4	170	(38.2)	0.310	(0.122)	0.935	(0.368)	0.193	(0.076)	0.185	(0.073)	1.06	76.4	(69.5)	...
FM-2 5	171	(38.4)	0.310	(0.122)	0.935	(0.368)	0.193	(0.076)			1.06	76.8	(69.9)	...
FM-2 6	171	(38.4)	0.310	(0.122)	0.935	(0.368)	0.193	(0.076)	0.193	(0.076)	1.06	76.8	(69.9)	...
FM-2 7	171	(38.4)	0.322	(0.127)	0.975	(0.384)	0.201	(0.079)			1.07	79.0	(71.9)	...
FM-2 8	170	(38.3)	0.330	(0.130)	0.998	(0.393)	0.206	(0.081)	0.203	(0.080)	1.07	79.9	(72.7)	...
FM-2 9	168	(37.9)	0.348	(0.137)	1.052	(0.414)	0.216	(0.085)			1.08	81.8	(74.4)	...
FM-2 10	166	(37.3)	0.358	(0.141)	1.082	(0.426)	0.224	(0.088)	0.221	(0.087)	1.09	82.4	(75.0)	...
FM-2 11	162	(36.4)	0.378	(0.149)	1.143	(0.450)	0.234	(0.092)			1.11	83.8	(76.3)	...
FM-2 12	159	(35.8)	0.394	(0.155)	1.189	(0.468)	0.244	(0.096)	0.241	(0.095)	1.12	85.0	(77.4)	...
FM-2 13	155	(34.8)	0.411	(0.162)	1.242	(0.489)	0.254	(0.100)			1.13	85.2	(77.5)	...
FM-2 14	151	(34.0)	0.422	(0.166)	1.275	(0.502)	0.259	(0.102)	0.259	(0.102)	1.14	84.7	(77.1)	...
FM-2 16	144	(32.3)	0.450	(0.177)	1.359	(0.535)	0.274	(0.108)	0.277	(0.109)	1.17	84.9	(77.3)	...
FM-2 18	137	(30.8)	0.483	(0.190)	1.458	(0.574)	0.292	(0.115)	0.300	(0.118)	1.20	85.7	(78.0)	...
FM-2 20	129	(29.0)	0.503	(0.198)	1.519	(0.598)	0.302	(0.119)	0.312	(0.123)	1.21	82.7	(75.3)	no dimple
FL-3 1	185	(41.5)	0.366	(0.144)	0.980	(0.386)	0.206	(0.081)	...	...	1.07	72.2	(65.6)	no dimple
A-3 1	32.5	(7.3)	0.102	(0.040)	0.472	(0.186)	0.079	(0.031)	...	...	1.09	27.9	(27.9)	...
A-3 2	45.8	(10.3)	0.102	(0.040)	0.472	(0.186)	0.081	(0.032)	...	...	1.09	39.9	(39.9)	...
A-3 3	48.9	(11.0)	0.102	(0.040)	0.472	(0.186)	0.084	(0.033)	...	...	1.09	43.3	(43.3)	...
A-3 4	49.8	(11.2)	0.102	(0.040)	0.472	(0.186)	0.084	(0.033)	...	...	1.09	44.2	(44.2)	...
A-3 5	50.7	(11.4)	0.102	(0.040)	0.472	(0.186)	0.084	(0.033)	...	...	1.09	44.9	(44.9)	...
A-3 6	50.7	(11.4)	0.117	(0.046)	0.544	(0.214)	0.096	(0.038)	...	...	1.12	49.5	(49.5)	back-face dimpled
A-3 7	48.0	(10.8)					data invalid after dimpling							
A-3 8	49.8	(11.2)												
A-3 9	49.4	(11.1)												
A-4 1	23.4	(3.4)	0.020	(0.008)	0.142	(0.056)	0.020	(0.008)	...	...	1.05	25.9	(23.6)	back-face dimpled

[a]Numbers refer to specific slopes on the compliance curve, initial crack sizes are reported on the lines marked with 1.

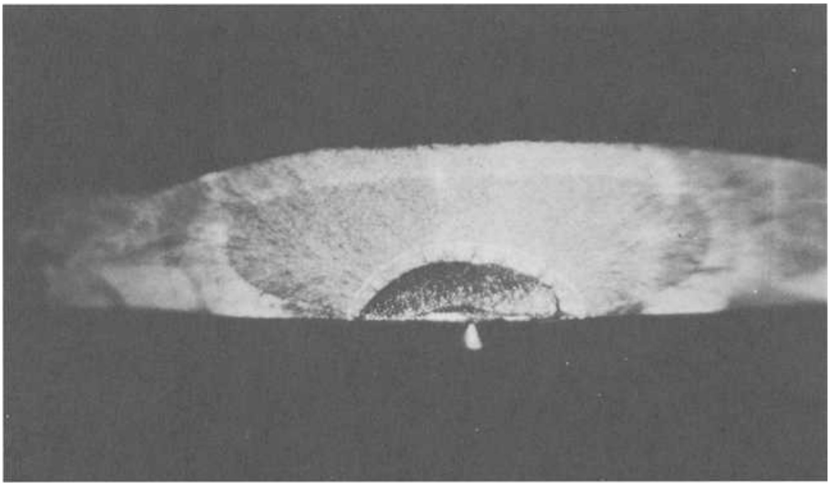

FIG. 1—*Fracture surface of Specimen FM-2 (×3.92 magnification).*

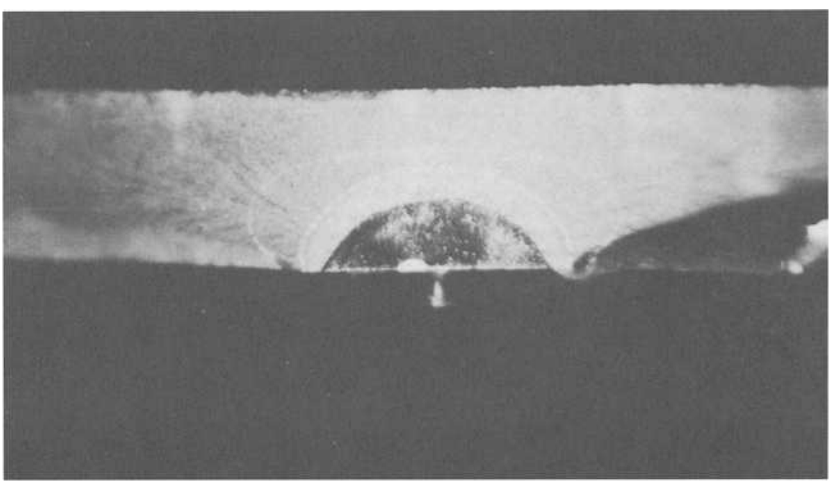

FIG. 2—*Fracture surface of Specimen FL-3 (×3.68 magnification).*

evidence of out-of-plane bending, "buckling," on unloading and reloading. This phenomenon is characteristic of the surface crack. Also, it is important to include loading-unloading steps in the early portion of the R-curve to distinguish physical crack growth from gross yielding because the crack depth cannot be observed directly.

Each specimen was subjected to an initial steadily increasing load to obtain the compliance test record. The stress rate was less than 690 000 KPa/min (100 000 psi/min). Clip-gage opening versus load was recorded to detect the onset of fracture. When possible, several different unloading slopes were taken on the compliance test record to permit calculation of the instantaneous crack size from Eq 3. The instantaneous values of K_I corresponding to each slope were then calculated using Eq 2. The maximum value of K_I of each specimen was assumed to be K_{Ie}, the fracture toughness as defined in ASTM Method E 740-80.

Once K_{Ie} was achieved, it was no longer possible to wait until the crack had stopped growing subcritically to take the unloading slope. Therefore, the load had to be dropped while the crack was still growing. This is a point of departure from ASTM Method E 561-78T. However, considerably more data and insight were gained by this testing procedure than if the crack had been allowed to grow to failure without dropping the load. The significance of this procedure is explained in the following.

Dimpling Determination

The onset of back-face dimpling was determined by looking at the back face at each of the unloading slope measurement points. The phenomenon of back-face dimpling is described in detail in Ref *13*.

Results and Discussion

The stress-intensity factors calculated from Eqs 2 and 3 for the different slopes on the compliance test records for selected specimens are listed in Table 2. The data for 12 other specimens are reported in Ref *4*.

Since the unloading slope of the compliance curve permits the calculation of a/Φ^2, the secant slope which includes plastic zone hinging should permit the calculation of a/Q. Values of a/Q calculated from the secant slopes are included in Table 2 for comparison with the values calculated from Eq 3 and the previously described assumption of a constant value of Φ. The maximum difference between Irwin's Q based on this assumption and the Q from the secant slope is about 4 percent. Since the stress-intensity factor is proportional to $Q^{1/2}$, the maximum difference between the two R-curves would be approximately 2 percent. This agreement is unexpected because the crack shapes shown in Figs. 1 and 2 are far from being ellipses with the major axes on the face as assumed for the Irwin model.

Figures 3–5 are the compliance test records for three of the specimens listed in Table 2. Notice in Fig. 3 that as the crack in Specimen FM-2 became larger, the load required to reinitiate subcritical crack growth after unloading became smaller on each successive reloading. However, the stress-intensity factor to reinitiate crack growth continued to increase above the tangency point of Fig. 6. Once the peak stress-intensity factor had been obtained in the

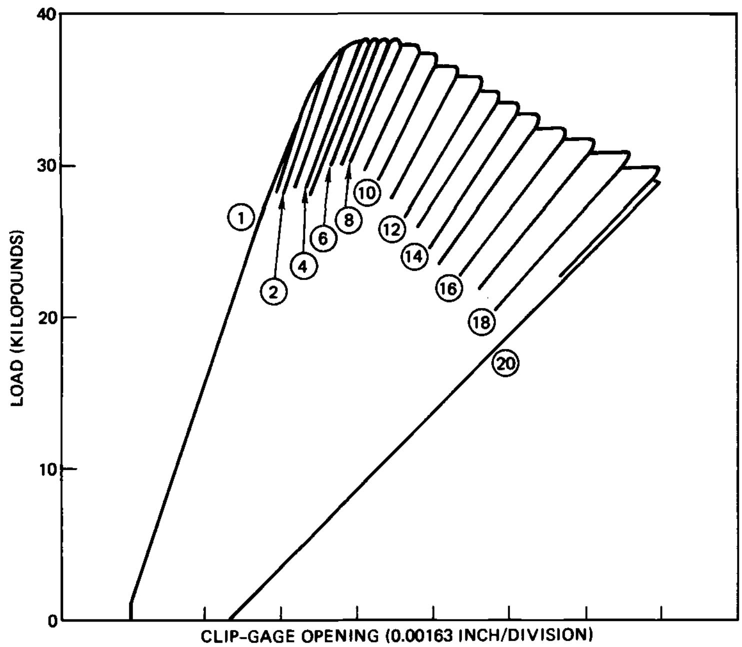

FIG. 3—*Compliance test record for Specimen FM-2 (1 kilopound = 4.448 kN; 1 in. = 2.54 cm).*

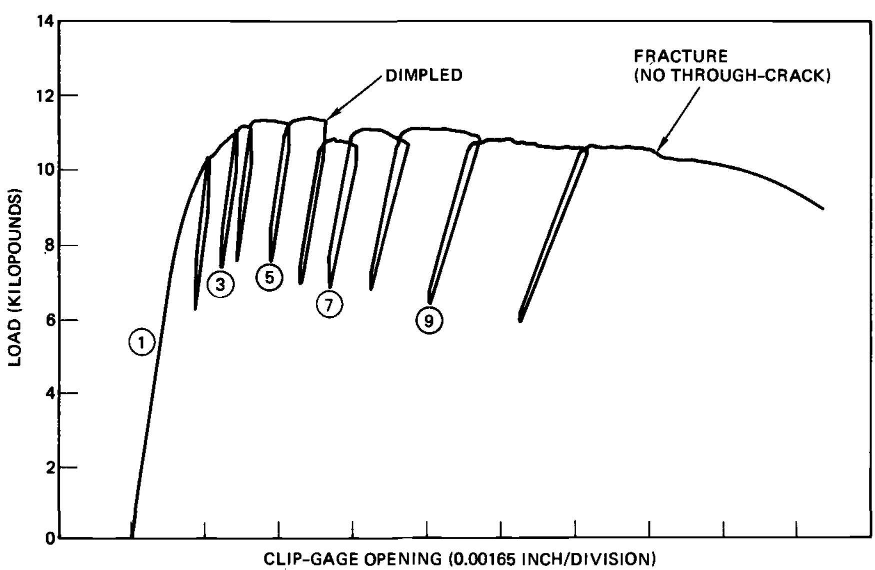

FIG. 4—*Compliance test record for Specimen A-3 (1 kilopound = 4.448 kN; 1 in. = 2.54 cm).*

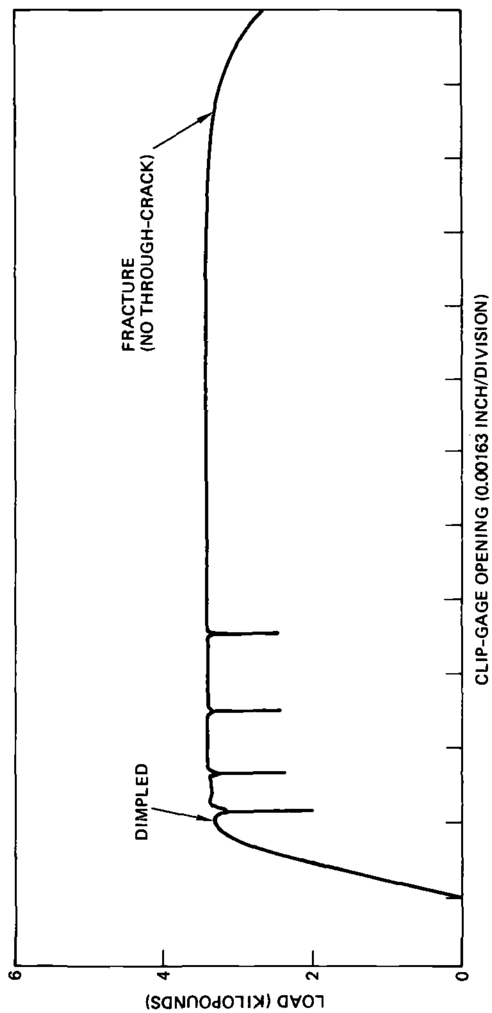

FIG. 5—*Compliance test record for Specimen A-4 (1 kilopound = 4.448 kN, 1 in. = 2.54 cm).*

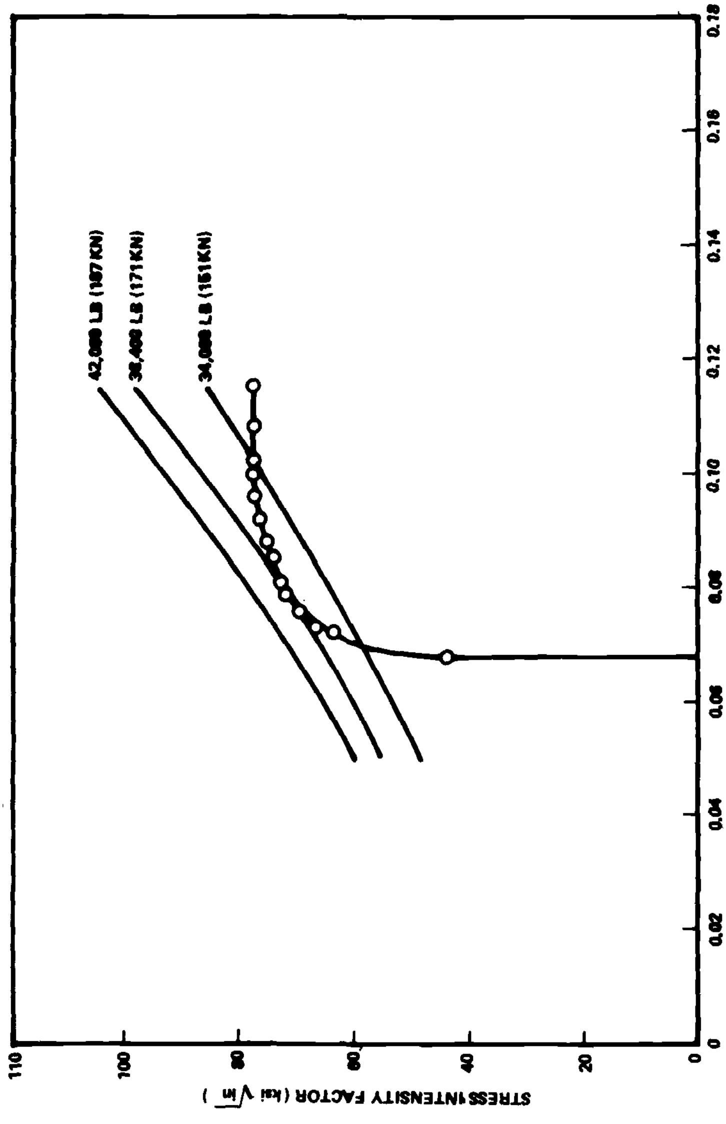

FIG. 6—*R-Curve for Specimen FM-2 (1 ksi $\sqrt{in.}$ = 1.10 MPa $\sqrt{m}$; 1 in. = 2.54 cm).*

material, reinitiation of subcritical crack growth for all subsequent unloading points occurred at this peak stress-intensity factor. This phenomenon was typical of the thicker specimen that did not dimple and resulted in an R-curve with a plateau (Fig. 6). In order not to exceed this peak stress-intensity factor, the load had to drop as the crack grew subcritically. Intrinsic material behavior of this nature is indicative of a material property. If unloading slopes had not been taken and only secant slopes had been used to calculate the R-curve based on the effective crack lengths, then only a monotonically increasing R-curve would have been produced and this plateau would not have been observed.

When the compliance test records of the two specimens that had been marked were continued after marking, the stress-intensity factors for reinitiation returned immediately to the peak stress-intensity factor of the plateau. The failure to regenerate the lower stress-intensity factor values of the R-curve could be interpreted to mean that these lower values result from nonelliptical crack geometry or from initial formation of the plastic zone or possibly a combination of these. More tests under more controlled conditions need to be run to determine the source of the lower initial stress-intensity factor values of the R-curve. The use of fatigue marking would mask this phenomenon [*5*–*8*].

It is noted in Fig. 4 that the back face of the 0.24-cm-thick (0.093 in.) annealed specimen dimpled before any physical crack growth occurred. Therefore, no stress-intensity factor solution was available for subsequent data; however, physical crack growth did occur after dimpling. The crack grew only in length with the dimple getting longer as the crack grew longer. Observation of the dimple showed that the crack never broke through the ligament to become a through-crack before fracture occurred. This phenomenon was true of all the specimens in all the thicknesses and casts doubt on whether leak-before-burst occurs in this alloy in these conditions.

After dimpling, physical crack growth occurs in length only in thin material under rising load. Analytical models must be developed if accurate life predictions are to be made for such structures. It is not sufficient to merely ignore this portion of the R-curve because analytical models do not yet exist.

Figure 5 shows that physical crack growth did not occur in the thinnest specimen (A-4) even after dimpling. In fact, the crack simply yielded out and had no effect on the compliance after dimpling. Note that the unloading slopes of the compliance test record are vertical after dimpling. The authors have no explanation for this but suspect an influence of out-of-plane bending on the clips. If only secant slopes had been taken from this curve, the crack size surviving proof would have been overestimated by compliance calculations; however, since partial unloading measurements were made, the constant value of the slopes revealed the lack of crack growth.

Vertical slopes are not generally observed with surface crack tension specimens that do not exhibit physical crack growth. Figure 7 is the compliance

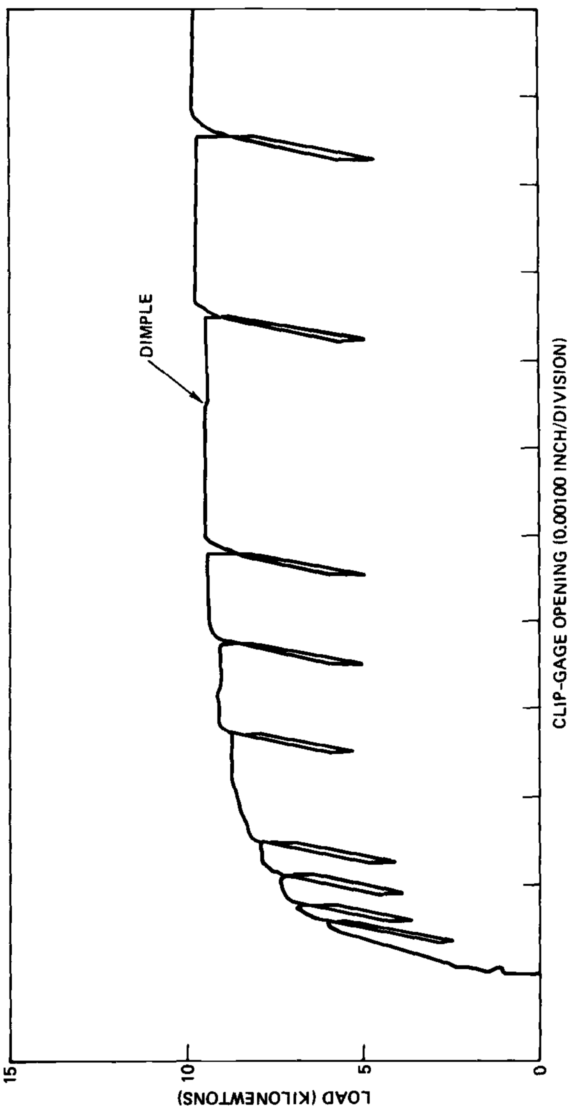

FIG. 7—*Compliance test record for 1100-0 aluminum (1 in. = 2.54 cm).*

test record for a 0.25-cm-thick (0.100 in.) specimen of 1100-0 aluminum with an 0.08-cm-deep (0.030 in.) surface crack. Note that the slope of the compliance test record did not change even though extensive yielding occurred.

Observation of the fracture surfaces in Figs. 1 and 2 shows that as the crack grew subcritically, the major axis moved from the surface to a point in the interior. In addition, crack growth proceeded along the front face along the 45-deg shear lip emanating from the corners of the initial fatigue crack. Therefore, the crack geometry was no longer a true surface crack. However, assuming a true surface crack geometry and its effect on the specimen compliance permitted very accurate calculations of the crack depth. We believe this is possible because the compliance test record is strongly affected by crack depth but only slightly affected by crack length (Eq 3).

Conclusions

Study of the subcritical growth behavior of surface cracks in thin materials requires testing techniques that are only slightly different from those of ASTM Method E 561-78T. Irwin's approximate stress-intensity factor solution and Ehret's compliance calibration for the surface crack can be used to accurately calculate the behavior of the growing crack until back-face dimpling occurs.

Analytical models need to be developed for surface crack growth after back-face dimpling occurs.

Acknowledgments

The authors wish to thank the following people and organizations for their support of this study; Mr. Ward Minkler of TIMET for contributing the plate for the additional specimens reported in Ref *4*; Mr. Howard Gapp and Mr. Ray Toosky of Cherry Fasteners Division of Townsend, a Textron Company for heat treating and hydrogenation; Mr. Ed Thomas of TiTech International, Inc., for hydrogen analysis; and Mr. James Kelley of the Jet Propulsion Laboratory for funding for specimen preparation.

References

[*1*] "Safety Policy and Requirements for Payloads Using the Space Transportation System (STS)," NHB 1700.7, National Aeronautics and Space Administration, Washington, D.C., May 1979.

[*2*] "NASA Aerospace Pressure Vessel Safety Standard," NSS/HP-1740.1, National Aeronautics and Space Administration, Washington, D.C., 22 Feb. 1974.

[*3*] *Fracture Toughness Evaluation by R-Curve Methods, ASTM STP 527,* American Society for Testing and Materials, 1973.

[*4*] Lewis, J. C., "Effect of Hydrogen on Fracture of Titanium," Thesis for Master of Science Degree in Engineering, University of California at Los Angeles, Los Angeles, Calif., 1979.

[*5*] Shaw, Ramesh C., "Effects of Proof Loads and Combined Nobe Loadings on Fracture and

Flaw Growth Characteristics of Aerospace Alloys," NASA CR-134611, The Boeing Company, Seattle, Wash., March 1974.
[6] Bixler, W. D., "Fracture Control Method for Composite Tanks with Load Sharing Liners," NASA CR-134758, The Boeing Company, Seattle, Wash., July 1975.
[7] Finger, R. W., "Proof Test Criteria for Thin-Walled 2219 Aluminum Pressure Vessels, Volume I," NASA CR-135036, The Boeing Company, Seattle, Wash., Aug. 1976.
[8] Finger, R. W., "Proof Test Criteria for Thin-Walled 2219 Aluminum Pressure Vessels, Volume II," NASA CR-135037, The Boeing Company, Seattle, Wash., Aug. 1976.
[9] Ehret, R. M., "Part-Through-Crack Elastic Compliance Calibration," Internal Document No. SD71-329, North American Rockwell, Downey, Calif., 1 Oct. 1971.
[10] Irwin, G. R., *Journal of Applied Mechanics,* Series E, Vol. 29, No. 4, pp. 651-654.
[11] Master, J. N., Haese, W. P., and Finger, R. W., "Investigation of Deep Flaws in Thin-Walled Tanks," NASA CR-72606, The Boeing Company, Seattle, Wash., Dec. 1969.
[12] Waisman, J. L., Sines, G., and Toosky, R. F., in *Proceedings, Second International Congress on Hydrogen in Metals,* Paris, France, 11 June 1977.
[13] Lewis, J. C. in *Proceedings,* 1980 JANNAF Propulsion Meeting, CPIA Publication 315, Chemical Propulsion Information Agency, Laurel, Md., March 1980, pp. 245-268.

D. O. Harris[1] *and E. Y. Lim*[1]

Stress-Intensity Factors for Complete Circumferential Interior Surface Cracks in Hollow Cylinders

REFERENCE: Harris, D. O. and Lim, E. Y., **"Stress-Intensity Factors for Complete Circumferential Interior Surface Cracks in Hollow Cylinders,"** *Fracture Mechanics: Thirteenth Conference, ASTM STP 743,* Richard Roberts, Ed., American Society for Testing and Materials, 1981, pp. 375–386.

ABSTRACT: An approximate expression is developed for the stress-intensity factor due to concentrated point loads applied to the surfaces of a complete circumferential interior surface crack in a hollow circular cylinder. This expression is derived from existing results for a point load on an embedded penny-shaped crack and a concentrated "ring" load on a complete circumferential interior surface crack in a hollow cylinder. Results for a particular loading case were obtained using the approximate solution and comparing with three-dimensional results obtained using boundary integral equation techniques. Since the agreement was good, it is concluded that the approximate expression provides a sufficiently accurate means of estimating K for an arbitrary loading on an interior complete circumferential surface crack. Results for bending of a cracked cylinder are then presented as an example of the use of the approximate K solution. Convenient curve fits of relevant results are included in the Appendix.

KEY WORDS: stress-intensity factor, cylinder, point load, boundary integral equation method

Nomenclature

- a Depth of a complete circumferential crack
- f_γ Function of geometrical parameters in K due to a point load (see Eq 1)
- F Applied point load
- $g(\theta)$ Angular variation of K due to point load (see Eq 1)
- h Pipe wall thickness

[1]Division managers, Science Applications, Inc., San Jose and Palo Alto, respectively, Calif. 94304.

K Stress-intensity factor
K_{max} Maximum K along crack tip
m Weight function for a "ring" load on a complete circumferential crack
r_i Pipe inside radius
u Equals x/a
x Distance into pipe wall from inside radius
y Distance from neutral axis for bending stress
α Equals a/h
γ Equals r_i/h
θ Angular coordinate of position along crack front
θ_0 Angle over which loading is applied in example problem (see Fig. 2)
θ_{max} Maximum value of θ in pipe segment used in boundary integral equation calculation (see Fig. 2)
ρ Equals $(r_i + x)/(r_i + a) = (\gamma + \alpha u)/(\gamma + \alpha)$
σ Applied stress
σ_{max} Maximum bending stress
σ' Maximum applied nominal stress at location of crack tip
ϕ Angular coordinate for applied stress

The purpose of this paper is to present an approximate expression for the stress-intensity factor for a concentrated point load on the surfaces of a complete circumferential interior surface crack in a hollow circular cylinder. Such results are of use in the analysis of subcritical and catastrophic crack growth in hollow cylinders such as pressure vessels and piping.

The application of linear elastic fracture mechanics to the analysis of crack behavior requires stress-intensity factor solutions for the body and crack configuration stressed in the appropriate manner. The number of such solutions is increasing rapidly, thereby allowing increasingly sophisticated and accurate analyses of crack behavior to be performed. Tada et al [*1*][2] provide a convenient summary of many of the solutions available in 1973. Stress-intensity results for cracks in hollow cylinders have been of particular interest for a number of years due to the increased concern for the integrity of pressure vessels and piping in applications such as petrochemical and electric power generation. The increasing cost of plant downtime and the safety considerations in nuclear power generation have led to the need for stress-intensity solutions for cracks in cylindrical components.

The number of available stress-intensity solutions for cracked hollow cylinders is too large to be reviewed in detail here. However, such solutions are generally for longitudinal cracks in cylinders where the stresses in the uncracked wall are either uniform or vary radially according to the plane elasticity solution for an internally pressurized cylinder. Hence, most ex-

[2]The italic numbers in brackets refer to the list of references appended to this paper.

isting solutions cannot be applied to circumferential cracks, and cannot treat cases where the stresses have steep gradients through the wall of the cylinder. Furthermore, no known solutions are capable of treating stress systems which vary with position in the direction parallel to the surface length of the crack.

The need to account for steep thickness gradients of the stresses arises in the treatment of thermal and residual stresses. The need to treat circumferential cracks arises in the analysis of weld defects in piping, where most of the welds are usually circumferential, and the largest tensile stresses are usually in the axial pipe direction. In the case of circumferential cracks, the need to account for angular variations in the stresses arises in treatment of bending (which is usually a major contributor to piping stresses) and residual stresses, which often exhibit strong angular variations [*2*].

Stress-intensity factor results presented by Labbens et al [*3*] and Buchalet and Bamford [*4*] are applicable to complete interior surface cracks in hollow circular cylinders subjected to arbitrary *axisymmetric* axial stresses. Additionally, Erdol and Erdogan [*5*] present results applicable to circumferential cracks which also include subsurface defects. The results of Refs *3* and *4* overcome the shortcomings noted in the foregoing, with the exception of not being applicable to cases in which angular variations in the applied stresses occur. The following sections provide an approximate expression for the stress-intensity factor for concentrated point loads on the surfaces of a complete circumferential interior surface crack in a hollow cylinder. This approximate expression is deduced by requiring it to reduce to known results in limiting cases, and is applicable by suitable superposition to the determination of stress intensities for pipes subjected to arbitrary axial stresses (axisymmetry no longer required). The accuracy of the approximate result is then checked by comparing a particular case to the results of three-dimensional numerical calculations obtained by the boundary integral equation (BIE) technique [*6*]. Finally, results obtained for bending and uniform tension are presented.

Results and Discussion

A concentrated point load on the surfaces of a complete circumferential interior surface crack in a hollow circular cylinder is shown in Fig. 1*a*. The loading, crack, and body geometry are symmetric about the crack plane. Hence, only Mode I loading is present [*1*], and the subscript "I" for the stress intensity factor, *K*, will be omitted. Sectioning the cylinder on the crack plane provides the plane view shown in Fig. 1*b*, which also shows the geometric variables involved.

The following expression for the stress-intensity factor, *K*, will be assumed based on dimensional considerations

$$K = \frac{F}{a^{3/2}} f_\gamma(x/a,\ a/h) g(\theta) \tag{1}$$

$g(\theta)$ may depend on the other variables such as a, h, and r_i. The function $g(\theta)$ can be determined from the solution for a point load on a penny-shaped crack in an infinite body [*1, 7*]. In the present notation this solution can be written as

$$K = \frac{F}{(\pi a)^{3/2}} \frac{(1 - \rho^2)^{1/2}}{(1 - 2\rho \cos\theta + \rho^2)} \tag{2}$$

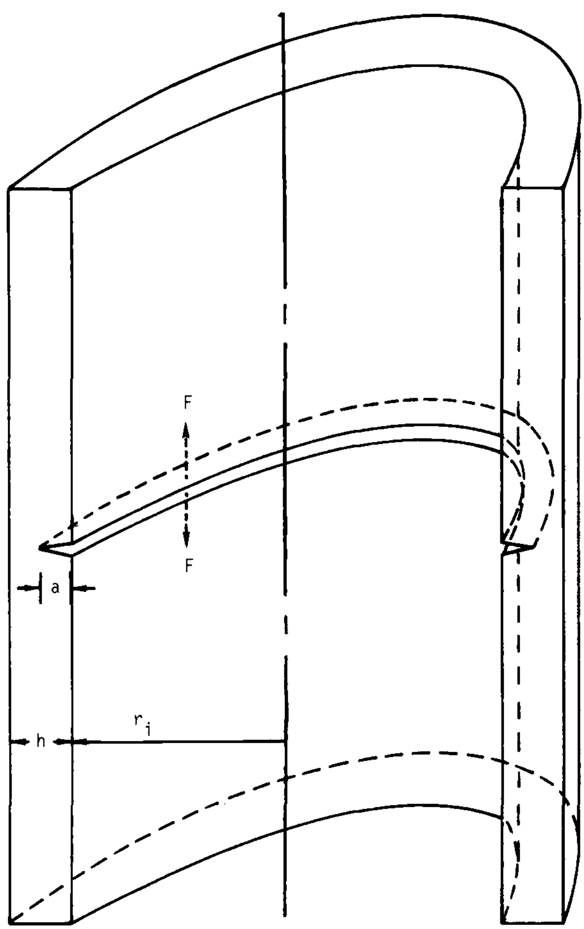

FIG. 1(*a*)—*Complete circumferential interior surface crack in a hollow circular cylinder subjected to concentrated point loads on the crack surfaces.*

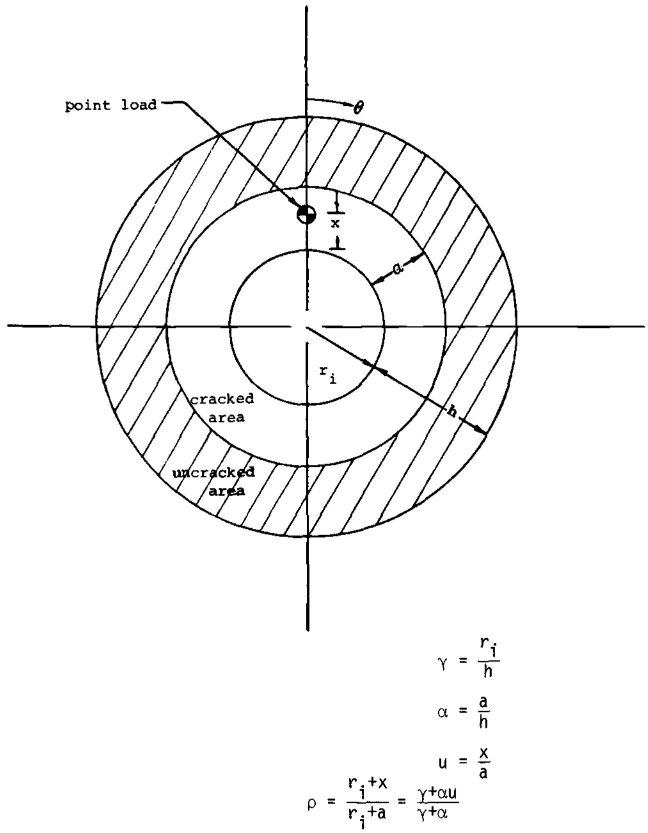

FIG. 1(*b*)—*Complete circumferential interior surface crack in a hollow circular cylinder subjected to concentrated point loads on the crack surfaces.*

($r_i = 0$ for a penny shaped crack). A comparison of Eqs 1 and 2 shows that $g(\theta) = (1 - 2\rho \cos \theta + \rho^2)^{-1}$. Equation 1 can be rewritten as

$$K = \frac{F}{a^{3/2}} f_\gamma(u, \alpha) \frac{1}{1 - 2\rho \cos \theta + \rho^2} \tag{3}$$

The function $f_\gamma(u, \alpha)$ is determined by integrating Eq 3 to provide the result for a complete concentrated "ring" load, and then comparing the results with the Labbens et al solution [3]. This provides the following end result for a point load

$$K = \frac{\alpha F}{(\pi a)^{3/2} 2^{1/2}} \frac{m(u, \alpha)}{(\gamma + \alpha)(1 - u)^{1/2}} \frac{1 - \rho^2}{1 - 2\rho \cos \theta + \rho^2} \tag{4}$$

$m(u, \alpha)$ is the Labben et al weight function, which does depend on $\gamma(= r_i/h)$. m for circumferential cracks with $\gamma = 5$, 10, and ∞ is provided by Labbens [3] in graphical form. The results of Ref 3 were obtained by finite-element solutions for the axisymmetric two-dimensional problem, and are estimated to be accurate within 5 percent [3]. For convenience, the Labbens results for circumferential cracks with $\gamma = 5$ and 10 have been curve-fitted. The results are presented in the Appendix.

The simplicity of Eq 4, which makes use of currently available results for $m(u, \alpha)$ or requires only two-dimensional numerical calculations, makes it desirable for general use in analysis of circumferentially cracked cylinders. However, it is difficult to assess its accuracy, even though it satisfies all the known special cases for which solutions are available. In order to obtain some idea of its accuracy, three-dimensional numerical calculations were performed using the BIE technique [6, 8, 9]. The BIE code described in Ref 8 was utilized. This code breaks the surface of the body into flat triangular segments, and assumes that the displacements and surface tractions vary linearly within a triangular segment. The stress-intensity factors were calculated directly from the nodal displacements on the row of nodes on the crack surface closest to the crack front. Even though energy release rates or contour integrals provide more accurate results [9], the use of nodal displacements close to the crack front is particularly simple. The total number of nodes utilized was generally about 120, which resulted in fast, easy, and economical computer runs.

The accuracy of the BIE code and the suitability of using only the closest nodal displacements to determine K were assessed by applying the code to the solution of a complete ring load and comparing the results with axisymmetric results of Labbens [3]. For $a/h = 1/2$, $r_i/h = 5$, and the row of nodes closest to the crack front being $a/10$ away, the BIE results for K were 6.7 percent below Labbens. For the closest row of nodes, being $a/5$ away from the crack front, the BIE results were 10 percent below Labbens. This is sufficient accuracy for the present case.

The BIE code was then applied to the three-dimensional distributed-load problem shown in Fig. 2. Due to symmetry, only half of the problem has to be solved. Due to the rapid decrease of K away from $\theta = 0$, only a portion of the pipe has to be modeled. BIE results were obtained for θ_{max} (see Fig. 2) of 30 and 90 deg. The 30-deg results were obtained for a free surface at $\theta = 30$ deg, and the 90-deg results were obtained for a zero angular displacement at 90 deg ("roller" boundary conditions).

Results for the problem shown in Fig. 2 can be obtained by integrating the preceding approximate point-load solution (Eq 4). The integration on the radial coordinate was performed numerically. The results of the two BIE solutions and the corresponding results obtained by integration are shown in Fig. 3. Also shown is the result for a concentrated point load of the same total force as the distributed pressure load applied at the center of

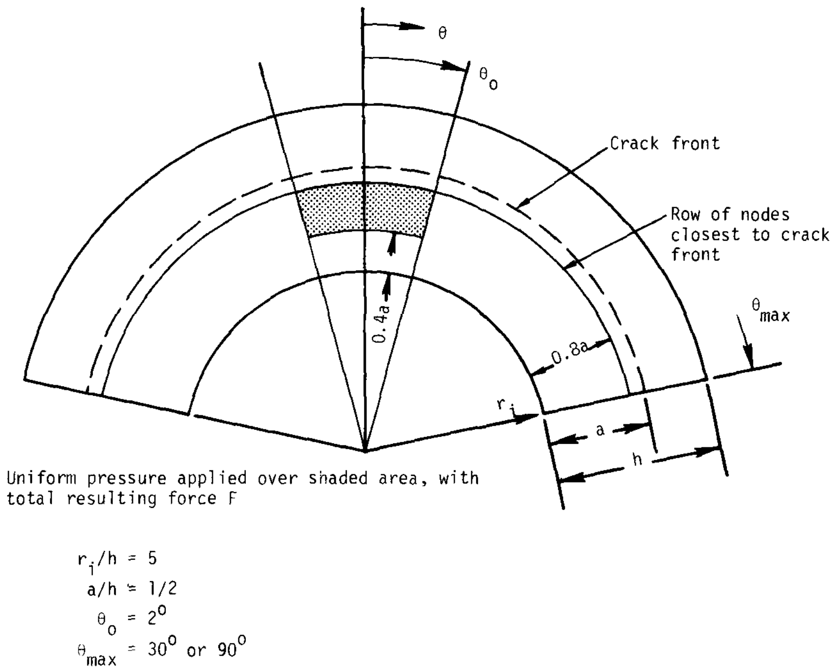

FIG. 2—*Localized pressure loading problem solved by boundary integral equation techniques for comparison with results obtained by use of Eq 4 in order to assess the accuracy of the approximate point load solution.*

the area of the distributed load. The following observations can be made from Fig. 3:

1. The concentrated and distributed load results obtained from Eq 4 agree well with one another except at θ-locations close to the load.
2. The 90-deg roller and 30-deg free BIE results agree well with one another, especially at locations well away from θ_{max}. This observation, and the one immediately preceding, are expected results—by St. Venant's principle.
3. The BIE results and the distributed load results from Eq 4 agree well with one another, especially in regions where K is largest (and where nodes were therefore concentrated). The BIE results were low by roughly 10 percent, which is consistent with the results for axisymmetric problems discussed in the foregoing. Thus, it can be concluded that the approximate expression for K due to a point load provides reasonable accuracy for engineering purposes, and provides a suitable means for estimating stress-intensity factors for complete circumferential cracks in pipes subjected to arbitrary axial stresses.

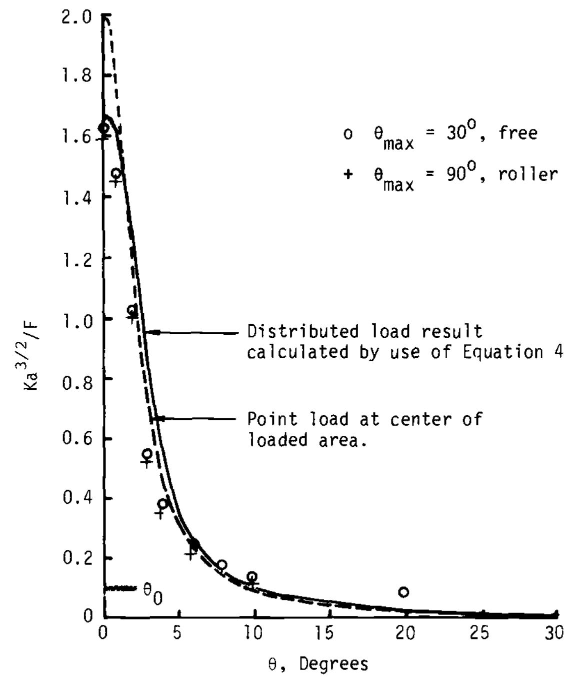

FIG. 3—*Comparison of approximate solution for* K *with boundary integral equation results.*

The application of the preceding results to the case of a pipe subjected to bending is straightforward, and provides an example of the usefulness of Eq 4. The applied stress is taken to be

$$\sigma = \sigma_{max} \frac{y}{r_i + h} = \sigma_{max} \frac{r_i + x}{r_i + h} \cos \phi$$

where y is the distance from the neutral axis and ϕ is an angular coordinate.[3] Using Eq 4 and integrating over the crack surface eventually leads to the following result

$$K = \frac{\sigma_{max} \cos \theta}{(\gamma + 1)(\gamma + \alpha)^2} \left(\frac{2a}{\pi} \right)^{1/2} \int_0^1 (\gamma + \alpha u)^3 \frac{m(u, \alpha)}{(1 - u)^{1/2}} du \quad \text{(bending)} \quad (5)$$

This expression neglects the possible influence of crack closure in the regions where nominal bending stresses are compressive. The corresponding

[3]In the present notation, ϕ is the angular coordinate for the applied stress and θ is the angular coordinate of position along the crack front.

result for uniform tension is directly obtainable from Labbens [3]. In the present notation the result is

$$K = \sigma\left(\frac{2a}{\pi}\right)^{1/2} \int_0^1 \frac{\gamma + \alpha u}{\gamma + \alpha} \frac{m(u, \alpha)}{(1 - u)^{1/2}} du \quad \text{(tension)} \tag{6}$$

Stress-intensity factor results for tension and bending for $\gamma = 5$ are presented in Fig. 4. Results are presented in terms of $K_{max}/\sigma' a^{1/2}$ where K_{max} is the maximum K around the crack front, and σ' is the maximum applied nominal stress at the crack-tip location. For tension $\sigma' = \sigma$, and for bending, $\sigma' = \sigma_{max}(r_i + a)/(r_i + h) = \sigma_{max}(\gamma + \alpha)/(\gamma + 1)$. Also shown is the single-edge-notch result for a flat plate in tension [1]. This corre-

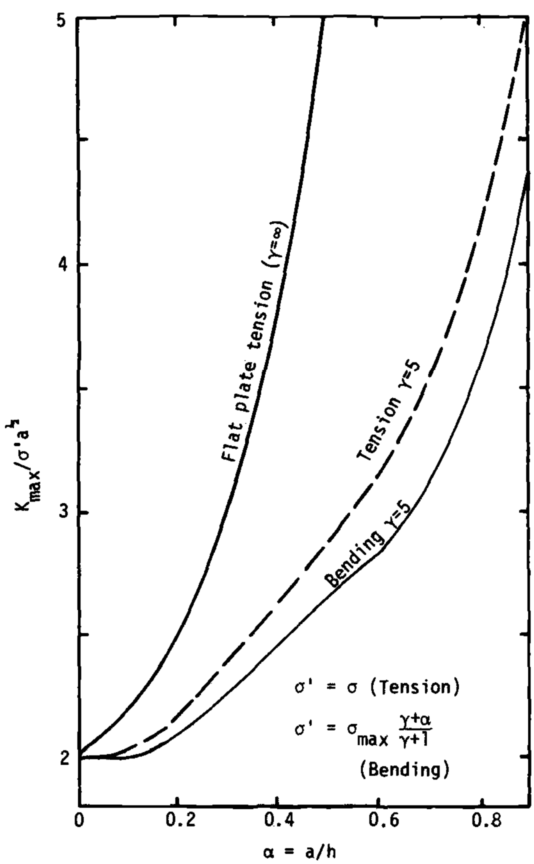

FIG. 4—*Stress-intensity factor results for a complete circumferential interior surface crack in a pipe with $\gamma = r_i/h = 5$ subjected to uniform axial tensile stress or bending. Also shown is the corresponding tension result for a flat plate. See text for σ'.*

sponds to $\gamma = \infty$. The similarity of the tension and bending results for $\gamma = 5$ in Fig. 4 is not surprising because, as shown in Fig. 3, K at a given angular location is influenced most strongly by the stresses close by, and the bending stresses in a pipe with $\gamma = 5$ are nearly uniform through the wall thicknesses at the angular location corresponding to the maximum stress ($\phi = 0$). Results for uniform tension are of particular interest, and curve fits obtained by use of $m(u, \alpha)$ [*3*] are presented in the Appendix for $\gamma = 5$ and 10. Such results were also presented in graphical form in Refs *3* and *4*.

A comparison of the flat-plate tension results with the $\gamma = 5$ tension results shows that the use of the flat-plate solution is very conservative when applied to a hollow cylinder. Additional comparisons with available solutions, and discussions of the influence of γ and the presence of nearby nozzles, are included in Ref *10*. It was found that γ was not too influential in the range from 5 to 10, and that the results for a circumferential crack in a long pipe were very similar to those for a circumferential crack at a pipe-to-pressure vessel nozzle. Reference *10* also applies Eq 4 to the calculation of K for a crack in a weldment due to residual axial stresses that have strong angular variations, and then discusses the implication of these results to the growth of stress corrosion cracks in boiling water reactor piping.

In closing, analogous results for longitudinal cracks could be obtained by means similar to those employed in the foregoing and in Ref *3*. Reference *11* should prove useful in such an effort.

Summary and Conclusions

An approximate stress-intensity factor expression for a concentrated point load on the surfaces of a complete circumferential interior surface crack in a hollow circular cylinder was presented (Eq 4). This expression was deduced from existing solutions for a point load on an embedded penny-shaped crack and for a concentrated ring load on a complete circumferential interior surface crack in a hollow cylinder. Hence, the approximate expression reduces exactly to these particular cases. The accuracy of the approximate K expression was assessed by comparing it with the numerical results for a particular three-dimensional case. The numerical results were obtained by the BIE technique. Good agreement was observed, from which it can be concluded that the approximate three-dimensional expression provides reasonable accuracy for engineering purposes, and provides a suitable means for estimating stress-intensity factors for complete circumferential interior surface cracks in pipes subjected to arbitrary axial stresses. The point-load solution was then applied to determine K for a pipe in bending, and additional uses of the solution were discussed.

Acknowledgments

The support provided by the Electric Power Research Institute, Palo Alto, Calif., is gratefully acknowledged. The cooperation of Dr. T. A. Cruse of Pratt and Whitney Aircraft Division, East Hartford, Conn., and the generous assistance and cooperation of Mr. P. M. Besuner of Failure Analysis Associates, Palo Alto, Calif., were indispensable in the performance of the BIE calculations. Lawrence Livermore Laboratory, through their Load Combinations Program, provided support for the BIE calculations, which it is a pleasure to acknowledge. Finally, considerable assistance in this work was provided by Mr. Rick Northrup of the authors' organization and the University of Cincinnati.

APPENDIX

Curve Fits for Some Results of Interest

The weight functions $m(u, \alpha)$ for $\gamma = 5$, 10, and ∞ are provided by Labbens et al [3] for complete circumferential and longitudinal cracks. The results are presented in graphical form, and were obtained by finite-element techniques. Curve fits to the graphical results of Ref 3 are of use in numerical calculations that utilize them, and such results for circumferential cracks for $\gamma = 5$ and 10 are as follows:

$$
\begin{aligned}
v &= 1 - u \\
m(u, \alpha) &= 1 + b_1(\alpha)v + b_2(\alpha)v^2 + b_3(\alpha)v^3 + b_4(\alpha)v^4 \\
b_1(\alpha) &= c_0 + c_1\alpha + c_2\alpha^2 + c_3\alpha^3 + c_4\alpha^4 \\
b_2(\alpha) &= d_0 + d_1\alpha + d_2\alpha^2 + d_3\alpha^3 + d_4\alpha^4 \\
b_3(\alpha) &= e_0 + e_1\alpha + e_2\alpha^2 + e_3\alpha^3 + e_4\alpha^4 \\
b_4(\alpha) &= f_0 + f_1\alpha + f_2\alpha^2 + f_3\alpha^3 + f_4\alpha^4
\end{aligned}
$$

The constants in the expressions for $b_i(\alpha)$ depend on γ, and Table 1 gives values for circumferential cracks with $\gamma = 5$ and 10. Values of $m(u, \alpha)$ calculated from the foregoing curve fits generally agree within less than 2 percent with values read from the graphs in Ref 3. Hence, inaccuracies in addition to the 5 percent in the finite-element results mentioned in Ref 3 are felt to be minimal. These results are applicable out to $\alpha = 0.9$; the upper limit considered by Labbens [3].

The case of a uniform stress in the pipe wall is of particular interest in the analysis of the behavior of circumferential cracks in pipes. Curve fits to results obtained by numerical integration using the foregoing results for $m(u, \alpha)$ were obtained:

$$
\frac{K}{\sigma a^{1/2}} = \frac{2 + c_1\alpha + c_2\alpha^2 + c_3\alpha^3 + c_4\alpha^4}{(1 - \alpha)^{1/2}}
$$

	$\gamma = 5$	$\gamma = 10$
c_1	−1.00250	−0.625027
c_2	4.79463	3.58965
c_3	−6.21135	−0.968876
c_4	1.79864	−2.73242

These polynominal curve fits agreed with the numerical integration results within 2 percent, and the accuracy is felt to be consistent with the accuracy in Ref *3*. These results are applicable to at least $\alpha = 0.9$, which is the limit of the results provided by Labbens et al [*3*].

TABLE 1—*Values of constants.*

	$\gamma = 5$	$\gamma = 10$		$\gamma = 5$	$\gamma = 10$
c_0	0.72805	1.96985	e_0	0.044577	7.594051
c_1	−2.78297	−23.03093	e_1	−1.3464	−125.27237
c_2	42.8153	129.60957	e_2	37.6152	553.73778
c_3	−93.6387	−221.6217	e_3	−92.69887	−854.8676
c_4	69.2408	130.8334	e_4	75.8054	435.2845
d_0	0.18587	−5.07745	f_0	0.114636	−3.655956
d_1	0.85491	87.82169	f_1	−0.70486	60.66035
d_2	−42.5302	−407.90414	f_2	−8.46211	−263.0722
d_3	122.3899	676.17251	f_3	23.29726	395.173
d_4	−100.5542	−370.3413	f_4	−21.29696	−194.234

References

[*1*] Tada, H., Paris, P. C., and Irwin, G. R., *The Stress Analysis of Cracks Handbook*, Del Research Corp., Hellertown, Pa. 1973.

[*2*] Shack, W. J., Ellingson, W. A., and Pahis, L. E., "The Measurement of Residual Stresses in Type 304 Stainless Steel Piping Butt Weldments," Final Report on Electric Power Research Institute Research Project RP449-1, Palo Alto, Calif., Dec. 1978.

[*3*] Labbens, R., Pellisier-Tanon, A., and Heliot, J. in *Mechanics of Crack Growth, ASTM STP 590*, American Society for Testing and Materials, 1976, pp. 368–384.

[*4*] Buchalet, C. B. and Bamford, W. H. in *Mechanics of Crack Growth, ASTM STP 590*, American Society for Testing and Materials, 1976, pp. 385–402.

[*5*] Erdol, R. and Erdogan, F., *Journal of Applied Mechanics*, Vol. 45, No. 2, June 1978, pp. 281–286.

[*6*] *Boundary-Integral Equation Method: Computational Applications in Applied Mechanics*, American Society of Mechanical Engineers AMD, Vol. 11, T. A. Cruse and F. J. Rizzo, Eds., New York, 1975.

[*7*] Smith, F. W., Kobayashi, A. S., and Emery, A. F., *Journal of Applied Mechanics*, Vol. 34, No. 4, Dec. 1967, pp. 947–952.

[*8*] Cruse, T. A., "An Improved Boundary-Integral Equation Method for Three Dimensional Elastic Stress Analysis," Report SM-73-19, Department of Mechanical Engineering, Carnegie-Mellon University, Pittsburgh, Pa., Aug. 1973.

[*9*] Cruse, T. A. in *Boundary-Integral Equation Method: Computational Applications in Applied Mechanics*, American Society of Mechanical Engineers AMD, Vol. 11, T. A. Cruse and F. J. Rizzo, Eds., New York, 1975, pp. 31–46.

[*10*] Harris, D. O., "The Influence of Crack Growth Kinetics and Inspection on the Integrity of Sensitized BWR Piping Welds," Electric Power Research Institute Report EPRI NP-1163, Project 1325-2, Palo Alto, Calif., Sept. 1979.

[*11*] Harris, D. O., *International Journal of Fracture*, Vol. 9, No. 1, March 1973, pp. 21–32.

J. W. Phillips[1] *and R. J. Sanford*[2]

Effect of Higher-Order Stress Terms on Mode-I Caustics in Birefringent Materials

REFERENCE: Phillips, J. W. and Sanford, R. J., "**Effect of Higher-Order Stress Terms on Mode-I Caustics in Birefringent Materials,**" *Fracture Mechanics: Thirteenth Conference, ASTM STP 743,* Richard Roberts, Ed., American Society for Testing and Materials, 1981, pp. 387-402.

ABSTRACT: A general theory is developed for determining the sizes, shapes, and locations of the double caustics produced in statically loaded birefringent plates containing Mode-I cracks. Particular attention is paid to the effect of the first few higher-order, nonsingular stress terms on the determination of the stress-intensity factor K_I associated with the singular stress field.

It is found that the transverse diameters of the inner and outer parts of the double caustic have an average value essentially equal to the transverse diameter of the single caustic produced by an optically isotropic material having the same optical constant. Furthermore, with the superposition of a constant (tensile or compressive) stress parallel to the crack, each part of the double caustic deforms independently but in such a way as to maintain this average transverse diameter.

Other higher-order effects are also investigated and it is concluded that birefringent materials offer the potential of "feature extraction" concerning crack-tip stress fields, in addition to being suitable for the accurate determination of K_I-values experimentally.

KEY WORDS: caustics, shadow-spot patterns, Mode-I deformation, linear elastic fracture mechanics, optical methods, crack-tip stress fields

The optical method of caustics, or shadow patterns, is a relatively new experimental method that can be used to determine stress-intensity factors associated with cracks in bodies. Potentially, it has application to a wide variety of problems, including static and dynamic crack propagation studies in both opaque and transparent materials.

In the mid-1960's, Manogg [*1*][3] published the first fundamental papers on

[1]Associate professor, Department of Theoretical and Applied Mechanics, University of Illinois at Urbana-Champaign, Urbana, Ill. 61801.

[2]Head, Structural Reliability Section, Marine Technology Division, Naval Research Laboratory, Washington, D. C. 20375.

[3]The italic numbers in brackets refer to the list of references appended to this paper.

caustics; he demonstrated that the shape of the shadow zone that would be produced by the square-root-singular stress distribution for a Mode-I loaded crack [2] in an optically isotropic plate would be an epicycloid-like figure having a circular generating curve of radius r_0 given by

$$r_0^5 = \left(\frac{3}{2} \frac{K_I}{\sqrt{2\pi}} \frac{Cdz_0}{M}\right)^2 \tag{1}$$

where K_I is the Mode-I stress-intensity factor and the other quantities, such as the magnification factor M, are experimental parameters. The caustic itself, which is viewed on a screen or recorded on film, is typically a dark spot surrounded by a bright halo having dimensions proportional to r_0; see Fig. 1. Thus, in principle, the value of K_I can be determined easily by measuring a characteristic dimension of the caustic, such as its transverse diameter D_t (which is equal to 3.170 Mr_0 in the case of Manogg's "classical" caustic).

Subsequent to Manogg's initial work, Beinert, Kalthoff, and Maier in Germany [3,4] and Theocaris and his co-workers in Greece [5-7], among others, have made major advances in the state of the art of caustics. Much of the work reported by the German workers involves the use of optically anisotropic (birefringent) materials for both static and dynamic crack propagation experiments, whereas Theocaris's work centers mainly on the use of optically isotropic materials for studies of static stress fields surrounding crack tips and other discontinuities in bodies or in surface loadings.

Recently Theocaris and Ioakimidis [8] investigated, for optically isotropic materials, one of the factors that can influence the accuracy of data reduction associated with caustics, namely, the effect of nonsingular stress fields on the size and shape of the caustic. For optically isotropic materials they showed

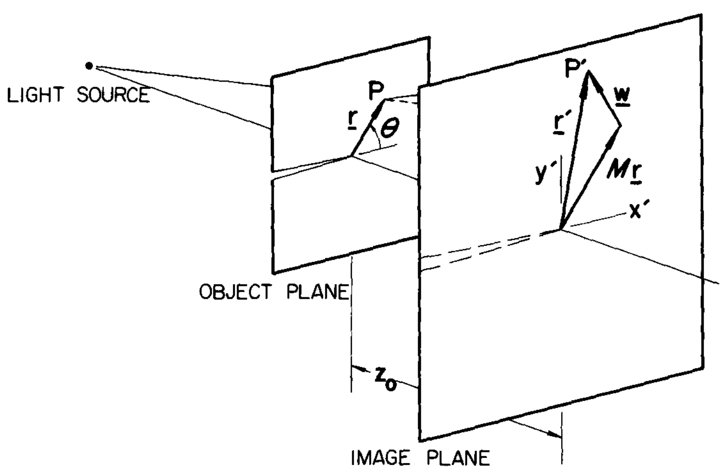

FIG. 1—*Experimental arrangement for producing transmitted-light caustics.*

that, of the first four admissible stress terms (those that vary as $r^{-1/2}$, r^0, $r^{+1/2}$ and r^{+1}, where r is the polar distance from the crack tip), only the $r^{-1/2}$ and the $r^{+1/2}$ terms influence the size and shape of the caustic; furthermore, by proper measurement of the caustic, the effect of a small $r^{+1/2}$ component in the stress field can be nullified as far as the accurate determination of the value of K_I is concerned.

The purpose of this paper is to study the effects of the first few nonsingular stress terms on the sizes and shapes of the caustics that are produced in optically anisotropic (birefringent) materials. The introduction of optical anisotropy complicates the governing image equations, gives rise to a double caustic instead of a single one, increases by one the number of parameters to be considered, and makes the shapes of the caustics dependent upon all higher-order stress terms. It will be shown, however, that a benefit of the increased complexity due to birefringence is an ability to discriminate, at least partially, between some of the low-order nonsingular terms that arise experimentally. The work may be regarded as an extension of a previous effort [*9*] in which the effect of the first nonsingular term (a constant-stress component) was studied.

Analysis

Formation of Caustics

When a light ray traverses a plate of thickness d in a normal or near-normal direction, it suffers an optical path length change Δs given by [*5*]

$$\Delta s = C d\,[(\sigma_1 + \sigma_2) \pm \xi(\sigma_1 - \sigma_2)] \tag{2}$$

where

C = elasto-optic material constant that depends upon the generalized state of stress [*4, 9*],

σ_1, σ_2 = principal stresses in the plane of the plate, and

ξ = another material constant [*4, 9*] called the optical anisotropy parameter.

The value of ξ is zero for optically isotropic materials such as polymethylmethacrylate and is nonzero for birefringent materials such as Homalite-100 and Araldite-B. When $\xi \neq 0$, two path length changes are predicted by Eq 2 and consequently caustics produced by birefringent materials appear in distinctive double sets.

If the plate is placed between a light source and an image plane, as illustrated in Fig. 1, a light ray passing through a generic point P located by position vector $\mathbf{r}$ in the midplane of the plate will strike the image plane at a point P' located by position vector $\mathbf{r}'$; from the theory of the eikonal the transformation $\mathbf{r} \rightarrow \mathbf{r}'$ is given by

$$\mathbf{r}' = M\mathbf{r} - z_0 \nabla(\Delta s) \tag{3}$$

where M is the magnification factor for the optical arrangement (> 1, $= 1$, or < 1 for a divergent, parallel, or convergent light source, respectively) and z_0 is the distance between the plate midplane and the image plane. A caustic is formed whenever the Jacobian $J(r, \theta)$ of the transformation $\mathbf{r} \rightarrow \mathbf{r}'$ vanishes, that is, when

$$J(r, \theta) \equiv \frac{\partial x'}{\partial r}\frac{\partial y'}{\partial \theta} - \frac{\partial y'}{\partial r}\frac{\partial x'}{\partial \theta} = 0 \tag{4}$$

x' and y' being the Cartesian components of $\mathbf{r}'$ and r and θ being the polar coordinates of $\mathbf{r}$.

From Eqs 2, 3, and 4 it will be seen that it is the spatial distribution of the principal stresses σ_1 and σ_2 that determines whether or not a caustic is formed, and if a caustic is formed, what size and shape it will have.

Assumed Stress Distribution

It is well known that the singular stress distribution surrounding a Mode-I loaded crack [2] having free faces at $\theta = \pm\pi$ varies inversely as the square root of r, each stress component varying trigonometrically with respect to θ; and that the stress-intensity factor K_I defined by

$$K_I = \lim_{r \to 0} \sigma_\theta(r, \theta)\sqrt{2\pi r}\,\bigg|_{\theta=0} \tag{5}$$

plays a fundamental role in fracture mechanics studies. As a very special case of the analysis to follow, it can be shown that the principal stress sum $(\sigma_1 + \sigma_2)$ associated with the Mode I singular stress solution alone is given by

$$\sigma_1 + \sigma_2 = \frac{2K_I}{\sqrt{2\pi r}} \cos\frac{\theta}{2} \tag{6}$$

and that, for this singular stress distribution, a caustic will be formed in an optically isotropic material ($\xi = 0$) by points (r, θ) satisfying $r = r_0$ (independent of θ) where r_0 is given by Eq 1.

The emphasis in this paper, however, will be on birefringent materials ($\xi \neq 0$) in which the stresses consist not only of the singular term but also of higher-order, nonsingular terms. For purposes of analysis, it is useful to employ the recent generalization [*10*] of the Westergaard formulation [*11*] for crack problems. In this generalization [*10*], two analytic functions $Z(z)$ and $\eta(z)$ are introduced, where $z = re^{i\theta} = x + iy$, subject to the restrictions

$$Re\{Z\} = 0 \quad \text{for}\ \theta = \pm\pi \quad \text{and} \quad Im\{\eta\} = 0 \quad \text{for} \quad y = 0. \tag{7}$$

Then the Cartesian stress components derived from the relations

$$\sigma_x\,(r,\,\theta) = Re\{Z\} - y\,Im\{Z'\} + y\,Im\{\eta'\} - 2Re\{\eta\} \tag{8}$$

$$\sigma_y\,(r,\,\theta) = Re\{Z\} + y\,Im\{Z'\} - y\,Im\{\eta'\} \tag{9}$$

$$\tau_{xy}\,(r,\,\theta) = -y\,Re\{Z'\} + y\,Re\{\eta'\} + Im\{\eta\} \tag{10}$$

automatically satisfy the compatibility, static equilibrium, and traction boundary conditions of the problem. Suitable expressions for $Z(z)$ and $\eta(z)$ are [9]

$$Z(z) = \frac{K_{\mathrm{I}}}{\sqrt{2\pi z}} \sum_{n=0}^{\infty} \gamma_n \left(\frac{z}{r_0}\right)^n, \qquad \eta(z) = \frac{K_{\mathrm{I}}}{\sqrt{2\pi z}} \sum_{m=0}^{\infty} \delta_m \left(\frac{z}{r_0}\right)^{m+1/2} \tag{11}$$

where γ_n and δ_m are real dimensionless constants and r_0 is any characteristic length scale, which for convenience is taken to be the radius of the generating curve for the "classical" caustic (see Eq 1 and Fig. 2). Using Eqs 9 and 11 and definition Eq 5, one can demonstrate that γ_0 must be equal to unity. All the other γ_n and δ_m are completely arbitrary and can be selected so as to match far-field stress conditions. For example, δ_0 is related to Irwin's [12] constant-stress term σ_{0x} by the relation

$$\sigma_{0x} = \frac{2K_{\mathrm{I}}}{\sqrt{2\pi r_0}}\,\delta_0 \tag{12}$$

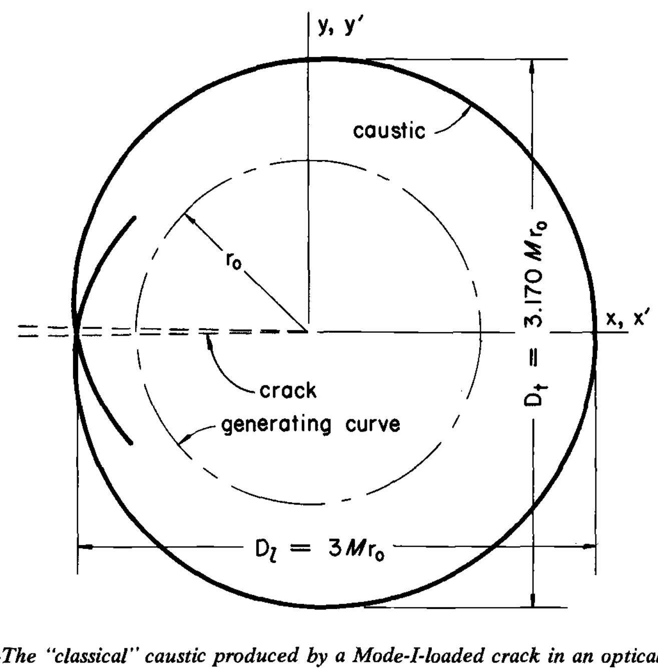

FIG. 2—*The "classical" caustic produced by a Mode-I-loaded crack in an optically isotropic material.*

It is already well known [3-8] that the value of σ_{0x} does not influence in any way the size, shape, or location of the single caustic produced by an optically isotropic material. However, it has also been demonstrated that the constant-stress term will affect the sizes and shapes of the double caustics produced in an optically anisotropic material [9].

Numerical Calculation of the Caustics

The image equation (Eq 3), when examined for the case of an optically anisotropic material, is found to be considerably more complex than for the isotropic case because the optical path length change Δs given by Eq 2 will involve not only the principal stress sum $(\sigma_1 + \sigma_2)$, which by Eqs 8–10 is seen to be linear in the stress functions $Z(z)$ and $\eta(z)$

$$\sigma_1 + \sigma_2 = 2Re\{Z\} - 2Re\{\eta\} \tag{13}$$

but also the difference $(\sigma_1 - \sigma_2)$, which is nonlinear in the stress functions

$$\sigma_1 - \sigma_2 = [(2y\, Im\{\eta'\} - 2\, Re\{\eta\} - 2y\, Im\{Z'\})^2 + (2y\, Re\{\eta'\} + 2Im\{\eta\} - 2y\, Re\{Z'\})^2]^{1/2} \tag{14}$$

Nevertheless, it is a rather straightforward procedure to substitute the assumed forms of $Z(z)$ and $\eta(z)$, Eq 11, into Eqs 13 and 14 and thereby to derive, by means of Eq 2, an expression for Δs that can be substituted into the image equation (Eq 3); the result can be found in Ref *9*.

Subsequent evaluation of the Jacobian $J(r, \theta)$ analytically by the use of Eq 4, however, becomes a prohibitively complicated task, and it is at this point that a resort is made to numerical techniques in an effort to generate theoretical caustics. Central finite differences, for example, are used to evaluate the partial derivatives $\partial x'/\partial r$, $\partial y'/\partial \theta$, etc., appearing in the definition of $J(r, \theta)$, and a Newton iteration on the variable r is used to satisfy the equality $J(r, \theta) = 0$ for regularly spaced values of θ in the upper half of the object plane $(0 \leq \theta \leq \pi)$. Symmetry arguments appropriate for Mode-I deformation can be used to extend the results into the lower half-plane. Generally speaking, for any admissible θ, a unique value of r can be found that renders $J(r, \theta) = 0$, but occasionally one encounters small angular subintervals in which $J(r, \theta) = 0$ apparently has no solution [9].

Results

Typical values of the anisotropy parameter ξ for common photoelastic materials vary between 0.1 and 0.5, depending upon the generalized state of stress [4, 9]. In all the calculations to be presented here, ξ has been set equal to 0.4.

Near-Field (Singular) Solution

When $\xi \neq 0$, a double caustic is produced for all stress fields under consideration, even for the near-field [2] distribution with no higher-order terms present. In Figs. 3 through 11, the double caustic for the near-field solution is drawn as a dashed line and will be called the reference (double) caustic in the discussion to follow; the transverse diameters of the inner and outer reference caustics are found to be

$$\left.\begin{aligned}(D_t)_{\text{inner(ref)}} &= 3.011\, Mr_0 \\ (D_t)_{\text{outer(ref)}} &= 3.375\, Mr_0\end{aligned}\right\} \text{for } \xi = 0.4 \tag{15}$$

It is interesting to note that the average of the inner and outer transverse diameters of the reference caustic is 3.173 Mr_0, which is remarkably close to the transverse diameter of the classical caustic (3.170 Mr_0). Also, the average

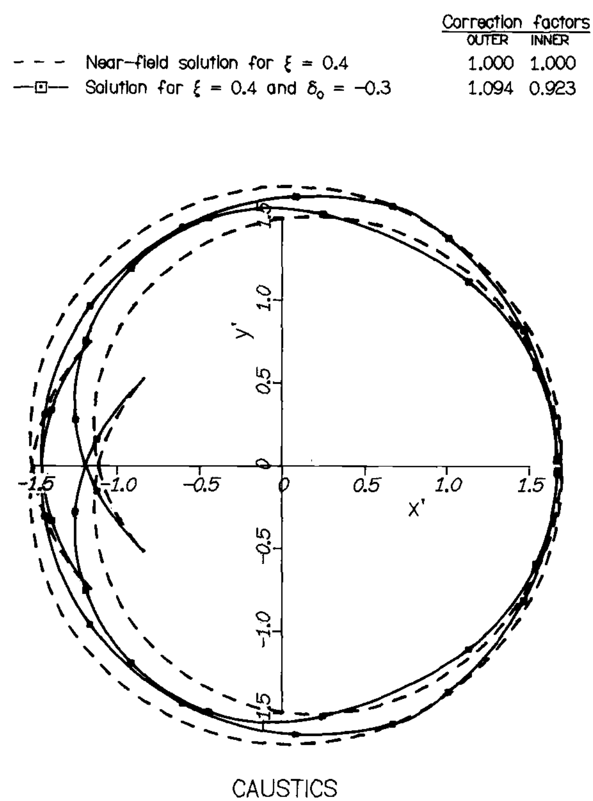

FIG. 3—*Comparison of reference caustic with caustic produced when tensile stress parallel to crack (r^0-term) is superposed on singular solution. In this figure, as well as in Figs. 4 through 11, the length scales have been normalized with respect to* Mr_0.

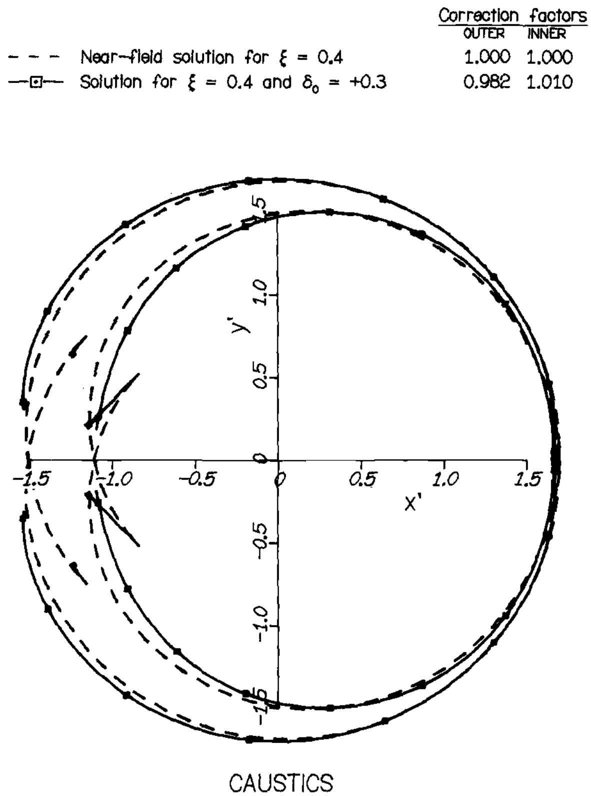

FIG. 4—*Effect of compressive stress parallel to crack (*r^0*-term).*

of the longitudinal diameters of the reference caustic, measured between the points of intersection of the caustics with the x'-axis, is found to be $3.006\,Mr_0$, which is again remarkably close to the longitudinal diameter of the classical caustic (exactly $3\,Mr_0$).

Suppose one is attempting to determine K_I by measuring, say, the outer transverse diameter $(D_t)_{outer}$ of the double caustic when higher-order terms are present; then one can appeal to Eqs 1 and 15 and write

$$K_I = f_{outer} K_I^* \tag{16}$$

where K_I^* is a "provisional" value of K_I that does not account for the presence of higher-order terms

$$K_I^* = \frac{2}{3} \frac{\sqrt{2\pi}\, M}{|Cdz_0|} \left(\frac{(D_t)_{outer}}{3.375\, M} \right)^{5/2} \tag{17}$$

and f_{outer} is a correction factor given by

$$f_{outer} = \left(\frac{(D_t)_{outer(ref)}}{(D_t)_{outer}}\right)^{5/2} \tag{18}$$

A similar procedure can be established for working with inner caustics. In Figs. 3 through 11, the values of the correction factors so defined appear in the upper right-hand corner.

Effect of the Constant-Stress Term

When the singular stress term is augmented by a constant-stress component σ_{0x} parallel to the crack, each caustic in the double set suffers a distortion, as illustrated in Figs. 3 and 4 for tensile ($\delta_0 = -0.3$) and compressive ($\delta_0 = +0.3$) values of σ_{0x}, respectively. (See Eqs 8-12 with γ_0 set equal to 1, $\delta_0 \neq 0$, all other γ_n, and $\delta_m = 0$.) In Fig. 3 it will be seen that a tensile value of σ_{0x} tends to increase the transverse diameter of the inner caustic and to decrease that of the outer one. As might be expected, a compressive σ_{0x} produces just

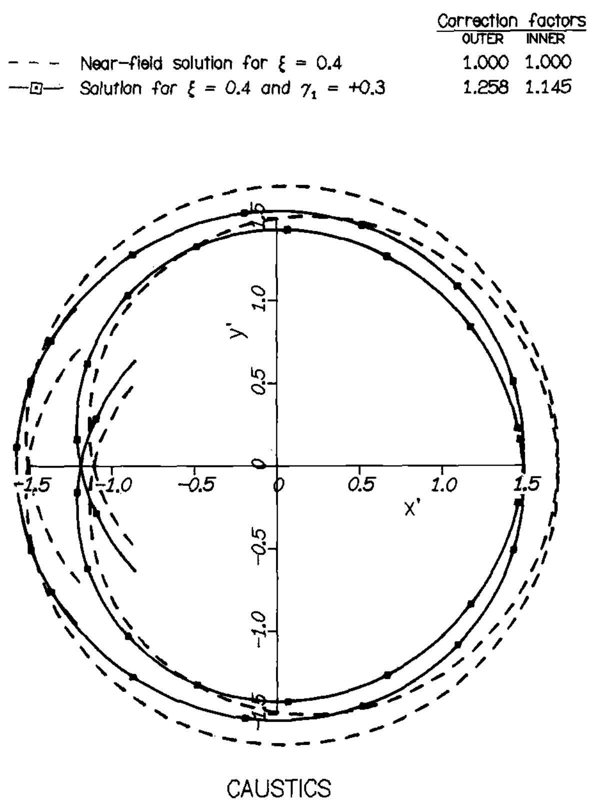

FIG. 5—*Effect of* $r^{1/2}$*-term (positive* γ_1*).*

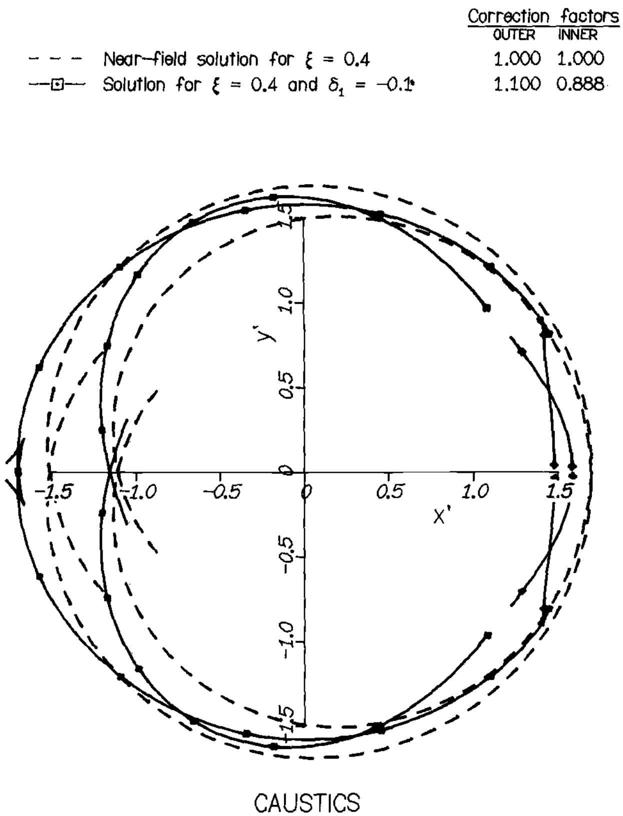

FIG. 6—*Effect of linear term in* r *(negative* δ_1*).*

the opposite effects (Fig. 4), although the effects are not as pronounced as in the tensile case.

The straightforward use of these correction factors requires a knowledge of the values of the higher-order terms, such as δ_0 in the present context, but some important observations can be made just by examining the nature of the correction factors. For δ_0 in particular, the fact that the inner and outer correction factors fall to either side of unity by approximately the same amount indicates that the average of the transverse diameters of the double caustics produced when $\delta_0 \neq 0$ is about the same as the average of the transverse diameters of the reference (double) caustic. This is regarded as an important finding because it means that virtually no correction for ξ or δ_0 is required if the constant-stress term is the only dominant higher-order term and if the average of the transverse diameters of a double caustic, call it $(D_t)_{avg}$, is used to determine r_0 (and hence K_I) by setting D_t of the "classical" caustic equal to $(D_t)_{avg}$, that is, $r_0 = (D_t)_{avg}/(3.170\ M)$.

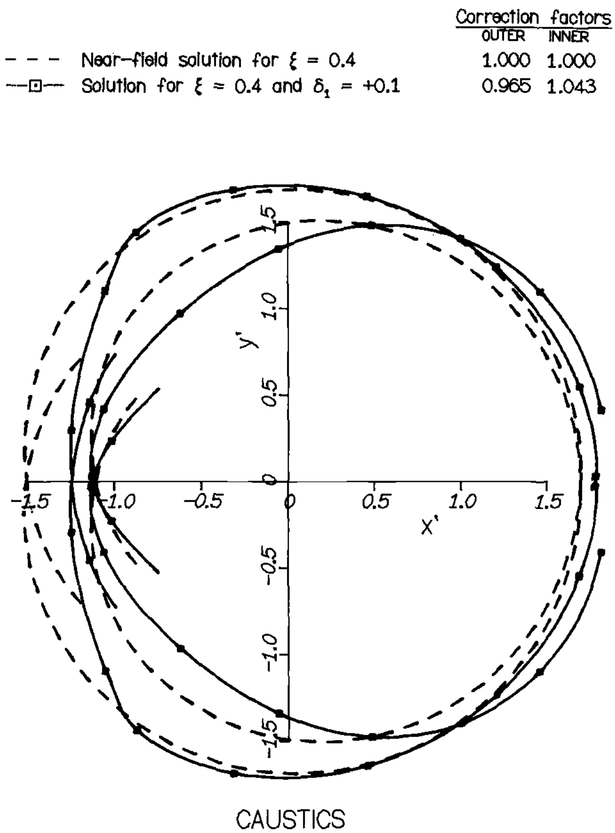

FIG. 7—*Effect of linear term in* r *(positive* δ_1*).*

Effect of Terms of Order $r^{1/2}$, r^1, $r^{3/2}$, r^2

It turns out that, of the next four possible terms in the stress field representation (Eq 11), only the δ_1-term produces correction factors that tend to be self-cancelling in the sense just described for δ_0. The δ_1-term controls the strength of the stress term varying linearly with r, and it is perhaps not surprising that the δ_0- and δ_1-terms, which have no influence on the size or shape of the caustic in an optically isotropic material [8], are the only low-order nonsingular terms that have this property.

Typical results for the $r^{1/2}$-type dependence are shown in Fig. 5. It is seen that both parts of the double caustic are reduced in size and shifted to the left when $\gamma_1 > 0$; just the opposite effects (not illustrated) are noted for $\gamma_1 < 0$. Although the correction factors are affected, the distortion of the caustics is observed to be minimal.

Considerable distortion of the double caustic is produced, however, when

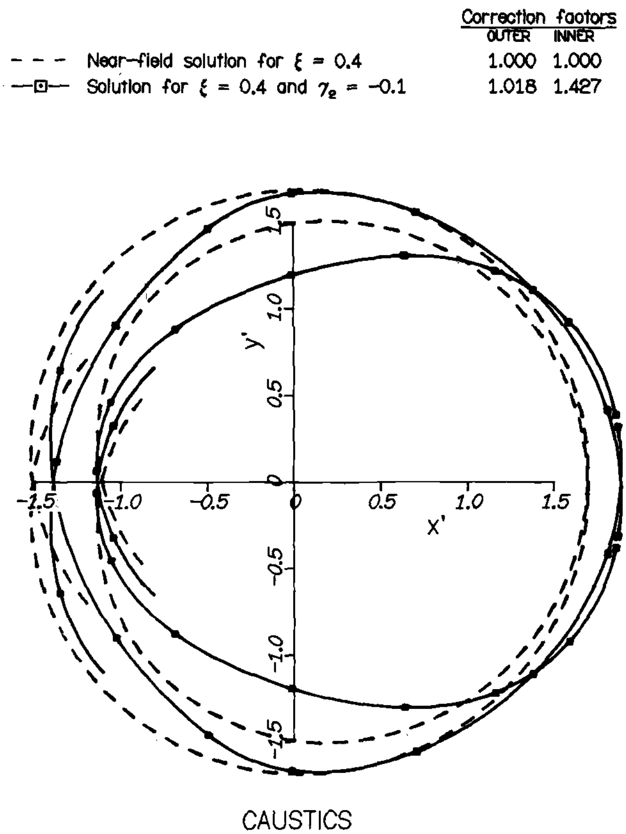

FIG. 8—*Effect of* $r^{3/2}$*-term (negative* γ_2*).*

the coefficient of the r^1-term is allowed to vary, as noted in Figs. 6 and 7 for negative and positive values of δ_1, respectively. For negative δ_1, a noticeable blunting of what was originally the outer caustic occurs along the $+x'$-axis, whereas, in the same region, what was originally the inner caustic is developing a nose. Also, the inner and outer caustics no longer coincide where they cross the $+x'$-axis. For positive δ_1, blunting and sharpening of the outer and inner caustics, respectively, are observed along the $-x'$-axis (see Fig. 7).

The curves in Figs. 8 and 9 illustrate the effect of the $r^{3/2}$-type variation in stress. A considerable foreshortening of the double caustic longitudinally, coupled with a considerable expansion of the inner caustic transversely, leads to a rather distorted double caustic for the chosen positive value of γ_2 (Fig. 9). A negative value of γ_2 of equal magnitude produces opposite effects, including a left-to-right inversion of the "tail" of the outer caustic (Fig. 8). Also, regardless of the sign of γ_2, the inner and outer caustics cross in an "X" pattern at the $+x'$-axis; a similar effect is seen in Fig. 6 (for γ_1).

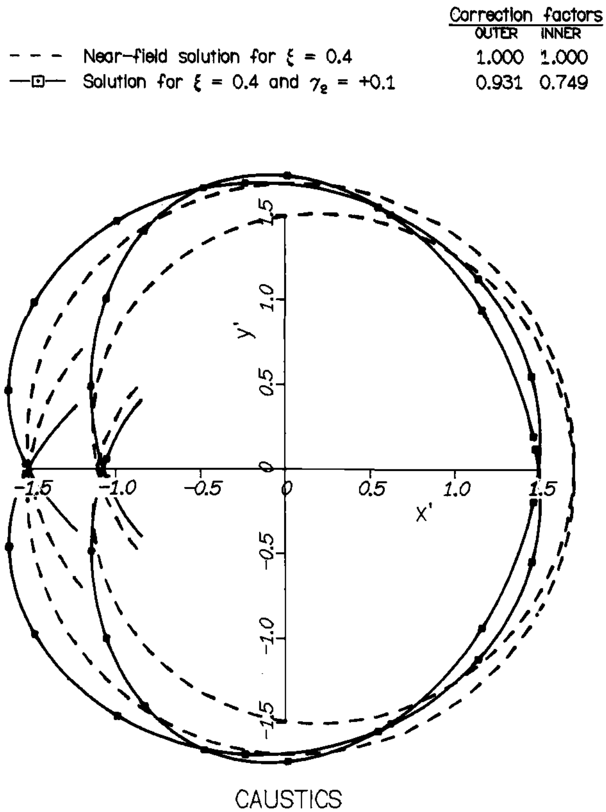

FIG. 9—*Effect of* $r^{3/2}$*-term (positive* γ_2*).*

The highest-order stress term considered in this paper is the one that varies as r^2 (Figs. 10 and 11). Note that the *outer* caustic, although distorted by either positive or negative values of δ_2, maintains a nearly constant transverse diameter, but the same cannot be said of the *inner* one. In this respect the r^2-term and the $r^{3/2}$-term have similar effects. A peculiar deviation of the outer caustic where it crosses the $+x'$-axis is noted for negative δ_2. For positive δ_2, no solution was found for the outer caustic for small values of θ, which is somewhat unusual.

Conclusions

Examination of the effects of the first five higher-order stress terms, namely, those that vary as r^0, $r^{1/2}$, r^1, $r^{3/2}$, and r^2, on the sizes and shapes of the double caustics produced by Mode-I loaded cracks in birefringent materials reveals the following:

1. All higher-order terms affect the sizes and shapes of both parts of the double caustic.

2. The constant (r^0, or σ_{0x}) and the linear (r^1) terms are the only terms that produce self-cancelling errors when the average of the transverse diameters is used to compute the stress-intensity factor K_I according to the classical formula.

3. The r^1-and r^2-terms are the lowest-order terms that produce a separation of the double caustic where it crosses the $+x'$-axis.

4. All terms of order r^1 and higher produce somewhat similar blunting and sharpening effects, depending upon the signs of the terms, and a transverse "double crossing" of the inner and outer caustics near the $\pm y'$-axis is not uncommon.

5. The inner and outer caustics produced by nonzero $r^{1/2}$- and $r^{3/2}$-terms tend to cross in an X-pattern at the $+x'$-axis, whereas all caustics produced by integer-order powers of r cross the $+x'$-axis perpendicularly.

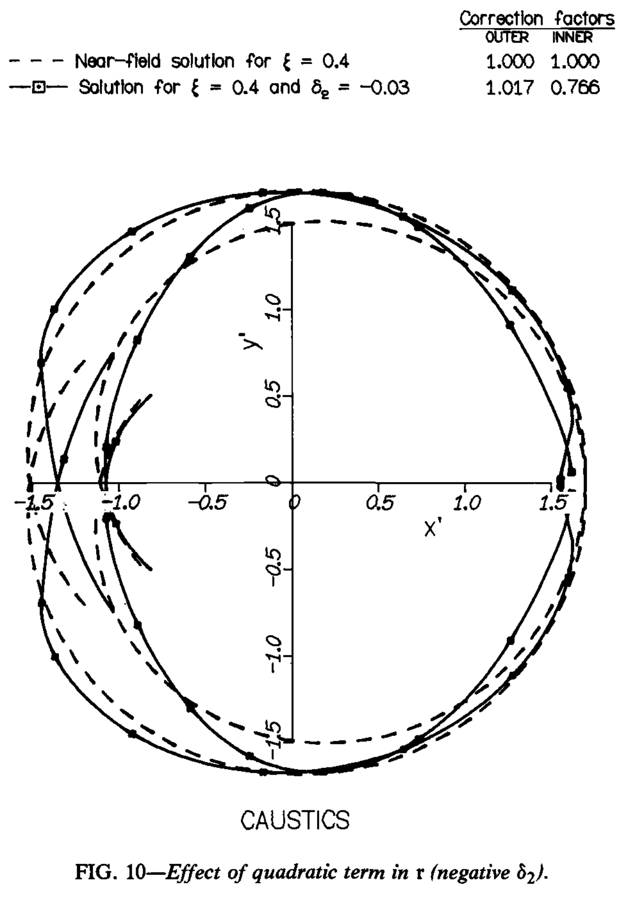

FIG. 10—*Effect of quadratic term in* r *(negative* δ_2*).*

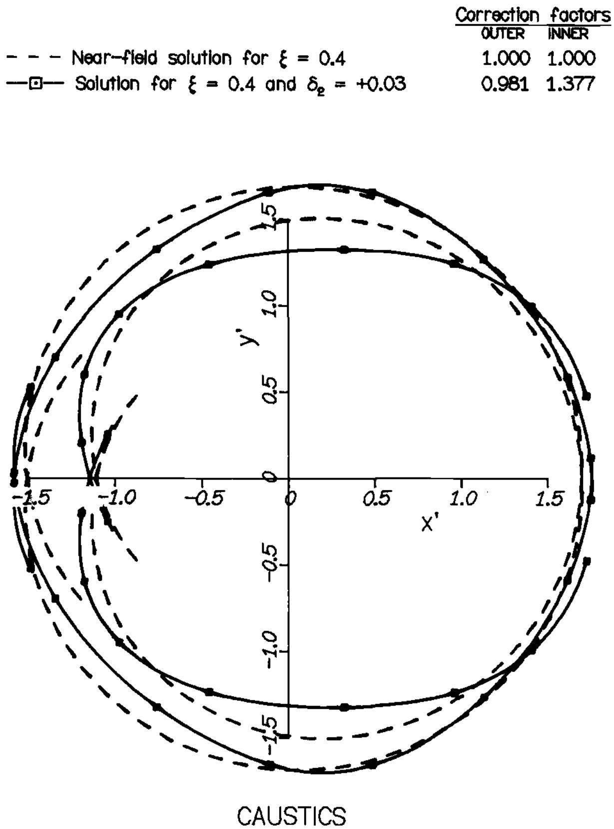

FIG. 11—*Effect of quadratic term in r (positive δ_2).*

It would appear that the use of birefringent materials for experimental work in caustics offers a potential for "feature extraction" that is not available with the use of nonbirefringent, or optically isotropic, materials. With double caustics, accurate values of K_I can be determined by a simple transverse-diameter averaging technique that essentially eliminates the effect of the constant and linear terms in r. It is probable that an averaging technique involving the longitudinal diameters of the double caustics can be used to minimize the effect of the $r^{1/2}$-term as well, as Theocaris and Ioakimidis have done in the case of optically isotropic materials [8], but this is yet to be demonstrated.

Acknowledgments

The work reported here was initiated while the authors were associated with the Mechanical Engineering Department of the University of Maryland at College Park, Md. Valuable discussions with Dr. J. Beinert, who was also visiting at that time, and with Drs. W. L. Fourney, J. W. Dally, and G. R. Irwin, are gratefully acknowledged. Computing services were provided by the Computing Services Office of the University of Illinois at Urbana-Champaign.

References

[1] Manogg, P., *Glastechnische Berichte*, Vol. 39, 1966, pp. 229-329. *See also*, Manogg, P., "Anwendung der Schattenoptik zur Untersuchung des Zerreissvorgangs von Platten," ["Application of Shadow Optics to the Investigation of the Tearing Process in Plates,"] Ph.D. Dissertation, Freiburg, Germany, 1964.
[2] Sneddon, I. N. in *Proceedings*, The Physical Society (London), Vol. 187, 1946, pp. 229-260.
[3] Beinert, J., Kalthoff, J. F., and Maier, M. in *Proceedings*, Sixth International Conference on Experimental Stress Analysis, Verlag des Vereins Deutscher Ingenieure, Düsseldorf, Germany, 1978, pp. 791-798.
[4] Beinert, J. and Kalthoff, J. F., *Mechanics of Fracture*, Vol. 7, G. C. Sih, Ed. (to appear).
[5] Theocaris, P. S., *Journal of Applied Mechanics*, Vol. 37, 1970, pp. 409-415.
[6] Theocaris, P. S., *Applied Optics*, Vol. 10, 1971, pp. 2240-2247.
[7] Theocaris, P. S. and Gdoutos, E. E., *Journal of Applied Mechanics*, Vol. 39, 1972, pp. 91-97.
[8] Theocaris, P. S. and Ioakimidis, N. I., *Journal of Strain Analysis*, Vol. 14, 1979, pp. 111-118.
[9] Phillips, J. W., Sanford, R. J., and Beinert, J., "Effect of the Constant-Stress Term on Mode-I Caustics," Technical Report No. 436, Department of Theoretical and Applied Mechanics, University of Illinois at Urbana-Champaign, Ill., 1979.
[10] Sanford, R. J., *Mechanics Research Communications*, Vol. 6, No. 5, 1979, pp. 289-294.
[11] Westergaard, H. M., *Journal of Applied Mechanics*, Vol. 6, 1939, pp. 49-53.
[12] Irwin, G. R., Discussion of paper by A. Wells and D. Post, *Proceedings*, The Society for Experimental Stress Analysis, Vol. 16, No. 1, 1958, pp. 69-92; Discussion, pp. 93-96.

J. Heliot,[1] *R. Labbens,*[1] *and F. Robisson*[2]

Influence Functions for Stress-Intensity Factors at a Nozzle Corner

REFERENCE: Heliot, J., Labbens, R., and Robisson, F., "**Influence Functions for Stress-Intensity Factors at a Nozzle Corner,**" *Fracture Mechanics: Thirteenth Conference, ASTM STP 743,* Richard Roberts, Ed., American Society for Testing and Materials, 1981, pp. 403-421.

ABSTRACT: Influence functions are computed for the calculation of stress-intensity factors along partly circular cracks in nozzle corners subjected to pressure hoop stress linearly represented in the plane of the crack. The boundary integral equations method is used. The results are compared with those of previous studies.

KEY WORDS: stress-intensity factors, elastic theory, three-dimensional problems, nozzle crack corners

Nomenclature

a	Crack depth
c	Radius of crack
t	Reference length in nozzle
x,y	Coordinates in plane of crack
θ	Angle from internal surface of vessel
$K(\theta)$	Stress-intensity factor
$h_{ij}(\theta)$	Polynomial influence functions
r	Short distance along a normal to crack front
v	Displacement of a point on surface of crack
E	Young's modulus
ν	Poisson's ratio

The nozzle corners in pressure vessels may be more sensitive than other areas of the vessel to cracks initiated in the fabrication process or in the life of the vessel, since rather high stresses develop locally. As a counterpart, the high

[1]Research engineer and scientific manager, respectively, Creusot-Loire, Paris, France.
[2]Engineer, Framatome, Division des Fabrications, B. P. 13-71380 Saint-Marcel, France.

stresses are rather localized, and the geometry of the nozzles makes them very stiff. Due to the steep gradients and the geometry, no simple formula exists and numerical computations are necessary.

As will be seen in the next section, the research on nozzle crack corners has become important. Some of the methods presented could be used for other problems; but there is a need for functions depending only on the geometry which allow a simple calculation of the stress-intensity factors resulting from any load.

The authors have calculated, for plane problems and semi-elliptical cracks in cylinders *[1,2]*[3] influence functions depending only on the geometry, so that the stress-intensity factors along the crack front are easily calculated for any applied stress approximated by a polynomial in two coordinates in the plane of the crack.

The geometry studied is the lower corner of an inlet nozzle of a pressurized water reactor (PWR), the dimensions of which are shown in Fig. 1. The method, already documented in Ref *2*, is that of the boundary integral equations (BIE). The applied stress is defined by (Fig. 2)

$$\sigma(x,y) = \sigma_{ij}\left(\frac{x}{t}\right)^i \left(\frac{y}{t}\right)^j \tag{1}$$

and the polynomial influence functions are

$$h_{ij}(\theta) = \frac{\pi}{2} \frac{K_{ij}(\theta)}{\sigma_{ij}\left(\frac{c}{t}\right)^{i+j} \sqrt{\pi c}} \tag{2}$$

The individual stress-intensity factors are this way normalized with respect to a circular crack in an infinite solid subjected to a uniform stress $\sigma_{ij}(c/t)^{i+j}$.

As will be seen in a subsequent section, for the studied cracks

depth $a = 15, 60, 90$ mm

radius $c = 57, 102, 132$ mm

only the constant and linear terms are significant in the representation of the pressure hoop stress by a polynomial; due to the nearly symmetry, the term in y is small. As a consequence, only the influence functions $h_{00}(\theta)$ and $h_{10}(\theta)$ were calculated. Other functions could be calculated if more complete polynomials were necessary either for deeper or noncircular cracks or for other loads.

[3]The italic numbers in brackets refer to the list of references appended to this paper.

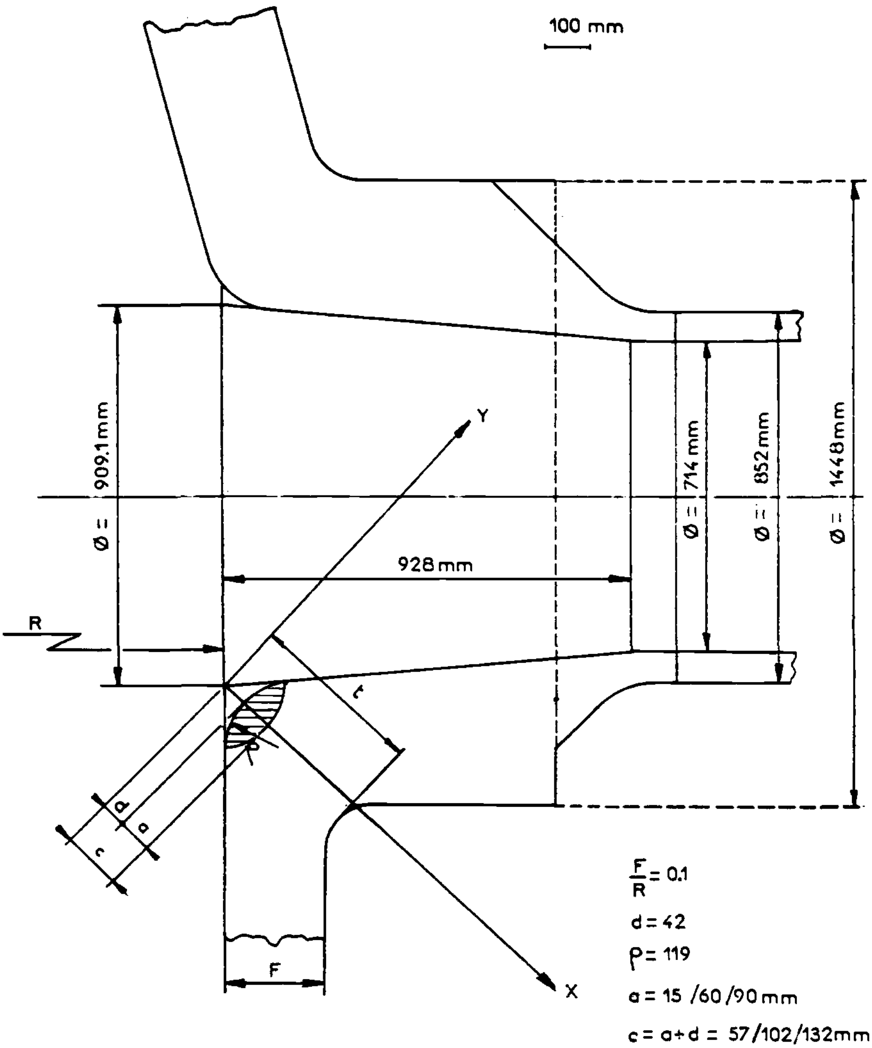

FIG. 1—*Dimensions of nozzle studied.*

Previous Research on Nozzle Corner Cracks

Distribution of Hoop Stress in a Reinforced Nozzle

Rashid and Gilman [*3*] were likely the first who investigated the problem of a nozzle corner subjected to an internal pressure. Their results on the distribution of the hoop stress were confirmed by subsequent studies [*4,5*] (Fig. 3), although Ref *5* is for a nozzle in a plate subjected to tensions σ and $\sigma/2$. A peak

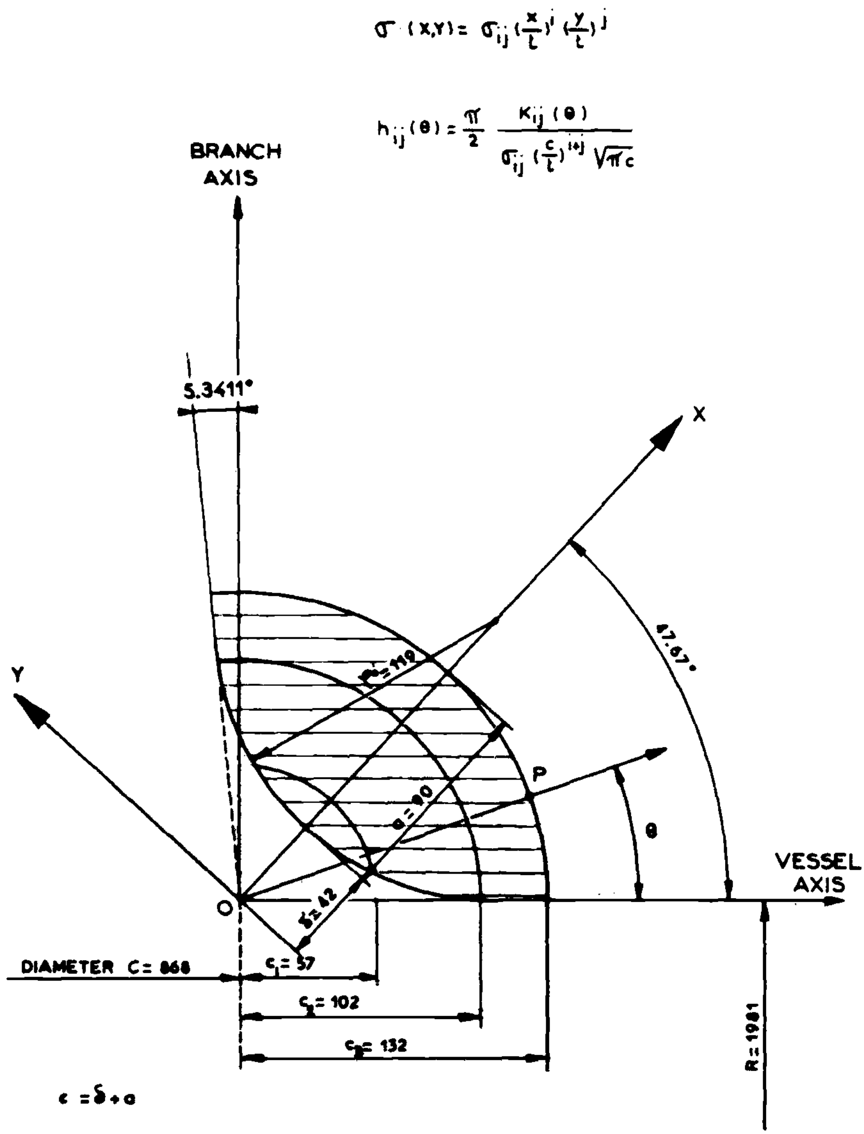

FIG. 2—*Detail of nozzle corner cracks.*

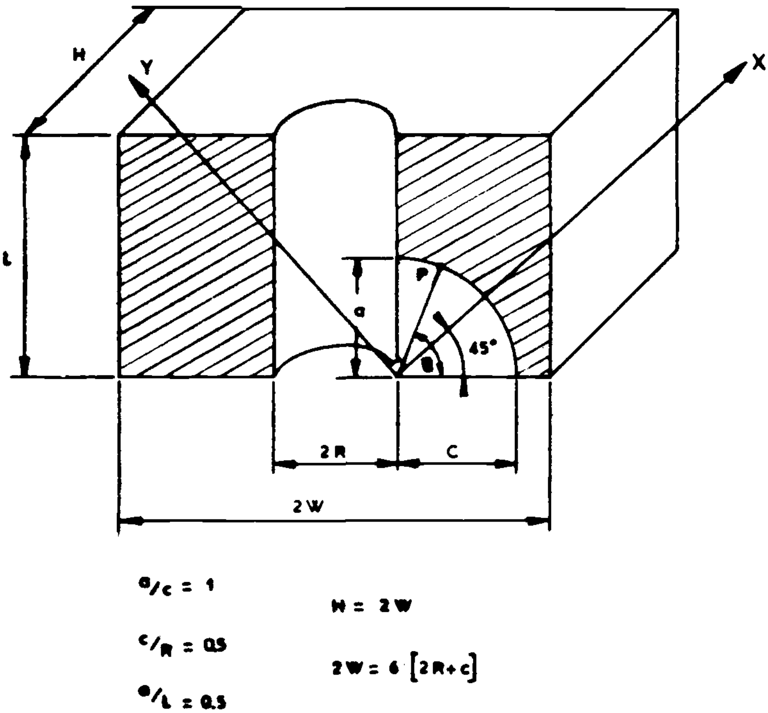

FIG. 3—*Benchmark Problem No. 2.*

exists at the corner, with a steep decrease along the bissector; on the surface the decrease is first slower in the branch than in the vessel, as far as the effect of the hole in the vessel is dominant; next, due to the reinforcement the decrease is steeper in the branch while in the vessel the decrease is limited to the stress in the wall.

Finite-Element Methods

In 1971 Rashid and Gilman [*3*] showed that the stress-intensity factor on a partly circular crack was always smaller than it would be for a crack of the same depth emanating from a hole in a plate subjected to the hoop and axial stresses resulting from pressure.

Later Hellen and Dowling [*4*] calculated the stress-intensity factors of partly circular cracks at the corner of a nozzle of a PWR subjected to a pressure with radii varying between 0.4 and 76 mm. The results were nearly constant K along the crack front, with variations less than 10 percent for radii 19 and 45 mm, slowly variable for a radius 76 mm, and increasing by 20 to 25 percent near the branch end.

Reynen [6] reported similar calculations on a boiling water reactor (BWR) for pressure and thermal hoop stresses, in a paper which deals more with the method than with the results. The results for rather deep cracks show that K increases with pressure from the vessel wall to the branch.

Schmitt et al [7] calculated stress-intensity factors for straight cracks subjected to a pressure hoop stress.

Broekhoven [5] proved for quarter circular cracks subjected to a pressure hoop stress nearly constant stress-intensity factors for medium radii, and for higher radii a minimum of the stress-intensity factor with the highest values on the branch surface.

Atluri and Katherisan used their hybrid displacement finite-element method [8] for calculating stress-intensity factors along any crack in a nozzle corner, and particularly the so-called natural shape longer along the cylinder than along the branch.

These studies do not clarify when the stress-intensity factor is nearly constant and when it increases from the vessel to the branch; quantitative comparisons are difficult since the geometries are not identical or very completely defined.

Semi-Analytical Method for Any Stress Gradient

Kobayashi et al [9-11] used the alternating method to calculate the stress-intensity factors resulting from any stress gradient approximated by a polynomial of the third degree on the crack surface.

In Refs *9* and *10* circular and elliptical cracks are studied, and compared with Broekhoven's results. In Ref *11* a simplified method for flattened cracks is proposed; the crack front is replaced by a part of a similar semi-elliptical crack in a plate, for which results had already been published. The authors justified their approximation by comparison with results obtained on semicircular cracks in a plate and in the nozzle corner; they found differences less than 10 percent. This coincidence may result from the fact that for such cracks the rigidity of a plate may be not very different from that of the nozzle considered; as these solids are actually very different, it may be thought that the calculation in a semi-infinite solid would also not have been very different. One can therefore wonder if the coincidence will still be good with slender or deeper elliptical cracks.

Bhandari et al [12] treated the problem in a quarter infinite solid, and found the highest stress-intensity factors at the branch surface. This approximation does not take into account the limited thickness of the wall, thinner than the reinforcement, and likely obliterates the decrease of the pressure hoop stress in the reinforcement.

Experimental Results by Photoelasticity

Smith et al [13] studied several flaw shapes in a PWR nozzle corner subjected to pressure. The results were that for a medium-size quarter circular crack the stress-intensity factor did not vary much along the crack front, in agreement with finite-element calculations; deeper cracks evolved toward the so-called natural shape, calculated by Atluri [*8*], deeper on the vessel surface than on the branch.

Boundary Integral Equation Method

The BIE method and the program Equations Integrales Tridimensionnelles (EITD) used have already been documented in [*2,14,15*]; Ref *2* shows how the EITD program was validated for three-dimensional crack problems.

Further validations were obtained with good agreement by McGowan and Raymund [*16*], Newman and Raju [*17*], and Atluri [*8*] for semi-elliptical cracks in cylinders. A report on the solutions of "Benchmark Problem No. 1" [*18,19*], prepared by the Society for Experimental Stress Analysis (SESA), showed agreement within ±5 percent with the results of McGowan and Raymund and those of Raju and Newman.

Before dealing with the nozzle problem, the EITD program was again tested by solving "Benchmark Problem No. 2" [*18*], a quarter circular crack at the corner of a hole in a plate (Fig. 3).

Benchmark Problem No. 2

Definition

In Ref *18*, only a uniform traction σ at infinity is considered; the stress on the crack surface is governed by the hole; an influence function is defined as

$$h_0(\theta) = \frac{\pi}{2} \frac{K_0(\theta)}{\sigma\sqrt{\pi c}} \tag{3}$$

Influence functions were also calculated for a linearly varying load

$$\sigma(x,y) = \sigma_{00} + \sigma_{10} \frac{x}{c}$$

on the crack surface, with influence functions

$$h_{ij}(\theta) = \frac{\pi}{2} \frac{K_{ij}(\theta)}{\sigma_{ij}\sqrt{\pi c}} \tag{4}$$

Results

The solid was meshed according to the same principles as for the semi-elliptical cracks [*2*], isoparametric elements with 8 nodes and 24 degrees of freedom, quarter-point crack front elements. The first results were inconsistent; the stresses on certain sections were not balanced. It was thought that this difficulty did not result from the BIE method or the elements chosen but from three imposed coordinates at one point on the boundary, what the program could not handle. For cost and time reasons, this could not be fully checked.

Because consistent though inaccurate results had been obtained with a coarse mesh with 8-node elements, 12 degrees of freedom on 4 nodes, and no quarter-point crack front elements, the calculation was continued this way with a more refined mesh: 8 crack front elements, 55 on the crack surface, and other displacement imposed conditions on the boundary.

The results are shown in Fig. 4.

Comparison with Other Solutions

The results for a uniform traction at infinity were compared with the solutions of Palusamy and Raymund [*20*], Raju and Newman [*21*], and Hechmer and Bloom [*22*] (Fig. 5). The geometries are not exactly identical (see Table 1) but the influence of the differences seems negligible.

In Fig. 5 it is difficult to distinguish this solution from those of Refs *20* and *22* except near the hole, where the differences are about 10 percent. Raju and Newman's solution is higher by about 10 percent for θ near 60 deg, and lower near the hole; this decrease is likely related to the lower singularity at the surface, which cannot be evidenced with other meshes. As a whole the results are satisfactory for engineering purposes.

For the other influence functions, the differences with Ref *20* were less than 3 percent for $\theta < 75$ deg; near the hole ($\theta = 90$ deg) they were 5 percent for h_{00} and h_{10}.

Part Circular Cracks in a Nozzle Corner

Geometry and Mesh

The nozzle is defined by Fig. 1 with crack radii $c = 57$, 102, 132 mm. The solid meshed for the deepest crack is defined by Fig. 6; for reasons of accuracy it was limited by the complete meridional plane of the vessel containing the axis of the branch. For the other cracks it was only half this solid, limited by a perpendicular plane by the axis of the branch. As the results for $c = 132$ and 102 mm were consistent with each other, it was thought that the smaller solid was sufficient.

As the difficulties met with Benchmark Problem No. 2 were no longer expected, isoparametric elements with 8 nodes, 24 degrees of freedom were used, as for the semi-elliptical cracks [*2*]; actually no difficulty was met (Fig. 7). The total number of elements and nodes is given in Table 2.

The external boundaries of the meshed solid were free; this is possible because only the singular problem of a loaded crack, with no load on the exter-

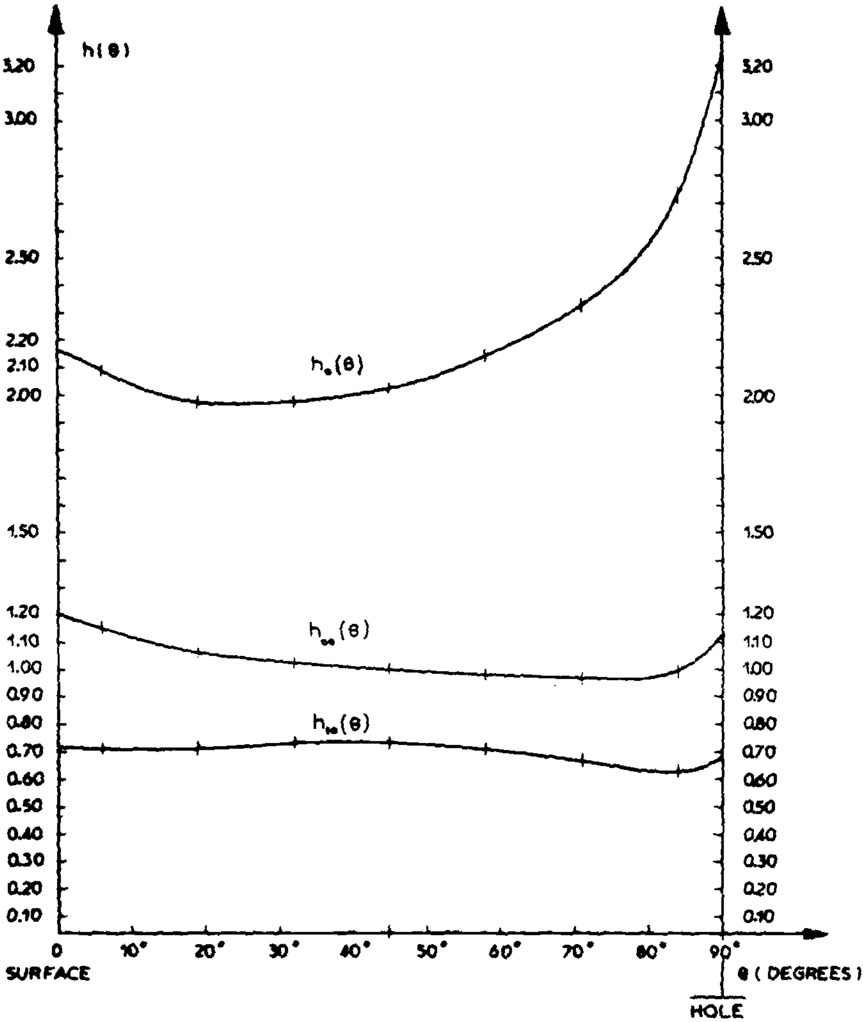

FIG. 4—*Benchmark Problem No. 2—influence functions.*

nal boundaries, is solved, with displacements and stresses negligible at such distances from the crack.

Choice of Influence Functions Necessary for a Pressure Hoop Stress

A representation was attempted of the hoop stress on the crack surface resulting from an internal pressure by a polynomial of five terms

$$\frac{\sigma_h(x,y)}{-} = \alpha_{00} + \alpha_{10}\frac{x}{t} + \alpha_{01}\frac{y}{t} + \alpha_{20}\left(\frac{x}{t}\right)^2 + \alpha_{02}\left(\frac{y}{t}\right)^2 \qquad (5)$$

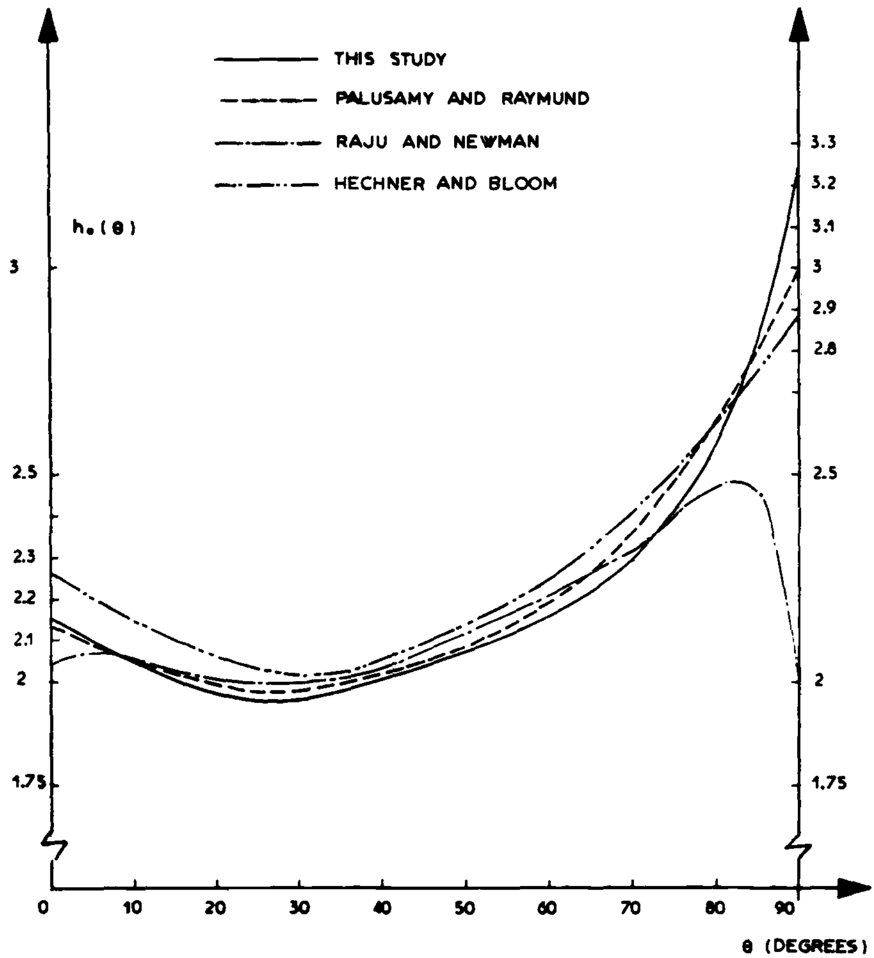

FIG. 5—*Benchmark Problem No. 2—comparison of solutions to* $h_0(\theta)$.

TABLE 1—*Results for uniform traction at infinity.*

	Benchmark No. 2 This Study Ref *20*	Refs *21* and *22*
a/c	1	1
a/t	0.5	0.2
a/R	0.5	0.4

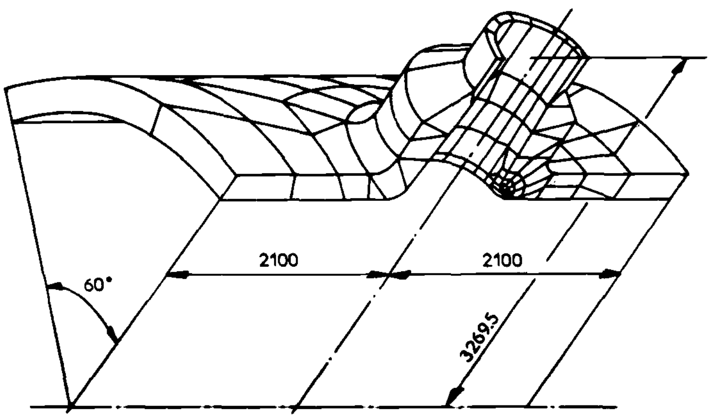

FIG. 6—*Nozzle corner crack—meshed solid.*

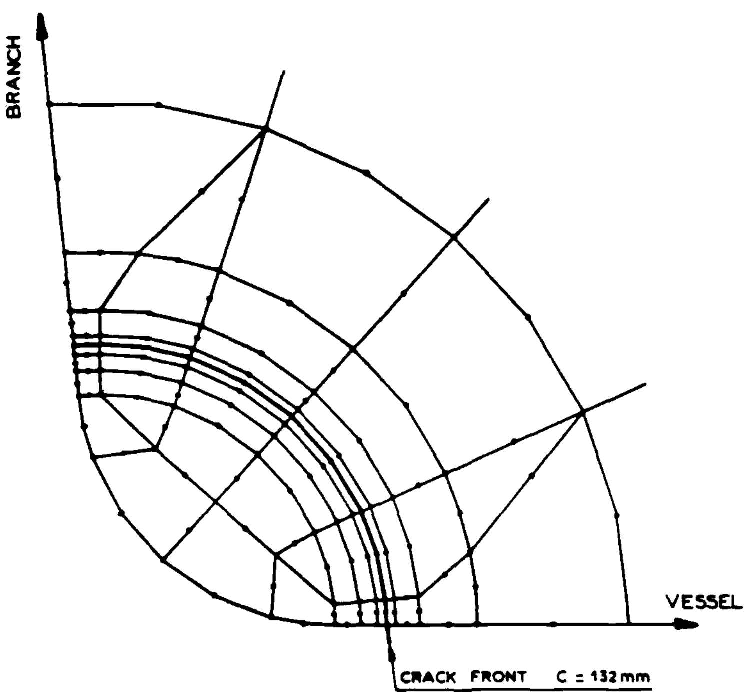

FIG. 7—*Grid in plane of crack.*

TABLE 2—*Total number of elements and nodes.*

	Crack Radii		
	57 mm	102 mm	132 mm
No. of subregions	5	5	8
Total No. of elements	220	242	398
Total No. of nodes	568	626	1013
Total No. of degrees	1704	1878	3039
Nodes in plane of crack:			
total	79	93	93
surface of crack	76	80	80
crack front	13	13	13

t, arbitrary, is chosen the distance from the origin to the external surface on Ox (Fig. 1), or 0.390 m. On the surface of the crack studied, the following nondimensional α_{ij} yield a difference less than 2 percent with the finite-element hoop stress

$$\begin{aligned} \alpha_{00} &= 27.583 \\ \alpha_{10} &= -32.331 \\ \alpha_{01} &= 1.911 \\ \alpha_{20} &= 10.708 \\ \alpha_{02} &= 10.084 \end{aligned}$$

The stress-intensity factor is

$$\frac{K(\theta)}{\frac{2}{\pi} p\sqrt{\pi c}} = \alpha_{00} h_{00}(\theta) + \alpha_{10} \frac{c}{t} h_{10}(\theta) + \alpha_{01} \frac{c}{t} h_{01}(\theta)$$

$$+ \alpha_{20} \left(\frac{c}{t}\right)^2 h_{20}(\theta) + \alpha_{02} \left(\frac{c}{t}\right)^2 h_{02}(\theta) \quad (6)$$

Due to the near symmetry, α_{01} is small. It is also known that the $h_{ij}(\theta)$ must decrease for higher $i + j$; as $(c/t)^2$ is small, the terms $h_{20}(\theta)$ and $h_{02}(\theta)$ are not significant, and the first two terms only can be kept.

Calculation of Influence Functions

Tractions

$$\sigma_{ij} = x^0 y^0, xy^0$$

were applied on the crack surface. The corresponding stress-intensity factors

$K'_{ij}(\theta)$ were calculated along the front; as with these particular stresses $\sigma_{ij}/t^{i+j} = 1$, according to Eq 2, the nondimensional influence functions are

$$h_{ij}(\phi) = \frac{\pi}{2} \frac{K'_{ij}(\phi)}{c^{i+j}\sqrt{\pi c}} \tag{7}$$

The stress-intensity factors were calculated by extrapolation of the displacements on the crack surface in planes normal to the crack front, or more precisely of

$$\sqrt{\frac{\pi}{2}} \frac{E}{2(1 - \nu)^2} \frac{\nu}{\sqrt{r}}$$

Parabolic extrapolation was kept because it was less scattered than linear extrapolation.

The computed influence functions are shown in Fig. 8.

Accuracy

It is shown in Ref *2* that the errors depend very much on the relative variation of the load in the front elements. As this variation is here zero for the uniform stress and 3 percent for the linear stress, an underestimation less than 2.5 percent can be expected, with a possible error somewhat higher on the surfaces. The results were corrected by 2.5 percent for taking this error into account.

Discussion of Results

Symmetry of Influence Functions

The curves of the influence functions are nearly perfectly symmetrical with respect to the axis *Ox;* the functions differ very little on the walls of the vessel and the branch; in Fig. 1 it is clear that the cracks considered are only little affected by the dissymmetry of the vessel and the branch. But this symmetry would not hold for deeper cracks.

The curves for the shallow crack (c = 57 mm) exhibit a rather rapid decrease near the surfaces, which does not exist for the other cracks. The same functions were calculated for a penny-shaped crack in an infinite solid loaded only on an area corresponding to the crack in the nozzle (Fig. 9); the results were evidently smaller than for the nozzle crack; for the small crack depth the functions also exhibited rapid decreases.

Comparison with Benchmark Problem No. 2

In Fig. 10, Curves $h_{00}(\theta)$ and $h_{10}(\theta)$ have been drawn for the benchmark problem and the two medium cracks in the nozzle c = 132 and 102 mm. It appears that the difference is always smaller than 10 percent except for $h_{00}(\theta)$ near the surface. The solution to the Benchmark Problem is not a bad approximation for the influence functions of these medium cracks; this might not be exact for deeper cracks; if these functions are used, it should be with the stress distribution in a nozzle, and the result would likely be different from $h_0(\theta)$ for the benchmark problem, even in a qualitative way.

Calculation of Stress-Intensity Factors Resulting from Pressure

Calculation with a Two-Term Polynomial

Equation 6 reduced to two terms is

$$\frac{K(\theta)}{\frac{2}{\pi} p\sqrt{\pi c}} = \alpha'_{00} h_{00}(\theta) + \alpha'_{10} \frac{c}{t} h_{10}(\theta) \tag{8}$$

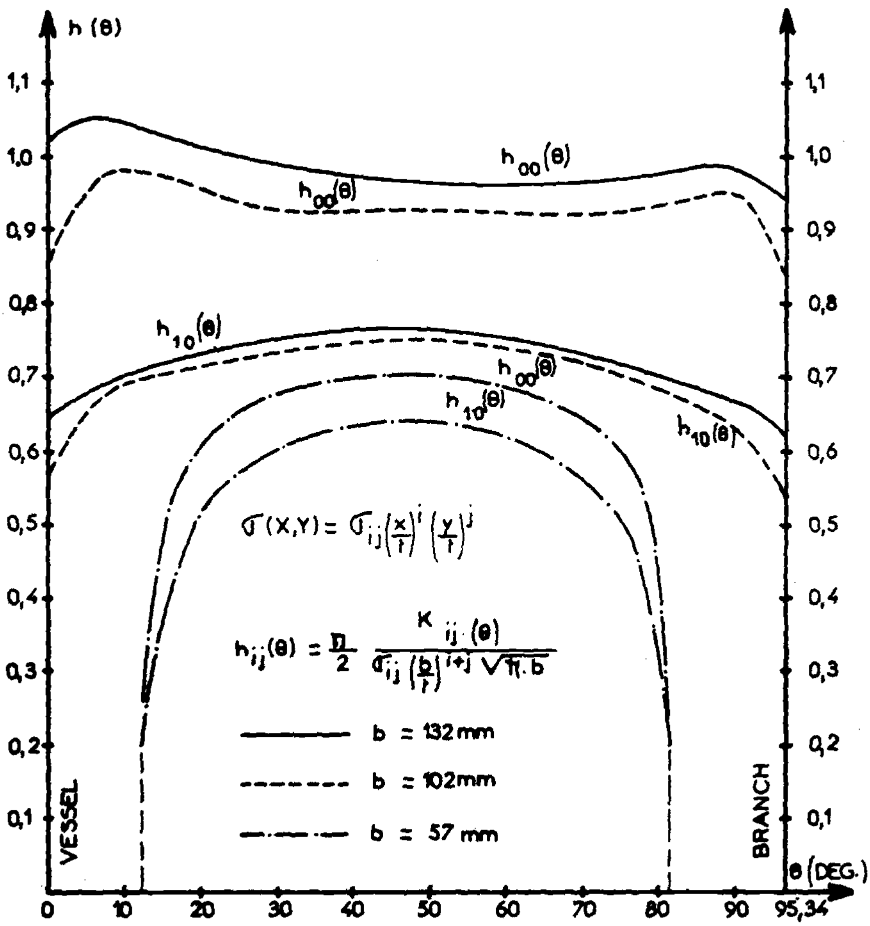

FIG. 8—*Nozzle corner cracks—influence functions.*

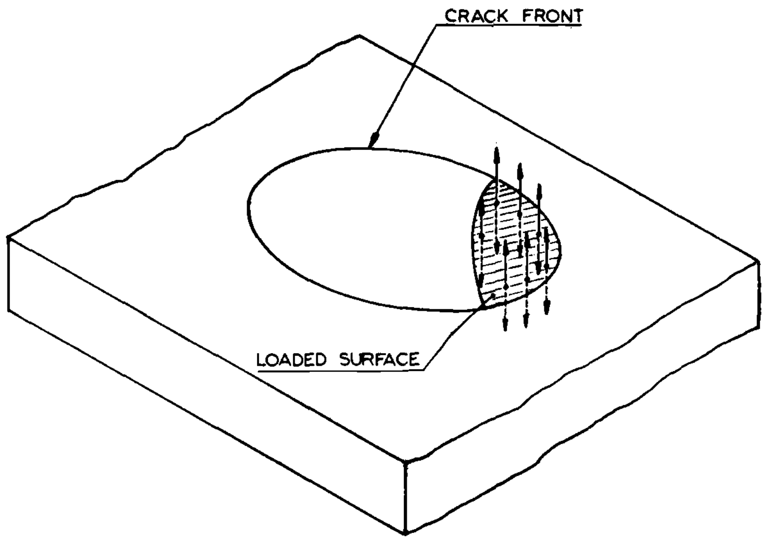

FIG. 9—*Partially loaded circular crack.*

These nondimensional stress intensity factors are shown for the three calculated cracks in Fig. 11.

Discussion

For the shallow crack the stress-intensity factors are low with a quick decrease near the surface; this results very likely from the angle smaller than 90 deg between the front and the boundary (Fig. 2).

For the two other cracks, the nondimensional stress-intensity factors are practically the same, since the difference is less than 2 percent. The differences on the surfaces of the vessel and the branch are of no practical importance, but may be significant because the smaller crack (c = 102 mm) is just at the limit of the corner and the larger (c = 132 mm) reaches the surfaces in the straight profiles, with angles of 90 deg.

These results confirm the practically constant stress-intensity factors evidenced by previous researchers for certain crack depths. They are rather far from curves similar to $h_0(\theta)$ for the Benchmark Problem which might be obtained with a hole in a plate subjected to the hoop and axial stress in the cylinder.

Deeper cracks were not studied. For such cracks the thickness of the reinforcement, more than twice the thickness of the wall, plays an important role.

If the reinforcement was not substantially thicker than the wall, deep cracks would likely evolve to a situation similar to the Benchmark Problem in pure tension, corrected for the axial stress, with a maximum stress-intensity factor

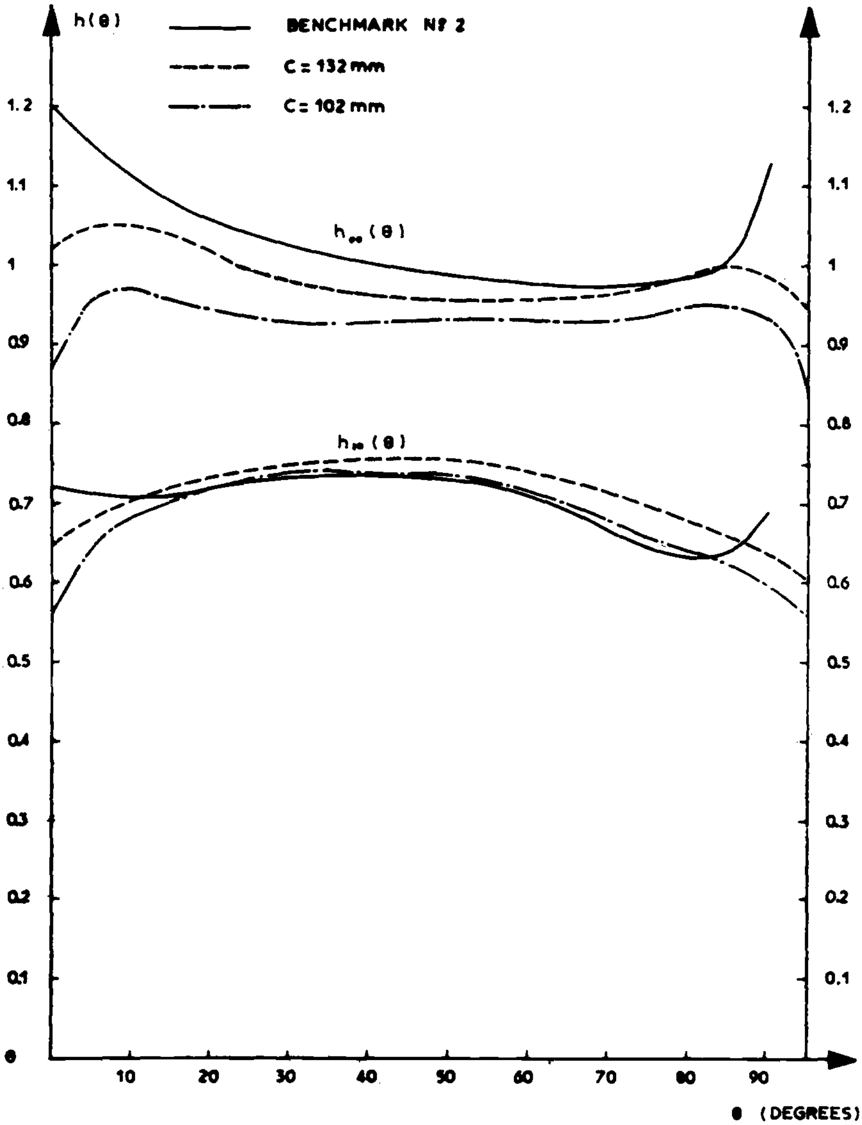

FIG. 10—*Comparison of influence functions for Benchmark Problem No. 2 and a nozzle corner crack.*

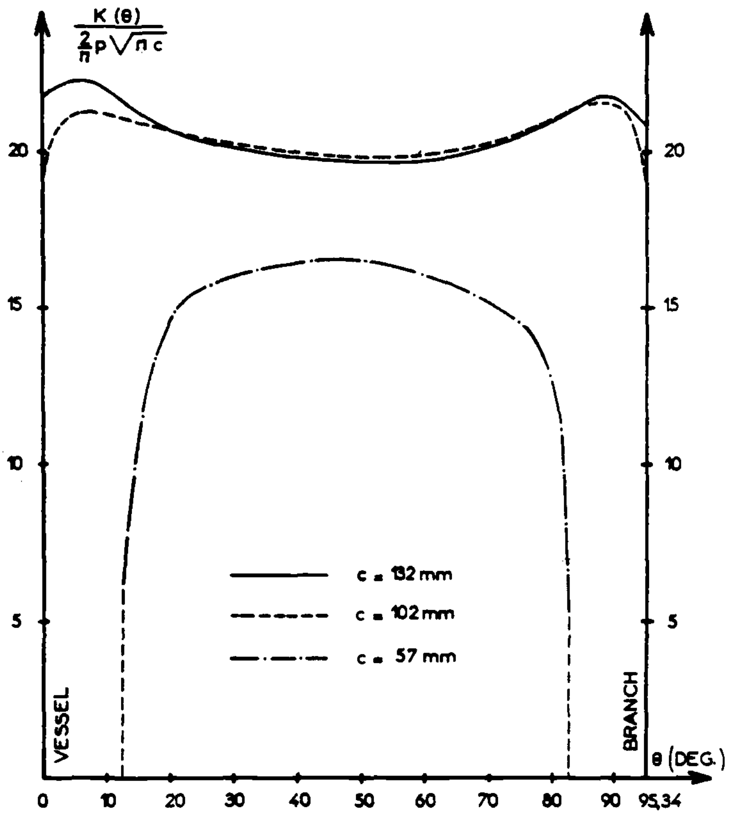

FIG. 11—*Nozzle corner cracks—pressure loading—nondimensional stress-intensity factors.*

at the surface of the branch. But due to the higher thickness of the reinforcement the hoop stress will not decrease so much in the wall direction as in the branch; this would likely result in higher stress-intensity factors on the vessel, and an extension might occur in this direction. Previous studies on slender semi-elliptical cracks, with axes ratio up to 10 to 1 [*23*], show that when such a crack extends along the surface with a constant depth, the stress-intensity factor at the surface decreases. This is consistent with the natural crack shapes in nozzle corners observed by Smith [*13*] and calculated by Atluri [*8*], and might result in an arrest of the crack.

Summary and Conclusions

The BIE method was used for computing polynomial influence functions for partly circular cracks in a nozzle corner, with an accuracy about ±5 percent or better.

The results applied to pressure hoop stress were qualitatively consistent with other studies. A quantitative comparison is difficult because the sizes of the crack are not the same and also the geometries are not completely defined.

Shallow cracks are sensitive to the radius of the corner. Medium cracks, up to about the quarter of the thickness of the nozzle along the bissector, are little sensitive to the vessel wall and the branch; they exhibit small variations of the stress-intensity factor; a two-terms approximation is practically sufficient.

With cracks deeper than those studied and the conventional reinforcements, it does not seem that the evolution is toward a benchmark-like situation, even corrected for the longitudinal stress. It can be expected, as experimentally shown by photoelastic experimentation, that the highest stress-intensity factor will be on the vessel surface, and that an extension in this direction would result in a decreasing stress-intensity factor, and possibly in an arrest of the crack.

References

[1] Labbens, R., Pellissier-Tanon, A., and Héliot, J. in *Mechanics of Cracks Growth, ASTM STP 590,* American Society for Testing and Materials, 1976, pp. 368-384.

[2] Héliot, J., Labbens, R., and Pellissier-Tanon, A. in *Fracture Mechanics, ASTM STP 677,* American Society for Testing and Materials, 1979, pp. 441-464.

[3] Rashid, Y. R. and Gilman, J. D., "Three Dimensional Analysis of Reactor Pressure Vessel Nozzles," First International Conference on Structural Mechanics in Reactor Technology, 1971, Paper G 2/6.

[4] Hellen, T. K. and Dowling, A. R., *International Journal of Pressure Vessels and Piping,* 1975, pp. 57-74.

[5] Broekhoven, M. J. G. in *Proceedings,* Third International Conference on Pressure Vessel Technology, Tokyo, 1977, pp. 839, 952.

[6] Reynen, J., "Analysis of Cracked Pressure Vessel Nozzles," Third Conference on Structural Mechanics in Reactor Technology, London, 1975.

[7] Schmitt, W., Bartholomé, G., Gröstadt, A., and Miksch, M., *International Journal of Fracture,* 1976, pp. 381-390.

[8] Atluri, S. N. and Kathiresan, K., "Influence of Flaw Shapes on Stress Intensity Factors for Pressure Vessel Surface Flaws and Nozzle Corner Cracks," American Society of Mechanical Engineers, Paper 79-PVP-65, San Francisco, 1979.

[9] Kobayashi, A. S. and Enetanya, A. N. in *Mechanics of Cracks Growth, ASTM STP 590,* American Society for Testing and Materials, 1976, pp. 477-495.

[10] Kobayashi, A. S. et al, "Stress Intensity Factors of Corner Cracks in Two Nozzle-Cylinder Intersections," Fourth International Conference on Structural Mechanics in Reactor Technology, San Francisco, 1977.

[11] Kobayashi, A. S., Emery, A. F., Love, W. J., and Antipas, A., "A Procedure for Estimating the Stress Intensity Factor of a Flattened Surface Crack at a Nozzle Corner," American Society of Mechanical Engineers, Paper 78-PVP-95, Montreal, 1978.

[12] Bhandari, S. K., Barrachin, B., and Picou, J. L., "Part Circular Cracks at Various Openings under Complex Loading Conditions," ASME Pressure Vessel and Piping Conference, American Society of Mechanical Engineers, Paper 79-PVP-61, San Francisco, 1979.

[13] Smith, C. W., Jolles, M., and Peters, W. H., "Stress Intensity for Nozzle Cracks in Reactor Vessels," Virginia Polytechnic Institute and State University, Blackburg, Va., Report VPI-E-76-25.

[14] Cruse, T. A. in *The Surface Crack,* American Society of Mechanical Engineers, 1972, pp. 153-170.

[15] Lachat, J. C. and Watson, J. O., Symposium on Boundary Integral Equation Method, American Society of Mechanical Engineers, 1975.

[16] McGowan, J. J. and Raymund, M. in *Fracture Mechanics, ASTM STP 677*, American Society for Testing and Materials, 1979, pp. 365–380.
[17] Newman, J. C. and Raju, I. S., National Aeronautics and Space Administration Technical Memorandum 80073, Langley Research Center, Hampton, Va., 1979.
[18] Hulbert, L. E., *International Journal of Fracture*, Feb. 1977, pp. 87–91.
[19] McGowan, J. J., "A Critical Evaluation of Numerical Solution to the 'Benchmark' Surface Flaw Problem," Society for Experimental Stress Analysis, 1980.
[20] Palusamy, S. S., Raymund, M., and Petsche, J. F., "Stress Intensity Factors for a Corner Crack at the Edge of Hole in a Plate," Westinghouse Report WCAP 9597.
[21] Raju, I. S. and Newman, J. C., "Stress Intensity Factors for Corner Cracks at the Edge of a Hole," National Aeronautics and Space Administration Technical Memorandum 78728, Langley Research Center, Hampton, Va.
[22] Hechmer, J. L. and Bloom, J. M., *International Journal of Fracture*, 1977, pp. 732–735.
[23] Héliot, J., Labbens, R., and Pellissier-Tanon, A., Pressure Vessel and Piping Conference, American Society of Mechanical Engineers, Paper 80-C2/PVP 119, 1980.

C. W. Smith,[1] *W. H. Peters,*[1] *G. C. Kirby,*[1] *and A. Andonian*[2]

Stress-Intensity Distributions for Natural Flaw Shapes Approximating 'Benchmark' Geometries

REFERENCE: Smith, C. W., Peters, W. H., Kirby, G. C., and Andonian, A., **"Stress-Intensity Distributions for Natural Flaw Shapes Approximately 'Benchmark' Geometries,"** *Fracture Mechanics: Thirteenth Conference, ASTM STP 743,* Richard Roberts, Ed., American Society for Testing and Materials, 1981, pp. 422-437.

ABSTRACT: Because of its importance and frequency of occurrence, considerable effort has been devoted to the modeling of subcritical surface crack growth in recent years. Due to the geometrical complexities involved, available solutions are generally constrained to elastic numerical models implying self-similar crack growth. By selecting specific geometries (known as 'benchmark' geometries) and solving for stress-intensity factor distributions, several of these numerical models have recently exhibited reasonable agreement by assuming semi-elliptic crack shapes (see Ref *6*). Over the past decade, the first author and his colleagues have evolved an experimental technique which couples the field equations of linear elastic fracture mechanics with the frozen stress photoelastic method for generating natural crack shapes and their corresponding stress-intensity distributions where neither are known *a priori.* The present paper focuses upon the application of this technique to two surface crack geometries approximating benchmark geometries and comparing with results from the recent literature in order to assess the validity of the semi-elliptic crack shape assumption for the surface crack in numerical models and to quantify any observed deviations. Results show that shallow crack shapes ($a/2c \approx 0.30$ $a/T \approx 0.30$) are accurately described by the semi-ellipse assumption, and the experimental stress-intensity distributions seem to be predicted with reasonable accuracy in regions of highest values. The deeper cracks, however ($a/2c \approx 0.30$ $a/T \approx 0.75$), exhibit a deviation in shape from a quarter-ellipse in the form of bulging near the points of intersection of the flaw border with the plate front surface, and the accompanying maximum stress intensities are some 25 percent higher than the values predicted in Ref *6* using semi-elliptic crack models with the same aspect ratio and a/T.

KEY WORDS: frozen stress analysis, stress-intensity distributions, surface flaws, photoelasticity

[1] Professor, assistant professor, and graduate research assistant, respectively, Department of Engineering Science and Mechanics, Virginia Polytechnic Institute and State University, Blacksburg, Va. 24061.

[2] Assistant professor, Department of Materials Engineering, University of Chicago at Chicago Circle, Chicago, Ill. 60680.

Since the growth of surface cracks under fatigue loading is generally recognized as a primary cause of service failures, it is not surprising to find that a substantial fraction of the fracture mechanics literature has been devoted to the subject. Beginning with Irwin's classic paper in 1962 [*1*][3] characterizing the shallow, semi-elliptic crack, many investigations, both analytical and experimental, have been conducted. Recently, the surface crack has been the subject of two symposia [*2,3*] and perusal of the *Proceedings* of the Eleventh National Fracture Symposium [*4*] will show that nearly two thirds of those papers dealt with fatigue crack growth.

Although the surface crack in a large body is generally conceded to be well characterized both as to shape (semi-elliptic) and stress-intensity factor (SIF) distribution, this characterization becomes questionable when the crack penetrates a significant portion of the thickness of a finite plate. Most such problems remain intractable to closed-form solution even in the elastic sense due to geometric complexity and lack of knowledge of the proper flaw shape, which is usually needed as input data for a numerical analysis of the problem. Nevertheless, continued improvements are being made in both the hardware and software needed in order to render three-dimensional (3D) cracked-body problems tractable. Despite these improvements, differences still exist between numerical models in this problem area.

In 1976, a meeting of active researchers in 3D crack problems was convened at the Battelle-Columbus Laboratories, and a set of 'benchmark' problems [*5*] was formulated with fixed geometries to be solved by various analysts using various approximate methods. Such solutions have recently been collected by McGowan and have been synthesized into a "state-of-the-art" paper [*6*]. One of the benchmark problems included in McGowan's work involves both shallow and deep semi-elliptic surface cracks under Mode I loading.

Beginning a decade ago, the first author and his colleagues undertook an effort to develop an experimental technique which would be capable of providing independent estimates of SIF distributions in 3D cracked body problems for use in providing computer code verification for the numerical models. The original method for analyzing Mode I problems, summarized in Ref *7*, consists of a marriage between the "frozen stress" photoelastic method and the equations of linear elastic fracture mechanics (LEFM). The method has since been simplified [*8*] and extended to cover all three local modes of deformation [*9*]. It has been successfully applied to a number of surface flaw problems to date [*10–21*].

Quite recently, it has been observed [*22,23*] that, if natural starter cracks are grown in photoelastic models under monotonic load above critical temperature under classical small-scale yield conditions, the resulting flaw shapes will be identical to those produced by fatigue crack extension in

[3] The italic numbers in brackets refer to the list of references appended to this paper.

geometrically similar metal models. Thus the frozen stress method applied to cracked bodies possesses the potential for obtaining both crack shapes and SIF distributions where neither is known *a priori.*

In the authors' experience, the simple geometric crack shapes and self-similar flaw growth implied by most numerical models are valid only for a limited range of crack growth in 3D cracked-body problems. In the Mode I surface crack problem, for example, a typical crack growth pattern is pictured in Fig. 1. This figure [*24*] shows the change in crack shape as it starts from a part circular slot and moves through an aluminum plate. It is clear that, as the flaw passes middepth, its shape varies significantly from that of a semi-ellipse. This implies an accompanying change in the SIF distribution from that predicted for a semi-elliptic crack shape of the same semi-axes.

The present paper deals with the application of the "frozen stress" method to both shallow and deep surface cracks under Mode I loading using geometries approaching the 'benchmark' geometries and comparing results with analytical results in order to assess the influence of the differences between idealized and real crack behavior. Before describing the results, a brief description of the frozen stress method for estimating SIF distributions is included.

Frozen Stress Method

The details of the frozen stress method have been described elsewhere [*8,25*]. Its application to the Mode I problem is briefly restated here for the convenience of the reader.

For the case of Mode I loading, one begins with equations of the form

$$\sigma_{ij} = \frac{K_\mathrm{I}}{r^{1/2}} f_{ij}(\theta) + \sigma_{ij}{}^0(r, \theta) \qquad (i, j = n, z) \tag{1}$$

for the stresses in a plane mutually orthogonal to the crack surface and the crack border referred to a set of local rectangular Cartesian coordinates as pictured in Fig. 2, where the terms containing K_I, the SIF, are identical to Irwin's equations for the plane case and $\sigma_{ij}{}^0$ represent the contribution of

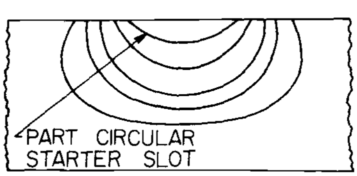

FIG. 1—*Fatigue crack shapes in an aluminum plate [24].*

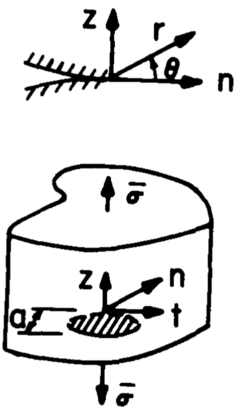

FIG. 2—*Problem geometry and notation.*

the regular stresses to the stress field in the measurement zone. The σ_{ij}^0 are normally taken to be constant for a given point along the crack border, but may vary from point to point. Observing that stress fringes tend to spread approximately normal to the crack surface (Fig. 3), Eqs 1 are evaluated along $\theta = \pi/2$ (Fig. 2) and

$$\tau_{max} = \tfrac{1}{2}[(\sigma_{nn} - \sigma_{zz})^2 + 4\sigma_{nz}^2]^{1/2} \tag{2}$$

which, when truncated to the same order as Eq 1, leads to the two parameter equation

$$\tau_{max} = \frac{A}{r^{1/2}} + B \text{ where } \begin{array}{l} A = K_I/\sqrt{8\pi} \\ B = f(\sigma_{ij}^0) \end{array} \tag{3}$$

which can be rearranged into the normalized form

$$\frac{K_{AP}}{q(\pi a)^{1/2}} = \frac{K_I}{q(\pi a)^{1/2}} + \frac{f(\sigma_{ij}^0)(8)^{1/2}}{q}\left(\frac{r}{a}\right)^{1/2} \tag{4}$$

where

$$K_{AP} = \tau_{max}(8\pi r)^{1/2}$$

and, from the Stress-Optic Law,

$\tau_{max} = Nf/2t'$
N = stress fringe order,
f = material fringe value,
t' = slice thickness in t-direction,
q = remote loading parameter (such as uniform stress, pressure), and
a = characteristic crack depth.

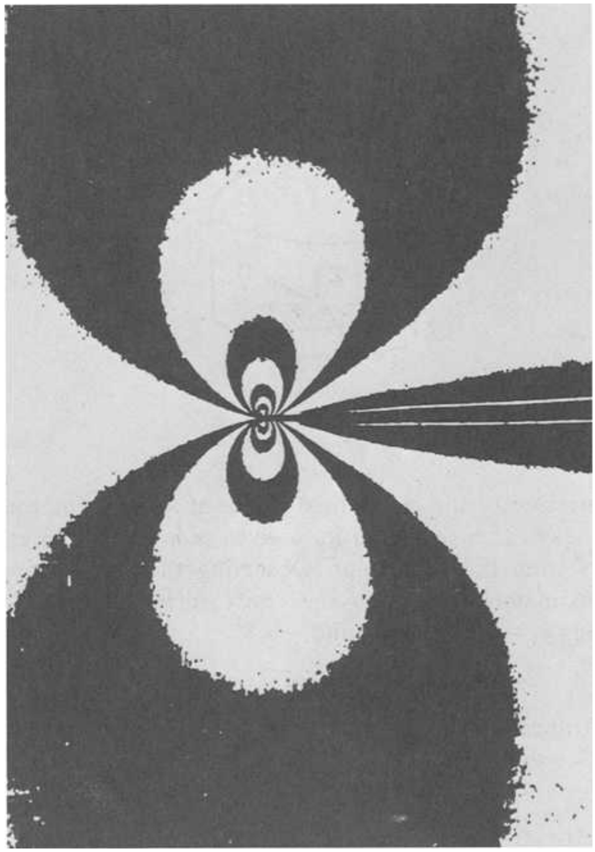

FIG. 3—*Spreading of Mode I fringes away from crack plane.*

Equation (4) prescribes that, within the zone dominated by Eqs 1 with σ_{ij}^0 as described in the foregoing, a linear relation exists between the normalized apparent SIF and the square root of the normalized distance from the crack tip. Thus, one need only locate the linear zone in a set of photoelastic data and extrapolate across a very-near-field nonlinear zone to the crack tip in order to obtain the SIF. An example of this approach using data from one of the tests described in the sequel is given in Fig. 4.

By following similar arguments, but not specifying $\theta = \pi/2$, equations for the mixed-mode case can also be developed [*9,26*].

In applying the method, starter cracks are inserted at desired locations by striking a sharp blade held normal to the specimen surface, causing a crack to propagate dynamically into the specimen normal to the specimen surface, after which the crack arrests. The cracked model is then placed in an oven in a loading device, heated to critical temperature, and then loaded

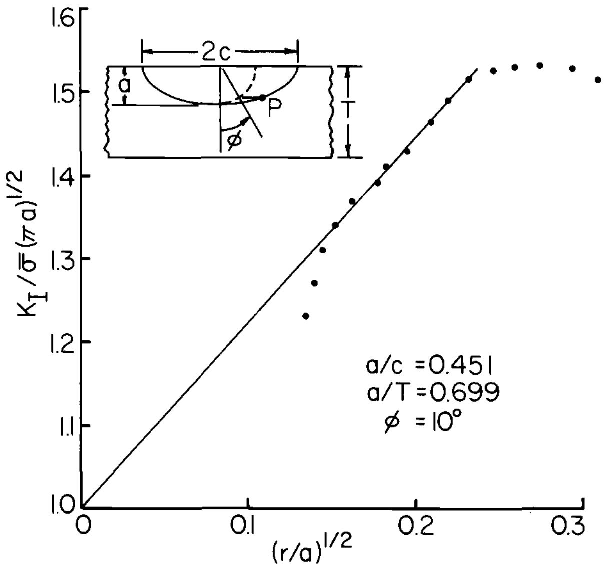

FIG. 4—*Typical set of data from a specimen taken mutually orthogonal to crack surface and crack border.*

monotonically until the crack begins to grow. The crack will take the shape dictated by the loads and geometry, and when it reaches the desired size (several times larger than the initial crack), loads are reduced, terminating flaw growth. Upon cooling under load, the frozen cracked model containing crack-tip fringe and deformation fields is obtained. All slices for analysis are taken parallel to the nz-plane (Fig. 2), coated with matching index fluid, and analyzed in a crossed circular polariscope with white light, using the Tardy Method and reading tint of passage at $\times 10$ magnification.

Experimental Results

A series of nine frozen stress photoelastic tests was run in an effort to produce cracked-body geometries similar to the two benchmark geometries for the surface crack problem. Both model and benchmark geometries together with the notation employed herein are given in Table 1.

In order to produce the geometries shown in Table 1, it was necessary to flex the plates above critical temperature. However, once the desired crack shapes were reached, the bending was removed and only uniaxial tension was used in order to develop the frozen stress pattern. This is permissible since stress freezing materials respond in a linear elastic fashion above critical temperature.

All of the shallow cracks (Models 1 through 5) exhibited a perfect semi-elliptic shape. Figure 5 shows how the SIF distribution is altered as the

TABLE 1—*Benchmark geometries, loads, and dimensions of test models.*

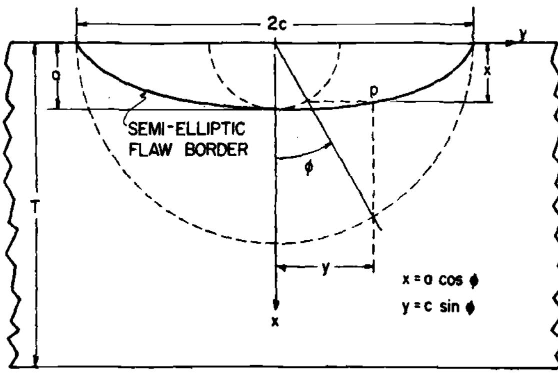

W = plate width

Shallow Flaws

	$\bar{\sigma}$	a	c	a/c	a/T	2c/W
Benchmark Geom.				0.500	0.250	≤0.20
Model 1	122.5	3.20	3.52	0.910	0.252	.0894
" 2	135.0	5.16	8.03	0.644	0.403	.2040
" 3	110.0	4.12	6.92	0.588	0.297	.1560
" 4	122.2	4.04	6.21	0.648	0.304	.1485
" 5	139.7	3.68	5.60	0.658	0.288	.1450
Avg. of 3,4 & 5		3.94	6.24	0.630	0.296	.1498
			Deep Flaws			
Benchmark Geom.				0.500	0.750	≤0.20
Model 6	92.7	8.66	22.60	0.382	0.675	0.314
" 7	42.0	11.85	32.80	0.360	0.916	0.382
" 8	82.9	9.02	20.00	0.451	0.699	0.229
" 9	93.2	10.28	21.60	0.474	0.794	0.282
Avg. of 8 & 9		9.64	20.80	0.463	0.746	0.255

crack grows deeper and changes its aspect ratio while maintaining a semi-elliptic shape. By comparing the crack fronts in Fig. 5 we see that, in changing its aspect ratio, the crack grows more along the surface than through the depth and this growth results in a lowering of the SIF along the surface. This behavior has been observed many times by the authors. All of the deep cracks exhibited a deviation from the semi-elliptic shape (Fig. 6) similar to that of the deep crack in Fig. 1. SIF values are found in Table 2. Figure 7 shows how the SIF distribution varies for deep cracks of the same "aspect ratio" as semi-elliptic cracks. By comparing Figs. 6 and 7, we see that a severe local bulge, Test 6, produces a sharp drop in the normalized SIF in the bulge region. However, when the bulge becomes more evenly distributed along the crack border, then the SIF gradient is reduced.

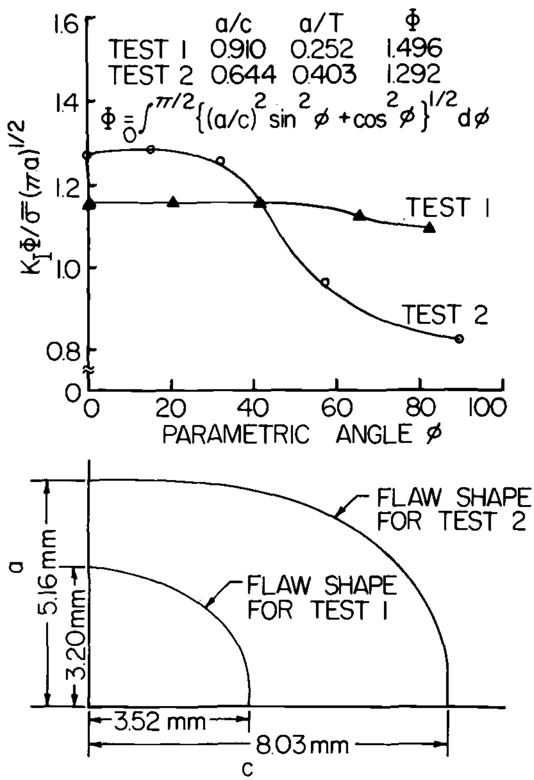

FIG. 5—*Variation in SIF distribution in semi-elliptic shallow cracks of varying depth and aspect ratio.*

From the shallow crack tests, Models 3 through 5 were selected for comparison with analytical results on the shallow-benchmark problem and Models 8 and 9 were selected for comparison with the deep-crack benchmark geometries. As seen in Table 1, there are still some discrepancies between the benchmark and average model test geometries. An attempt was made to correct for these discrepancies using the analysis of Newman and Raju [*27*]. The procedure is briefly described in the Appendix. After correcting the experimental results to the benchmark geometries, they are compared with the analytical results for the shallow-crack benchmark geometry in Fig. 8 and with the deep-crack benchmark geometry in Fig. 9. These analytical models are briefly described in Ref *6*. They consist of finite element, Schwarz Alternating, and boundary-integral methods of approach to the benchmark problems with assessments for accuracy made for each. Included is a ±5 percent scatter band expected in the experimental results and a ±4 percent variation between the several numerical models [*6*].

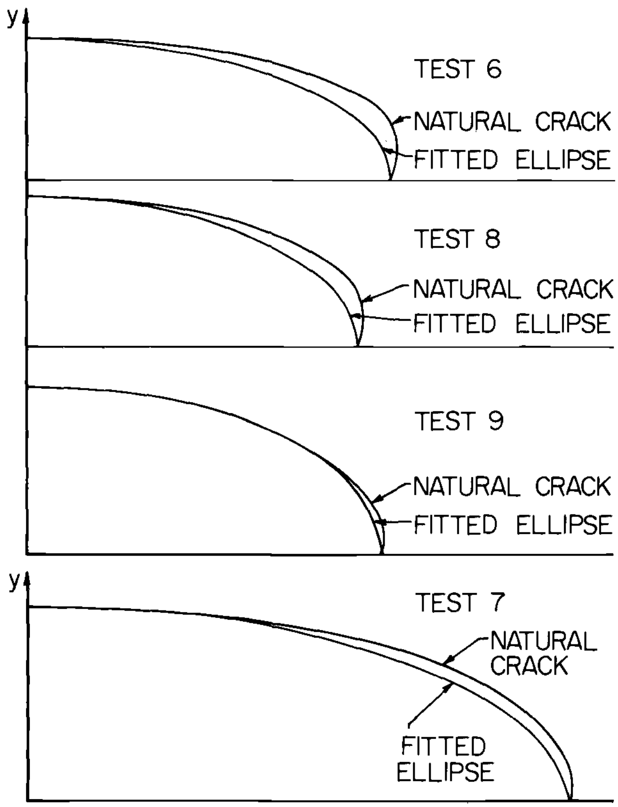

FIG. 6—*Variation of deep cracks from semi-elliptic shape.*

Discussion of Results

As shown by Fig. 5, significant changes in the SIF distributions occur in semi-elliptic, shallow surface cracks due to changes in crack size and aspect ratio. Moreover, in deep cracks of similar nonsemi-elliptic shape, significant changes in SIF distributions result from changes in crack size and local bulging. In the present study, we are focusing upon the effect of deviations of the deep cracks from semi-elliptic shapes.

From Fig. 8 we see reasonable agreement and overlapping between the analytical and experimental results for the shallow, semi-elliptic cracks in the region of highest SIF, and this agreement was expected. However, in the regions of lower SIF close to the plate front surface, the experimental results diverge from the analytical solutions and show significantly smaller SIF values than predicted analytically. In prior studies, the authors have found that the experimental method tends to produce SIF values near mid-

TABLE 2—*Stress intensity factors.*

Model No.	ϕ	$K_I\Phi/\bar{\sigma}(\pi a)^{1/2}$
1	0.0	1.160
	21.1	1.160
	42.3	1.160
	66.1	1.123
	82.3	1.093
2	0.0	1.273
	14.9	1.286
	32.8	1.260
	59.3	0.961
	90	0.819
Avg 3, 4, 5	0	1.056
	15	1.036
	30	0.982
	45	0.890
	60	0.768
	75	0.637
	90	...
6	0	0.544
	9.2	1.416
	20.9	1.586
	33.5	1.654
	55.0	1.626
	90.0	1.643
7	0	1.851
	8.7	1.851
	19.8	1.795
	41.7	1.683[a]
	90	1.279
Avg 8, 9	0	1.622
	15	1.630
	30	1.566
	45	1.442
	60	1.285
	75	1.069
	83.5	0.828

[a] Reading from one side only.
ϕ = parametric angle from mid-flaw position (Fig. 7).
Φ = as defined in Fig. 7.

crack which are some 5 percent higher than theory due to the fact that Poisson's ratio of the stress freezing material is ≈ 0.5 above critical temperature. This suggests that the experimental curve of Fig. 8 may still lie 10 or 15 percent below its proper location at the midcrack ($\phi = 0$) location.

In searching for an explanation of these discrepancies, the authors took measurements on remaining parts of the model and found that a small

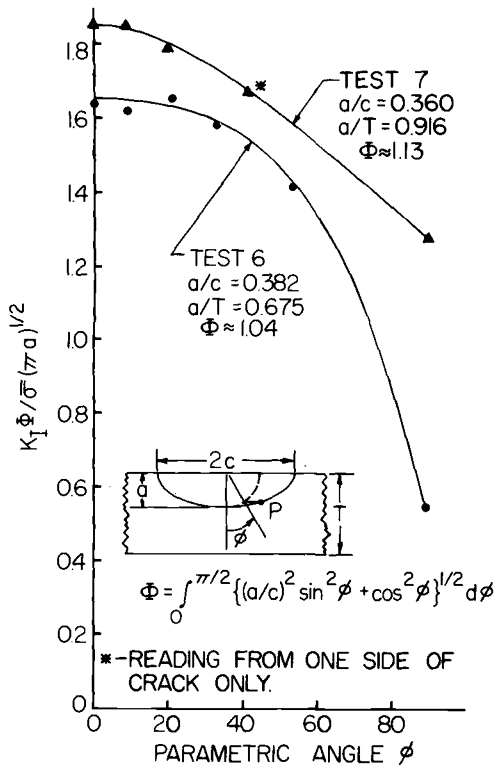

FIG. 7—*Variation in SIF distribution in deep cracks with same 'aspect ratio.*

amount of out-of-plane curvature existed which implied the presence of some bending in the plates which produced, upon loading, an additional compression on the side of the plate where the flaw was located and tension on the opposite side. From these measurements, a nominal bending stress was estimated and, using the results of Ref *27* for the bending case for semi-elliptic flaws, normalized SIF values due to bending were qualitatively estimated. These estimates indicated that, if the bending were not present, the experimental curve in Fig. 8 would shift upwards by about 15 percent with slight counterclockwise rotation about $\phi = 0$ so as to agree with the theoretical results to within the indicated scatter bands. A similar shift would be achieved by applying the correction to the results in Fig. 9. However, the experimental value would still be well above the theoretical result using semi-elliptic flaws (from 20 to 40 percent at maximum flaw depth) and this is the result of technological importance which we wish to focus upon here. Finally, due to uncertainty of the quantitative accuracy of the bending calculations, their effect is not included in Figs. 8 or 9.

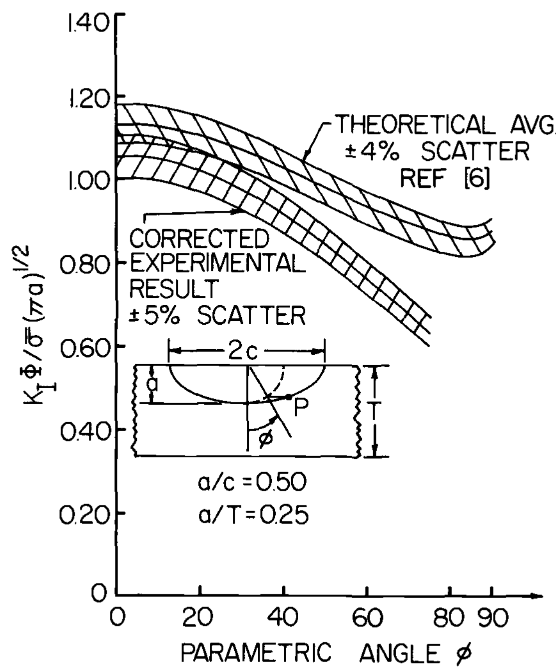

FIG. 8—*Comparison of average of experimental results with average of numerical models [6] for shallow-crack benchmark geometry.*

Summary

A series of "frozen stress" photoelastic experiments was carried out on model geometries approaching the geometries of "Benchmark Problem No. 1," a plate containing a surface crack loaded in remote simple tension. Natural shallow cracks were exact semi-ellipses and reasonable engineering correlation was observed between the average of several analytical results and the average of several model test replications in regions of maximum SIF values after correcting for deviation of test model geometries from the benchmark geometry. Natural deep cracks deviated from the semi-elliptic crack shape and SIF levels were some 25 percent higher in the region of maximum SIF values than predicted by the numerical models using semi-elliptic crack shapes.

There are several factors which might influence the experimental results presented in addition to random experimental scatter:

1. the fact that Poisson's ratio for the photoelastic material was greater than the value used in the numerical models (that is, 0.5 > 0.3),

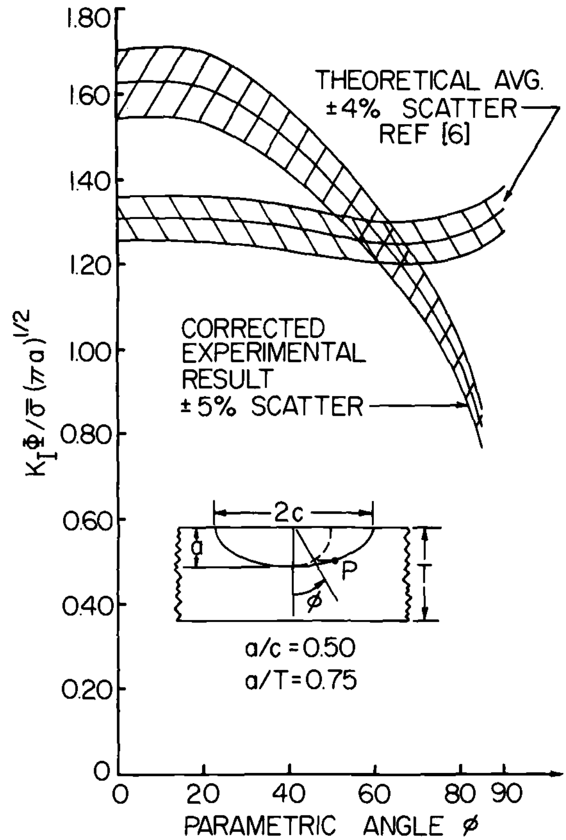

FIG. 9—*Comparison of average of experimental results with average of numerical models [6] for deep-crack benchmark geometry.*

2. the accuracy of the corrections for geometric deviations of the test models from the benchmark geometries used in the analyses,
3. the use of bending loads to produce the natural crack shapes, and
4. the presence of warpage in the plates when loaded in tension.

In prior work, the authors have found the first effect to be less than the order of experimental scatter. The second effect should be small, since the corrections were applied only to geometries closely approximating the benchmark geometries. The influence of the third effect is more difficult to judge. It is possible that the bulging produced by combined tension and bending could produce a flaw shape which deviates more from a semi-ellipse than one produced by only simple remote tension. Although bending loads were also used to grow the perfectly elliptical shallow flaws, stronger bending effects are present in deep flaws. Finally, the data do appear to contain an effect which the authors conjecture to be residual warpage resulting from the flex loading rig used to grow the cracks. The important point here is that, if flaw shapes deviate from semi-elliptic crack shapes as pictured in Fig. 1, a significant SIF elevation in the region of maximum SIF may be expected in the absence of other effects. Studies are currently underway toward further clarification of this point.

Acknowledgments

The authors wish to acknowledge the support of the staff and facilities of the Department of Engineering Science and Mechanics at Virginia Polytechnic Institute and State University, the work of their colleagues, especially J. J. McGowan and J. C. Newman, Jr., the encouragement of C. J. Astill, and they gratefully acknowledge the support of the National Science Foundation under Grant No. Eng. 76-20824-01.

APPENDIX

Corrections for Deviation of Test Geometries from Benchmark Geometries

Based upon a three dimensional finite-element solution for a flat plate under remote tension containing a semi-elliptic surface crack under Mode I loading, Newman and Raju [27] developed a series of expressions for defining the influence of the various problem parameters. Using the basic form

$$K_{\mathrm{I}} = \bar{\sigma}\sqrt{\pi a/\Phi^2}F(a/T,\ a/c,\ 2c/W,\ \phi) \tag{5}$$

where

$\bar{\sigma}$ = remote tensile stress,
a = crack depth,

$$\Phi = \int_0^{\pi/2} \left\{\left(\frac{a}{c}\right)^2 \sin^2\phi + \cos^2\phi\right\}^{1/2} d\phi,$$

T = plate thickness,
$2c$ = crack width in plate surface,
W = plate width, and
ϕ = parametric angle measured from maximum crack depth position.

They provide the following expressions

$$F = \left[M_1 + M_2\left(\frac{a}{T}\right)^2 + M_3\left(\frac{a}{T}\right)^4\right] f\left(\frac{a}{c}, \phi\right) g\left(\frac{a}{T}, \phi\right) h\left(\frac{2c}{W}, \frac{a}{T}\right) \tag{6}$$

where

$$M_1 = 1.13 - 0.09\left(\frac{a}{c}\right)$$

$$M_2 = -0.54 + \frac{0.89}{0.2 + \frac{a}{c}}$$

$$M_3 = 0.5 - \frac{1.0}{0.65 + \frac{a}{c}} + 14\left(1.0 - \frac{a}{c}\right)^{24}$$

$$f\left(\frac{a}{c}, \phi\right) = \left[\left(\frac{a}{c}\right)^2 \sin^2\phi + \cos^2\phi\right]^{1/4}$$

$$g\left(\frac{a}{T}, \phi\right) = 1 + \left[0.1 + 0.35\left(\frac{a}{T}\right)^2\right](1 - \cos\phi)^2$$

$$h\left(\frac{2c}{W}, \frac{a}{T}\right) = \left[\sec\frac{\pi}{4}\left(\frac{2c}{W}\right)\left(\frac{a}{T}\right)^{1/2}\right]^{1/2}$$

In this paper, the experimental geometries were corrected to the benchmark geometries by computing F_{EXPR} using test model geometries and F_{THEOR} using benchmark geometries and multiplying the normalized experimental SIF

$$\frac{K_I\Phi}{\bar{\sigma}(\pi a)^{1/2}} \text{ by } \frac{F_{\text{THEOR}}}{F_{\text{EXPR}}} \text{ to get } \left[\frac{K_I\Phi}{\bar{\sigma}(\pi a)^{1/2}}\right]_{\text{CORRECTED}} \tag{7}$$

References

[1] Irwin, G. R., *Journal of Applied Mechanics*, Vol. 29, *Transactions*, American Society of Mechanical Engineers, Vol. 79, Series E, Dec. 1962, pp. 651-654.

[2] *Proceedings*, ASME Committee for Computing in Applied Mechanics of AMD, J. L. Swedlow, Ed., American Society of Mechanical Engineers, Nov. 1972.

[3] *Part-Through Crack Fatigue Life Prediction, ASTM STP 687*, J. B. Chang, Ed., American Society for Testing and Materials, 1979.

[4] *Fracture Mechanics, ASTM STP 677*, C. W. Smith, Ed., American Society for Testing and Materials, 1979.

[5] *Proceedings*, Workshop on Three Dimensional Fracture Analysis, L. E. Hulbert, Ed., Battelle-Columbus Laboratories, Columbus, Ohio, Sept. 1976.

[6] *Journal of Experimental Mechanics*, J. J. McGowan, Ed., Vol. 20, No. 8, Aug. 1980, pp. 253-264.

[7] Smith, C. W. in *Experimental Techniques in Fracture Mechanics*, Vol. 2, Society for Experimental Stress Analysis, Monograph No. 2, 1975, pp. 3-58.

[8] Jolles, M., McGowan, J. J., and Smith, C. W. in *Computational Fracture Mechanics*, ASME-AMD-SP, *Proceedings*, Second National Congress on Pressure Vessels and Piping, E. F. Rybicki and S. E. Benzley, Eds., American Society of Mechanical Engineers, 1975, pp. 63-82.

[9] Smith, C. W. in *Mechanics of Fracture*, Vol. 6, Sitjhoff-Noordhoff International, The Netherlands, 1980.

[10] Smith, D. G. and Smith, C. W., *International Journal of Fracture Mechanics*, Vol. 6, No. 3, Sept. 1970, pp. 305-318.

[11] Smith, C. W. in *Proceedings*, Third International Congress on Experimental Mechanics, Dec. 1974, pp. 287-292.
[12] Marrs, G. R. and Smith, C. W. in *Stress Analysis and Growth of Cracks, ASTM STP 513*, American Society for Testing and Materials, 1972, pp. 22-36.
[13] Schroedl, M. A. and Smith, C. W. in *Progress in Flaw Growth and Fracture Toughness Testing, ASTM STP 536*, American Society for Testing and Materials, 1973, pp. 45-68.
[14] Schroedl, M. A., McGowan, J. J., and Smith, C. W., *Experimental Mechanics*, Vol. 14, No. 10, Oct. 1974, pp. 392-399.
[15] Harms, A. E. and Smith, C. W., *Recent Advances in Engineering Science*, Vol. 7, No. 2, Feb. 1973.
[16] McGowan, J. J. and Smith, C. W. in *Mechanics of Crack Growth, ASTM STP 590*, American Society for Testing and Materials, 1975, pp. 460-476.
[17] Smith, C. W., McGowan, J. J., and Jolles, M. in *Proceedings*, Twelfth Annual Meeting of the Society for Engineering Science, Austin, Texas, 1975, pp. 353-362.
[18] Jolles, M., McGowan, J. J., and Smith, C. W., *Journal of Engineering Materials and Technology, Transactions*, American Society of Mechanical Engineers, Vol. 97, 1, Jan. 1975, pp. 45-51.
[19] Smith, C. W. and Jolles, M. in *Proceedings*, Symposium on Developments in Theoretical and Applied Mechanics (Eighth SECTAM), 1976, pp. 151-161.
[20] Smith, C. W. in *Fracture Mechanics in Engineering Application*, Sijthoff and Noordhoff, Alphen aan den Rijn, The Netherlands, 1979.
[21] Smith, C. W., Peters, W. H., and Andonian, A., *Journal of Engineering Fracture Mechanics*, 1980.
[22] Smith, C. W. and Peters, W. H., *Developments in Theoretical and Applied Mechanics*, Vol. 9, May 1978, pp. 225-234.
[23] Smith, C. W. and Peters, W. H. in *Preprints of the 6th International Conference on Experimental Stress Analysis*, Sept. 1978, pp. 861-864.
[24] Sommer, E., Hodulak, L., and Kordisch, H., *Journal of Pressure Vessel Technology*, Feb. 1977, pp. 106-111.
[25] Smith, C. W. in *Fracture Mechanics and Technology*, Vol. 1, G. C. Sih and C. L. Chow, Eds., Sijthoff and Noordhoff, Alphen aan den Rijn, The Netherlands, 1979, pp. 591-605.
[26] Smith, C. W., Peters, W. H., and Gou, S. F. in *Fracture Mechanics, ASTM STP 677*, American Society for Testing and Materials, 1979, pp. 431-445.
[27] Newman, J. C., Jr., and Raju, I. S., "Analyses of Surface Cracks in Finite Plates Under Tension or Bending Loads," NASA TP 1578, National Aeronautics and Space Administration, Washington, D.C., Dec. 1979.

S. S. Palusamy[1] *and M. Raymund*[1]

Stress-Intensity Factor for a Corner Crack at the Edge of a Hole in a Plate

REFERENCE: Palusamy, S. S. and Raymond, M., "**Stress-Intensity Factor for a Corner Crack at the Edge of a Hole in a Plate,**" *Fracture Mechanics: Thirteenth Conference, ASTM STP 743,* Richard Roberts, Ed., American Society for Testing and Materials, 1981, pp. 438–455.

ABSTRACT: A corner-cracked hole in a plate, subjected to remote tension loading, is one of the three benchmark problems identified for the validation of three-dimensional techniques at the workshop held in Battelle Columbus Laboratories. Stress-intensity factor results for the case of circular corner crack obtained by the macroelement technique is presented in this paper. Results for the remote tension loading are compared with those obtained by the boundary-integral equation (BIE) method and three-dimensional finite-element technique based on singular elements.

Since this investigation was carried out as a part of an overall program aimed at developing stress-intensity factor values for cracks in reactor vessel nozzles, results for six other crack surface loadings were obtained and compared with the results obtained by BIE method.

For the case of remote tension loading, the results of the macroelement technique in the regions removed from the free surface agree within 2.5 percent of those obtained by BIE and the singularity finite-element method. For the case of crack surface loadings, the results of the macroelement technique are shown to be in good agreement with the BIE method throughout the crack front. Comparisons with the limited results available in the literature which take into account constraint variation at the free surface show that the macroelement results for the free surface will be too conservative for thermal shock applications. However, it is concluded that the macroelement technique will give reasonably accurate results for nozzle corner crack problems except in the regions of free surface.

KEY WORDS: corner crack, stress-intensity factors, surface flaws, fatigue (materials), finite-element analysis, pressure vessels

Corner-cracked holes, being among the most commonly encountered flaws in structures, have attracted several investigators. Average K_I estimates for some corner-crack configurations have been obtained by Hall and Finger [*1*],[2] Liu [*2*], and Newman [*3*]. Employing the alternating method, Shah [*4*]

[1]Fellow engineer and senior scientist, respectively, Westinghouse Nuclear Technology Division, Pittsburgh, Pa. 15230.

[2]The italic numbers in brackets refer to the list of references appended to this paper.

calculated the distribution of K_I at the crack front for corner-crack geometry subjected to either remote tension or pin loading. Three-dimensional photoelastic techniques were used by McGowan and Smith [5], Smith, Jolles, and Peters [6], and Smith, Peters, and Gou [7] to obtain stress-intensity factors for a variety of corner-crack configurations. Recently, the three-dimensional finite-element technique has been used by Kathiresan [8], Heckmer and Bloom [9], and Raju and Newman [10] to obtain K_I solutions to several different corner-cracked hole problems.

A corner-cracked hole in a plate, subjected to a remote uniform tension loading, is one of the three benchmark problems identified for the validation of three-dimensional fracture analysis methods at the workshop held in Battelle Columbus Laboratories [11]. Four cases of the corner-crack geometry were proposed at the workshop. The case of circular corner crack is considered in this report.

Hall, Raymund, and Palusamy [12] had developed the macroelement technique for the determination of Mode I stress-intensity factors (K_I) for cracks in three-dimensional bodies subjected to arbitrary loadings. McGowan and Raymund [13,14] applied this technique successfully to longitudinal semi-elleptical surface flaws in reactor vessel beltline and finite-thickness plates. They demonstrated that the macroelement technique gave consistently good results within 8 percent of the results available in the literature. A stress-intensity factor solution to the corner-cracked hole benchmark problem is sought in this investigation as a preliminary step towards the application of the macroelement technique to the determination of K_I solutions to nozzle corner cracks. The corner-cracked hole problem represents somewhat the constraint and stress concentration effects in the region of the nozzle corner crack and therefore would serve as a reasonable basis for validating the application of the macroelement technique to the nozzle problems. Further, solutions to this problem are being obtained by investigators around the world with which the macroelement results can be compared to evaluate their accuracy.

Presented in this report are K_I distributions for a circular corner crack at the edge of a hole in a plate, obtained by the macroelement technique. Results were obtained for several crack surface component loadings as well as uniform remote tension loading. The crack surface load components were chosen to be capable of representing severe stress gradients at nozzel corners due to thermal shock loadings. The results obtained in this investigation are compared with those obtained by Heliot, Lebans, and Pellissier-Tanon [15] using the boundary integral technique and by Raju and Newman [10] using the finite-element technique.

Geometry and Loading

The corner-cracked hole geometry considered in this investigation is shown in Fig 1. It consists of a hole of radius R, in a solid plate of length $2H$, width

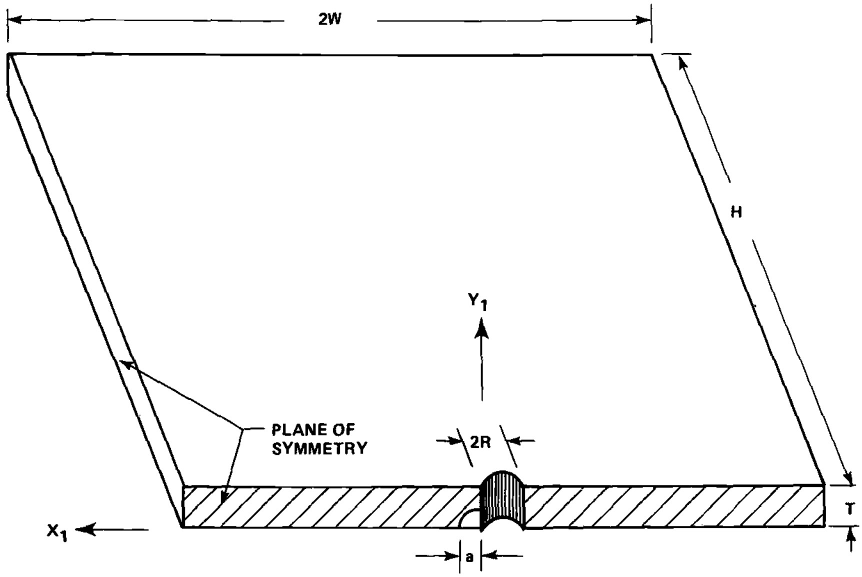

FIG. 1—*Corner-cracked hole geometry.*

$2W$, and thickness T. A quarter-circular crack of radius a is considered at one corner of the hole. The plane containing the crack and the plane $X_1 = W$ are assumed to be planes of symmetry. The ratios of crack radius to the hole radius and the crack radius to the plate thickness are both chosen to be 0.5. The dimensional values chosen for this investigation are

$$\begin{aligned} H &= 375 \text{ mm} \\ 2W &= 375 \text{ mm} \\ T &= 25 \text{ mm} \\ R &= 25 \text{ mm} \\ a &= 12.5 \text{ mm} \end{aligned} \tag{1}$$

These values were chosen to satisfy the following restrictions specified in Ref *11*

$$2W = 6(2R + a), H = 2W \tag{2}$$

The plate is subjected to an arbitrary crack-opening loading, denoted by σ, which in general is a function of X_1 and Y_1.

The values of modulus of elasticity and Poisson's ratio for the plate material were assumed to be 200 000 MPa and 0.3, respectively.

Both remote and crack surface loadings were considered. The remote loading consisted of a uniform tension, σ_0, at the edge of the plate in a direction normal to the plane of the crack

$$\sigma = \sigma_0 \tag{3}$$

The following six different crack surface loadings were considered

$$\begin{aligned}
\sigma &= \sigma_{00} \\
\sigma &= \sigma_{10}\left(\frac{x}{a}\right) \\
\sigma &= \sigma_{20}\left(\frac{x}{a}\right)^2 \\
\sigma &= \sigma_{01}\left(\frac{y}{a}\right) \\
\sigma &= \sigma_{02}\left(\frac{y}{a}\right)^2 \\
\sigma &= \sigma_{12}\left(\frac{x}{a}\right)\left(\frac{y}{a}\right)^2
\end{aligned} \tag{4}$$

where σ_{00}, σ_{10} ..., σ_{12} are arbitrary coefficients and x and y are coordinates rotated through 45 deg with respect to X_1 and Y_1, Fig. 2. The loadings were chosen after extensive numerical curve-fitting studies carried out to represent the crack-opening stress profile at the uncracked nozzle corner due to thermal shock loading to a reasonable degree of accuracy. Using superposition principle, the loadings [*4*] can be used to represent any crack-opening stress profile due to thermal shock loading.

Finite-Element Model

The finite-element model of the corner-cracked hole plate was formulated by dividing the plate into two substructures, Fig. 3. The crack-tip region was modeled by a single macroelement [*12*] and was treated as one substructure. Figure 4 shows the dimensions of the macroelement substructure. As described in Ref *12*, the macroelement is built out of 45 microelements consisting of blended brick and wedge elements. The blended brick elements permit a variable number of nodes and therefore the number of nodes on and in the vicinity of crack tip can be chosen by the analyst. In this problem, 22 nodes were chosen to represent the crack tip. The macroelement had 1656 degrees of freedom. The macroelement is basically built as a unit cube and a transformation is carried out to represent elliptical flaw shapes and curved surfaces. The macroelement in the form of unit cube prior to transformation is shown in Fig. 5.

The remainder of the plate called mother structure (Fig. 3) was modeled

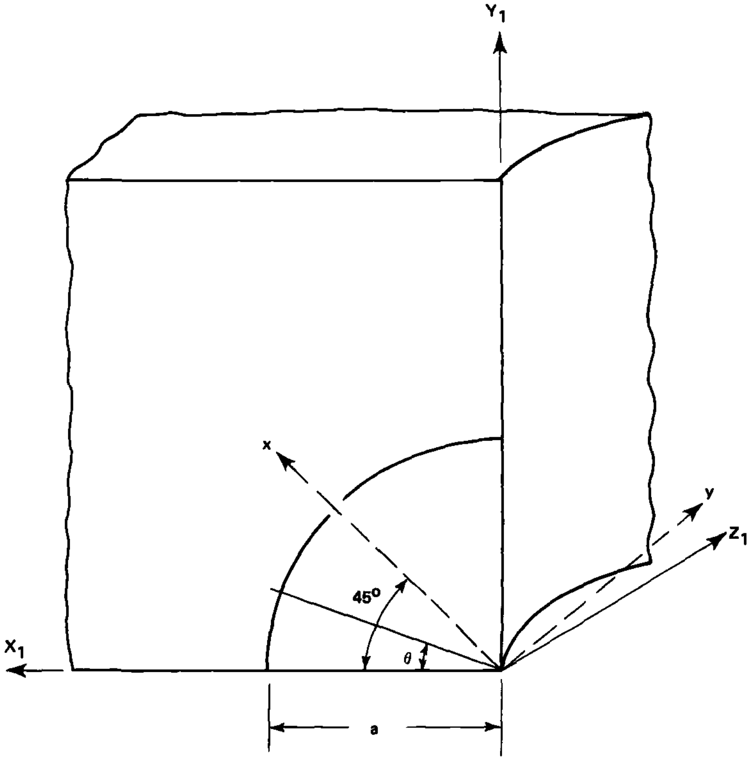

FIG. 2—*Definition of coordinate systems.*

using conventional 20-node isoparametric elements. The macroelement is designed to be compatible with these 20-node elements. The computer-plotted three-dimensional view of the finite-element model of the mother structure is shown in Fig. 3, whereas the plan view of the model is shown in Fig. 6. The model consists of 99 elements and 1931 degrees of freedom.

Stress-Intensity Factor for Arbitrary Loading

For each of the loadings specified in Refs *3* and *4*, Park's stiffness derivative method [*16*] was used to obtain the stress-intensity factor at every node point on the circular crack front. The implementation of the stiffness derivative method is described elsewhere by Hall, Raymund, and Palusamy [*12*]. The stress-intensity factor for an arbitrary loading can be obtained by employing the principle of superposition. As reported before, the stress profile formed by the summation of the crack surface loadings defined in Ref *4* could adequately represent the crack-opening stress profile due to thermal shock loading in the unflawed plate with a hole

$$\sigma(x, y) = \sigma_{00} + \sigma_{10}\left(\frac{x}{a}\right) + \sigma_{20}\left(\frac{x}{a}\right)^2 + \sigma_{01}\left(\frac{y}{a}\right) + \sigma_{02}\left(\frac{y}{a}\right)^2 + \sigma_{12}\left(\frac{x}{a}\right)\left(\frac{y}{a}\right)^2 \quad (5)$$

The resulting stress-intensity factor K_I can then be expressed as follows

$$K_I = \sigma_{00} H_{00}(\theta) + \sigma_{10} H_{10}(\theta) + \sigma_{20} H_{20}(\theta) + \sigma_{01} H_{01}(\theta) + \sigma_{02} H_{02}(\theta) + \sigma_{12} H_{12}(\theta) \quad (6)$$

where $H_0(\theta), \ldots, H_{12}(\theta)$ are functions of positions along the crack front and are numerically derived by the macroelement technique for the loadings $\sigma_{00}, \ldots, \sigma_{12}(x/a)(y/a)^2$, respectively. The parameter θ defines the angular position along the crack front as shown in Fig. 2.

It is convenient to nondimensionalize the functions $H_{00}(\theta), \ldots, H_{12}(\theta)$, and the stress-intensity factor for a buried circular flaw in an infinite medium subjected to uniform remote tension loading is chosen as a reference value. As a result, Eq 6 can be rewritten as follows

$$K_I = \frac{2}{\pi}\sqrt{\pi a}\,[\sigma_{00} h_{00}(\theta) + \sigma_{10} h_{10}(\theta) + \sigma_{20} h_{20}(\theta) + \sigma_{01} h_{01}(\theta) + \sigma_{02} h_{02}(\theta) + \sigma_{12} h_{12}(\theta)] \quad (7)$$

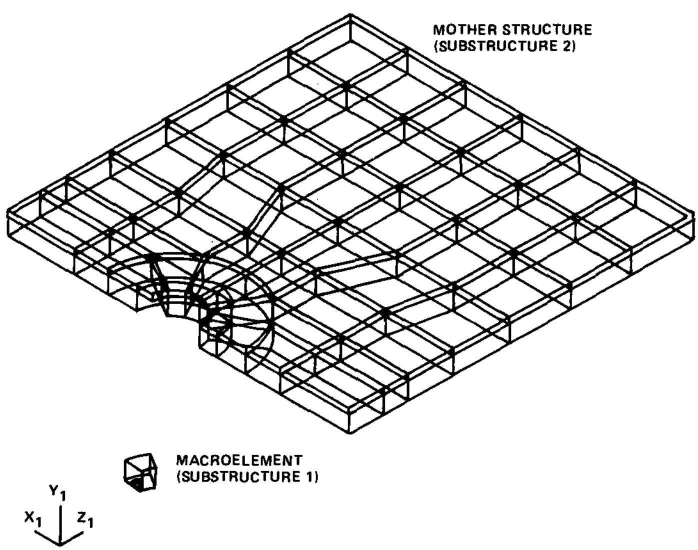

FIG. 3—*Finite-element model of plate with a corner-cracked hole.*

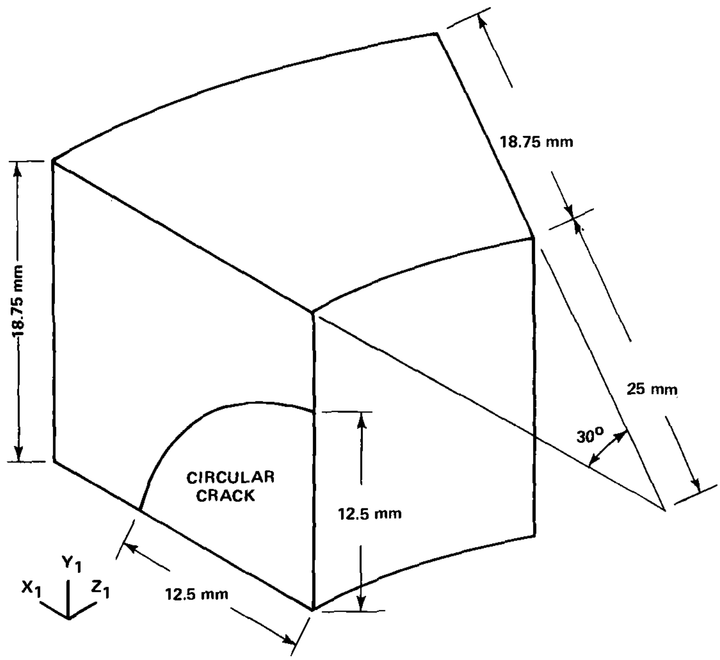

FIG. 4—*Macroelement substructure.*

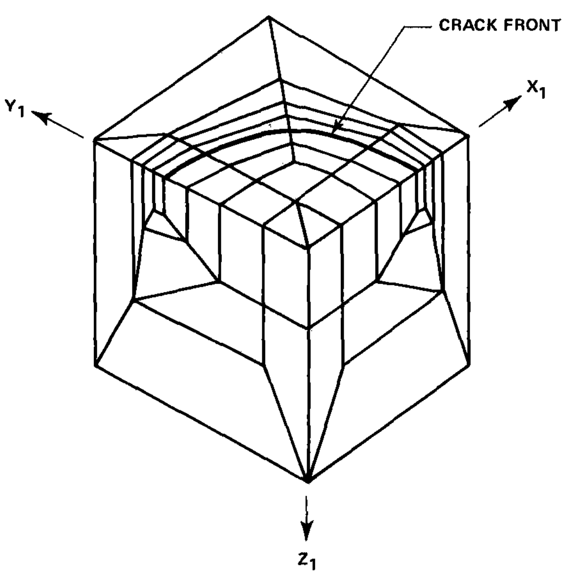

FIG. 5—*Undeformed macroelement geometry.*

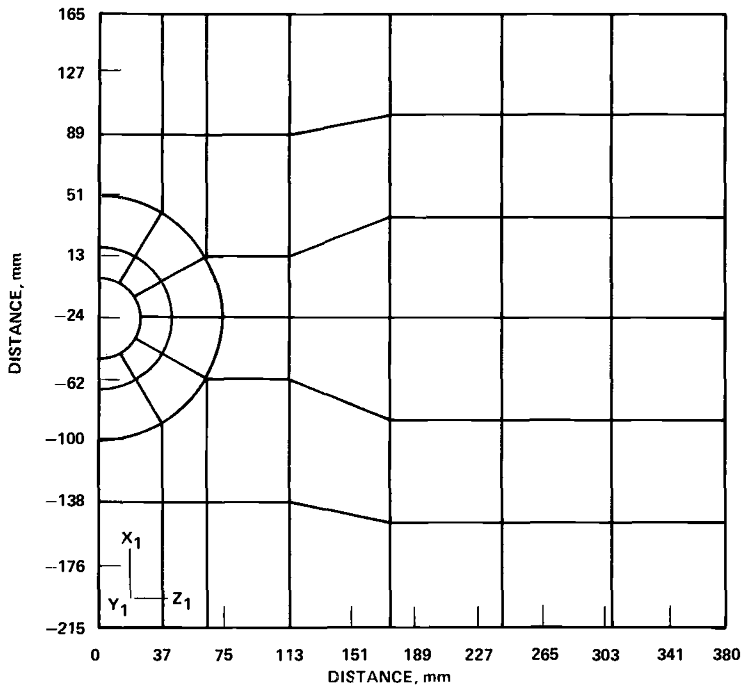

FIG. 6—*Plan view of the finite-element model.*

where

$$h_{00}(\theta) = \frac{H_{00}(\theta)}{\frac{2}{\pi}\sqrt{\pi a}}$$

$$\vdots \tag{8}$$

$$h_{12}(\theta) = \frac{H_{12}(\theta)}{\frac{2}{\pi}\sqrt{\pi a}}$$

Similarly, the stress-intensity factor due to the remote loading given by the Eq 3 is written as

$$K_I = \frac{2}{\pi}\sqrt{\pi a}\,[\sigma_0 h_0(\theta)] \tag{9}$$

The results for the dimensionless influence functions h_0 (θ), h_{00} (θ), ..., h_{02} (θ) are presented in Figs. 7-13 and Table 1.

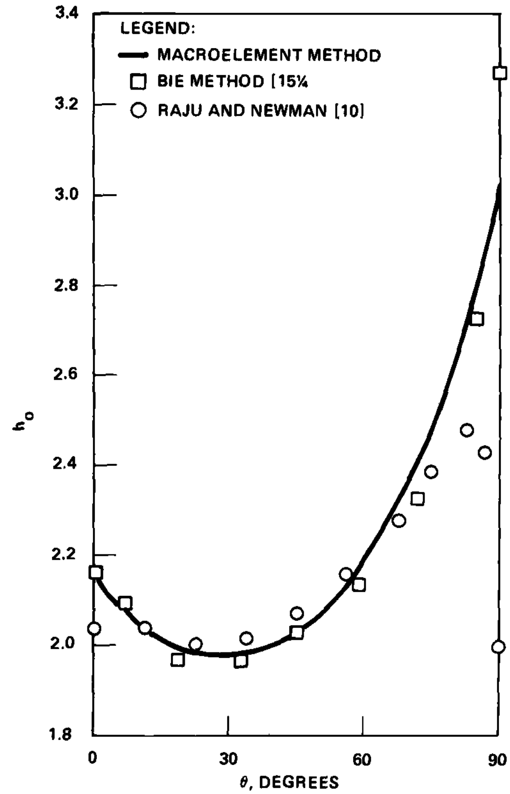

FIG. 7—*Influence function for remote tension loading.*

Results for Remote Tension Loading

The numerical values h_0 (θ) obtained for the remote tension loading are included in Table 1. Figure 7 shows the plot of h_0 (θ) with respect to (θ). In order to evaluate the accuracy, the results obtained by the macroelement method are compared in Fig. 7 with the results obtained by two other investigators for identical and near-identical problems. Raju and Newman [*10*], using three-dimensional singularity elements, solved the identical problem except they considered cracks on both sides of the hole. For the purposes of comparison in Fig. 7, the value of h_0 for a single crack is obtained by multiplying the results given in Ref *10* by a factor 0.96, based on the suggestion by Shah [*4*]. Heliot et al [*15*] solved the identical problem using the boundary-integral equation (BIE) method.

The results of BIE and three-dimensional singularity element methods, are compared with those of the macroelement in Fig. 7. The agreement between the results of macroelement and BIE method are excellent and the results agree within less than 2.5 percent except at the angular location θ equal to 90

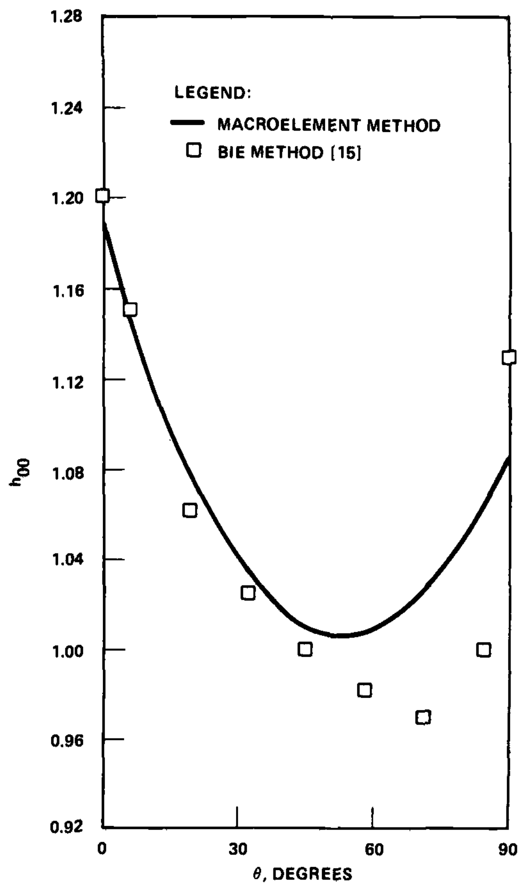

FIG. 8—*Influence function for constant crack surface loading.*

deg. In the region removed from the free surface, the results of Raju and Newman [*10*] are about 2 percent greater than those of the macroelement technique.

In the region of the free surface, a significant difference exists and this is expected due to the differences in the assumption made in the various techniques. The stiffness derivative method used for the computation of stress-intensity factor in the macroelement technique requires an *a priori* assumption of plane stress or plane strain. In reality, the constraint around the crack-tip region probably varies as some function of position. Unless this functional variation is known, the stiffness derivative method cannot be used to accurately determine the stress-intensity factor close to the region of free surface. For this reason, a plane-strain condition was conservatively assumed over the entire crack front in the macroelement technique. Therefore, the

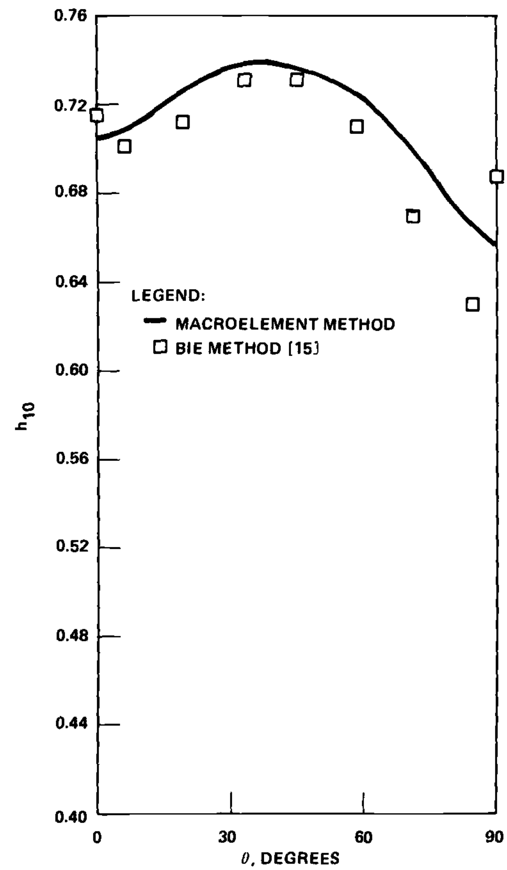

FIG. 9—*Influence function for* x*-component loading.*

macroelement results in the region of the free surface should be considered as upper bound only. On the other hand, the method used by Raju and Newman [*10*] does not require an *a priori* assumption regarding the crack-tip constraint. Consequently, these results can be considered to be a more realistic value. However, because of the large difference in results, experimental data for this region would be extremely valuable in establishing and improving the accuracy of various methods.

Plane-stress constraint values can be calculated from the macroelement results by multiplying by $(1 - \nu^2)$. By comparing these results with those of Raju and Newman at the free surfaces, certain observations can be made. At $\theta = 0$ deg, the plane-stress constraint value is exactly equal to that of Raju and Newman after accounting for the increase due to quarter-symmetry. On the other hand, at $\theta = 90$ deg, the Raju and Newman result after accounting

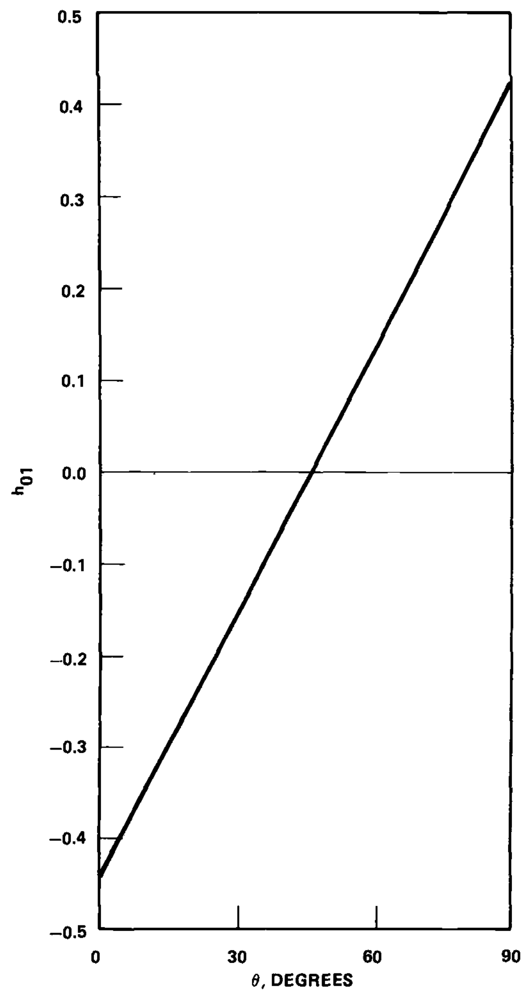

FIG. 10—*Influence function for* y*-component loading.*

for the quarter-symmetry (1.92) is only 70 percent of the value corresponding to the plane-stress condition (2.73).

Results for Crack Surface Loadings

The values of dimensionless influence functions h_{00}, h_{10}, h_{20}, h_{01}, h_{02}, and h_{12} due to the six component crack surface loadings defined in Eq 4 are plotted in Figs. 8–13. The numerical values for these functions are listed in Table 1. For most of the loadings, Heliot et al [*15*] have computed the influence

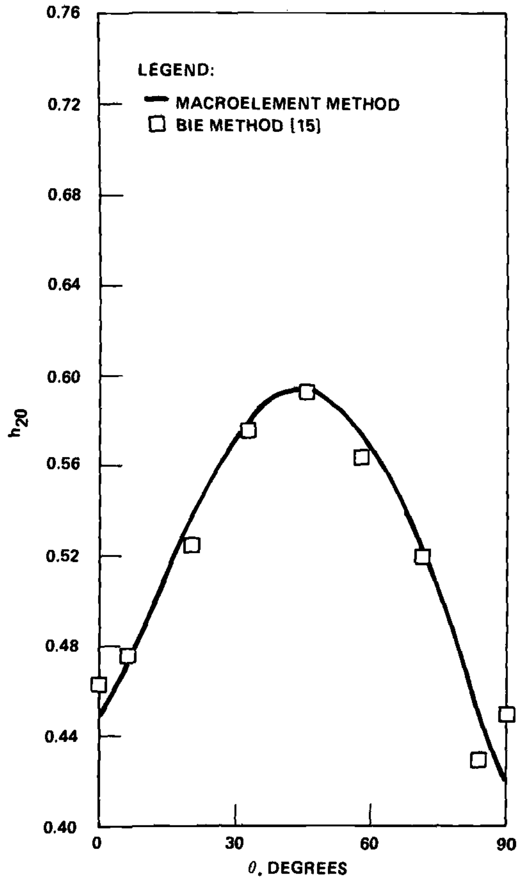

FIG. 11—*Influence function for* x^2*-component loading.*

function values using the BIE method. These results are compared with macroelement results in Figs. 8, 9, 11, and 12. The values of h_{00} due to the macroelement method agree with the BIE values within 6 percent. The corresponding agreement for h_{10} is within 5 percent. In the case of h_{20} and h_{02}, the agreement between the two methods is within 2 percent except in the vicinity of the free surface, where the maximum disagreement is 7 percent.

Crack-Opening Displacements

In Ref *11* it was suggested that crack-opening displacements be provided on the crack surface at 10-deg increments of θ on concentric ellipses or circles for the case considered in this paper. The macroelement computer program used in solving the corner-cracked hole problem has not been programmed

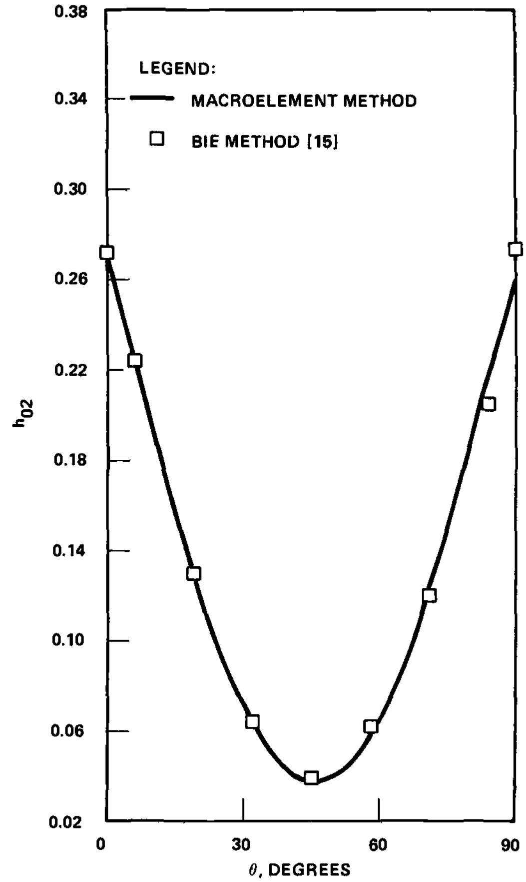

FIG. 12—*Influence function for* y^2*-component loading.*

for calculating the displacements in such detail as suggested in Ref *11* without major computer program development. Therefore the displacements were computed at 25 nodal points on the crack surface. The nodal point locations are defined by the parameter

$$\lambda = \left(\frac{X_1^2 + Y_1^2}{a^2}\right)^{1/2} \tag{9}$$

where X_1, Y_1, and a are defined in Fig. 2.

The crack-opening displacement U_{Z1} is normalized with respect to the crack opening displacement U_{Z1_e} of an embedded circular flaw of radius a, in an infinite medium, subjected to a crack-opening stress of σ_{ij}. Thus, the normalized displacement is expressed as

$$u_{Z1} = \frac{U_{Z1}}{U_{Z1e}} \tag{10}$$

where

$$u_{Z1e} = \frac{4\,(1 - \nu^2)\,\sigma_{ij}}{\pi E}\left[1 - \left(\frac{X_1^2 + Y_1^2}{a^2}\right)^{1/2}\right] \tag{11}$$

E and ν are the modulus of elasticity and Poisson's ratio of the material. The factor σ_{ij} stands for σ_0, σ_{00}, . . ., σ_{12}, defined in Eqs 3 and 4. The values of u_{Z1} for the 25 node points due to the seven load components are listed in Table 2. The corresponding values of λ and θ are also listed in Table 2.

Summary and Conclusions

The investigation of corner-cracked hole in a plate was carried out as a part of an overall program aimed at developing stress-intensity factor values

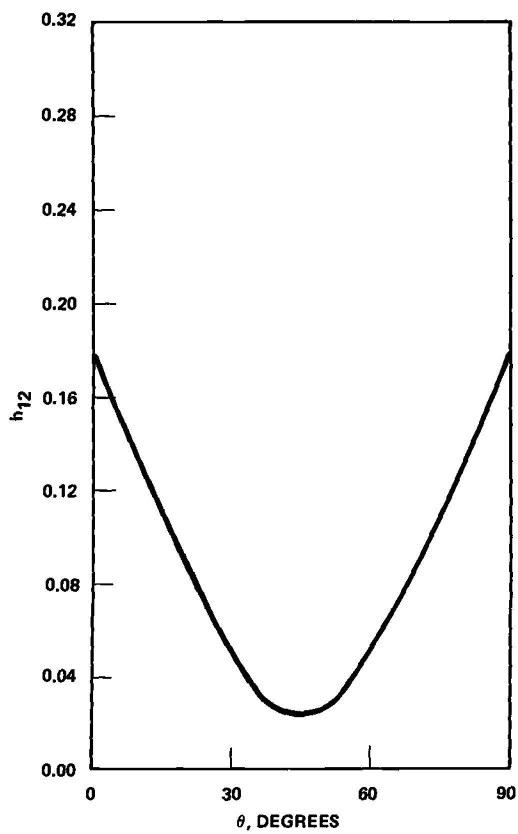

FIG. 13—*Influence function for* xy^2*-component loading.*

TABLE 1—*Numerical values of influence functions obtained by Westinghouse macroelement technique.*

Location	θ, deg	h_0	h_{00}	h_{10}	h_{20}	h_{01}	h_{02}	h_{12}
1	0.0	2.160	1.189	0.705	0.449	−0.446	0.267	0.180
2	4.36	2.101	1.159	0.708	0.467	−0.406	0.237	0.162
3	8.72	2.060	1.130	0.711	0.486	−0.365	0.204	0.143
4	13.08	2.031	1.106	0.718	0.508	−0.321	0.169	0.122
5	20.89	1.990	1.070	0.730	0.547	−0.246	0.114	0.085
6	24.34	1.979	1.057	0.731	0.557	−0.214	0.097	0.072
7	27.79	1.977	1.046	0.734	0.568	−0.180	0.079	0.058
8	31.24	1.979	1.038	0.736	0.576	−0.149	0.066	0.048
9	34.69	1.986	1.030	0.739	0.584	−0.113	0.053	0.037
10	38.14	1.993	1.022	0.738	0.589	−0.084	0.045	0.031
11	41.59	2.001	1.012	0.736	0.593	−0.044	0.039	0.025
12	48.48	2.052	1.002	0.733	0.591	0.038	0.038	0.025
13	51.92	2.089	1.006	0.730	0.586	0.076	0.044	0.030
14	55.35	2.134	1.007	0.729	0.580	0.106	0.051	0.036
15	58.79	2.178	1.009	0.724	0.570	0.141	0.064	0.047
16	62.23	2.229	1.012	0.719	0.560	0.173	0.076	0.057
17	65.66	2.288	1.015	0.713	0.548	0.206	0.094	0.071
18	69.10	2.356	1.022	0.708	0.536	0.236	0.111	0.084
19	76.90	2.551	1.038	0.684	0.490	0.310	0.164	0.120
20	81.27	2.687	1.052	0.671	0.465	0.350	0.198	0.140
21	85.63	2.832	1.070	0.663	0.442	0.388	0.230	0.158
22	90.0	3.000	1.086	0.656	0.419	0.425	0.260	0.177

for cracks in reactor vessel nozzles. The primary objective was to validate the macroelement technique by comparing its results with those obtained by BIE and other methods reported in the literature.

A corner-cracked hole in a plate, subjected to remote tension loading, is one of the three benchmark problems identified for the validation of three-dimensional techniques at the workshop held in Battelle Columbus Laboratories. Stress-intensity factor results for the case of a circular corner crack obtained by the macroelement technique are presented in this report. Results for the remote tension loading are compared with those obtained by the BIE method and the three-dimensional finite-element technique based on singular elements. In addition, results for six other crack surface loadings necessary to represent severe stress gradients such as those due to thermal shock loadings were obtained and compared with those of the BIE method. Based on these comparisons the following conclusions are reached:

1. In the case of remote tension loading, the results of the macroelement technique for the regions removed from the free surface agree within 2.5 percent of those obtained by the BIE and singularity finite-element method.

2. Only solutions available for crack surface loadings are due to the BIE method and of the six loadings solved by the macroelement technique, BIE solutions are available for only four of them. Comparison of results for these

TABLE 2—*Crack-opening displacement*, u_{ZI}.

θ, deg	λ	σ_0	σ_{00}	σ_{10}	σ_{20}	σ_{01}	σ_{02}	σ_{12}
0.0	0.825	1.83	0.981	6.79	51.2	−3.69	25.1	192.0
5.5	0.819	1.74	0.925	6.52	50.3	−3.18	21.1	164.0
10.8	0.821	1.69	0.890	6.44	51.2	−2.77	17.7	142.0
16.0	0.829	1.65	0.863	6.45	52.9	−2.40	14.8	121.0
20.9	0.843	1.61	0.840	6.49	55.2	−2.04	12.1	102.0
23.9	0.838	1.62	0.837	6.53	56.2	−1.78	10.6	89.7
26.9	0.835	1.63	0.833	6.57	57.2	−1.53	9.36	78.2
29.9	0.834	1.63	0.828	6.59	58.1	−1.29	8.20	67.9
33.0	0.836	1.63	0.822	6.61	58.8	−1.04	7.21	59.0
36.0	0.840	1.63	0.814	6.61	59.5	−0.789	6.39	51.7
39.0	0.848	1.62	0.804	6.59	59.9	−0.538	5.76	45.9
42.0	0.857	1.61	0.792	6.56	60.2	−0.287	5.31	41.8
45.0	0.869	1.60	0.778	6.51	60.3	−0.352	5.04	39.5
47.9	0.857	1.64	0.785	6.52	59.9	0.207	5.22	41.1
50.9	0.848	1.67	0.791	6.51	59.3	0.448	5.58	44.5
53.9	0.840	1.71	0.795	6.49	58.6	0.691	6.12	49.5
56.9	0.836	1.74	0.797	6.45	57.7	0.933	6.85	56.3
60.0	0.834	1.77	0.798	6.40	56.7	1.17	7.76	64.6
63.0	0.835	1.80	0.796	6.33	55.4	1.41	8.86	74.4
66.0	0.838	1.83	0.794	6.25	54.1	1.65	10.1	85.6
69.0	0.843	1.85	0.790	6.16	52.6	1.90	11.5	98.1
73.9	0.829	1.94	0.800	6.03	49.9	2.22	13.9	115.0
79.1	0.821	2.03	0.812	5.93	47.4	2.54	16.5	132.0
84.4	0.819	2.14	0.830	5.89	45.5	2.88	19.4	151.0
90.0	0.825	2.30	0.865	6.01	45.4	3.30	22.9	175.0

cases show that the maximum disagreement is 7 percent, which includes the results for the region of the free surface.

3. Since the macroelement technique assumes plane-strain behavior throughout the crack front, the results for the region of free surface are only upper bounds. In the case of remote loading, comparison with singularity finite-element results shows that macroelement results are 50 percent larger.

4. Comparisons with the limited results available in the literature show that the macroelement results for the free surface may be too conservative for thermal shock applications. Investigations should be continued to reduce the conservatism in these results.

Acknowledgment

The authors wish to acknowledge the contribution of J. F. Petsche for performing a major part of the computing work and to thank the senior author's manager, J. N. Chirigos, for his constant encouragement.

References

[1] Hall, L. R. and Finger, R. W., *Fracture and Fatigue Growth of Partially Embedded Flaws*, AFFDL-TR-70-144, Air Force Flight Dynamics Laboratory, Wright-Patterson AFB, Ohio, Dec. 1970.

[2] Liu, A. F., *Engineering Fracture Mechanics*, Vol. 4, 1972, pp. 175-179.
[3] Newman, J. C., Jr., "Predicting Failure of Specimens With Either Surface Cracks or Corner Cracks at Holes," NASA TND-8244, National Aeronautics and Space Administration, Washington, D.C., June 1976.
[4] Shah, R. C. in *Mechanics of Crack Growth, ASTM STP 590*, American Society for Testing and Materials, 1976, pp. 429-459.
[5] McGowan, J. J. and Smith, C. W. in *Mechanics of Crack Growth, ASTM STP 590*, American Society for Testing and Materials, 1976, pp. 460-476.
[6] Smith, C. W., Jolles, M. I., and Peters, W. H., "Stress Intensity for Cracks Emanating From Pin Loaded Holes," VPI-E-76-13, Virginia Polytechnic Institute and State University, Blacksburg, Va., Aug. 1976.
[7] Smith, C. W., Peters, W. H., and Gou, S. F., "Influence of Flaw Geometries in Hole-Crack Stress Intensity," presented at the Eleventh National Symposium on Fracture Mechanics, Blacksburg, Va., June 1978.
[8] Kathiresan, K., "Three-Dimensional Linear Elastic Fracture Mechanics Analysis by a Displacement Hybrid Finite Element," Ph.D. Thesis, Georgia Institute of Technology, Atlanta, Ga., Sept. 1976.
[9] Heckmer, J. L. and Bloom, J. M., *International Journal of Fracture*, Oct. 1977.
[10] Raju, I. S. and Newman, J. C., Jr., in *Fracture Mechanics, ASTM STP 677*, American Society for Testing and Materials, 1979, pp. 411-430.
[11] Hulbert, L. E., *International Journal of Fracture*, Vol. 13, 1977, pp. 87-91.
[12] Hall, C. A., Raymund, M., and Palusamy, S., *International Journal of Fracture*, Vol. 15, 1979, pp. 231-245.
[13] McGowan, J. J. and Raymund, M. in *Fracture Mechanics, ASTM STP 677*, C. W. Smith, Ed., American Society for Testing and Materials, 1979, pp. 365-380.
[14] McGowan, J. J. and Raymund, M., "Stress Intensity Factor Solutions for Surface Flaws in Finite Thickness Plates Under Arbitrary Loading," WCAP-9318, Westinghouse Nuclear Technology Division, Pittsburgh, Pa., 1978.
[15] Heliot, J., Labbens, R., and Pellissier-Tanon, A., "Application of the Boundary Integral Equation Method to Three Dimensional Crack Problems," presented at the ASME Pressure Vessel Conference, American Society of Mechanical Engineers, San Francisco, Aug. 1980.
[16] Parks, D. M., *International Journal of Fracture*, Vol. 10, 1974, pp. 487-502.
[17] Smith, F. W. and Kullgren, T. E., "Theoretical and Experimental Analysis of Surface Cracks Emanating from Fastener Holes," AFFDL-TR-76-104, Defense Documentation Center, Alexander, Va., Feb. 1977.

L. M. Barker[1]

Short Rod and Short Bar Fracture Toughness Specimen Geometries and Test Methods for Metallic Materials

REFERENCE: Barker, L. M., **"Short Rod and Short Bar Fracture Toughness Specimen Geometries and Test Methods for Metallic Materials,"** *Fracture Mechanics: Thirteenth Conference, ASTM STP 743,* Richard Roberts, Ed., American Society for Testing and Materials, 1981, pp. 456–475.

ABSTRACT: There is an increasing interest in using short rod and short bar fracture toughness specimens to measure the plane-strain critical stress-intensity factor of metallic materials. In this paper, short rod and short bar specimen design considerations are discussed, and various specimen geometries with essentially equivalent test behavior and calibration are presented. A recent experimental study was conducted on three steels and two aluminum alloys to determine the sensitivity of the test result to variations in the chevron slot thickness and the sharpness of the slot bottoms. The results give strong indications that plane-strain constraint along the crack front is enhanced by thinness of the chevron slots and sharpness of the slot bottoms. The desirable aspects of loading configurations for short rod testing are discussed, and a successful loading mechanism is described.

KEY WORDS: fracture toughness, test methods, calibrations, fracture tests

It is generally agreed that a need exists for simpler, less-expensive methods of measuring the fracture toughness of metallic materials in terms of their plane-strain critical stress-intensity factor. One promising method makes use of the relatively new test specimen of circular cross section called the short rod [*1,2*],[2] and its rectangular-shaped counterpart called the short bar [*3*] (Figs. 1*a* and 1*b*). These specimens appear to be applicable to a wide range of materials, including metals, ceramics, polymers, and rocks. The required precrack is created automatically during the fracture toughness test without any fatigue cycling, and no postmortem crack length measurements are required. A recently published theory and data analysis technique [*4*] indicates that valid measurements are attainable using smaller specimens than those

[1]Senior staff consultant, Terra Tek, Inc., Salt Lake City, Utah 84108.
[2]The italic numbers in brackets refer to the list of references appended to this paper.

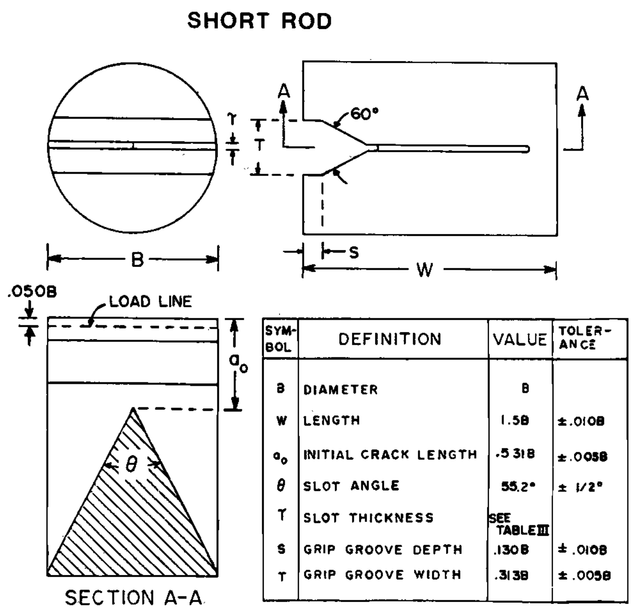

SYMBOL	DEFINITION	VALUE	TOLERANCE
B	DIAMETER	B	
W	LENGTH	1.5B	±.010B
a_o	INITIAL CRACK LENGTH	.531B	±.005B
θ	SLOT ANGLE	55.2°	± 1/2°
Υ	SLOT THICKNESS	SEE TABLE III	
S	GRIP GROOVE DEPTH	.130B	±.010B
T	GRIP GROOVE WIDTH	.313B	±.005B

(a)

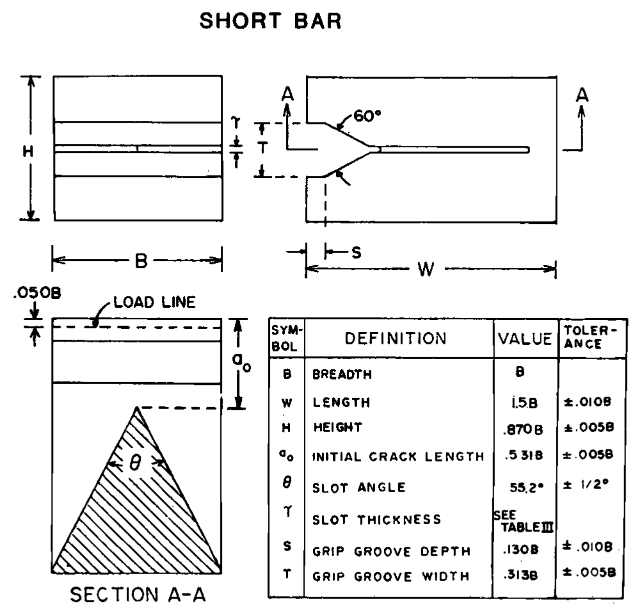

SYMBOL	DEFINITION	VALUE	TOLERANCE
B	BREADTH	B	
W	LENGTH	1.5B	±.010B
H	HEIGHT	.870B	±.005B
a_o	INITIAL CRACK LENGTH	.531B	±.005B
θ	SLOT ANGLE	55.2°	± 1/2°
Υ	SLOT THICKNESS	SEE TABLE III	
S	GRIP GROOVE DEPTH	.130B	±.010B
T	GRIP GROOVE WIDTH	.313B	±.005B

(b)

FIG. 1—*Short rod (a) and short bar (b) specimens with straight chevron slots. The* LOAD LINE *is the line along which the opening load is applied in the mouth of the specimen.*

required by the Test for Plane-Strain Fracture Toughness of Metallic Materials (E 399-78a).

These attributes and others have generated considerable interest in the short rod[3] test specimen and its associated test methods [*5-10*]. A recent study [*11*] compared short rod fracture toughness measurements of a number of metallic materials against measurements made according to the ASTM Method E 399-78a. The results were encouraging, and have stimulated a number of laboratories to begin using short rod and short bar specimens to measure the fracture toughness of metallic materials. Also, a task group within the ASTM E 24 Committee on Fracture Testing is beginning to coordinate comparison tests and computer calculations on the short rod specimen to determine the extent of its applicability to metallic materials.

This paper reports on the short rod and short bar specimen geometries and specimen loading methods which have been developed for testing metallic materials. It includes the results of a recent experimental study of the effects of varying the chevron slot thickness and the sharpness of the slot bottom. A subsequent paper will describe data reduction procedures which have been found to be useful.

Short Rod/Short Bar Geometry

Background

The short rod specimen uses a chevron slot similar to that of Tattersall and Tappin [*12*] in their three-point bend "work of fracture" specimen. Bluhm [*13*] has done analytical work on the fracture specimen, but Simpson [*14*] and Davidge and Tappin [*15*] reported difficulties in achieving the required stable crack growth. Pook [*16*] suggested using a chevron-slotted three-point bend specimen as a fracture toughness quality-control test specimen based on the peak load to fracture. He pointed out that no fatigue precracking should be necessary, because the required precrack can be obtained before the peak load as a result of initially stable crack growth inherent in the specimen design.

The short rod specimen has the test characteristics suggested by Pook, but uses much less material than the bend specimen. In addition, the test and data analysis techniques have progressed beyond the point of using only the peak load in the test, a procedure which is valid only when the assumptions of linear elastic fracture mechanics (LEFM) are well satisfied. Good test results are now possible even when the LEFM assumptions are violated to a significant degree [*4*].

[3]Specimens of the rectangular short bar configuration have been found to have test characteristics which appear experimentally indistinguishable from those of the round short rod specimens [*3*]. Thus, the statements about short rod specimens in this paper are equally applicable to short bar specimens.

Selection of the Short Rod Geometry

The configuration of the short rod specimen was selected on the basis of a large number of tests of specimens with different length-to-diameter ratios and various chevron slot geometries. The criteria on which the current geometry was selected were as follows.

1. The tendency for the crack to "pop in" at initiation should be minimized; that is, the crack initiation should be as smooth as possible.
2. The crack should tend to be well guided by the chevron slot.
3. The width of the crack front should be an appreciable portion of the specimen diameter at the time of the toughness measurement.
4. The crack should be near the center of the specimen (far from the ends) at the time of the toughness measurement.
5. The load should be at or near its peak value at the time of the toughness measurement.
6. The specimen geometry should be as simple as possible for ease of specimen fabrication.
7. The specimen should be economical in its use of sample material.

Some of these criteria are mutually exclusive, of course. The short rod and short bar specimen configurations of this paper were selected as a reasonable compromise in an attempt for an optimum geometry.

Specimen Geometry Options

Four basic specimen geometries are illustrated in Figs. 1 and 2, where the specimen size parameter, B, is the specimen diameter (short rod) or breadth (short bar). Figures 1 and 2 show two slot bottom geometries which result from two useful methods of machining the chevron slots. Figure 1 shows the straight slot geometry which results from feeding the saw or cutter through the specimen, while Fig. 2 shows the curved slot geometry which is obtained from a plunge-type feed of the saw blade into the specimen. Notice that the plan views (Sections A-A) of the rectangular short bars are identical with those of the round short rods. The height of the short bar specimens, which is 0.870 B, was selected in order that the compliance derivative with respect to crack length would be equal to that of the short rod. Thus, the short rod and short bar calibrations should be equivalent, and an experimental study has shown that the two specimens can indeed be considered as equivalent [*3*].

It would also be desirable to have the calibration of the straight-slotted specimens of Fig. 1 equivalent to the calibration of the curved-slotted specimens of Fig. 2. This can be accomplished to well within experimental uncertainties by superimposing the plan views of the two geometries, and by adjusting the slot configurations until the straight and curved slot bottoms are tangent to each other at the critical crack length, a_c, where the peak load occurs in an LEFM test, that is, where the fracture toughness measurement is

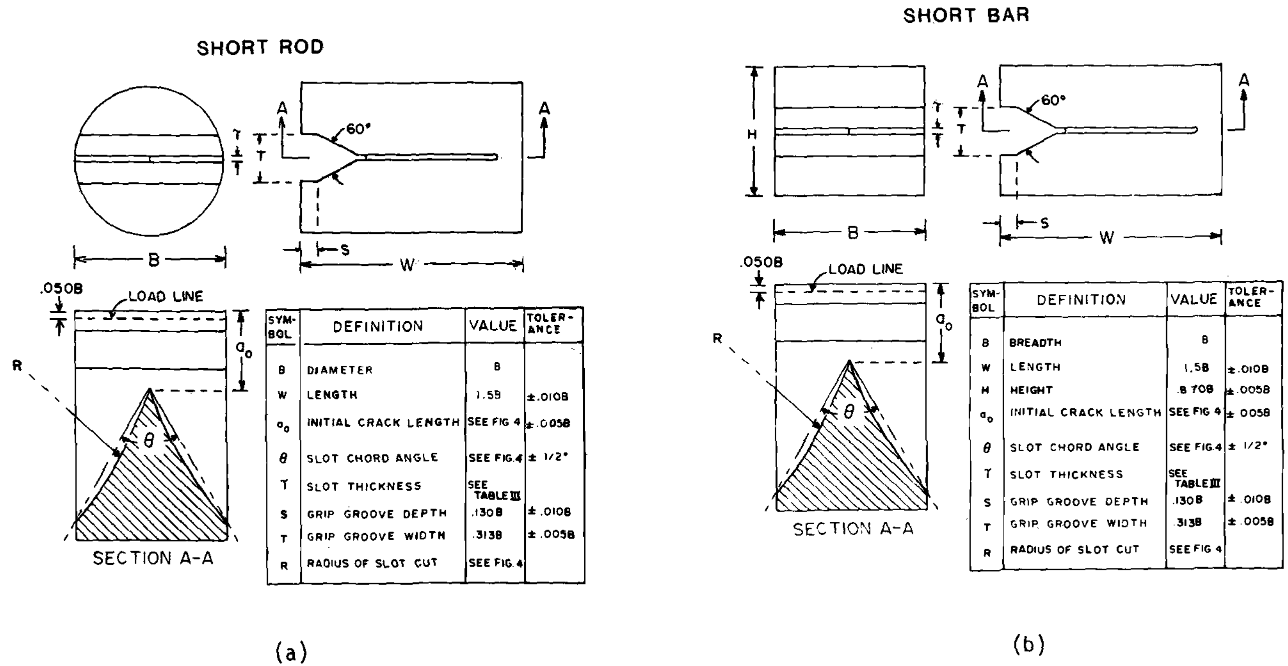

SYM-BOL	DEFINITION	VALUE	TOLER-ANCE
B	DIAMETER	B	
W	LENGTH	1.5B	±.010B
a_o	INITIAL CRACK LENGTH	SEE FIG 4	±.005B
θ	SLOT CHORD ANGLE	SEE FIG.4	± 1/2°
T	SLOT THICKNESS	SEE TABLE III	
S	GRIP GROOVE DEPTH	.130B	±.010B
T	GRIP GROOVE WIDTH	.313B	±.005B
R	RADIUS OF SLOT CUT	SEE FIG.4	

SYM-BOL	DEFINITION	VALUE	TOLER-ANCE
B	BREADTH	B	
W	LENGTH	1.5B	±.010B
H	HEIGHT	.870B	±.005B
a_o	INITIAL CRACK LENGTH	SEE FIG 4	± .005B
θ	SLOT CHORD ANGLE	SEE FIG.4	± 1/2°
T	SLOT THICKNESS	SEE TABLE III	
S	GRIP GROOVE DEPTH	.130B	±.010B
T	GRIP GROOVE WIDTH	.313B	±.005B
R	RADIUS OF SLOT CUT	SEE FIG 4	

FIG. 2—*Short rod (a) and short bar (b) specimens with curved chevron slots. The* LOAD LINE *is the line along which the opening load is applied in the mouth of the specimen.*

made (Fig. 3). Thus, when the crack is near the position where the toughness measurement is taken, both geometries have essentially the same crack-front width, rate of change of crack-front width with crack length, and compliance derivative, which causes their calibrations to be essentially equivalent. The calibrations of all four specimen geometries of Figs. 1 and 2 are therefore nominally the same, which allows the user some flexibility in choosing the most convenient short rod or short bar specimen geometry.

In machining the chevron slots in a curved-slotted specimen, it is much more convenient to measure the distance to the point of the chevron slot, a_0, and the chord angle, θ (Fig. 2), than to measure directly whether the slots pass through the desired tangency points at the proper angle. Therefore, the values of a_0 and θ which produce the desired tangency have been calculated as a function of the saw blade diameter. These functions are plotted in Fig. 4. By always using the a_0 and θ found from Fig. 4 for the saw blade diameter (the diameter of the slot curvature) in question, one can be assured of an essentially constant specimen calibration, regardless of specimen size, when the crack is in the vicinity of the critical crack length, a_c.

Specimen Machining Tolerance

It was recognized very early that the variation in the specimen's calibration as a function of a_0, θ, and W (Figs. 1 and 2), assuming a constant B, should be measured in order to determine the allowable tolerances on these parameters in fabricating specimens. A sensitivity study of these parameters was reported in 1976 [*2*]. Based on that study, the tolerances listed in Figs. 1 and 2 were selected to keep the effect of within-tolerance variations of any one parameter to within about ± 0.5 percent of the calculated toughness.

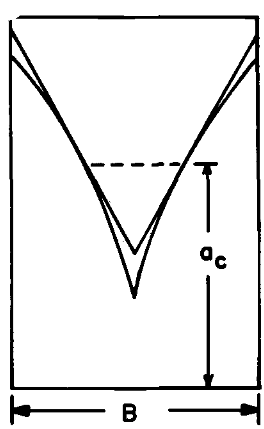

FIG. 3—*Curved and straight slots tangent at* a_c. *In the short rod specimen geometries of this paper,* $a_c = 0.85B$ *(see Ref* 18*).*

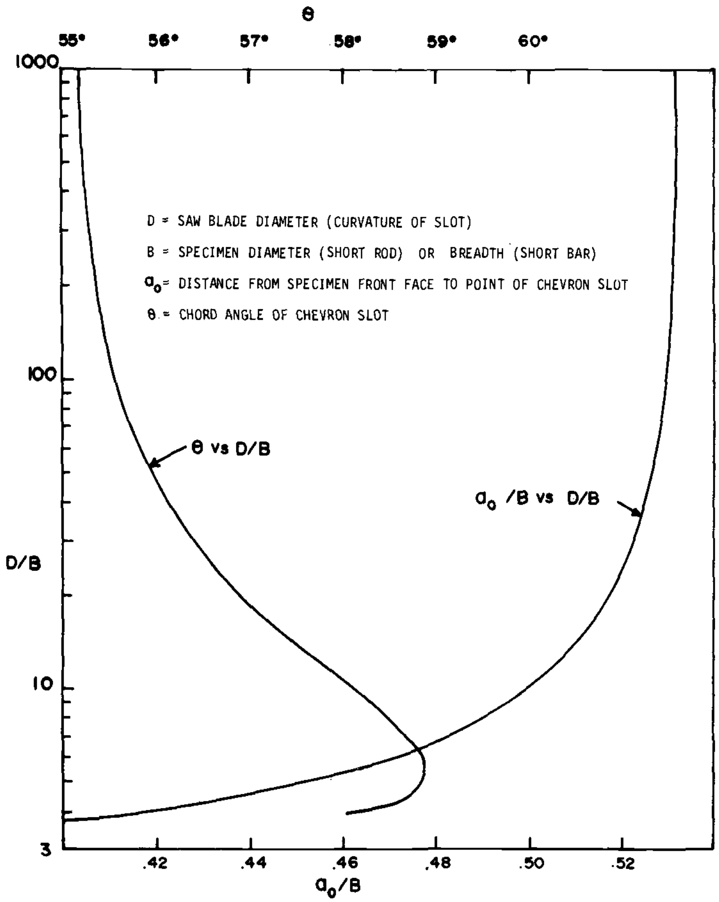

FIG. 4—*Chevron slot angle, θ, and initial crack length,* a_0, *for curved chevron slots.*

The sensitivities of the test results to variations in a_0, θ, and W are well-enough known to allow the application of a correction factor whenever one or more of these parameters is somewhat out of tolerance. The equations of Table 1 are used in the calculation of a configuration correction factor, C_c, which is multiplied by the test result to correct for somewhat imperfect specimen geometries. By using the C_c factor, test results for specimens which are out of tolerance by up to three times the tolerances of Figs. 1 and 2 can be corrected to within the ± 0.5 percent (per parameter) toughness uncertainty of nominal specimens.

Slot Thickness and Sharpness of the Slot Bottom

A crack tip is said to be in plane strain if the strains in the plane of the crack are zero along the crack front. Any crack which intersects a lateral free

TABLE 1—*Equations for the specimen configuration correction factor,* C_c.

Tolerances			
$W \pm 0.010\,B$ $a_0 \pm 0.005\,B$ $\theta \pm 1/2^0$	for tolerance up to three times these, use the C-factors.	$C_W = 1 - 1/2\,\Delta W/B$ $C_a = 1 + \Delta a_0/B$ $C_\theta = 1 - 0.01\,\Delta\theta$	$C_c = C_W C_a C_\theta$

Nomenclature
a_0 = distance from specimen front end face to the point of the chevron slot,
Δa_0 = a_0 minus the nominal value of a_0,
B = diameter (short rods) or breadth (short bar),
H = specimen height (short bars only),
W = specimen length,
ΔW = W minus the nominal value of W, that is, $W - 1.5\,B$,
θ = chord angle of chevron slot, and
$\Delta\theta$ = θ minus the nominal value of θ.
C-factors: factors which correct the toughness measurement for relatively small deviations of the specimen dimensions from the nominal values.

surface cannot be in perfect plane strain because the boundary condition at the lateral free surface is plane stress rather than plane strain. The condition gradually changes from plane stress to plane strain with distance from the free surface. Hertzberg [*18*] shows that the depth of penetration of significantly nonplane strain effects is the same order of magnitude as the radius of the crack-tip plastic zone size under plane-stress conditions (see Fig. 5). The non-plane-strain region can be detrimental because metals are generally much tougher in plane stress than in plane strain. Therefore, attempts to measure the plane-strain fracture toughness in specimens with substantial non-plane-strain regions at the flank ends of the crack can result in high values of the fracture toughness.

The existence of the non-plane-strain region at the flank end of a crack intersecting a lateral free surface is readily apparent in ductile material because of the inward dimpling which occurs there (Fig. 5), proving that lateral plastic straining has occurred. It would seem that the non-plane-strain region could be minimized by not allowing the crack to intersect a lateral free surface at all, but instead by causing the crack flanks to follow thin slots such

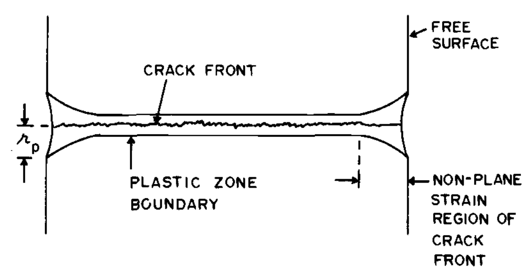

FIG. 5—*Schematic of the plastic zone boundary at a crack front. The crack is advancing perpendicular to the page. Note the inward dimpling of the free surfaces at the flank ends of the crack.*

as those of the short rod specimen. The inward plastic straining which appears as dimpling at the flank ends of the crack should be drastically reduced by sufficiently thin slots, that is, slots whose thickness is much smaller than the plane-stress plastic zone size, which is approximately [*19*]

$$r_p = \frac{1}{2\pi} (K_{\mathrm{Ic}}/\sigma_{\mathrm{ys}})^2$$

Alternatively, sharp-bottomed slots or side grooves should accomplish the same effect. Of course, whenever r_p is very much smaller than the distance along the crack front, the crack should be in good plane-strain constraint regardless of the specimen geometry at the flank ends of the crack.

To test these ideas, and to determine the magnitude of the non-plane-strain effects in short rod specimens, a study was made of the effects of slot thickness and the sharpness of the slot bottom. Two aluminum and three steel materials were chosen to span a wide range of crack-tip plastic zone sizes. The materials and their mechanical properties are listed in Table 2. Over 130 short rod specimens with B = 25.4 mm (1 in.) were tested in the study. Slot thicknesses of from 0.38 to 1.6 mm (0.015 to 0.062 in.) were tried, and square, round, and 60-deg included angle pointed slot bottoms were used for each slot thickness. The radius of curvature at the tips of the pointed slot bottoms was always less than 0.08 mm (0.003 in.).

It was found, as expected, that the slot bottom geometry made no detectable difference for the very brittle material [440 C stainless steel at a Rockwell C hardness (HRC) of 56], in which the plane-stress plastic zone size was only about 0.03 mm (0.001 in.). The plastic zone size, and thus the non-plane-strain region, was so small compared with the specimen dimensions that the crack front was always in very good plane-strain constraint for all three of the slot bottom geometries. The slot thickness had a slight effect on the specimen calibration, however, because a consistent decrease in apparent toughness with increasing slot thickness was observed. The 440 C stainless steel specimens with 1.6-mm slots gave toughness readings about 3 percent lower than the specimens with 0.38-mm slots.

TABLE 2—*Properties of the materials of the slot geometry study.*

Material	*Yield,* MPa	*Hardness* HRC	*Crack* Orientation	r_p[a], mm	K_{IcSR},[b] MPa$\sqrt{\mathrm{m}}$
4340 steel	807	25	T-L	1.50	78.4
4340 steel	1210	42	S-L	0.64	77.0
440C stainless	1860	56	C-L	0.03	26.0
2419-T851 Al	334	...	T-L	1.41	31.4
7075-T651 Al	469	...	C-L	0.27	19.4

[a] Radius of the plane-stress crack-tip plastic zone.
[b] Plane-strain critical stress-intensity factor as measured by the short rod method.

The effects of the non-plane-strain regions were quite apparent in the materials with larger r_p's. In the specimens with round and square slot bottoms, there was a consistent increasing trend in the apparent toughness with increasing slot thickness, in spite of the decreasing trend due to specimen calibration deduced from the 440 C stainless steel tests. The increase was generally smaller for the round-bottom specimens than for the square-bottom specimens of the same slot thickness, indicating, as might be expected, that the round slot bottoms are more effective at limiting the non-plane-strain regions than square slot bottoms. Among the specimens with sharp-pointed slot bottoms, however, the plane-strain constraint appeared to be excellent, regardless of the slot thickness. In fact, the apparent toughness appeared to *decrease* about 3 percent as the slot thickness was increased from 0.38 to 1.6 mm. The 3 percent decrease is undoubtedly caused by the same change in the specimen calibration with increasing slot thickness which was observed in the 440 C stainless steel specimens with the extremely small crack-tip plastic zone size.

The specimen slot configurations, their effects on the specimen calibration, and their plane-strain constraint ratings based on these tests are shown in Table 3. From this study, it would seem that the 0.38-mm sharp-pointed, the 0.8-mm sharp-pointed, and the 0.38-mm round-bottom slot geometries may be considered as equally preferable and interchangeable. The 1.6-mm sharp-pointed slot has excellent plane-strain constraint, but its calibration is significantly different from the other configurations rated "excellent." In addition, the thicker slots significantly weaken the specimen, causing it to be more limited in its ability to test tough, low-yield-strength materials.

It is also important to note the rather dramatic effect which the degree of plane-strain constraint has on the general appearance of the load-displacement test record. Figure 6 shows two test records of the same 4340 steel which are typical of the "excellent" and the "poor" plane-strain constraint specimens. The records of the "excellent" specimens had the general shape of ideal LEFM records,[4] and the maximum load occurred close to the point at which the crack passed through the critical crack length, a_c. The poor plane-strain constraint records, on the other hand, had rapidly decreasing loads when the crack passed through a_c.

It is recognized, of course, that the chevron slots in short rod specimens are, in effect, side grooves. Side-grooving of other fracture toughness specimens has been tried many times in the past with varying degrees of success. In some cases it has seemed beneficial in promoting flat fracture surfaces and plane-strain conditions [*20–22*], while in others it seems to have complicated the fracture toughness test results in an unpredictable way [*23–25*]. In the case of the short rod specimen the side grooves are an integral part of the specimen configuration and the data analysis equations. The slot

[4]Patent No. 4,198,870.

TABLE 3—*Summary of slot geometry study results.*

SLOT CONFIGURATION	SLOT THICKNESS (mm)	EFFECT ON SPECIMEN CALIBRATION	PLANE-STRAIN CONSTRAINT*
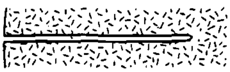	0.38	0	Excellent
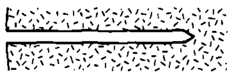	0.8	-1%	Excellent
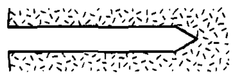	1.6	-3%	Excellent
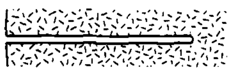	0.38	0	Excellent
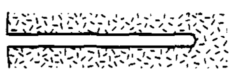	0.8	-1%	Good
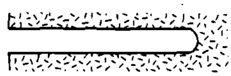	1.6	-3%	Poor
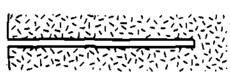	0.38	0	Good
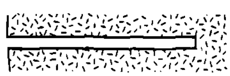	0.8	-1%	Poor
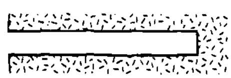	1.6	-3%	Poor

* Excellent = less than +2% effect on the measurement
Good = less than +5% effect on the measurement
Poor = more than +5% effect on the measurement

configuration study reported in the foregoing indicates very strongly that properly designed slots can greatly enhance the degree of plane-strain constraint along the crack front. It is also noteworthy that the short rod is a crack-line-loaded specimen, and that side grooving has appeared to be the most beneficial and the least confusing in crack-line-loaded specimens [*20,21*].

Test Configuration

Not only are specimen geometry and preparation important in short rod measurements of fracture toughness, but the testing procedure must also be controlled in order to obtain valid toughness data. In this section the

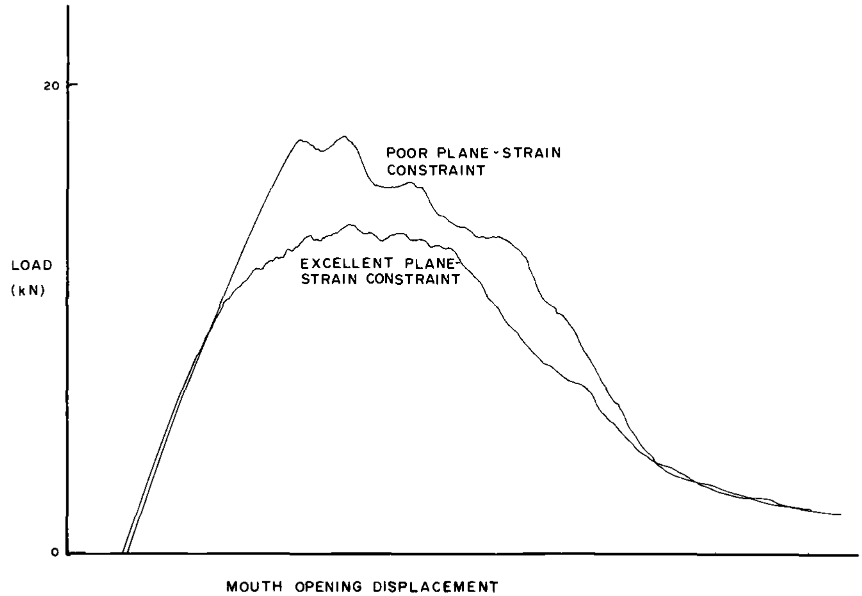

FIG. 6—*Test records of two 4340 steel specimens with excellent and poor plane-strain constraint.*

desirable characteristics of the test machine and the loading geometry are discussed, after which the test configuration is described. First, however, a brief description of the mechanics of a short rod test is in order.

Short Rod Test Description

In fracture toughness testing of short rod specimens, an opening load is applied near the mouth of the specimen, causing a crack to initiate at the point of the chevron slot. Ideally, the opening load at crack initiation is smaller than the load that will further advance the crack just after initiation, and a continually increasing load must be supplied until the crack length reaches a critical value, a_c. Beyond a_c, the crack-advancing load begins to decrease, as shown in Fig. 7.

Accurate short rod tests of metallic materials usually require the measurement of the load versus mouth opening displacement curve during the test [*4*]. Such curves can often be of value also when testing the more brittle nonmetals. Two unloading and reloading cycles are normally drawn during the test, as shown in Fig. 8.

Test Configuration Requirements

Test Machine Stiffness—Some materials can exhibit a "pop-in" crack initiation behavior in which the load to initiate the crack at the point of the

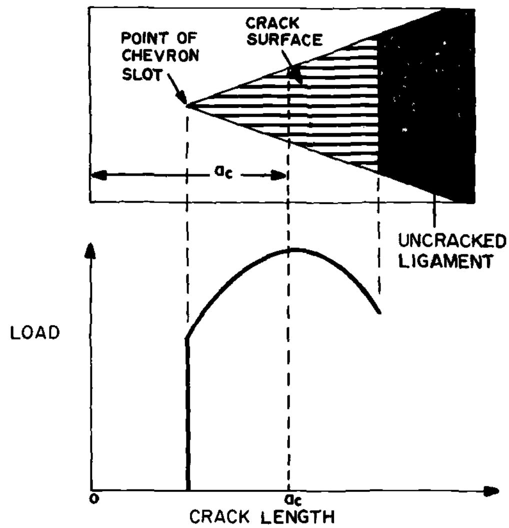

FIG. 7—*Variation of the crack-advancing load with crack length in a short rod specimen.*

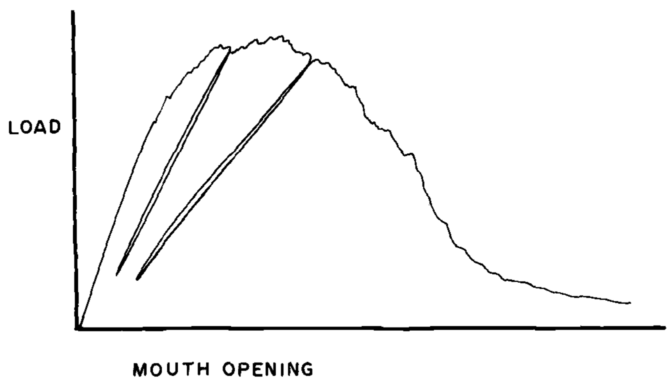

FIG. 8—*A short rod test record.*

chevron slot can be higher than the load during the rest of the test. When this occurs, a stiff testing machine is necessary to keep the specimen mouth opening nearly constant as the load suddenly drops due to crack growth. Minimal additional mouth opening after the initial pop-in allows the crack to arrest immediately upon the dissipation of the stored elastic energy of the specimen (Fig. 9). If the testing machine is not sufficiently stiff, it tends to increase the mouth opening of the specimen by contributing additional elastic energy in response to the sudden load drop. This can invalidate the test by causing the initial pop-in crack to catastrophically propagate through the entire specimen, as indicated by the dashed line of Fig. 9.

Minimum Load-Line Change—For accurate and repeatable short rod test

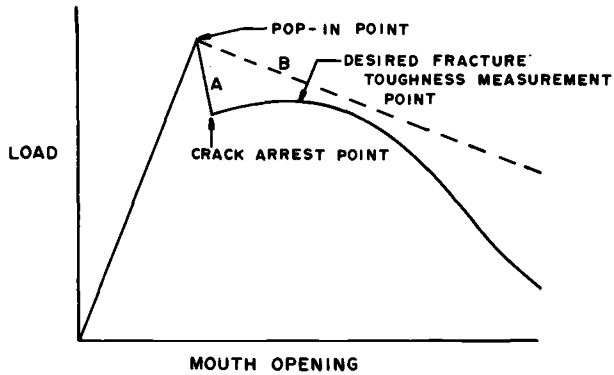

FIG. 9—*Stiff machine characteristic (A) allows crack arrest soon after pop-in. Soft machine characteristic (B) maintains more load, causing the crack to run through the entire specimen and to bypass the desired measurement point. The pop-in load does not relate to the fracture toughness.*

results, it is important to mount the specimen on the test machine so that the opening load will be applied along the intended load line within the grip groove (Figs. 1 and 2). The reason, of course, is that the specimen calibration is a function of the load-line location. Furthermore, the location of the load line must not change during the test. If the loading configuration is not carefully designed, the flexing of the specimen during the test can result in significant changes in the location of the load line. Variation of the load line during the test produces an uncertainty not only in the specimen calibration, but also in the unloading slopes which are used in the data analysis.

Minimum Friction—It is well-known that friction in the load train between the load transducer and the specimen, and friction resulting from the flexing of the specimen during the test, can adversely affect the accuracy of the test result. The ASTM Method E 399-78a, for example, specifies loading mechanisms designed to accommodate the specimen flexing through rolling friction, rather than sliding friction. Similarly, any system for accurate testing of short rod specimens must minimize any deleterious friction effects.

Minimum Plastic Deformation—It is important to minimize any plastic deformation which may occur where the loading mechanism contacts the specimen. Plastic deformation of the specimen at the loading lines can result in friction due to specimen flexing, and can also change the location of the load line. The deformation itself, being irreversible, can have an effect similar to friction in producing measurement errors. Thus, the lines of contact between the specimen and the loading machine must be carefully designed to minimize any plastic deformation.

The Fracjack Loading Mechanism[4]

A short rod fracture toughness test configuration which is remarkably successful at meeting the above requirements makes use of a loading mechanism called a Fracjack [26]. The Fracjack, shown schematically in Fig. 10, has the added attributes that it allows for easy control of the specimen's temperature during the test, that the specimen installation and alignment are very simple, and that a very wide variety of materials can be tested. Various aspects of the Fracjack testing configuration are described in the following.

Grip Design—The grip design in use is shown schematically in Fig. 11*b*, while less-desirable alternative designs are shown in Figs. 11*a* and 11*c*. The grips of Fig. 11*b* have cylindrically crowned contact surfaces with a radius of curvature of $^1/_2B$; that is, they have the same curvature as the outside surface of the short rod specimen. Using the cylindrically crowned contact surface rather than a flat one (Fig. 11*a*) allows adequate control of the load line position (see features described in the following). Using an angle-crowned contact surface (Fig. 11*c*) would further improve the control of the load-line position, but would also lead to excessive plastic deformation of the specimen along the load line. The cylindrically crowned surface produces very limited plasticity even in the softest and toughest specimens which can be tested.

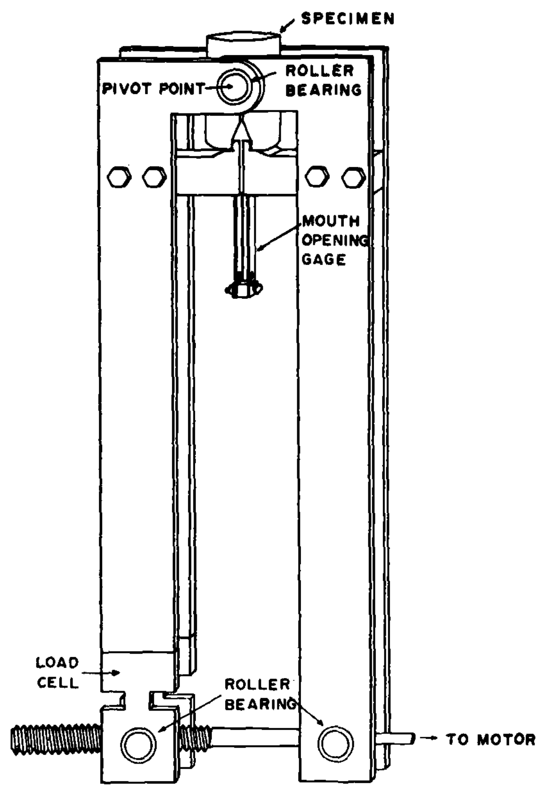

FIG. 10—*Schematic drawing of the Fracjack specimen loading mechanism. The strain-gaged members serve as the load transducer.*

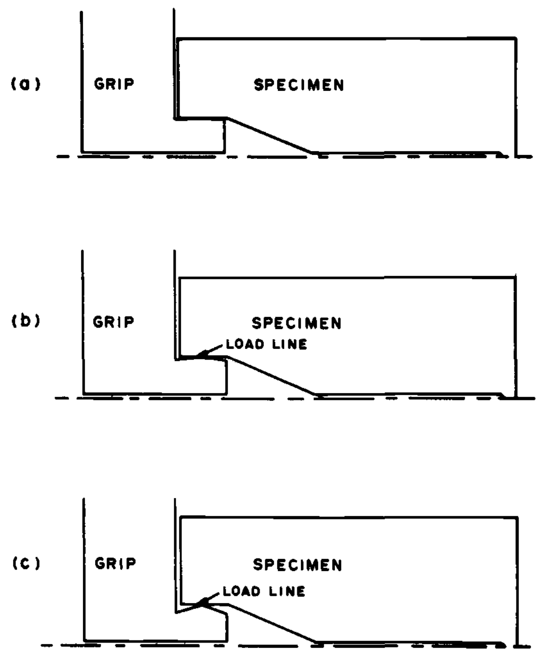

FIG. 11—*Grip designs with (a) flat, (b) cylindrical-crown, and (c) angle-crown contact surfaces.*

Automatic compensation for any small variation in the load line position is discussed next.

Specimen Flexing and Grip Rotation—As the grips apply a load to the specimen, the specimen mouth flexes open. If the grips are pulled apart along a straight line as by a conventional tension test machine, the location of the load line will change as the angle of the specimen's grip contact surface changes, as can be visualized from Fig. 11*b*. The change in the load line location is further aggravated if the specimen grip contact surfaces experience any plastic yielding. In some materials the load-line change can easily exceed five times the tolerance normally allowed on the distance from the load line to the point of the chevron slot. Finally, the amount of plastic deformation is increased due to the "rolling down" of the specimen's grip contact surfaces by the grips. The increase in plastic deformation constitutes an irrecoverable work expenditure which is attributable to the flexing of the specimen. Thus, as discussed previously, it produces a further degradation in the accuracy of the test.

To prevent the "wandering" of the load line during the test, the Fracjack rotates the grips as they load the specimen. The rotation closely matches that of the specimen's grip contact surface, thus minimizing any change in the location of the load line during the test. Friction and plastic deformation due to flexing of the specimen are also minimized by matching the grip rotation to that of the specimen. The rotating grip concept thus alleviates most of the problems associated with the testing of short rod specimens. The major remaining concern (addressed next) is the accurate location of the original load line. Although the rotating grips tend to maintain a constant load-line position, the small curvature of the crown on the grips still prevents a completely precise location of the initial load line position.

Automatic Compensation for Load Line Variance—The reason for the concern over the load-line location, of course, is that the load required to advance the crack is a function of the load-line location. The larger the distance from the specimen front face to the load line, the larger will be the load necessary to advance the crack at any given crack length. Suppose, now, that we apply the load through a device which has a mechanical advantage between the measured input load and the load actually applied to the specimen. Suppose further that the mechanical advantage is a function of the load-line location, and that it increases as the distance from the specimen's front face to the load line increases. Then, if the load line is somehow deeper into the specimen mouth than its nominal location, the load applied to the specimen will be larger than that calculated from the input load and the nominal mechanical advantage. However, a larger load *is required* to advance the crack when the load line is too deep in the specimen mouth. Thus, the errors in the required load and in the load actually applied to the specimen tend to cancel. The Fracjack is designed such that the mechanical advantage variation with load-line position compensates for at least 90 percent of the variation in the load required to advance the crack.

The automatic compensation for variation of the load line position is important primarily because of machining tolerances on the grips and the specimen's grip surfaces, which can affect the location of the initial load line. In addition, the automatic compensation corrects for any slight load line changes which may still occur during the test due to imperfect matching of the grip rotation to the flexing of the specimen.

Specimen Mouth-Opening Gage: Short rod tests of ductile material involve the recording of the load applied to the specimen versus the opening of the specimen mouth. For accuracy, the mouth-opening transducer must sense the specimen itself, rather than sensing some related motion, such as the parting of the grips. For maximum convenience in aligning the specimen with respect to the grips and in installing the mouth-opening transducer, the arrangement of Fig. 12 is used, which shows a short rod specimen about to be mounted on the grips. The grips are horizontal, and the specimen axis is vertical as it is mounted. The specimen is lowered over the grips until it rests on the specimen landing surface, where it is held by gravity until the test is started. Before specimen installation, the mouth-opening gage arms are spring-loaded against the slots in the Fracjack grips through which they protrude. As the specimen is lowered, the specimen's grip slot rides down over

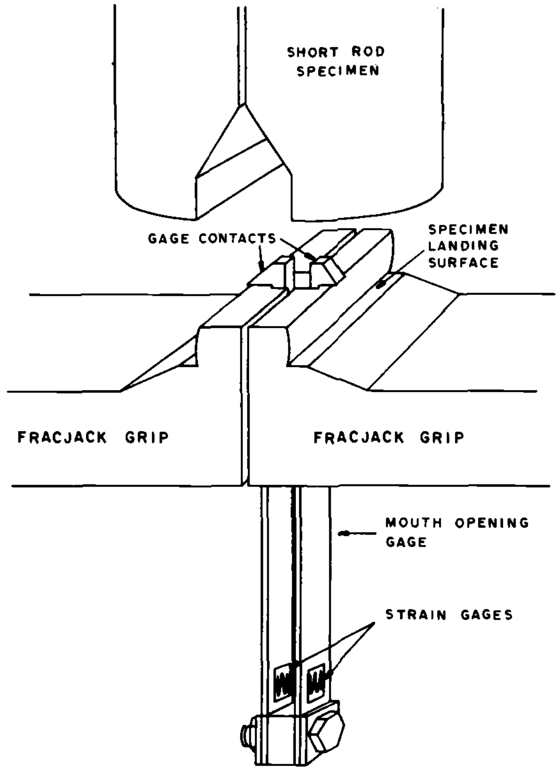

FIG. 12—*Short rod specimen about to be installed on the Fracjack grips, showing the mouth-opening gage configuration.*

the slanted surfaces of the gage contacts, flexing the gage arms slightly closer together. Thus, when the specimen is in position on its landing surface, the mouth-opening gage is also automatically installed and ready for the test. Note that this arrangement also keeps the mouth-opening gage completely out of the way, allowing maximum access to the specimen for temperature or environment control purposes. The mouth-opening gage arms are made sufficiently resistant to heat transfer so that the strain-gaged section experiences little temperature change even when the specimen is held at a relatively high temperature.

Summary

Certain short rod and short bar fracture toughness test methods for metallic materials have evolved as a result of considerable research, development, and testing experience. The studies which led to the particular geometries in use have been reviewed. Some flexibility in geometry is possible

without changing the calibration of the specimen; that is, circular-cross-section short rods or rectangular short bars can be used interchangably, and the chevron slots can be either straight or curved, provided the appropriate dimensions are used. The results of a recent study on the effects of chevron slot thickness and the sharpness of the slot bottoms indicate that slot thinness and bottom sharpness both help to promote good plane-strain conditions along the crack front.

The various desirable aspects of the specimen loading configuration have been discussed. A Fracjack mechanism which meets the desired test machine characteristics remarkably well has been developed. The Fracjack freatures enhance the accuracy, convenience, and versatility of short rod and short bar fracture toughness testing.

Acknowledgment

The author gratefully acknowledges the contributions of Mr. Randall V. Guest, whose expertise in design and whose technical consultations have been invaluable in developing the short rod technique. This work was supported in part by the National Science Foundation.

References

[1] Barker, L. M., *Engineering Fracture Mechanics*, Vol. 9, 1977, p. 361.
[2] Barker, L. M. in *Proceedings* ICM-II Conference, Boston, Mass., 1976, p. 1547.
[3] Barker, L. M. in Fracture Mechanics Applied to Brittle Materials, *ASTM STP 678*, American Society for Testing and Materials, 1979, pp. 73-82.
[4] Barker, L. M., *International Journal of Fracture*, Vol. 15, No. 6, 1979, pp. 515-536.
[5] Koblitz, F. F., Luna, V. R., Glenn, J. F., and DeVries, K. L. in *Organic Coatings and Plastics Chemistry*, Vol. 38, 1978, p. 322.
[6] Munz, D., Bubsey, R. T., and Srawley, J. E., *International Journal of Fracture*, Vol. 16, 1980.
[7] Munz, D., Bubsey, R. T., and Shannon, J. L., *ASTM Journal of Testing and Evaluation*, 5 June 1979.
[8] Smyth, R. R., Bentsen, L., and Youngblood, G. E., "Corrosion Effects in a Fused-Cast $MgO:MgAl_2O_4$ Refractory," presented at the 81st Annual Meeting of the American Ceramic Society, Cincinnati, Ohio, 29 April 1979.
[9] Marion, R. H. and Cuthrell, R. E., "Effect of Various Liquids on Crack Propagation in Glass," presented at the 81st Annual Meeting of the American Ceramic Society, Cincinnati, Ohio, 29 April 1979.
[10 Drake, E. F. and Krawitz, A. D., "Fatigue Damage and Crack Propagation in a WC-Cemented Carbide Composite," presented at the 7th National Science Foundation Hard Materials Workshop, Illinois Institute of Technology, Chicago, Ill., 29 June 1979.
[11] Barker, L. M. and Baratta, F. I., *ASTM Journal of Testing and Evaluation*, May 1980.
[12] Tattersall, H. B. and Tappin, G., *Journal of Material Science*, Vol. 1, 1966, p. 296.
[13] Bluhm, J. I., *Engineering Fracture Mechanics*, Vol. 7, 1975, pp. 593-604.
[14] Simpson, L. A., *Journal of the American Ceramic Society*, Vol. 56, No. 1, 1973, p. 7.
[15] Davidge, R. W. and Tappin, G., *Journal of Materials Science*, Vol. 3, 1968, p. 165.
[16] Pook, L. P., *International Journal of Fracture Mechanics*, Vol. 8, 1972, pp. 103-104.
[17] Barker, L. M. and Guest, R. V., "Compliance Calibration of the Short Rod Fracture Toughness Specimen," Terra Tek Report TR 78-20, Salt Lake City, Utah 1978.
[18] Hertzberg, R. W., *Deformation and Fracture Mechanics of Engineering Materials*, Wiley, New York, 1976, p. 279 and 280.

[19] McClintock, F. A. and Irwin, G. R. in *Fracture Toughness Testing and Its Applications, ASTM STP 381,* American Society for Testing and Materials, 1965, pp. 84–113.
[20] Mostovoy, S., Crosley, P. B., and Ripling, E. J., *Journal of Materials,* Vol. 2, 1967, pp. 661-681.
[21] Marcus, H. L. and Sih, G. C., *Engineering Fracture Mechanics,* Vol. 3, 1971, p. 453.
[22] Shih, C. F., Andres, W. R., DeLorenzi, H. G., Van Stone, R. H., Yukawa, S., and Wilkinson, J. P. D., "Crack Initiation and Growth Under Fully Plastic Conditions: A Methodology for Plastic Fracture," Report No. 78CRD038, General Electric Corporate Research and Development, Schenectady, N.Y., 1978.
[23] Freed, C. N. and Krafft, J. M., *Journal of Materials,* Vol. 1, 1966, p. 770.
[24] Brown, W. F., Jr. and Srawley, J. E. in *Plane Strain Crack Toughness Testing of High-Strength Metallic Materials, ASTM STP 410,* American Society for Testing and Materials, 1966, pp. 48-51.
[25] Nelson, F. G., Schilling, P. E., and Kaufman, J. G., *Engineering Fracture Mechanics,* Vol. 4, 1972, pp. 33-50.
[26] Barker, L. M., "Development of the Fractometer II System for Fracture Toughness Testing Using Short Rod and Short Bar Specimens," Terra Tek Report TR 79-32, Salt Lake City, Utah, June 1979.

H. A. Ernst,[1] *P. C. Paris,*[2] *and J. D. Landes*[1]

Estimations on J-Integral and Tearing Modulus *T* from a Single Specimen Test Record

REFERENCE: Ernst, H. A., Paris, P. C., and Landes, J. D., "**Estimations on J-Integral and Tearing Modulus *T* from a Single Specimen Test Record**," *Fracture Mechanics: Thirteenth Conference, ASTM STP 743,* Richard Roberts, Ed., American Society for Testing and Materials, 1981, pp. 476-502.

ABSTRACT: This paper presents methods for evaluating the J-integral and the tearing moduli from a single test record. Several different aspects of the problem have been combined in this work. An overview of the conditions for separability of the load into multiplicative functions of displacement and crack length as well as for the existence of η-factors is presented. The consequences of expressing J by a Merkle-Corten type formula are explored in terms of the crack increment, da, the tearing modulus, T, and J itself, including the case of growing cracks. A simple method is suggested to obtain the correct J for crack growth and T from nothing more than the test record itself; the procedure is applied to available experimental data and the results are compared with those obtained by other formulae. Additional physical interpretation is given on the T_{mat}-versus-T_{app} stability criterion and the remaining compliance capacity C_{CR} is defined.

KEY WORDS: cracks, mechanical properties, load-displacement records, analysis, structure, J-integral, J-R curves, tearing modulus T, single record

With the development of elastic-plastic fracture mechanics methods the J-integral [*1-3*][3] has been accepted as the principal parameter for characterizing fracture behavior. Since the introduction of the multispecimen technique by Begley and Landes [*4,5*] significant effort has been devoted to obtain J using the smallest possible number of specimens. Among others, most notable is the analysis of Rice et al [*6*], which allows the calculation of J from a single load-displacement record for different configurations where the remaining ligament, b, is the only significant length parameter (that is, b is very small compared with any other planar dimension). In particular, their

[1] Senior engineer and advisory engineer, respectively, Materials Engineering Department, Westinghouse R&D Center, Pittsburgh, Pa. 15235.
[2] Professor, Center for Fracture Mechanics, Washington University, St. Louis, Mo. 63130.
[3] The italic numbers in brackets refer to the list of references appended to this paper.

result for pure bending, $J = (2/b) A$ (where A is the area under the generalized force per unit thickness—generalized force point displacement diagram), has been widely used since then for all bending configurations.

A modification of the preceding expression was presented by Merkle and Corten [7] for the compact specimen, which takes into account the tensile component of the load. The resulting expression for J is $J = (\eta/b) A$ where $\eta = 2 + (0.522)(b/W)$ [8].

At the same time J had been tentatively regarded as the controlling parameter in the presence of crack growth and the J-R curve concept was introduced.

Hutchinson and Paris [9], in a recent work, proved that there is indeed a J-controlled crack growth regime for limited amounts of crack extension. Thus, lately, it has become common practice to characterize the material resistance to fracture by means of the J-R curve. For the compact specimen, this curve is obtained by using the Merkle-Corten expression for J, and by measuring the crack length change by the unloading compliance method [10]. But, although some formulas were developed (dealt with later), the matter on how to evaluate J in the presence of crack growth was not completely settled for some investigators.

A method to calculate J was proposed by Hutchinson and Paris [9] and generalized later by Ernst et al [11,12]. This method takes into account the influence of crack growth on J, and the presented formulas are regarded as exact from an analytical point of view. This result demonstrated that J had not been always correctly evaluated.

Although exact, these methods require a significant amount of numerical work in order to evaluate the P-δ record. Thus it is necessary, for convenience, to develop simpler formulas for the correct J for crack growth.

In this work, the consequences of expressing J by the Merkle-Corten formula are explored in terms of J itself, the crack increment, da, and the tearing modulus, T [13,14]. Additional physical interpretation is given on the material versus applied tearing modulus stability criterion, and a simple method for evaluating J, following the actual path of the P-δ record, is suggested. The procedure is applied to available experimental data and the modified J-R curves are shown. Comparisons with other proposed expressions for J corrected for crack growth are also discussed.

The J-Integral

Consider an homogeneous body which exhibits an elastic (linear or nonlinear) behavior, free of body forces, with a crack or notch parallel to the x-axis and subjected to a 2-D deformation field [all $\sigma_{ij} = \sigma_{ij}(x, y)$]. Define now the integral

$$\int W_s dy - T_i \frac{\partial u_i}{\partial x} ds \tag{1}$$

where

W_s = strain energy density,
T_i = traction vector components,
u_i = displacement vector components,
x, y = rectangular coordinates as noted,
ds = element of arc along the path of integration.

Rice [1] proved that if the integral is evaluated along any closed curve S lying completely inside the body (not encompassing any singularity), the result is identically zero

$$\int_S W_s dy - T_i \frac{\partial u_i}{\partial x} ds = 0 \tag{2}$$

As a consequence, if now the integral is taken along an open curve Γ, surrounding the crack tip, going from the lower surface to the upper one, and lying completely inside the body, the result of evaluating the integral is a unique value for all contours Γ, which Rice called J.

$$\int_\Gamma W_s dy - T_i \frac{\partial u_i}{\partial x} ds = J \tag{3}$$

The uniqueness of the result implies that J is a crack-tip characterization parameter, the crack tip being the only point enclosed by all Γ-type curves. In fact, it has been shown by Hutchinson [2] and Rice and Rosengren [3] that the crack-tip singular stress-strain fields can be completely characterized in terms of J; thus J is a measure of the intensity of the crack-tip singularity.

An alternative, equally valid definition was also provided by Rice [15]: J can be interpreted as the rate of change of potential energy per unit cracked area. That is

$$J = -\frac{dU}{Bda} \tag{4}$$

where U is the potential energy and b is the thickness. This definition relates J to exteriorly measurable quantities like the load and the displacement. In fact, in P-δ records (where P is load per unit thickness and δ is the load-point displacement) for slightly different crack lengths in otherwise identical specimens, the area between curves is $J\,da$. Therefore, and alternative definition of J is

$$J = -\frac{dU}{Bda} = -\int_0^\delta \frac{\partial P}{\partial a} d\delta = \int_0^P \frac{\partial \delta}{\partial a} dP \tag{5}$$

where δ is the load-point displacement due to the crack only.

This result enabled Begley and Landes [*4,5*] to do the first experimental evaluation of J. Using the so-called multispecimen technique they obtained J as a function of crack length and level of applied deformation (δ or P) for different configurations.

A Convenient Form of the J-Integral

It is sometimes convenient, as will be seen later, to divide the displacement in a P-δ record into its elastic δ_{el} and nonlinear (plastic) δ_{pl} parts, as shown in Fig. 1. At any given point in the P-δ diagram, the δ_{el} can be calculated as load times the elastic compliance, the δ_{pl} being the difference between the total displacement δ and δ_{el}

$$\delta = \delta_{el} + \delta_{pl} \tag{6}$$

Then following Eq 5

$$J = \int_0^P \left.\frac{\partial \delta}{\partial a}\right)_P dP = \int_0^P \left.\frac{\partial \delta_{el}}{\partial a}\right)_P dP + \int_0^P \left.\frac{\partial \delta_{pl}}{\partial a}\right)_P dP \tag{7}$$

The first term of Eq 7 is the linear component of J: J_{el} or simply the Griffith [*16*] G. The second term is the nonlinear component, J_{pl}, of J. As shown by Ernst et al [*10,11*], if second-order differentials are neglected, this term can be written as

$$\int_0^P \left.\frac{\partial \delta_{pl}}{\partial a}\right)_P dP = -\int_0^{\delta_{pl}} \left.\frac{\partial P}{\partial a}\right)_{\delta_{pl}} d\delta_{pl} = \int_0^{\delta_{pl}} \left.\frac{\partial P}{\partial b}\right)_{\delta_{pl}} d\delta_{pl} \tag{8}$$

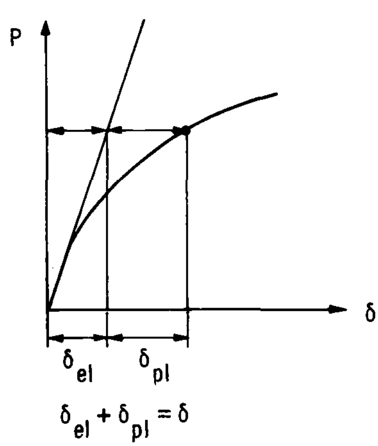

FIG. 1—*Load displacement record. Separation of the displacement in its elastic and plastic parts.*

giving then as a result

$$J = G + \int_0^{\delta_{pl}} \left. \frac{\partial P}{\partial b} \right)_{\delta_{pl}} d\delta_{pl} \tag{9}$$

where b is the remaining ligament. Equation 9 gives a convenient method for computing J without any loss in analytical precision compared with the original form, Eq 5. Without ambiguity G is always to be computed using linear elastic fracture mechanics (LEFM) formulas, using the actual load and crack length a (without plastic zone correction).

In particular for bending configurations, it has proven convenient [*9,11,12*] to express the load per unit thickness, P (as an extension of Rice et al [*6*], as

$$P = \frac{b^2}{W} F(\delta_{pl}/W, a/W) \tag{10}$$

This form is completely general and has the advantage that F is very weakly dependent on a/W. In other words, the main dependence of P on a/W is given by b^2. In fact for $a/W \to 1$

$$\frac{\partial F}{\partial(a/W)} \to 0$$

also, for the three-point bending specimen (3 PB), it can be considered that

$$\frac{\partial F}{\partial(a/W)} \approx 0$$

for all a/W of interest.

Substituting now Eq 10 into Eq 9, the expression for J for bending configurations becomes

$$J = G + \frac{2b}{W} \int_0^{\delta_{pl}} F d\delta_{pl} - \frac{b^2}{W^2} \int_0^{\delta_{pl}} \frac{\partial F}{\partial(a/W)} d\delta_{pl} \tag{11}$$

$$J = G + \frac{2}{b} \int_0^{\delta_{pl}} P d\delta_{pl} - \frac{b^2}{W^2} \int_0^{\delta_{pl}} \frac{\partial F}{\partial(a/W)} d\delta_{pl} \tag{12}$$

Note that if

$$\frac{\partial F}{\partial(a/W)} = \alpha F\left(\frac{a}{W}\right) \tag{13}$$

then Eqs 11 and 12 become

$$J = G + \left(\frac{2b}{W} - \frac{b^2}{W^2}\alpha\right)\int_0^{\delta_{pl}} F d\delta_{pl} \tag{14}$$

$$J = G + \frac{1}{b}\left(2 - \frac{b}{W}\alpha\right)\int_0^{\delta_{pl}} P d\delta_{pl} \tag{15}$$

The conditions for Eq 13 to hold and its eventual implications are discussed in much greater detail in the next sections.

Work Factors

Although J can be experimentally obtained in general by using the multi-specimen technique [*4,5*], the possibility of its evaluation using the smallest possible number of specimens has been always of obvious importance. In particular, since the pioneer work by Rice et al [*6*], significant effort has been devoted to relate J to work done or area under the P-δ diagram.

In Ref *6* several configurations in the limit of very deep crack were analyzed in terms of J. In particular, the result for pure moment applied to a very small remaining ligament b was

$$J = \frac{2}{b}A \tag{16}$$

where A is the area under the P-δ record. Since then, this expression has been commonly used for all bending configurations.

More recently, modifications of the factor 2 in Eq 16 following Sumpter and Turner [*30*] have been attempted for compact tension (CT), in order to account for the tensile component. Thus, in general

$$J = \frac{\eta}{b}A \tag{17}$$

where η is a function of a/W only.

Obviously, this expression gives a very convenient way for evaluating J for bending configuration from single P-δ records. Nevertheless, from a analytical viewpoint it was not apparent why Eq 17 appeared to work, or, in other words, under which conditions J can be expressed as area times a factor depending solely on a/W, being independent of the level of deformation. In this matter some light was shed by the analysis of Paris et al [*17*] and Ernst and Paris [*12*]. In that work, necessary and sufficient conditions for the existence of the η-factor were explored (where by existence of η is meant here that Eq 17 holds with η as a function of a/W only).

The Elastic η-Factor

Among other things, it can be seen in Ref *12* that an elastic η-factor always exists. In other words, the elastic part of J, that is, G, can always be written as

$$G = \frac{\eta_{el}}{b} A_{el} \tag{18}$$

In fact if load and displacement are related by

$$PC = \delta_{el} \tag{19}$$

then applying the definition of Eq 7

$$G = \frac{P^2}{2} \frac{\partial C}{\partial a} \tag{20}$$

But also the area under the P-δ_{el} diagram is

$$A_{el} = \frac{P\delta_{el}}{2} \tag{21}$$

And then substituting in Eq 20

$$G = \frac{\eta_{el}}{b} A_{el} \text{ with } \eta_{el} = \frac{b}{C} \frac{\partial C}{\partial a} \tag{22}$$

The Plastic η-Factor

It was shown also in Ref *12* that a plastic η-factor; that is, η_{pl}, will always exist if and only if a separation of variables can be found for the expression of the load P in terms of a/W and the plastic displacement δ_{pl}

$$P = \frac{b^2}{W} F(\delta_{pl}/W, a/W) \tag{23}$$

Plotting now F versus δ_{pl}, as shown in Fig. 2, if all curves for each constant a/W-value are of height F in constant scale to each other, then the separation exists. Further, if this scaling exists for some range of a/W-values from $\delta_{pl} =$

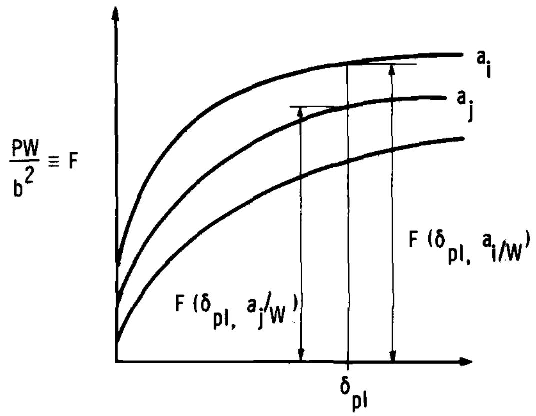

FIG. 2— F *versus* δ_{pl} *for different crack lengths.*

0 to some limiting value of δ_{pl}, that is, δ_{pl}^{limit}, then the separation of variables exists over that region; that is to say, if the condition

$$\frac{F(\delta_{pl}/W,\ a_i/W)}{F(\delta_{pl}/W,\ a_j/W)} = C_{ij} \tag{24}$$

where the C_{ij} constants for any value of a_i/W, a_j/W and for all δ_{pl} values for that region

$$\frac{a_i}{W} \leq \frac{a}{W} \leq \frac{a_j}{W}$$

and (25)

$$0 \leq \delta_{pl} \leq \delta_{pl}^{limit}$$

Then within that region, the separation of variables will exist and therefore η_{pl} will exist for that region.

It can be readily seen now that the condition of Eq 13 is equivalent to that of Eq 24; thus the term in brackets in Eq 15 can be defined as the η_{pl}. Moreover, if Eq 24 holds, F is separable in multiplicative functions of a/W and δ_{pl}, that is

$$F\left(\delta_{pl}/W, \frac{a}{W}\right) = g\left(\frac{a}{W}\right) \cdot H(\delta_{pl}/W) \tag{26}$$

and thus the load P is

$$P = \frac{b^2}{W}F = \frac{b^2}{W}g\left(\frac{a}{W}\right) \cdot H(\delta_{pl}/W) \tag{27}$$

The Eq 15 becomes

$$J = G + \frac{1}{b}\eta_{pl}\int_0^{\delta_{pl}} P d\delta_{pl} \tag{28}$$

with

$$\eta_{pl} = \left(2 - \frac{b}{W}\frac{g'}{g}\right) \tag{29}$$

It can be seen that the η_{pl} approach will give approximately correct results sufficiently accurate to be practically useful, if the condition of Eq 24 is only slightly violated.

Taking a more practical view, the accuracy of Eq 24 can be tested experimentally by testing identical configurations with identical material, differing only in their a/W-values to produce P versus δ_{pl} records, which can be plotted and tested numerically. Subsized (or blunt notch) specimens of the same configuration-material combination may be utilized for this purpose, which will avoid having crack growth prior to the $\delta_{pl}{}^{limit}$ of applicability. In this way the existence of η_{pl} can be directly experimentally decided.

A Compact Expression for J

In the previous section, it was proven that the ηs will exist provided that scaling factors exist, independent of the level of deformation, Eq 24. For this case J is

$$J = \frac{1}{b}(\eta_{el}A_{el} + \eta_{pl}A_{pl}) \tag{30}$$

It can be readily seen that the scaling factors mentioned do not have to be necessarily the same in the linear elastic and in the nonlinear elastic (plastic) region, thus giving in general $\eta_{el} \neq \eta_{pl}$. Nevertheless, if the scaling factors are the same (or nearly the same for practical purposes) throughout the region of interest (in displacement δ), then

$$\eta_{el} \simeq \eta_{pl} = \eta \tag{31}$$

the expression for J is

$$J = \frac{\eta}{b}A \tag{32}$$

and the load P is separable in functions of a/W and displacement δ ($\delta = \delta_{el} + \delta_{pl}$)

$$P = g_0\left(\frac{a}{W}\right)H(\delta/W) \tag{33}$$

Recently, it has been found experimentally [18] that values of J for the compact specimen could be obtained using Eq [32]. In fact, if the displacement is measured at the load line (instead of load point) and a single η ($\eta = \eta_{el} = \eta_{pl}$) is used, the resulting J is in excellent agreement with J obtained from the multispecimen techniques, the expression for η being

$$\eta = 2 + (0.522)\frac{b}{W} \tag{34}$$

It is emphasized here that this is a rather surprising result. In fact, J should be obtained by measuring the displacement at the load point and no single η should be used. As was shown before, the η_{pl} does not always exist, and if it does, is not expected to be, in general, equal to η_{el}. Nevertheless, the two simultaneous violations seem to produce an acceptable result in terms of experimental accuracy for J. Presently, this expression has been accepted and used by several investigators [8,19].

In the next sections, the consequences of assuming Eq 32 are explored in terms of J itself, the crack increment da, and the tearing modulus T—although no attempt is made to justify the starting assumption.

J for the Growing Crack

As was mentioned before, in this work the deformation theory interpretation of J is followed: J is a unique function of any two of the variables a, δ, P. In particular, consider a and δ as the independent ones from here on. Then J is a potential function of a and δ. In fact, for a given value of a and δ there is one and only one value of J associated with that particular pair (a, δ). This value is history-independent; it does not depend on the particular path followed in the a-δ plane to get to the point of interest.

Now if J is expressed as

$$J = \frac{\eta}{b}\int_0^\delta P\,d\delta \tag{35}$$

with $\eta = \eta(a/W)$, the separability of the load is automatically implied [11,12]

$$P = g_0\left(\frac{a}{W}\right)H(\delta/W) \tag{36}$$

as well as the existence of scaling factors for all a/W and δ of interest.

Using the more convenient form for bending

$$P = \frac{b^2}{W}g\left(\frac{a}{W}\right)H(\delta/W) \tag{37}$$

J becomes

$$J = \eta g \frac{b}{W} \int_0^\delta H d\delta = \frac{\eta}{b} \int_0^\delta P d\delta \tag{38}$$

with

$$\eta = \left(2 - \frac{b}{W} \frac{g'}{g}\right) \tag{39}$$

Note that the function g is automatically implied by Eq 39 combined with Eq 34

$$\frac{dg}{d(a/W)} + (0.522)g = 0 \tag{40}$$

$$g = k e^{(0.522)\, b/W} \tag{41}$$

In particular, the arbitrary constant k can be set equal to unity. In doing so, $g \rightarrow 1$ for $b/W \rightarrow 0$

$$g = e^{(0.522)\, b/W} \tag{42}$$

Replacing then Eq 42 in Eq 37 gives the load P

$$P = \frac{b^2}{W} e^{(0.522)\, b/W} H(\delta/W) \tag{43}$$

In the limit for $b/W \rightarrow 0$, the foregoing expression can be rearranged to give

$$\frac{PW}{b^2} = \frac{M}{b^2} = H(\delta/W) \equiv H(\theta) \tag{44}$$

where M is the applied bending moment per unit thickness and θ is the angle change between points of moment application. In this way, the result of Ref *6* is recovered.

Equation 38 is valid only for constant crack length a, although, as will be seen later, it can be used also for growing cracks if a correct interpretation of the quantities is made.

In general, taking a and δ as the independent variables, Eq 38 can be differentiated to give

$$dJ = \left\{ -\left(\eta - 1 - \frac{b}{W} \frac{\eta'}{\eta}\right) \frac{\eta g}{W} \int_0^\delta H d\delta \right\} da + \left\{ \frac{\eta b}{W} g H \right\} d\delta \tag{45}$$

and reintegrating

$$J = \int_{a_0}^{a} \left(-\gamma \frac{\eta g}{W} \int_0^{\delta} H d\delta \right) da + \int_0^{\delta} \frac{\eta b g}{W} H d\delta$$
$$= \int_{a_0}^{a} -\frac{J}{b} \gamma \, da + \int_0^{\delta} \frac{\eta b g}{W} H d\delta \tag{46}$$

where $\eta' = d\eta/d(a/W)$ and $\gamma(a/W)$ has been defined as

$$\gamma = \left(\eta - 1 - \frac{b}{W} \frac{\eta'}{\eta} \right) \tag{47}$$

Using Eq 34, γ can be approximated as

$$\gamma = 1 + (0.76) \frac{b}{W} \tag{48}$$

Thus, J can be obtained for any point in the P-δ record by evaluating Eqs 45 or 46 along any desired path from the origin to the point of interest. In particular the P-δ test record itself can be followed, as a special case. Joyce et al [*20,21*] obtained complete J-R curves from single test specimens using this method.

In what follows, some paths shown in Fig. 3 are analyzed in some detail.

Consider a path like Path 1; that is, crack length a, constant at current value of interest, a_i. This is the same curve that an identical specimen with initial crack a (constant) would have had. Thus in Eq 46 the first term vanishes and J is

$$J = \int_0^{\delta} \frac{\eta b g}{W} H d\delta = \frac{\eta b g}{W} \int_0^{H} d\delta = \frac{\eta}{b} \int_0^{\delta} P d\delta \tag{49}$$

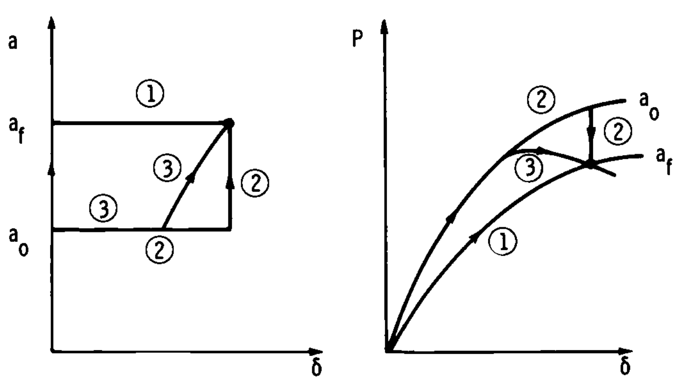

FIG. 3.—*Different possible paths in the* a-δ *and* P-δ *planes.*

where η/b is evaluated at the current crack length value and $\int_0^{\delta} P d\delta$ refers to the area under the P-δ record of the corresponding nongrowing crack curve. As was mentioned before, Eqs 38 and 49 are still correct for growing cracks provided the aforementioned interpretation is used.

Consider a path like Path 2; that is, constant $a = a_0$ up to final δ; then $\delta =$ constant and crack length growing from a_0 to current value a_i. The expression for J is

$$J = \tilde{J} - \int_{a_0}^{a} \gamma \frac{J}{b} da \tag{50}$$

where $\tilde{J}$ is

$$\tilde{J} = \frac{\eta b g}{W} \int_0^{\delta} H d\delta \tag{51}$$

with η, b, and g evaluated at initial crack length $a = a_0$ and δ is the displacement of the point of interest.

Crack Length Change and the Test Record as a Special Path

The crack length change can also be directly obtained from the P-δ record [*11,12*] without further instrumentation such as unloading compliance.

Using as the starting assumption the separability of the load, Eq 37 can be differentiated to give

$$\begin{aligned} dP &= -\frac{bgH}{W}\left(2 - \frac{b}{W}\frac{g'}{g}\right) da + \frac{b^2}{W^2} g H' d\delta \\ &= -\frac{\eta P}{b} da + \frac{b^2}{W^2} g H' d\delta \end{aligned} \tag{52}$$

$$da = \frac{b}{\eta}\left(-\frac{dP}{P} + \frac{H'}{H}\frac{d\delta}{W}\right) \tag{53}$$

where $H' = [dH]/d(\delta/W)$. This expression allows the change in crack length to be calculated directly from a single P-δ record. It can be also used to further simplify Eq 45 if the actual test record is followed, that is, Path 3 in Fig. 3. In fact, Eq 53 can be restated as

$$\frac{da}{d\delta} = \frac{b}{\eta}\left(\frac{H'}{WH} - \frac{dP}{P d\delta}\right) \tag{54}$$

Replacing now Eq 54 in Eq 45 gives

$$dJ = \left\{ -\frac{J}{\eta}\gamma\left(\frac{H'}{WH} - \frac{dP}{Pd\delta}\right) + \eta\frac{P}{b} \right\} d\delta \tag{55}$$

where P and $dP/d\delta$ are to be taken from the actual P-δ test record; the rest of the quantities in the bracket are evaluated at current values of a and δ.

As Eq 45, Eq 55 is ideal for a step-by-step integration procedure to obtain J, the advantage of the latter being its simpler form involving only one differential, that is, $d\delta$.

Method to Correctly Evaluate J in the Presence of Crack Growth from a Single Test Record

The differential expression for J, Eq 45, and the resulting expressions for different paths are exact, but knowledge of the $H(\delta/W)$ function is needed (g is automatically implied by the form of η as discussed previously).

In this section a method is presented to correctly evaluate J, in the presence of crack growth from the test record only.

Consider a point [A] in Fig. 4, J at [A]; J_A can be calculated following Eq 42 as

$$J_A = \frac{\eta g b}{W} \int_0^{\delta_A} H d\delta = \frac{\eta}{b} \int_0^{\delta_A} P d\delta \tag{56}$$

where δ_A is the value of δ at [A] and η, g, and b are evaluated at the corresponding crack length value, say a_1.

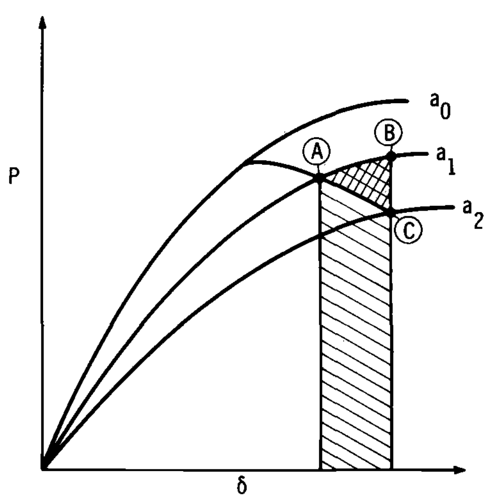

FIG. 4.—P-δ *diagram for nongrowing cracks and actual test record.*

Consider now a point [B], lying on the same nongrowing crack curve (δ_B, a_1); J at [B] is

$$J_B = \frac{\eta b g}{W} \int_0^{\delta_B} H d\delta = \frac{\eta}{b} \int_0^{\delta_B} P d\delta \tag{57}$$

Relating now Eqs 56 and 57

$$J_B = J_A + \frac{\eta}{b} \int_{\delta_A}^{\delta_B} P d\delta \tag{58}$$

where as before the integral represents the area under the nongrowing crack curve.

If now a point [C] is considered, J at [C], J_C, can be related to J_B by Eq 43

$$J_C = J_B - \int_{a_0}^{a} \gamma \frac{J}{b} da \tag{59}$$

Or using Eq 58, J_C and J_A can be related as

$$J_C = J_A + \frac{\eta}{b} \int_{\delta_A}^{\delta_B} P d\delta - \int_{a_0}^{a} \gamma \frac{J}{b} da \tag{60}$$

Note that up to this point no approximation has been made (besides the starting one, Eq 35 and so Eq 60 is completely general. Now if Points [A], [B], and [C] are close to each other, some approximations can be made in order to simplify the foregoing expression.

In fact, in the limit for differential steps, the integral in the second term in Eq 60 can be approximated by the area A_{AB} enclosed by the actual test record and lines of constant δ; that is, δ_A and δ_B, as shown in Fig. 4

$$\int_{\delta_A}^{\delta_B} P d\delta \simeq A_{AB} \tag{61}$$

At the same time under the same conditions the integral of the third term in Eq 60 can be replaced by the integrand times the increment in crack length.

$$\int_{a_0}^{a} \gamma \frac{J}{b} da \simeq \frac{\gamma}{b} J_B (a - a_0) \tag{62}$$

Replacing now Eqs *61* and *62* in *60* gives

$$J_C = J_A + \frac{\eta}{b} A_{AB} - \frac{\gamma}{b} J_B (a - a_0)$$

$$J_C = \left(J_A + \frac{\eta}{b} A_{AB}\right)\left(1 - \frac{\gamma}{b}(a - a_o)\right) \tag{63}$$

Or in general

$$J_{(i+1)} = \left(J_i + \left(\frac{\eta}{b}\right)_i A_{i,i+1}\right)\left(1 - \left(\frac{\gamma}{b}\right)_i (a_{i+1} - a_i)\right) \tag{64}$$

where the subscript i (or $i + 1$) indicates functions evaluated at that step. The term $A_{i,i+1}$ refers to the area enclosed by the actual test record and lines of constant displacement δ_i and δ_{i+1}. For the first step, $\delta = 0$, J is equal to zero. Note that if, up to a certain point $j + 1$, no crack growth has occurred, Eq 64 reduces to

$$\begin{aligned} J_{j+1} &= J_j + \left(\frac{\eta}{b}\right)_j A_{j,j+1} \\ &= \frac{\eta}{b} \int_0^{\delta_{j+1}} P d\delta \end{aligned} \tag{65}$$

which coincides with the already familiar form, Eq 38. Thus Eq 64 is completely general and can be used for the whole test record, starting from the origin.

The method presented here is an extension of the work of Refs *12* and *22*. Since then it has already been adopted by some investigators. Joyce [*21*] used this procedure to correct J in already existent J-R curves and other investigators have expressed their interest in adopting it [*23*].

Discussion of the Method

As was mentioned in the foregoing, the present method does not require information from other specimens [that is, the $H(\delta/W)$ function], making instead full use of the test record itself.

Joyce [*21*] used this J procedure to modify previously obtained A533B J-R curves [*24*]. In Figs. 5-7 values of J with and without correction for crack growth are compared with those obtained by the calibration curve analysis

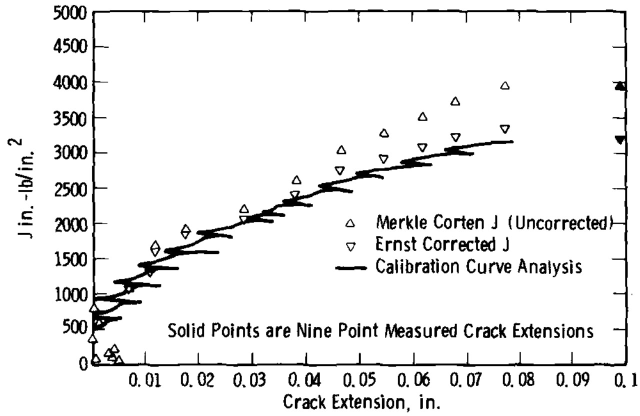

FIG. 5—*J-R curve comparison for Specimen No. 1-18,* a/W = *0.7, 0 percent side grooves. A533 B steel IT-CT from Joyce et al [21].*

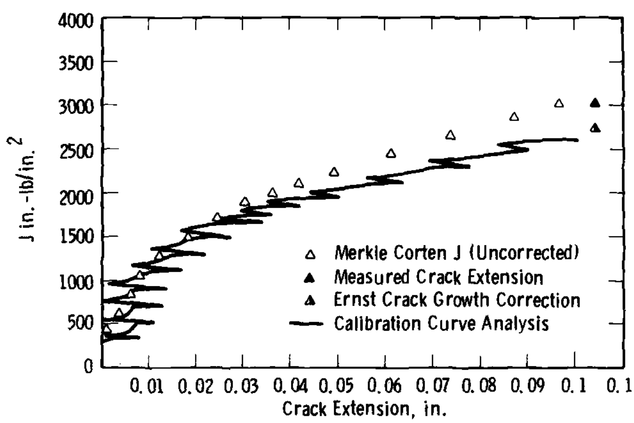

FIG. 6—*J-R Curve comparison for Specimen No. 1-13,* a/W = *0.6, 20 percent side grooves. A533B steel IT-CT from Joyce et al [21].*

developed by Ernst et al [*11,12*] implemented by Joyce et al [*21*], and considered as exact.

As can be seen, the Merkle-Corten (without correction) expression tends to overestimate J, whereas J corrected by the present method (Ernst-corrected J in Joyce's work) seems to give a very good agreement with the exact procedure. On the other hand, some investigators have previously proposed formulas to correctly evaluate J in the presence of crack growth.

Garwood et al [*25,26*] presented a formula for J-corrected

$$J_n = J_{n-1}\left[\frac{W - a_n}{W - a_{n-1}} + \frac{2\,U_4}{B(W - a_{n-1})}\right] \tag{66}$$

where the subscript $n(n-1)$ indicates that the corresponding quantity is evaluated at the step $n(n-1)$; the term U_4 refers to the area under the actual test record limited by lines of constant displacement δ_{n-1} and δ_n. This formula can be considered a special case of the proposed Eq 64. In fact both equations coincide (to a second-order differential) in the limit η = constant = 2. Thus this formula is limited to the case of pure bending of a very small remaining ligament (eventually three-point bend specimen, as is discussed later). The proposed Eq 64 is thus a generalization of Eq 66. Moreover, the sufficient conditions for Eq 64 to be valid are clearly stated here.

Hutchinson and Paris [9] proposed a formula for J for the case of pure bending of a small remaining ligament, with a built-in correction for crack extension

$$J = \int_0^\delta \frac{2M}{b} d\delta - \int_{a_0}^a \frac{J}{b} da \tag{67}$$

In fact this expression, considered as exact from an analytical viewpoint, served as the basis for the more general formulas developed by Ernst et al [11,12] on which this method is, in its turn, based. Equation 64 is a straightforward derivation of Eq 12 when Eq 32 is assumed.

The foregoing expression can be rearranged, as proposed by McMeeking [27], to give J in a more compact form. Differentiating and reintegrating Eq 67 gives

$$dJ = 2\frac{M}{b} d\delta - \frac{J}{b} da$$

$$\begin{gathered}\frac{dJ}{b} + \frac{J}{b^2} da = \frac{2M}{b^2} d\delta \\ \int_0^{(J/b)} d\left(\frac{J}{b}\right) = \int_0^\delta \frac{2M}{b^2} d\delta\end{gathered} \tag{68}$$

$$J = 2\, b_i \int_0^\delta \frac{M}{b^2} d\delta$$

Based on Eq 67, this expression is also exact from an analytical viewpoint, but as before is valid for the case of a very deep crack subject to pure bending.

Finally, Andrews [28] presented an empirical formula to correct J for crack growth

$$J = J_0 \left[1 - \frac{0.75\eta - 1}{b} \Delta a\right] \tag{69}$$

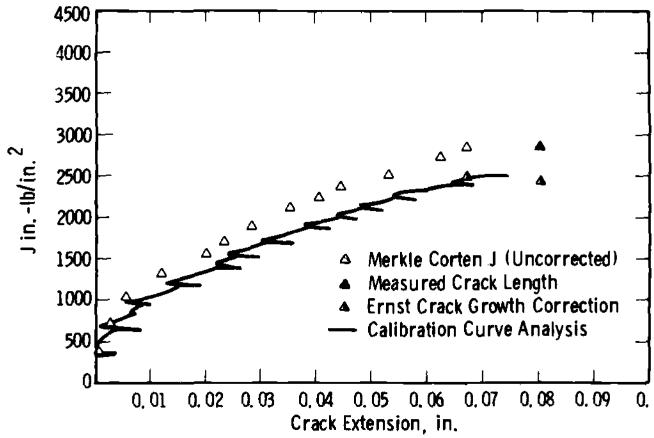

FIG. 7—*J-R curve comparison for Specimen No. 1-27,* a/W = *0.8, 20 percent side grooves. A533B steel IT-CT from Joyce et al [21].*

where J_0 is the area under the actual test record times η/b evaluated at initial crack length. As can be seen, Eq 69 has the same general form as the proposed Eq 64. Nevertheless, the latter is based on analytical considerations which presumably give more confidence in the actual coefficients.

In conclusion, the presented method is a direct derivation of Eq 12 with the assumption of Eq 32, the former being considered exact from an analytical viewpoint, thus consistent (although more general) with other exact formulas. Conditions for its validity were clearly stated.

The method is not limited to deep cracks and does not require any information other than the test record itself. It has already been successfully applied and interest seems to be growing in its recommendation [23]. In Figs. 8

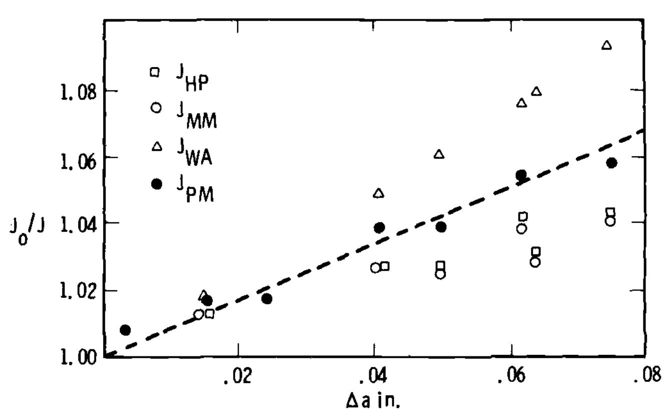

FIG. 8—J_0/J *versus* Δa *from various correction schemes. A533B IT-CT.*

and 9, J-R curves obtained by different scheme of calculating J, as reported by Landes [29], are shown in addition to that obtained by the present method, J_{PM}, Eq 64. J_{HP}, J_{MM}, and J_{WA} correspond to Eqs 67, 68, and 69, respectively. J_0 refers to J as defined in Eq 69. Differences between values obtained using Eqs 67 and 68 should be attributed to numerical evaluation.

The Tearing Modulus

Even though the potential of J as the governing parameter of the crack-tip stress-strain field was established earlier, the question of stable versus unstable tearing remained unresolved until very recently. In fact, a model capable of predicting stable/unstable behavior, taking into account specimen geometry, a/W ratio, material properties, and overall behavior of the structure, was simply nonexistent.

In 1977 Paris et al [13,14] proposed a theory to explain stable versus unstable crack growth. They introduced a nondimensional quantity called the tearing modulus, T, that in general has the form

$$T = \frac{E}{\sigma_0^2} \frac{dJ}{da} \tag{70}$$

where E is the Young's modulus and σ_0 is the flow stress.

To better illustrate these concepts, consider the particular example shown in Fig. 10. A specimen is loaded in series with a linear spring of constant K_M, in a displacement-controlled test. The total displacement, δ_{tot}, can be separated into a part due to the crack, δ, and the remaining part, δ_M, which will be associated with the spring and eventually the rest of the structure

$$\delta_{tot} = \delta + \delta_M \tag{71}$$

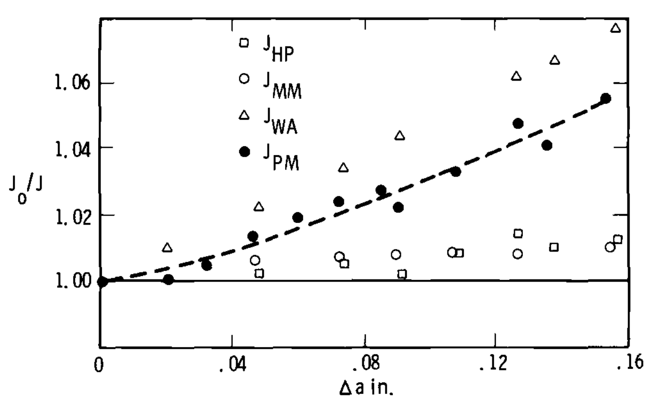

FIG. 9—J_0/J *versus* Δa *from various correction schemes A533B 1.6T-CT.*

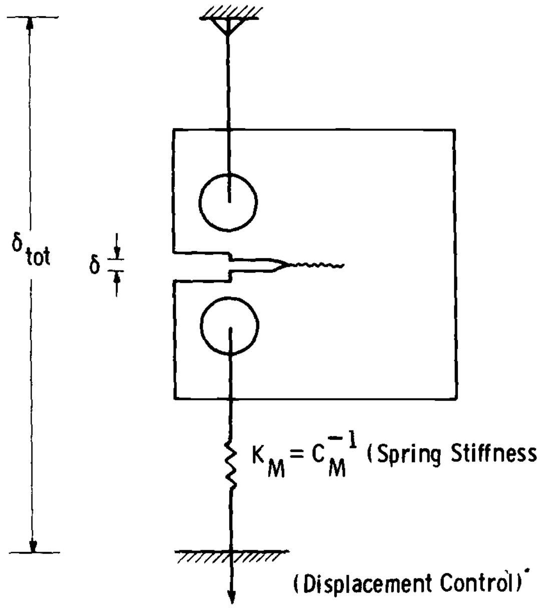

FIG. 10—*Displacement control test of a bend specimen in series with a spring bar.*

Note that only the part of the displacement due to the crack, δ, affects J. It is important at this point to make a distinction between the values of J lying on the material resistance J-R curve, and the applied values of J. The former will be called J_{mat} and will be regarded as a function of the crack length increment Δa only

$$J_{mat} = J(\Delta a) \tag{72}$$

The latter will be called J_{app} and can be regarded as a function of load (or displacement) and current crack length a ($a = a_0 + \Delta a$)

$$J_{app} = J(a, P) = J(a, \delta) \tag{73}$$

Now if Eq 70 is evaluated using Eq 72, the resulting T is the material tearing modulus

$$T_{mat} = \frac{E}{\sigma_0^2}\left(\frac{dJ}{da}\right)_{mat} \tag{74}$$

If instead dJ/da in Eq 70 is calculated as the rate of change of J_{app} per unit virtual crack extension with the condition δ_{tot} = constant (or other similar condition specified), the resulting T is the applied tearing modulus

$$T_{app} = \frac{E}{\sigma_0^2}\left(\frac{dJ}{da}\right)_{\delta_{tot}} \tag{75}$$

And so following Refs *13* and *14*, instability will be ensured if

$$T_{\text{app}} > T_{\text{mat}} \tag{76}$$

In the next sections explicit expressions are obtained for T_{mat} and T_{app} for the compact specimen using the starting assumption of Eq 32.

Material Tearing Modulus T_{mat}

As has been mentioned, T_{mat} is defined as the rate of change of J with crack length along the J-R curve, or actual test record

$$T_{\text{mat}} = \frac{E}{\sigma_0^2}\left(\frac{dJ}{da}\right)_{\text{mat}} = \frac{E}{\sigma_0^2}\left(\frac{\partial J}{\partial a} + \frac{\partial J}{\partial \delta}\frac{d\delta}{da}\right)_{\text{mat}} \tag{77}$$

Thus, T_{mat} can be calculated from a test record by using Eq 45 divided by da or simply Eqs 54 and 55, giving

$$T_{\text{mat}} = \frac{E}{\sigma_0^2}\left\{-\gamma\frac{J}{b} + \frac{\eta^2}{b^2}P\left(\frac{1}{\dfrac{H'}{WH} - \dfrac{1}{P}\dfrac{dP}{d\delta}}\right)\right\} \tag{78}$$

where all quantities are evaluated at current values of a and δ, and the ratio $dP/d\delta$ is to be taken from the actual test record.

Applied Tearing Modulus T_{app}

The applied tearing modulus T_{app} is defined as the rate of change of J_{app} with crack length under the condition that the overall displacement is kept constant (or equivalent condition). Thus, T_{app} is given by

$$T_{\text{app}} = \frac{E}{\sigma_0^2}\left(\frac{dJ}{da}\right)_{\delta_{\text{tot}}} = \frac{E}{\sigma_0^2}\left(\frac{\partial J}{\partial a} + \frac{\partial J}{\partial \delta}\frac{d\delta}{da}\right)_{\delta_{\text{tot}}} \tag{79}$$

The condition δ_{tot} = constant is equivalent to $d\delta_{\text{tot}} = 0$

$$\begin{aligned} d\delta_{\text{tot}} &= d\delta + d\delta_M = 0 \\ &= d\delta + C_M dP = 0 \end{aligned} \tag{80}$$

where

$$C_M = K_M^{-1} = d\delta_M/dP$$

can be associated with the compliance of the system (spring + testing machine + uncracked specimen). T_{app} can then be calculated using Eqs 47 and 48 subject to the condition of Eq 80 to give

$$T_{\text{app}} = \frac{E}{\sigma_0^2}\left\{-\gamma\frac{J}{b} + \frac{\eta^2}{b^2}P\left(\frac{1}{\frac{H'}{WH} + \frac{K_M}{P}}\right)\right\} \tag{81}$$

(For alternative expression, see Appendix.) Using Eqs 78 and 81 the instability condition of Eq 76 can be restated as

$$T_{\text{app}} > T_{\text{mat}}$$

or

$$-dP/d\delta > C_M^{-1} = K_M \tag{82}$$

Alternate Physical Interpretation of the Instability Condition

The condition for instability can be obtained using a different approach.

Consider the P-δ record of a bend specimen tested under displacement control, and the corresponding calibration (nongrowing crack) curves as shown in Fig. 11*a*.

It is assumed that the fracture process is described in terms of the J-R curve; that is, every point in the P-δ record has associated a value of J, J_i and a value of a, a_i which are connected according to the J-R curve.

Suppose now that an identical specimen (same a/W) is tested, this time in series with a spring (as described before), Fig. 11*b*. It can be seen that the effect of the spring on the calibration functions is just to shift every point in Fig. 11*a* to the right by an amount

$$\delta_M = PC_M$$

or

$$\delta_{A'} = \delta_A + P_A C_M \tag{83}$$

$$\delta_{B'} = \delta_B + P_B C_M \tag{84}$$

where P_A and P_B are the loads at Points [A-A'] and [B-B'], respectively. Note that corresponding points, [A-A'], [B-B'], etc., have the same value of

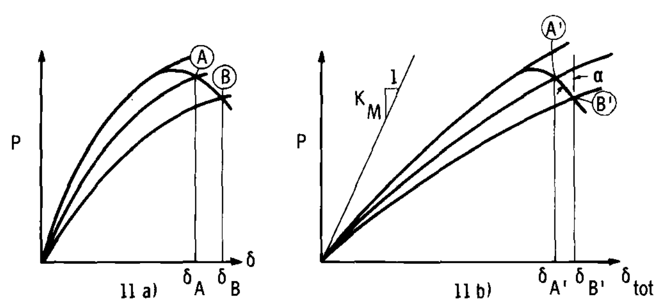

FIG. 11—*Test record for identical specimen (a) without and (b) with spring.*

J (J depending on a/W and displacement only due to the crack, δ). Thus the resulting test record is expected to go through these corresponding points [A'], [B'], etc. in order to follow the J-R curve as before. Combining Eqs 83 and 84 gives

$$\delta_{B'} - \delta_{A'} = \delta_B - \delta_A + C_M(P_B - P_A) \tag{85}$$

Is important to note that for the portion of the test record where $P_B - P_A < 0$ (dropping part), the relative distance of subsequent points is diminished by the addition of the spring

$$\delta_B - \delta_A > \delta_{B'} - \delta_{A'} \quad \text{if } P_B < P_A \tag{86}$$

In fact, if enough compliance is added, this relative distance can even turn out to be negative; that is, Point [B'] lying to the left of [A']. If this is the case the test record would have to go backwards (in δ) to pass through [B'] in order to follow the J-R curve. But this is not compatible with the boundary condition, which asks for a monotonically increasing displacement. Thus, the test record gets as near to Point [B'] as it is allowed to (vertical drop), corresponding to unstable growth.

The conditions for stability can be then expressed as

$$\begin{aligned} \delta_{B'} - \delta_{A'} &< 0 \quad \text{unstable} \\ \delta_{B'} - \delta_{A'} &> 0 \quad \text{stable} \end{aligned} \tag{87}$$

Replacing Eqs 83 and 84 in the preceding expression gives

$$\begin{aligned} &\delta_{B'} - \delta_{A'} = \delta_B - \delta_A + (P_B - P_A)\, C_M < 0 \\ &\frac{\Delta\delta}{\Delta P} < -\, C_M \\ &C_M{}^{-1} = K_M < -\, dP/d\delta \quad \text{for instability} \end{aligned} \tag{88}$$

which coincides with Eq 82.

It can be seen from Eq 88 that, under the specified testing conditions, instability cannot occur in the part of the P-δ record where the load is increasing ($dP/d\delta > 0$ would imply $C_M < 0$).

The value of C_M which satisfies Eq 88 can be interpreted as the necessary compliance to be added to the system in order to set subsequent points to the same displacement

$$\delta_{B'} = \delta_{A'} \tag{89}$$

causing then instability.

Note that by examining a test record (with or without the spring) a remaining compliance capacity C_{CR} can be defined as

$$C_{CR} = t_g\, \alpha = (-\, dP/d\delta)^{-1} \tag{90}$$

where α is shown in Fig. 11*b*.

This value of C_M represents the additional compliance the system can handle without going unstable (or additional compliance needed to satisfy Eq 89).

The Three-Point Bend Specimen

In all of the foregoing the three-point bend specimen (3 PB) can be considered a special case. In fact, it has been recommended for the 3 PB (with span/width ratio = 4) to use Eq 32 with $\eta = 2$. That being the case, all of the foregoing formulas are still valid for 3 PB if the following substitutions are made.

$$\begin{aligned} \eta &= 2 \\ \gamma &= 1 \\ g &= 1 \\ g' &= 0 \\ \eta' &= 0 \end{aligned} \tag{91}$$

for any a/W

Conclusions

1. An overview of the problem of relating J to work done through the η-factor was presented. The conditions for the existence of η (as independent of the level of deformation) were set in connection with the separability of the load into multiplicative functions of crack length and displacement. Using the starting assumption of Eq 32

$$J = \eta/b \quad \text{work}$$

Formulas for calculating J, T_{mat}, T_{app} and da from the test record itself were derived. As a result a method for correctly evaluating J in general, including the case of crack growth, was proposed.

2. Experimental data corrected with this method seem to agree very well with those obtained by the calibration curve analysis, which is considered to be exact.

3. Additional physical interpretation is given in the T_{mat}-versus-T_{app} stability criterion and a remaining compliance capacity, C_{CR}, is defined.

4. It is emphasized here that in this work the strict deformation theory interpretation of J is followed: J is a function of two variables (a and δ, for example), and its value does not depend on the particular path chosen to get to the point of interest.

5. J is the parameter which can be used to describe the stable tearing pro-

cess but its limits of validity are still an open question which was not intended to be addressed here.

Acknowledgments

This work was supported in part by the U.S. Nuclear Regulatory Commission, Contract NRC 04-78-277, with Washington University, St. Louis, Mo. The remaining part of the work was supported by Westinghouse Corporate Research Funds. The authors are particularly indebted to Mrs. Donna Gongaware for her patient typing of the manuscript.

APPENDIX

To evaluate T_{mat} and T_{app} from Eqs 78 and 81, *in any number of tests*, information is needed on the characterization (that is, the H-function) of the particular material-specimen combination used. This means that only one extra test has to be run to obtain H, and thus the number of tests results is basically the number of tests run.

By proper manipulation, however, even this need of running the extra test can be avoided. In fact Eqs 78 and 81 can be combined in order to eliminate the term involving the H-function, giving

$$T_{app} = \frac{E}{\sigma_0{}^2} \left\{ -\gamma \frac{J}{b} + \frac{\eta^2 P}{b^2} \right. \\ \left. \times \frac{1}{\left[\dfrac{K_M}{P} + \dfrac{1}{P}\dfrac{dP}{d\delta} + \dfrac{\eta^2 P}{b^2} \left(\dfrac{1}{\dfrac{\sigma_0{}^2}{E} \cdot T_{mat} + \gamma \dfrac{J}{b}} \right) \right]} \right\} \quad (92)$$

As can be seen *all* the terms involved in the foregoing expression are known from one test record. Note that T_{mat} is just the normalized slope of the J-R curve, which in its turn can be obtained from a single record according to the method suggested in the text.

Thus as a result, the T_{mat}, following the mentioned procedure, and then T_{app} using Eq 92 can be obtained from nothing else but one single test record.

References

[1] Rice, J. R., *Journal of Applied Mechanics*, Vol. 35, 1968, pp. 379-386.
[2] Hutchinson, J. W., *Journal of the Mechanics and Physics of Solids*, Vol. 16, No. 1, 1968, pp. 13-31.

[3] Rice, J. R. and Rosengren, G. F., *Journal of the Mechanics and Physics of Solids*, Vol. 16, No. 1, 1968, pp. 1-12.
[4] Begley, J. A. and Landes, J. A. in *Fracture Toughness, ASTM STP 514*, American Society for Testing and Materials, 1972, pp. 1-23.
[5] Landes, J. D. and Begley, J. A. in *Fracture Toughness, ASTM STP 514*, American Society for Testing and Materials, 1972, pp. 24-39.
[6] Rice, J. R., Paris, P. C., and Merkle, J. G. in *Progress in Flaw Growth and Fracture Toughness Testing, ASTM STP 536*, American Society for Testing and Materials, 1973, pp. 231-245.
[7] Merkle, J. and Corten, H., *Journal of Pressure Vessel Technology, Transactions, American Society of Mechanical Engineers*, 1974, pp. 286-292.
[8] Clarke, G. A. and Landes, J. D., *Journal of Testing and Evaluation*, Vol. 7, No. 5, Sept. 1979, pp. 264-269.
[9] Hutchinson, J. W. and Paris, P. C. in *Elastic-Plastic Fracture, ASTM STP 668*, American Society for Testing and Materials, 1979, pp. 37-64.
[10] Clarke, G. A., Andrews, W. R., Paris, P. C., and Schmidt, D. W. in *Mechanics of Crack Growth, ASTM STP 590*, American Society for Testing and Materials, 1976, pp. 27-42.
[11] Ernst, H. A., Paris, P. C., Rossow, M., and Hutchinson, J. W. in *Fracture Mechanics, ASTM STP 677*, American Society for Testing and Materials, 1979, pp. 581-599.
[12] Ernst, H. A. and Paris, P. C., "Techniques of Analysis of Load-Displacement Records by J Integral Methods," Nuclear Regulatory Commission, NUREG/CR-1222, Jan. 1980; also available as H. A. Ernst Ph.D. Thesis, Department of Mechanical Engineering, Washington University, St. Louis, Mo., Dec. 1979.
[13] Paris, P. C., Tada, H., Zahoor, A., and Ernst, H. A. in *Elastic-Plastic Fracture, ASTM STP 668*, American Society for Testing and Materials, 1979, pp. 5-36.
[14] Paris, P. C., Tada, H., Ernst, H., and Zahoor, A. in *Elastic-Plastic Fracture, ASTM STP 668*, American Society for Testing and Materials, 1979, pp. 251-265.
[15] Rice, J. R. in *Fracture*, Vol. 2, H. Liebowitz, Ed., Academic Press, New York, 1968, pp. 191-311.
[16] Griffith, A. A., *Transactions of the Royal Society of London*, Vol. 221, 1920.
[17] Paris, P. C., Ernst, H. A., and Turner, C. E. in *Fracture Mechanics*, Proceedings of the 12th National Symposium, *ASTM STP 700*, American Society for Testing and Materials, 1980, pp. 338-351.
[18] Landes, J. D., Walker, H., and Clarke, G. A. in *Elastic-Plastic Fracture, ASTM STP 668*, J. D. Landes, J. A. Begley, and G. A. Clarke, Eds., American Society for Testing and Materials, 1979, pp. 266-287.
[19] Clarke, G. A., this publication, pp. 553-575.
[20] Joyce, J. A., Ernst, H. A., and Paris, P. C. in *Fracture Mechanics*, Proceedings of the 12th National Symposium, *ASTM STP 700*, American Society for Testing and Materials, 1980, pp. 222-236.
[21] Joyce, J. A., "Application of the Key Curve Method to Determining J-R Curve for A533B Steel," Nuclear Regulatory Commission Report, NUREG/CR-1290, Feb. 1980.
[22] Ernst, H. A., private communication, to the ASTM E24.08 J-R Curve Working Group, Washington University, St. Louis, Mo., May 1979.
[23] Gudas, J. P., private communication.
[24] Vassilaros, M. G., Joyce, J. A., and Gudas, J. P., *Fracture Mechanics*, Proceedings of the 12th National Symposium, *ASTM STP 700*, American Society for Testing and Materials, 1980, pp. 251-270.
[25] Garwood, S. J., Robinson, N., and Turner, C. E., *International Journal of Fracture*, Vol. 11, No. 3, June 1975.
[26] Garwood, S. J. and Turner, C. E., *International Journal of Fracture*, Vol. 14, 1976.
[27] McMeeking, R. M., private communication.
[28] Andrews, W. R., private communication.
[29] Landes, J. D., technical presentation at the ASTM E24.08 meeting, Pittsburgh, Pa., Nov. 1979.
[30] Sumpter, J. D. G. and Turner, C. E. in *Cracks and Fracture, ASTM STP 601*, American Society for Testing and Materials, 1976, pp. 3-18.

K. W. Carlson[1] *and J. A. Williams*[1]

A More Basic Approach to the Analysis of Multiple-Specimen R-Curves for Determination of J_c

REFERENCE: Carlson, K. W. and Williams, J. A., "**A More Basic Approach to the Analysis of Multiple-Specimen R-Curves for Determination of J_c**," *Fracture Mechanics: Thirteenth Conference, ASTM STP 743*, Richard Roberts, Ed., American Society for Testing and Materials, 1981, pp. 503–524.

ABSTRACT: Multiple specimen J-R curves were developed for groups of 25.4-mm-thick (1T) compact specimens with different a/W values and depth of side grooving. The purpose of this investigation was to determine J_c (J at the onset of crack extension) for each group. Judicious selection of points on the load versus load-line deflection record at which to unload and heat-tint specimens permitted direct observation of approximate onset of crack extension. It was found that the present recommended procedure for determining J_c from multiple-specimen R-curves, which is being considered for standardization, consistently yielded nonconservative J_c-values. A more basic approach to analyzing multiple-specimen R-curves is presented, applied, and discussed. This analysis determined J_c-values that closely corresponded to actual observed onset of crack extension.

KEY WORDS: J-integral, J_{Ic}, J_c, J-R curve, ductile fracture toughness, crack initiation, crack extension, crack-opening stretch, multiple-specimen R-curve.

In recent years a considerable effort has been expended on the development of a ductile fracture toughness criterion to characterize the fracture behavior of structural materials employed at temperatures where they exhibit elastic-plastic behavior. This effort has focused, to a large extent, on the J-integral, first proposed by Rice [*1,2*][2] and later advanced as a failure criterion by Begley and Landes [*3,4*]. Subsequently, methodology for J-integral testing and analyses have evolved [*5–9*]. However, the optimum procedures of analyses have yet to be conclusively defined and standardized. In this investigation observed phenomena were used to compare the critical J-integral values at the onset of crack extension, J_c, determined by both the recommended analysis [*9*] and a more basic J-R curve analysis.

[1]Advanced engineer and senior engineer, respectively, Westinghouse Hanford Co., Richland, Wash. 99352.

[2]The italic numbers in brackets refer to the list of references appended to this paper.

While the crack initiation and the stable crack extension regions on the J-R curve are generally recognized to be nonlinear, the recommended procedure [9] models the crack extension process as a straight line; the intersection of this line with a blunting line is taken as J_c. The J_c-value can be determined (within bounds) by direct observation when data near the onset of crack extension are obtained by the multiple-specimen technique. Direct observation demonstrated that the recommended procedure consistently yielded high J_c-values. The recommended analysis modified to account for nonlinear crack initiation and crack propagation was found to be in much better agreement with observed values.

The J_c-value obtained by the recommended procedure is an artifact of the procedure itself while the J_c-value obtained from the modified analysis represents a phenomenological event, the onset of crack extension. It is anticipated that such a quantity would be more suitable as a material parameter and would be more useful in resolving related questions such as size and geometry effects.

Material

The material used in this investigation was ASTM A533, Grade B, Class 1 steel (A533-B, 1). The material was removed from the Heavy Section Steel Technology (HSST) plate 02. The heat treatment for Plate 02 consisted of normalizing at 913°C (1675°F), austenitizing at 871°C (1600°F), water-quenching, tempering at 663°C (1225°F), and stress-relieving at 607°C (1125°F). The chemical composition, given in Table 1, and the heat treatment were reported by Childress [10]. The specimens were removed from between the 1/4 and 3/4 thickness of the 30.48-cm (12 in.) plate. Mechanical properties [11-13] are given in Table 2. All specimens tested for this investigation were 25.4-mm-thick (1T) compact specimens machined in the T-L orientation.

TABLE 1—*Chemical composition of ASTM A533-B1 steel (HSST plate 02) (weight %).*

C	Mn	Ni	Mo	Si	S	P	Cu	Fe
0.22	1.48	0.68	0.52	0.25	0.018	0.012	0.012	balance

TABLE 2—*Strength and impact mechanical properties of ASTM A533-B1 steel at 149°C (300°F).*

Yield strength	= 434 MPa	(63 000 psi)
Ultimate strength	= 579 MPa	(84 000 psi)
C_v energy	= 126 joules	(93 ft-lb)
Modulus of elasticity, E	= 2.1×10^2 GPa	(30.7×10^6 psi)

Testing and Analysis

All specimens were standard 1T compact specimens modified to permit the measurement of load-line deflection on the crack plane (see Fig. 1). Four groups of five to eight specimens each were tested. The specimens within a group were machined to a single notch depth. The specimens within the various groups were cut to varying notch depths so that after fatigue precracking, two groups had an a/W ratio of 0.5, one group had $a/W = 0.6$, and one group had $a/W = 0.8$. Since side grooving the remaining ligament is a commonly employed means of producing straight crack fronts [*14-16*], one of the groups having $a/W = 0.5$ was given 45-deg V-shaped side grooves to a total depth of 20 percent (10 percent on each side) of the thickness, shown in Fig. 1. To ensure consistently sharp crack tips, all specimens were precracked in fatigue at least 2.5 mm (0.100 in.) at loads sufficiently low that plastic flow at the crack tip was minimized as recommended in Ref *9*. Precracking was completed prior to specimen side-grooving.

The fracture toughness tests were conducted at 149°C (300°F), where stable crack extension was controlling failure. The temperature was controlled to approximately ±2 deg C in an air-circulating electrically heated furnace. The specimen temperature was sensed with a thermocouple attached to the specimen surface. The 1T specimens were brought to test temperature in the

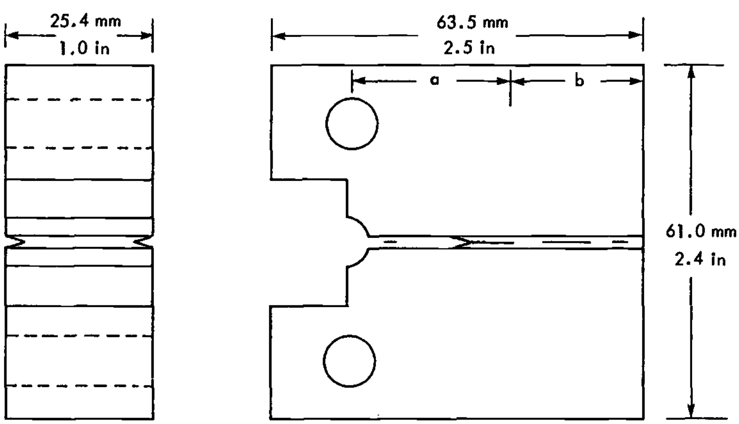

inches

a/W	B	a	b
.50	1.00	1.00	1.00
.60	1.00	1.20	.80
.70	1.00	1.40	.60
.80	1.00	1.60	.40

mm

a/W	B	a	b
.50	25.4	25.4	25.4
.60	25.4	30.5	20.3
.70	25.4	35.6	15.2
.80	25.4	40.6	10.2

FIG. 1—*1T compact specimen.*

furnace and then allowed to soak at test temperature for at least an hour prior to testing.

A J-integral test requires an accurate load versus load-point deflection record. The tests were performed on an 89.0-kN-capacity (20 000 lb) closed-loop servo-controlled hydraulic test system. The tests were conducted in stroke control at a rate of 0.5 mm/min (0.02 in./min). Loading clevises with "flat bottom" holes were used to test the compact specimens. The load was monitored by the system load cell. Load-line deflection was measured with either an electrical resistance clip gage or a pair of linear variable differential transducers (LVDT's) mounted in a rigid frame. The clip gage was mounted on razor blades attached at the load line on the crack plane. The LVDT frame was mounted in the same screw holes that were used to attach the razor blades. The signals from the LVDT's were added to give average load-line displacement measurements. Note that either one extensometer or the other was used for a given test. The extensometers yield identical results as discussed elsewhere [*17*]. The extensometers are shown in Fig. 2.

To compute J for the compact specimens the formula developed by Rice et al [*6*], modified for the tensile component of load after Merkle and Corten [*18*] and shortened by the ASTM Task Group E24.01.09 [*9*], was used. This equation is

$$J = \frac{2A}{Bb} \frac{(1 + \alpha)}{(1 + \alpha^2)} \tag{1}$$

where

$$\alpha = \left[\left(\frac{2a_0}{b}\right)^2 + \frac{4a_0}{b} + 2\right]^{1/2} - \left(\frac{2a_0}{b} + 1\right) \tag{2}$$

and

A = area (energy) under load deflection record,
B = thickness (net section thickness for side-grooved specimens),
b = remaining uncracked ligament, and
a_0 = initial crack length.

After completion of a test, the specimen was heat-tinted in a furnace at 649°C (1200°F) and then fractured after cooling in liquid nitrogen. The blue oxide coating clearly delineates the fatigue crack and crack extension; these quantities were measured at nine equally spaced points along the crack front under a microscope with a vernier-calibrated traveling stage at ×48 magnification. The crack extension was taken as the mean of eight points: the seven interior measurements plus the average of the two surface measurements. The initial crack length as measured on the specimen fracture surface was used to compute the J-values.

To facilitate data acquisition and computation, a minicomputer system was used. The system consisted of a magnetic tape programmable computer,

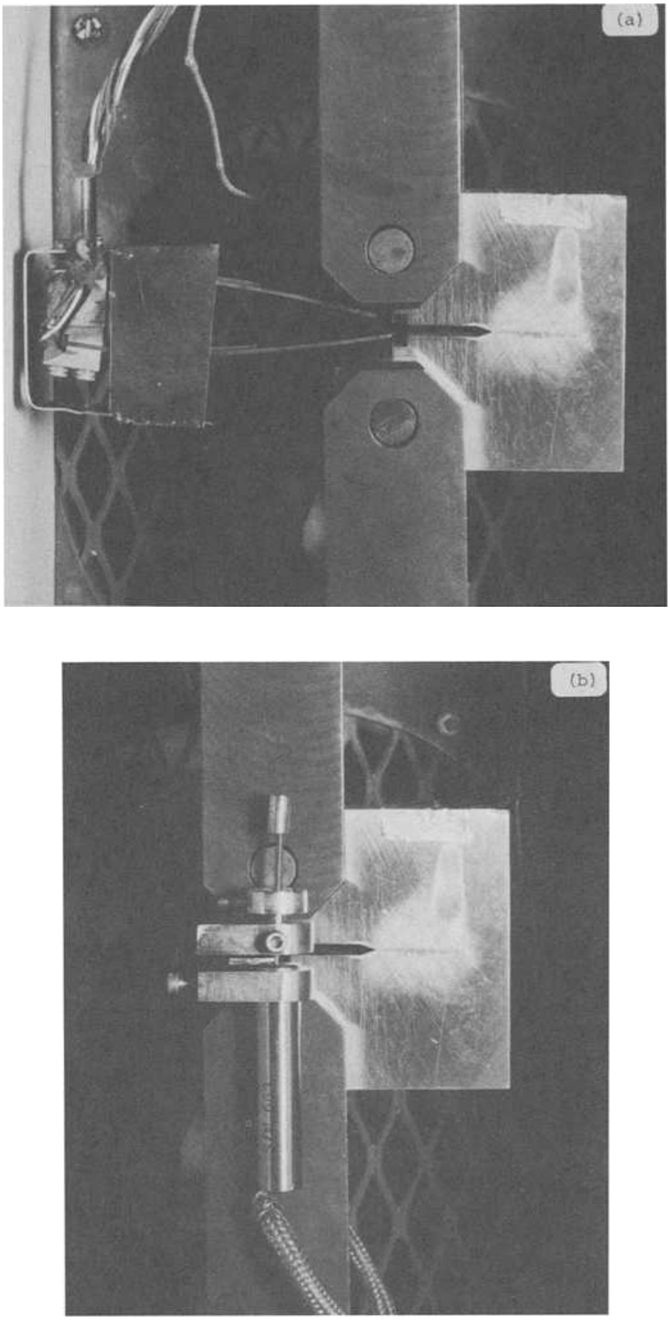

FIG. 2—*Load-line extensometers: (a) electrical resistance clip gage; (b) load-line LVDT system.*

X-Y plotter, thermal printer, and a magnetic disk drive for data storage. The system was programmed to accurately record load and displacement. All data were stored on magnetic disks. Simultaneously, the X-Y recorder was autographically producing the load-deflection record. Upon completion of the test and subsequent crack length measurement from the broken specimen, the data were recalled from the magnetic disk and accurate J- and Δa-values were computed. With all data permanently stored on the magnetic disks, the data were easily retrievable for subsequent analyses or replay.

All test recording and measurement equipment was calibrated to National Bureau of Standards traceable standards as a normal requirement. Test machines were checked for calibration prior to test. Extensometers were calibrated at test temperature and for a deflection range exceeding that required for the maximum deflection encountered during testing; for the extended ranges accuracy was better than 1 percent.

Results and Discussion

J-R Curves

The current recommended J-integral test procedure [9] entails determining the critical J-value at the onset of crack extension, J_c, from the J-R curve, which is a plot of J as a function of crack extension, Δa. The most widely used method of obtaining a J-R curve is the multiple-specimen heat-tint method where a number of identical specimens (usually five to ten) are loaded to various points on the load-deflection record corresponding to different amounts of crack extension. Each specimen is unloaded, heat-tinted in a furnace, and broken. The tinted crack extension can then be measured. The J-value at the point where each test was halted is plotted as a function of its measured crack extension.

The progress of ductile fracture commencing from a sharp crack has been described [19] as being separable into four regimes: (1) crack-opening stretch (COS) or crack-tip blunting by plastic flow at the crack tip, (2) crack growth initiation, (3) stable crack growth by material separation at the crack tip, and (4) unstable crack propagation. These four events determine the shape of the R-curve. Of these four regimes, crack-tip blunting and stable crack extension predominate during the fracture process described by an R-curve. Crack initiation occurs over a short interval and unstable crack propagation usually occurs at some point beyond where the useful R-curve terminates (if it occurs at all).

In the current recommended procedure, the R-curve is analyzed by modeling the crack-tip blunting regime and the stable crack extension regime by two linear relationships. The crack-tip blunting line is assumed to follow the theoretical relationship [1]

$$\Delta a = J/2\sigma_0 \tag{3}$$

where the flow stress, σ_0, is taken as the mean of the yield and ultimate uniaxial tensile stresses. The data points utilized for the construction of the crack extension line are recommended to be those contained in an interval defined by lines parallel to the blunting line, Eq 3, but offset by 0.15 mm (0.006 in.) and 1.5 mm (0.060 in.) from the origin. The crack extension portion of the R-curve is proposed to be represented by a least-squares linear regression through these points. This R-curve analysis is shown schematically in Fig. 3. The intersection of the two straight lines is taken as the onset of crack extension and the J-value at this point is considered J_c. In this investigation, data points slightly to the right (in all cases less than about 20 percent of the allowable Δa) were included in the analysis by the recommended procedure. These were included so that the required data spread and the required number of data points in the recommended procedure could be met. Because of their proximity to the area defined by the "exclusion lines," it is very unlikely that their inclusion in the recommended analysis significantly affects the result attributed to the recommended analysis.

If one test is halted during the latter stages of blunting and another test is halted during initiation of crack extension, a reasonable determination of J_c can be made by direct observation. In this investigation it was found that the J_c-values obtained from the recommended analysis were consistently higher than those determined by direct observation for all five R-curves generated; the magnitude of overestimation by the recommended analysis ranged from approximately 31 to 65 percent. The overestimation was observed to be an artifact of the analysis and not a consequence of the actual data. A modification of the recommended analysis (to be referred to as "modified analysis")

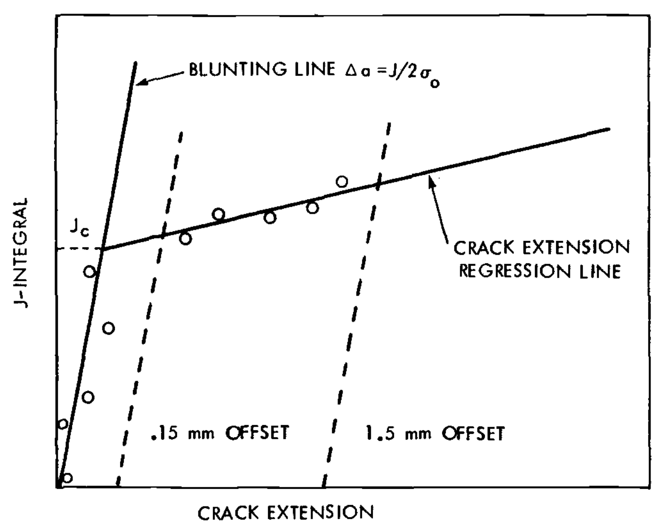

FIG. 3—*Schematic representation of the recommended R-curve analysis.*

was found to give J_c results that closely agreed with the directly observed J_c-values.

The modified analysis recognizes that while the regime of crack initiation is small relative to crack-tip blunting and stable crack growth, it is extremely significant in the determination of J at the onset of crack extension. As noted in previous investigations [*20,21*], it was also observed in this study that crack initiation on the R-curve was actually nonlinear. During this period of transition from crack-tip blunting with its steep slope on the R-curve to stable crack growth, which has a relatively shallow slope, there is a gradual change of slope (shown schematically in Fig. 4) rather than the abrupt change suggested by the recommended analysis. Thus, a linear regression of data collected in the stable crack extension regime is not, in general, an accurate representation of R-curve behavior in the crack initiation regime. As a consequence of this, J_c is often lower than the value obtained by extrapolating the linear crack extension line back to the blunting line.

The modified analysis accommodates the nonlinear crack extension line by including data points from all specimens which show any macroscopic (or low-power microscopic) crack extension; all data are analyzed with a statistical curve-fitting computer program of a family regression analysis of nonlinear curves, one of which is a straight line. The curve equation which produces the highest correlation coefficient is employed in the analysis. It should be noted that some subjectivity must be exercised in choosing the ap-

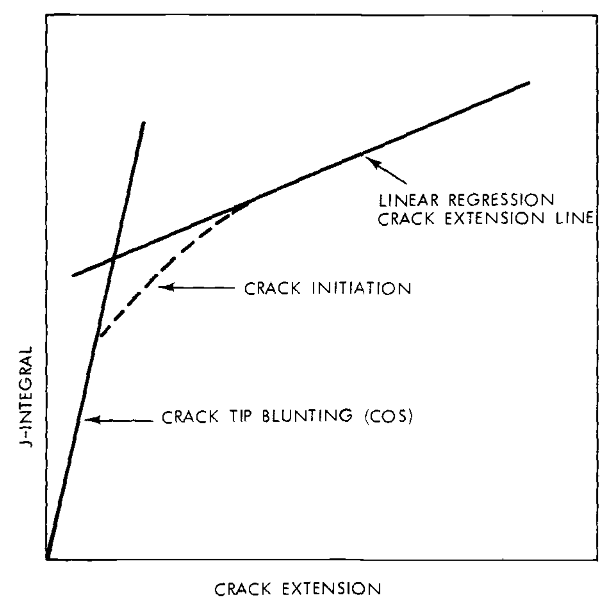

FIG. 4—*Schematic representation of the nonlinear nature of crack extension during the initiation regime.*

propriate equation; an appropriate equation must not exhibit an instability within the region of data used to obtain the fit. In other words, J and Δa must continually increase. To be effective, at least one datum point for an R-curve must be obtained near the onset of crack extension; this implies the necessity of a datum point which is to the left of the 0.15 mm (0.006 in.) exclusion line of the recommended analysis. The intersection of the blunting line and this nonlinear crack extension line is taken as J_c. Table 3 lists the equation forms used by the family regression program. The equation form

$$Y = Ax^B \tag{4}$$

was found to give the best fit for four out of the five curves analyzed; it was the second best fit for the other curve. Equation form

$$Y = A + Bx^{1/2} \tag{5}$$

gave the best fit for the fifth set of data analyzed, it was also the second best fit for the first four sets of data.

A multiple-specimen heat-tint R-curve was developed for each of the four groups of specimens tested. Each group had different dimensions varying the a/W ratio and the depth of side grooving (percentage SG). The groups were:

Group 1: a/W = 0.5 percent SG = 0
Group 2: a/W = 0.5 percent SG = 20
Group 3: a/W = 0.6 percent SG = 0
Group 4: a/W = 0.8 percent SG = 0

The results from each group are discussed separately prior to a general discussion of all results.

TABLE 3—*Family regression of functions used for statistical curve-fitting.*

$$
\begin{aligned}
Y &= A + Bx \\
Y &= A + B/x \\
1/Y &= A + B/x \\
Y &= A + B\sqrt{x} \\
Y &= A \exp (Bx) \\
Y &= Ax^B \\
Y &= A + B \ln (x) \\
Y &= A + Bx + CX^2 \\
Y &= A + Bx + Cx^2 + Dx^3 \\
&\cdot \\
&\cdot \\
&\cdot \\
Y &= A + Bx + Cx^2 + Dx^3 + Ex^4 + Fx^5 + Gx^6 + Hx^7 + Ix^8 + Jx^9 + Kx^{10}
\end{aligned}
$$

where A, B, C . . . K are constants; $Y = J$, and $x = \Delta a$.

R-Curve Analysis for Group 1: a/W = *0.5, Percent SG = 0*

Eight specimens were tested in this group; the relevant J-R curve data are listed in Table 4. The fracture surfaces are shown in Fig. 5. It was observed from the fracture surfaces that Specimen 02JH4 had undergone only COS as only a stretched zone was apparent. The specimen with the next largest measured crack extension, 02JH3, showed a considerable amount of crack extension. Since both specimens were consistent with the other specimens in the group (see Fig. 6), these two tests provide lower- and upper-bound values of J_c for this group. Thus, strictly from direct observation it can be established that

$$168 < J_c < 264 \text{ kJ/m}^2$$

$$(961 < J_c < 1510 \text{ in.-lb/in.}^2)$$

The multiple-specimen R-curve is shown in Fig. 6. The modified analysis crack extension line was obtained from the best fit in the family regression analysis of all data points except 02JH4 (no extension), 02GAA1-47, and 02GA593 (too much extension). The data show a rapidly increasing slope as the blunting line is approached. The intersection of the modified analysis crack extension line with the blunting line gives the result

$$J_c = 226 \text{ kJ/m}^2$$

$$(J_c = 1290 \text{ in.-lb/in.}^2)$$

Also shown in Fig. 6 is the recommended analysis (the dashed crack extension line). This analysis yielded a J_c-value of 309 kJ/m^2 (1762 in.-lb/in.^{2}). Certainly, using direct observation as a basis for judgment, the modified analysis gives a J_c-value much closer to the observed J_c than does the recommended analysis.

R-Curve Analysis for Group 2: a/W = *0.5, Percent SG = 20*

In this group six specimens were tested. The data from these tests are tabulated in Table 4. Figure 7 shows the fracture surfaces for the specimens in this group. The fracture surfaces of all specimens indicated that all had undergone some crack extension. The test of Specimen 02JM3 was interrupted at the lowest load-line deflection and, consequently, it had the least amount of crack extension. The small amount of crack extension in 02JM3 indicates that onset occurred shortly before the test was interrupted. Thus, direct observation permits the conclusion

$$J_c < 239 \text{ kJ/m}^2$$

$$(J_c < 1362 \text{ in.-lb/in.}^2)$$

TABLE 4—*J-R curve results.*

Specimen No.	B, mm	a, mm	a/W	% SG	J, kJ/m^2	Δa, mm
02JH4	25.4	27.20	0.536	0	168	0.1067
02JH3[c]	25.4	26.77	0.527	0	264	0.3251
02JG4[c,d]	25.4	26.67	0.525	0	361	0.6655
02GA614[c,d]	25.4	26.52	0.522	0	415	0.8814
02JG3[c,d]	25.4	26.68	0.525	0	440	1.0541
02GA612[c,d]	25.4	27.24	0.536	0	638	2.2352
02GAA1-47	25.4	26.75	0.526	0	725	2.7254
02GA593	25.4	27.13	0.534	0	698	3.0226
02JM3[c]	25.4	27.12	0.533	20	239	0.3048
02JL1[c,d]	25.4	27.17	0.530	20	360	0.8357
02JL3[c,d]	25.4	26.60	0.523	20	396	1.0947
02GAA1-36[c,d]	25.4	26.14	0.518	20	494	2.1844
02JG5[c,d]	25.4	26.73	0.525	20	469	1.4249
02JL4[c,d]	25.4	26.28	0.516	20	560	2.5451
02GA605	25.4	30.78	0.606	0	91	0.0533
02GA613	25.4	30.61	0.603	0	147	0.1270
02GA604[c]	25.4	31.15	0.613	0	235	0.2337
02GA606[c,d]	25.4	30.74	0.605	0	281	0.4242
02GA611[c,d]	25.4	30.83	0.607	0	396	0.6655
02GAA1-143[c,d]	25.4	31.24	0.615	0	625	2.3952
02GAA1-WRD[a,c,d]	25.4	31.37	0.618	0	589	1.8034
02GAA1-14[b,c,d]	25.4	31.50	0.620	0	524	1.7018
02GAA1-15[b,c,d]	25.4	32.00	0.630	0	642	2.3114
02JL6[c]	25.4	41.72	0.821	0	159	0.1473
02JL5[c]	25.4	41.03	0.808	0	217	0.2565
02JH5[c,d]	25.4	41.24	0.812	0	333	0.6096
02JH6[c,d]	25.4	41.77	0.822	0	498	1.2649
02GAA1-28[c,d]	25.4	43.42	0.855	0	498	1.4732
02JM6[c,d]	25.4	42.13	0.829	0	591	1.9609
02JG6[c,d]	25.4	40.70	0.801	0	652	2.2403

[a]Private communication with G. A. Clarke, Westinghouse Research and Development Center.
[b]Reference *16*.
[c]Data used for crack extension analysis by modified procedure.
[d]Data used for crack extension analysis by recommended procedure.

The multiple-specimen R-curve for this group is shown in Fig. 8. All specimens in the group behaved in a consistent manner relative to one another. All data points were included in the family regression analysis. Again the best-fit curve was concave downward. The intersection of the blunting line and the crack extension line gave

$$J_c = 205 \text{ kJ/m}^2$$

$$(J_c = 1170 \text{ in.-lb/in.}^2)$$

The recommended analysis, on the other hand, yielded a J_c-value of 326 kJ/m^2 (1860in.-lb/in.^{2}). Again the modified analysis gives a J_c-value which is in better agreement with direct observation.

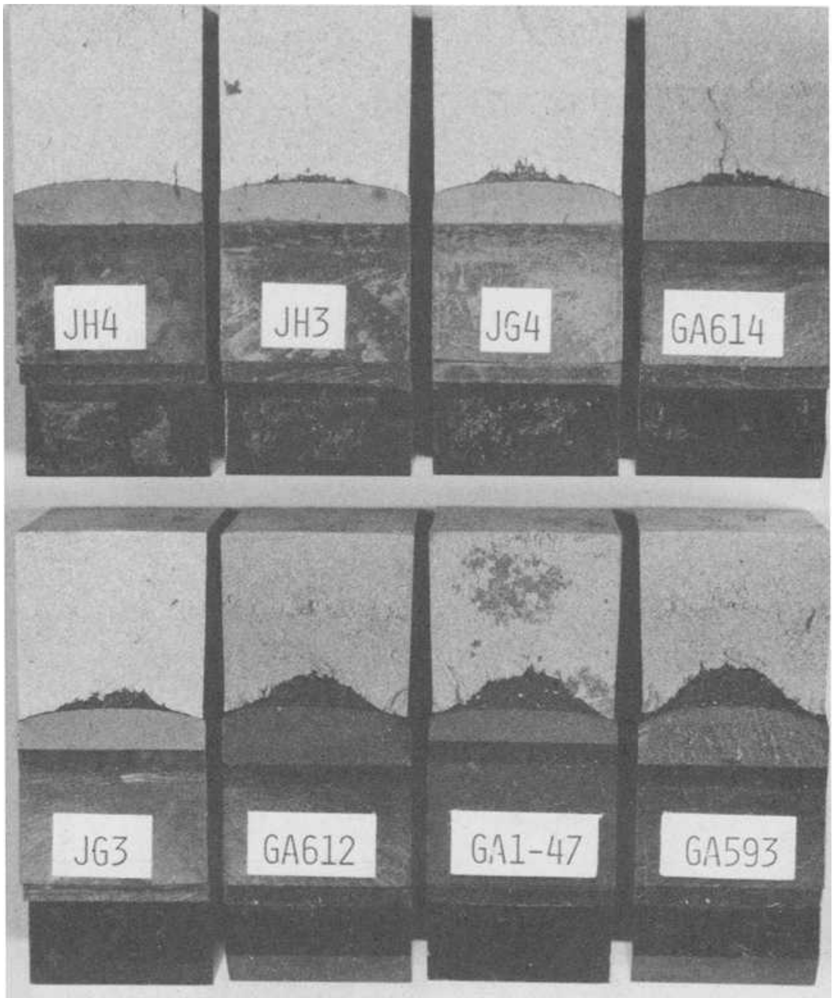

FIG. 5—*Fracture surfaces for Group 1;* a/W = *0.5, percent SG = 0.*

R-Curve Analysis for Group 3: a/W = *0.6, Percent SG = 0*

The results of nine tests were available for the construction of the R-curve for this group. Fracture surfaces are shown in Fig. 9 (note that three specimens were not available for the photograph, but all three had more crack extension than the specimens shown). The results are listed in Table 4. Examination of fracture surfaces showed that two specimens, 02GA605 and 02GA613, underwent COS only; the remainder showeu crack extension. Specimen 02GA604 showed the least amount of crack extension. Therefore,

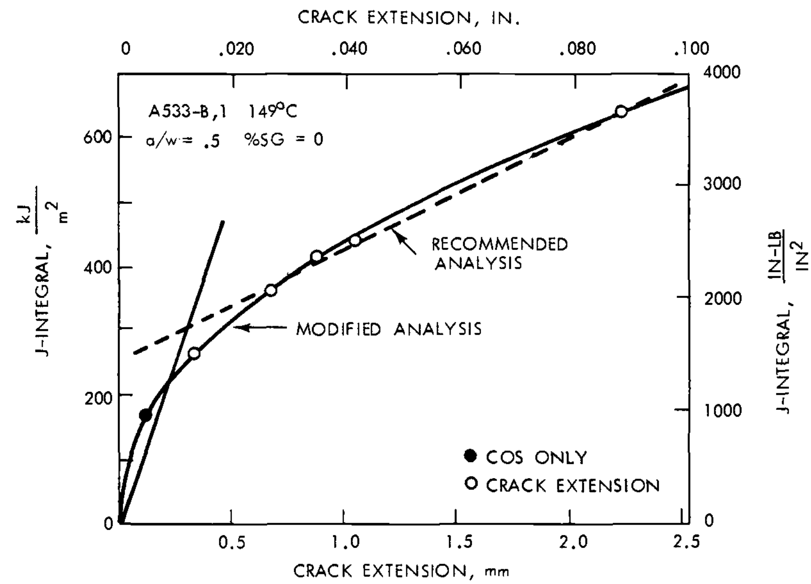

FIG. 6—*R-curve for Group 1; a/W = 0.5, percent SG = 0.*

direct observation reveals that onset of crack extension occurred at a J-value between the J-values for 02GA613 and 02GA604

$$147 < J_c < 235 \text{ kJ/m}^2$$

$$(839 < J_c < 1340 \text{ in.-lb/in.}^2)$$

In Fig. 10 the multiple-specimen R-curve is shown. All data points except 02GA605 and 02GA613 were used in the family regression analysis to obtain the crack extension line. As in the previous two R-curves, the curve is again concave downward. Using the modified analysis, it was found that

$$J_c = 228 \text{ kJ/m}^2$$

$$(J_c = 1300 \text{ in.-lb/in.}^2)$$

The recommended analysis yielded a J_c-value of 297 kJ/m^2 (1697 in.-lb/in.^{2}). The modified analysis again showed better agreement between the computed and directly observed J_c.

The data in this group lend themselves to comparison with the ASTM round-robin results [*22*]. In the round-robin, 12 separate laboratories tested four to six 1T compact specimens ($a/W = 0.6$) each, to generate 12 separate R-curves. Then all the data were assembled to construct one aggregate R-curve. The aggregate R-curve is of primary interest. In spite of a lack of data points near the blunting line, when the round-robin data were analyzed by the modified analysis (see Fig. 11), a concave-downward curve again proved

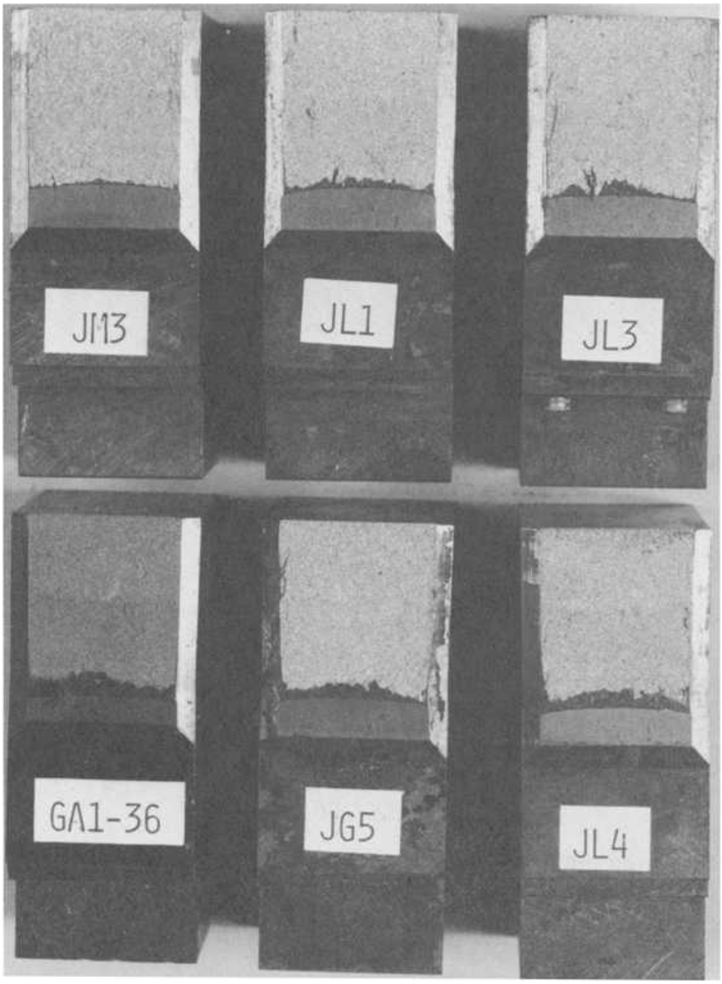

FIG. 7—*Fracture surfaces for Group 2;* a/W = *0.5 percent SG* = *20.*

to be the best fit (the two data points which lie on the blunting line were not included as it was not certain crack extension had occurred). The nonlinear regression had a correlation coefficient of 0.9089 compared with 0.8773 for the linear regression. The J_c-value obtained from the modified analysis was 182 kJ/m^2 (1040 in.-lb/in.^{2}). The recommended analysis yielded a J_{Ic}-value of 255 kJ/m^2 (1456 in.-lb/in.^{2}) which again appears to be an overestimation of 40 percent. It might be noted that both analyses considered only data falling within the "exclusion lines" and the systematic overestimation of J_c was still apparent. A comparable over-estimation (30 percent) was obtained by the recommended analysis for the data in Fig. 10 even though some data beyond the 1.5-mm "exclusion line" were included in the analysis.

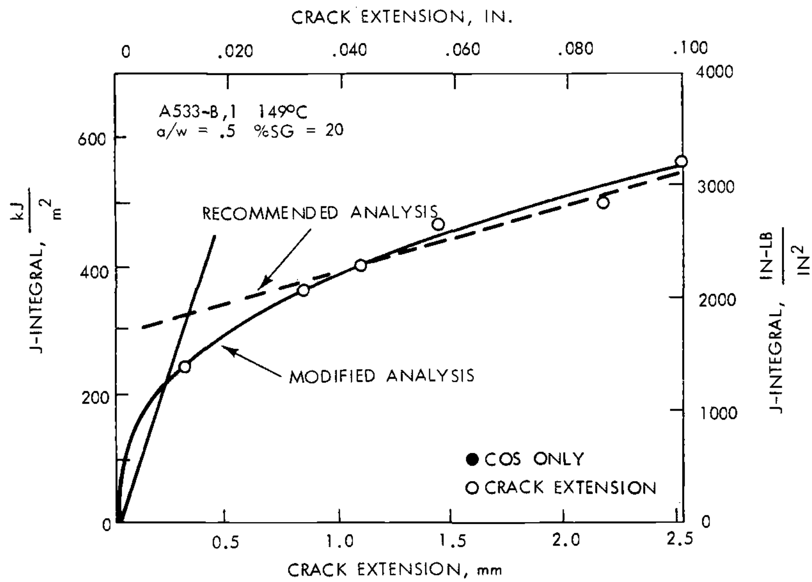

FIG. 8—*R-curve for Group 2;* a/W = *0.5, percent SG = 20.*

R-Curve Analysis for Group 4: a/W = *0.8, Percent SG = 0*

Seven specimens were tested in this group. The fracture surfaces are seen in Fig. 12 and the results tabulated in Table 4. All specimens were observed to exhibit crack extension. However, Specimen 02JL6 was observed to have very little crack extension in the form of three or four isolated locations of initiation. This specimen was estimated to very nearly represent the onset of crack extension and, therefore

$$J_c \lesssim 159 \text{ kJ/m}^2$$

$$(J_c \lesssim 906 \text{ in.-lb/in.}^2)$$

The R-curve for this group is shown in Fig. 13. The data points from all specimens tested in the group were used in the family regression analysis to obtain the best-fit crack extension line. The subsequent curve was again concave downward. The intersection of the crack extension line and the blunting line indicate that

$$J_c = 170 \text{ kJ/m}^2$$

$$(J_c = 970 \text{ in.-lb/in.}^2)$$

The current recommended analysis, also shown in Fig. 13, yields a J_c-value of 281 kJ/m² (1605 in.-lb/in.²).

FIG. 9—*Fracture surfaces for Group 3;* a/W = *0.6, percent SG* = *0.*

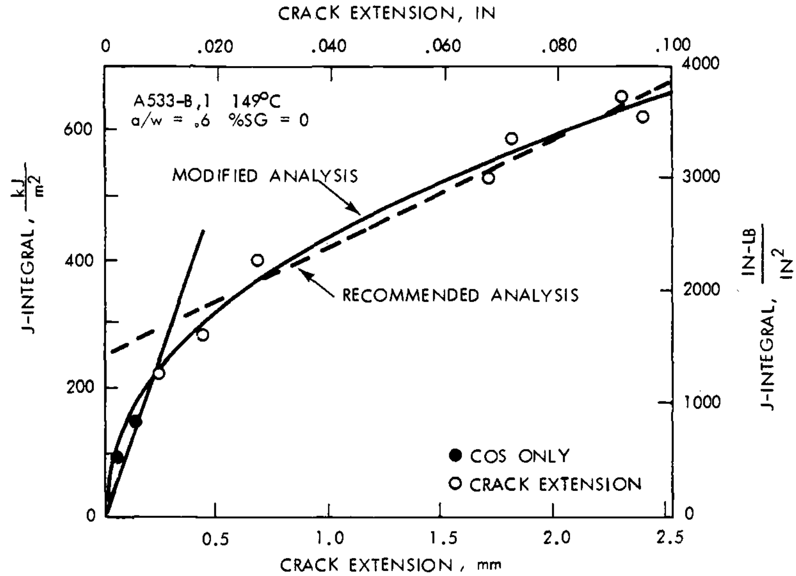

FIG. 10—*R-curve for Group 3;* a/W = *0.6, percent SG* = *0.*

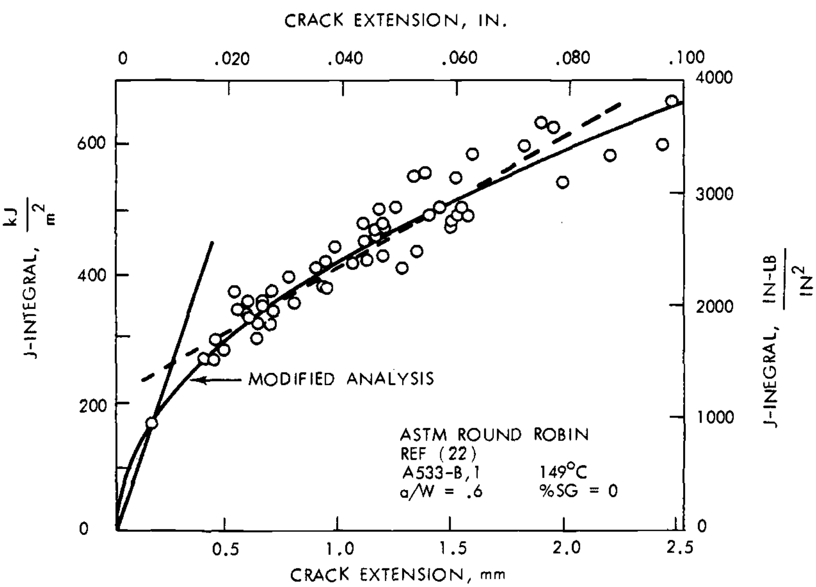

FIG. 11—*R-curve for data from ASTM round robin [22].*

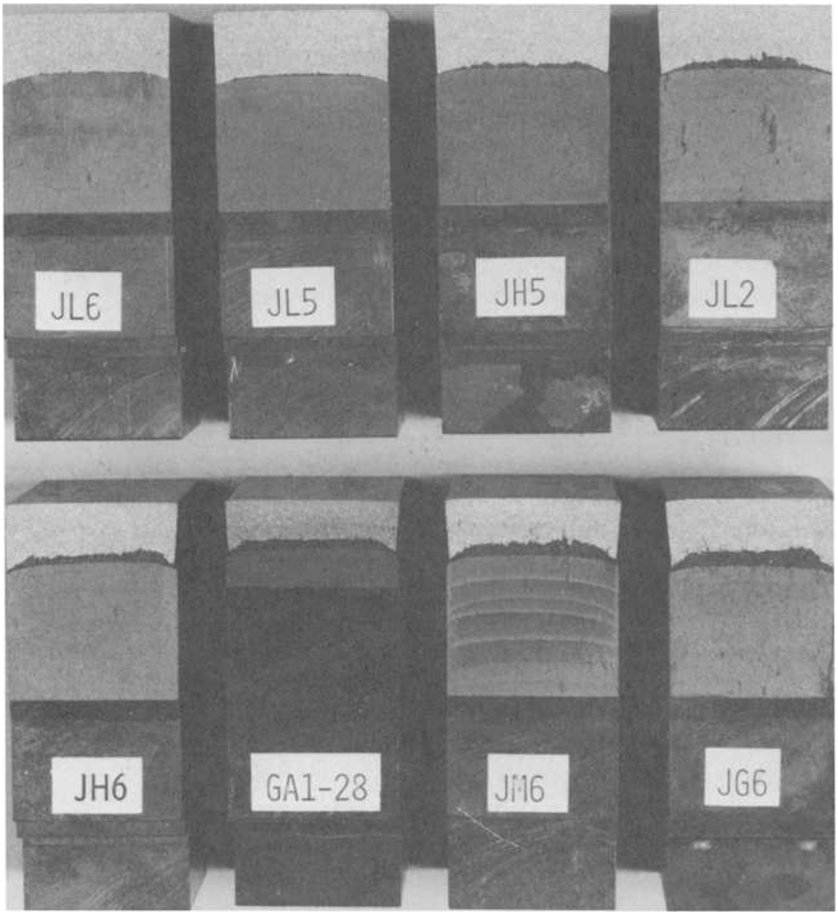

FIG. 12—*Fracture surfaces for Group 4;* a/W = *0.8, percent SG* = *0.*

Discussion

A number of similarities were noted in the R-curves developed for the various specimen configurations studied. In each case the recommended analysis overestimated the observed approximate onset of crack extension. The results are summarized in Table 5. On the R-curves this was observed as the inability of the linear regression crack extension line in the recommended analysis to accommodate the nonlinear behavior of that portion of the R-curve where crack initiation was taking place. The J-value increases rapidly during initiation but at a decreasing rate as the crack grows; the abrupt change in rate suggested by the straight-line construction of the recommended procedure does not accurately reflect the data. By using care to obtain at least one datum point in the crack initiation regime and by employing a family

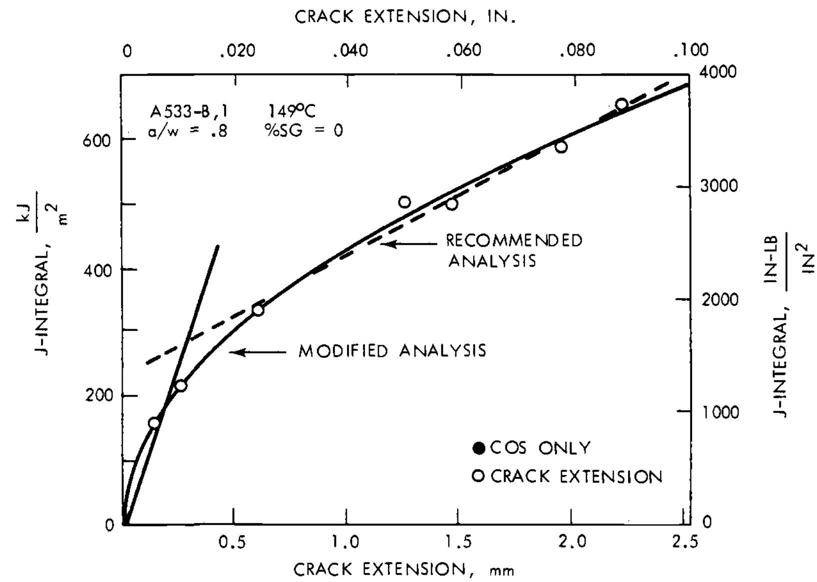

FIG. 13—*R-curve for Group 4;* a/W = *0.8, percent SG = 0.*

TABLE 5—*Comparison of* J_c *results.*

Specimen Group		J_c, kJ/m²		
a/W	% SG	Direct Observation	Modified Analysis	Recommended Analysis
0.5	0	$168 < J_c < 264$	226	309
0.5	20	$J_c < 239$	205	326
0.6	0	$147 < J_c < 235$	228	297
0.6 (round robin)	0	...	182	255
0.8	0	$J_c \lesssim 159$	170	281

regression analysis of data points from tests where crack extension occurred, a J_c-value which agrees with observations can be determined.

The use of the data points slightly beyond the 1.5-m (0.06 in.) "exclusion line" appeared to have little effect on J_{Ic} results obtained by the recommended analysis. The recommended procedure was strictly adhered to for the ASTM round-robin data ($a/W = 0.6$, percent SG = 0) and still the systematic over-estimation was evident. Furthermore, it is likely that if those tests which lie beyond the 1.5-mm (0.06 in.) "exclusion line" had been terminated at slightly shorter crack extensions [so that they would have fallen to the left of the 1.5-mm (0.06 in.) exclusion line], the shift of these data points would have had an insignificant effect on the results of the linear regression. This is particularly true because the data exhibited little curvature in this portion of the J-R curve.

On the basis of the results obtained in this investigation, it is suggested that recommended analysis of multiple-specimen R-curves be modified in two ways: (1) Data points which comprise the crack extension line should include at least one test interrupted in the crack initiation regime; (2) a family regression analysis should be used to identify the best-fit curve through the data for the establishment of the crack extension line, and the intersection of the best-fit data curve and the blunting line should be used to determine J_c.

It is significant that the recommended analysis overestimates the critical J-integral at initiation by 31 to 65 percent for ASTM A 533-B1, the material on which the recommended analysis was largely based. Such variations, due principally to nonlinear R-curve behavior, can contribute to confusion in the determination or clarification of possible size and geometry effects on J_c. For example, a possible effect of remaining ligament on J_c is observed for data in Table 5 when the nonlinear R-curve analysis is employed, while such an effect is obscured by the current recommended analysis. Alternately, analysis procedures which employ statistical curve-fitting of the observed crack extension data points (from which either a linear or nonlinear analysis may result) would possibly resolve potential specimen materials, specimen size, and specimen geometry effects on J_c. Nonlinear analysis may be particularly applicable to single-specimen techniques of J_c determination. This is the subject of a continuing investigation.

Conclusions

1. The current recommended analysis of J-R curve data gave high J_c-values (nonconservative) while nonlinear J-R curve analysis gave values in close agreement with observed J_c.

2. The nonlinearity of the crack initiation and the crack extension regime was confirmed by this study. Therefore, a linear regression analysis through data points in the stable crack extension regime is not an accurate representation of R-curve data.

3. The recommended analysis should be modified to yield analytical J_c-values in closer agreement with observed J_c. The modified analysis will require data points in the crack initiation region of the R-curve and should employ a statistical family regression to obtain the best-fit curve through the data points.

4. While the recommended analysis may provide an operational definition of J_{IC}, it appears unlikely that it will provide a parameter by which a quantitative description of the ductile fracture process can be made. The J_c-value obtained from the modified analysis is a more viable parameter.

Acknowledgments

The authors would like to extend their thanks to G. C. Massie, senior technician, for his careful attention in conducting the tests reported herein. They would also like to acknowledge L. D. Blackburn, manager of Structural Properties and R. L. Knecht, manager of Structural Engineering at Westinghouse Hanford Co. for their support and encouragement during this investigation.

References

[1] Rice, J. R., *Journal of Applied Mechanics*, Vol. 35, 1968, pp. 379-386.
[2] Rice, J. R. in *Fracture*, H. Liebowitz, Ed., Vol. 2, Academic Press, New York, 1968, pp. 191-311.
[3] Begley, J. A. and Landes, J. D. in *Fracture Toughness, ASTM STP 514*, American Society for Testing and Materials, 1972, pp. 1-23.
[4] Landes, J. D. and Begley, J. A. in *Fracture Toughness, ASTM STP 514*, American Society for Testing and Materials, 1972, pp. 24-39.
[5] Bucci, R. J., Paris, P. C., Landes, J. D., and Rice, J. R. in *Fracture Toughness, ASTM STP 514*, American Society for Testing and Materials, 1972, pp. 40-69.
[6] Rice, J. R., Paris, P. C., and Merkle, J. G. in *Progress in Flaw Growth and Fracture Toughness Testing, ASTM STP 536*, American Society for Testing and Materials, 1973, pp. 231-245.
[7] Landes, J. D. and Begley, J. A. in *Fracture Analysis, ASTM STP 560*, American Society for Testing and Materials, 1974, pp. 170-186.
[8] Begley, J. A. (on behalf of ASTM Task Group E-24:01:09), "Recommended Practices for the Determination of the J_{Ic} Point from the J Versus Δa R-Curve," presented at the American Society for Testing and Materials E-24 Committee Meeting, Philadelphia, Pa., 7 Oct. 1976.
[8] Clarke, G. A., Andrews, W. R., Begley, J. A., Donald, J. K., Embley, G. T., Landes, J. D., McCabe, D. E., and Underwood, J. H., *Journal of Testing and Evaluation*, Vol. 7, No. 1, Jan. 1979, pp. 49-56.
[10] Childress, C. E., "Fabrication History of the First Two 12-Inch Thick ASTM A533 Grade B, Class 1 Steel Plates of the Heavy Section Steel Technology Program," Documentary Report 1, ORNL-4313, Oak Ridge National Laboratory, Oak Ridge, Tenn., Feb. 1969.
[11] Williams, J. A., "The Irradiation and Temperature Dependence of Tensile and Fracture Properties of ASTM A533, Grade B, Class 1 Steel Plate and Weldment," HEDL-TME 73-75, HSSTP Technical Report 31, Hanford Engineering Development Laboratory, Richland, Wash., Aug. 1973.
[12] Steichen, J. M. and Williams, J. A., "High Strain Rate Tensile Properties of Irradiated ASTM A533-B Pressure Vessel Steel," HEDL-TME 73-74, HSSTP Technical Report 32, Hanford Engineering Development Laboratory, Richland, Wash., July 1973.
[13] Stelzman, W. J. and Berggren, R. G., "Radiation Strengthening and Embrittlement in Heavy Section Steel Plates and Welds," ORNL-4871, Oak Ridge National Laboratory, Oak Ridge, Tenn., June 1973.
[14] Andrews, W. R. and Shih, C. F. in *Elastic-Plastic Fracture, ASTM STP 668*, J. D. Landes, J. A. Begley, and G. A. Clarke, Eds., American Society for Testing and Materials, 1979, pp. 426-450.
[15] Gudas, J. P., Joyce, J. A., and Davis, D. A. in *Fracture Mechanics, ASTM STP 677*, C. W. Smith, Ed., American Society for Testing and Materials, 1979, pp. 474-485.
[16] Vassilaros, M. G., Joyce, J. A., and Gudas, J. P. in *Fracture Mechanics, Proceedings of the National Symposium, ASTM STP 700*, American Society for Testing and Materials, 1980, pp. 251-270.
[17] Williams, J. A. and Carlson, K. W., "An Evaluation of a Load-Line Extensometer for

Elastic-Plastic Fracture Toughness Evaluation," paper to be published in *Journal of Testing and Evaluation,* Sept. 1981.

[*18*] Merkle, J. G. and Corten, H. T., *Journal of Pressure Vessel Technology,* American Society of Mechanical Engineers, 1974.

[*19*] Shih, C. F., deLorenzi, H. G., and Andrews, W. R. in *Elastic-Plastic Fracture, ASTM STP 668,* J. D. Landes, J. A. Begley, and G. A. Clarke, Eds., American Society for Testing and Materials, 1979, pp. 65–120.

[*20*] Berger, C., Keller, H. P., and Munz, D. in *Elastic-Plastic Fracture, ASTM STP 668,* J. D. Landes, J. A. Begley, and G. A. Clarke, Eds., American Society for Testing and Materials, 1979, pp. 378–405.

[*21*] Carlson, K. W., "A Study of the Experimental Implementation and the Resulting Characteristic Behavior of the J-Integral Fracture Toughness Parameter Applied to Two Controlled-Rolled Steels," Ph.D. Thesis, University of Illinois, Urbana, Ill., June 1978.

[*22*] Clarke, G. A., "Evaluation of the J_{Ic} Testing Procedure by Round-Robin Tests on A533B Class 1 Pressure Vessel Steel," Westinghouse Scientific Paper 79-1D3-JINTF-P5, Westinghouse R&D Center, Pittsburgh, Pa., 28 Sept. 1979.

J. A. Joyce[1] *and M. G. Vassilaros*[2]

An Experimental Evaluation of Tearing Instability Using the Compact Specimen

REFERENCE: Joyce, J. A. and Vassilaros, M. G., **"An Experimental Evaluation of Tearing Instability Using the Compact Specimen,"** *Fracture Mechanics: Thirteenth Conference, ASTM STP 743,* Richard Roberts, Ed., American Society for Testing and Materials, 1981, pp. 525–542.

ABSTRACT: The objective of this investigation was to produce experimental verification of the tearing instability theory proposed by Paris and co-workers [*10*].[3] This theory states that ductile crack extension will occur in an unstable fashion whenever the applied tearing force is greater than the material tearing resistance. In this investigation a series of compact specimens of aluminum, titanium, and steel alloys was tested in a variably compliant test machine to generate a range of applied tearing force. The material tearing resistance was measured from the J_I-R curves of the stable specimens and compared with the applied tearing force necessary to generate ductile tearing instability in each material. The Paris theory was found to accurately predict the onset of gross instability behavior. Some limited instability behavior was found, however, at values of tearing force less than the average material tearing resistance obtained from an unloading compliance J_I-R curve test. Limited instability behavior was characterized by repeated short steps of rapid but ductile crack extension, separated by regions of slow stable tearing.

KEY WORDS: fracture crack instability, tearing instability, tearing modulus, elastic-plastic fracture, ductile fracture, crack propagation, stable crack growth, compact tension specimen

During the past few years it has become increasingly common to characterize materials' resistance to static crack extension in terms of the J resistance curve (J-R curve) as introduced by Begley and Landes [*2*]. The usual application of this J-R curve has been to extrapolate back to the crack initiation parameter J_{Ic}, which is then considered to be a material parameter. Crack extension is then avoided in the structural element by limiting applied

[1]Associate professor of mechanical engineering, U. S. Naval Academy, Annapolis, Md. 21402.
[2]Project engineer, Fatigue and Fracture Branch, David W. Taylor Naval Ship R&D Center, Annapolis Laboratory, Annapolis, Md. 21402.
[3]The italic numbers in brackets refer to the list of references appended to this paper.

loads to values which keep the J-integral parameter at existing cracks below the material J_{Ic}-value.

In many applications overloads can be envisioned which could reach or exceed the loading required to initiate ductile crack extension. An added requirement for structural integrity then is that the crack growth be stable and not self-propagating and that it cease immediately when the overload is removed.

To address this problem Paris and co-workers [*1*] have defined a tearing modulus quantity T given by

$$T = \frac{E}{\sigma_0^2} \frac{dJ}{da} \tag{1}$$

where

a = crack length,
E = elastic modulus, and
σ_0 = material flow stress.

A material tearing modulus, T_{material} can then be defined by taking dJ/da as the slope of the material J_I-R curve beyond J_{Ic}.

The applied tearing force, T_{applied}, depends on the material properties E and σ_0 but also on the value of dJ/da applied to the crack tip by the combination of crack geometry, type of loading, and structural stiffness. Calculations of T_{applied} have been accomplished by Paris and co-workers [*1,3,4*] for several simple geometries.

The tearing instability theory of Paris [*1*] states that a flawed member will tear stably when it is beyond J_{Ic}, and at its limit load, as long as the T_{applied} is less than the T_{material}. Tearing instability will occur whenever the T_{applied} equals or exceeds the material tearing modulus.

The objective of this investigation is to evaluate the validity of the Paris tearing instability theory by testing a series of compact specimens in a test apparatus of variable compliance. A range of materials including aluminum, titanium, and steel alloys was chosen to encompass a broad range of elastic moduli. Both side-grooved and non-side-grooved specimens were tested since earlier work [*5,6*] has demonstrated that this geometry modification has a distinct effect on the material J_I-R curve, tending to give lower T_{material} values when side grooves were present. Application of a range of T_{applied} values would allow the determination of whether the T_{material} value was geometry dependent, or if not, which T_{material} accurately predicted the instability conditions. Two crack lengths were studied to verify the accuracy of the expression for T_{applied} over a range of this variable as well as elastic modulus, flow stress, and machine stiffness.

For each material, standard single-specimen J_I-R curves were developed using a stiff test machine and the technique of Joyce and Gudas [*7*], to characterize the T_{material} for each material. Then by increasing the test machine compliance the T_{applied} was increased until it exceeded the T_{material} value, at which point the previously stable specimens would be expected to fail in a rapid, unstable, but ductile fashion. Previous work of this type has been completed by Paris [8] for one steel using bend specimens. For all tests the J-integral size criterion [9] was met to keep the tests initially in the region of J-controlled growth [10].

T_{applied} was calculated for the compact specimen geometry in a compliant test machine using the general analysis scheme outlined by Paris et al [1], assuming elastic-fully plastic material behavior. The details of this analysis for a compact specimen are included herein.

Materials and Experimental Method

The experimental tearing instability analysis study was performed on a series of 36 25.4 mm (1 in.) (1T) compact specimens machined in the T-L orientation. These plate materials, which were chosen to encompass a wide range of elastic moduli, included aluminum 5456 H117, Ti-3Al-2.5V titanium alloy, HY-130 steel, and as-quenched ASTM A533B steel. The mechanical properties of the materials are presented in Table 1. All specimens were tested at room temperature except the as-quenched A533B, which was tested at 150°C. The tests were performed with a screw-driven Tinius Olsen tensile machine modified with a variable-stiffness titanium spring in the load train as shown in Fig. 1. The spring was composed of two titanium beams in series loaded in three-point bending. The spring stiffness was a function of the span distance between the two rollers.

All the J-integral fracture tests were conducted using a single-specimen computer interactive unloading compliance method utilizing a minicomputer for data acquisition and analysis as developed by Joyce and Gudas [7]. The results of each unloading compliance test were plots of load versus load line crack-opening displacement (COD), load versus test machine head displacement, and a J_I-R curve which included corrections for crack growth [11] and for specimen rotation [12].

The computer program was modified to calculate the machine compliance, the T_{applied} using the machine compliance, applied J_I, and crack length from each unloading. The machine compliance was calculated by measuring the total system crosshead deflection versus applied load during the initial loading of a specimen, and subtracting the compliance contribution of the specimen. In addition to the digitally recorded data, an analog plot of load versus crosshead displacement was recorded during each test. This plot supplemented the load-versus-COD curves and was used to identify instability events during the test.

Table 2 is the test matrix for this tearing instability investigation, which summarizes the materials, specimen geometries, and ranges of T_{applied}.

TABLE 1—*Mechanical properties of materials used in tearing instability study.*

Material	Modulus, psi	Modulus, (MPa)	Flow Stress, KSI	Flow Stress, (MPa)	J_{Ic}, in.-lb in^2	J_{Ic}, (KJ/m^2)	$T_{material}$ with 20% Side Grooves a	$T_{material}$ with 20% Side Grooves b	Yield Stress, ksi	Yield Stress, (MPa)	Tensile Stress, ksi	Tensile Stress, (MPa)	Elongation, % in 2 in.
Al 5456 H117	10.3×10^6	(71×10^3)	42.5	(293)	177	(31)	12	4	34	(234)	51	(351)	19
Ti-3Al-2.5V	15.4×10^6	(106×10^3)	80.5	(555)	450	(79)	22	11	73	(503)	88	(607)	22
ASTM A533B steel (as-quenched)	29×10^6	(200×10^3)	65	(448)	1500	(262)	36[c]	26[c]	51	(352)	79	(545)	30
HY-130 steel	29×10^6	(200×10^3)	145	(999)	870	(152)	14	9	138	(951)	152	(1048)	20

[a]These values were calculated from J_I-R curve data with crack extensions up to 1.5 mm, $a_0/W = 0.65$.
[b]These values were calculated from J_I-R curve data with crack extensions up to 5 mm, $a_0/W = 0.65$.
[c]These were non-side-grooved specimens.

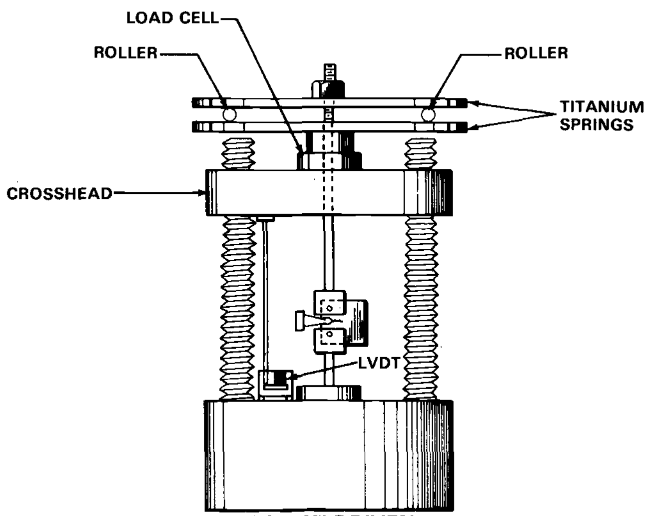

FIG. 1—*Schematic of modified test machine.*

The T_{material} values listed in Table were calculated from conventional J-integral tests in two ways. The first method was to use a least-squares linear regression analysis as prescribed by Clarke et al [*9*] up to a crack extension of 1.5 mm and the second method was to use a similar method but to include all test points up to a crack extension of 5 mm.

Analysis

This section presents the derivation of an expression for the tearing force T_{applied} for a compact specimen loaded in a compliant test machine.

For the specimen and test configuration shown in Fig. 2 a fixed Δ_{TOT} is applied and held rigidly so that

$$\Delta_{TOT} = \Delta_{EL} + \Delta_{PL} + \Delta_M = \text{Constant} \tag{3}$$

where Δ_{TOT}, Δ_{EL}, Δ_{PL}, and Δ_M are the total, elastic, plastic and machine displacements, respectively. During crack extension, then, the sum of the differentials of Δ_{EL}, Δ_{PL}, and Δ_M must be zero, that is

$$d\Delta_{EL} + d\Delta_{PL} + d\Delta_M = 0 \tag{4}$$

For the compact specimen the elastic displacement component can be evaluated from the relationship that

$$\Delta_{EL} = \frac{P}{BE} f\left(\frac{a}{W}\right) \tag{5}$$

TABLE 2—*Results of tearing instability study on 1T compact specimens.*

Material	a/W	% Side Grooves	$T_{material}$	$T_{applied}$ at Max Load	Fracture Behavior
5456 H117 aluminum	0.65	0.0	19	3.5	stable
				4.0	semistable
				5.5	semistable
				9.7	semistable
				39.0	unstable
5454 H117 aluminum	0.65	20.0	4	−1.4	semistable
				1.5	semistable
				4.7	unstable
5456 H117 aluminum	0.80	0.0	17	−.5	stable
				4.7	stable
				7.7	semistable
				14.2	semistable
				134.0	unstable
5456 H117 aluminum	0.80	20.0	5	−7.2	semistable
				3.4	semistable
				10.0	unstable
				21.0	unstable
Ti-3Al-2.5V	0.65	0.0	20	−1.0	stable
				6.0	stable
				15.0	stable
				29.0	unstable
Ti-3Al-2.5V	0.65	20.0	11	−1.0	stable
				5.0	semistable
				13.0	semistable
				17.0	unstable
A533B [as-quenched test at 149°C (300°F)]	0.65	0.0	26	5	stable
				5	semistable
				23	semistable
				34	unstable
HY-130	0.65	0.0	22	3	stable
				13	semistable
				17	semistable
				26	unstable
				37	unstable
HY-130	0.65	20.0	9	1.0	semistable
				2.0	semistable
				9.0	semistable
				11.0	unstable

NOTE: All tests conducted at room temperature except the A533B tests.

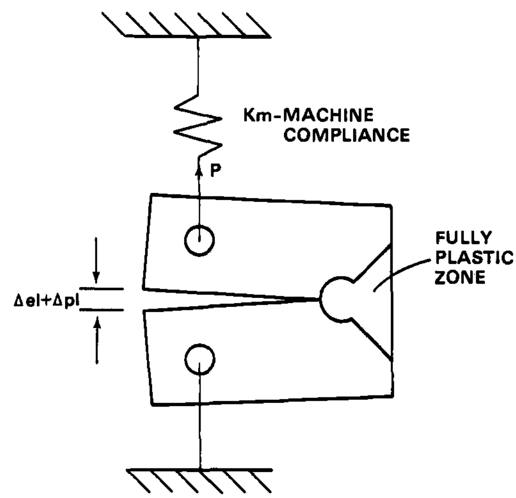

FIG. 2—*Illustration of specimen displacement notation.*

where from Saxena and Hudak [13]

$$f\left(\frac{a}{W}\right) = \left(\frac{1+\frac{a}{W}}{1-\frac{a}{W}}\right)^2 \left[2.16299 + 12.219\frac{a}{W} - 20.065\left(\frac{a}{W}\right)^2 - 0.9925\left(\frac{a}{W}\right)^3 + 20.609\left(\frac{a}{W}\right)^4 - 9.9314\left(\frac{a}{W}\right)^5\right] \quad (6)$$

where

W = specimen width,
E = elastic modulus,
B = specimen thickness, and
P = applied load.

The plastic displacement component can be expressed as

$$\Delta_{PL} = \delta_t g\left(\frac{a}{W}\right) \quad (7)$$

where from Merkle and Corten [14]

$$g\left(\frac{a}{W}\right) = \left(\frac{2W}{W-a} + \alpha - 1\right)\frac{\delta_t}{1+\alpha} \quad (8)$$

where δ_t is the crack-opening stretch and

$$\alpha = \{[4a^2 + 4a(W - a) + 2(W - a)^2]^{1/2} - (a + W)\}/(W - a) \quad (9)$$

The testing machine is assumed here to behave like a linear elastic spring so the testing machine displacement is given simply by

$$\Delta_M = \frac{P}{K_M} \quad (10)$$

where K_M, the machine stiffness, is a constant.

Assuming now that the load is at the specimen limit load gives

$$P = P_L = \sigma_0 B W h \left(\frac{a}{W}\right) \quad (11)$$

where from Merkle and Corten [14]

$$h\left(\frac{a}{W}\right) = \left(1 - \frac{a}{W}\right) \alpha \quad (12)$$

with α given by Eq 9. The final relationship needed here is from Paris [15] and Rice [16]—that the crack-tip opening displacement is proportional to J as

$$\delta_t = \alpha^* \frac{J}{\sigma_0} \quad (13)$$

where α^* is a constant $\approx$ 1 for plane stress and $\approx$ 0.7 for plane strain.

Taking the differentials of Eqs 5, 7, and 10, substituting into Eq 4, and rearranging gives the relationship

$$T_{\text{applied}} = \frac{E}{\sigma_0{}^2} \frac{\partial J}{\partial a} = - \frac{W}{\alpha^* g\left(\frac{a}{W}\right)} \left\{ \frac{\partial}{\partial a} \left[h\left(\frac{a}{W}\right) f\left(\frac{a}{W}\right) \right\} \right.$$

$$\left. + \frac{EB}{K_M} \frac{\partial h\left(\frac{a}{W}\right)}{\partial a} + \frac{\alpha^* JE}{W \sigma_0{}^2} \frac{\partial g\left(\frac{a}{W}\right)}{\partial a} \right] \quad (14)$$

where by differentiation of Eqs 6, 8, and 12

$$\frac{\partial f}{\partial a} = \frac{2}{W} \frac{1 + \frac{a}{W}}{1 - \frac{a}{W}} \frac{2}{\left(1 - \frac{a}{W}\right)^2} \left[2.16299 + 12.219 \frac{a}{W} - 20.065 \left(\frac{a}{W}\right)^2 \right.$$

$$- 0.9925\left(\frac{a}{W}\right)^3 + 20.609\left(\frac{a}{W}\right)^4 - 9.9314\left(\frac{a}{W}\right)^5\Bigg] + \frac{1}{W}\left(\frac{1+\dfrac{a}{W}}{1-\dfrac{a}{W}}\right)^2$$

$$\left[12.219 - 40.13\frac{a}{W} - 2.9775\left(\frac{a}{W}\right)^2 + 82.436\left(\frac{a}{W}\right)^3 - 49.657\left(\frac{a}{W}\right)^4\right] \tag{15}$$

$$\frac{\partial g}{\partial a} = \frac{\left\{1 + \dfrac{\partial[\alpha(W-a)]}{\partial a}\right\}[W - a + (W-a)\alpha]}{(W-a)^2(1+\alpha)^2}$$

$$- \frac{\left\{-1 + \dfrac{\partial[\alpha(W-a)]}{\partial a}\right\}}{(W-a)^2}\,\frac{[(W+a) + \alpha(W-a)]}{(1+\alpha)^2} \tag{16}$$

$$\frac{\partial h}{\partial a} = \frac{1}{W}\frac{\partial[\alpha(W-a)]}{\partial a} \tag{17}$$

with from Eq 9

$$\frac{\partial[\alpha(W-a)]}{\partial a} = \frac{2a}{[4a^2 + 4a(W-a) + 2(W-a)^2]^{1/2}} - 1 \tag{18}$$

Substitution of Eqs 15–18 into Eq 14 gives the final form of $T_{applied}$ used throughout this investigation, expressing the dependence of $T_{applied}$ on J_I, E, σ_0, a/W, and K_M for the compact specimen.

Discussion of Results

Description of Specimen Instability Behavior

During the loading of the specimens described in the test matrix, three general types of load displacement behavior were demonstrated as shown in Fig. 3. Figure 3*a* shows the result of a J_I-R curve done in a rigid test machine so that $T_{material} \gg T_{applied}$. This behavior is typical of a stable J_I-R curve test.

For cases where $T_{applied} > T_{material} > 0.1\ T_{applied}$ the behavior shown in Fig. 3*b* was observed. This behavior was characterized by repeated rapid steps of crack growth of relatively small magnitude, typically on the order of $0.1 \rightarrow 0.5$ mm, with larger steps being observed as $T_{applied}$ approached $T_{material}$. Often, unloadings were taken during the stable interval to reestablish the new crack length, but this was not always done and did not appear to affect the spacing or magnitude of the rapid crack growth increments. This phenomenon is termed "limited instability behavior" in the discussion which follows.

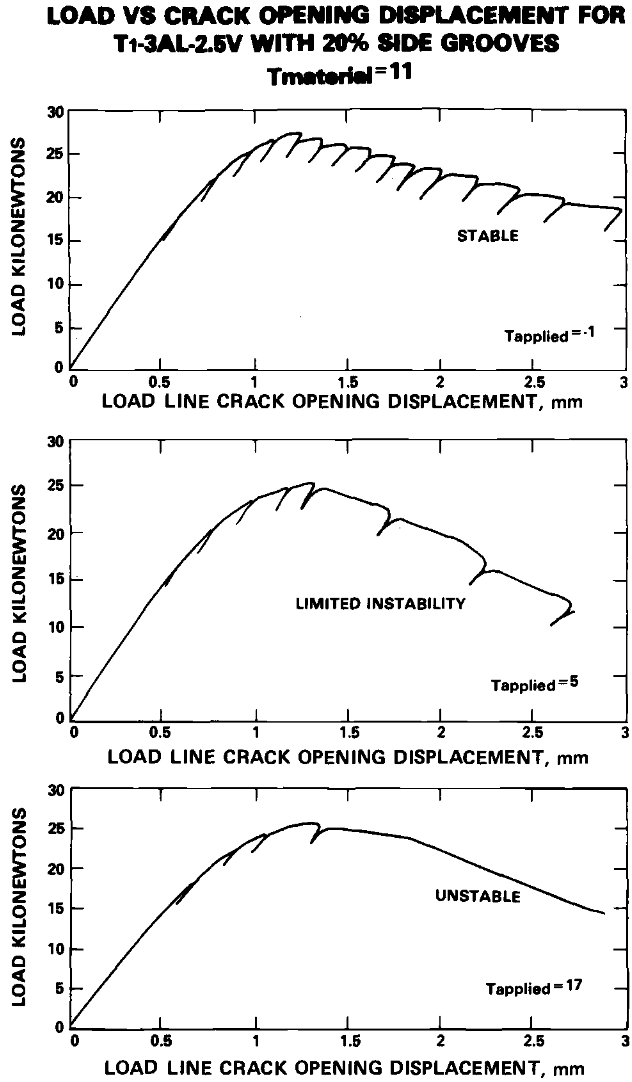

FIG. 3—*Load displacement records for three general types of tearing behavior.*

For cases where $T_{\text{applied}} > T_{\text{material}}$ the typical behavior is as shown in Fig. 3*c*. At maximum load a sudden instability occurs, producing a large enough increment of crack extension to either separate the specimen completely or leave only a small remaining ligament or the shear lip region holding the specimen together.

Figures 3*a* and 3*b* show that the load displacement records for stable specimens and specimens of limited instability are similar in shape in spite of the presence of the small instabilities, and likewise the J-R curves obtained from stable and limited instability specimens are similar in shape as shown in Fig. 4 for the aluminum alloy. This insensitivity of the J_I-R curve to the $T_{applied}$ was seen for all materials tested.

Both macroscopic observation and scanning electron microscope (SEM) analysis of all materials studied here showed that the fracture surfaces were fully ductile and very similar whether they resulted from the stable tearing fracture or the rapid instability. No evidence of cleavage was observed in any of the test specimens either near the beginning of the unstable tearing or during the growth of the rapidly propagating crack.

Verification of Instability Theory

The results of the complete series of tests are plotted in Figs. 5 and 6 with each point representing a single specimen. Solid points denote specimens which demonstrated instability to such a degree that the test was stopped. The half-filled data points represent specimens which demonstrated limited instability. The hollow data points represent specimens that behaved in a stable fashion throughout the test as they would have been expected to behave in a standard stiff test machine. The only difference between Fig. 5 and Fig. 6 is that the $T_{material}$ plotted in Fig. 5 were calculated from J_I-R curves with crack

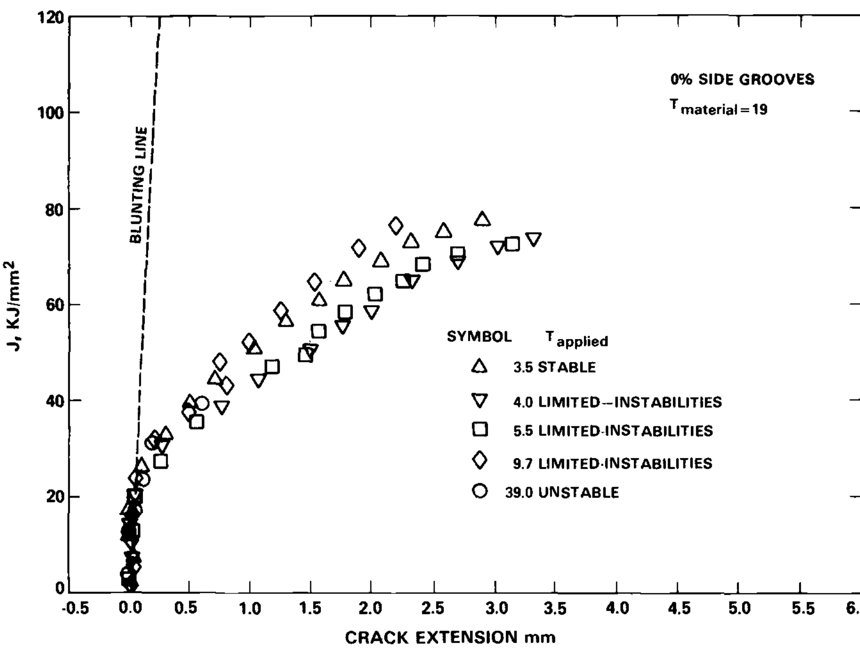

FIG. 4—*J_I-R curves for non-side-grooved 5456-H117 aluminum alloy specimens (*a/W *= 0.65).*

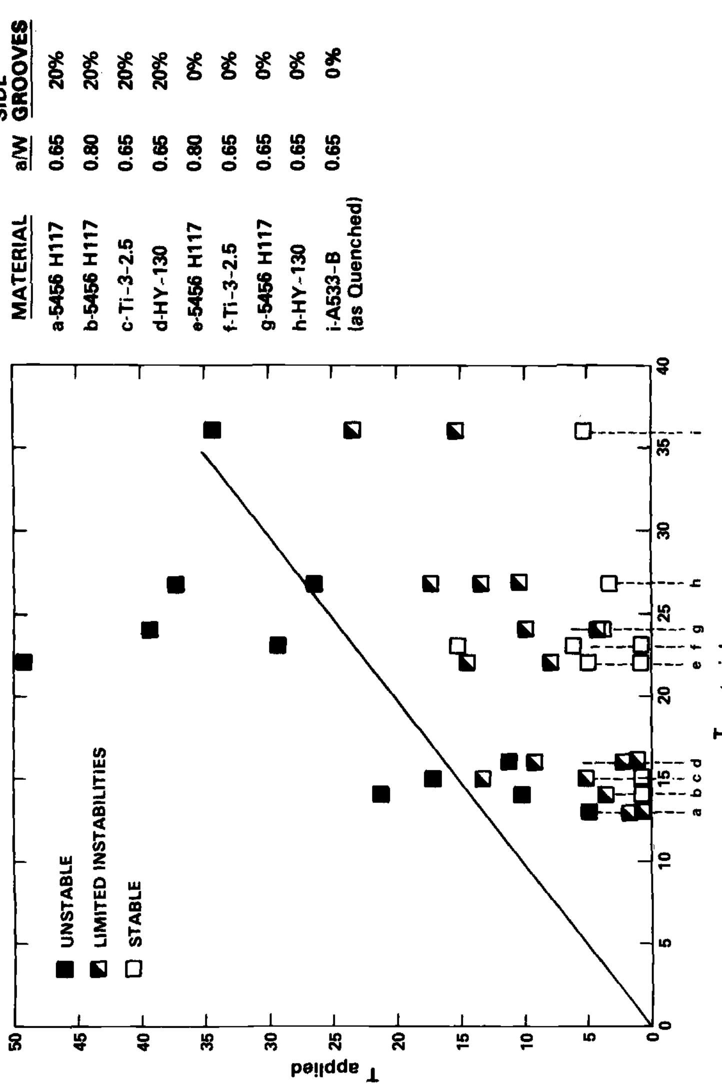

FIG. 5—$T_{applied}$ *versus* $T_{material}$ *calculated from* J_I*-R curve slope taken to crack extension of 1.5 mm.*

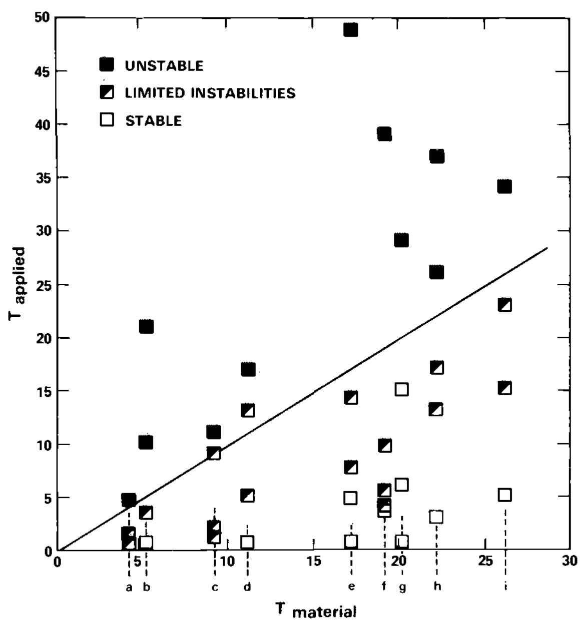

MATERIAL	a/W	SIDE GROOVES
a-5456 H117	0.65	20%
b-5456 H117	0.80	20%
c-HY-130	0.65	20%
d-T_I-3-2.5	0.65	20%
e-5456 H117	0.80	0%
f-5456 H117	0.65	0%
g-T_I-3-2.5	0.65	0%
h-HY-130	0.65	0%
i-A533-B (as Quenched)	0.65	0%

FIG. 6—*$T_{applied}$ versus $T_{material}$ with $T_{material}$ calculated from J_I-R curve slope taken to crack extension of 5.0 mm.*

extension up to 1.5 mm while Fig. 6 used T_{material} calculated from J_I-R curves with crack extension up to 5 mm.

Both Figs. 5 and 6 demonstrate the validity of the Paris tearing instability criterion that, when $T_{\text{material}} < T_{\text{applied}}$, unstable fracture behavior will occur. Figures 5 and 6 also show that T_{material} calculated from J_I-R curves with crack extension to 5 mm are a more accurate measure of the material tearing modulus. This effect was more pronounced on specimens with 20 percent side grooves than on specimens with no sided grooves.

The effect of 20 percent side grooves on the materials test was to produce a different T_{material} from the non-side-grooved specimens and correspondingly required a different T_{applied} to produce unstable behavior. Figure 6 thus shows that the T_{material} produced with 20 percent side-grooved specimens is a real change in the effective material behavior due to the change in constraint. Further research is necessary to prove if the constraint produced by side grooving models the constraint present in very thick parts.

Discussion of Limited Instability

In previous work on tearing instability using bend bar specimens, Paris et al [*8*] did not report observing the wide range of limited instability behavior observed in this work. They did report one case of "marginal behavior" and two other cases termed stable that showed instantaneous load drops of about 5 percent just beyond maximum load and possibly some other load drops later in the tests—in specimens with $T_{\text{applied}} = 0.6 - 0.8\ T_{\text{material}}$.

To explain the observed range of limited instability two possibilities seemed to present themselves. First it was conjectured that the T_{applied} would fall rapidly with the increased crack length, causing instability to be reestablished. The second possibility was that T_{material} varied considerably about the average value obtained by the single-specimen J_I-R curve methodology, leaving the possibility that occasionally the T_{applied} would exceed the T_{material}, giving a limited instability behavior. To investigate these alternatives a load-load line COD plot was obtained from a non-side-grooved specimen of the HY130 alloy without any unloadings. Since this alloy was identical to the alloy used by Joyce et al [17] a "key curve" analysis could be applied to develop a J_I-R curve for this specimen directly from the load displacement curve of the specimen. The resulting J_I-R curve is shown in Fig. 7. The key curve analysis result has a (J, Δa) pair for each point on the original load displacement curve and thus it allows a determination of the variability in both T_{material} and T_{applied} during a test.

Using the J and a/W values defined by the J_I-R curve of Fig. 7 allows calculating the T_{applied} which would have been present if the test had been run in a compliant test machine with the given stiffness. These results are plotted in Fig. 8 and show that T_{applied} does vary during a typical test, but only slowly,

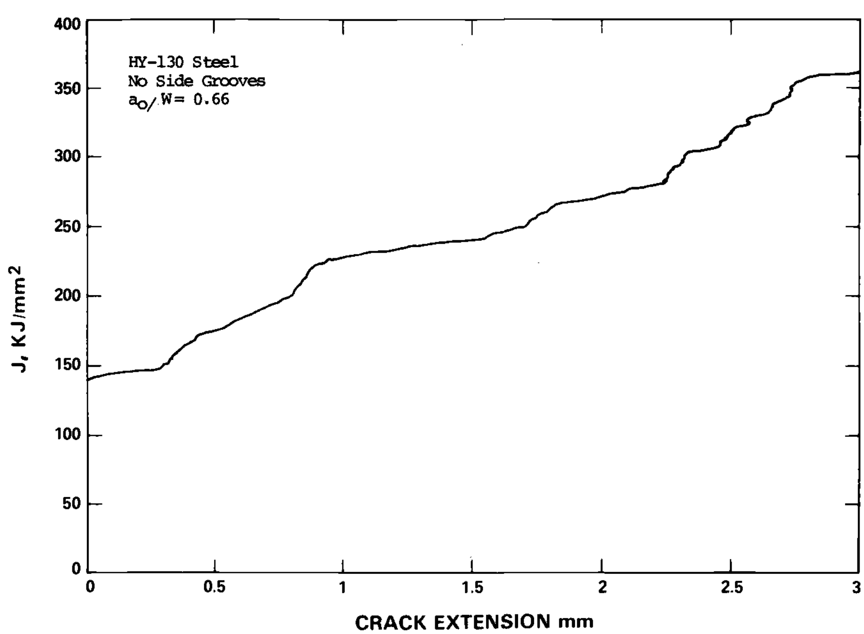

FIG. 7—*Key curve analysis J_I-R curve for HY130 steel specimen.*

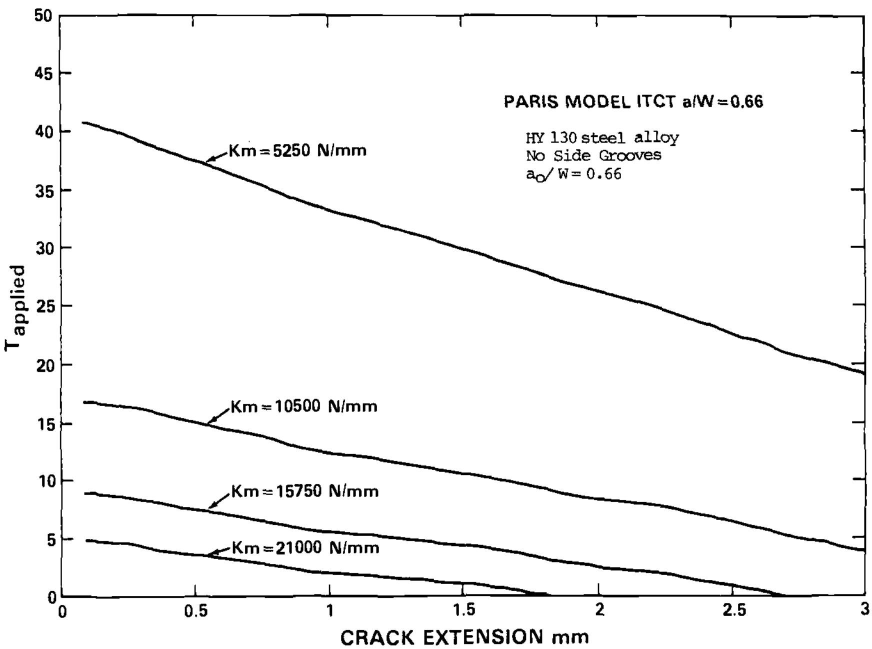

FIG. 8—$T_{applied}$ *versus crack extension for HY130 steel compact specimen tested in a compliant test machine.*

decreasing as a/W and J_I increase. No sudden and pronounced reduction in T_{applied} occurs as the result of a slight increase in crack length. If the situation occurred where T_{applied} was slightly above T_{material} at maximum load, a small step of crack extension could occur with stability being reestablished when T_{applied} fell below T_{material}. This phenomenon then could not recur during this test since T_{applied} would fall only with further increases in a/W or J_I.

To test the second possibility an iterated quadratic polynomial fit procedure was used to evaluate the local slopes of the J_I-R curve presented in Fig. 7, and hence the local T_{material} defined by Eq 1. In the technique used here the polynomial was fit to all J-Δa pairs in a fixed region of Δa instead of to a set number of data points. This procedure applied to the J_I-R curve of Fig. 7 gives the results shown in Fig. 9. Here, even when fitting the polynomial over a relatively large region of 0.25 mm of crack extension, a wide band of T_{material} values is found ranging from 5 to 35. Overplotted on this figure are the T_{applied} curves from Fig. 7 which tend to bound the T_{material} scatter band. The implication of this plot is that a mixture of stable and unstable behavior should exist for this material for T_{applied} values ranging from 5 to 35. This effect is not unexpected considering the inhomogeneity of structural materials, producing, in turn, irregular crack growth. The wide variation of T_{material} observed here is, however, somewhat surprising.

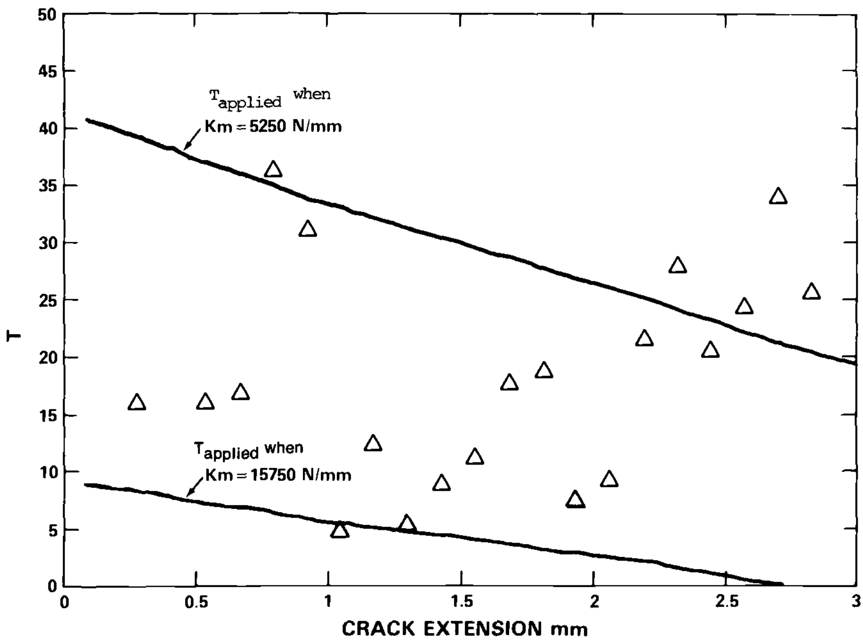

FIG. 9—*Local* $T_{material}$ *values for HY130 steel alloy demonstrating material variability.*

Conclusions

The following conclusions can be drawn from the work described herein:

1. Tearing instability was assured in a compact specimen if the $T_{applied}$ produced by the compliant test machine exceeded the $T_{material}$ defined by a stable single specimen unloading compliance J_I-R curve for a similar specimen for the range of aluminum, titanium, and steel alloys tested here.
2. $T_{material}$ was most accurately defined by taking the least-squares slope of the J_I-R curve from 0.15 mm beyond the blunting line to a crack extension of 5 mm, which here was as far as the stable J_I-R curves were measured.
3. Macroscopic and SEM analysis showed that the stable and unstable specimens fracture surfaces were very similar. No evidence of cleavage was observed on fracture surfaces of the unstable specimen.
4. In all materials tested here a region of limited instability behavior was observed for a range of $T_{applied}$ below the average $T_{material}$ value, with a gradual reduction in the severity of the unstable behavior as $T_{applied}$ is reduced.
5. For $T_{applied}$ less than one tenth of the average $T_{material}$, no unstable behavior was observed in these tests.
6. The existence of the limited instability region was apparently due to variability of $T_{material}$ about the average value obtained from the single-

specimen J_I-R curve and not to variations in T_{applied} resulting from the crack extension.

7. The J_I-R curves for the materials tested were unaffected by the value of T_{applied} experienced by the compact specimen.

8. The added constraint present in the side-grooved specimens produced a T_{material} value distinctly different from that of non-side-grooved specimens of the same material. Tearing instability was then controlled by the applicable T_{material} in these specimens.

Acknowledgment

The authors wish to acknowledge Dr. H. H. Vanderveldt of the Naval Sea System Command (NAVSEA 05R15), and Mr. J. P. Gudas of the David W. Taylor Naval Ship Research and Development Center (Code 2814) for supporting this research.

References

[*1*] Paris, P. C., Tada, H., Zahoor, A., and Ernst, H. in *Elastic-Plastic Fracture, ASTM STP 668,* J. D. Landes, J. A. Begley, and G. A. Clarke, Eds., American Society for Testing and Materials, 1979, pp. 5-36.

[*2*] Landes, J. D. and Begley, J. A. in *Fracture Analysis, ASTM STP 560,* American Society for Testing and Materials, 1974, pp. 170-186.

[*3*] Ernst, H., "Techniques of Analysis of Load Displacement Records by J-Integral Methods," Ph.D. Thesis, Sever Institute, Washington University, St Louis, Mo., 10 Aug. 1979.

[*4*] Tada, W., Paris, P. C., Gomez, M., and Gamble, R., "A Stability Analysis of Circumferential Cracks for Reactor Piping System," Nuclear Regulatory Commission, 1979.

[*5*] Gudas, J. P., Joyce, J. A., and Davis, D. A. in *Fracture Mechanics, ASTM STP 677,* C. W. Smith, Ed., American Society for Testing and Materials, 1979, pp. 474-485.

[*6*] Vassilaros, M. G., Joyce, J. A., and Gudas, J. P. in *Fracture Mechanics,* Proceedings of the 12th National Symposium, *ASTM STP 700,* American Society for Testing and Materials, 1980, pp. 251-270.

[*7*] Joyce, J. A. and Gudas, J. P. in *Elastic-Plastic Fracture, ASTM STP 668,* J. D. Landes, J. A. Begley, and G. A. Clarke, Eds., American Society for Testing and Materials, 1979, pp. 451-468.

[*8*] Paris, P. C., Tada, H., Ernst, H., and Zahoor, A. in *Elastic-Plastic Fracture, ASTM STP 668,* J. D. Landes, J. A. Begley, and G. A. Clarke, Eds., American Society for Testing and Materials, 1979, pp. 251-265.

[*9*] Clarke, G. A., Andrews, W. R., Begley, J. A., Donald, K., Embley, G. T., Landes, J. D., McCabe, D. E., and Underwood, J. H., *Journal of Testing and Evaluation,* Vol. 1, Jan. 1979.

[*10*] Hutchinson, J. W. and Paris, P. C., *Elastic-Plastic Fracture, ASTM STP 668,* J. D. Landes, J. A. Begley, and G. A. Clarke, Eds., American Society for Testing and Materials, 1979, pp. 37-64.

[*11*] Ernst, H. A., Paris, P. C., Landes, J. D., this publication, pp. 476-502.

[*12*] "NRL-DPRI Research Program (RP 886-2), Evaluation and Predictions of Neutron Embrittlement in Reactor Pressure Vessel Materials, Annual Progress Report for 1978," J. C. Hawthorne, Ed., National Research Laboratory, Report 327, 30 Aug. 1979, p. 40.

[*13*] Saxena, A. and Hudak, S. J., *International Journal of Fracture,* Vol. 14, 1978, pp. 453-468.

[*14*] Merkle, J. G. and Corten, H. T., *Journal of Pressure Vessel Technology, Transactions,* American Society of Mechanical Engineers, Vol. 96, Nov. 1974, pp. 286-292.

[*15*] Paris, P. C. in *Flow Growth and Fracture, ASTM STP 631,* American Society for Testing and Materials, 1976, pp. 3-27.
[*16*] Rice, F. R., *The Mechanics of Fracture,* F. Erdogan, Ed., American Society of Mechanical Engineers, 1976.
[*17*] Joyce, J. A., Ernst, H., and Paris, P. C. in *Fracture Mechanics,* Proceedings of the 12th National Symposium, *ASTM STP 700,* American Society for Testing and Materials, 1980, pp. 222-236.

Phuc Nguyen-Duy[1]

Relationship Between Critical Stretch Zone Width, Crack-Tip Opening Displacement, and Fracture-Energy Criterion: Application to SA-516-70 Steel Plates

REFERENCE: Nguyen-Duy, Phuc, **"Relationship Between Critical Stretch Zone Width, Crack-Tip Opening Displacement, and Fracture-Energy Criterion: Application to SA-516-70 Steel Plates,"** *Fracture Mechanics: Thirteenth Conference, ASTM STP 743*, Richard Roberts, Ed., American Society for Testing and Materials, 1981, pp. 543–552.

ABSTRACT: Relationships are developed between the crack-tip opening displacement (CTOD), fracture-energy criterion (J_{Ic}), and critical stretch zone width (W_{SZc}) using a simple geometrical model of the crack tip. Stretch zone width is directly measured from micrographs of fracture surfaces.

For three-point-bend specimens of SA-516-70 steel, J_{Ic} evaluated from measured values of W_{SZc} is equal to 0.173 MJ-m^{-2} compared with 0.200 MJ-m^{-2} determined from the single-specimen method in which the crack onset point is detected by the electrical potential method.

KEY WORDS: stretch zone, J-integral, crack-tip opening displacement, fracture

Nomenclature

a_0	Precrack length
B	Specimen thickness
CTOD	Crack-tip opening displacement
(CTOD)$_c$	Critical value of crack-tip opening displacement
E_{Sc}	Strain energy at crack initiation point
G	Magnification

[1]Scientist, Materials Sciences Directorate, Institut de Recherche d'Hydro-Québec (IREQ), Varennes, Québec, Canada.

J_{Ic} Critical value of energy criterion of fracture for Mode I
L Width of stretch zone measured on micrographs
W_{SZc} Critical value of stretch zone width
W Specimen depth
δ Angle formed by incident and vertical line
σ_f Flow stress $(\sigma_y + \sigma_u)/2$
σ_u Ultimate stress
σ_y Yield stress
θ Angle formed by stretch zone and horizontal line

The stretch zone is an intermediate fracture surface between the end of the fatigue precrack and the beginning of the crack produced by monotonic loading. The appearance of this zone, ductile like the fatigue precrack zone, is distinguished by a more hilly relief and more elongated dimples. Theoretically, the stretch zone width is related by crack-tip opening displacement (CTOD). CTOD can be then defined as the displacement of the original crack-tip position, namely, the tip of the fatigue precrack in a COD specimen or a natural crack in a structure.

Mathematical Analysis

Considering a symetric blunt crack relative to the original line of fatigue precrack, an equation relating stretch zone width (W_{SZ}) to CTOD can easily be established. In Fig. 1, the stretch zone is represented by arc AB and forms an angle θ with the horizontal line. If AB is the critical stretch zone width, we can write

$$(\mathrm{CTOD})_c = 2\, W_{SZc} \sin\theta \tag{1}$$

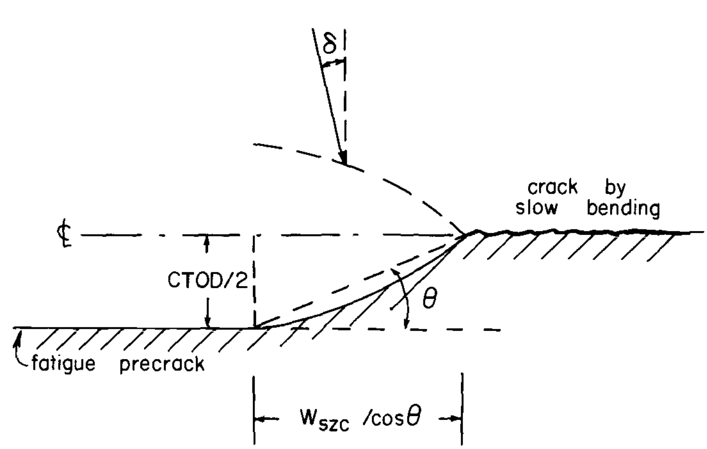

FIG. 1—*Profile of stretch zone of a broken specimen half.*

The scanning electron microscope (SEM) is frequently used to observe the stretch zone of fractured specimens. If the incident angle is δ and the magnification is G, the stretch zone width can be evaluated by

$$W_{SZc} = \frac{L}{\cos(\theta - \delta)} \times \frac{1}{G} \tag{2}$$

where L is the measured length of the stretch zone on micrographs. Substituting Eq 2 in Eq 1, the value of CTOD can be derived directly from experimental data for L, δ, and G

$$(\text{CTOD})_c = 2\frac{L \sin\theta}{\cos(\theta - \delta)} \times \frac{1}{G} \tag{3}$$

In Eqs 2 and 3 the only unknown on the right-hand side is the angle θ, which is intimately related to critical values of stretch zone width and CTOD. This angle represents the capacity of material to resist crack initiation and appears to be approximately 45 deg [*1,2*].[2] With this assumption, we can rewrite Eqs 2 and 3

$$W_{SZc} = \frac{\sqrt{2}\,L}{\cos\delta + \sin\delta} \times \frac{1}{G} \tag{4}$$

$$(\text{CTOD})_c = \frac{2\,L}{\cos\delta + \sin\delta} \times \frac{1}{G} \tag{5}$$

Equations 4 and 5 indicate clearly that critical values of W_{SZ} and CTOD can be simply determined by measuring the length L on micrographs.

The relationship between CTOD and J_{Ic} was developed elsewhere [*3,4*]. This can be extended to critical values of J_I and CTOD, and the following equation can be written

$$J_{Ic} = m\sigma_f(\text{CTOD})_c \tag{6}$$

In the case of uniaxial loading and under plane-strain conditions, for three-point-bend specimens, finite-element calculation gives $m = 2$ [*5*]

$$J_{Ic} = 2\sigma_f(\text{CTOD})_c \tag{7}$$

It was also reported that m decreases when plasticity increases. Inserting Eq 5 in Eq 7, we obtain

$$J_{Ic} = \frac{4\sigma_f L}{\cos\delta + \sin\delta} \times \frac{1}{G} \tag{8}$$

[2]The italic numbers in brackets refer to the list of references appended to this paper.

It is important to mention that $(\mathrm{CTOD})_c$ and J_{Ic} are stable crack initiation criteria.

The coefficient $m = 2$ in Eq 7 can be verified eventually by using the J_{Ic}-value determined by the single-specimen method and CTOD determined via the critical stretch zone width.

Application to SA-516-70 Steel

Fatigue precracked three-point-bend specimens of different dimensions

$$B = 1 \text{ cm}, \ W = 2 \text{ cm}$$

$$B = 1.75 \text{ cm}, \ W = 3.50 \text{ cm}$$

in SA-516-70 steel were used. J_{Ic} was determined by the single-specimen method. The electrical potential method was used to determine the crack onset point [6]

$$J_{Ic} = (2/Bb)E_{Sc} \tag{9}$$

E_{Sc} varies as a function of a_0/W and can be expressed, for specimens of different dimensions, by

$$E_{Sc}/WB = (-J_{Ic}/2)(a_0/W) + (J_{Ic}/2) \tag{10}$$

where $a_0/W = 1$ and $E_{Sc} = 0$. The variation of (E_{Sc}/WB) in terms of a_0/W is a straight line passing through the point (1,0) with slope $(-J_{Ic}/2)$.

The linearity is an indication that the J_{Ic}-value determined by the single-specimen method is correct.

An average value of J_{Ic} was determined and equal to

$$J_{Ic} = 0.200 \text{ MJ} - \text{m}^{-2}$$

Fracture surfaces of broken specimen halves were examined by SEM to determine W_{SZc} and CTOD according to Eqs 4 and 5.

An incident angle δ of 45 deg and magnification factor G of 200 were used. The length L is an average value of 16 measurements taken at equal intervals in the central third region of a specimen of thickness B.

Results and Discussion

The results are reported in Table 1. In Fig. 2, micrographs of the stretch zone of four observed specimens are shown. In these micrographs, the limits of the stretch zone are clearly defined, characterized by a ductile appearance with particularly hilly relief and elongated dimples.

In considering $\sigma_f = 424$ MPa, the average values of CTOD and of the energy-fracture criterion J_{Ic} determined via W_{SZc} are

$$\overline{\text{CTOD}} = 2.037 \times 10^{-4} \text{m}$$

$$\overline{J_{Ic}} = 0.173 \text{ MJ} - \text{m}^{-2}$$

TABLE 1—*Values of stretch zone width, crack-tip opening displacement, and fracture-energy criterion for different SA-516-70 steel specimens.*

Measurement	Specimen				Avg
	1 (1 by 2 cm)	2 (1 by 2 cm)	3 (1 by 2 cm)	4 (1.75 by 3.50 cm)	
L, m	2.95×10^{-2}	2.965×10^{-2}	3.01×10^{-2}	2.60×10^{-2}	2.88×10^{-2}
W_{SZc}, m	1.475×10^{-4}	1.483×10^{-4}	1.505×10^{-4}	1.30×10^{-4}	1.44×10^{-4}
CTOD, m	2.086×10^{-4}	2.096×10^{-4}	2.128×10^{-4}	1.838×10^{-4}	2.037×10^{-4}
J_{Ic}, MJ − m^{-2}	0.177	0.178	0.180	0.156	0.173

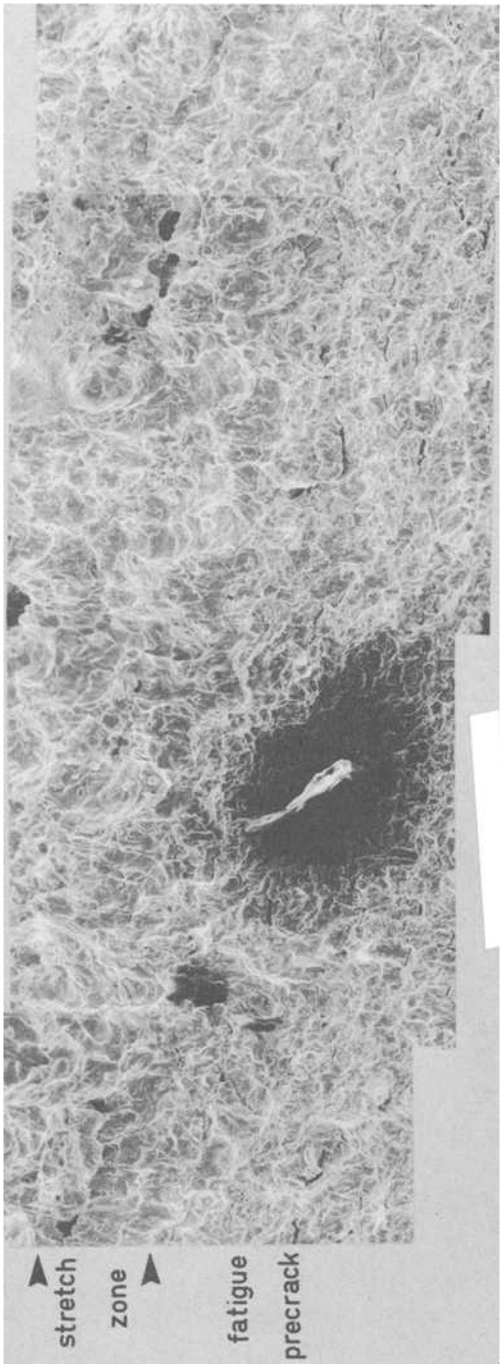

FIG. 2—*Micrographs of the stretch zone of the four observed specimens (×140).*

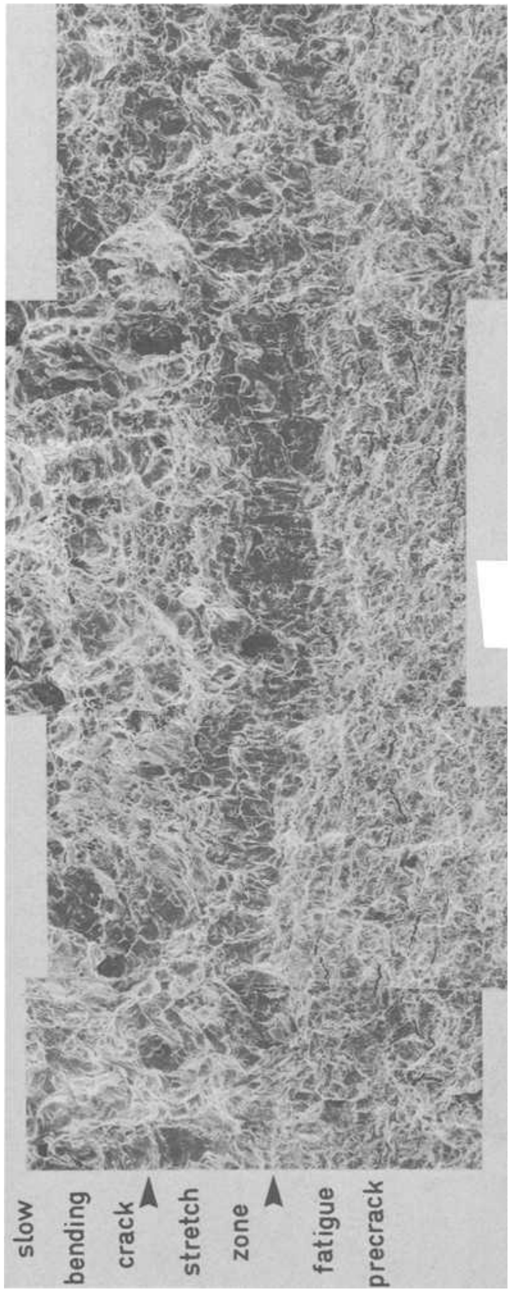

FIG. 2—*Continued.*

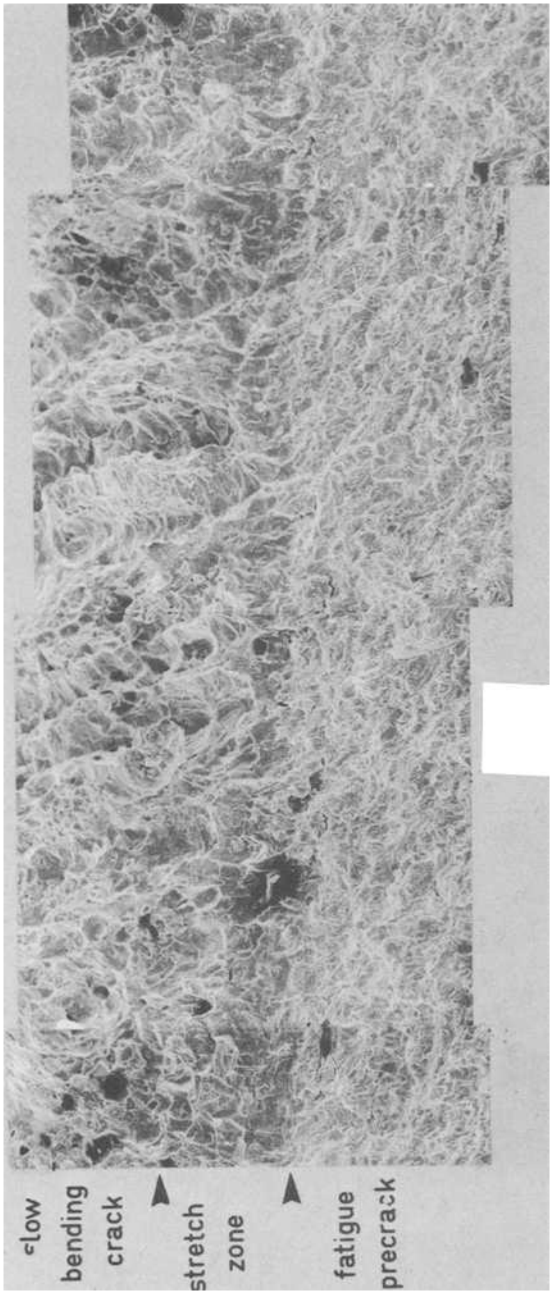

FIG. 2—*Continued.*

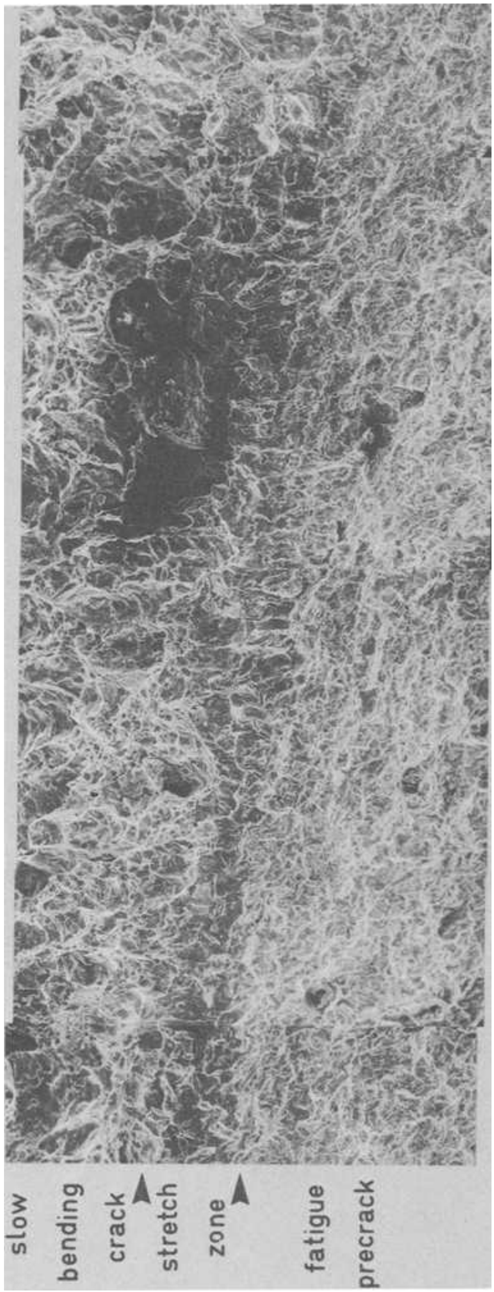

FIG. 2—*Continued.*

This average value of J_{Ic} compares favorably with

$$J_{Ic} = 0.200 \, \text{MJ} - \text{m}^{-2}$$

determined by the single-specimen method [*6*].

Inserting this value of J_{Ic} and the value of CTOD, 2.037×10^{-4} m, in

$$m = \frac{J_{Ic}}{\sigma_f (\text{CTOD})} \tag{11}$$

we obtain $m \sim 2,3$.

Using certain geometrical assumptions concerning the crack tip, it is possible to evaluate the critical value of CTOD and J from the critical stretch zone width, W_{SZc}, as measured directly on SEM micrographs.

Acknowledgments

The author is pleased to acknowledge Dr. E. A. Dancy for reading the manuscript and Mr. M. Dugré for taking SEM micrographs.

References

[*1*] Landes, J. D. and Begley, J. A. in *Fracture Analysis, ASTM STP 560,* American Society for Testing and Materials, 1974, pp. 170-186.

[*2*] Robinson, J. N. and Tetelman, A. S., *Engineering Fracture Mechanics,* 1976, Vol. 8, pp. 301-313.

[*3*] Dawes, M. G., *Elastic-Plastic Fracture, ASTM STP 668,* J. D. Landes, J. A. Begley, and G. A. Clarke, Eds., American Society for Testing and Materials, 1979, pp. 307-333.

[*4*] Rice, J. R., "Elastic-Plastic Fracture Mechanics," Mechanics of Fracture, Winter Annual Meeting, American Society of Mechanical Engineers, 1976.

[*5*] Turner, C. E. in *Proceedings,* First International Conference on Numerical Methods in Fracture Mechanics, A. R. Luxmoore and D. R. J. Owen, Eds., Swansea, U.K., 1978.

[*6*] Nguyen-Duy, P. and Phélippeau, G., *Journal of Testing and Evaluation,* Vol. 7, No. 6, Nov. 1979, pp. 310-316.

G. A. Clarke[1]

Single-Specimen Tests for J_{Ic} Determination—Revisited

REFERENCE: Clarke, G. A., "**Single-Specimen Tests for J_{Ic} Determination—Revisited,**" *Fracture Mechanics: Thirteenth Conference, ASTM STP 743,* Richard Roberts, Ed., American Society for Testing and Materials, 1981, pp. 553–575.

ABSTRACT: Since the development of the unloading compliance method, numerous improvements to this J_{Ic} and J-R curve testing procedure have occurred over the past five years. This paper presents a description of many of these test technique improvements along with the results of the improvements.

Improvements in both mechanical and electrical systems are shown to greatly improve the reproducibility of the unloading compliance data. Computerization of the data reduction has led to a better understanding of the requirements necessary for an accurate J-versus-Δa R-curve.

KEY WORDS: crack growth, J-R curve, unloading compliance method, plasticity, computers

Since the initial paper by Clarke et al [*1*][2] which described the unloading compliance procedure used for J_{Ic} testing, numerous papers have been published [*2–6*] detailing the experiences of various authors with this method. To describe these experiences as varied would be an understatement. A common experience with all experimenters using the unloading compliance method is that careful attention to experimental procedure results in more reliable data. More sophisticated techniques are now available to the experimentalist in the pursuit of reliable data, including the use of data acquisition systems coupled to computers [*7,8*].

The use of computers has provided a means of more accurately evaluating the measurement capability of both the load and displacement measuring devices. This evaluation has allowed a more realistic appraisal of the scatter likely in the value of J_{Ic} when using unloading compliance methods. Prior to the use of computers, the data reduction time necessary for the development

[1] Special marketing representative, Westinghouse R&D Center, Pittsburgh, Pa. 15235.
[2] The italic numbers in brackets refer to the list of references appended to this paper.

of J-versus-Δa R-curves was in the order of 4 to 5 h. Present systems are capable of developing J-versus-Δa R-curves within 20 to 30 min from the test start. The advantages of computerized systems are speed, accuracy, and a more extensive data base. However, many experimenters have found computers to be more of a bane than a boon.

Without data massaging (removal of erroneous data), computer systems become unforgiving tools in the determination of J-versus-Δa data. It should be realized that these systems only reflect the condition of the data being generated during the J-integral test. Therefore, almost all of the improvements necessary for accurate J-versus-Δa R-curves must be in the testing procedures used. The purpose of this paper is to describe many of the improvements in the unloading compliance procedure that have occurred since its inception in 1974. It is hoped that experimentalists involved in J_{Ic} testing will benefit from these improvements and eventually develop an accurate and simple test using single-specimen techniques to determine the elastic-plastic toughness, J_{Ic}, of materials.

Requirements for Unloading Compliance Testing

The use of any single-specimen technique to determine J_{Ic} has the advantage over the multiple-specimen heat-tint technique of requiring only one specimen. However, unless the R-curves developed by these single-specimen techniques are identical to those developed using the multispecimen method, they should be regarded with suspicion. It is necessary, therefore, not only to demand the same accuracy requirements as used in the multiple-specimen tests, but also to require that the single-specimen technique give similar J and Δa values as those found by the multiple-specimen method at comparable measurement points. One such comparable measurement point is the crack extension value at the end of the J-integral test. In both multispecimen and single-specimen tests, this point is defined by heat-tinting the specimen at the conclusion of the test.

The present recomended practice for J_{Ic} determination [9], developed by the ASTM task group on J_{Ic} and initiation concepts, E24.08.04, was based on determining the value of J_{Ic} within a scatter band of ± 10 percent. In keeping within this scatter band, it was found that for the unloading compliance procedure to determine J_{Ic} accurately, it is necessary to predict the final amount of crack extension within ± 15 percent of the heat-tint value.

To ensure that the displacement and load measurements are accurate at the beginning of each test, a measure of the compliance of the specimen is made. From the known relationship between the compliance measured at the load line and the crack length of commonly used bend specimens (three-point-bend and compact specimens), the initial crack length of the specimen can be predicted from

$$U_x = \frac{1}{\sqrt{\frac{BEV}{P}} + 1} \tag{1}$$

where

B = specimen thickness,
E = Young's modulus, and
V/P = compliance of specimen measure at load line.

For compact specimens [*10*]

$$a/w = 1.0002 - 4.0632\, U_x + 11.242\, U_x^2 - 106.04\, U_x^3 + 464.33\, U_x^4 - 650.68\, U_x^5 \tag{2}$$

For three-point-bend specimens with a span-to-width ratio of 4

$$a/w = 0.99231 - 3.08319\, U_x - 19.13138\, U_x^2 + 158.24593\, U_x^3 - 5.0453738\, U_x^4 \tag{3}$$

where a/W is the crack length normalized by the specimen width. Using the preceding equations along with the measured initial crack length, we can determine the value of Young's modulus for the material being tested. This value should be in agreement with the experimentally determined value of Young's modulus, within ± 5 percent. If care is taken to calibrate both the displacement and load measuring devices and the Young's modulus value is within the specified limits, then we can be reasonably assured that the values of J for the specimens can be accurately determined. The J calculation procedure is independent of testing method (single-specimen or multiple heat-tint techniques) and is determined from the area swept out by the load-versus-displacement plot. As long as only small partial unloadings are used for the unloading compliance procedure, experimental evidence [*1*] has shown that the area under the load-displacement curve is independent of the number of partial unloadings occurring during the test. These partial unloadings, however, should be approximately 10 percent of the maximum load obtained during the test.

The number of J-versus-Δa points generated during the unloading compliance test should be sufficient to develop an acceptable R-curve as defined by the J_{Ic} recommended procedure [*9*]. The data points should be within the required limits of J and crack extension Δa, as shown in Fig. 1.

Testing Requirements and Equipment

The aim of the unloading compliance method is to monitor the amount of crack extension occurring during the J_{Ic} test. To accomplish this it is necessary

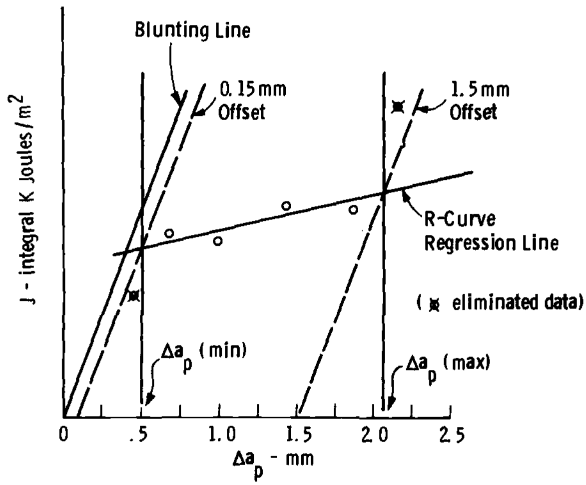

FIG. 1—*Valid data range after linear regression fit to R-curve data.*

to produce a linear elastic partial unloading curve during the test. Any nonlinearity in the curve will cause unacceptable crack length predictions. There are numerous reasons why nonlinearity can occur during these partial unloadings; however, by using careful testing procedures, much of this nonlinearity can be eliminated. While most of the improvements to the testing procedure can come under the heading of mechanical improvements, electronic improvements can also be made. A discussion of both the mechanical and electrical equipment used to develop unloading compliance J-R curves is presented next.

Mechanical Equipment

Much of the blame for hysteresis in the partial unloading curves has been placed on friction. Friction effects between the loading pins and the clevises or between the clip gage and the specimen knife edges have received considerable attention. The friction effects between pins and clevises were found when comparisons were made of the partial unloading load-displacement curves using clevises with round-bottom pinholes and clevises with flat-bottom pinholes. To further improve the linearity of the unloading curves, roller bearings were used by some investigators [*3,11*] to reduce the friction between pins and clevises even more. However, a careful examination of the comparative quality of the curves (developed using both flat-bottom holes and roller-bearing clevises) shows no advantage of one clevis design over the other [*11*]. Either design of clevis shown in Fig. 2 can be used to develop friction-free unloading curves. However, if bearings are to be used, care must be taken not to exceed the static load bearing capability of the roller bearings; otherwise friction effects may be evident.

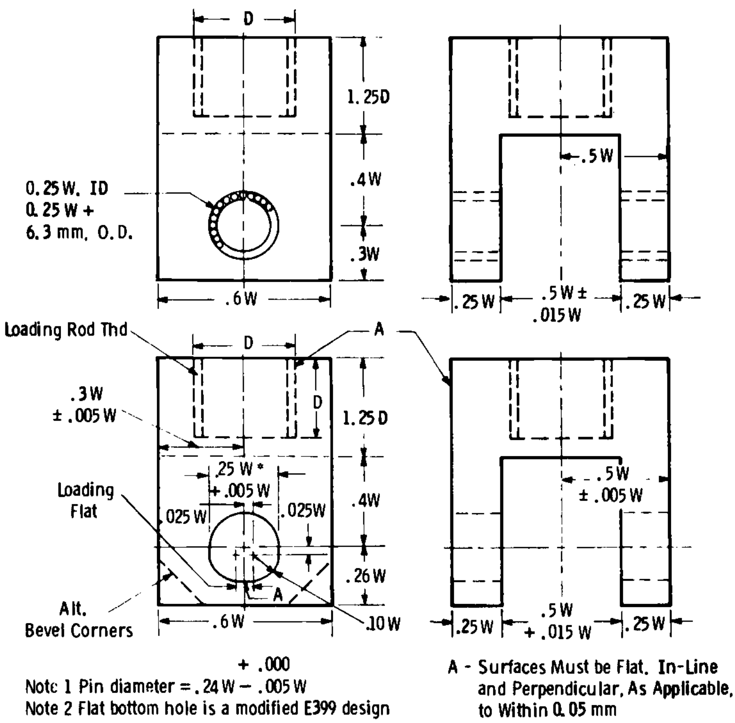

FIG. 2—*Two clevis designs for compact specimen testing.*

The more commonly used displacement measurement devices are the clip gage and the linear variable displacement transducer (LVDT). The clip gage can, in most cases, be attached directly to the load-line measurement position of the compact specimen. As this is the displacement value used in the calculation of J, the clip gage is especially useful for compact specimens. The calibrated voltage output for the clip gage is usually 0 to 10 V for the full range of the clip gage. As the partial unloading displacements are generally less than 1/2 percent of the full displacement range of the specimen test, amplification of the unloading voltage signal is often necessary to achieve a clear definition of the linear unloading slope.

Amplification of the signal would not of course be necessary if the output voltage of the measurement device were calibrated to 10 V for the total range of a single partial unloading displacement. To develop a J-versus-Δa R-curve using such a scheme would of course require two measurement devices, one to measure the full range of specimen displacement and the other to be continuously reset to zero until the partial unloading displacement measurement is required. As the output voltage of the rezeroed measurement device is calibrated to approximately the full partial unloading displacement, a very high degree of linearity is expected between the output voltage and the displacement values. While such a rezeroing scheme is not practical for clip gages, it is well suited to the LVDT. Such a system was developed, as shown in Fig. 3. This system is particularly useful for large specimens which require a high degree of sensitivity from the measurement devices [11].

As can be seen in Fig. 3, the displacement measurement device is not attached to the load line of the compact specimen but rather to the front face. While the displacements used in J-versus Δa R-curve calculations are measured at the load line, the displacement values measured need not necessarily be load-line displacements. By using linear interpolation, front-face displacement readings can be converted to load-line displacements with sufficient accuracy to determine J within ± 1 percent of the J calculated directly from load-line displacements [12]. It should also be pointed out that compliance values are used to determine values of crack extension, Δa, rather than absolute crack lengths. Therefore, any small errors in the linear interpolation of front-face compliances to load-line compliance values should not affect the calculation of Δa. Recent work by Landes [12] has shown that while it is necessary to determine the stress reversal point in the compact specimen, as shown in Fig. 4, any small errors in determining its position do not result in

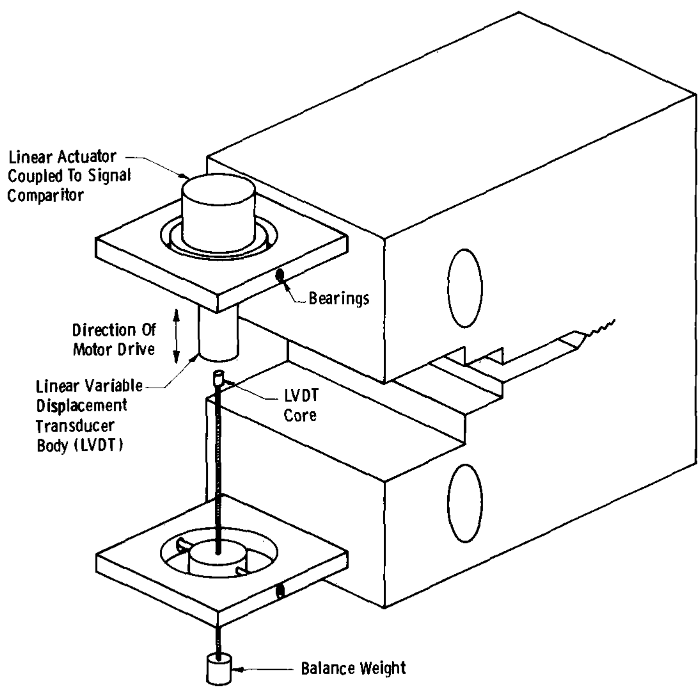

FIG. 3—*Schematic of front face rezeroing LVDT system for compact specimens.*

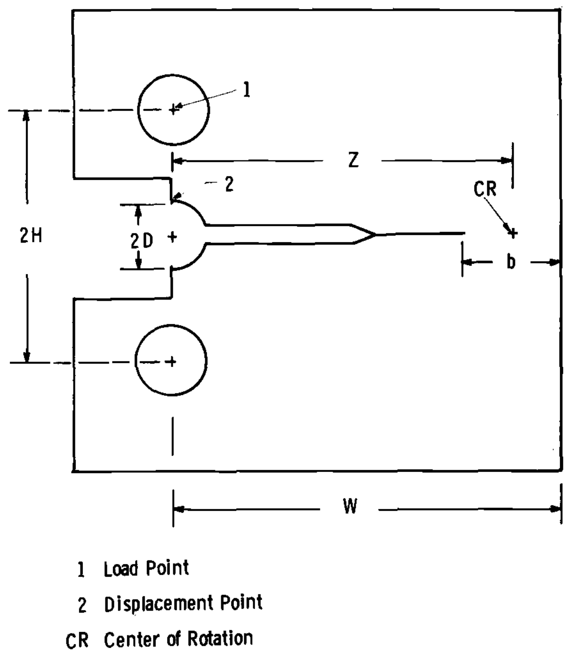

FIG. 4—*Schematic of compact specimen with points for large rotation corrections.*

significant errors when converting non-load-line displacements to load-line values.

Electrical Equipment

Probably the single largest cause of error in compliance data, as determined from a computerized system, is electrical noise. There are a number of ways to reduce the effect of this noise, including the use of active low band pass filters or data-averaging techniques. High-frequency noise suppression is not so critical when using an X-Y recorder to determine the compliance, as most X-Y recorder systems cannot respond at the rate of these high frequencies. However, high-speed data acquisition systems read signals at the instant the system is triggered. Hence any reading affected by high-frequency noise will be read by a high-speed data acquisition system. One method successfully used by the author to reduce the effects of this noise is an analog active low band pass filter coupled with an averaging procedure. This averaging procedure uses 10 data points taken at ultrahigh speed (that is, 100 kHz), and averages them for use as a single load and displacement point.

Amplification of the partial unloading signal may also be necessary when using computer systems. This is especially true if the data acquisition system has a 12-bit or less word length. A 12-bit data acquisition system is capable of only ±2024 digits, requiring that the 0 to 10-V input signal be digitized over a 4048-digit range. While this sensitivity is more than adequate to describe the overall load-displacement record, it is hardly sufficient to describe the partial unloading curve, whose total displacement may be only 1/2 percent of the overall displacement (that is, 20 digits). Most data acquisition systems have a ± digit repeatability accuracy which can result in as much as ± 3 percent inaccuracy in a compliance reading. While this does not appear to be a large error, it can result in a 0.762-mm (0.03 in.) difference in crack extension value for a [25.4-mm (1 in.)] (1T) compact specimen with $a/W = 0.5$. By amplifying the partial unloading signal, this ±1-digit repeatability factor has less effect on the overall accuracy of the data. Care should be taken to use only precision amplifiers for this operation.

Evaluation of the Calculation Methods for J and Δa

The analytical procedures used to calculate J from the load-displacement records of commonly used specimens have gone through some minor changes since first developed by Rice et al. These changes range from correction factors for the tension component in compact specimens [13] to adjustments in the J-integral value to account for crack extension [14]. Experimental methods [15] have been used to evaluate the accuracy of these J-integral calculation procedures for compact, three-point-bend, and center-cracked panel specimens. It was from an experimental J-integral calibration that the simplified form of the J equation accounting for the tension component in the compact specimen [13] resulted

$$J_0 \frac{2A}{Bb}\left(\frac{1+\alpha}{1+\alpha^2}\right) \tag{4}$$

where

A = area under the load-displacement curve,
b = remaining ligament $(W - a)$,
W = specimen width,
B = specimen thickness, and
α = function of the normalized crack length, a/W or a/b, and is found from

$$\alpha = 2\sqrt{\left(\frac{a}{b}\right)^2 + \frac{a}{b} + \frac{1}{2}} - 2\left(\frac{a}{b} + \frac{1}{2}\right) \tag{5}$$

or from Ref *18*

$$\eta = 2\left(\frac{1+\alpha}{1+\alpha^2}\right) = 2\left[1 + 0.261\left(1 - \frac{a}{W}\right)\right]$$

$$\eta = 2\left[1 + 0.261\left(\frac{b}{W}\right)\right] \tag{6}$$

hence

$$J_0 = \frac{\eta A}{Bb} \tag{7}$$

Recently work by Hutchinson and Paris [16] has shown that the effect of crack extension on the value of J for bend-type specimens should be included when developing accurate J-versus-Δa R-curves. The following form for calculating J should be used to account for crack extension [14]

$$J = J_0 - \int_{a_0}^{a} \frac{J_0}{b}\left(\eta - 1 - \frac{b}{W}\frac{\eta'}{\eta}\right) da \tag{8}$$

If the values of J are limited to very small crack extension values, such as those used to determine J_{Ic}, then a simple approximation to these J-values can be determined from [17]

$$J = J_0\left[1 - \frac{(0.75\,\eta - 1)}{b}\Delta a\right] \tag{9}$$

Again, it should be pointed out that this formula should be used only when small crack extension values are involved [that is, less than 2.0 mm (0.08 in.)].

Probably the least understood part of developing the J-R curve by the unloading compliance method is the relationship between compliance data and the crack extension values generated. It should first be pointed out that compliance data are not used to calculate crack lengths, rather to calculate crack extension values. While the compliance calibration equations are used to determine the difference in crack lengths, absolute values of crack length can be erroneously predicted due to the use of incorrect Young's modulus values. An equation used to calculate the crack extension values in compact specimens directly without the usual compliance tables was first shown in the paper by Clarke [1] and is given by

$$da = \frac{dC}{C}\frac{(W-a)}{2}\cdot g\left(\frac{a}{W}\right) \tag{10}$$

where C is the compliance and dC is the change in compliance of the specimen. The function $g(a/W)$ acts in the same manner as the tension component correction factor in J calculations. Equation 10 was developed in the following manner. For the pure bend specimen, the strain-energy release rate G can be found from

$$G = \frac{P^2}{2B}\frac{dC}{da} \tag{11}$$

and for purely elastic conditions

$$G = \frac{2A}{B(W-a)} \tag{12}$$

where A is the area under the load-displacement curve $P\delta/2$

$$G = \frac{P\delta}{B(W-a)} = \frac{P^2}{2B}\frac{dC}{da} \tag{13}$$

or

$$da = \frac{dC}{\delta/P}\frac{(W-a)}{2} = \frac{dc}{C}\frac{(W-a)}{2} \tag{14}$$

If the tension component in a compact specimen is accounted for in the area estimation of G, then

$$G = \frac{2A}{Bb}\cdot\left(\frac{1+\alpha}{1+\alpha^2}\right) = \frac{P^2}{2B}\frac{dC}{da} \tag{15}$$

or

$$da = \frac{dC}{C}\cdot\frac{W-a}{2}\cdot\frac{1+\alpha^2}{1+\alpha} \tag{16}$$

If we convert Eq 16 to its original form; that is

$$da = \frac{dC}{C}\cdot\frac{W-a}{2}\cdot g\left(\frac{a}{W}\right) \tag{17}$$

then

$$g\left(\frac{a}{W}\right) = \frac{1+\alpha^2}{1+\alpha} \tag{18}$$

A second, and possibly more accurate, means of determining the function $g(a/W)$ comes from the K-calibration of the specimen, or

$$G = \frac{K^2}{E} = \frac{P^2(1 - a/W)Y^2}{EB^2b} = \frac{2A}{Bb} \cdot \frac{1}{g(a/W)} \tag{19}$$

$$\frac{P^2(1 - a/W)Y^2}{EB^2B} = \frac{P\delta}{Bb} \cdot \frac{1}{g(a/W)} \tag{20}$$

or

$$g(a/W) = \frac{EB\delta}{PY^2} \frac{1}{(1 - a/W)} \tag{21}$$

The use of a linear relationship between $EB\delta/P$ versus Y^2 will give

$$g(a/W) = 0.315\,(a/W) + 0.652 \tag{22}$$

The equation for crack extension in a compact specimen is therefore

$$da = \frac{dC}{C} \frac{(W - a)}{2} [0.315\,(a/W) + 0.652] \tag{23}$$

By extending the crack extension value, da, by 0.05-mm (0.002 in.) increments and using the same value for compliance at $a/W = 0.5$ as used in Eqs 1 and 2, a normalized compliance versus normalized crack length curve is developed, as shown in Fig. 5. When larger increments of crack extension are used, such as 0.125 and 0.25 mm (0.005 and 0.01 in.), increasingly larger deviations from the compliance curve generated by Saxena and Hudak are found. These differing curves are also shown in Fig. 5.

As the three-point-bend specimen ($S/W = 4$) closely resembles the pure-bend situation, the crack extension for the three-point-bend specimen is simply

$$da = \frac{dC}{C} \frac{(W - a)}{2} \tag{24}$$

When compact specimen tests result in large displacements, it is necessary to account for rotational effects of the specimen. Both the load point, P, and the displacement point rotate around the stress reversal point in the remaining ligament of the specimen. The rotation correction factor [3] for both the load P and the displacement δ is given by

$$\frac{\delta_c}{P_c} \text{ (corrected} = \frac{\delta_m}{P_m} \text{ (measured)} \left\{ \frac{1}{(1 - x/Z)(1 - y/Z)} \right\} \tag{25}$$

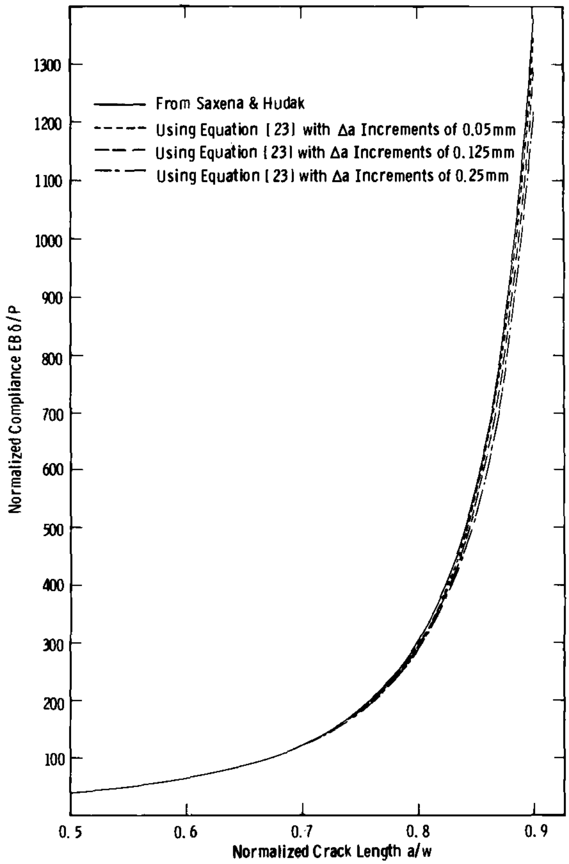

FIG. 5—*Normalized compliance versus normalized crack length curve as developed by Eq 23, with various incremental crack extensions, compared with the curve developed by Eq 2.*

where Z is the distance from the load line to the stress reversal point and x and y are given by

$$X = \frac{\delta_m H + \frac{\delta_m^2}{2}}{Z} \tag{26}$$

$$Y = \frac{\delta_m D + \frac{\delta_m^2}{2}}{Z} \tag{27}$$

where D is the vertical distance between the crack plane and the displacement measuring point and H is the vertical distance between the crack plane and the load point. A much better agreement between the final heat-tint value of crack extension and the predicted value of crack extension occurs when the rotation correction is applied. Examples of the effect of the rotation correction are shown in Figs. 6 and 7. Figure 6 shows the effect of the rotation correction on the blunting line, while Fig. 7 shows the effect of correcting significant crack extension values.

Evaluation of Specimen Geometry

The testing procedures used to develop unloading compliance data have been in a state of flux since the first test was completed. While improvements in the testing procedures are still continuing, drastic changes are far less commonplace than they were at the procedure's inception. Many papers have been written describing the experiences of investigators [*18–20*] who have used the unloading compliance method. I hope that by relating the experiences of myself and others in improving experimental procedures, the learning curve will show a steep increase for future users of this method.

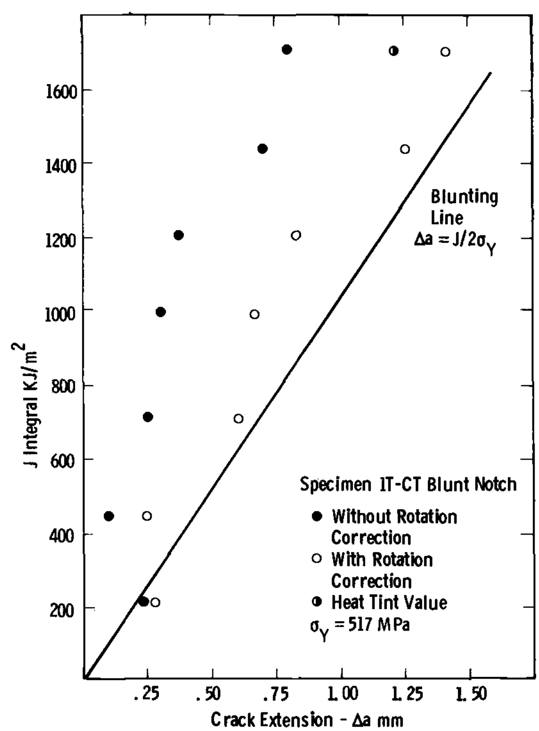

FIG. 6—*Effect of rotation on a 1T-CT blunt-notch specimen of A508 material tested at room temperature.*

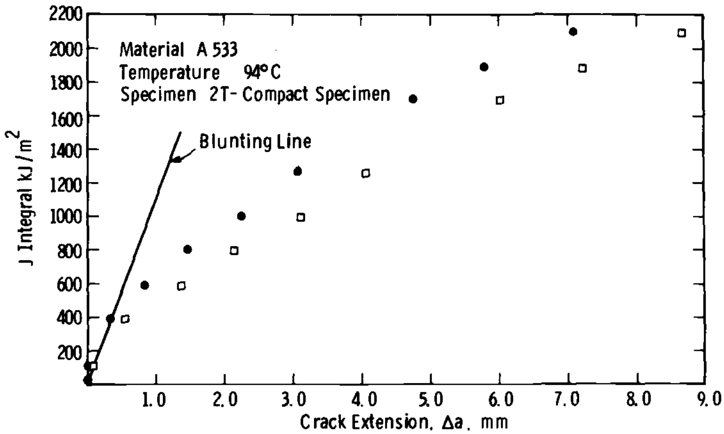

FIG. 7—*J-versus-*Δa *R-curve showing effects of compact specimen rotation on predicted crack extension values.*

For a number of years the effect of crack tunneling on the unloading compliance predictions of crack extension has resulted in controversy between experimentalists. Some investigators [*19-21*] have shown that the straight crack front, produced by the side-grooving of specimens, results in a much closer agreement between the heat-tint measurement values of crack extension and those predicted by unloading compliance. On the other hand, I have found little difference in the accuracy of predictions by unloading compliance tests on either non-side-grooved specimens (with a tunneled crack front) or a side-grooved specimen [*11*] (with a straight crack front) when considering a limited amount of crack extension [less than 2.0 mm (0.08 in.)].

An investigation into the effects of crack tunneling on compliance was recently completed by Loss et al [*22*]. A blunt-notch specimen with a machined-in crack front as shown in Fig. 8 was tested. It was found that the compliance of the specimen significantly underestimated the averaged crack front as would be predicted from the compliance calibration for this specimen. This result is shown in Fig. 9 along with data recently generated at Westinghouse. The principal difference between the two data sets is that the blunt-notch specimen tested by Loss et al [*22*] was tested within the linear elastic regime, while the specimens tested in this investigation were tested in the fully plastic regime. If the material along the sides of the tunneled crack is not yielded as shown in Fig. 10, then the measured stiffness of the specimen may well differ from the stiffness as measured by the unloading compliance when in the fully plastic regime.

The blunt-notch specimens tested at Westinghouse R&D Center are shown in Fig. 11. The compliance values, taken at various displacements during the test, are listed in Table 1. It can be seen that all the averaged crack lengths are predicted by the unloading compliance values within 0.127 mm (0.005 in.)

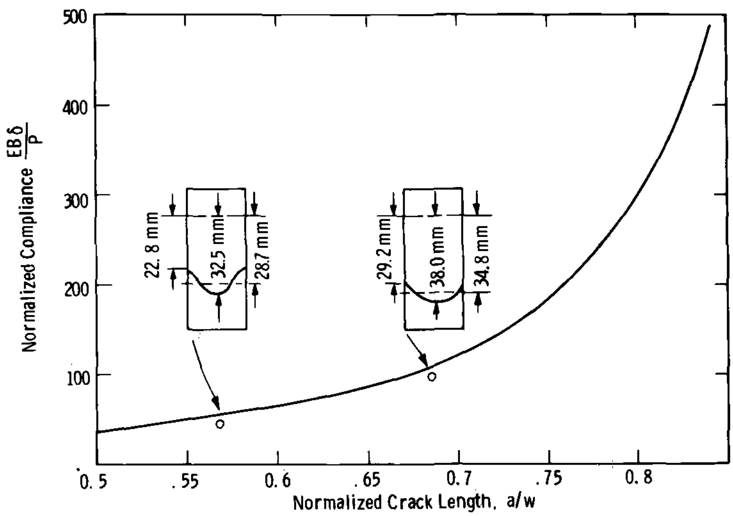

FIG. 8—*Compliance data for tunneled crack (machined into specimen) using data generated in purely elastic regime [22].*

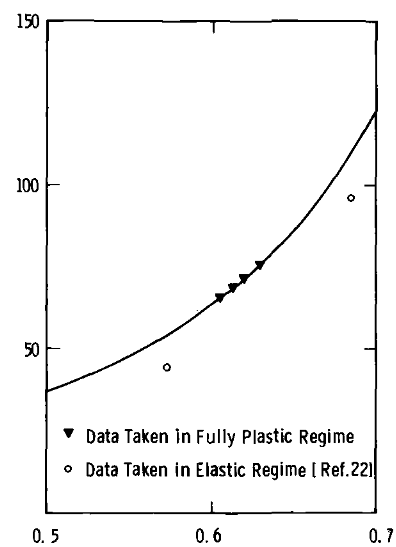

FIG. 9—*Comparison of blunt-notch data taken in elastic and fully plastic portions of the load-displacement curve.*

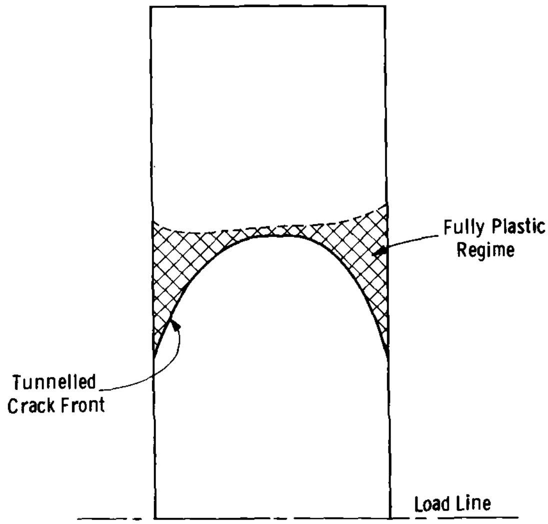

FIG. 10—*Schematic of yielding ahead of a tunneled crack front on the fracture surface of a compact specimen.*

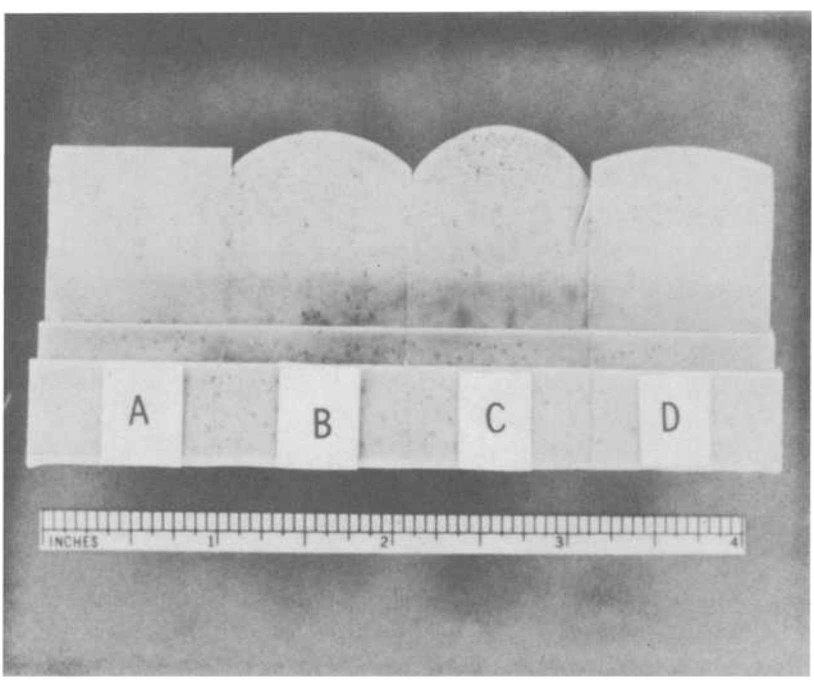

FIG. 11—*Rubber impressions of blunt-notch tunneled crack fronts in compact specimens.*

TABLE 1—*Blunt-notch tunneled crack results.*

Unload No.	Compliance Value, mm/kg $\times 10^{-3}$	Uncorrected Crack Length, mm	Rotation Corrected Crack Length, mm	Displacement Value at Unloading Point, mm	Correlation Coefficient
			Specimen A		
1	1.222	30.77	30.77	0.33	0.999992
2	1.228	30.81	30.84	0.56	0.999986
3	1.239	30.88	30.93	0.89	0.999990
4	1.239	30.88	30.96	1.19	0.999993
5	1.244	30.91	31.01	1.55	0.999989
Nine-point avg of machined notch = 30.83 mm					
			Specimen B		
1	1.335	31.50	31.52	0.58	0.999971
2	1.336	31.52	31.57	0.94	0.999981
3	1.330	31.47	31.54	1.24	0.999964
Nine-point avg of machined notch = 31.52 mm					
			Specimen C		
1	1.418	32.00	32.00	0.33	0.999966
2	1.418	32.00	32.03	0.61	0.999972
3	1.418	32.00	32.05	0.94	0.999982
4	1.420	32.03	32.10	1.27	0.999978
5	1.423	32.03	32.13	1.57	0.999981
6	1.423	32.03	32.16	1.91	0.999967
7	1.413	31.98	32.08	2.23	0.999971
8	1.415	31.98	32.13	2.51	0.999953
Nine-point avg of machined notch = 32.00 mm					
			Specimen D		
1	1.291	31.22	31.24	0.48	0.999986
2	1.295	31.24	31.29	0.81	0.999992
3	1.298	31.27	31.34	1.12	0.999987
4	1.294	31.24	31.34	1.42	0.999990
5	1.296	31.24	31.37	1.73	0.999958
6	1.298	31.27	31.39	2.11	0.999984
7	1.291	31.22	31.37	2.39	0.999957
8	1.294	31.24	31.42	2.74	0.999948
Nine-point avg of machined notch = 31.24 mm					

NOTE: 1 mm = 0.04 in.

regardless of the amount of tunneling in the specimen. It may be argued that even the specimen with the largest amount of crack tunneling, as shown in Fig. 11, does not have a significant amount of tunneling when compared with some specimens which have no side grooves. However, with such close agreement between actual crack lengths and the unloading compliance values, I would not expect to see radically differing results for a moderately increased amount of tunneling.

With such controversy existing for non-side-grooved specimens, we may well be justified in using side-grooved specimens for J_{Ic} testing. However, the side-grooving of specimens is not without its own controversy. The results of some investigations [*19,22*] have shown that side-grooving lowers both the value of J_{Ic} and the slope of the R-line dJ/da. Most of these observations have been made using the unloading compliance technique. Tests on A533B material using the multiple-specimen heat-tint technique [*23*] have resulted in similar values of J_{Ic} for both side-grooved and non-side-grooved specimens. The slope of the R-line dJ/da is lower for the side-grooved specimens, as shown in Fig. 12. This trend of lower slopes has also been noted by other investigators [*19,21,22*].

It may be of interest at this point to evaluate the pros and cons of side-grooving specimens used in J_{Ic} testing. If the effect of side-grooving is a lower J_{Ic} and dJ/da value, then serious consideration must be given to standardizing the amount of side-grooving necessary for the measurement of the material property, J_{Ic}. If, on the other hand, these effects are the result of inaccurate data developed on non-side-grooved specimens (due to crack tunneling), then side-grooving the specimens may indeed help us to develop a more accurate R-line. The value of thickness, B, used in the expressions to determine J for side-grooved specimens is assumed to be the net value of B. While this appears to be a reasonable assumption to use in the determination of J, an experimental verification similar to that used to evaluate J for the non-side-grooved specimens [*15*] has yet to be completed.

The effects of time-dependent plasticity and soft testing machines (machines with highly compliant structural frames) go hand in hand to cause inaccurate unloading slopes during the test. If the specimen is held in a position of constant stroke, then time-dependent plasticity along with machine

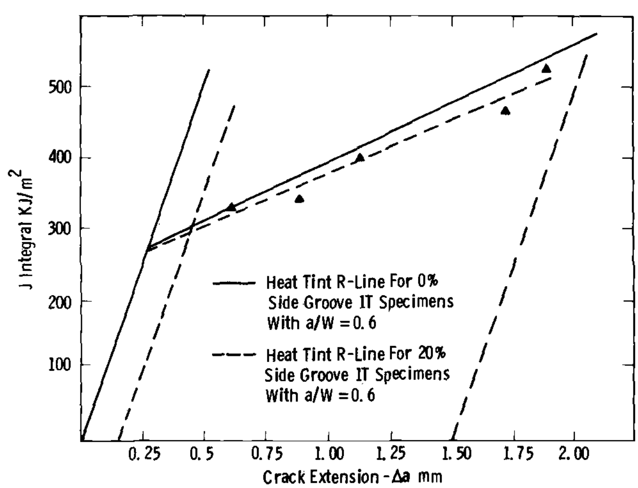

FIG. 12—*Results of a series of multispecimen heat-tint tests on 20 percent side-grooved 1T compact specimens of A533B Cl.102 baseplate material tested at 149°C (300°F) with* a/W *= 0.6.*

stiffness effects will cause a drift in the load-displacement record similar to that shown in Fig. 13. If the specimen is partially unloaded prior to allowing these time-dependent phenomena to settle out, then the load and displacement curve will have these time-dependent effects included. This can result in a significant hysteresis loop in the load-versus-displacement trace, as shown in Fig. 14.

Time-dependent plasticity effects are found to be greater for specimens with significant crack tunneling than for specimens with straight crack fronts, as can be seen in Fig. 15. This may well be due to the large local plastic displacements occurring in the plane-stress regime, at the specimen sides. The removal of the plane-stress region by side-grooving the specimens results in a more uniform plastic zone size across the crack front. As time-dependent plasticity effects depend upon the maximum-obtained plastic strains, it is easy to see why these effects are more noticeable in non-side-grooved specimens made of low-strength material. While the side grooving of specimens will certainly reduce these effects, care should always be taken to allow the time-dependent plastic displacements to diminish before partially unloading the specimen.

The use of slightly undersized loading pins, when using flat-bottom hole clevises, will aid in reducing the friction between the pins and the side of the

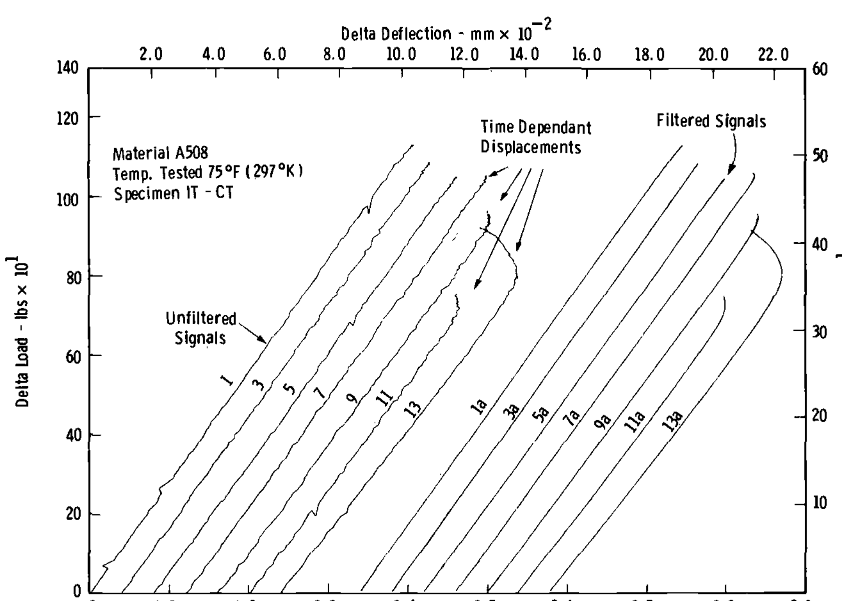

FIG. 13—*Amplified load-displacement records showing increased time-dependent effects with increased total displacements. (The overall displacement value increases with increasing unloading numbers.)*

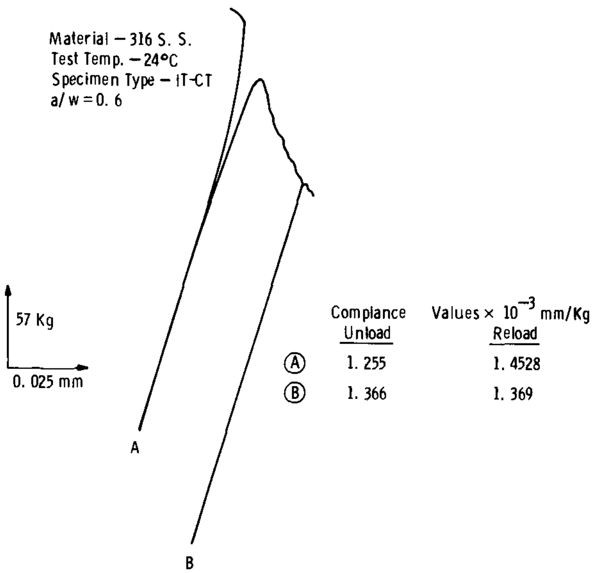

FIG. 14—*Amplified unload and reload curves taken at 2.3-mm (0.092 in.) total displacement by* A *unloading the specimen immediately and* B *allowing time-dependent plasticity effects to settle out prior to unloading.*

clevis hole by allowing the pins to rotate freely on the flat-bottom surface. Care should be taken to ensure that the pins are at the midpoint of the flat bottom surface and are properly aligned with respect to the loading axis.

Conclusions

A general conclusion from the sum total of all our experiences with the unloading compliance test is that the amount of accuracy and reliability in this test method is directly proportional to the amount of care taken in the test procedure. Pin friction, clip-gage linearity, and specimen alignment all go hand in hand in the development of reliable data. There are additionally a number of other more important observations which significantly affect the accuracy of the J-and-Δa values. These observations follow.

1. Time-dependent plasticity effects should be allowed to diminish prior to partially unloading the specimen. By holding the test machine in a constant stroke position for an adequate time period such that all specimen displacements are diminished, the linearity of the partial unloading slopes is greatly improved.
2. A more sensitive measurement of the unloading compliance value can be obtained by using a rezeroing displacement measurement system. Such a

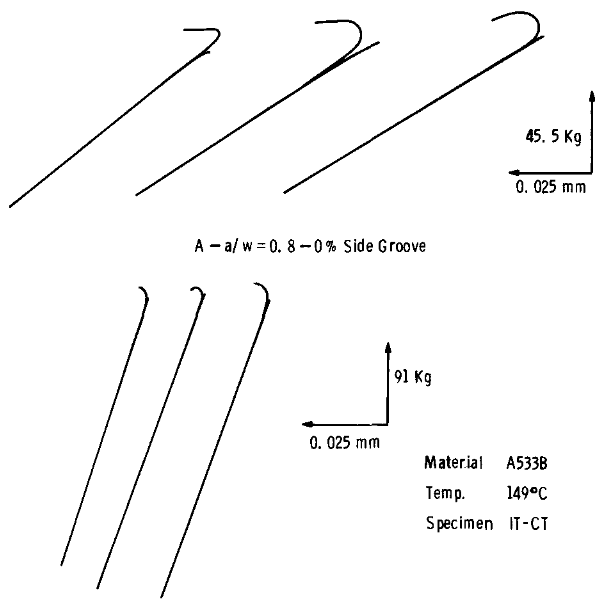

FIG. 15—*Amplified unload and reload curves showing time-dependent plasticity effects on A533B for specimens with (*A*) 0 percent side-grooving and (*B*) 20 percent side-grooving.*

system allows almost the full range of the measurement device to be used for each partial unloading.

3. The nine-point averaged crack lengths of four blunt-notched specimens (with varying amounts of crack tunneling) were predicted quite closely by the compliance method. It should be noted that all compliance values were measured once the specimens exhibited plastic behavior.
4. A simplified formula to calculate J when accounting for crack extension of less than 2.0 mm (0.08 in.) can be used to develop an accurate R-curve while determining J_{Ic}.
5. A J calibration curve using the potential energy rate definition of J is needed to evaluate compact specimens with varying depths of side grooves.
6. The side-grooving of specimens aids in accurate predictions of crack extensions when using unloading compliance procedures.
7. A simple equation using the change in compliance can accurately predict crack extension values in bend-type specimens.

Acknowledgments

The author is grateful to Professor Paul C. Paris of Washington University for his pioneering work on this procedure. All the credit for this method of testing should be directed to him. It was he who, when confronted with the problem of developing a single specimen test for J-integral testing, conceived the unloading compliance technique.

I would also like to thank my colleagues at the Westinghouse R&D Center for their help in computerizing the unloading compliance technique.

References

[1] Clarke, G. A., Andrews, W. R., Paris, P. C., and Schmidt, D. W. in *Mechanics of Crack Growth, ASTM STP 590,* American Society for Testing and Materials, 1976, pp. 27-42.

[2] Bamford, W. H. and Bush, A. J. in *Elastic-Plastic Fracture, ASTM STP 668,* J. D. Landes, J. A. Begley, and G. A. Clarke, Eds., American Society for Testing and Materials, 1979, pp. 553-577.

[3] Clarke, G. A. and Landes, J. D., "Toughness Testing of Materials by J-Integral Techniques," *Toughness Characterization and Specifications for NSLA and Structural Steels,* P. L. Mangonon, Jr., Ed., The Metallurgical Society of the American Institute of Mining, Metallurgical and Petroleum Engineers, 1979.

[4] Logsdon, W. A., "Static and Dynamic Fracture Toughness of ASTM A508 Cl 2 and ASTM A533 Gr B Cl 1 Pressure Vessel Steels at Upper Shelf Temperatures," *Ductility and Toughness Considerations in Elevated Temperature Service,* MPC-8, George V. Smith, Ed., The American Society of Mechanical Engineers, 1978, pp. 149-165.

[5] Logsdon, W. A., Kossowsky, R., and Wells, J. M. in *Advances in Cryogenic Engineering,* K. D. Timmerhaus, R. P. Reed, and A. F. Clark, Eds., 1978, pp. 197-209.

[6] Loss, F. J., Menke, B. H., Gray, R. A., Jr., Hawthorne, J. R., and Watson, H. E., "J-R Curve Characterization of Irradiated Submerged Arc Weld Deposit," *Structural Integrity of Water Reactor Pressure Boundary Components,* F. J. Loss, Ed., U.S. Nuclear Regulatory Commission Report NUREG/CR0943, Sept. 1979.

[7] Joyce, J. A. and Gudas, J. P. in *Elastic-Plastic Fracture, ASTM STP 668,* J. D. Landes, J. A. Begley, and G. A. Clarke, Eds., American Society for Testing and Materials, 1979, pp. 451-468.

[8] Clarke, G. A. and Brown, G. M. in *Computer Automation of Materials Testing, ASTM STP 710,* American Society for Testing and Materials, 1980, pp. 110-126.

[9] Clarke, G. A., Andrews, W. R., Begley, J. A., Donald, J. K., Embley, G. T., Landes, J. D., McCabe, D. E., and Underwood, J. H., *Journal of Testing and Evaluation,* Vol. 7, No. 1, Jan. 1979.

[10] Saxena, A. and Hudak, S. J., Jr., *International Journal of Fracture,* Vol. 14, No. 5, Oct. 1978.

[11] Clarke, G. A., "An Evaluation of the Unloading Compliance Procedure for J Integral Testing in the Hot Cell," Nuclear Regulatory Commission Report NUREG/CR-1070.

[12] Landes, J. D., "J Calibration from Front Face Displacement Measurement on a Compact Specimen," to be published.

[13] Clarke, G. A. and Landes, J. D., *Journal of Testing and Evaluation,* Vol. 7, No. 5, Sept. 1979, pp. 264-269.

[14] Ernst, H. A. and Paris, P. C., "Techniques of Analysis of Load-Displacement Records by J-Integral Methods," U.S. Nuclear Regulatory Commission Report NUREG/CR-122, Jan. 1980.

[15] Landes, J. D., Walker, H., and Clarke, G. A. in *Elastic-Plastic Fracture, ASTM STP 668,* J. D. Landes, J. A. Begley, and G. A. Clarke, Eds., American Society for Testing and Materials, 1979, pp. 266-287.

[16] Hutchinson, J. W. and Paris, P. C. in *Elastic-Plastic Fracture, ASTM STP 668,* J. D. Landes, J. A. Begley, and G. A. Clarke, Eds., American Society for Testing and Materials, 1979, pp. 37-64.

[17] Ernst, H. A., Paris, P. C., and Landes, J. D., this symposium, pp. 476-502.

[18] Logsdon, W. A. in *Mechanics of Crack Growth, ASTM STP 590,* 1976, pp. 43-60.

[*19*] Gudas, J. P., Joyce, J. A., and Davis, D. A. in *Fracture Mechanics, ASTM STP 677,* American Society for Testing and Materials, 1979.
[*20*] Clarke, G. A., Landes, J. D., and Begley, J. A., *Journal of Testing and Evaluation,* Vol. 8, No. 5, Sept. 1980.
[*21*] Shih, C. F., DeLorenzi, H. G., and Andrews, W. R., *International Journal of Fracture,* Vol. 13, 1977, pp. 544–548.
[*22*] Loss, F. J., Menke, B. H., Gray, R. A., Jr., Hawthorne, J. R., and Waterson, H. E. in *Structural Integrity of Water Reactor Pressure Vessel Boundary Components,* Annual Report, FY1979, F. J. Loss, Ed., U.S. Nuclear Regulatory Commission Report NUREG/CR-1128, 1979.
[*23*] Clarke, G. A. in *Journal of Testing and Evaluation,* Vol. 8, No. 5, Sept. 1980.

W. R. Andrews,[1] *V. Kumar,*[1] *and M. M. Little*[1]

Small-Specimen Brittle-Fracture Toughness Testing

REFERENCE: Andrews, W. R., Kumar, V., and Little, M. M., **"Small-Specimen Brittle-Fracture Toughness Testing,"** *Fracture Mechanics: Thirteenth Conference, ASTM STP 743,* Richard Roberts, Ed., American Society for Testing and Materials, 1981, pp. 576-598.

ABSTRACT: Accurate estimates of valid plane-strain fracture toughness, K_{Ic}, for low-alloy steels in the ductile-to-brittle transition temperature range may be made by using J_{Ic}-valid specimens and accounting for a size effect evident for cleavage fracture. The size effect is explained using a "weakest link" theory that predicts variance in test results using constant-size specimens and decreasing average results when the specimen size is increased. Cleavage fracture occurs when the maximum tensile stress near the crack tip equals or exceeds the cleavage stress, σ_f^*, over a microstructurally significant distance, the process-zone diameter. Variation in specimen toughness arises due to variations in the microstructure within the process zone; the weakest feature in the process zone causes catastrophic cleavage fracture of the specimen.

Our work indicates that the size effect on J_{Ic} is represented by

$$J_1/J_2 = (B_2/B_1)^{1/m}$$

where m is the Weibull modulus, B_i is the specimen thickness for specimen i, and J_i is the mean J_{Ic} for several specimens. Experimental evidence supporting the theory is shown.

KEY WORDS: brittle fracture, K_{Ic}, J_{Ic} testing, low-alloy steels, cleavage, ductile-brittle transition, size effect

Fracture toughness characterization of materials is an essential element in the evaluation of the integrity of a highly stressed structure. With material samples at a premium, small-specimen toughness tests are highly desirable. The J_{Ic} test [*1*][2] is an appropriate small-specimen fracture toughness test for ductile tearing. Herein, the J_{Ic} test methodology is adapted to situations involving the brittle (cleavage) fracture of low-alloy steels. Experimental and

[1]Engineer, Advanced Mechanics of Materials, mechanical engineer, Corporate Research and Development Center, and stress analysis engineer, Large Steam Turbine-Generator Department, General Electric Co., Schenectady, N. Y. 12345.

[2]The italic numbers in brackets refer to the list of references appended to this paper.

theoretical investigations are discussed which answer several fundamental questions pertaining to observed size effects in small-specimen brittle-fracture toughness testing.

The present efforts to develop a methodology for small-specimen brittle-fracture toughness testing were motivated by the need to determine fracture toughness values for generator rotor forgings placed in service before 1959. These forgings are made of low-alloy steel and typically operate at temperatures at which test specimens fracture in a brittle (cleavage) mode. Material samples can be obtained from these forgings by radially trepanning coupons from the periphery of the rotor. Of course, the size of these trepans is limited by the component geometry. Typically, 19-mm-diameter (3/4 in.) by 140-mm-long (5 1/2 in.) coupons are obtained but are too small to obtain valid fracture toughness results.

The methodology for directly determining material fracture toughness in terms of a critical stress-intensity factor under plane-strain conditions, K_{Ic}, is contained in the ASTM Standard Test Method for Plane-Strain Fracture Toughness of Metallic Materials (E 399-78a). In order to comply with the requirements of that standard, the characteristic dimensions, that is, crack length (a), thickness (B), and uncracked ligament (c) must be large such that the criterion

$$a, B, c > 2.5\,(K_{Ic}/\sigma_y)^2 \tag{1}$$

is satisfied, where σ_y is the yield strength. For the steels of interest, the ratio of toughness to yield strength is such that specimens 127 by 305 by 356 mm (5 by 12 by 14 in.) could be required. This size requirement is obviously prohibitive for testing existing forgings using trepan coupons.

Present practice is to machine Charpy V-notch bars from the trepanned samples. These bars are broken according to the ASTM Standard Method for Notched Bar Impact Testing of Metallic Materials (E 23-72) and a 50 percent fracture appearance transition temperature (FATT) is determined. This is defined as the temperature at which the broken faces of the Charpy bars exhibit 50 percent cleavage fracture and 50 percent ductile fracture. With the value of the 50 percent FATT and the operating temperature known, the fracture toughness, K_{Ic}, can be estimated by means of a correlation based on extensive materials testing [*2*]. This method is an empirical one; no theoretical means exists for calculating K_{Ic} from the 50 percent FATT. Significant scatter is evident in the available data, hence a lower-bound curve is used to correlate the data in order to provide conservative (safe) estimates of material toughness. It is evident that small specimens for obtaining material fracture toughness values would be of considerable value, particularly in light of the fact that the defect size needed to cause fracture is proportional to the square of K_{Ic}. The use of small specimens leads to gross plastic deformation, a state precluded by the K_{Ic} method.

The theoretical considerations for treating plastic deformation use Rice's J-integral J as a crack-tip stress-and-strain field descriptor [3,4] and are now well known. At first thought, it would seem reasonable that a single value of J could be used to characterize cleavage fracture as long as the specimen size requirements for providing plane-strain and J-dominance conditions at the crack tip are met (see later section "Limits of Applicability"). Hence, a continuing effort has been made to verify the use of the J_{Ic} test methodology for cleavage fracture. A great advantage of this methodology is that test specimens are required to be only 3/100 as large as needed for valid K_{Ic} testing. In addition, a relationship of the form

$$(K_{Ic})^2 = (J_{Ic} \times E)/(1 - \nu^2) \equiv (K_{IJ})^2 \tag{2}$$

is expected to exist but has yet to be conclusively shown.

Although J_{Ic} specimens meet the size requirement for their validity, assuming full plastic constraint at the crack tip [5], a size effect has been observed by several investigators [6–10] using low-alloy steel specimens and testing in the brittle-fracture or transition temperature range. This size effect for cleavage fracture that is not accounted for by elastic or elastic-plastic fracture mechanics is accounted for in this investigation.

Milne and Chell [9] described the size effect as arising from varied constraints using a model of cleavage fracture from sharp cracks based on the postulate that fracture will occur when the stress normal to the crack plane (σ_{yy}) exceeds the cleavage stress, σ_f^*, over a characteristic distance, l_o^*, ahead of the crack tip [11]. Using this model, the size effect is claimed to arise from a lower-stress triaxiality for smaller specimens due to an increased through-thickness deformation. Indeed, much of the data used to support this model were obtained using shallow-notched, three-point-bend bars and single-edge-notched tension specimens which were too small to achieve plane-strain constraint. This point is amplified later under "Limits of Applicability." Thus, for a given value of J, σ_{yy} over l_o^* will be lower in the smaller specimen. Since the criterion for fracture is σ_f^*, the smaller-specimen test would be expected to result in a "J_{Ic}" or K_{IJ} which exceeds K_{Ic} using Eq 2.

The preceding rationale, summarized from Ref 9, while interposing an alternative fracture criterion, σ_f^*, does not adequately predict the frequent observation of a large scatter in smaller-specimen test results in which the lowest values represented in that scatter are actually equal to, and occasionally below, K_{Ic} [10].

Landes and Shaffer [10] observed that the scatter of J_{Ic} data might be characterized by a Weibull distribution. This characterization implies a "weakest-link-controlling-fracture" hypothesis. Using compact specimens of similar dimension ($B : W = 1 : 2$) where W is the specimen width, and using the assumption that the length of the crack front is proportional to the volume, or the number of "links" sampled, it was possible to predict $4T\ K_{Ic}$ results from results of $1T\ J_{Ic}$ tests using nickel-chromium-molybdenum-vanadium rotor steel.

The present series of tests was designed to give evidence from which the better of two size effect descriptions could be selected. The test plan was designed to distinguish whether the constraint hypothesis (called H1) [9] or the weakest-link hypothesis (called H2) [10] is operative. The H1 hypothesis would logically predict that a loss of constraint, and thus an increase in J_{Ic}, would accompany either a decrease in the ligament, c, or a decrease in the thickness, B. It is assumed that both dimensions are equally effective in controlling constraint as is implied by the ASTM size requirements, Eq 1. The H2 hypothesis would predict that J_{Ic} would, on the average, increase with decreasing B (equal to crack-front length) but not with decreasing ligament. Thus, the test strategy consisted of testing various thickness compact or bend specimens having equal plan size, repeating the array for several plan size selections.

Materials

The steel tested is ASTM A469, a rotor forgoing steel. A typical analysis for this grade of steel is given in Table 1. The mechanical properties and some Charpy V-notch impact properties are given in Table 2. These specimens were cut from core bars taken from two large rotor forgings and designated K462 and P217.

The grain sizes for these materials were ASTM Grain Size Nos. 6 and 7. A micrograph of the structure is shown in Fig. 1, and of the polished surface showing inclusion population in Fig. 2

TABLE 1—*Test material composition (typical) of ASTM A469 steel.*

Element	Weight %
C	0.21
Mn	0.31
P	0.01
S	0.013
Si	0.20
Ni	3.55
Cr	0.07
Mo	0.26
V	0.10

TABLE 2—*ASTM A469 steel, mechanical and Charpy V-notch properties.*

	Material K462	Material P217
0.2% yeild strength, MPa	468	496
Ultimate tensile strength, MPa	634	634
Elongation in 50.8 mm (2 in.), %	17	19.5
Reduction in area, %	41	33
50% FATT (°C)	21	21
CV energy at room temperature, *J*	50	66
CV energy at 52°C (125°F), *J*	88	111

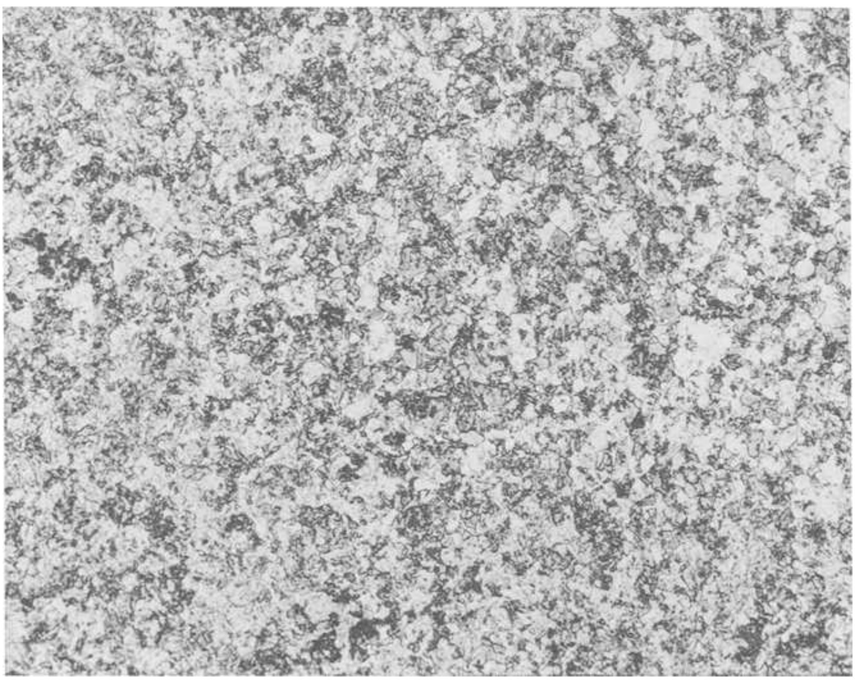

FIG. 1—*Microstructure of the steels tested—×100, 2 percent nital etchant.*

Procedures

The specimens tested were round-profile compact (RCT) specimens (Fig. 3) in sizes 3/4T, 1 1/2T, and 3T. Additional specimens included 1T three-point-bend bars (Fig. 4) and 1/2T four-point-bend bars (Fig. 5).

The test specimens were fatigue precracked prior to side-grooving using maximum loads, $P_{f\,max}$, indicated in Table 3. Only the 1 1/2T, RCT [B_N =

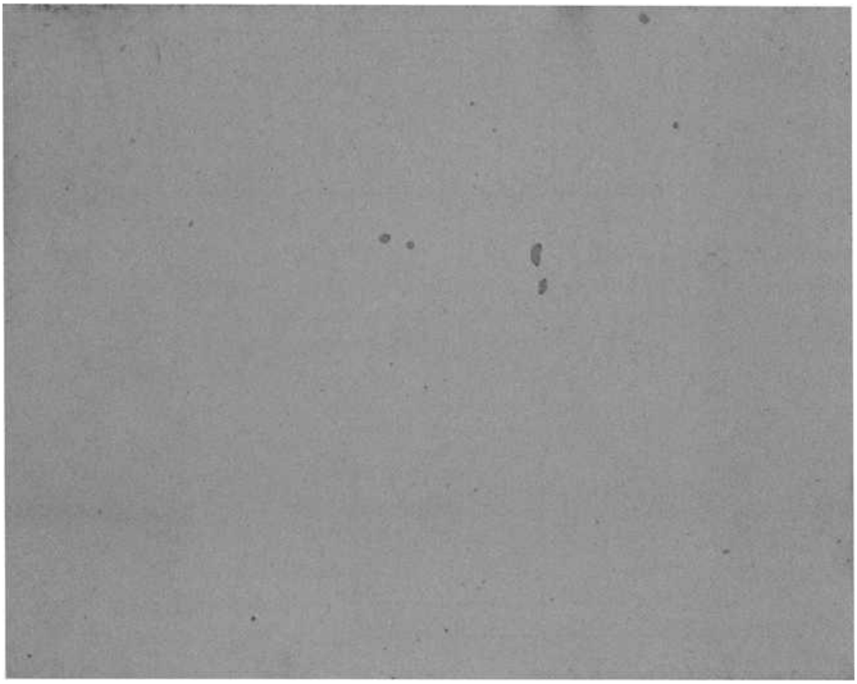

FIG. 2—*Inclusions found in the steels tested, ×100, as polished.*

36.2 mm (1.448 in.) specimens were side-grooved (Fig. 3). The fracture surfaces were examined to determine the mode of fracture. All tests were performed at −23°C (−10°F) and the mode of fracture was predominantly cleavage. Example fractographs are shown in Fig. 6.

The tests were conducted using a monotonically rising load at a rate calculated to produce fracture in 3 to 15 min. The load-line displacement and crack-tip opening displacement were monitored for RCT tests using the frame extensometer fixture (Fig. 7) and two clip-gage extensometers.

Data Reduction

The test data, recorded in digital format, were processed using a computer or programmable calculator to evaluate J_I, elastic compliance, and crack length.

For bend bars, J_I was calculated using the estimation formula [*12*]

$$J_I = \frac{\eta_e (a/W) A_e}{B_N (W - a)} + \frac{\eta_p (a/W) A_p}{B_N (W - a)} \tag{3}$$

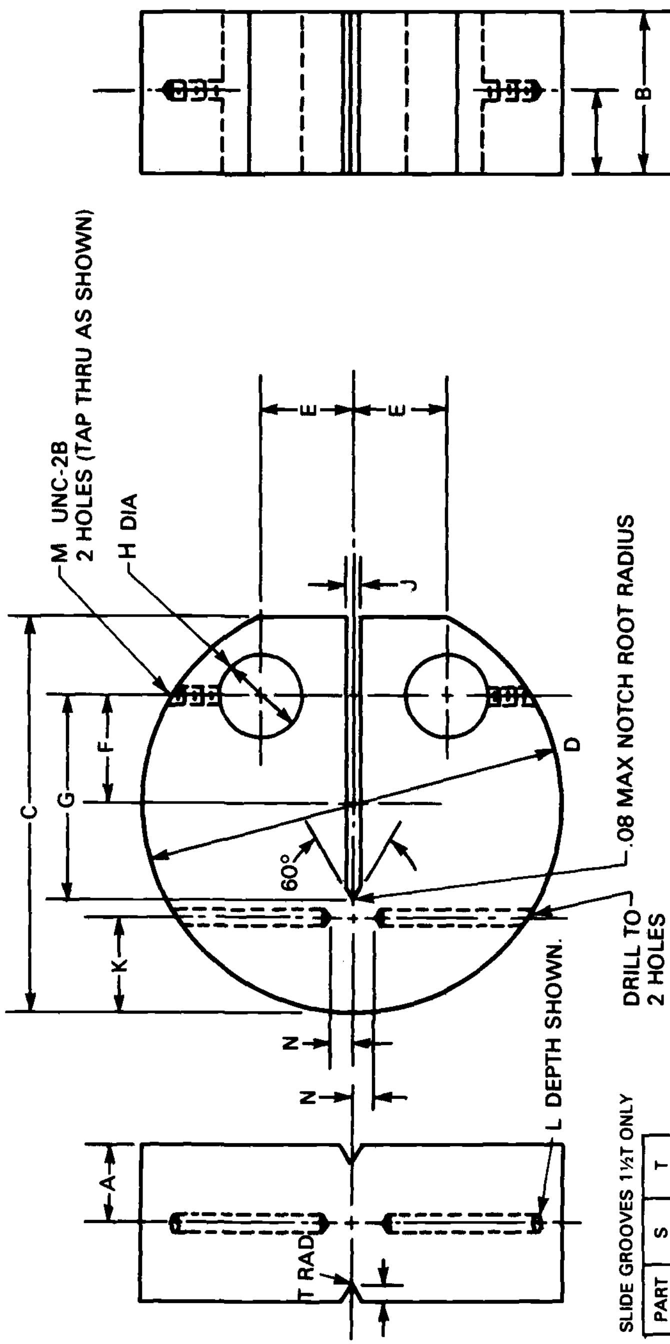

SLIDE GROOVES 1½T ONLY

PART	S	T
1	4.78	0.51
2	0.97	0.51

DIMENSIONS IN mm (in.)

SIZE	A	B	C	D	E	F	G	H	J	K	L (*DRILL)	M	N
3/4T	9.53	19.05	47.63	50.80	11.13	12.70	24.77	9.53	1.91	13.97	1.70 (#51)	#8-32	2.54
(IN.)	(0.375	(0.750)	(1.875)	(2.000)	(0.438)	(0.500)	(0.975)	(0.375)	(0.075)	(0.550)	(0.067) (#51)	#8-32	(0.100)
1½T	19.05	38.10	95.25	101.60	22.23	25.40	49.53	19.05	3.81	27.94	3.45 (#29)	#8-32	5.08
(IN.)	(0.750)	(1.500)	(3.750)	(4.000)	(0.875)	(1.000)	(1.950)	(0.750)	(0.150)	(1.100)	(0.136) (#29)	#8-32	(0.200)
1½T½	9.53	19.05	95.25	101.60	22.23	25.40	49.53	19.05	3.81	27.94	3.45 (#29)	#8-32	5.08
(IN.)	(0.375)	(0.750)	(3.750)	(4.000)	(0.875)	(1.000)	(1.950)	(0.750)	(0.150)	(1.100)	(0.136) (#29)	#8-32	(0.200)
1½T¼	4.76	9.53	95.25	101.60	22.23	25.40	49.53	19.05	3.81	27.94	3.45 (#29)	#8-32	5.08
(IN.)	(0.1875)	(0.375)	(3.750)	(4.000)	(0.875)	(1.000)	(1.950)	(0.750)	(0.150)	(1.100)	(0.136) (#29)	#8-32	(0.200)
3T	38.10	76.20	190.50	203.20	44.45	50.80	68.58	38.10	7.62	X	X	X	X
(IN.)	(1.500)	(3.000)	(7.500)	(8.000)	(1.750)	(2.000)	(2.700)	(1.500)	(0.300)				
3T½	19.05	38.10	190.50	203.20	44.45	50.80	68.58	38.10	7.62	X	X	X	X
(IN.)	(0.750)	(1.500)	(7.500)	(8.000)	(1.750)	(2.000)	(2.700)	(1.500)	(0.300)				
3T¼	9.53	19.05	190.50	203.20	44.45	50.80	68.58	38.10	7.62	X	X	X	X
(IN.)	(0.375)	(0.750)	(7.500)	(8.000)	(1.750)	(2.000)	(2.700)	(1.500)	(0.300)				

FIG. 3—*The round-profile compact specimens.*

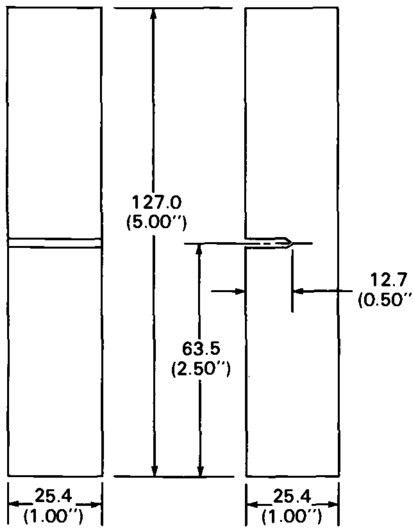

FIG. 4—*The 3-point-bend bar specimen.*

where

A_e = (for four-point bending) area under the load-versus-elastic deflection (deflection due to crack only) record,
A_e = (for three-point bending) area under the load-versus-elastic deflection (total deflection) record,
A_p = area under the load-versus-plastic-deflection record,
B_N = specimen net thickness,
W = specimen width,
a = original fatigue-crack depth,
η_p = 2.0,
η_e = a function of a/W (See Table 4).

The area under the load-deflection record was calculated using the trapezoidal rule

$$A = \left[\frac{P_n + P_{n-1}}{2}\right] \times \left[V_n - V_{n-1}\right] \tag{4}$$

where

P_i = loads,
n = sequence number of data line, and
V_i = load-point displacements (see Fig. 7).

For RCT specimens, J_{I} was calculated using the estimation formula with the Merkle-Corten correction [*13*]

$$J = \frac{2A}{B(W - a)} \times f(a/W) \tag{5}$$

where

$$f(a/W) = \frac{(1 + \alpha)}{(1 + \alpha^2)} \tag{6}$$

and

$$\alpha = \sqrt{\left[\frac{2a}{(W - a)}\right]^2 + \frac{4a}{(W - a)} + 2} - \left[\frac{2a}{W - a} + 1\right] \tag{7}$$

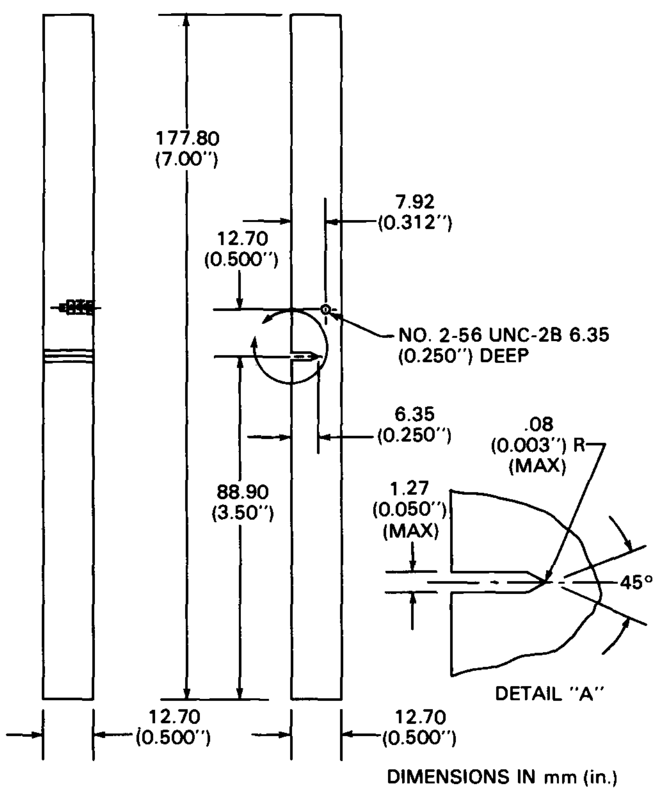

FIG. 5—*The 4-point-bend bar specimen.*

TABLE 3—*Tests at −23°C (−10°F), specimen size effects.*

σ_Y, MPa	Specimen No.	Plan Size, T	Thickness, mm	$(W - a)$ Ligament, mm	$P_{f\,max}$, kN	P_{max}, kN	P_{lim}, kN	J_Q, $\frac{kN}{m^2}$	$\frac{B\sigma_Y}{J_Q}$
593	K462-C5	1/2 BB	12.7	4.78	1.07	2.80	2.94	42	179
600	P217-35	1/2 BB	12.7	4.83	1.07	2.38	2.94	91	83
593	K462-1	3/4 RCT	19.0	9.53	4.09	9.17	12.30	51	221
593	K462-2	3/4 RCT	19.0	9.89	4.09	9.03	13.30	42	268
593	K462-3	3/4 RCT	19.1	10.01	4.09	8.21	13.71	32	358
593	K462-4	3/4 RCT	19.1	11.00	4.45	11.0	16.72	56	202
593	K462-13	1 BB	25.4	9.89	8.45	17.39	21.0	69	218
600	P217-44	1 BB	25.4	9.58	8.45	17.26	20.0	116	131
593	K462-9	1 1/2 RCT 1/4	9.8	23.61	2.9	12.44	19.90	152	38
593	K462-10	1 1/2 RCT 1/4	9.8	24.27	2.9	10.78	21.10	43	135
593	K462-11	1 1/2 RCT 1/4	9.8	23.42	2.9	11.01	19.57	62	94
600	P217-1	1 1/2 RCT 1/4	9.8	23.92	2.9	11.29	20.71	56	104
600	P217-2	1 1/2 RCT 1/4	9.8	23.63	2.9	12.61	20.18	176	33
600	P217-3	1 1/2 RCT 1/4	9.8	23.46	2.9	11.74	19.88	119	49
593	K462-104	1 1/2 RCT 1/2	19.2	22.90	5.8	20.67	36.57	51	223
593	K462-105	1 1/2 RCT 1/2	19.2	22.98	5.8	20.22	36.84	44	259
593	K462-106	1 1/2 RCT 1/2	19.2	23.42	5.8	18.59	38.35	33	345
600	P217-5P1	1 1/2 RCT 1/2	19.2	23.42	5.8	22.52	38.80	58	199

600	P217-5P2	1 1/2 RCT 1/2	19.2	22.72	5.8	23.50	36.39	102	112
600	P217-5P3	1 1/2 RCT 1/2	19.2	22.97	5.8	23.13	37.24	75	154
593	K462-64[a]	1 1/2 RCT	36.2	23.34	15.6	39.05	71.78	40	537
600	P217-54[a]	1 1/2 RCT	36.2	24.26	15.6	39.28	78.82	79	275
593	K462-7	3 RCT 1/4	19.1	78.23	22.9	70.06	230.46	46	246
593	K462-8	3 RCT 1/4	19.1	83.69	22.9	106.31	267.61	81[b]	140
593	K462-9	3 RCT 1/4	19.1	75.03	22.9	71.17	211.22	45	252
600	P217-2	3 RCT 1/4	19.1	77.34	22.9	95.63	227.37	94	122
600	P217-3	3 RCT 1/4	19.1	70.66	22.9	64.50	186.51	48	239
600	P217-4	3 RCT 1/4	19.1	79.27	22.9	93.41	240.08	70	164
593	K462-4	3 RCT 1/2	38.1	78.50	45.8	146.80	463.23	41	551
593	K462-5	3 RCT 1/2	38.1	79.65	45.8	179.30	478.35	57	396
593	K462-6	3 RCT 1/2	38.1	76.99	45.8	196.20	443.81	81[b]	279
593	K462-1	3 RCT	76.2	78.94	91.6	284.70	937.96	39	1159
593	K462-2	3 RCT	76.2	79.71	91.6	260.21	958.30	28	1614
593	K462-3	3 RCT	76.2	78.00	91.6	258.43	913.48	33	1369
600	P217-1	3 RCT	76.2	77.27	91.6	278.00	905.31	39	1172

[a]Thickness is net, B_N, $P_{\lim} = \dfrac{1.26 B_N \sigma_Y (W - a)^2}{(2W + a)}$

[b]Fatigue crack not acceptable.

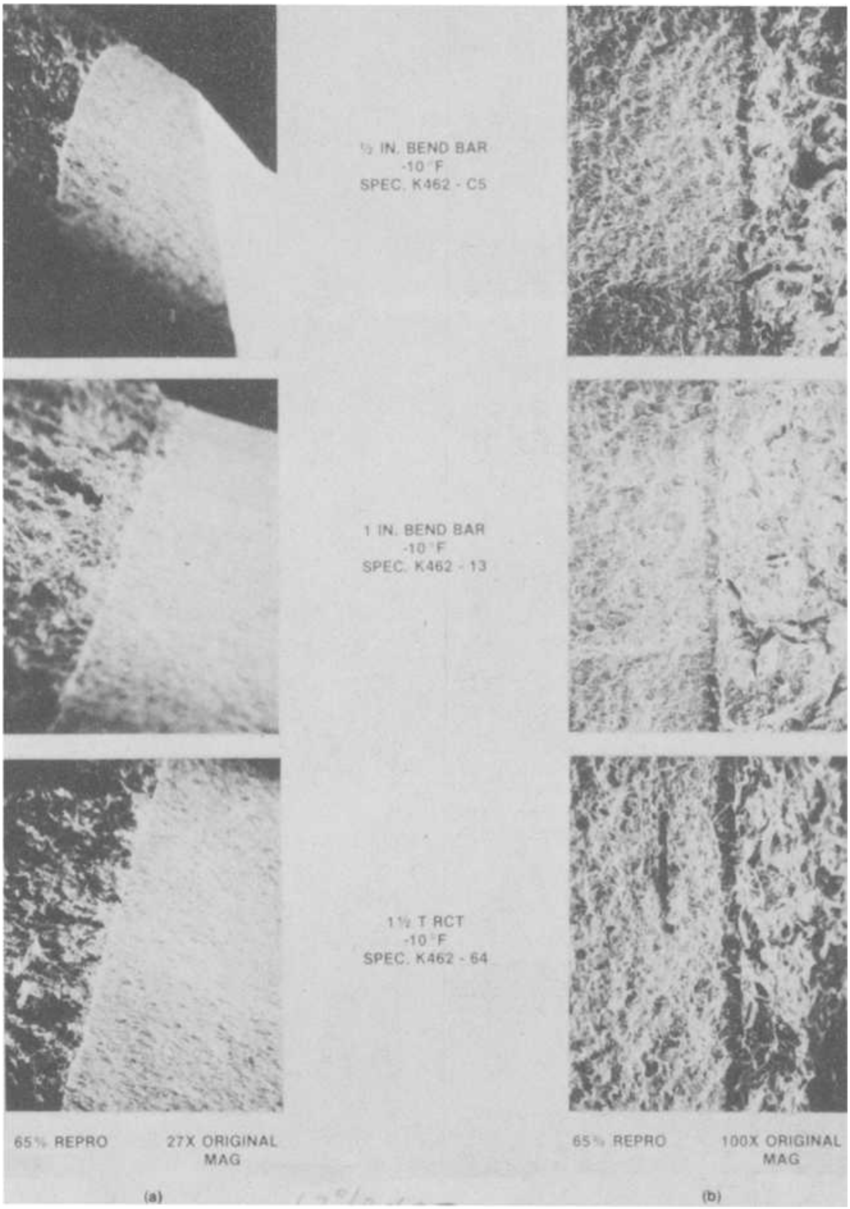

FIG. 6—*Fractographs of tested specimens showing the stretch zone and cleavage fracture.*

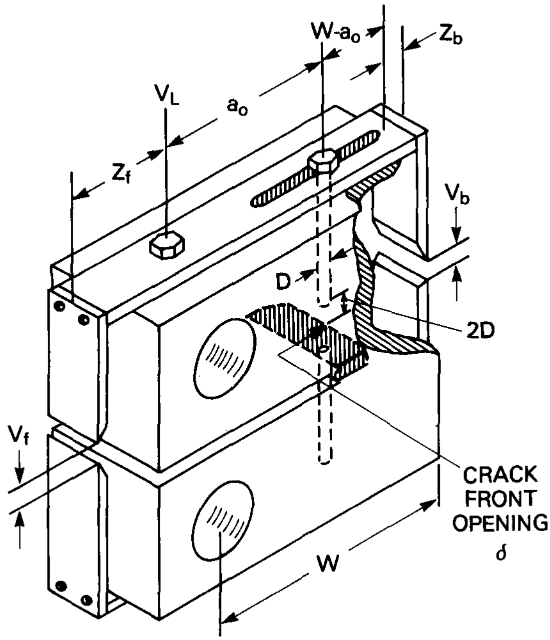

FIG. 7—*The "frame" fixture for clip-gage instrumentation.*

TABLE 4—*J-estimation weights.*

$$J = J_e + J_p = \frac{\eta_e A_e}{(W-a)B} + \frac{\eta_p A_p}{(W-a)B}$$

	a/W								
Specimen Type	0.2	0.3	0.4	0.5	0.6	0.7	0.8	0.9	1.0
4-point bend[a]:									
η_e	...	...	4.09	3.12	2.56	2.26	2.14	2.13	2.02
η_p	...	...	2.00	2.00	2.00	2.00	2.00	2.00	2.00
3-point bend[b]:									
η_e	1.44	1.75	1.96	2.08	2.14	2.18	2.21	2.21	2.00
η_p	2.00	2.00	2.00	2.00	2.00	2.00	2.00	2.00	2.00

[a] $A_e = A$ due to crack only.
[b] $A_e = A$ total.

Results

The test results are shown in Table 3 and Fig. 8. In Table 3, the first column is the flow stress, σ_Y, defined as the average of the yield stress, σ_y, and the ultimate tensile strength, σ_u. The flow stress is used to calculate the theoretical limit load, $P_{\lim}$. The loads $P_{f\,\max}$ are the maximum loads used in the final stages of precracking, shown here to demonstrate that the results

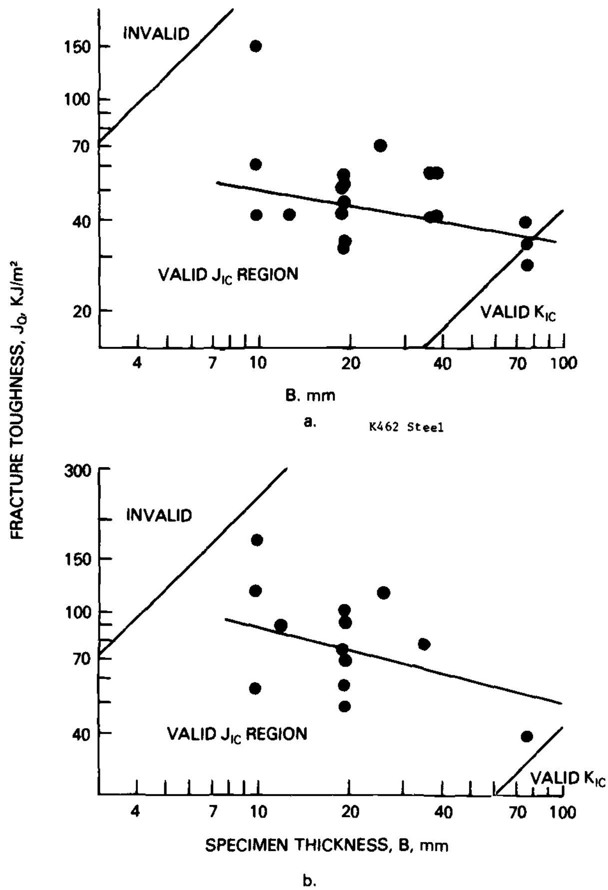

FIG. 8—*Fracture test results—regression line was projected from 19-mm (3/4 in.) data per Appendix I.*

were not reasonably affected by virtue of the low (< 0.5) values of the ratios $P_{f\,max} : P_{max}$ and $P_{fmax} : P_{lim}$.

The validity of the fracture toughness results, J_Q, were evaluated by comparison with the criterion $B\sigma_Y/J_Q \geq 25$. See the right-hand column in Table 3. Valid results having acceptable fatigue precracks are called J_{Ic} elsewhere in the report on these bases only.

The results are plotted in Fig. 8 to show the trend of J_{Ic} decreasing with increasing thickness, irrespective of ligament length. The data for 19-mm-thick (3/4 in.) specimens and for both heats of steel, shown in Fig. 9, indicate that ligament length has no effect on the results. Had specimens of differing ligament lengths produced differing results, they would have fallen on different lines in Fig. 9. The close correspondence of the results for the

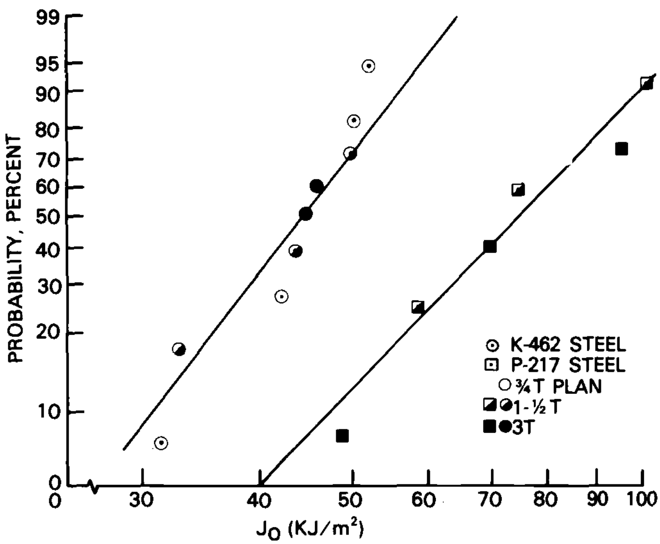

FIG. 9—*Probability plot for Weibull distribution of fracture toughness, K462 and P-217 steels, 19-mm-thick (3/4 in.) specimens.*

specimens of equal thickness but differing plan size demonstrates that the H2, or weakest-link, hypothesis is better than H1 for these results.

Discussion

Fractographic observations [*14*] in low-alloy steels have shown that, microscopically, low-temperature (lower shelf) fractures occur by a transgranular cleavage mechanism along low-energy crystallographic cleavage planes. Failure at the lower shelf has been modeled as slip-initiated cleavage fracture using the critical stress criterion proposed by Ritchie, Knott, and Rice (RKR) [*11*].

The RKR model, also used by Milne and Chell [*9*], assumes that cleavage fracture occurs when the maximum principal tensile stress (σ_{yy}) ahead of a crack exceeds a critical value (σ_f*) which is insensitive to both temperature and strain rate [*15,16*] and acts over a microstructurally significant length (l_0*). The model is capable of relating low-temperature fracture toughness to the material yield and fracture stresses determined in a smooth-bar tension test. The length l_0* is characteristic of the order of two ferritic grain diameters [*10*]. The details for quantitative application of the model are given in Ref *17*.

The model as described in the foregoing also gives a basis for understanding the variability observed in the results of fracture toughness tests of low-alloy steel. The largest source of variation is the physical dimension related to the parameter l_o*. This parameter was related to the ferrite grain size [16] and to the prior austenite grain size [17]; both grain sizes vary within any one specimen of steel.

Assuming the grain size is actually the physical feature that is associated with l_o*, the crack front in a specimen will sample a variety of grain sizes and orientations. The "sample" size (volume) is directly proportional to the crack-front length. Fracture will then occur when the local stress exceeds the fracture stress, σ_f*, over the characteristic length, l_o*, for the weakest grain within that sample volume. The fracture event in this weakest grain will initiate fracture in the neighboring grains due to the elevation of the flow stress with dynamic loading associated with the running crack, and the specimen will fail catastrophically.

The appropriate mathematical model for describing variation of the initiation and fracture event and the resulting size effects is a statistical model representing a weakest-link hypothesis. The Weibull distribution [18] is consistent with that hypothesis and is given by

$$P(J_1) = 1 - \exp(-J_1/J_o)^m \tag{8}$$

where $P(J_1)$ is the probability that a specimen will have a toughness less than J_1, J_o is a scale parameter proportional to the mean value of J_{Ic}, and m is the Weibull modulus or slope parameter.

The accuracy of the model for representing any data set may be evaluated using a graph plotting lnln $[1/(1 - P)]$ versus ln J_{Ic} for data obtained from equal-sized specimens. The probability, P, is calculated using [19]

$$P = \frac{n - 0.5}{N} \tag{9}$$

where n is the rank-order number for the J_{Ic}-value and N is the number of specimens in the sample. If the data are well represented by the Weibull distribution, they will plot as a straight line of slope m. Figure 9 shows examples using the data for 19-mm-thick (3/4 in.) specimens of the K469 and P217 materials. These data are well represented with straight lines. An example calculation is given in Appendix I.

The value of m obtained for these specimens is in excellent agreement with the value obtained by Landes and Shaffer [10] for a nickel-chromium-molybdenum-vanadium rotor steel.

The size effect is related to the scatter for a given size, and may be estimated using the relationship [10]

$$\frac{J_1}{J_2} = \left[\frac{B_2}{B_1}\right]^{1/m} \tag{10}$$

where J_1 is the mean J_{Ic} for specimens of thickness B_1 and J_2 is the mean J_{Ic} for specimens of thickness B_2. Using this relationship, a prediction of J_{Ic} for any size specimen is projected from the 19-mm-thick (3/4 in.) specimen data in Fig. 8.

Limits of Applicability

The foregoing estimates of size effects are applicable only within certain size limits. The stress and strain distributions in the vicinity of the crack tip must be characterizable by the Hutchinson, Rice, and Rosengren (HRR) field [*3,4*] with J_I as the amplitude, and the full constraint of the near tip stresses must be effective. McMeeking and Parks [*20*] and Shih and German [*5*] carried out detailed finite-element calculations to establish the size requirements for center-cracked plates in tension and single-edge-cracked plates under pure bending. Their studies suggest that the requirements

$$(B, c_o, a_o) > 25J_{Ic}/\sigma_y \tag{11}$$

must be adhered to for bend specimens and

$$(B, c_o, a_o) > 150J_{Ic}/\sigma_y \tag{12}$$

for tension specimens. The more stringent requirements for tension specimens arise because of the loss of HRR field dominance as discussed by Shih and German [*5*]. The present test program employed mostly RCT specimens where the uncracked ligament is subjected to both bending and tension; however, for sufficiently deep cracks the remaining ligament is predominantly in bending and the requirement given by Eq 11 may be assumed to be valid. To ensure that this indeed is the case, a J-dominance study along the lines of Shih and German [*5*] was performed for a $3T$ RCT specimen with $a_o/W = 0.6$ of ASTM 469 steel. As detailed in Appendix II, the finite-element stress and strain distributions near the crack tip are compared with the HRR singular fields due to Hutchinson [*3*] and Rice and Rosengren [*4*]. The results show that the requirements given by Eq 11 remain valid for RCT configurations also, as long as $a_o/W = 0.6$ (it is noted that $a_o/W = 0.6$ is only a necessary condition and may not be sufficient). This is not surprising because for $a_o/W > 0.6$ the tensile stresses are small compared with the bending stresses in the uncracked ligament and, therefore, the pure bending results would still be applicable as demonstrated in Appendix II.

An additional consideration needed for comparing specimens loaded in bending with those loaded in tension is the contribution of the σ_{xx}, the stress parallel to the crack, to the hydrostatic tension [*21*]; σ_{xx} is not described by the J-integral, which describes only the singular stresses. Since σ_{xx} is non-singular at the crack tip, J cannot characterize it. The values taken by σ_{xx} increase with specimen geometry from center-cracked plates to single-edge-notched tension, to deeply cracked bend specimens, tending to place less stringent requirements on bend specimens. Since the specimens used in this study were loaded primarily in bending, this effect was neglected.

The use of bend specimens is further constrained to deeply precracked ($a_0/W > 0.5$) specimens to avoid the misapplication of the J_I-calculation to regions of crack length for which J_I is not applicable; short cracks allow a loss of constraint through yielding along slip lines intersecting the notched face of the specimen.

A frequent occurrence while using J_{Ic}-sized specimens is the advent of slow crack growth prior to cleavage [22]. For specimens which show this behavior, a conservative estimate of J_{Ic} is that for slow crack growth initiation, however, these tests produced no slow crack growth and the resulting recommendations do not cover such behavior.

Conclusions

The tests performed support the argument that accurate estimates of valid plane-strain fracture toughness, K_{Ic}, for low-alloy steels in the ductile-to-brittle transition temperature range, for example, ASTM A469 rotor forging steel, may be made using a statistical sampling of J_{Ic}-valid specimens, the number depending on the confidence required, and accounting for a size effect evident for cleavage fracture. This conclusion is applicable to valid J_{Ic} specimens which show no slow crack growth prior to cleavage.

APPENDIX I

Weibull Analysis of J_{Ic} Data

K462 specimens 19 to 19.2 mm (0.76 to 0.768 in.) thick

Specimen	Plan Size	J_{Ic}	Rank Order, n	$P(J_c)$
K462-3	3/4 T	32	1	0.06
K462-106	1 1/2 T	33	2	0.17
K462-2	3/4 T	42	3	0.28
K462-105	1 1/2 T	44	4	0.39
K462-9	3 T	45	5	0.50
K462-7	1 1/2 T	46	6	0.61
K462-104	1 1/2 T	51	7	0.72
K462-1	3/4 T	51	8	0.83
K462-4	3/4 T	56	9	0.94
	$J_{B=19}$ =	44		

1. $P(J_c) = n - 0.5/N$
2. $\ln\ln [1/(1 - P)] = a_0 + m \ln (J_{Ic})$
   m = Weibull modulus by least-squares assuming equation form

$$y = a_0 + mx$$
$$a_0 = 23.36, m = 6.04$$

3. Estimating $3T$ K_{Ic} using Eq 10

$$J_{B=76} = J_{B=19} \times \left[\frac{19}{76}\right]^{1/6.04}$$

$$= 35 \text{ kJ/mm}^2 \text{ (200 in.-lb/in.}^2\text{)}$$

$$[K_{Ic} = 88 \text{ MPa} \sqrt{\text{m}} \text{ (80 ksi} \sqrt{\text{in.}}\text{)]}$$

APPENDIX II

In order to establish size requirements for J_{Ic} tests employing RCT specimens, a J-dominance analysis of this crack configuration has been carried out in a manner similar to Shih and German [5]. The J_{Ic} approach is valid as long as the size R of the region over which the HRR field is dominant completely encloses the fracture process zone. Since the fracture process zone, governed by grain size and inclusion spacing, etc., is of the order of crack-tip opening displacement, δ_t, the foregoing condition can be stated as requiring R to be equal to several times δ_t.

The size R of the HRR field is obtained by comparing the finite-element results for stress and strains with the singular field. The finite-element analysis is based on small strain theory and employs the J_2 flow theory of plasticity. The material behavior in uniaxial tension is modeled by the following piecewise power hardening law

$$\frac{\epsilon}{\epsilon_0} = \frac{\sigma}{\sigma_0} \quad \text{for} \quad \sigma \leq \sigma_0 \tag{13}$$

$$\frac{\epsilon}{\epsilon_0} = \alpha\left(\frac{\sigma}{\sigma_0}\right)^n \quad \text{for} \quad \sigma > \sigma_0 \tag{14}$$

where $\sigma_0 = E\,\epsilon_0$. The elastic modulus E was taken to be 200 GPa (29 000 ksi), the yield stress σ_0 to be 468 MPa (68 ksi), and the Poisson's ratio ν to be 0.3. The parameters α and n are determined by least-squares fitting to be 6.17 and 6.07, respectively. Eight-noded isoparametric elements with 3-by-3 Gauss points are employed in the calculations. The elements also allow the modeling of crack-tip blunting through the use of the collapsed-node technique. Ten wedge-shaped degenerate eight-noded elements are used to model the upper half of the crack tip. The finite-element mesh of the upper-half specimen is illustrated in Fig. 10. The finite-element code ADINA was employed for these computations.

The actual stress and strain fields as given by the finite-element solution are compared against the asymptotic or HRR singularity. The variation of the normalized tensile stress σ_{yy}/σ_0 with distance along the ligament normalized by J/σ_0 is shown in Figs. 11–13 for small-scale yielding, large-scale yielding, and fully plastic conditions, respectively. The level of plastic deformation is represented by $c/(J/\sigma_0)$. It is clearly seen that in all cases the finite-element results are in good agreement with the HRR singularity over the interval $X\sigma_0/J < 3$. Using the relation $\delta_t = d_n J/\sigma_0$ [22] with $d_n = 0.37$ for this steel, it is evident that the size R of the HRR field for the present case is about eight times δ_t at all levels of plastic deformation, including fully plastic condi-

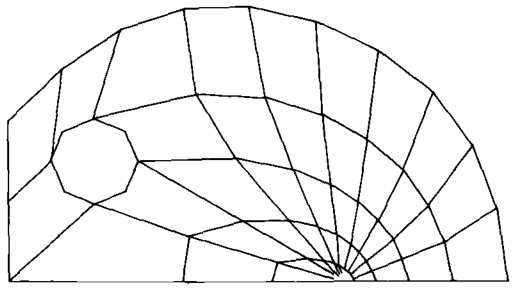

FIG. 10—*Finite-element mesh for the upper half of an RCT specimen.*

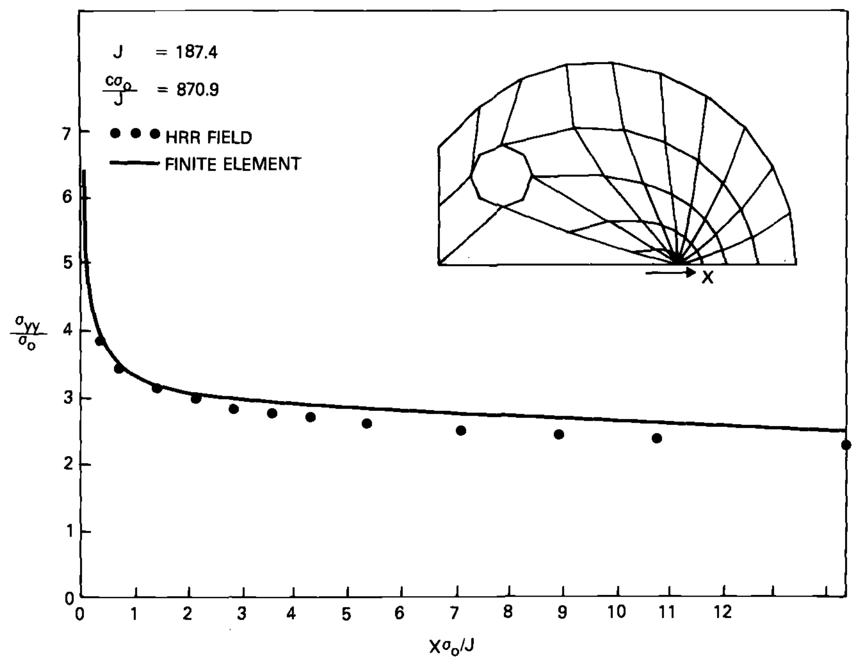

FIG. 11—*Comparison of finite-element and HRR field solution for normal stress ahead of crack under small-scale yielding. X is the distance from the crack tip. The shaded area shows the plastic zone.*

tions corresponding to $c\sigma_0/J = 25$. Similar results are observed for the strain distribution near the crack tip.

To summarize, the HRR singularity governs the near-tip stress and strain fields over a region which completely encloses the fracture process zone up to $c_0\sigma_0/J = 25$. Thus, the size requirement expressed by Eq 11 will also hold for the present specimen.

Although this analysis is for $a_0/W = 0.6$, these results will also hold for $a_0/W > 0.6$ because the bending stresses will increasingly dominate the tensile stresses approaching pure bending, for which condition the results assuredly would be valid.

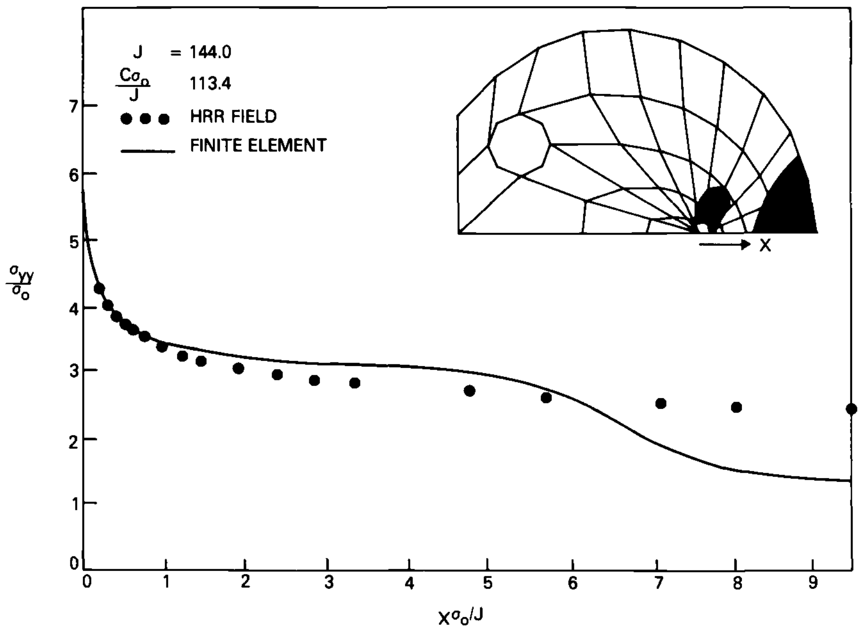

FIG. 12—*Comparison of finite-element and HRR field solutions for normal stress ahead of crack under large-scale yielding. The shaded area shows the plastic zone.*

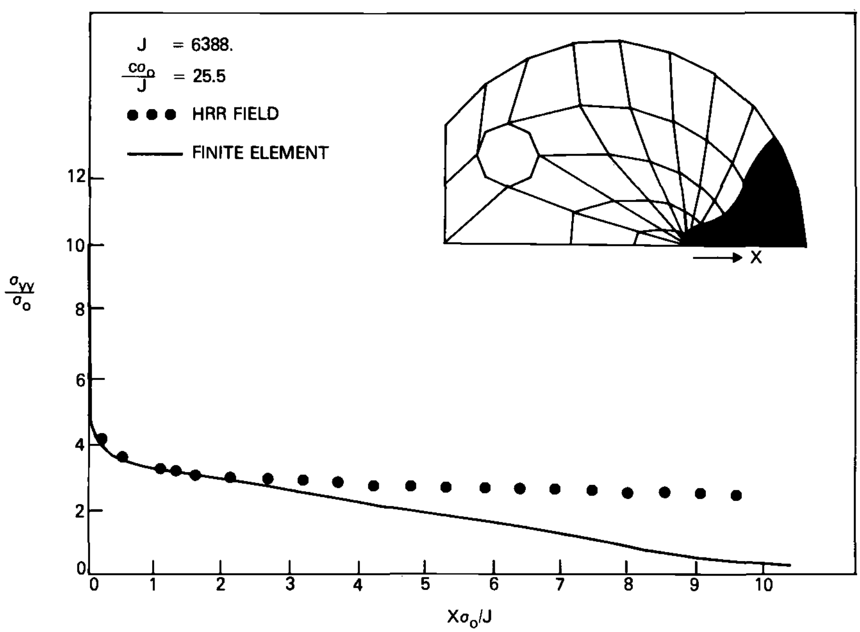

FIG. 13—*Comparison of finite-element and HRR field solutions for normal stress ahead of the crack under full plastic conditions.*

References

[1] Clarke, G. A., Andrews, W. R., Begley, J. A., Donald, J. K., Embly, G. T., Landes, J. D., McCabe, D. E., and Underwood, J. H., *ASTM Journal of Testing and Evaluation*, Vol. 7, No. 1, Jan. 1979, pp. 49-56.
[2] Newhouse, D. L. and DeForest, D. R., "Meeting Requirements for Larger Generator Rotors. ... A Metallurgical Challenge," presented at the Internal Forgemasters' Meeting, Terni, Italy, 6-9, May 1970.
[3] Hutchinson, J. W., *Journal of the Mechanics and Physics of Solids*, Vol. 16, 1968, pp. 13-31 and 337-347.
[4] Rice, J. R. and Rosengren, G. F., *Journal of the Mechanics and Physics of Solids*, Vol. 16, 1968, pp. 1-12.
[5] Shih, C. F. and German, M. D., "Requirements for a One-Parameter Characterization of Crack-Tip Fields by the HRR Singularity," General Electric Company Technical Information Series No. 79CRD076, April 1979.
[6] Landes, J. D. and Begley, J. A. in *Fracture Analysis, ASTM STP 560*, American Society for Testing and Materials, 1974, pp. 170-186.
[7] Logsdon, W. A. in *Mechanics of Crack Growth, ASTM STP 590*, American Society for Testing and Materials, 1976, pp. 43-60.
[8] Sumpter, J. D. G., *Metal Science*, Oct. 1976, pp. 354-356.
[9] Milne, I. and Chell, G. G. in *Elastic-Plastic Fracture, ASTM STP 668*, American Society for Testing and Materials, 1979, pp. 358-377.
[10] Landes, J. D. and Shaffer, D. H., "Statistical Characterization of Fracture in the Transition Region," Westinghouse Corp. Scientific Paper 79-1D3-JINTF-P4, 8 June, 1979.
[11] Ritchie, R. O., Knott, J. F., and Rice, J. R., *Journal of the Mechanics and Physics of Solids*, Vol. 21, 1973, p. 395.
[12] Sumpter, J. D. G. and Turner, C. E. in *Cracks and Fracture, ASTM STP 601*, American Society for Testing and Materials, 1976, pp. 3-18.
[13] Merkle, J. G. and Corten, H. T., *Journal of Pressure Vessel Technology, Transactions*, American Society of Mechanical Engineers, Nov. 1974, pp. 286-292.
[14] VanStone, R. H., General Electric Report No. SRD-78-116 for the Electric Power Research Institute, July 1978, pp. 5.1-5.13.
[15] Orowan, E., *Report on Progress in Physics*, Vol. 12, 1948, p. 185.
[16] Knott, J. F., *Journal of the Iron and Steel Institute*, Vol. 204, 1976, pp. 104-111.
[17] Ritchie, R. O., Server, W. L., and Wullaert, R. A., *Metallurgical Transactions*, Vol. 10A, Oct. 1979, pp. 1557-1570.
[18] Weibull, W., "A Statical Theory of the Strength of Materials," Royal Swedish Institute of Engineering Research, No. 151, 1939.
[19] Weibull, W., *Fatigue Testing and Analysis of Results*, Pergamon Press, New York, 1961, pp. 198-199.
[20] McMeeking, R. M. and Parks, D. M. in *Elastic-Plastic Fracture, ASTM STP 668*, American Society for Testing and Materials, 1979, pp. 175-194.
[21] Rice, J. R., *Journal of the Mechanics and Physics of Solids*, Vol. 22, 1974, pp. 17-26.
[22] Blauel, J. G. and Hollstein, T., "An Evaluation of Fracture Mechanics Material Parameters for the Reactor Pressure Steel 22 NiMoCr 37 from WOL-X Specimens," presented at SMIRT 5 Post-Conference Seminar: Assuring Structural Integrity of Steel Reactor Pressure Vessels, Berlin, 21-22 Aug. 1979.
[23] Shih, C. F., "Relationships Between the J-Integral and the Crack Opening Displacement for Stationary and Extending Cracks", *Journal of the Mechanics and Physics of Solids*, to appear.

M. E. Taylor[1] *and J. M. Barsom*[1]

Effect of Cyclic Frequency on the Corrosion-Fatigue Crack-Initiation Behavior of ASTM A517 Grade F Steel

REFERENCE: Taylor, M. E. and Barsom, J. M., "**Effect of Cyclic Frequency on the Corrosion-Fatigue Crack-Initiation Behavior of ASTM A517 Grade F Steel,**" *Fracture Mechanics: Thirteenth Conference, ASTM STP 743,* Richard Roberts, Ed., American Society for Testing and Materials, 1981, pp. 599–622.

ABSTRACT: This study was conducted to investigate the effect of cyclic frequency on the corrosion-fatigue crack-initiation behavior in regions of stress concentration in ASTM A517 Grade F steel. The tests were conducted on notched compact tension specimens at a stress ratio of 0.1 in a room-temperature 3.5 percent solution of sodium chloride. The test results showed that the corrosion-fatigue crack-initiation life under full immersion conditions was significantly less than the fatigue-crack-initiation life in air. Moreover, the test results showed no effect of cyclic frequency in the range of 12 to 300 cpm on the corrosion-fatigue life. The data indicate the possible existence of a corrosion-fatigue crack-initiation limit, below which cracks did not initiate, at a $\Delta K/\sqrt{\rho}$ of about 172 MPa (25 ksi). This value of $\Delta K/\sqrt{\rho}$ corresponds to a maximum stress range, $\Delta\sigma_{max}$, of about 207 MPa (30 ksi) and is one-fourth the value for the fatigue-crack-initiation limit in air.

Fatigue-crack-initiation test results on precorroded notched specimens showed a 25 percent reduction in the fatigue-crack-initiation limit. This decrease was attributed to an increase in the stress concentration caused by corrosion pits on the surface of the notch radius.

Metallographic investigations showed that corrosion-fatigue cracks initiate at corrosion pits on the surface of the notch tip. These cracks initiate as microcracks that form by a sharpening of the corrosion-pit tip under the combined influence of the environment and cyclic loads. No relationship was found between microstructure and corrosion-pit sites.

KEY WORDS: corrosion, corrosion fatigue, crack initiation, cyclic loads, cyclic frequency, crack propagation

Failure of structural components subjected to fluctuating loads is caused by the initiation and propagation of cracks. The total useful life of such components is determined by the time necessary to initiate the crack and to prop-

[1]Cooperative student and division chief, Materials Technology, respectively, Research Laboratory, U. S. Steel Corp., Monroeville, Pa. 15146.

agate the crack to a critical size. Crack initiation and subcritical crack propagation may be caused by cyclic stresses in the absence of an aggressive environment (fatigue) or by the combined effects of cyclic stresses and an aggressive environment (corrosion fatigue). The relative magnitude of crack-initiation life and crack-propagation life in the total life of a component depends on material properties, structural geometry, applied stresses, and environment.

Fatigue-Crack Initiation

Initiation of cracks in structural components that are subjected to fluctuating loads occurs in the neighborhood of stress raisers or notches. Stress raisers or notches in structural components cause stress intensification in the vicinity of the notch tip. Thus, the material element at the tip of the notch is subjected to the maximum stress (strain) magnitude and fluctuation. Consequently, this material element is most susceptible to fatigue damage and is, in general, the initiation site of fatigue cracks. The higher the stress concentration, the shorter is the fatigue-crack-initiation life. Thus, under identical test conditions, the total fatigue life of a notched specimen is shorter than that for a smooth specimen or for a specimen containing a less severe stress raiser.

The maximum-stress range, $\Delta\sigma_{max}$ (or maximum stress, σ_{max}), on the material element at the tip of a deep notch can be related to the stress-intensity-factor range, ΔK_I (or stress-intensity factor, K_I), as follows [*1*][2]

$$\Delta\sigma_{max} = \frac{2}{\sqrt{\pi}}\frac{\Delta K_I}{\sqrt{\rho}} = \Delta\sigma(k_t) \tag{1}$$

where

ρ = notch-tip radius,
$\Delta\sigma$ = applied nominal-stress range, and
k_t = stress-concentration factor.

Although Eq 1 is considered exact only when ρ approaches zero, Wilson and Gabrielse [*2*] showed that this relationship is accurate to within 10 percent for notch radii up to 4.6 mm (0.180 in.).

The behavior of specimens containing notches that correspond to various stress-concentration factors is shown in Fig. 1 for zero-to-tension axial loading [*1,3*]. The data are presented in terms of the number of cycles for fatigue-crack initiation, N_i, at the tip of a notch versus the nominal-stress fluctuation, $\Delta\sigma$. The same data are presented in Fig. 2 in terms of N_i versus the stress-intensity-factor range divided by the square root of the notch-tip

[2]The italic numbers in brackets refer to the list of references appended to this paper.

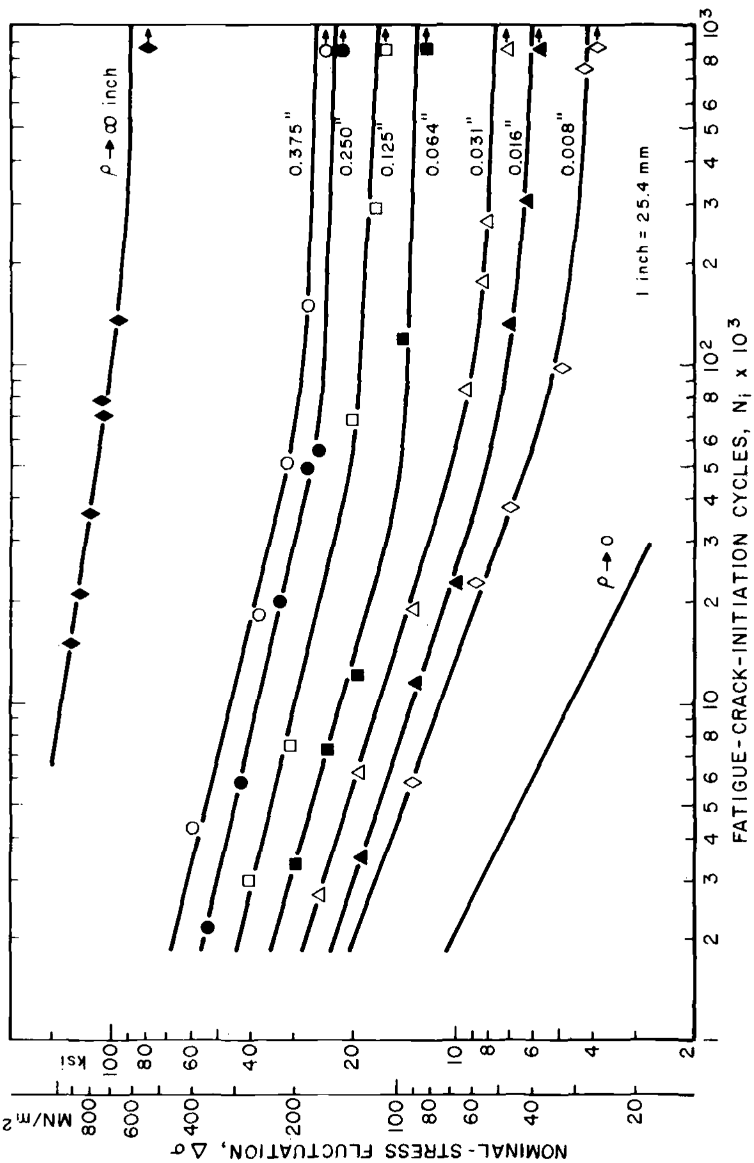

FIG. 1—*Dependence of fatigue-crack initiation of HY-130 steel on nominal-stress fluctuations for various notch geometries.*

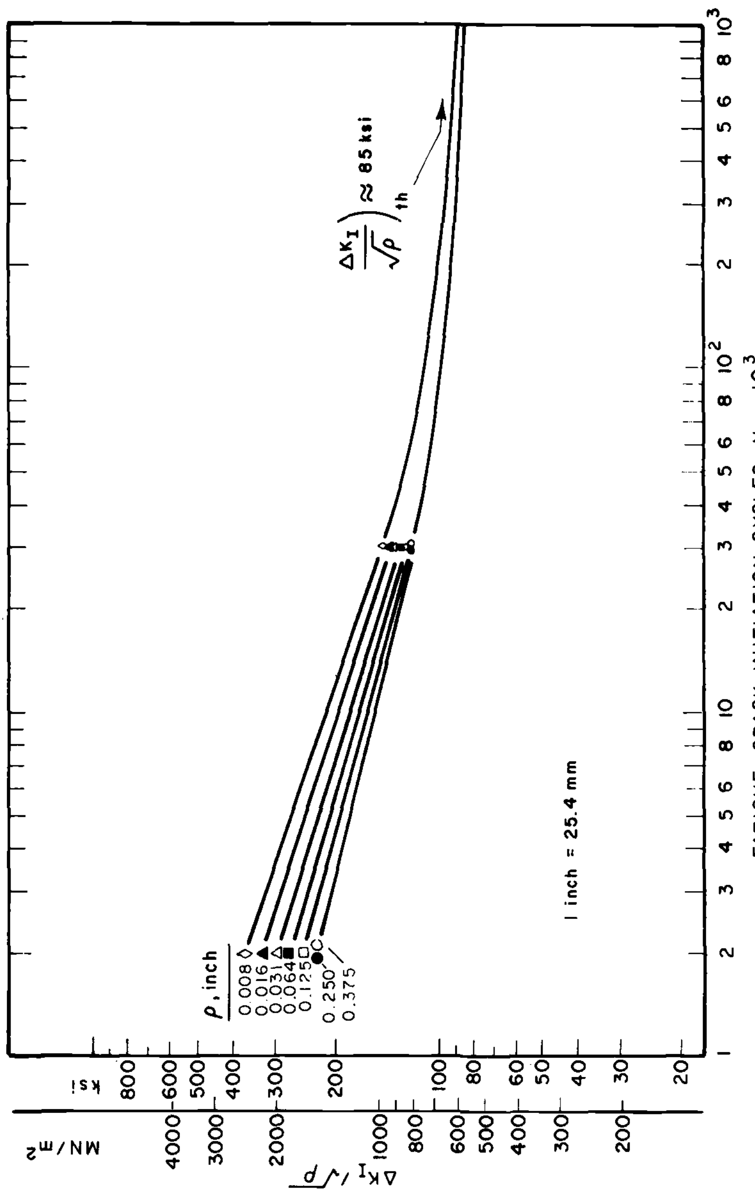

FIG. 2—*Correlation of fatigue-crack-initiation life with the parameter* $K_I/\sqrt{\rho}$ *for HY-130 steel.*

radius, $\Delta K_I/\sqrt{\rho}$, which corresponds to the maximum-stress range at the tip of the notch. The data in Fig. 1 show a significant decrease in the fatigue-crack-initiation life for a given nominal-stress range with an increased stress-concentration factor. The data in Fig. 2 show that $\Delta K_I/\sqrt{\rho}$, and therefore $\Delta\sigma_{max}$, is the primary parameter that governs the fatigue-crack-initiation behavior in regions of stress concentration for a given steel.

The fatigue-crack-initiation behavior of various steels is presented in Fig. 3 for specimens subjected to zero-to-tension bending stress and containing a notch that resulted in a stress concentration of about 2.5 [2]. Similar data have been published for Type 403 stainless steel [4] and for ASTM A517 Grade F steel, Fig. 4 [5]. Because the stress-concentration factor was constant for all specimens and for the various steels, the differences in the fatigue-crack-initiation behavior shown in Fig. 3 are related primarily to inherent differences in the fatigue-crack-initiation characteristics of the steels. The data show that fatigue cracks do not initiate in steel structural components when the body configuration, the notch geometry, and the nominal-stress fluctuations are such that the magnitude of the parameter, $\Delta K_I/\sqrt{\rho}$, and therefore $\Delta\sigma_{max}$, at the root of the notch is less than a given value that is characteristic of the steel. The value of this fatigue-crack-initiation threshold, $(\Delta K_I/\sqrt{\rho})_{th}$, increases with increased yield strength or tensile strength of the steel. The data show that the fatigue-crack-initiation life of a structural detail subjected to a given nominal-stress range increases with increased tensile strength of the steel. However, this difference in fatigue-crack-initiation life for various steels decreases with an increased magnitude of the stress-concentration factor.

Finally, fatigue-crack-initiation data for various steels subjected to stress ratios (ratio of nominal minimum-applied stress to nominal maximum-applied stress) ranging from -1.0 to $+0.5$, Fig. 5, indicate that the fatigue-crack-initiation life is governed by the total maximum-stress (tension plus compression) range at the tip of the notch [6].

Corrosion-Fatigue Crack Initiation

Corrosion-fatigue behavior of a given environment-material system refers to the characteristics of the material under fluctuating loads in the presence of the particular environment. Different environments have different effects on the cyclic behavior of a given material. Similarly, the corrosion-fatigue behavior of different materials is different in the same environment.

The corrosion-fatigue behavior of metals subjected to load fluctuation in the presence of an environment to which the metal is immune is identical to the fatigue behavior of the metal in the absence of that environment. Consequently, the corrosion-fatigue behavior of an environment-material system can be studied by establishing the deviation of the corrosion-fatigue behavior

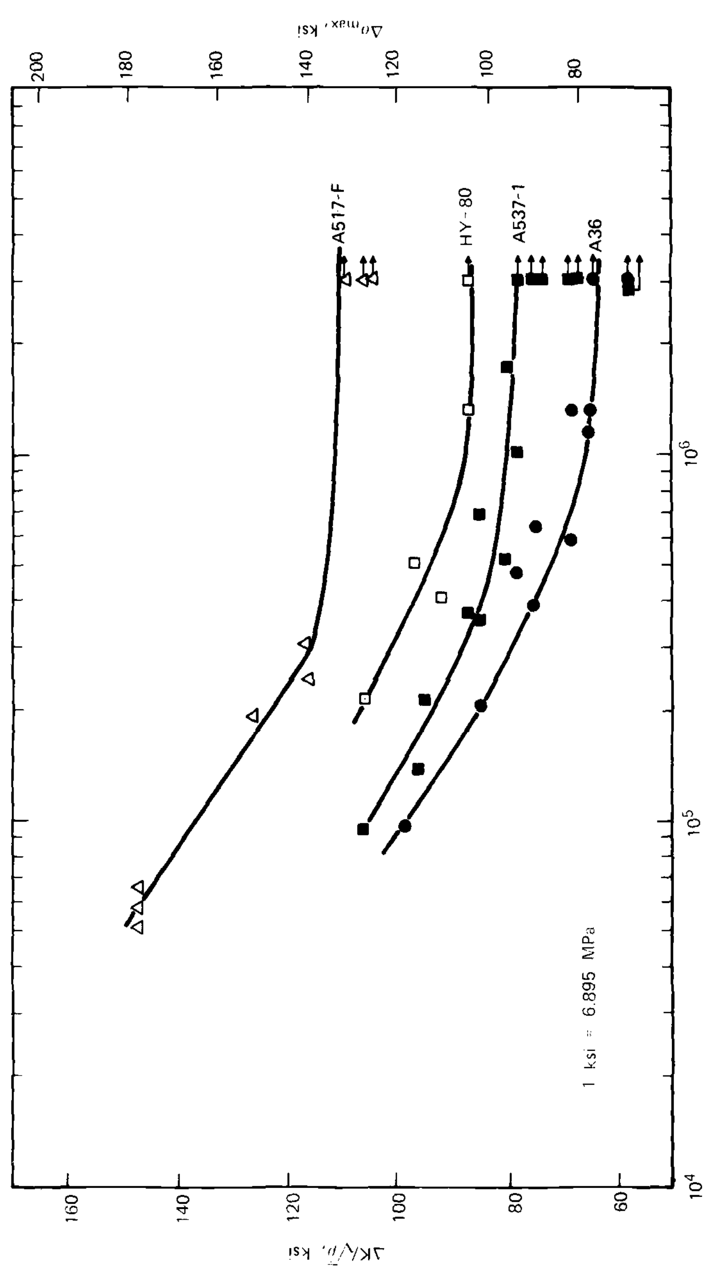

FIG. 3—*Fatigue-crack-initiation behavior of various steels at stress ratio of +0.1.*

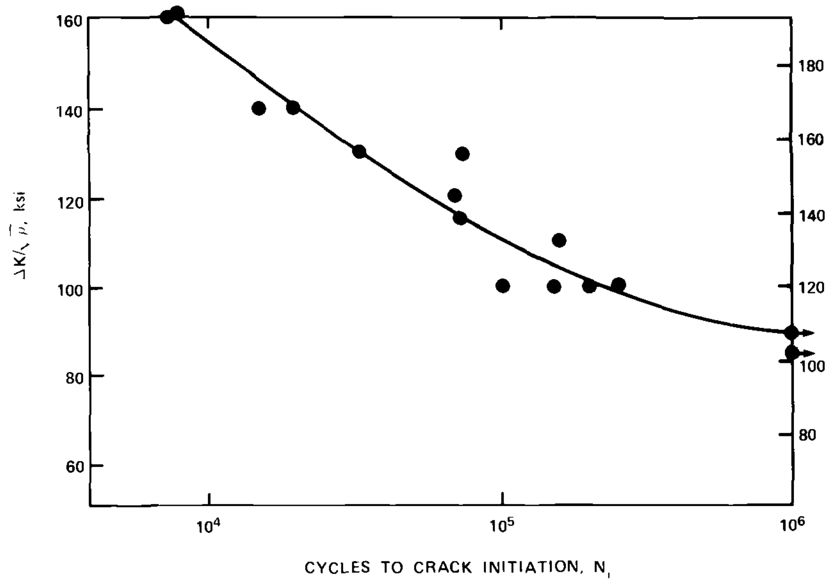

FIG. 4—*Fatigue-crack-initiation behavior of A517 Grade F steel.*

for the environment-material system from the fatigue behavior of the material in a benign environment.

Various aspects of the corrosion-fatigue behavior of metals in various environments have been investigated [*7*]. However, the corrosion-fatigue crack-initiation behavior in regions of stress concentration has not been investigated systematically for constructional steels. Recently, Novak and McKelvey [*8*] established the corrosion-fatigue crack-initiation behavior for notched specimens of ASTM A517 Grade F steel in a room-temperature 3.5 percent solution of sodium chloride. The tests were conducted with notched specimens ($k_t \approx 2.5$) subjected to zero-to-tension loads in bending and at a cyclic frequency of 12 cpm, Fig. 6. The data show a substantial decrease in the corrosion-fatigue crack-initiation life at stress ranges significantly lower than that corresponding to the fatigue limit in a room-temperature air environment.

Extensive research has been conducted to establish the corrosion-fatigue crack-propagation behavior for constructional steels [*1*]. The test results show that an environment can increase the rate of fatigue crack growth and that the magnitude of this increase depends on the material-environment system. The data also show that for a given material-environment system, the rate of corrosion-fatigue crack growth depends strongly on the shape of the applied load cycle (waveform) and its frequency. However, the effect of waveform and cyclic frequency on corrosion-fatigue crack-initiation life has not been investigated. Consequently, the present investigation was conducted

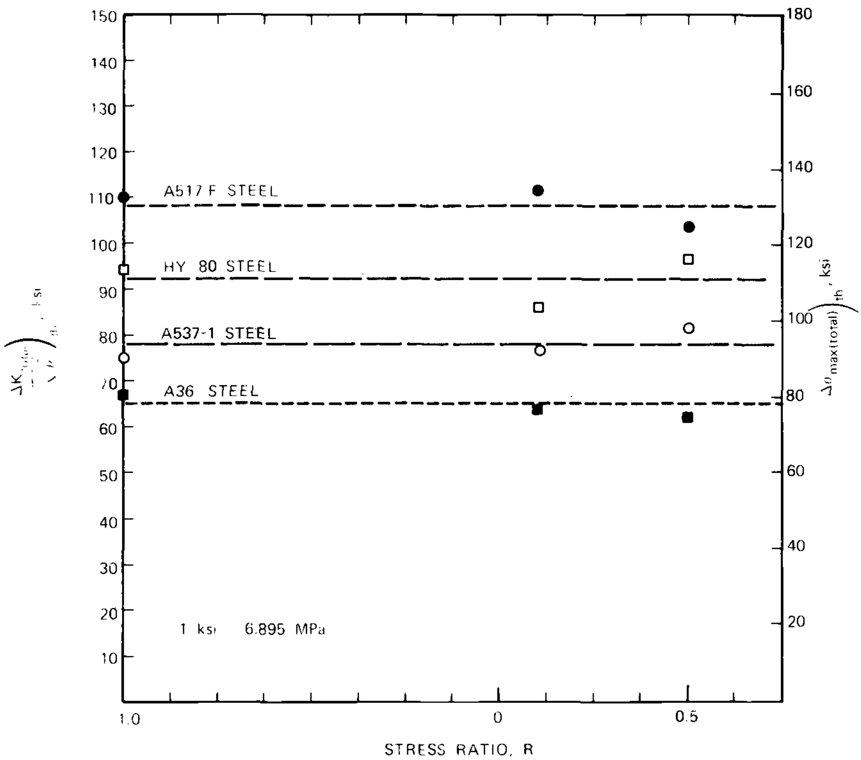

FIG. 5—*Independence of fatigue-crack-initiation threshold from stress ratio.*

to determine the effect of cyclic frequency for sinusoidal loading on the corrosion-fatigue crack-initiation behavior of ASTM A517 Grade F steel in a room-temperature 3.5 percent solution of sodium chloride. Moreover, the effect of corrosion under stress on the subsequent fatigue-crack-initiation behavior was investigated by fatigue-testing notched specimens that had been subjected to static loading in the environment.

Material and Experimental Work

Material

The present investigation was conducted with ASTM A517 Grade F steel obtained from the same plate used by Barsom [*6*], Fig. 3, and by Novak and McKelvey [*8*], Fig. 6. The chemical composition and mechanical properties of this steel are presented in Tables 1 and 2, respectively.

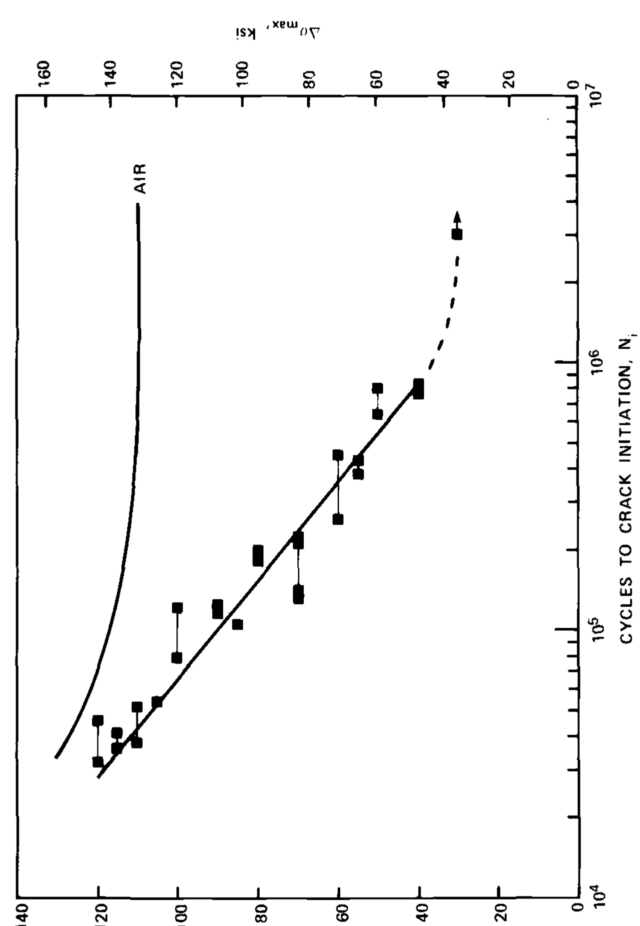

FIG. 6—*Corrosion-fatigue crack-initiation behavior of A517 Grade F steel in 3.5 NaCl solution at 12 cpm (Novak and McKelvey).*

TABLE 1—*Chemical composition of ASTM A517 Grade F steel tested—percent (check analysis).*

C	Mn	P	S	Si	Cu	Ni	Cr	Mo	V	B
0.17	0.89	0.015	0.015	0.19	0.30	0.84	0.52	0.42	0.04	0.003

Test Specimens

Because of limited material from the A517 Grade F plate previously investigated by Barsom [*6*] and Novak and McKelvey [*8*], the available plate was split at midthickness and specimens were machined from the two halves. The test specimens were 9.4-mm-thick (0.372 in.) modified compact tension (CT) specimens [ASTM Standard Test Method for Plane-Strain Fracture Toughness of Metallic Materials (E399-78a)] having in-plane dimensions equal to a 25.4-mm-thick (1 in.) CT specimen, Fig. 7. All specimens contained notches that were milled to a length (a) of about 17.0 mm (0.67 in.) or 25.4 mm (1.0 in.) and had tip radii (ρ) of 3.3 mm (0.128 in.). The sides of the specimens were ground to a No. 6 finish or better and the surfaces in and around the notch root were then diamond-polished to a 6-μm finish.

Experimental Procedure

The specimens were corrosion-fatigue-tested in a room-temperature 3.5 percent solution of sodium chloride in distilled water at frequencies of 300, 120, and 60 cpm. These tests were conducted with 100-kip (45 000 kg) and 50-kip (22 500 kg) Materials Testing System (MTS) machines. Alignment was obtained by carefully machining specimens and other auxiliary parts and by using universal joints to load the specimens.

In all tests the specimens were cyclically loaded in tension at a stress ratio, R (ratio of minimum and maximum loads), of 0.1. The cyclic load was sinusoidal and the maximum and minimum loads were controlled within ± 1.0 percent. For each cyclic frequency the tests were conducted at various $\Delta K/\sqrt{\rho}$-values that ranged from 137.9 to 896.4 MPa (20 to 130 ksi). Specific $\Delta K/\sqrt{\rho}$-values, test frequencies, and range of cycles for crack initiation for each test are presented in Table 3. The range of cycles for crack initiation is bounded by the number of cycles corresponding to the last inspection of the notch tip where no crack was observed and the following inspection where a crack existed.

The environmental tank, Fig. 8, was made of polymethylmethacrylate (Plexiglas), and all auxiliary parts and the universal joints were made of ASTM A517 Grade F steel to minimize galvanic corrosion. The solution was maintained at a pH of 6.5 ± 0.5 and was replaced every 100 h for all tests that exceeded this period of time. The oxygen content of the solution was not controlled; however, some aeration of the solution would have occurred as a

TABLE 2—*Mechanical properties of ASTM A517 Grade F steel tested.*

Yield, Strength (0.2% Offset), MPa (ksi)	Tensile Strength, MPa (ksi)	Elongation in 25.4 mm (1 in.), %	Reduction of Area, %	2/3-Size Charpy V-Notch Energy Absorption, J (ft-lb)				
				22°C (+72°F)	0°C (+32°F)	18°C (0°F)	−40°C (−40°F)	−73°C (−100°F)
754 (109.3)	862 (125.0)	20.3	67.5	47 (35)	41 (30)	30 (22)	23 (17)	12 (9)

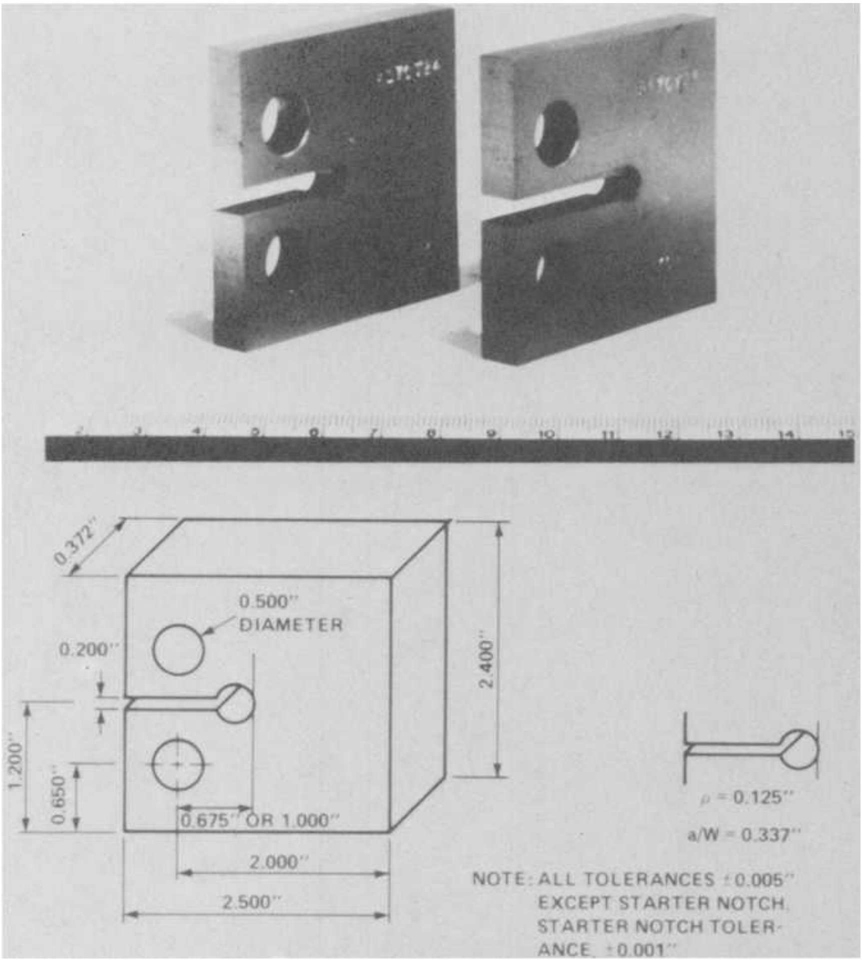

FIG. 7—*Modified compact-tension specimens.*

result of movement of the specimen and exposure of the surface of the solution to the room air.

The notch-tip surface was inspected periodically by lowering the tank, Fig. 9, drying the notch tip with absorbent cotton swabs, and observing the notch-tip surface at ×17 magnification with a microscope. The test was terminated when a crack of 0.25 mm (0.010 in.) or longer was observed at the surface of the notch tip. For the 300-cpm tests, the frequency was temporarily lowered to about 120 cpm during inspection to facilitate observation of cracking at the notch tip. Specimens that did not exhibit cracking after 4×10^6 cycles were considered runout tests.

Testing of Precorroded Specimens—To investigate the effect of corrosion

TABLE 3—*Crack-initiation data for various test conditions.*

Test Condition	$\Delta K/\sqrt{\rho}$, MPa (ksi)	Last Reading Without Crack	First Reading With Crack
Air,	1034 (150)	13 870	21 880
120 cpm	896 (130)	75 600	89 960
	827 (120)	87 660	106 500
	758 (110)	4×10^6	...
	690 (100)	4×10^6	...
Precorroded,	1034 (150)	19 750	24 440
120 cpm	896 (130)	53 940	60 160
	827 (120)	63 720	81 990
	690 (100)	554 000	735 000
	621 (90)	2 320 000	2 430 000
	552 (80)	729 470	973 710
Corrosion	690 (100)	59 300	71 340
fatigue,	552 (80)	153 480	196 600
300 cpm	414 (60)	290 250	365 360
	345 (50)	304 370	409 340
	310 (45)	772 580	921 970
	276 (40)	4×10^6	...
	241 (35)	2 231 750	2 691 650
Corrosion	827 (120)	31 400	46 550
fatigue,	690 (100)	89 500	111 000
120 cpm	552 (80)	163 700	207 920
	414 (60)	328 630	357 410
	276 (40)	1 139 510	1 360 730
	207 (30)	1 346 000	1 791 000
	138 (20)	4×10^6	...
Corrosion	896 (130)	27 830	30 240
fatigue,	552 (80)	177 900	208 220
60 cpm	276 (40)	889 560	921 800

under stress on the subsequent fatigue behavior of ASTM A517 Grade F steel, CT specimens were statically loaded in the 3.5 percent solution of sodium chloride, Fig. 10. The solution was replaced once a week.

Two specimens, each with different notch lengths, were immersed in the solution and were loaded in series. Because the specimens had different notch lengths, the value of $\Delta K/\sqrt{\rho}$ (and $\Delta\sigma_{max}$) at the notch tip corresponding to a given deadweight load was about 50 percent higher for the long notches than for the short notches. The specimens were statically loaded in the environment for about one month. Then they were unloaded, rinsed in distilled water, dried thoroughly with absorbent cotton, and cyclically loaded in room-temperature air. The specimens were tested under sinusoidal loading at a frequency of 120 cpm and at an R-value of 0.1. Each specimen was tested at a $\Delta K/\sqrt{\rho}$ level equal to the $K/\sqrt{\rho}$ level at which it had been previously stress-corroded. Periodic observations of the notch tip were made at $\times 17$ magnification until crack initiation occurred.

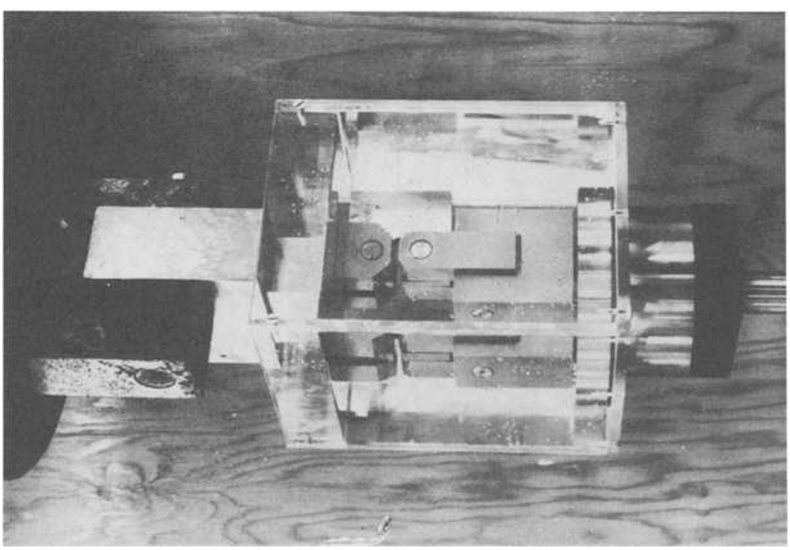

FIG. 8—*Corrosion tank in operating position.*

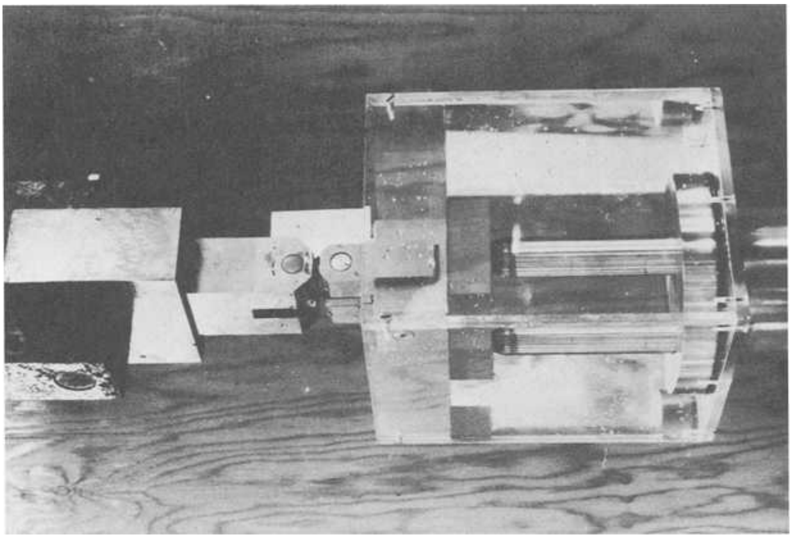

FIG. 9—*Corrosion tank in inspection position.*

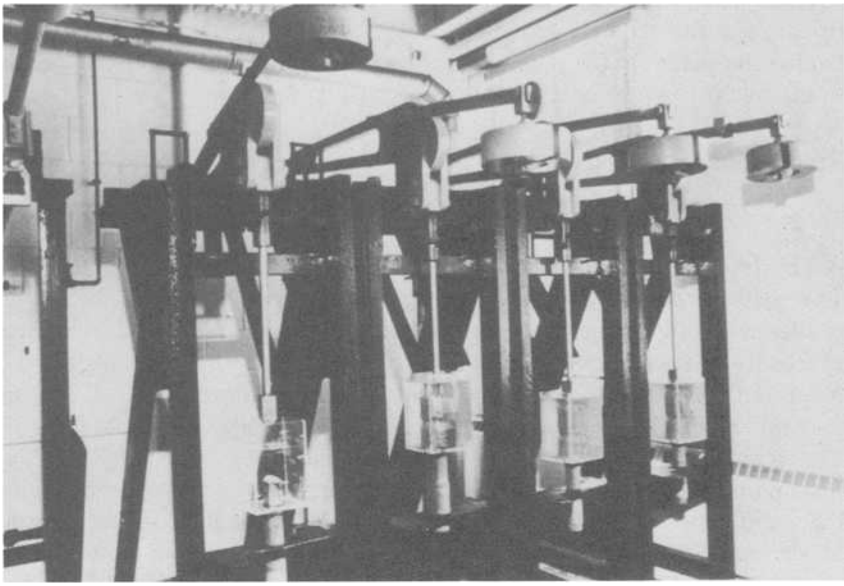

FIG. 10—*Static loading facility.*

Specimens with polished notches were also tested in air to compare the effect of precorrosion on the fatigue-crack-initiation behavior of ASTM A517 Grade F steel and to ensure that the fatigue-crack-initiation behavior obtained by testing the CT specimens was similar to the behavior established previously [*6,8*] by using other specimens and loadings. These tests were conducted on specimens with $\Delta K/\sqrt{\rho}$ values of 1034, 896, and 827 MPa (150, 130, and 120 ksi) in an MTS machine and with values of 758 and 690 MPa (110 and 100 ksi) in an Amsler Vibraphore machine. All these tests were conducted in room-temperature air at $R = 0.1$. Crack initiation for the tests conducted in the Vibraphore machine was observed at $\times 30$ magnification by using a stereomicroscope and a strobe light.

Metallographic Analyses—Various metallographic analyses with a scanning electron microscope (SEM) were conducted on selected specimens to characterize the corrosion-fatigue crack-initiation site. One specimen that contained a corrosion-fatigue crack at the notch tip was broken at liquid-nitrogen temperature. The entire surface of the thumbnail crack was then studied with the SEM at magnifications between $\times 15$ and $\times 3000$.

Small blocks that contained the notch were cut from four specimens. After a thorough mapping of the pitting and cracking on the notch, the blocks were ground and polished incrementally in the through-thickness direction. SEM observations were made so that the polished surface, profile of the notch-radius surface, and the notch-radius surface were observed simultaneously at 30, 30, and 60-deg angles, respectively.

Finally, a mechanically polished surface of one specimen was electropolished and studied with the SEM to determine the magnitude of activated slip planes at the notch tip and the location of crack-initiation relative to the microstructure of the steel.

Results and Discussion

Fatigue-Crack Initiation

The fatigue-crack-initiation behavior in air of the ASTM A517 Grade F steel plate tested in the present investigation is presented in Fig. 11. The test results in this figure include data obtained by Barsom [*6*] using 3-point-bend specimens subjected to R-values of -1.0, $+0.1$, and $+0.5$; data obtained by Novak and McKelvey [*8*] using cantilever-bend specimens at $R = 0.1$; and data obtained in the present investigation by using CT specimens at $R = 0.1$. The data show that fatigue-crack-initiation life is governed by the total maximum-stress (tension plus compression) range at the tip of the notch and that different specimen geometries and loading give similar results. Moreover, the data show a distinct fatigue-crack-initiation limit that occurred at a $\Delta K/\sqrt{\rho}$ of about 690 MPa (100 ksi) for ASTM A517 Grade F steel and this corresponds to a $\Delta\sigma_{max}$ of about 828 MPa (120 ksi).

Corrosion-Fatigue-Crack Initiation

The corrosion-fatigue crack-initiation behavior of ASTM A517 Grade F steel in a 3.5 percent solution of sodium chloride at 60, 120, and 300 cpm is presented in Fig. 12. Superimposed on this figure are data obtained at 12 cpm [*8*] and the lower-bound fatigue-crack-initiation curve from Fig. 11. The combined corrosion-fatigue data fall within a narrow scatter band and, within experimental scatter, showed no consistent ordering with respect to test frequency. Moreover, the data showed no effect of cyclic frequency on the corrosion-fatigue crack-initiation life for the material-environment system investigated. However, under the full-immersion conditions used in the present investigation, the environment caused a substantial reduction in the fatigue life at $\Delta\sigma_{max}$-values that were significantly lower than the value corresponding to the fatigue limit in air.

The data indicate the possible existence of a threshold below which corrosion-fatigue-crack initiation would not occur. This threshold behavior for full-immersion conditions occurred at a $\Delta\sigma_{max}$ of about 207 MPa (30 ksi) [$\Delta K/\sqrt{\rho} \approx$ 172 MPa (25 ksi)] and is more apparent on a linear plot of $\Delta K/\sqrt{\rho}$ versus N_i.

Fatigue-Crack Initiation of Precorroded Specimens

Notched CT specimens were immersed in the 3.5 percent sodium chloride solution and subjected to static loads for a period of about one month. The

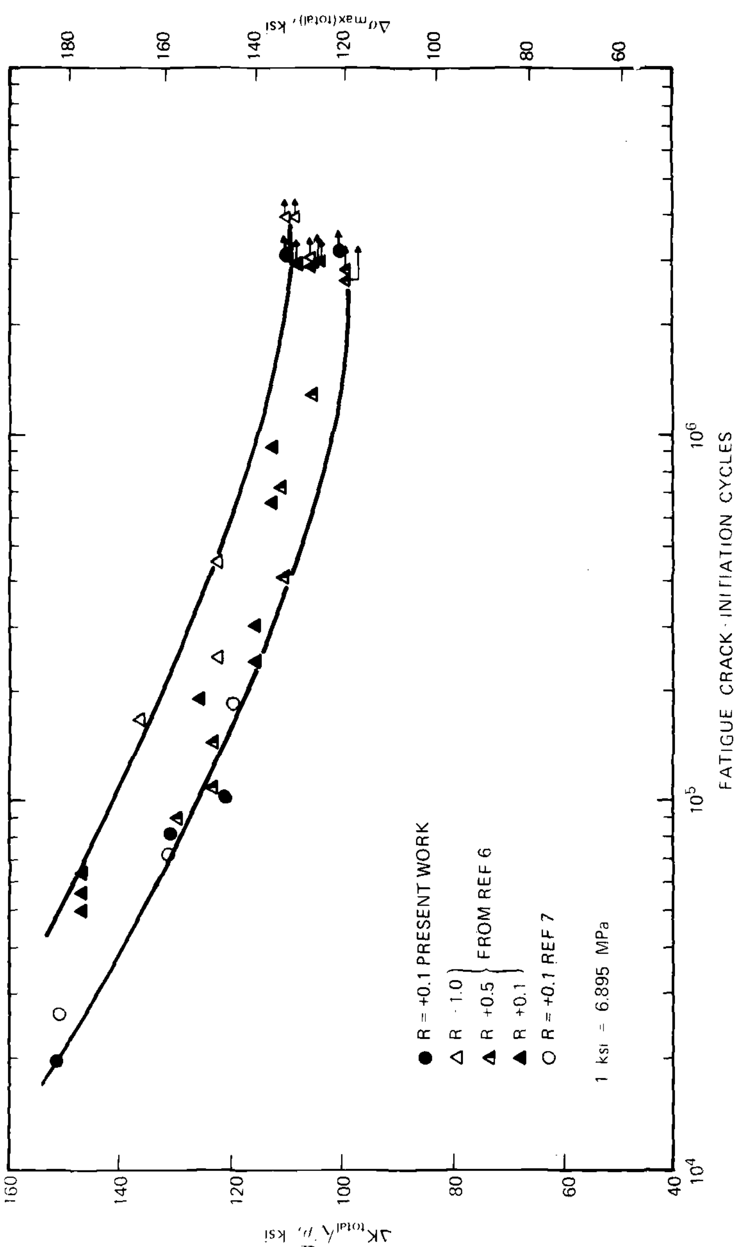

FIG. 11—*Relationship between fatigue-crack initiation and various stress ratios for A517 Grade F steel.*

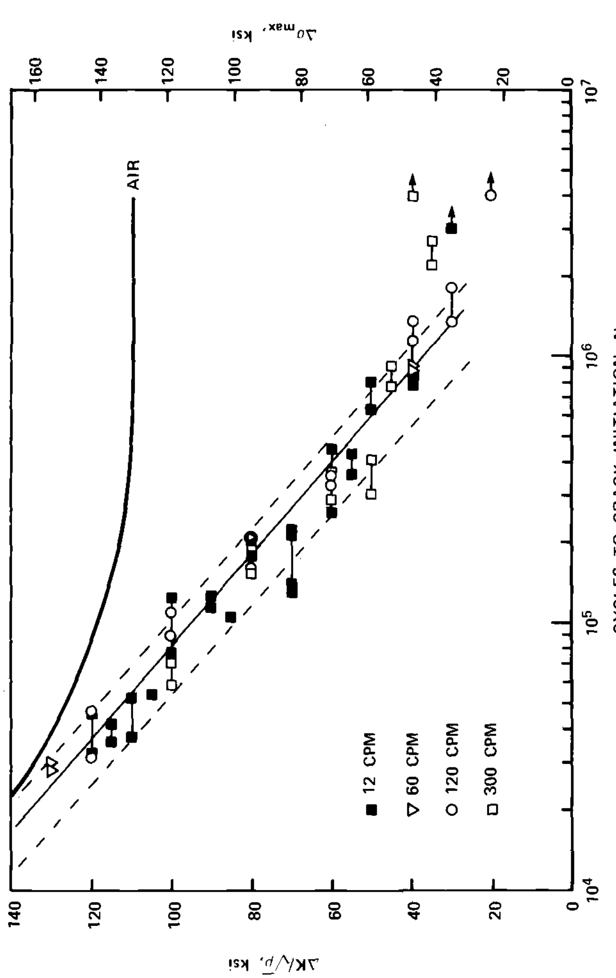

FIG. 12—*Effect of frequency on corrosion-fatigue crack initiation of A517 Grade F steel in 3.5NaCl solution.*

static loads for the six specimens corresponded to $\Delta K/\sqrt{\rho}$-values of 552, 621, 689, 827, 896, and 1034 MPa (80, 90, 100, 120, 130, and 150 ksi). After the one-month test period, the specimens were dried and subjected to tensile cyclic loads of $R = 0.1$ such that the $\Delta K/\sqrt{\rho}$-value for each specimen was equal to the $K/\sqrt{\rho}$-value in the static test. The scatter in the fatigue-crack-initiation data obtained by testing these specimens was larger than observed in the other tests, Fig. 13. The data show that the fatigue-crack-initiation limit for the precorroded specimens was about 25 percent lower than for specimens with machined and polished notches. This decrease in fatigue limit was attributed to an increase in the stress concentration caused by corrosion pits on the surface of the notch radius.

The decrease in the fatigue life of precorroded specimens is significantly less than the decrease obtained under corrosion-fatigue conditions. Consequently, the significant decrease in the corrosion-fatigue crack-initiation life must be caused, primarily, by synergistic effects of the environment and cyclic loading operating under full-immersion conditions. The actual corrosion-fatigue mechanism that caused the degradation in the crack-initiation life for the material-environment system investigated was not established.

Metallographic Analysis

A corrosion-fatigue specimen was broken in liquid nitrogen after it had been tested at a $\Delta K/\sqrt{\rho}$ of 552 MPa (80 ksi) and 120 cpm. The test was terminated when an 0.76-mm (0.03 in.) crack was observed on the notch surface. On the fracture surface, the crack was semicircular with an 0.38-mm (0.015 in.) depth.

The thumbnail crack surface was observed with the SEM at various magnifications between ×15 and ×3000. These observations revealed that the crack-initiation site in the material-environment system investigated contained mixed regions of intergranular and transgranular fracture whereas the fatigue-crack-initiation zone in air was primarily transgranular.

Four corrosion-fatigue specimens that were tested under different test conditions were selected for further metallographic analysis. Two specimens were tested at 120 cpm and at $\Delta K/\sqrt{\rho}$-values of 827 and 276 MPa (120 and 40 ksi), respectively. The other two specimens were tested at 300 cpm and at $\Delta K/\sqrt{\rho}$-values of 690 and 276 MPa (100 and 40 ksi), respectively. Small blocks that contained the notch tip were cut from each of the specimens. The surfaces of the blocks were ground and polished incrementally in the through-thickness direction and each new surface was observed in the SEM.

SEM observations of the notch-tip surfaces for these specimens revealed discrete, random areas of localized corrosion, Fig. 14. Moreover, SEM investigations of cross sections through these corrosion zones showed that they corresponded to corrosion pits of various depths. The tips of some of these

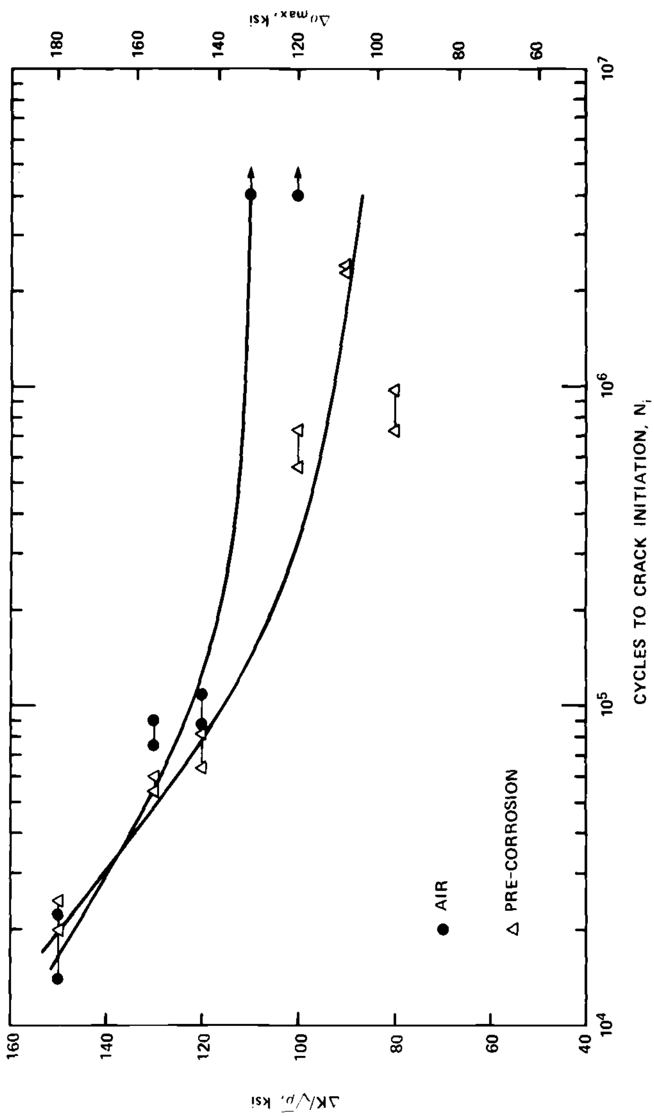

FIG. 13—*Effect of precorrosion on fatigue-crack initiation of A517 Grade F steel in air.*

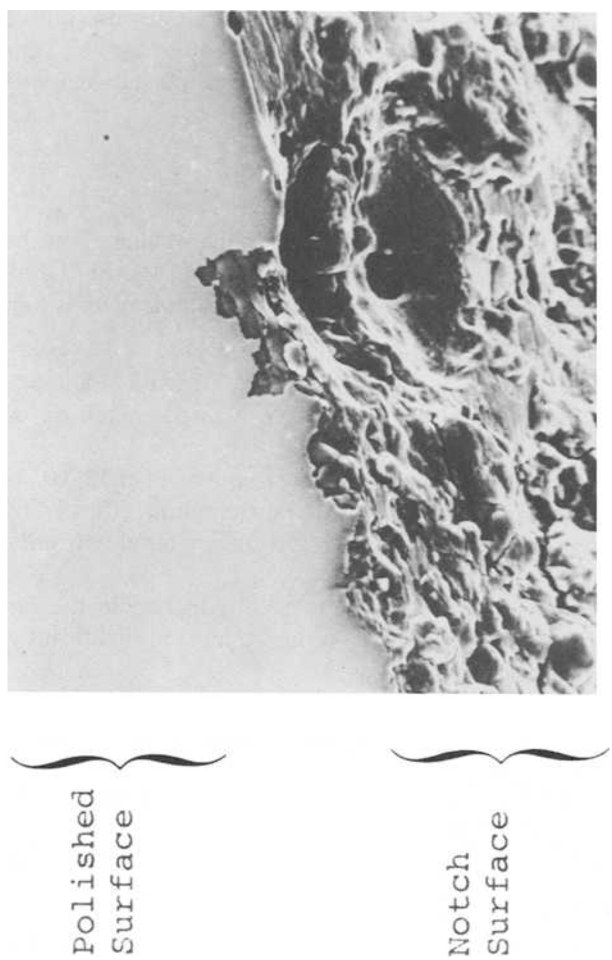

FIG. 14—*Scanning electron micrograph of polished transverse cross section and notch surface showing corrosion pits (×600).*

pits were sharpened during testing, resulting in microcracks, Fig. 15, that eventually grew to the terminal size of 0.25 mm (0.01 in.) or longer along the notch surface and about 0.13 mm (0.005 in.) or greater in depth.

SEM observations of electropolished sections through the corrosion pits revealed the tempered martensite microstructure of the ASTM A517 Grade F steel under investigation, Fig. 16. However, no relationship was observed between the microstructure and the location of the pits. Furthermore, activated slip planes at the tip of the notch were not observed on the electropolished sections that could have, as suggested by Laird and Duquette [9], accounted for the environmental degradation of the fatigue-crack-initiation life.

Summary

The results of this study on the effect of cyclic frequency on the corrosion-fatigue crack-initiation behavior for notches in ASTM A517 Grade F steel in a 3.5 percent sodium chloride solution can be summarized as follows:

1. The fatigue-crack-initiation behavior of ASTM A517 Grade F steel exhibited a fatigue limit at a $\Delta K/\sqrt{\rho}$ of about 690 MPa (100 ksi), which corresponds to a maximum stress range, $\Delta\sigma_{max}$, at the notch tip of about 828 MPa (120 ksi).
2. The corrosion-fatigue data for cyclic frequencies of 12, 60, 120, and 300 cpm fell within a narrow scatter band and showed no effect of frequency on corrosion-fatigue crack-initiation life for the material-environment system investigated.
3. The environment caused a significant reduction in the fatigue life of ASTM A517 Grade F steel at $\Delta\sigma_{max}$-values that were significantly lower than the value for the fatigue limit in air.
4. The data indicate the possible existence of a threshold at $\Delta\sigma_{max}$ of about 207 MPa (30 ksi) below which corrosion-fatigue-crack initiation did not occur.
5. The fatigue-crack-initiation limit, for notched specimens in air, was decreased by about 25 percent when the specimens were precorroded for about one month under static loads in the environment. This decrease was related to an increase in the stress concentration at the notch tip caused by corrosion pits on the surface of the notch radius.
6. The decrease in the corrosion-fatigue crack-initiation life was attributed, primarily, to synergistic effects of the environment and cyclic loading operating under full-immersion conditions. The actual corrosion-fatigue mechanism that caused the degradation was not established.
7. Metallographic investigations showed that corrosion-fatigue cracks initiate at corrosion pits on the surface of the notch tip. These cracks initiated as microcracks that were formed by a sharpening of the corrosion-pit tip under the combined influence of the environment and cyclic loads.

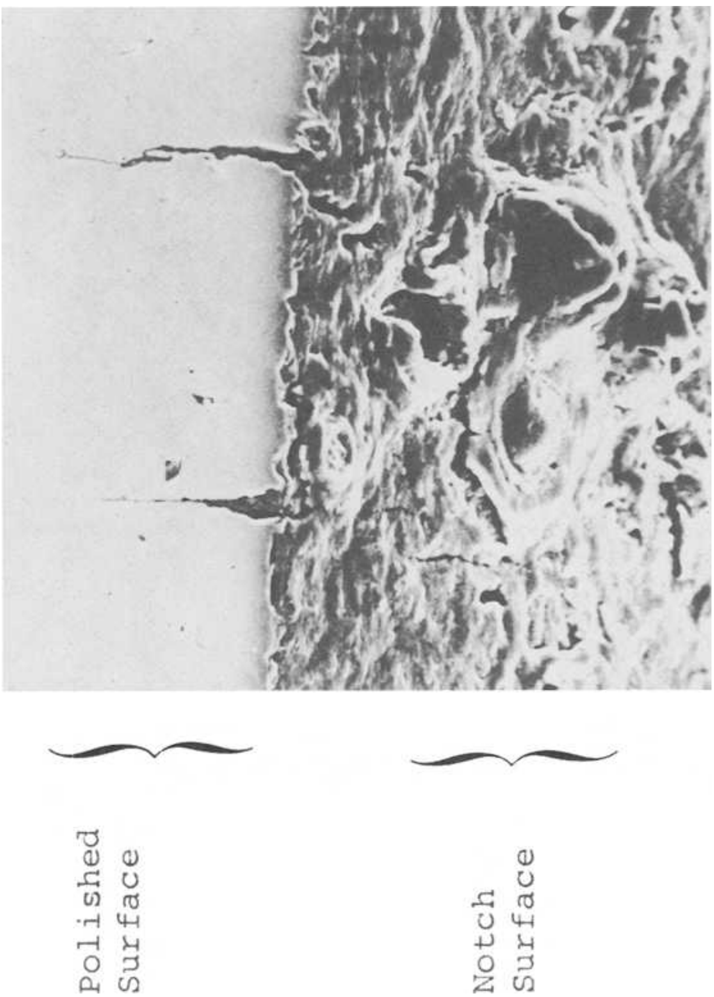

FIG. 15—*Scanning electron micrograph of polished transverse cross section and notch surface showing microcracks (×600).*

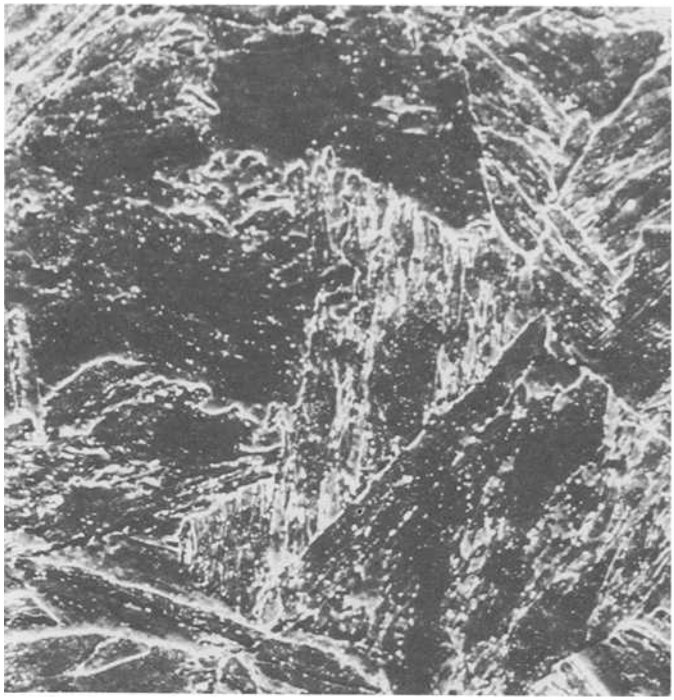

FIG. 16—*Scanning electron micrograph of A517 Grade F steel. Electropolished and nital etch (×3000).*

References

[1] Rolfe, S. T. and Barsom, J. M., *Fracture and Fatigue Control in Structures: Application of Fracture Mechanics,* Prentice-Hall, New York, 1977.

[2] Wilson, W. K. and Gabrielse, S. E., "Elasticity Analysis of Blunt Notched Compact Tension Specimens," Research Report 71-1E7-LOWFA-R1, Westinghouse Research Laboratory, 5 Feb., 1971.

[3] Barsom, J. M. and McNicol, R. C. in *Fracture Toughness and Slow-Stable Cracking, ASTM STP 559,* American Society for Testing and Materials, 1974.

[4] Clark, W. G., Jr. in *Fracture Toughness and Slow-Stable Cracking, ASTM STP 559,* American Society for Testing and Materials, 1974.

[5] May, R. A., Stuber, A., and Rolfe, S. T., "Effective Utilization of High Yield Strength Steels in Fatigue," WRC Bulletin 243, Welding Research Council, New York, Nov. 1978.

[6] Barsom, J. M. in *Fracture Mechanics for Bridge Design,* Federal Highway Administration, U. S. Department of Transportation, P. O. No. 5-3-0209, 1977.

[7] *Corrosion Fatigue: Chemistry, Mechanics and Microstructure,* NACE-2, National Association of Corrosion Engineers, 1972.

[8] Novak, S. R. and McKelvey, G. C., manuscript in preparation.

[9] Laird, C. and Duquette, D. J. in *Corrosion Fatigue: Chemistry, Mechanics and Microstructure,* NACE-2, National Association of Corrosion Engineers, 1972.

C. R. Saff[1] *and D. R. Holloway*[2]

Evaluation of Crack Growth Gages for Service Life Tracking

REFERENCE: Saff, C. R. and Holloway, D. R., **"Evaluation of Crack Growth Gages for Service Life Tracking,"** *Fracture Mechanics: Thirteenth Conference, ASTM STP 743,* Richard Roberts, Ed., American Society for Testing and Materials, 1981, pp. 623-640.

ABSTRACT: An analysis and test program was performed to evaluate the ability of a crack growth gage to monitor crack growth damage in fatigue-critical areas of F-4C/D aircraft structure. Crack growth gages were designed and manufactured for use on the F-4 lower wing skin. The crack growth behavior of the gage and relationship of gage crack growth to potential crack growth in the wing skin were determined through analysis and test. Eight gages were bonded on the Air Force F-4C/D full-scale fatigue test article at Wright-Patterson Air Force Base. Assessments were made of (1) the capability to predict crack growth behavior of the gages mounted on the fatigue test article, (2) the ability of crack growth gage to monitor potential crack growth damage at specified control points, and (3) the impact of manufacturing, installation, and data collection procedures on the utility of the gage as a damage monitoring device. Sheet thickness was found to have a profound effect on crack growth retardation under spectrum loading in 7075-T6 aluminum.

KEY WORDS: crack growth, crack growth gages, aircraft, fleet management, spectrum loads

Crack growth gages have received considerable attention as an aircraft fatigue life tracking system, since this use was proposed by Crane et al [*1*].[3] The fundamental concept of the crack growth gage (Fig. 1) is that potential crack growth in the structure can be determined by monitoring crack growth in the gage. This concept is based on the assumption that one can determine a relationship between potential flaw growth at a fatigue-critical location in the aircraft structure and crack growth in a coupon attached to the structure such that it experiences a similar stress history. A particular

[1] Lead engineer, McDonnell Aircraft Co., McDonnell Douglas Corp., St. Louis, Mo. 63166.
[2] Captain, USAF; aerospace engineer, Air Force Flight Dynamics Laboratory, Wright-Patterson AFB, Ohio.

[3] The italic numbers in brackets refer to the list of references appended to this paper.

relationship of potential structural flaw length and gage crack length is shown in Fig. 1. Because the gage is subjected to a stress history similar to that in the fatigue-critical location, use of the crack growth gage for service life tracking is potentially more accurate than the more complex systems based on flight parameter tracking used currently. The objective of this program was to evaluate the ability of a crack growth gage to monitor potential crack growth damage in fatigue-critical areas of F-4C/D aircraft structure.

Crack Growth Gage Design

The crack growth gage studied in this program (Fig. 1) was designed specifically for application to the lower wing skin of the F-4C/D aircraft. The design was based on the following criteria: (1) The gage must be small enough that it can be bonded to fighter wing skins without encompassing large strain differences, or degrading beneficial residual stresses near fastener patterns during bonding; (2) the gage must give measurable crack growth for each 1000 spectrum hours of test life; (3) the gage must be capable of being durably bonded to the aircraft; and (4) the gage must not buckle under the maximum compressive stress in the spectrum. The selected design satisfies all of these criteria.

Crack growth increments of about 0.25 cm (0.1 in.) per 1000 spectrum hours were selected as the minimum growth which might be visually measurable in the gage when bonded to the fatigue test article. Since the F-4 fatigue test was scheduled to obtain 12 000 flight hours following bonding

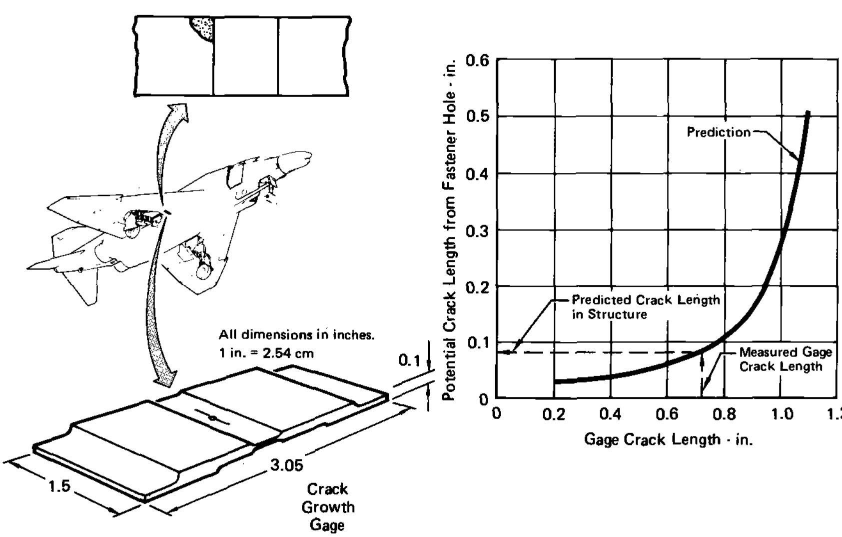

FIG. 1—*Use of crack growth gage to monitor potential crack growth in structure.*

of the gages, the total crack growth desired was 2.54 to 3.05 cm (1.0 to 1.2 in.). This growth, coupled with an initial flaw size of 0.51 cm (0.2 in.), required the gage width to be 3.81 cm (1.5 in.). The remaining gage dimensions are consequences of this width selection.

The stress-intensity factor for the gage was compounded from available solutions [2]. In terms of the gross stress in the gage at the plane of the crack, the gage stress-intensity factor can be expressed as

$$K = \sigma_g \beta \sqrt{\pi a} \tag{1}$$

where

σ_g = gross stress in gage,
a = half crack length in gage, and
$\beta = f_1 f_2$, where f_1 is Isida's stress-intensity correction for finite-width and finite-length plates subjected to a gross stress [3], and
f_2 = Hilton and Sih's stress-intensity correction for a stepped plate [4].

Crack surface displacements in the gage were determined from NASTRAN finite-element analyses and were used to compute gage stress-intensity factors at several crack lengths to verify the stress-intensity factor solution of Eq 1. Comparison of the results in Fig. 2 shows good agreement.

Parametric studies of crack growth gage geometries were performed using the stress-intensity factor solution of Eq 1. Variations in length-to-width ratio, step length to overall length ratio, and step-thickness ratio were studied to determine configurations predicted to attain 2.54 mm (1 in.) of crack growth in 12 000 flight hours. Results of crack growth analysis for

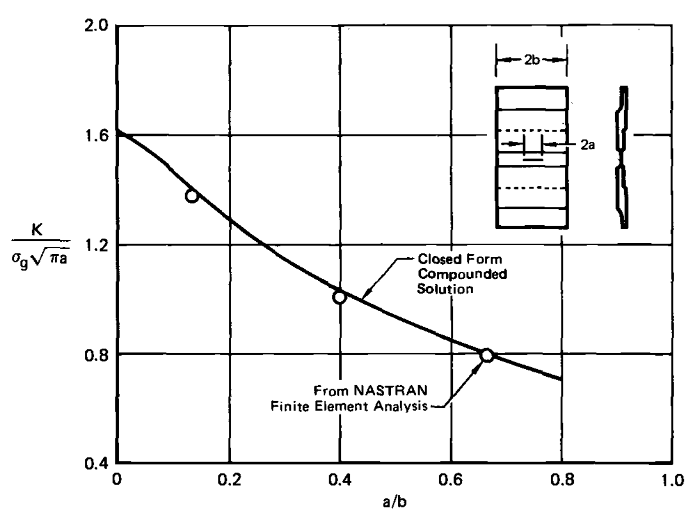

FIG. 2—*Finite-element results confirm gage stress-intensity factor computation.*

the selected gage configuration, shown in Fig. 3, indicate that the gage is predicted to produce nearly a constant crack growth rate.

Gage geometry optimization was based on the assumption that the gage displacements were equal to the displacement of the wing skin. Actually the displacement of a crack growth gage bonded to a carrier plate (be it wing skin or test coupon) depends on the stiffness of the gage, the stiffness of the carrier plate, and the stiffness of the bondline. Load transfer to the gage and bonded joint strength were determined using the bonded joint analysis of Hart-Smith [*5*]. These analyses, as well as buckling analyses, are presented in detail in Ref *2*.

Element Test Program

The majority of tests in this program were intended to determine the crack growth behavior of the gage. The test program is summarized in Table 1 and consists of tests for material characterization, load transfer to the gage, gage calibration under constant-amplitude and spectrum loadings, and gage validation under spectrum loading.

Load transfer tests and constant-amplitude gage calibration test results confirmed the stress-intensity factor prediction for bonded gages. Typical results of the constant-amplitude gage calibration tests are compared with predicted behavior in Fig. 4. In general, analysis and test results under constant-amplitude loadings were in good agreement and showed little gage-to-gage variability.

Gage calibration tests under spectrum loadings indicated that crack growth retardation was greater for the gages than that predicted using the

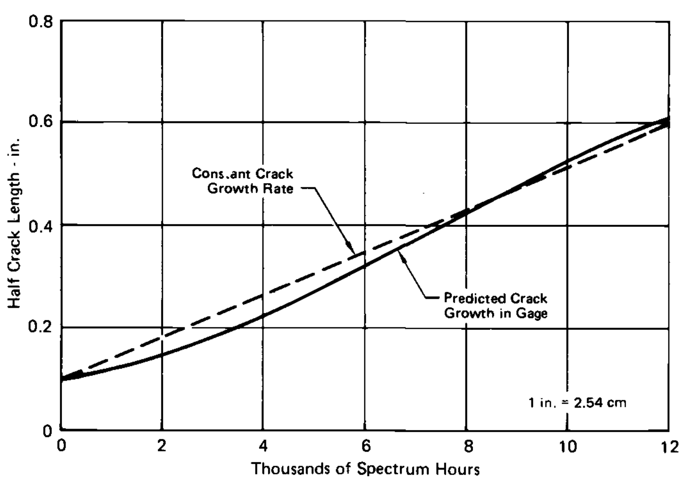

FIG. 3—*Crack growth for gage design is close to linear growth.*

TABLE 1—*Test program summary.*

Test Series	Number of Specimens	Test Purpose	Test Specimen
1	4	Measure da/dN of the lot of material used in gage manufacture	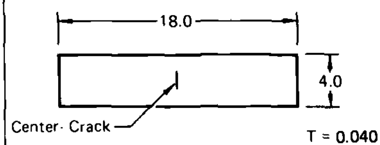
2	5	Measure load transfer characteristics of gage in order to interpret crack growth behavior. Gages on one specimen were precracked.	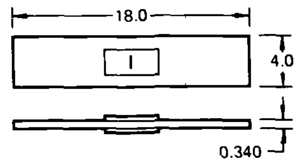
3	4	Gage calibration, constant amplitude loading	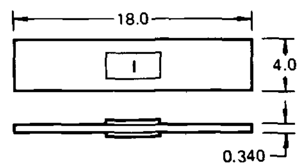
	11	Gage calibration, spectrum loading	
4	4	Validation of ability of gage to track spectrum loading	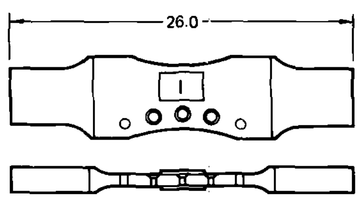
Total	28		

Note: All dimensions in inches. 1 in. = 2.54 cm

contact-stress model [*6*] and assuming plane-stress plastic zone conditions. As shown in Fig. 5, gage crack growth initially was faster than predicted, then slowed to a rate far less than predicted. Based on data presented by Shih and Wei [*7*] and Mills and Hertzberg [*8*], sheet thickness effects were felt to be responsible for the excessive retardation found in gage response.

Effect of Thickness on Crack Growth Retardation

To determine the effect of sheet thickness on crack growth retardation, a series of constant-amplitude and spectrum tests of center-cracked panels in several thicknesses was performed, as outlined in Table 2. Constant-amplitude results for tests at 33 $MN/m^{3/2}$ (30 ksi), $R = 0$, are shown in Fig. 6. The scatter shown is no more than would be expected for multiple

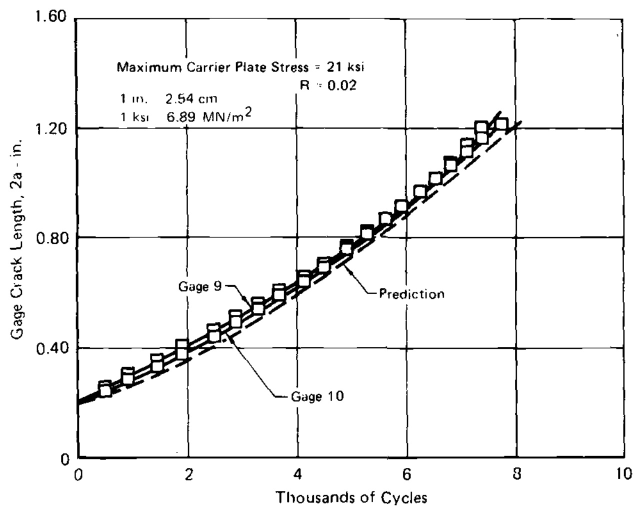

FIG. 4—*Predicted and measured crack growth for constant-amplitude gage calibration test.*

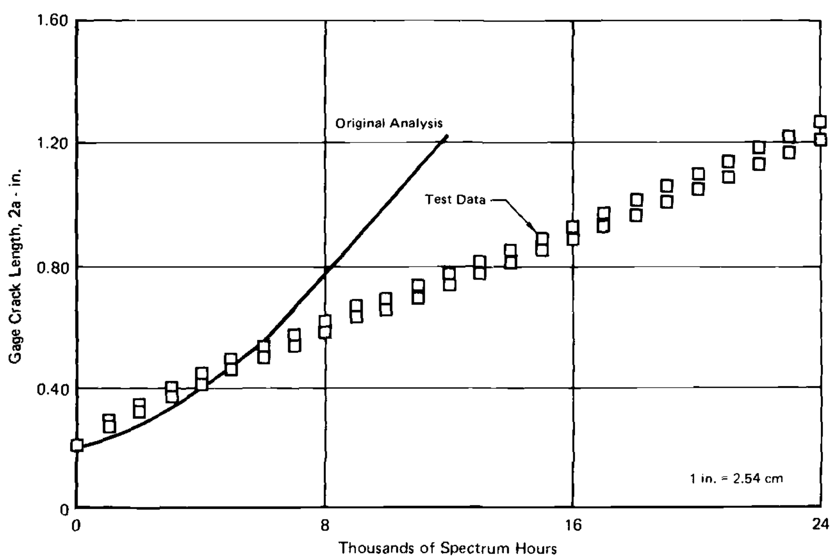

FIG. 5—*Comparison of predicted and measured crack growth in gage under F-4 lower wing skin spectrum.*

TABLE 2—*Constant-amplitude and spectrum tests to investigate sheet thickness effects.*

Stress Levels, ksi	Sheet Thickness, in.					
	0.02	0.04	0.08	0.15	0.25	0.50
15	...	X	...	...	X	...
30	X	X	X	X	X	X
45	...	X	...	...	X	...

NOTE—1 in. = 2.54 cm; 1 ksi = 6.89 MN/m².

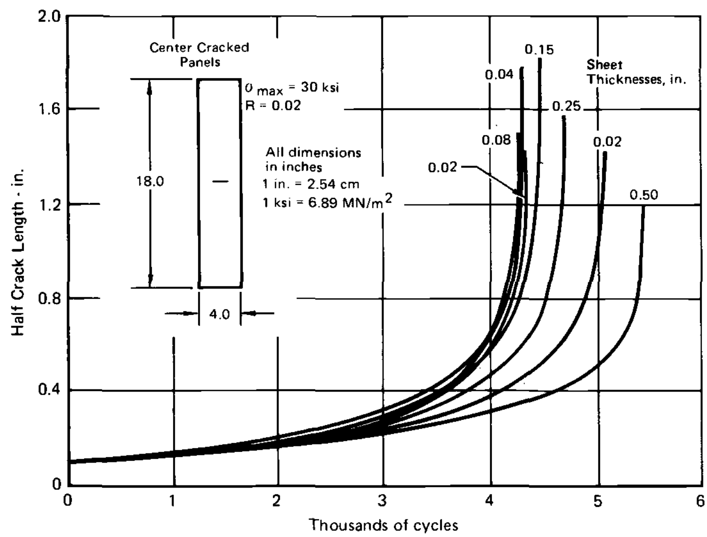

FIG. 6—*Results of crack growth tests in several sheet thicknesses.*

tests of material in the same thickness. This is shown by the two test results in 0.051-cm (0.02 in.) thickness.

Spectrum test results for identical center-cracked panels are shown in Fig. 6. An F-4 lower wing skin stress spectrum was applied at 33-MN/m$^{3/2}$ (30 ksi) limit stress. The maximum stress level was 1.07 times limit stress and the minimum stress level was −0.12 times limit stress. Buckling guides prevented both panel buckling and crack buckling in thin sheets. Spectrum crack growth lives generally tend to increase with decreasing thickness. The scatter in lives for thicknesses greater than 0.25 cm (0.1 in.) is within the scatter of the constant-amplitude results. Life for the 0.10-cm-thick (0.04 in.) panel is four times that for thicker panels and life for 0.05-cm (0.02 in.) thickness is six times that for thicker panels.

While previous investigations [*7,8*] have shown that thickness affects crack growth retardation following discrete high loads, the magnitude of this effect and its insensitivity to stress level were not anticipated. Fracture surfaces of the thicker specimens tested under spectrum loading showed evidence of crack-tip tunneling at the midplane and tearing at the surface. This behavior is felt to be due to the transition from plane-strain behavior at the specimen midplane to plane-stress behavior at the free surface.

Hartranft and Sih [*9*] have postulated that the thickness of this transition layer is a function of crack length and plate thickness

$$\xi/t = \frac{1}{4 + \dfrac{16t}{a}} \tag{2}$$

Finite-element results obtained by Raju and Newman [*10*] have provided support for this boundary effect, Fig. 7.

To obtain correlation with the data, crack growth retardation in thin sheets would have to exceed that analytically determined under plane-stress conditions using the contact-stress model. In this model, retardation is predicted by determining a minimum effective stress level which reduces the stress ranges used for computation of spectrum crack growth. The relationship of the minimum effective stress level to the applied stress levels is indicated in Fig. 8.

By selecting a minimum effective stress level (closure stress), assumed to be constant throughout the fatigue life as suggested by Elber [*11*], crack growth analyses were "tuned" to provide correlation with data from the

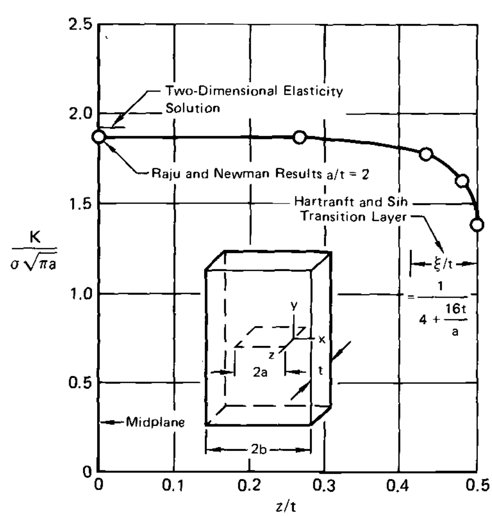

FIG. 7—*Comparison of finite-element analysis results with predicted boundary-layer depth.*

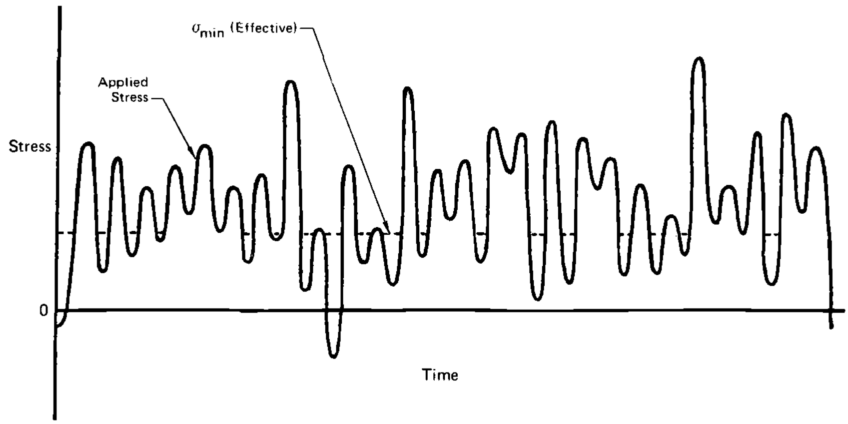

FIG. 8—*Relationship of effective minimum stress level to applied stress levels.*

spectrum tests performed at 33 $MN/m^{3/2}$ (30 ksi). A plot of the minimum effective stress level, used to match test data versus the boundary effect parameter, ξ/t, is shown in Fig. 9.

Crack growth lives for all constant-amplitude and spectrum tests are summarized as a function of specimen thickness in Figs. 10 and 11, respectively. Also shown are the crack growth life predictions obtained from the contact-stress model using the empirical relationship of Fig. 9 to compute the minimum effective stress level. While the empirical relationship was

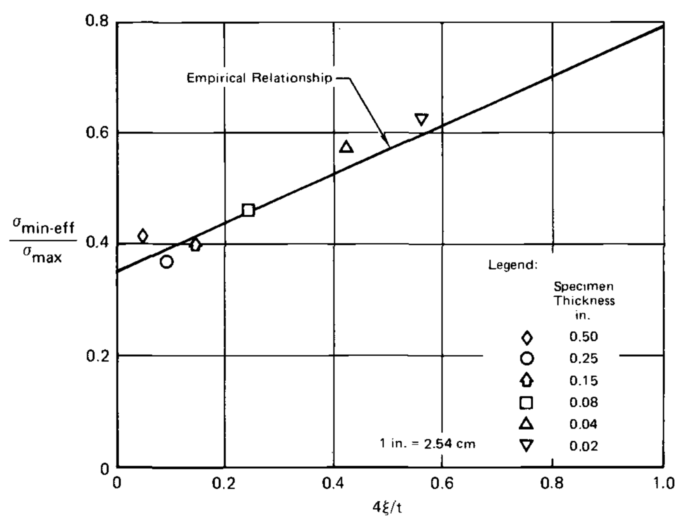

FIG. 9—*Relationship of effective minimum stress level to boundary-layer depth.*

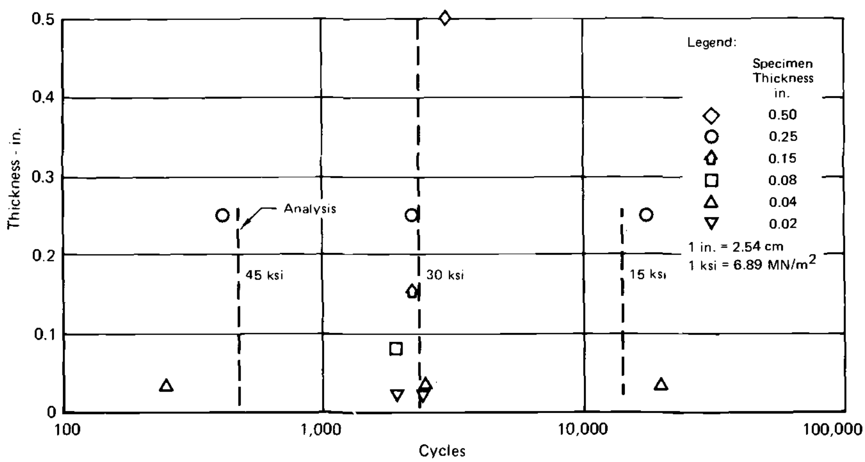

FIG. 10—*Effect of thickness on constant-amplitude crack growth lives—comparison of analysis and test results.*

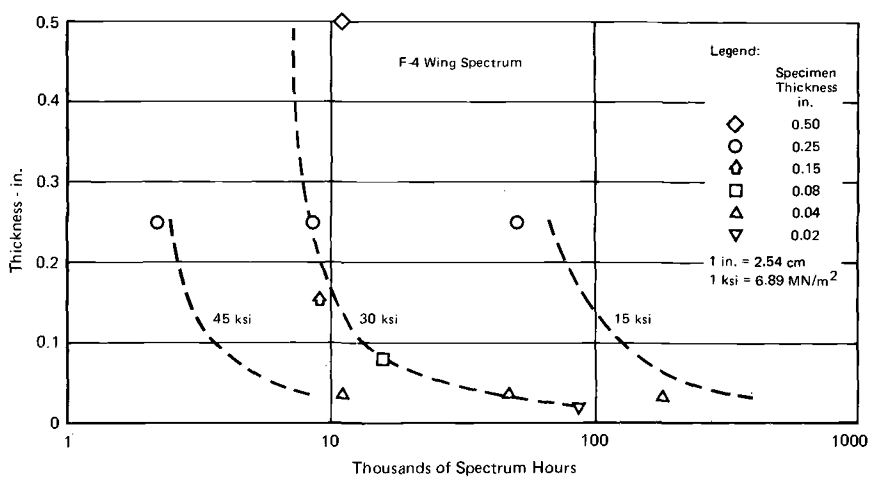

FIG. 11—*Effect of thickness on spectrum crack growth lives—comparison of analysis and test results.*

developed from the results at 33 $MN/m^{3/2}$ (30 ksi), good correlation is found with lives at other stress levels. One constant-amplitude test at 49.5 $MN/m^{3/2}$ (45 ksi), Fig. 10, appears to have an abnormally short life. Using the contact-stress model and the empirical relationship of Fig. 9, good correlation was obtained between the adjusted analysis and gage calibration and verification test results, as indicated by Fig. 12.

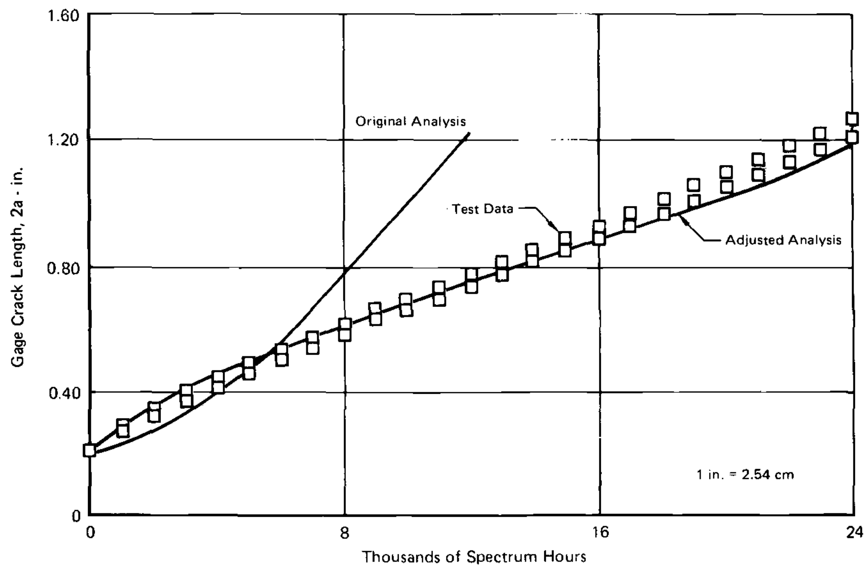

FIG. 12—*Comparison of adjusted analysis and measured crack growth in gage under F-4 lower wing skin spectrum.*

Gage Attachment to F-4 Fatigue Test Article

The primary gage sites on the F-4 fatigue test article, identified as Sites 1-4 in Fig. 13, were located on the lower wing skin. Most of the gages were attached to the right lower wing skin, but some sites were duplicated on the left lower wing skin, indicated in Fig. 13 by duplicate site numbers. Based on the gage configuration, predicted behavior, and bonding procedure, several criteria for site selection were defined.

Sites were selected to be near fracture-critical areas so that the stress histories experienced by the gages would be similar to those experienced by the fracture-critical areas.

Wing skin areas experiencing limit stress levels of 33 $MN/m^{3/2}$ (30 ksi) were selected to obtain the maximum possible gage crack growth during the full-scale fatigue test.

Areas near high stress gradients, fastener patterns, Taper-loks, and other stress concentrations were avoided for two reasons. First, the gage behavior would be sensitive to position and alignment in such areas. This could lead to variations in gage response from aircraft to aircraft if the gage were applied to fleet aircraft. Second, areas immediately adjacent to the gage will receive some heating during the bonding cure cycle. Heating to 177°C (350°F) can cause relaxation of plastic strains in high stress-concentration areas and reduce beneficial residual stresses near Taper-loks, which are

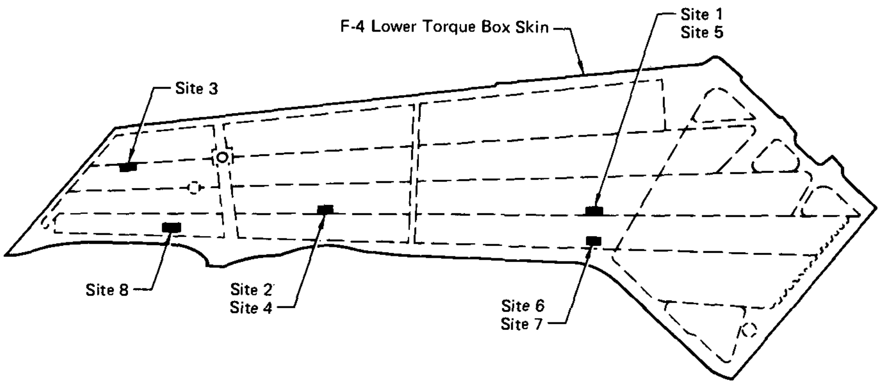

FIG. 13—*Crack growth gage sites on lower wing skin of F-4 fatigue test article.*

used in such areas on the F-4 lower wing skin. Fastener patterns in general were avoided because of the local strain distributions they create.

FM-73 adhesive was used to bond gages to test coupons and to the wing skin of the F-4 test article. FM-73, an epoxy adhesive requiring a 121°C (250°F) cure cycle, was selected based on strength, durability, service environment, and cure temperature considerations. A standard field repair surface treatment and bonding technique was used. While bonding to test coupons was successful, bonding to the F-4 fatigue test article was beset by problems. On the first attempt the adhesive was not cured at a high enough temperature. On the second attempt the adhesive was properly cured; however, the additional heating evidently broke down the silicone spray corrosion inhibitor used on the fatigue test article. Silicone, which is a release agent for FM-73 adhesive, was absorbed by that adhesive during the bonding, causing it to fail upon application of load to the test article.

After the four original gages disbonded, the areas and gages were cleaned and eight gages were bonded to the lower wing skins using the room-temperature-cure EA9309.1 adhesive [*12*]. The room-temperature cure allowed bonding of gages much closer to rib and spar fasteners than on the original sites. The locations of the eight crack growth gages are identified in Fig. 13. Four of these gages produced measurable crack growth through 4000 spectrum hours of full-scale fatigue testing.

Gage Performance on Test Article

Crack lengths in gages bonded to the fatigue test article were determined through microscopic examination of impressions of the crack made in Faxfilm replicating tape [*12*]. To obtain the impression, the film was pressed onto the gage step containing the crack. Measurements of the Faxfilm impressions could be made more easily than direct measurement of gage crack length, and the Faxfilm impressions make a good record of measurements.

Comparisons of predicted and measured crack growth in the gages are shown in Fig. 14. In general, the agreement between predicted and measured crack lengths is good. In those cases in which the gages separated from the wing skin, measured crack growth was close to that predicted until the gages separated.

Crack Growth Gage as Usage Monitor

Use of the crack growth gage as an aircraft fatigue life usage monitor is complicated by the fact that the relationship of potential crack growth in the structure to crack growth in the gage is predicted to vary markedly for small changes in usage (Fig. 15). This variation is due to the difference in crack growth retardation between the crack in the structure and the crack in the gage. In order for the relationship of potential crack growth in the structure to crack growth in the gage to be unique, unaffected by spectrum changes, the stress state at the tip of the gage crack must be similar to that at the tip of the crack in the structure. The difference in material thickness between gage and structure precludes similitude at the crack tips and,

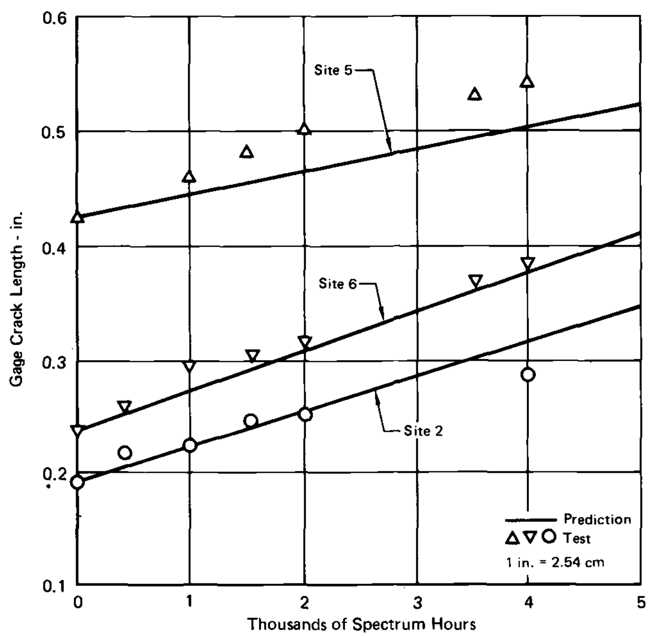

FIG. 14—*Comparison of gage crack length measurements from fatigue test article with predicted lengths.*

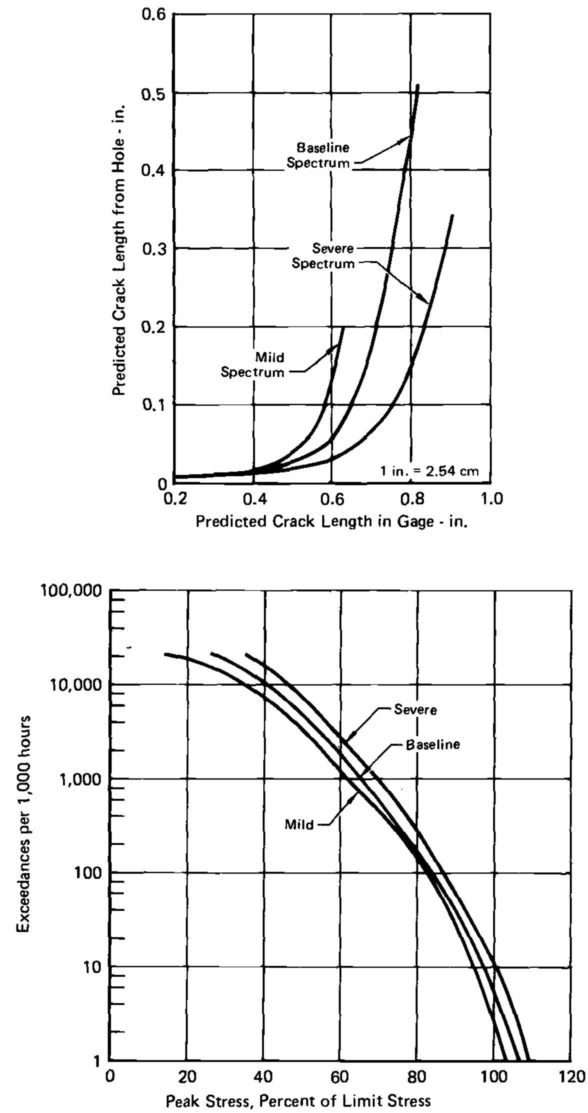

FIG. 15—*Relationship of potential crack growth in structure to gage crack growth varies with aircraft usage.*

consequently, precludes development of a unique relationship between gage crack length and crack length in the structure.

A procedure was developed to account for the variation in structure/gage flaw growth relationship based on predictions of crack growth in the gage and in the structure for a baseline spectrum under several limit stress levels. Relationships between potential crack growth from a hole and crack growth in the gage were determined for each stress level, Fig. 16. These relationships were used to predict potential flaw growth from a hole based on the crack length in the gage at a given time.

As an example of this technique for service life monitoring using the crack growth gage, five variations of an F-4 wing load spectrum were considered: baseline, mild, and severe variations used in the earlier evaluations (Fig. 15), the baseline with the maximum load per 1000 h increased to 125 percent of limit, and the baseline clipped at 80 percent of limit load. The latter spectrum variations were among the most severe of those reported in Ref *13*.

The predictions of crack growth from the hole based on gage analyses were compared with straightforward crack growth predictions using the contact-stress model for each of the spectrum variations. Comparison of the two predictions (Fig. 17) is reasonably good and indicates that gage crack growth interpretations will be consistent with the trends, at least, of potential crack growth in the structure, as long as the gage remains attached to the structure.

The comparison of predictions shown in Fig. 17 is the only available measure of the ability of the gage to monitor service usage. The comparison must be substantiated by test before acceptance of the gage as a usage monitor. The predictions of crack growth from a hole are based on improved analyses of the test results reported in Ref *13*. The predictions of gage response are based on test results for limit stress levels between 28.6 and 33 MN/m$^{3/2}$ (26 and 30 ksi) and are subject to greater question at limit stress levels that are higher or lower.

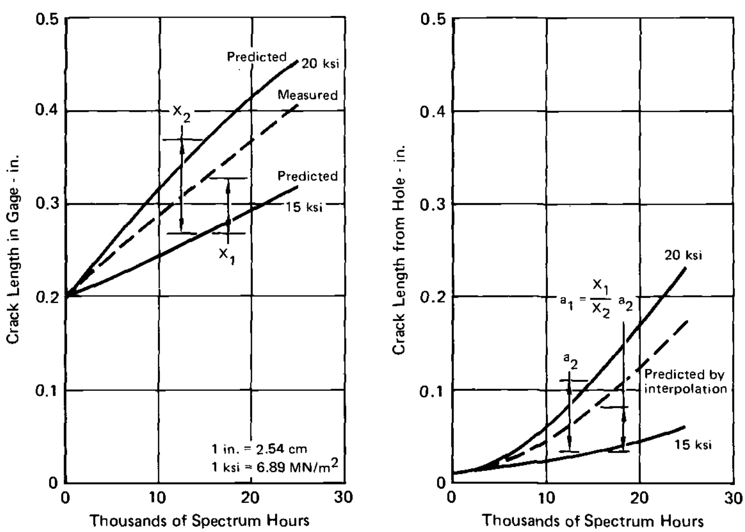

FIG. 16—*Crack growth from hole prediction interpolated from gage crack growth.*

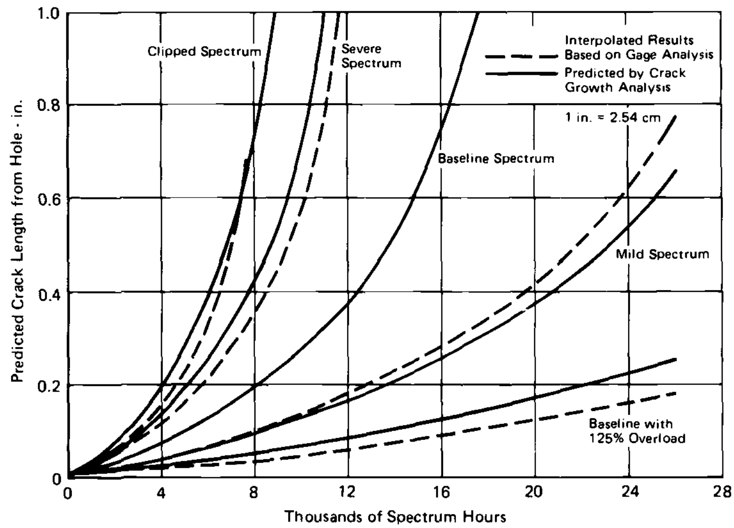

FIG. 17—*Comparison of predictions for crack growth from hole for several spectra.*

Conclusions

Results of this program indicate that crack growth in gages bonded to an aircraft can be correlated with the stress history of the gage site on that aircraft.

Knowledge of the gage crack length alone is not sufficient to determine the potential crack growth in the structure. Crack growth retardation in thin sheets [less than 0.25 cm (0.1 in.) thick] is much greater than in thicker fighter wing skins. Consequently, the relationship of gage crack length to potential flaw length in the structure is dependent on the usage (spectrum severity) of the aircraft. Spectrum severity and potential crack growth in the structure can be determined by tracking both the number of aircraft flight hours and crack length in the gage.

Gage manufacturing tolerances were predicted to have little impact on gage response; however, a comprehensive qualification program is required before accepting an adhesive and bonding procedure for gage attachment to fleet aircraft. Bonding of gages to the fatigue article using FM-73 adhesive was not successful due to circumstances peculiar to that application. EA 9309.1 room-temperature-cure adhesive was successfully used to bond gages to the fatigue article. In element tests, FM-73 was found to predictably transfer strains to the gage until either adhesive or gage failure occurred. Applications of fatigue load cycles were not found to change load transfer to the gage prior to adhesive failure.

The potential usefulness of a gage for monitoring crack growth in aircraft structure has not been fully explored. Considerable further research is required to verify the techniques used to determine the potential growth of structural flaws from measured gage crack growth, to determine the ability of a gage to track variations in service usage, to demonstrate reproducibility of growth from gage to gage, to develop simple procedures to reliably bond gages in a depot maintenance environment, to demonstrate adequate gage service lives in fleet use, and to determine procedures to collect and summarize individual aircraft gage data.

Acknowledgments

This work was accomplished under the sponsorship of the Air Force Air Logistics Center, Hill Air Force Base, Contract No. F42600-78-D-0014, with technical monitoring by the Air Force Wright Aeronautical Laboratories/FIBEC, Wright-Patterson Air Force Base. The element test program was performed by K. C. Garland of the Metallurgical Laboratory of McDonnell Aircraft Co.

References

[1] Crane, R. L., Grandt, A. F., and Gallagher, J. P., "A Crack Growth Gage for Assessing Flaw Growth Potential in Structural Components," AFML-TR-76-174-R, Air Force Materials Laboratory, Wright-Patterson AFB, Ohio, Oct. 1976.

[2] Saff, C. R., "F-4 Service Life Tracking Program (Crack Growth Gages)," AFFDL-TR-79-3148, Air Force Flight Dynamics Laboratory, Wright-Patterson AFB, Ohio, Dec. 1979.

[3] Isida, M., *International Journal of Fracture Mechanics*, Vol. 7, No. 3, Sept. 1971.

[4] Sih, G. C., *Handbook of Stress Intensity Factors*, Lehigh University, Bethlehem, Pa., 1973.

[5] Hart-Smith, L. J., "Adhesive-Bonded Scarf and Stepped-Lap Joints," NASA-CR-112237, National Aeronautics and Space Administration, Washington, D.C., 1973.

[6] Dill, H. D. and Saff, C. R. in *Fatigue Crack Growth Under Spectrum Loads, ASTM 595*, American Society for Testing and Materials, 1976, pp. 306-319; and *Cyclic Stress-Strain and Plastic Deformation Aspects of Fatigue Crack Growth, ASTM 637*, American Society for Testing and Materials, 1977, pp. 141-152.

[7] Shih, T. T. and Wei, R. P., *Journal of Testing and Evaluation*, Vol. 3, No. 1, Jan. 1975, pp. 46-47.

[8] Mills, W. J. and Hertzberg, R. W., *Engineering Fracture Mechanics*, Vol. 7, 1975, pp. 705-711.

[9] Hartranft, R. J. and Sih, G. C., *International Journal of Engineering Science*, Vol. 8, 1970, pp. 711-729.

[10] Raju, I. S. and Newman, J. C., Jr., "Three-Dimensional Finite-Element Analysis of Finite-Thickness Fracture Specimens," NASA TN D-8414, National Aeronautics and Space Administration, Washington, D.C., May 1977.

[11] Elber, Wolf in *Fatigue Crack Growth Under Spectrum Loads, ASTM STP 595*, American Society for Testing and Materials, 1976, pp. 236-250.

[12] Holloway, D. R., "Experimental Investigation of the Crack Growth Gage," AFWAL-TR-80-3045, Air Force Wright Aeronautical Laboratories, Wright-Patterson AFB, Ohio, June 1980.

[13] Dill, H. D. and Saff, C. R., "Effects of Fighter Attack Spectrum on Crack Growth," AFFDL-TR-76-112, Air Force Flight Dynamics Laboratory, Wright-Patterson AFB, Ohio, March 1977.

Summary

The papers contributed to the 13th National Symposium on Fracture Mechanics cover a wide range of topics. Approximately 35 percent of the papers deal with the subject of fatigue crack propagation in engineering materials. These fatigue-related papers cover subjects such as variable-amplitude loading, residual stresses, overloads, crack closure, hold time, and temperature. In addition to the papers on fatigue crack propagation, approximately 15 percent of the conference papers deal with the calculation of stress-intensity factors for various crack geometries and an additional 15 percent deal with elastic-plastic fracture mechanics as related to J_{Ic} and the tearing modulus T. The remaining papers deal with a wide range of subjects such as creep-crack growth, correlations of fracture behavior with Charpy V-notch response, the effect of root radius on fracture behavior, behavior of composite materials, R-curves, and applications of fracture mechanics methods.

As in previous national symposia on fracture mechanics, the preponderance of papers contributed deal with fatigue crack propagation. The effect of variable-amplitude loading was investigated by J. B. Chang, R. M. Engle, and J. Stolpestad. Their study examines the fatigue crack growth behavior of 2219-T851 aluminum subjected to variable-amplitude loading. This loading includes single and periodic tensile and compressive overloads as well as high-low or low-high block loading. A load interaction model is developed which accounts for the overload retardation and compressive load acceleration effects on fatigue crack growth. Analysis of the experimental data was performed using a computer program which employed this model. The results show reasonable agreement with the experimental data. The effect of residual stress on fatigue crack growth measurements was investigated by R. Bucci. In his paper Bucci gives numerous examples to show how residual stresses can lead to an erroneous interpretation of fatigue crack growth rates as measured in accordance with current ASTM Test for Constant-Load-Amplitude Fatigue Crack Growth Rates Above 10^{-8} m/Cycles (E 647-78T). Bucci recommends various modifications to applicable ASTM documents so that proper recognition will be given to the effect of residual stresses on fatigue crack growth rate measurements. J. H. Underwood and J. A. Kapp investigated the benefits of overloads on fatigue crack initiation and growth from a 0.1-mm-radius notch in steel alloy K_{Ic} specimens. Other tests are described which measure the effect of tension overloads on fatigue crack growth and fatigue crack initiation from 3.4-mm-root-radius notches in similar specimens. Their results indicate that when one wishes to accelerate crack initiation from the root of the notch the compressive overload is a definite benefit. Also, the effect of the tensile overload is to provide an increased fatigue life for the notched specimens. A. U. de Koning describes the results of the simple crack closure model for the prediction of fatigue crack growth rates under variable-amplitude loading. This model is based on crack closure arguments and was designed to predict the crack acceleration and retardation observed under variable-amplitude loading. This model was incorporated into a computer program and used to analyze the behavior of specimens of 7075-T6 aluminum. B. N. Leis and T. P. Forte provide some insight into the fatigue crack growth behavior of physically short cracks in aluminum and steel plates. Their paper presents and analyzes an extensive data set related to the so-called short-crack problem. Included in the results are data for notched plates made from two aluminum alloys and a steel. Leis and Forte suggest that physically long as well as physically short cracks may behave in a manner inconsistent with linear elastic fracture mechanics (LEFM) descriptions. It can be implied from their arguments that in these cases this variation is principally due to the inability of LEFM to accurately describe the crack tip stress and strain conditions. The contribution of Saff and Holloway describes a study of crack growth gages for evaluation of service life. They show, based on the results of their program, that the response of the crack growth gages can be correlated with the stress history of the aircraft in the region of the gage site. However, the authors indicate that the potential usefulness of the crack growth gages for monitoring actual crack growth in aircraft structures has not been fully explored. They feel that considerable further research is required to verify this technique before it can be practically applied. G. Marci provides some insight into the effect of temperature on fatigue crack growth rates. He concludes that the fatigue crack growth threshold decreases linearly with increasing temperature. In Marci's paper a crack growth equation incorporating the effect of temperature on the fatigue crack growth threshold is demonstrated for Type 304 stainless steel. Saxena, Williams, and Shih provided discussion of an analytical modeling technique used to predict the effect of hold time on fatigue crack growth behavior at elevated temperatures. This model was evaluated for fatigue crack growth data with hold times of 0, 5, and 50 s for A470 Class 8 steel at 538°C (1000°F). Additional data on Inconel alloy 718 at the same temperature were also taken from the literature to evaluate this model. It is their conclusion that the model is capable of accurately representing and predicting the hold time effects on fatigue crack growth behavior at elevated temperatures. The authors describe some of the limitations of their model and some of the possible methods for eliminating these problems. Taylor and Barsom in their paper describe the effect of cyclic frequency on the corrosion fatigue crack initiation behavior of an A517 Grade F steel. Their tests were conducted on a compact tension specimen at a stress ratio of 0.1 in a room temperature 3.5 percent solution of sodium chloride. They show that the corrosion fatigue crack initiation life under full immersion conditions is significantly less than the fatigue crack initiation life in air. Metallographic studies indicate that the corrosion fatigue cracks initiate at corrosion pits on the surface of the notch tip in the specimens. It is proposed that these cracks initiate as microcracks that form by a sharpening of the corrosion pit tip under the combined influence of the environment and the cyclic loads.

In the conference session on stress-intensity factors a number of very important practical geometries were investigated. Smith, Peters, Kirby, and Andonian provide some insight into stress-intensity distributions for certain natural flaw shapes which approximate benchmark geometries. The studies described took the form of frozen stress photoelastic experiments carried out on certain model geometries which approach a so-called benchmark problem represented by a plate containing a surface crack loaded in remote simple tension. The authors describe the limitation of their studies with respect to flaw depth and surface flaw length. In the paper by Phillips and Sanford the effect of higher-order stress terms on Mode I caustics in birefringent materials is discussed. While being relatively new, this experimental technique can be used to determine stress-intensity factors for various crack configurations. The principal thrust of the work by Phillips and Sanford was to discuss how the first few non-singular stress terms affect the sizes and shapes of the caustic that are produced in the optically anisotrophic materials.

Along with the study of fatigue and the evaluation of stress-intensity factors, the elastic-plastic response as measured by J_{Ic} and T received considerable attention during the 13th National Fracture Mechanics Symposium. In the paper by Ernst, Paris, and Landes the evaluation of J and tearing modulus T from a single test record is investigated. The consequences of expressing J by the Merkel-Corton formula is explored in terms of J, the crack increment da, and the tearing modulus T. The authors provide additional physical interpretation to the material versus applied tearing modulus stability criterion. Also, a simpler method for evaluating J following the actual $P\Delta$ test record is suggested. This procedure is compared with other experimental data. Carlson and Williams present an attempt to provide a more basic approach to the analysis of multiple-specimen R-curves for the determination of J_c. Multiple-specimen J-R curves were developed for groups of 1T compact specimens with different A/W values and depths of side grooving. The purpose of the investigation was to determine J_c for each group. A more basic approach for the analysis of multiple-specimen R-curves is presented in the paper. This technique is applied and extensively discussed to show J_c estimates that closely corresponded to actual observed onset of crack extension. Joyce and Vassilaros present the results of an experimental investigation of tearing instability using compact tension specimens. They conclude for the range of aluminum, titanium, and steel alloys tested that whenever the T_{applied} obtained from the generalized Paris model exceeds the T_{material}, a tearing instability is assured.

They show that side-grooving of these materials effectively reduces the $T_{material}$ and this reduction is related to a reduction in the $T_{applied}$ for instability. Additionally, they found that the value of $T_{applied}$ does not have any effect on the resultant J_I-R curves. Further, the J_I-R curves seem to be independent of the mode of crack extension observed over the range of $T_{applied}$. A reevaluation of procedures for calculating J_{Ic} is provided by G. A. Clarke. Clarke provides some insight into the various improvements to J_{Ic} and J-R curve testing which have occurred during the past five years. A description of many of these improvements is presented in the paper. Clarke highlights many of the pitfalls which one can encounter in J_{Ic} and J-R testing. In the paper by Andrews the utilization of small specimens to provide accurate predictions of the brittle fracture response of low alloy steels is examined. Andrews concludes that an accurate estimate of valid plane-strain fracture toughness, K_{Ic}, for low-alloy steels in the ductile-to-brittle transition temperature range may be made using J_{Ic}-valid specimens if one also accounts for size effect, which is evident for cleavage fracture. This size effect is explained using a weakest-link theory.

It has already been noted that approximately 60 percent of the papers contributed to the 13th National Symposium on Fracture Mechanics were in the general categories of fatigue, stress-intensity evaluation, and elastic-plastic fracture mechanics. The remaining papers did not conveniently fit into any single grouping. These papers represented a wide range of subjects from creep crack growth to Charpy V-notch correlations, composite materials, and fracture mechanics applications to name a few. In an attempt to provide a better understanding of creep crack growth, Donat, Nicholas, and Fu presented the results of an experimental investigation of creep crack growth in IN-100. They determined sustained crack growth rates in IN-100 at 732°C (1350°F). Their studies were conducted on two specimen geometries over a range of thicknesses. A number of various parameters such as the stress-intensity factor, net section stress, and a compliance-related integral were studied as possible crack growth rate correlating parameters. None of these parameters provided an effective means of correlating the observed growth rates. An upper-shelf correlation between the fracture toughness and the energy required to initiate cracking as measured in a Charpy V-notch specimen is presented in the work of Norris, Reaugh, and Server. Their correlation was obtained using data from 23 steels which possessed a wide variation in yield strength, fracture toughness, and Charpy toughness. The authors state that their correlation is only marginally better than that obtained by Rolfe and Novak, and Barsom and Rolfe, whose correlations use the entire Charpy fracture energy curves. In a series of J-integral fracture toughness tests, Tobler, Read, and Reed studied the effect of carbon and nitrogen on the fracture properties of an austenitic stainless steel having a base composition corresponding to AISI 304. The fracture toughness measured was observed to decrease with increasing carbon and nitrogen content. While many problems are quite obvious to a researcher when trying to apply fracture mechanics to an actual situation, they are not obvious all the time to most people. W. G. Clark, Jr., describes in his paper some of the problems that will occur in a typical application of fracture mechanics. The problems described by Clark range from the development of adequate material property data to the analytical and defect characterization aspects of the technology. These problems and their interaction are discussed with regard to their potential impact on structural life predictions and quantitative risk analysis. The material characterization problems associated with data scatter, prior loading effects, and time-dependent behavior are included along with consideration of the probability of flaw detection and the analysis of small defects and interacting flaws. Clark provides suggestions and recommendations for experimental work required to resolve some of these problems. A paper by Denyer also highlights fracture mechanics technology and its application. In this particular paper, the application of fracture mechanics to individual aircraft tracking is discussed. Denyer describes a crack growth analysis method which is designed to meet the intents and objectives of the U.S. Air Force requirements for durability and damage tolerance in their structures. The methodology described is currently being incorporated into the overall life monitoring of the USAF T-39 Utility Trainer. This is the first system to use crack growth principles for both durability and damage tolerance tracking. The behavior of composite materials as related to fracture mechanics was highlighted by three papers presented at the conference. The dependence of strength on particle size in graphite is discussed by Kennedy and Kennedy. The authors examine the strength to particle size relationship for specially fabricated graphites. They demonstrate that the utilization of fracture mechanics will provide an adequate basis for the observed performance. An application of the Dugdale crack extension model with simple modifications accounting for nonspherical pores and variable defect concentrations is used to explain the observed experimental data. In their study they also consider the particle size effect on coefficient of thermal expansion, electrical resistivity, fracture strain, and Young's modulus. Shih and Logsdon in their paper examine the fracture behavior of a thick-section graphite/epoxy composite. It was the authors' intent to examine the possibility of using advanced structural composities in the specific application of generator retaining rings. One aspect of this was to demonstrate the fracture behavior of the composite material. In particular, their tests served to permit an evaluation of the applicability of LEFM to composite materials in general and to thick-section composites in particular. Their results show that LEFM is not directly applicable to thick-section composites with cracks perpendicular to the fiber orientation. They found that the test composite was insensitive to cracks in a plane perpendicular to the fibers and that the load-carrying capability could be calculated based on net section considerations solely. The failure mode they observed in their test of composites tested in 3-point bending was interply shear failure. The third paper on fracture behavior of fiber composites was offered by Avery, Bradley, and King. This paper deals with fracture control in ballistic damage fiber composite wing structures. Their paper presents the fracture test data and analysis related to the development of a skin configuration for a graphite/epoxy wing box capable of sustaining limit loads following damage from a 23-mm high-explosive-impact projectile.

While not described in this summary, other very interesting papers were contributed to the symposium as evidenced by the index to this *Special Technical Publication*. A paper on fatigue fracture micromechanism in broad molecular weight distribution poly(methyl methacrylate) is offered by Janiszewski, Hertzberg, and Manson. A discussion of a final stretch model of ductile fracture by Wnuk and Sedmack is also included. Additionally, such things as the anomaly of toughness behavior with notch root radius are discussed by Datta and Wood; the relationship between critical stretch zone width crack-tip opening and fracture energy is investigated by Nguyen-Duy; Baker describes a new test method for short rod and short bar fracture toughness specimens; and Heritier examines a fracture mechanics study of stress corrosion cracking in austenitic and austenitic-ferritic stainless steels.

Richard Roberts

Materials Research Center Lehigh University Bethlehem, Pa. 18015; symposium chairman and editor

Index